UNIVERSITY OF BIRMINGHAM

The Synthesis, Characterisation and Ion Exchange of Mixed Metal Phosphates

by

Victoria Anne Burnell

A thesis submitted to
The University of Birmingham
for the degree of
Doctor of Philosophy

The School of Chemistry
College of Engineering and Physical Sciences
University of Birmingham
August 2011

Abstract

This thesis presents work investigating the synthesis and characterisation of a range of mixed metal phosphates. The main aim of the project was to develop materials for the remediation of nuclear waste. In light of this, the materials developed were subject to ion exchange studies and leach testing. The thermal behaviour of the phosphates and nature of the decomposition products were also investigated. This study demonstrates that the true solid solution cannot be formed in any of the mixed metal series investigated, which included zirconium-titanium, germanium-titanium, germanium-zirconium, tin-titanium and tin-zirconium. In all cases a miscibility gap was observed and the reasons for these were established. The co-precipitates that formed were characterised by a variety of analytical techniques which included powder X-ray diffraction (PXRD), thermogravimetric analysis (TGA), pair distribution function (PDF) analysis and X-ray fluorescence (XRF). Structural characterisation was undertaken using both traditional Rietveld analysis of synchrotron X-ray powder diffraction data and PDF analysis of high energy synchrotron total scattering data.

The results of the ion exchange studies yielded four exchanged products: strontium exchanged zirconium phosphate, a strontium exchanged zirconium-titanium phosphate and two sodium exchanged titanium phosphate products. Although it was not possible to solve the structures of these phases, they were further characterised by a number of methods and their use as potential stores were investigated by leach testing. The strontium exchanged zirconium phosphate product demonstrated good strontium retention and is recommended for further investigation as a possible strontium waste form.

Acknowledgments

First and foremost I would like to acknowledge my supervisor, Dr. Joe Hriljac for all of his help and guidance throughout my PhD. I would also like to thank the members of fifth floor who have helped me over the last three years. Special mentions should go to Evin for her help with the SEM and to Colin, Julie and Jackie for the hours spent with the XRF!

I would like to thank the EPSRC and the University of Birmingham for funding. I am also grateful to the following people who have helped with the acquisition of results included in this thesis:

- Paul Jones from Bruker for his help with the XRF results.
- Steve Baker, University of Birmingham for the ICP analyses
- Peter Chupas and Karena Chapman at the APS for their help with the collection of the PDF data and for their guidance on how to use the PDF technique.
- Chiu Tang, Julia Parker and Stephen Thompson at Diamond Light Source for their help in collecting the synchrotron X-ray diffraction data.
- Dr. John Hanna, University of Warwick for the ^{31}P NMR analysis

Finally, but in no way insignificant in their part, I wish to thank my parents and Andy for their constant support and encouragement. Without them this work would not have been possible and though I may not say it enough they are very much loved. I would also like to thank my uncles Pat and Joe and Auntie Gina, who, had they have lived to see this would have been so very proud.

.....for Andy

私の人生の愛

xx

Abbreviations

α-TiP	α-Titanium Phosphate - $Ti(HPO_4)_2.H_2O$
α-ZrP	α-Zirconium Phosphate - $Zr(HPO_4)_2.H_2O$
α-GeP	α-Germanium Phosphate - $Ge(HPO_4)_2.H_2O$
α-SnP	α-Tin Phosphate - $Sn(HPO_4)_2.H_2O$
α-PbP	α-Lead Phosphate - $Pb(HPO_4)_2.H_2O$
α-HfP	α-Hafnium Phosphate - $Hf(HPO_4)_2.H_2O$

PXRD	Powder X-ray Diffraction
XRD	X-ray Diffraction
XRF	X-ray Fluorescence
PDF	Pair Distribution Function
TGA	Thermogravimetric Analysis
DTA	Differential Thermal Analysis
NMR	Nuclear Magnetic Resonance
SEM	Scanning Electron Microscopy
EDX	Electron Dispersive X-ray
GSAS	General Structural Analysis System

Table of Contents

Chapter 1: Introduction

Chapter 2: Experimental

Chapter 3: Synthesis and Characterisation of Mixed Metal Phosphates

Chapter 4: Ion Exchange Studies

Chapter 5: Characterisation and Structure Solution of the Ion Exchanged Products

Chapter 6: Leach Testing of Ion Exchanged Products

Chapter 7: Summary

Appendices (available on CD)

Chapter 1: Introduction

1.1 Background – 'The Big Picture'

Renewed interest in nuclear power, with an emphasis on the safe long-term removal of legacy waste combined with the rising threat of dirty bombs has led to an increased search for exchangers that are effective for the rapid removal of ions such as strontium, caesium and cobalt from aqueous solutions. Increased environmental awareness over the past few decades has resulted in stricter regulations for waste releases and consequently more effective treatment methods are required to meet these conditions. The need for efficiency is especially urgent in the nuclear industry where large amounts of radioactive effluents are generated in almost all stages of the nuclear cycle, and from the reprocessing of the waste for further use of some of the radioactive elements.

Driven by public concern over the safety of nuclear power plants since the accidents at Three Mile Island (1979), Chernobyl (1986) and more recently the concerns over the Fukishima plant in Japan following the tsunami and earthquakes, many governments have abandoned or restricted their plans for future nuclear plants. Both Switzerland and Germany have announced a complete withdrawal from nuclear power by 2034 and 2022 respectively[1,2]. However in these cases decommissioning of existing sites will still need to be addressed and the waste stored. On the other hand, countries such as the UK understand the potential of nuclear power to meet the growing energy concerns and will continue to expand their nuclear operations. Consequently waste solutions will continue to be produced, requiring safe and permanent disposal.

There are currently more than 400 nuclear reactors in operation at nuclear power plants around the world. These generate large amounts of waste that contain radioactive ^{137}Cs and ^{90}Sr as well as activation corrosion products such as ^{60}Co. The effluents are typically leakages from the primary circuit, spent fuel storage pond waters and floor drain waters[3]. These waste solutions are usually combined and concentrated by evaporation to reduce the volume required for long-term storage.

Higher activity radioactive wastes, including both intermediate and high-level waste, are generated by the reprocessing plants. Many countries, e.g. UK, Japan and Russia, reprocess their spent fuel in order to separate out and reuse the uranium and plutonium contained. This process involves dissolving the spent fuel in nitric acid and generates acidic high-salt waste containing ^{137}Cs, ^{90}Sr, ^{241}Am as well as the anionic nuclides ^{99}Tc and ^{106}Ru. Traditionally this waste is then concentrated by evaporation and stored in stainless steel tanks[4]. Although this has been regarded as acceptable in the short term, longer term solutions based on the immobilization of the radionuclides and waste solidification in deep underground repositories are now required.

Immobilisation of this waste by vitrification is a well-established process[5,6] whereby a suitable glass host, typically a borosilicate glass, is used to incorporate the waste salts into a vitreous product that can be cast into suitable forms. However, these processes and the final disposal of high level waste are very expensive and glasses are not suitable for the retention of all ions. A simpler method which involves the selective removal of radionuclides from liquid nuclear waste offers several advantages over the conventional methods of evaporation, precipitation or direct solidification into concrete, by:

(i) Minimising the volumes of solidified waste which have to be disposed of;

(ii) Reduction of radioactive discharge into the environment.

Once the radioisotopes are removed the residual waste can then be solidified as either a medium or low level waste which is subject to less rigorous regulations than high level waste. In nuclear waste processing, simplicity is key as fewer processing steps implies lower costs, less waste handling and therefore less risk. Once buried, assuming the vault remains undisturbed (i.e. no earthquakes, floods etc.) the only mechanism by which radionuclides could reach the biosphere would be dissolution of the waste form in ground water. Therefore one of the major factors in selecting a waste form material is resistance to leaching by groundwater that may eventually penetrate the repository environment.

Another source of high activity nuclear waste comes from the military sector. In both the USA and Russia there is an enormous legacy of radioactive waste that was generated during the period of nuclear weapon production. For over half a century this waste has been stored in large tanks, however some have already leached radioactivity into the ground and therefore remediation of these wastes is urgent. As an example, contamination of the Columbia River with ^{137}Cs and ^{90}Sr near to the US department of energy (USDOE) site at Hanford, WA has already occurred due to leakages from the 177 underground steel tanks containing radioactive waste housed at that site[7,8]. Plans[7,8] are therefore in place to retrieve, separate and immobilize the waste at this site as well as other DOE sites across the US. For long-term safe storage in underground repositories, the viable waste form must be chemically durable and thermally stable over geological time scales.

Another topic of growing concern in today's society is the increasing threat of terrorism involving dirty bombs. Caesium, cobalt and strontium are all considered to be 'suitable materials' for the construction of these bombs[9]. There have been two cases of caesium-containing bombs, both found undetonated in Chechnya in the mid to late 1990s. If, for example, a dirty bomb was dropped on London, mobile and efficient exchangers would be required to decontaminate the rivers and water supplies by sequestering the harmful elements released.

Immobilization and solidification of the hazardous cations ^{137}Cs and ^{90}Sr and ^{60}Co is therefore highly important. The focus of this work is to develop ion exchange materials that can sequester these cations from aqueous environments and keep them safely stored over long time periods. Given the half-life of these radionuclide's, provided in Table 1.1, the leachabily of these materials is also highly important and must be assessed.

Table 1.1: Half-Lives of the radionuclides

Radionuclide	Half Life / years
^{90}Sr	28.5
^{137}Cs	30.2
^{60}Co	5.27

1.2 Inorganic Ion Exchange Materials

The advent of nuclear technology in the 1940s demanded ion exchange materials with high thermal stability and good resistance towards ionising radiation. Organic resins, which were widely developed in the 1930s, lacked both of these properties and so attention was turned

towards inorganic exchangers. Of these, zeolites[10-13] and acid salts of metal oxides, such as phosphates, tungstates and molybdates[14] proved superior in this respect and also offered other advantageous properties needed for the efficient separation of ions - such as high selectivity and capacity. Many of the early preparations were amorphous with variable compositions[15] and so elucidation of the ion exchange mechanism, as well as their physical and chemical properties, was limited. In 1964 Clearfield *et al.*[16] synthesised the first crystalline phase of zirconium phosphate finally making it possible to explain the ion exchange behaviour in structural terms. This renewed the interest in inorganic ion exchangers and since then, the increased knowledge of the crystalline structures of many inorganic compounds has allowed for more in-depth studies into the correlation between the structure and the observed ion exchange properties of a given compound. From such studies it is now possible for one to tailor the properties of materials developed through synthetic design rather than the traditionally used 'trial and error' approach which was time consuming and often inefficient.

The field of inorganic ion exchangers is vast and so the discussion will be confined to a few compounds/classes of compounds with particular importance to the nuclear industry to date. Zeolites were the first materials to be used in large-scale nuclear waste treatments and have been applied for the separation of caesium for over 25 years[10]. Natural zeolites such as clinoptilolite are currently employed by BNFL for the removal of both ^{137}Cs and ^{90}Sr[12]. Zeolites have also found many other industrial applications owing to their ion exchange abilities including use as water softeners in detergents. Zeolites are crystalline hydrated aluminosilicates comprising $[SiO_4]^{4-}$ and $[AlO_4]^{5-}$ tetrahedra connected by oxygen bridges. They form rigid 3D structures with cavities and tunnels that can act as ion sieves. Due to

their relatively low selectivity, zeolites are often not adequate for the removal of radionuclides from high or medium salt concentrations. In addition to this, the dissolution of aluminium and silicon from the framework at high pH means their use is limited to a narrow pH range.

Several new efficient inorganic exchangers that can efficiently remove radionuclides from concentrated salt solutions, including titanantes[17], silicotitanates[18,19] and hexacyanoferrate compounds[18,20] have been developed and brought to the market. To date, crystalline silicotitanate (CST) is the most promising material for the removal of radioactive caesium from high salt waste solutions over a broad pH range[7,18]. It has also been shown effective at the removal of strontium radionuclides as well[8]. Sodium titanate, $Na_4Ti_9O_{20}.nH_2O$ is a layered material shown to be highly selective for strontium in basic conditions in the presence of high concentrations of sodium. The exact crystal structure remains unknown due to the poorly crystalline nature of the product[21], but it consists of three edge sharing TiO_6 octahedra which are corner linked to other similar chains of octahedra forming layers; with sodium atoms occupying positions between the layers. SrTreat® is a commercially available and industrially used sodium titanium oxide based inorganic ion exchanger that has proved to be highly effective in the removal of strontium from basic nuclear waste solutions[22]. However the performance is severely reduced in acidic conditions.

CoTreat and CsTreat® are two other commercially available exchangers currently being used for the removal of radionuclides in the nuclear industry[3]. CsTreat® is potassium cobalthexacyanoferrate used for the removal of caesium from high salt waste concentrations in column operations and from floor drain waters. CoTreat is a titanium oxide based compound successfully employed for the removal of cobalt and other activation

corrosion products from floor drain waters at the optimum pH range of 5-7[23]. This is particularly important as prior to its discovery only activated carbons had shown any success in the separation of cobalt[24]. The reasons for this lay in the complicated uptake mechanism of cobalt which seldom exists as a divalent cation, instead it is usually found in complexes with iron colloids.

1.3 Layered Metal (IV) Phosphates

The ion-exchange properties of the insoluble acid salts of tetravalent metal ions have been known for many years[25-30]; however there has been a renewed interest in them owing to their favourable ion exchange properties and high resistance towards temperature and radiation, making them ideal for use in the nuclear industry. The products exist in varying degrees of crystallinity ranging from amorphous gels through to large single crystals[16,31,32]. Many of the key properties of these compounds are dependent upon the crystalline structure rather than on the metal ion present or the acid used[33]. The degree of crystallinity as well as composition and water content within these materials depends on many preparative factors including the stoichiometry of the reagents used, the concentration of the acid used and rate of addition of reagents, to name just a few. Thus the synthetic method chosen plays a key role in determining the structural parameters and reactivity of the resultant material. Aside from the use of these materials in nuclear fields[26,34], other applications of these crystalline inorganic exchangers have been found in proton conduction, intercalation[35], catalysis[36,37], water desalination[38,39], fuel cells[40,41] and sensors[42] etc; therefore they have been intensively studied and widely reported in the literature[26,33,43-49].

The layered metal (IV) phosphates were initially obtained as amorphous materials[14] having readily hydrolysable acid groups. After 1964 the discovery that crystalline compounds could be obtained by prolonged refluxing of the amorphous products in concentrated acid[16] or directly by slow precipitation in HF[50] gave rise to a renewed interest in this class of compounds. The crystalline phosphates were found to be considerably more stable than the amorphous ones[34] and offered higher ion exchange capabilities due to the increased order within the structures. The first and most studied of the acid salts is zirconium bis(monohydrogenorthophosphate) monohydrate, termed α-ZrP for convenience. Crystalline α-ZrP was first prepared in 1964 by Clearfield and Stynes[16] and by Alberti and Torracca[50]. The crystal structure was solved by Clearfield *et al.*[31,51] using single crystal methods. The layered structure is monoclinic[31,51] with space group $P2_1/c$, although the related $P2_1/n$ space group , which features a smaller monoclinic angle, is sometimes used instead. The arrangement of the layers produce interconnected zeolytic type cavities[51], which should in theory allow the diffusion of spherical particles of a maximum size of ~2.64 Å. A full discussion of the alpha structure type is presented in Section 1.3.2. Over the years many different preparative methods for α-ZrP have been reported[52,53], the two most commonly used methods were described above but other notable methods include the oxalic acid[54] and sol-gel[55,56] methods.

As well as the alpha structure type, there is also a second layer type, first reported by Clearfield *et al.*[57] in 1968 denoted gamma; the hydrated material was named γ-ZrP and the anhydrous form β-ZrP. These forms have larger interlayer distances (see Table 1.2) which enable the uptake of large cations such as Cs^+; however they can become severely hydrolysed because of the closeness of the fixed charges. Whilst many layered phosphates

with the alpha structure type are known[16,25,58], the gamma compounds are relatively scarce[57,59]. Elucidation of the structure proved difficult until the mid-1990s[60] owing to a lack of single crystals large enough for XRD methods. It was originally believed that the alpha and gamma phases featured the same layer type but that a different arrangement of the layers was responsible for the increased interlayer spacing. The situation was later clarified by the ^{31}P MAS NMR studies on the two ZrP forms undertaken by Clayden[61]. Two resonances of equal integrated intensity were observed in the spectra of γ-ZrP rather than the single resonance observed for α-ZrP. The explanation given for this was that the gamma phase must contain two chemically different types of phosphate groups compared with the two similar but crystallographically inequivalent phosphorus groups present in the alpha form. It was therefore concluded that γ-ZrP contains tertiary phosphate groups and dihydrogen phosphate groups in equal amounts, leading to the formula γ -$Zr(PO_4)(H_2PO_4).2H_2O$. The structure was eventually solved by Poojary *et al.*[60] from powder XRD methods, and shown to crystallise in the $P2_1$ space group with a = 5.3825(2) Å, b = 6.6337(1) Å, c = 12.4102(4) Å and β = 98.687(2)° [60]. In addition to the gamma phases, several other crystalline phases of zirconium phosphate have been prepared, and some of these are noted in Table 1.2. However, the work in thesis is only concerned with those materials having the alpha structure type.

Table 1.2: Crystalline zirconium phosphate phases.

Formula	Designation	Interlayer Spacing / Å	Ref.
$Zr(HPO_4)_2.H_2O$	α-ZrP	7.56	[16]
$Zr(HPO_4)_2$	β-ZrP	9.4	[57]
$Zr(HPO_4)_2.2H_2O$	γ-ZrP	12.2	[57]
$Zr(HPO_4)_2.½H_2O$	δ-ZrP	7.13	[62]
$Zr(HPO_4)_2$	ε-ZrP	5.59	[62]
$Zr(HPO_4)$	ζ-ZrP	7.41	[62]
$Zr(HPO_4)_2$	η-ZrP	7.37	[62]
$Zr(HPO_4)_2.8H_2O$	θ-ZrP	10.4	[63]

Since the preparation of crystalline forms of zirconium phosphate, many crystalline compounds of group 4 and 14 metals, having the general formula $M(HPO_4)_2.H_2O$ and the alpha structure have been synthesized and characterized. In general they are prepared by similar methods and are isomorphous to α-ZrP[64], but with varying ion exchange ability/capacity as shown in Table 1.3. Based on a neutron powder diffraction study[65] it has also been suggested that the orientation of the water molecules within the structure may subtly vary between the materials. For obvious reasons these differences cannot be investigated or observed through X-ray diffraction methods.

Table 1.3: Insoluble acid salts of group 4 and 14 metals with α-layered structures.

Compound	Formula	Interlayer Distance / Å	Ion Exchange Capacity mequiv. of H^+/g	Ref.
Titanium Phosphate	$Ti(HPO_4)_2.H_2O$	7.56	7.76	51
Zirconium Phosphate	$Zr(HPO_4)_2.H_2O$	7.56	6.64	51
Hafnium Phosphate	$Hf(HPO_4)_2.H_2O$	7.56	4.17	66,67
Germanium(IV) phosphate	$Ge(HPO_4)_2.H_2O$	7.60	7.08	64,68
Tin (IV) phosphate	$Sn(HPO_4)_2.H_2O$	7.76	6.08	58
Lead (IV) phosphate	$Pb(HPO_4)_2.H_2O$	7.80	4.79	64

The change in the metal ion results in small changes in the interlayer distance and in the area available for guest species, which in turn affects their ion exchange behaviour. The thermal and chemical stability of the compounds are also affected; with the phosphates containing the more electronegative central ions being more hydrolysable[69].

Titanium phosphate is the second most studied of this class of compounds and can also be prepared in both amorphous[70] and crystalline[29] forms by addition of $TiCl_4$ solutions to phosphoric acid and, if desired, refluxing in strong phosphoric acid to improve crystallinity. The crystalline product can also be obtained directly by slow decomposition of titanium-fluoro complexes in the presence of phosphoric acid[50], by sol-gel methods[55,71] or by the precipitation from titanium (III) solutions[72]. In this method titanium powder is dissolved in phosphoric acid to give the titanium (III) solutions which are then heated to allow oxidation

to titanium (IV). Both the alpha[73] and gamma[59] structure types exist and have been characterised by the Rietveld analysis of powder XRD data[74]. The phase formed is determined by the preparative conditions employed; high pressure, low temperatures, low activity of titanium(IV) and high concentrations of phosphoric acid favour the formation of the gamma phase[59,75]. α-TiP is isomorphic with α-ZrP[34] but with narrower passageways, making the ion exchange of larger cations harder, indeed it has been shown that K^+ is exchanged with difficulty in α-TiP but with ease in α-ZrP[73].

Tin phosphate is a known ion exchanger used for separation applications in both the processing of radioactive effluents and in water purification[25]. The first preparations of tin phosphate by Merz[76] were gelatinous and of indefinite composition, although they displayed ion exchange behaviour similar to the amorphous ZrP gels. As with the other metal (IV) phosphates, successive heating of the amorphous gel in phosphoric acid was later found to give the crystalline product α-SnP[64,77]. The structure was refined by Rietveld analysis of powder XRD data[43] and found to be isomorphous with both α-ZrP and α-TiP. In contrast to α-ZrP and α-TiP, α-SnP cannot be synthesised by the HF method due to the low stability of the fluoro complexes formed. Tin phosphates are also strongly hydrolysed in neutral or alkaline pH by all alkali metal cations excluding lithium[58].

α-GeP is the least chemically stable of the known group 4 and 14 metal phosphates[78] which possibly explains the reduced number of studies concerning this material. The original structural studies reported unit cell parameters of a = 8.230(2) Å, b = 4.784(1) Å, c = 16.502(5) Å, β = 110.2(4)°. However this gave unusual germanium-oxygen and phosphorus-oxygen distances, so the structure was later redetermined by Peters and Evans[68] with a

smaller monoclinic angle to give the unit cell parameters; a = 8.2920(2) Å, b = 4.7880(1) Å, c = 16.4058(3) Å, β = 108.985(1)°.

1.3.1 Mixed Metal (IV) Phosphates

In several fields of study, investigation into mixed metal compounds is of increasing interest, as the specific properties of single materials can be improved by adding other, suitably chosen elements. More specifically it generates the potential for fine tuning of the ion exchange selectivity through chemical control. The mixed metal species generated are novel multifunctional substances that offer many interesting properties.

Mixed metal (IV) phosphates have recently been prepared in order to modify and/or improve certain properties of the single metal counterparts e.g. in order to stabilise the materials with respect to hydrolysis, acidic strength or cation exchange capacity. By changing the average radii of the metal species through doping of one element for another one can create subtle changes in the structure that further alters the bonding environment between the layers where entering radionuclides reside, thus modifying the ion exchange capabilities. A review of the literature shows that mixed materials of the class of tetravalent metal acid salts containing two different anions and a cation have been widely studied[79,80]. The compounds produced have exhibited improved ion exchange properties and selectivity for particular metal ions compared to their single salt counterparts. Studies on mixed materials containing two cations and an anion are more scarce.

Mixed zirconium-titanium phosphates have been prepared in both the amorphous [81-84] and crystalline[29,82,85-88] forms by a variety of different methods. The co-precipitates produced have been characterised and in some cases the ion exchange capabilities' examined[29,82,87-89].

Amorphous mixed zirconium-titanium phosphate has been shown to have a higher ion exchange capacity of 3.36 meq g^{-1} [81] compared with the single salts α-ZrP and α-TiP having capacities of 2.77 and 3.09 meq g^{-1} respectively[81]. Rationalisation for this is given by the structural changes caused by the metal substitution. Yazawa *et al*.[88] have previously observed that the lattice structure of mixed zirconium-titanium phosphates are less ordered than those of α-TiP and α-ZrP due to the considerable difference in size of the crystal ionic radii of Zr^{4+} and Ti^{4+} (0.79 Å and 0.68 Å, respectively). This difference leads to a tilting of the P-O bonds on the phosphate groups to which an exchangeable hydrogen is bonded. The slight layer expansion caused by this affects the ion exchange capacity of the compound. A review of the work on crystalline zirconium-titanium phosphates and the different synthetic methods used is given in Chapter 3 of this thesis. In general the co-precipitates formed have been found isomorphous to the single metal counterparts they are compositionally closest to and display similar ion exchange[29,89] and thermal behaviour[85,90]. Investigations into intercalated mixed zirconium-titanium phosphates have also been reported[91,92] including studies into the use of these intercalated mixed metal phosphates to form pillared porous materials for catalysis[92].

Mixed germanium-zirconium phosphates were previously investigated by Galli *et al*.[93]. It was hoped that the doping of zirconium into α-GeP could (a) stabilise it towards hydrolysis[29] and (b) improve the acidic strength of α-GeP for catalysis[85]. A review of this series and the results of this study are given in Chapter 3.

To date there have been two previous literature reports[94,95] on crystalline mixed titanium-tin phosphates. The first[95] describes the synthesis and characterisation of these materials and is reviewed in Chapter 3. The second report[94] details an investigation into the vanadium

loading of these phosphates to test the catalytic use in the oxidative dehydrogenation of ethane. The authors hoped that the inclusion of the redox cation, tin, into the vanadium oxide loaded TiP catalyst would improve its catalytic performance[94]. A review of the zirconium-tin phosphates previously reported[96] is also included in Chapter 3.

Other mixed metal layered phosphates previously reported but not investigated in this thesis include mixed titanium-vanadium phosphates[97].

1.3.2 The Alpha Structure

The single crystal structure of α-ZrP first reported by Clearfield and Smith[51] is monoclinic with space group $P2_1/c$ and having the lattice parameters shown in Table 1.4. In 1977 Troup and Clearfield[31] published another single crystal X-ray study of α-ZrP using high quality crystals which had been recrystallised from HF and boric acid. Rather than the traditionally used $P2_1/c$ space group they opted for the related $P2_1/n$ space group owing to the smaller beta angle. The refined structure was essentially the same as per the previous model[51] for the non hydrogen positions, however the estimated standard deviations (esds) were now one tenth of their original values. A neutron refinement of the structure was carried out by Albertsson *et al.*[98] in order to determine the hydrogen positions. From this study they proposed that there were no hydrogen bonds between the layers but that the layers were held together by Van der Waals forces alone. More recently Capitani *et al*.[54] have refined α-ZrP products obtained from two slightly different synthetic methods. One involved the direct precipitation from HF solutions as used previously[50], whilst in the second method the HF solution was replaced by oxalic acid. The refinement results showed good agreement between the two products and also to the single crystal refinement work published

previously[31,51]. A summary of the lattice parameters obtained from all of these α-ZrP refinements are included in Table 1.4.

Table 1.4: Parameters of α-ZrP obtained from structural refinements reported in the literature.

Formula	Space Group	*a*/Å	*b*/Å	*c*/Å	β(°)	Ref.
α-$Zr(HPO_4)_2.H_2O$	$P2_1/c$	9.076(3)	5.298(6)	16.22(2)	111.15(1)	[51]
α-$Zr(HPO_4)_2.H_2O$*	$P2_1/c$	9.061(1)	5.2873(7)	16.248(3)	111.41(1)	[98]
α-$Zr(HPO_4)_2.H_2O$	$P2_1/n$	9.060(2)	5.297(1)	15.414(3)	101.71(2)	[31]
α-$Zr(HPO_4)_2.H_2O$ *HF method*	$P2_1/n$	9.0599(1)	5.28813(5)	15.4525(2)	101.697(1)	[54]
α-$Zr(HPO_4)_2.H_2O$ *oxalic acid*	$P2_1/n$	9.0631(2)	5.2886(1)	15.4444(3)	101.717(2)	[54]

* Neutron refinement

The structure of α-TiP was first solved in 1990 from powder X-ray diffraction methods by Christensen *et al.*[74], confirming it to be isostructural to α-ZrP. A later study published in 1995 by Bruque *et al*.[43] reported the structure of α-TiP from single crystal data using the $P2_1/n$ space group. A neutron diffraction study was published in the following year[65] giving the complete crystal structure of α-TiP, including the hydrogen-atom positions. The results from these studies are summarized in Table 1.5.

The structure of α-GeP was originally determined by Romano *et al*.[99] to confirm the phase purity of the sample obtained. However, owing to some unusual germanium-oxygen and phosphorus-oxygen distances as well as some surprising intra-tetrahedral angles reported, the structure was later redetermined by Peters and Evans[68] using a smaller beta angle of 108.985° rather than the previously reported 110.2°. The new structure gave more plausible bond distances and angles. The cell parameters reported from both studies are included in Table 1.5.

Table 1.5: Parameters of metal (IV) phosphates with the alpha structure obtained from structural refinements reported in the literature.

Formula	Space Group	*a*/Å	*b*/Å	*c*/Å	β(°)	Ref.
α-$Ti(HPO_4)_2.H_2O$	$P2_1/c$	8.630(2)	5.006(1)	16.189(3)	110.20(1)	[74]
α-$Ti(HPO_4)_2.H_2O$	$P2_1/n$	8.6403(2)	5.0093(1)	15.5097(4)	101.324(2)	[43]
α-$Ti(HPO_4)_2.H_2O$*	$P2_1/n$	8.6110(3)	4.9933(2)	16.1507(7)	110.206(3)	[65]
α-$Ge(HPO_4)_2.H_2O$	$P2_1/c$	8.230(3)	4.784(1)	16.502(5)	110.2(4)	[99]
α-$Ge(HPO_4)_2.H_2O$	$P2_1/c$	8.2920(2)	4.7880(1)	16.4058(3)	108.985(1)	[68]
α-$Sn(HPO_4)_2.H_2O$	$C2/c$	8.6115(3)	4.9643(5)	15.861(2)	100.003(1)	[43]

* Neutron refinement

The crystal structure of α-SnP was elucidated by Bruque *et al.*[43] in the mid 1990s. The cell parameters obtained are also included in Table 1.5. Although α-SnP is isomorphic with the other metal (IV) phosphates, the $C2/c$ space group was chosen for the refinement of α-SnP as the intensity of the primitive peaks were extremely weak, with most not being observed at all[43]. The $C2/c$ group is an isomorphic *C*-centred supergroup of $P2_1/n$. This change resulted in slight modifications to the atomic parameters in the α-ZrP structural model being required.

Both α-ZrP and α-TiP have the alpha layered structure with interlayer spacing of 7.56 Å, which can increase as the water content increases or with larger counter ions. α-SnP and α-GeP have the same alpha layered structure but with slightly larger interlayer spacings of 7.76 Å and 7.60 Å respectively.

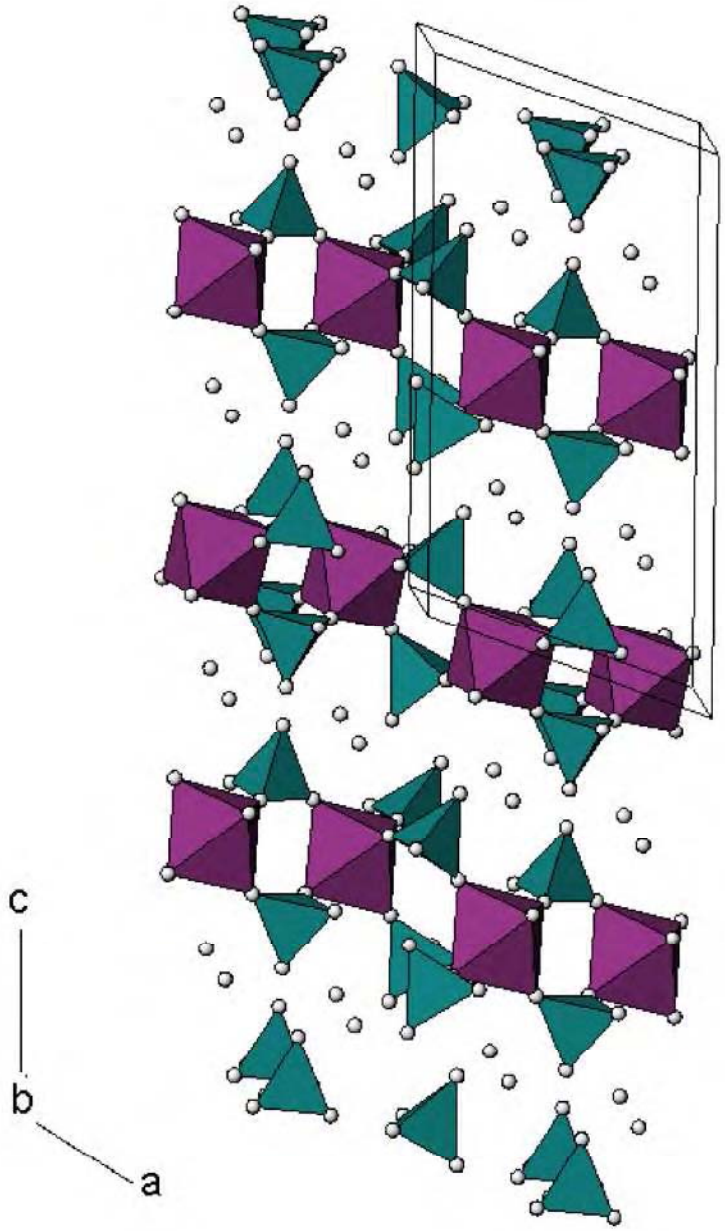

Figure 1.1: Polyhedral representation of the alpha structure ($M(HPO_4)_2.H_2O$) with phosphate tetrahedra in green, metal octahedra in purple and oxygen atoms as small spheres. The water molecules sit between the layers.

The alpha structure is a layered structure built up of slightly distorted MO_6 octahedra and alternating HPO_4 tetrahedra as shown in Figure 1.1. The layers consist of roughly coplanar metal atoms which are situated slightly above and below the *ab* planes at *z*=0 and ½. The

metal atoms are bridged by phosphate groups which alternate above and below this metal plane as shown in Figure 1.2.

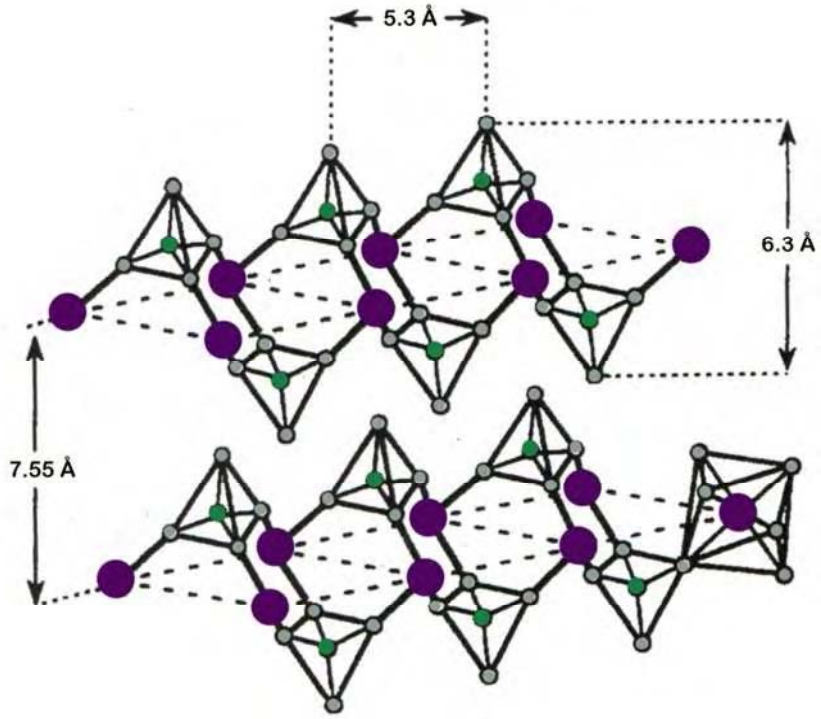

Figure 1.2: Schematic representation of two adjacent layers in α-ZrP – the protons and interlayer water have been omitted. The zirconium atoms are shown in purple, the phosphorus in green and the oxygen in grey.

Three of the oxygens from each tetrahedral phosphate group are bonded to three different zirconium atoms in the plane, thus the zirconium is octahedrally coordinated to six oxygens from six different phosphate groups. As the metal is in octahedral coordination and the phosphorus tetrahedral, there are T-O-T type layers as in smectic clays, but with inverted phosphate groups with respect to the silicate groups in the clay structure. The fourth oxygen on the phosphate group carries the negative charge and is bonded to a proton. This creates a longer P-O bond which is orientated perpendicular to the layers and which points into the interlayer space towards the adjacent layer. These P-OH groups act as hydrogen bond donors to the water molecules which sit in the cavities of the layered structure forming a

hydrogen bonding network with the phosphate groups[31,98] . The hydrogen is also the exchangeable site within the structure, allowing these protons to be exchanged with a number of different cations e.g. Li^+, Na^+ without significantly altering the layered structure[26]. The HPO_4^- groups in the interlayer region also serve as Brønsted acid sites[26] which allow the intercalation of organic molecules such as acetone[100], isopropanol[100] and *N*-methylformamide[100].

The packing of the layers is staggered so that each P-OH bond lies directly above and below the zirconium atoms in the adjacent layer, creating hexagonally shaped zeolitic-type[51] cavities between the layers (one for each zirconium atom).These cavities are depicted in Figure 1.3. A water molecule resides in the centre of each cavity and accepts two hydrogen bonds from nearby P-OH donor groups in the same layer forming short hydrogen bonds[31]. In turn the water molecule acts as a donor forming a hydrogen bond with the oxygen of a neighbouring POH group also within the same layer[31]. The other water hydrogen is not involved in hydrogen bond formation and instead points towards either the top or bottom of the cavity. Figure 1.4 provides an illustration of the hydrogen bonding within the cavities. There are no interlayer hydrogen bonds and only Van der Waals forces hold the layers together[98]. This allows the interlaying spacing to expand or contract as a result of ion exchange of intercalation processes. The interlayer forces become ionic when the hydrogen ions are replaced by other cations due to the fixed negative charges on adjacent layers; as hydrogen is no longer present to neutralize the charge.

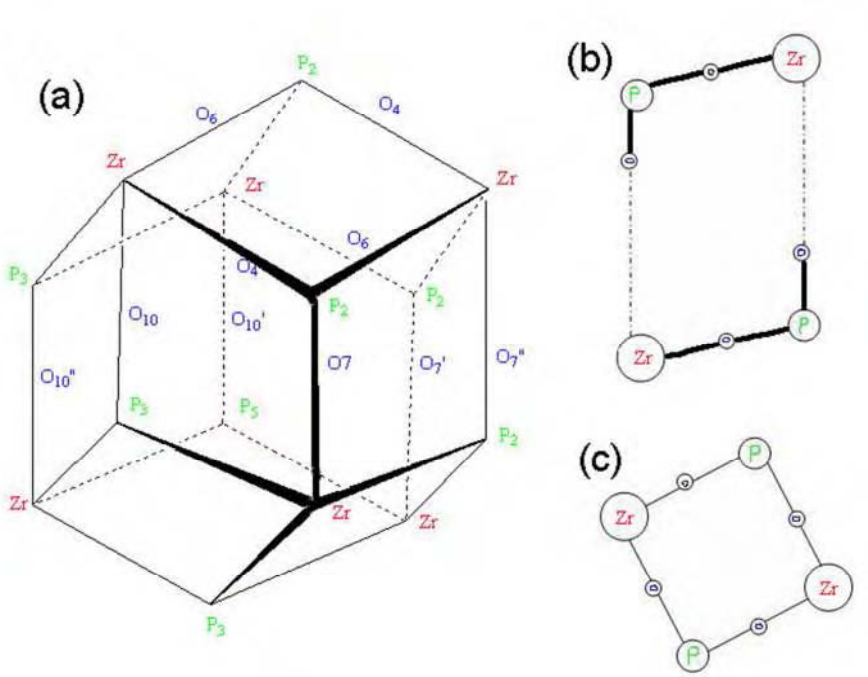

Figure 1.3: Schematic representation of (a) Cavity formed between the layers (b) Side of the cavity (c) Face of the cavity.

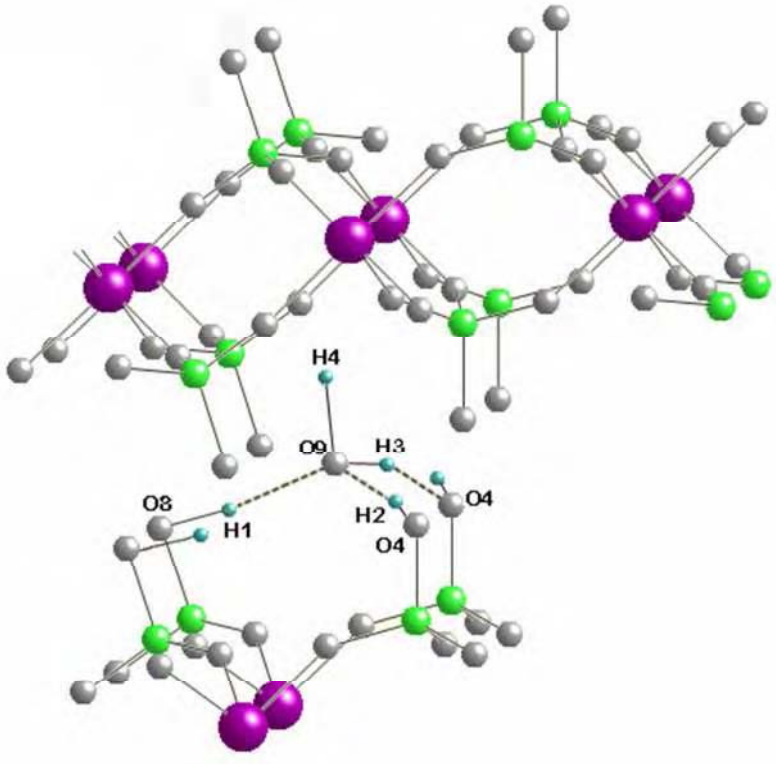

Figure 1.4: Illustration of the hydrogen-bonding within the cavities of α-TiP. The titanium atoms are shown in purple, the phosphorus in green, the oxygen in grey and the hydrogen in blue.

The cavities are also where incoming cations reside in the ion exchange process. However these cavities are interconnected by openings[63] which restrict counter ions with a larger diameter from diffusing in unless sufficient energy is supplied to spread the layers. Recalculation[31] of the size of the entrance ways (in α-ZrP) has shown that the largest opening is 2.61 Å rather than the originally reported 2.64 Å[30,101]. The more perfect the layers, the greater the attraction between them, thus metal (IV) phosphates with a high degree of crystallinity require appreciably more energy (usually in the form of a base) to initiate and sustain exchange compared with the amorphous and less crystalline forms[31]. Indeed, Troup *et al.*[31] found that as the crystallinity of the exchanger decreases, increasing amounts of the cation may be exchanged without the addition of a base. This is in keeping with the idea that in the less crystalline exchangers the phosphate groups are shifted or tilted away from their normal positions[102], resulting in the formation of cavities with a range of sizes rather than the uniform set of dimensions as in the fully crystalline exchanger. Exchange may then occur up to the point where the largest cavities are filled. In theory this would lead to a range of hydrogen bond energies and a weakening of the Van der Waals forces[31].

1.3.3 Ion Exchange of Layered Metal (IV) Phosphates

Ion exchange occurs in these layered phosphates by replacement of the orthophosphate protons by a variety of cations or by reactions with different organic reagents[33,103]. The presence of both Brønsted and Lewis acid sites on their surface give them $10^2 – 10^3$ times greater ion exchange capacity than commercial organic ion exchangers such as Dowex 50-X8[40]. They also offer many other advantages over organic exchange resins in that they

exhibit both high chemical and thermal stability as well as higher resistance towards radiation[33,34] and oxidation.

The ion exchange properties of both α-ZrP[16,26,30,33,40,46,104,105] and α-TiP[25,40,106,107] have been studied in great detail and it has been demonstrated that many factors affect the ion exchange properties[40,108] with pH[72] and the degree of crystallinity[32,49] of the exchanger being the most important (refer back to Section 1.3.2 for a discussion on the effect of crystallinity on the exchange process). Invariably exchange of α-TiP and α-ZrP with small cations results in a lowering of the crystallinity but without significant alteration of the layers – only an increase in the interlayer spacing which is proportional to the counter-ion diameters and the degree of hydration[33].

α-ZrP has shown ion exchange with ammonium[52], lithium[26,108], sodium[26,32], strontium[109-111] calcium[108] and potassium[26] ions amongst others. A summary of known exchanged phases is given in Table 1.6.

Table 1.6: Some known exchanged phases of α-ZrP.

Phase	Interlayer spacing /Å	Reference
$Zr(NH_4)_2(PO_4)_2.H_2O$	9.4	52
$ZrLi_2(PO_4)_2.4H_2O$	10.0	73,108
$ZrLi_2(PO_4)_2.2H_2O$	8.80	73
$ZrLi_2(PO_4)_2.H_2O$	7.90	73
$ZrHNa(PO_4)_2.5H_2O$	11.8	73
$ZrNa_2(PO_4)_2.3H_2O$	9.9	73
$ZrNa_2(PO_4)_2.H_2O$	8.4	73
$ZrK_2(PO_4)_2.3H_2O$	10.7	73
$ZrK_2(PO_4)_2.H_2O$	9.0	73
$ZrKH(PO_4)_2$	7.95	112
$ZrLiK(PO_4)_2$	7.6	113
$ZrCa_{0.55}(PO_4)_{1.1}(HPO_4)_{0.9}.3H_2O$	9.93	108
$ZrHSr_{0.5}(PO_4)_2.3.6H_2O$	10.2	110

Exchange with sodium results in two phases; at low loadings a half exchanged product, $ZrNaH(PO_4)_2.5H_2O$ and at higher loadings the fully exchanged $ZrNa_2(PO_4)_2.3H_2O$. The water contents are subject to the relative humidity and temperature with dehydration leading to the formation of several new phases[30]. The half exchanged phase is very unstable and loses water immediately upon separation[51]. In many cases both exchanged phases as well as unexchanged α-ZrP are found to coexist. The structures of both phases have been solved[114,115] and are depicted in Figures 1.5 and 1.6, a summary of structural parameters is included in Table 1.7.

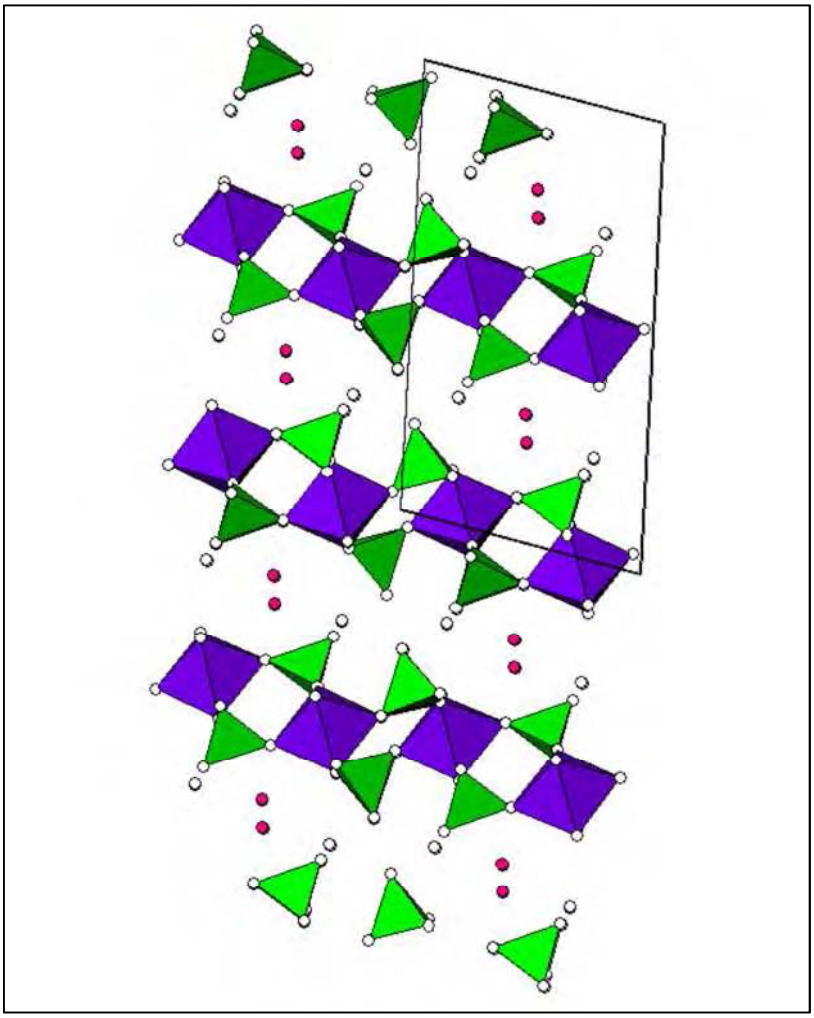

Figure 1.5: Polyhedral representation of $ZrNaH(PO_4)_2.H_2O$[114]. Phosphate tetrahedra in green, zirconium octahedra in purple, oxygen atoms as white sphere and sodium atoms as pink spheres.

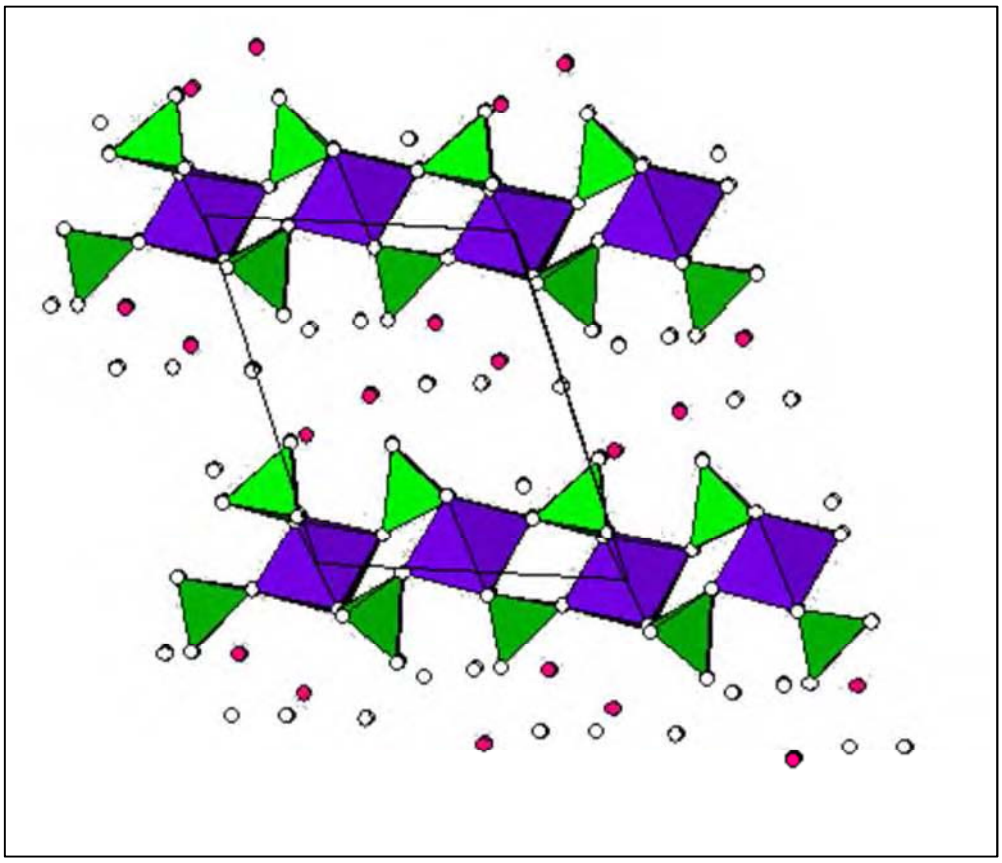

Figure 1.6: Polyhedral representation of $ZrNa_2(PO_4)_2.3H_2O$[115]. Phosphate tetrahedra in green, zirconium octahedra in purple, oxygen atoms as white sphere and sodium atoms as pink spheres.

Table 1.7: Structural parameters of the exchanged ZrP products.

Product	$ZrNaH(PO_4)_2.H_2O$	$ZrNa_2(PO_4)_2.3H_2O$	$Zr(NH_4)_2(PO_4)_2.H_2O$
Space group	$P2_1/c$	$P1$	$P2_1/c$
a /Å	8.8264(2)	8.9192(3)	9.131(5)
b /Å	5.3494(1)	10.5824(4)	5.417(5)
c /Å	16.0275(6)	5.4045(3)	19.19(1)
α /°	90	94.238(3)	90
β /°	101.857(4)	90.164(4)	102.7(1)
γ /°	90	111.013(3)	90
Reference	[114]	[115]	[116]

The structures of these exchanged phases are modified versions of the parent compound α-ZrP. Sodium exchange leads to a twisting of the phosphate groups away from the perpendicular to the layers resulting in the formation of alternating broad and constricted cavities[114,115]. In the half exchanged phase the sodium ions reside in the wider cavities in distorted octahedral environments[114]. Complete sodium exchange affects the arrangement of the layers sufficiently to lower the symmetry from monoclinic to triclinic. In this structure two sodium ions reside in each narrow and wide cavity[115]. The coordination polyhedra of the sodium ions are highly distorted because the oxygen atoms are constrained by their bonding to the layer atoms[115].

The structure of ammonium exchanged ZrP, $Zr(NH_4)_2(PO_4)_2.H_2O$ has also been solved[52,116] and is given in Figure 1.7 and Table 1.7. The reaction is essentially one of intercalation[117] whereby ammonia diffuses into the lattice and forms ammonium ions at the proton sites, thereby producing the diammonium phase in a single stage[118]. Consequently no shifting of the layers occurs and the ammonium ions occupy positions within the cavities described for the parent compound[51]. It has been shown to absorb ill smelling gases such as formaldehyde[52].

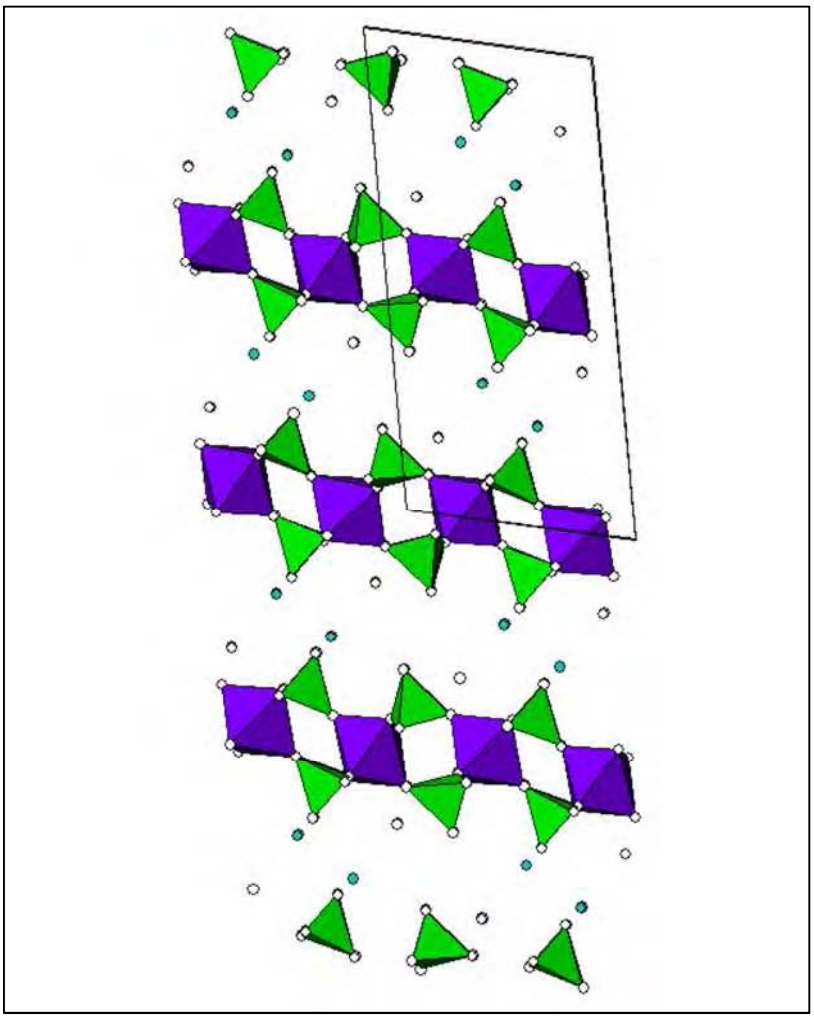

Figure 1.7: Polyhedral representation of $Zr(NH_4)_2(PO_4)_2.H_2O$[116]. Phosphate tetrahedra are in green, zirconium octahedra in purple, oxygen atoms as white sphere and sodium atoms as pink spheres.

For crystalline α-ZrP, caesium and rubidium uptake is negligible in acidic media[16,49] unlike the corresponding amorphous phase[16]. Exchange of magnesium is difficult even at high pH values.[119] This ion exchange behaviour can be explained by examination of the structure. The maximum size of the passageways leading into the cavities is 2.62 Å[30]. This is sufficient to allow unhydrated lithium, sodium and potassium to exchange, followed by rehydration of the ions. The interlayer distance must enlarge initially for the exchange of larger ions such as

rubidium and caesium. One way to achieve this is by the use of basic solutions whereby the hydroxide ions are believed[98] to create sorption sites via the reaction $–O_3POH + OH^- = -O_3PO^- + H_2O$. This reaction should produce enough energy to spread the layers apart and therefore allow diffusion of larger ions[98].

Although isomorphous to α-ZrP, differences are seen in the ion exchange behaviour of α-TiP due to its smaller unit cell dimensions. The tunnels connecting the cavities are narrower in α-TiP which leads to greater steric hindrance and so the ion exchange of large cations has greater activation energy. Consequently α-TiP exhibits high ion exchange capacity for lithium and sodium while potassium, rubidium and caesium uptakes are negligible in acid solutions[25,120]. Again this is unlike the amorphous form where these ions are readily exchanged[25]. At near neutral pHs potassium uptake is possible but is accompanied by destructive hydrolysis of the exchanger[72,121].Table 1.8 lists some of the known exchanged phases of α-TiP. As seen with α-ZrP, sodium exchange leads to the formation of both half and fully exchanged phases which are found to coexist at low sodium loadings[29,106]. Whilst the structures of these have not yet been solved, $^{47/49}$Ti solid state NMR data has shown that the titanium local environment is not significantly affected by the exchange in these materials[122].

Table 1.8: Known exchanged phases of α-TiP.

Phase	Interlayer distance /Å	Reference
$TiK_2(PO_4)_2.3H_2O$	10.4	107
$TiK_2(PO_4)_2.2H_2O$	9.6	107
$TiHNa(PO_4)_2.H_2O$	8.4	106
$TiHNa(PO_4)_2.4H_2O$	10.4	106
$TiNa_2(PO_4)_2.3H_2O$	9.7	72,106
$TiNa_2(PO_4)_2.H_2O$	8.3	72
$TiLi_2(PO_4)_2.H_2O$	7.5	72

In addition to the use of basic solutions to aid exchange of large cations, other options include increasing the interlayer spacing either by the intercalation of amines to form $M(HPO_4)_2(amine)_n.xH_2O$ species[123] or by the ion exchange of smaller ions e.g. sodium[119]. In the latter case, the low affinity for sodium of these phosphates means that when treated with other exchangeable cations only sodium and not H^+ undergo ion exchange[124]. Essentially the sodium ion behaves as a catalyst since the exchanges are strongly influenced by the presence of small amounts of sodium but the sodium does not feature in the global ion exchange reaction. Using this method both α-ZrP and α-TiP have been shown to exchange cations that were not possible in the pure forms e.g. magnesium and caesium[119,124]. Another advantage of this method is that it avoids the precipitation of insoluble metal hydroxides often observed when exchanges are conducted at high pH values[119].

1.4 Aims

The wider aim of this study has been to develop inorganic ion exchangers for the efficient removal of radionuclides including the important fission products ^{90}Sr and ^{137}Cs as well as the activation corrosion product ^{60}Co from aqueous nuclear effluents. Due to the obvious safety implications non radioactive forms of these cations were used in this research.

In principle, the main focus of the research described in this thesis was to investigate the synthesis, structure and ion exchange properties of mixed metal (IV) phosphates with the formula $(M1)_x(M2)_{1-x}(HPO_4)_2.H_2O$ where M1 and M2 include zirconium, titanium, germanium and/or tin, and x = 1, 0.9, 0.8, 0.7, 0.6, 0.5, 0.4, 0.3, 0.2, 0.1 and 0. The reasons for choosing these mixed metal layered phosphates lay in some inconclusive reports in the literature on

mixed zirconium-titanium phosphates[29,55,87,90] and on the premise that the properties of these materials – notably the ion exchange properties, could be fine tuned in such a manner. The products obtained were analysed by powder X-ray diffraction (XRD) and pair distribution function (PDF) methods, to allow insight into the structural changes occurring upon metal substitution and to allow a comparison of the two refinement methods.

Ion exchange with strontium, caesium, cobalt and sodium was also attempted on a selection of the products. The resultant materials were characterised by XRD, and in some cases attempts were made to index the XRD patterns obtained in order to identify the unit cells of the exchanged phases. Successfully exchanged products were also subject to further characterisation using a variety of methods including, PDF analysis, ^{31}P NMR spectroscopy, X-ray fluorescence and thermal treatment. Leach testing of these phases was also undertaken to establish their potential as long term waste stores.

1.5 References

(1) http://www.bfe.admin.ch/energie/00588/00589/00644/index.html?lang=en&msg-id=39337.
(2) http://www.bundesregierung.de/Content/EN/Artikel/__2011/06/2011-06-06-energiewende-text-breg__en.html.
(3) Harjula, R., Lehto, J., Paajanen, A., Tusa, E., Yarnell, P., *React. Funct. Poly.*, **60**, 85-95 (2004)
(4) Donald, I. W., Metcalfe, B. L., Taylor, R. N. J., *J. Mat. Sci.*, **32**, 5851-5887 (1997)
(5) Marples, J. A. C., *J. Mat. Sci.*, **29**, 230 (1988)
(6) Lutze, W., Ewing, R. C., *J. Mat. Sci.*, **32**, 699-740 (1997)
(7) Su, Y., Balmer, M. L., Wang, L., Bunker, B. C., Nyman, M., Nenoff, T., Navrotsky, A., *Mat. Res. Soc. Symp. Proc.*, **556**, 77-84 (1999)
(8) Nyman, M., Nenoff, T. M., Su, Y., Balmer, M. L., Navrotsky, A., Xu, H., *Mat. Res. Soc. Symp. Proc.*, **556**, 71-76 (1999)
(9) Koukouliou, V., In *NATO Science for Peace and Security Series C: Environmental Security*; Springer, Netherlands: Vienna, Austria; 3-14 (2010)
(10) Hutson, G. V. In *The Nuclear Fuel Cycle*; Wilson, P. D., Ed.; Oxford University Press: Oxford, (1996)
(11) Dyer, A., Aboujamous, J. K., *J. Radioanal. Nucl. Chem.*, **183**, 225-233 (1994)
(12) Howden, M., Pilot, J., In *Ion Exchange Technology*; Streat, D. N. a. M., Ed.; Ellis Horwood: Chichester, UK; 66 (1984)
(13) Dyer, A. K. D., *Zeolies*, **4**, 215-217 (1984)
(14) Amphlett, C. B., *Inorganic Ion Exchangers*; Elsevier: Amsterdam; Vol. 1964 (1964)

(15) Ahrland, S., Albertsson, J., Johansson, L., Nihlgard, B., Nilsson, L., *Acta. Chem. Scand.*, **18**, 707 (1964)
(16) Clearfield, A., Stynes, J. A., *J. Inorg. Nucl. Chem.*, **26**, 117-129 (1964)
(17) Lehto, J., Brodkin, L., Harjula, R., Tusa, E., *Nucl. Technol.*, **127**, 81 (1999)
(18) Clearfield, A., Bortun, L. N., Bortun, A. I., *React. Funct. Polym.*, **43**, 85 (2000)
(19) Poojary, D. M., Cahill, R. A., Clearfield, A., *Chem. Mater.*, **6**, 2364 (1994)
(20) Tusa, E., Paavola, A., Harjula, R., Lehto, J., *Nucl. Technol.*, **107**, 279 (1994)
(21) Lehto, J., Clearfield, A., *J. Radioanal. Nucl. Chem. Lett.,* **118**, 1 (1987)
(22) Lehto, J., Brodkin, L., Harjula, R., In *Radioactive Waste Man. Env. Remediation*: ASME; 245-248 (1997)
(23) Harjula, A., Lehto, J., Saarinen, L., Paajanen, A., Tusa, E., In *Proc. of the Waste Management 96 Symposium*: Tucson, Arizona, USA; 17-38 (1996)
(24) Paajanen, A., Lehto, J., Santapakka, T., Morneau, J. P., *Sep. Sci. Technol.,* **32**, 813 (1997)
(25) Alberti, G., Cardini-Galli, P., Costantino, U., Torracca, E., *J. Inorg. Nucl. Chem.*, **29**, 571-578 (1967)
(26) Clearfield, A., In *Ion Exchange Materials*; CRC Press: Boca Raton, FL (1982)
(27) Llavona, R., Suarez, M., Garcia, J. R., Rodriguez, J., *Inorg. Chem.*, **28**, 2863-2868 (1989)
(28) Nilchi, A., Ghanadi Maragheh, M., Khanchi, A., Farajzadeh, M. A., Aghaei, A. A., *J. Radio. Nucl. Chem.*, **261**, 393-400 (2004)
(29) Clearfield, A., Frianeza, T. N., *J. Inorg. Nucl. Chem.*, **40**, 1925-1932 (1978)
(30) Clearfield, A., Duax, W. L., Medina, A. S., Smith, G. D., Thomas, J. R., *J. Phys. Chem.*, **73**, 3424-3430 (1969)
(31) Troup, J. M., Clearfield, A., *Inorg. Chem.*, *16*, 3311-3313 (1977)
(32) Clearfield, A., Oskarsson, A., Oskarsson, C., *Ion Ex. Mem.*, **1** (1972)
(33) Alberti, G., *Am. Chem. Soc.*, **11**, 163-170 (1978)
(34) Clearfield, A., Nancollas, G. H., Blessing, R. H., In *Ion Exchange and Solvent Extraction*; Marcus, Y., SenGupta, A. K., Marinsky, J. A., Ed.; Dekker: New York; Vol. 5 (1973)
(35) Rodriguez-Castellon, E., Rodriguez, A., Bruque, S., *Inorg. Chem.*, **24**, 1187 (1984)
(36) Maireles-Torres, P., Jimenez-Lopez, A., Oliveira-Pastor, P., Rodriguez-Ramos, I., Guerrero-Ruiz, A., Garcia-Fierro, J. L., *J. Catal.*, **92**, 81 (1992)
(37) Clearfield, A., Thakkur, D. S., *Appl. Catal.*, **26**, 1 (1986)
(38) Gibert, O., Valderrama, C., Peterkova, M., Cortina, J. L., *Solvent Extract. Ion Exchan.*, **28**, 543-562 (2010)
(39) Bregman, J. I., Braman, R. S., *J. Colloid. Sci.*, **20**, 913 (1965)
(40) Parida, K. M., Sahu, B. B., Das, D. P., *J. Coll. Inter. Sci.*, **270**, 436-445 (2004)
(41) Hamlen, R. P., *J. Electrochem. Soc.*, **109**, 746 (1962)
(42) Park, S., Chung, T. D., Kang, S. K., Jeong, R. A., Boo, H., Kim, H. C., *Anal. Sci.*, **20**, 1635-1638 (2004)
(43) Bruque, S., Aranda, M. A. G., Losilla, E. R., Olivera-Pastor, P., Maireles-Torres, P., *Inorg. Chem.*, **34**, 893-899 (1995)
(44) Trobajo, C., Khainakov, A., Espina, Aranzazu, Garcia, J. R., *Chem. Mater.*, **12**, 1787-1790 (2000)
(45) Clearfield, A., Costantino, U. In *Comprehensive Supermolecular Chemistry*; 1st ed.; Alberti, G., Bein, T., Ed.; Pergamon: New York; Vol. 7; 108-149 (1996)
(46) Clearfield, A., *Mater. Chem. Phys.*, **35**, 257-263 (1993)
(47) La Ginestra, A., Patrono, P., *Mat. Chem. Phys.*, **17**, 161-179 (1987)
(48) Clearfield, A., *Chem. Rev.*, **88**, 125-148 (1988)
(49) Clearfield, A., *Ann. Rev. Mater. Sci.*, **14**, 205 (1984)
(50) Alberti, G., Torracca, E., *J. Inorg. Nucl. Chem.*, **30**, 317-318 (1968)
(51) Clearfield, A., Smith, G. D., *Inorg. Chem.*, **8**, 431-436 (1969)

(52) Hayashi, A., Fujimoto, Y., Ogawa, Y., Nakayama, H., Tsuhako, M., *J. Coll. Inter. Sci.*, **283**, 57-63 (2005)
(53) Gupta, J. P., Manning, N. J., Nowell, D. V., *J. Inorg. Nucl. Chem.*, **40**, 87 (1978)
(54) Capitani, D., Casciola, M., Donnadio, A., Vivani, R., *Inorg. Chem.*, **49**, 9409-9415 (2010)
(55) Farfan-Torres, E. M., Sham, E. L., Martinez-Lara, M., Jimenez-Lopez, A., *Mat. Res. Bull.*, **27**, 1255-1262 (1992)
(56) Caletka, R., Tympl, M., *J. Inorg. Nucl. Chem.*, **39**, 669 (1977)
(57) Clearfield, A., Blessing, R. H., Stynes, J. A., *J. Inorg. Nucl. Chem.*, **30**, 2249 (1968)
(58) Costantino, U., Gasperoni, A., *J. Chromatog.*, **51**, 289-296 (1970)
(59) Allulli, S., Ferragina, C., La Ginestra, A., Massucci, M. A., Tomassini, N., *J. Inorg. Nucl. Chem.*, **39**, 1043-1048 (1977)
(60) Poojary, D. M., Shpeizer, B., Clearfield, A., *J. Chem. Soc. Dalton Trans.*, 111 (1995)
(61) Clayden, N. J., *J. Chem. Soc. Dalton Trans.*, 1877-1881 (1987)
(62) Clearfield, A., Landis, A. M., Medina, A. S., Troup, J. M., *J. Inorg. Nucl. Chem.*, **35**, 1099 (1973)
(63) Clearfield, A., Duaz, W. L., Medina, A. S., Smith, G. D., Thomas, J. R., *J. Phys. Chem.*, **73**, 3424 (1969)
(64) Winkler, V. A., Thilo, E. *Z,. Anorg. Allg. Chem.*, **364**, 92-112 (1966)
(65) Salvado, M. A., Pertierra, P., Garcia-Granda, S., Garcia, J. R., Rodriguez, J., Fernandez-Diaz, M. T., *Acta. Cryst.*, **B52**, 896-898 (1996)
(66) Clearfield, A., Thomas, J. R., *Inorg. Nucl. Chem. Lett.*, **5**, 775 (1969)
(67) Nakai, I., Imai, K., Kawashima, T., Ohsumi, K., Izumi, F., Tomita, I., *Anal. Sci.*, ***6***, 689-693 (1990)
(68) Peters, L., Evans, J. S. O., *J. Solid State Chem.*, **180**, 2363-2370 (2007)
(69) La Ginestra, A., Galli, P., Berardelli, M. L., *J. Chem. Soc. Dalton Trans.*, 527-531 (1984)
(70) Kraus, K. A., Phillips, H. O., Carlson, T. A., Johnson, J. S., In *Proc. Int. Conf. Peaceful Uses At. Energy*: 2nd, Geneva; Vol. 15 (1985)
(71) Santamaria Gonzalez, J., Martinez Lara, M., Banares, M. A., Martinez-Huerta, M. V., Rodriguez-Castellon, E., Fierro, J. L. G., Jimenez Lopez, A., *J. Cat.*, **181**, 280-284 (1999)
(72) Tegehall, P.E., *Acta. Chem. Scan.*, **A40**, 507-514 (1986)
(73) Alberti, G., Costantino, U., Allulli, S., Tomassini, N., *J. Inorg. Nucl. Chem.*, **40**, 1113-1117 (1978)
(74) Norlund Christensen, A., Krogh Andersen, E., Krogh Andersen, I. G., Alberti, G., Nielsen, M., Lehmann, M. S., *Acta. Chem. Scan.*, **44**, 865-872 (1990)
(75) Alberti, G., Costantino, U, Luciani Giovagnotti, M. L., *J. Inorg. Nucl. Chem.*, **41**, 643 (1979)
(76) Merz, E., *Z. Electrochem.*, **63**, 288 (1959)
(77) Fuller, M. J., *J. Inorg. Nucl. Chem.*, **33**, 559 (1971)
(78) Patrono, P., La Ginestra, A., Ferragina, C., Massucci, M. A., Frezza, A., Vecchio, S., *J. Therm. Anal.*, **38**, 2603-2612 (1992)
(79) Varshney, K. G., Premadas, A., *Sep. Sci. Technol.*, 793-803 (1981)
(80) Sing, P. R., J. P., Rehman, N., *Talanta*, **59**, 443-452 (2003)
(81) Thakkar, R., Chudasama, U., *J. Hazard. Mat.*, **172**, 129-137 (2009)
(82) Jignasa, A., Rakesh, T., Uma, C., *J. Chem. Sci.*, **118**, 185-189 (2006)
(83) Amin, J., Thakkar, R., Chudasama, U., *J. Chem. Sci.*, **118**, 185-189 (2006)
(84) Shakshooki, S. K., Naqvi, N., Kowalczyk, J., Khalil, S., Rais, M., Tarish, F., *React. Poly.*, **7**, 221-226 (1988)
(85) Frianeza, T. N., Clearfield, A., *J. Catal.*, **85**, 398-404 (1984)
(86) Shakshooki, S. K., Szirtes, L., Khalil, S., Azzabi, O., Naqvi, N., Kowalczyk, J., *J. Radio. Nucl. Chem.*, **121**, 175-184 (1988)
(87) Thakkar, R., Chudasama, U., *J. Sci. Ind. Res.*, **68**, 312-318 (2009)
(88) Yazawa, Y., Eguchi, T., Takaguchi, K., Tomita, I., *Bull. Chem. Soc. Jap.*, **52**, 2923-2927 (1979)
(89) Tomita, I., Iwase, K., Saito, K., Sugiyama, Y., *Bull. Chem. Soc. Jap.*, **54**, 749-753 (1981)

(90) Szirtes, L., Poko, Z., Shakshooki, S. K., Ahmed, M., Dehair, A., Benhamed, A., *J. Therm. Anal.*, **35**, 895-902 (1989)
(91) Szirtes, L., Kern, J., Pavlovszki, L., Shakshooki, S. K., Elmismary, Y., Benfaid, N., Haraga, S., *J. Therm. Anal.*, **35**, 1527-1539 (1989)
(92) Farfan-Torres, E. M., Maza-Rodriguez, J., Martinez-Lara, M., Jimenez-Lopez, A., *Solid State Ionics*, **63-65**, 506-511 (1993)
(93) Galli, P., La Ginestra, A., Berardelli, M. L., Massucci, M. A., Patrono, P., *Thermo. Acta*, **92**, 615-618 (1985)
(94) Anillo, A., Rodriguez, M. L., Llavona, R., Rodriguez, J., Martinez-huerta, M. V., Banares, M. A., Fierro, J. L. G., *Inter. J. Inorg. Mat.*, **2**, 177-185 (2000)
(95) Trobajo, C., Rodriguez, M. L., Suarez, M., Garcia, J. R., Rodriguez, J., Parra, J. B., Salvado, M. A., Pertierra, P., Garcia-Granda, S., *J. Mat. Res.*, **13**, 754-759 (1998)
(96) Bagnasco, G., Ciambelli, P., Frezza, A., Galli, P., La Ginestra, A., *App. Cryst.*, **68**, 55-68 (1991)
(97) Ennaciri, S. A., R'Kha, C. R., Barboux, P., Livage, J., Maquet, J., *J. Sol-gel Sci. Tech.*, **34**, 197-203 (2005)
(98) Albertsson, J., Oskarsson, A., Tellgren, R., Thomas, J. O., *J. Phys. Chem.*, **81**, 1574-1578 (1977)
(99) Romano, R., Ruiz, A. I., Alves, O. L., *J. Solid State Chem.*, **177**, 1520-1528 (2004)
(100) Costantino, U., *J. Chem. Soc. Dalton.*, 402 (1979)
(101) Vesely, A., Pekarek, V., *Talanta*, **19**, 219-262 (1972)
(102) Clearfield, A., Oskarsson, A., Kullberg, L., *J. Phys. Chem.*, **78**, 1150 (1974)
(103) Espina, A., Parra, J. B., Garcia, J. R., Pajares, J. A., Rodriguez, J., *Mat. Chem. Phys.*, **35**, 250-256 (1993)
(104) Alberti, G., Costantino, U., Allulli, S., Massucci, M. A., Tomassini, N., *J. Inorg. Nucl. Chem.*, **36**, 661-664 (1974)
(105) Alberti, G., Costantino, U., Allulli, S., Massucci, M. A., *J. Inorg. Nucl. Chem.*, **35**, 1339-1346 (1973)
(106) Suarez, M., Garcia, J. R., Rodriguez, J., *J. Phys. Chem.*, **88**, 159-162 (1984)
(107) Garcia, J. R., Suarez, M., Llavona, R., Rodriguez, J., *J. Chem. Soc. Dalton Trans.*, 2605-2609 (1984)
(108) Alberti, G., Costantino, U., Allulli, S., Massucci, M. A., Pelliccioni, M., *J. Inorg. Nucl. Chem.*, **35**, 1347-1357 (1973)
(109) Alberti, A., Costantino, U., Pelliccioni, M., *J. Inorg. Nucl. Chem.*, **35**, 1327-1338 (1973)
(110) Alberti, G., Bertrami, R., Casciola, M., Costantino, U., Gupta, J. P., *J. Inorg. Nucl. Chem.*, **38**, 843-848 (1976)
(111) Clearfield, A., Hagiwara, H., *J. Inorg. Nucl. Chem.*, **40**, 907-914 (1978)
(112) Clearfield, A., McCusker, L. B., Rudolf, P. R., *Inorg. Chem.*, **23**, 4679-4682 (1984)
(113) Alberti, G., Costantino, U., Allulli, S., Massucci, M. A., Tomassini, N., *J. Inorg. Nucl. Chem.*, **36**, 653-659 (1974)
(114) Rudolf, P. R., Clearfield, A., *Inorg. Chem.*, **28**, 1706-1710 (1988)
(115) Poojary, D. M., Clearfield, A., *Inorg. Chem.*, **33**, 3685-3688 (1994)
(116) Clearfield, A., Troup, J. M., *J. Phys. Chem.*, **77**, 243-247 (1973)
(117) Alberti, G., Bertrami, R., Costantino, U., Gupta, J. P., *J. Inorg. Nucl. Chem.*, **39**, 1060 (1977)
(118) Clearfield, A., Hunter, R. A., *J. Inorg. Nucl. Chem.*, **38**, 1085-1089 (1976)
(119) Alberti, G., Costantino, U., Gupta, J. P., *J. Inorg. Nucl. Chem.*, **36**, 2109-2114 (1974)
(120) Alberti, G., Giammari, G., Grassini-Strazza, G., *J. Chromatog.*, *28* (1967)
(121) Alberti, G., Cardini-Galli, P., Costantino, U., Torracca, E., *J. Inorg. Nucl. Chem.*, **29**, 571-578 (1967)
(122) Zhu, J., Trefiak, N., Woo, T. K., Huang, Y., *J. Phys. Chem.*, **113**, 10029-10037 (2009)
(123) Clearfield, A., *Solvent Extr. Ion Exch.*, 18 (2000)
(124) Clearfield, A., Bortun, A. I., Khainakov, S. A., Bortun, L. N., Strelko, V. V., Khryaschevskii, V. N., *Waste Manag.*, **18**, 203-210 (1988)

Chapter 2: Experimental

2.1 Introduction

The techniques used for the synthesis and subsequent characterisation of all the materials produced in this research project will be discussed in this chapter. All materials once synthesised were characterised by X-ray diffraction (Section 2.4) and pair distribution function (Section 2.6) techniques. Rietveld refinements (Section 2.5) of the diffraction patterns were carried out using the GSAS program package[1]. Pair distribution functions (PDFs) of the products were calculated using the program PDFgetX2[2] and these were refined with the PDFGui[3] program. X-ray fluorescence (Section 2.8) was used to determine the chemical compositions of the materials and thermogravimetric analysis with mass spectroscopy (Section 2.7) enabled the thermal behaviour of many of the samples to be investigated and the decomposition products identified.

2.2 Synthetic Procedures

Most of the phosphates in this work were prepared by hydrothermal methods. Experiments were generally carried out using Parr acid digestion bombs (types 4749, 4744 or 4748) with the appropriate sized Teflon cups that had a maximum operating temperature of 250 °C. The chemicals used were of reagent grade obtained from Sigma Aldrich or Fisher Scientific.

2.2.1.1 α-$Ti_xZr_{1-x}(HPO_4)_2.H_2O$ for $0 \leq x \leq 1$

The experimental procedure used was similar to that previously reported by Clearfield and Frianeza[4] using 1 M titanium tetrachloride and zirconyl chloride solutions as the precursors. A 250 ml stock zirconyl chloride solution was prepared by dissolving 80.56 g (0.25 mol) of $ZrOCl_2.8H_2O$ in 1 M hydrochloric acid. The 1 M titanium tetrachloride solutions were prepared individually by the addition of stoichiometric amounts of $TiCl_4$ and 1 M acetic acid as indicated in Table 2.1. These solutions were mixed together in stoichiometric amounts to give the desired Zr/Ti ratios (see Table 2.1 for the quantities used). 50 ml of 4 M H_3PO_4 were added to each of these mixtures and they were stirred overnight at room temperature to give the crude products. Traditionally[4] the crude products are then refluxed in 12 M phosphoric acid for 14 days to afford the crystalline phosphates. In this work it was found that heating the crude products with 10 ml phosphoric acid (12 M) in a 25 ml autoclave at 150 °C for one week gave the same quality products in half the time. The final products were collected by centrifugation. Variations of this method, including increased temperatures and heating stage durations, were attempted to try and form the true solid solution for this system. These variations are discussed in more detail in section 3.1.2.8.

Table 2.1: Quantities of reagents used for the zirconium-titanium phosphate preparations.

Product	Moles of Ti /mol	Volume of $TiCl_4$ /ml	Volume of 1 M acetic acid /ml*	Moles of Zr /mol	Volume of 1 M $ZrOCl_2.8H_2O$ solution /ml
$Ti(HPO_4)_2.H_2O$	3.88×10^{-2}	4.26	34.54 *38.80*	0	0
$Ti_{0.9}Zr_{0.1}(HPO_4)_2.H_2O$	2.40×10^{-2}	2.64	21.36 *24.00*	0.27×10^{-2}	2.67
$Ti_{0.8}Zr_{0.2}(HPO_4)_2.H_2O$	2.10×10^{-2}	2.31	18.69 *21.00*	0.53×10^{-2}	5.26
$Ti_{0.7}Zr_{0.3}(HPO_4)_2.H_2O$	1.81×10^{-2}	1.99	16.11 *18.10*	0.78×10^{-2}	7.76
$Ti_{0.6}Zr_{0.4}(HPO_4)_2.H_2O$	1.53×10^{-2}	1.68	13.62 *15.30*	1.02×10^{-2}	10.18
$Ti_{0.5}Zr_{0.5}(HPO_4)_2.H_2O$	1.25×10^{-2}	1.37	11.13 *12.50*	1.25×10^{-2}	12.50
$Ti_{0.4}Zr_{0.6}(HPO_4)_2.H_2O$	0.98×10^{-2}	1.08	8.78 *9.86*	1.48×10^{-2}	14.80
$Ti_{0.3}Zr_{0.7}(HPO_4)_2.H_2O$	0.73×10^{-2}	0.80	6.46 *7.26*	1.70×10^{-2}	17.00
$Ti_{0.2}Zr_{0.8}(HPO_4)_2.H_2O$	0.48×10^{-2}	0.53	4.26 *4.79*	1.91×10^{-2}	19.12
$Ti_{0.1}Zr_{0.9}(HPO_4)_2.H_2O$	0.24×10^{-2}	0.26	2.10 *2.36*	2.12×10^{-2}	21.24
$Zr(HPO_4)_2.H_2O$	0	0	0 *0*	3.32×10^{-2}	33.20

*The volumes given in italics refer to the total volume of 1 M $TiCl_4$ acetic acid solution used.

α-$Ti_xZr_{1-x}(H_{1-x}P_{1-x}Si_xO_4)_2.H_2O$ for $0.75 \leq x \leq 0.25$

The substitution of silicon for phosphorus within the alpha structure was attempted to see if it could yield greater metal substitution. The silicon substituted phosphates were prepared in the same way as the standard mixed zirconium-titanium phosphates outlined above, the only exception being the partial substitution of 4 M phosphoric acid by Ludox HS-40 (40 wt % suspension of SiO_2 in H_2O). Details of the quantities of reagents used can be found in Table 2.2.

Table 2.2: Quantities of reagents used for the α-$Ti_xZr_{1-x}(H_{1-x}P_{1-x}Si_xO_4)_2.H_2O$ preparations.

x	Titanium			Zirconium		Phosphorus		Silicon	
	Moles /mol	Volume of $TiCl_4$ /ml	Volume of 1 M $TiCl_4$ acetic acid solution /ml*	Moles /mol	Volume of 1M $ZrOCl_2.8H_2O$ solution /ml	Moles /mol	Volume of 4 M H_3PO_4 /ml	Moles /mol	Mass of HS-40 /g
0.75	0.060	6.61	60.00	0.020	20.00	0.060	15.00	0.020	3.00
0.50	0.013	1.37	12.50	0.013	12.50	0.013	3.13	0.013	1.88
0.25	0.013	1.48	13.32	0.040	40.00	0.013	3.30	0.040	6.01

**Note this is the total volume of 1 M $TiCl_4$ acetic acid solution used. The volume of 1 M acetic acid is the difference between this value and the volume of $TiCl_4$ used.*

Sol gel Synthesis

The sol gel method used was based on that previously reported by Farfan-Torres *et al.* [5] except that the second reflux step was replaced with the use of an autoclave and oven. 1 M solutions of titanium isopropoxide and zirconium isopropoxide were prepared by the addition of 5.076 g (1.79×10^{-2} moles) of $Ti[OCH(CH_3)_2]_4$ and 5.85 g (1.79×10^{-2} moles) of $Zr[O(CH_2)_2CH_3]_4$ to 18 ml propanol respectively. The solutions were stirred together and hydrolysed by the slow addition of H_3PO_4 (3.80 g) in propanol (36 ml). After 5 hours, 12 M H_3PO_4 (100 ml) was added and the solution was heated under reflux for 15 hours to yield the crude product. The crude gel was heated at 150 °C for 120 hours in a 25 ml autoclave with 12 ml H_3PO_4 (9 M) to give the final product that was collected by centrifugation.

A literature method reported by Thakkar and Chudasama[6] and an oxalic acid preparation[7] were also attempted. These are discussed further in chapter 3.

2.2.1.2 α-$Zr_xGe_{1-x}(HPO_4)_2.H_2O$ for $0 \leq x \leq 1$

The mixed zirconium germanium phosphates were prepared using the experimental procedure reported by Losilla *et al.*[8]. Appropriate amounts (as indicated in Table 2.3) of zirconyl chloride and germanium dioxide were heated with 18.71 g H_3PO_4 (85% w/w) and 5.83 g of H_2O in a 25 ml autoclave at 125 °C for one week. The final products were collected by centrifugation.

Table 2.3: Quantities of reagents used for the zirconium-germanium phosphate preparations.

Product	Moles of Ge / mol	Mass of GeO_2 / g	Moles of Zr / mol	Mass of $ZrOCl_2.8H_2O$ /g
$Zr_{0.9}Ge_{0.1}(HPO_4)_2.H_2O$	0.81×10^{-3}	0.085	7.28×10^{-3}	2.346
$Zr_{0.8}Ge_{0.2}(HPO_4)_2.H_2O$	1.62×10^{-3}	0.169	6.47×10^{-3}	2.085
$Zr_{0.7}Ge_{0.3}(HPO_4)_2.H_2O$	2.43×10^{-3}	0.254	5.66×10^{-3}	1.825
$Zr_{0.6}Ge_{0.4}(HPO_4)_2.H_2O$	3.24×10^{-3}	0.339	4.85×10^{-3}	1.564
$Zr_{0.5}Ge_{0.5}(HPO_4)_2.H_2O$	4.04×10^{-3}	0.432	4.04×10^{-3}	1.303
$Zr_{0.4}Ge_{0.6}(HPO_4)_2.H_2O$	4.85×10^{-3}	0.508	3.24×10^{-3}	1.043
$Zr_{0.3}Ge_{0.7}(HPO_4)_2.H_2O$	5.66×10^{-3}	0.593	2.43×10^{-3}	0.782
$Zr_{0.2}Ge_{0.8}(HPO_4)_2.H_2O$	6.47×10^{-3}	0.677	1.62×10^{-3}	0.521
$Zr_{0.1}Ge_{0.9}(HPO_4)_2.H_2O$	7.28×10^{-3}	0.762	0.81×10^{-3}	0.261
$Ge(HPO_4)_2.H_2O$	8.09×10^{-3}	0.847	0	0

2.2.1.3 α-$Ti_xGe_{1-x}(HPO_4)_2.H_2O$ for $0 \leq x \leq 1$

α-TiP Based Method

The mixed titanium germanium phosphates were prepared using the same procedure that was used for the synthesis of the mixed zirconium-titanium phosphates outlined previously (Section 2.2.1.1). Stoichiometric amounts of titanium tetrachloride and germanium dioxide as indicated in Table 2.4 were used to form the crude products.

Table 2.4: Quantities of reagents used for the preparation of titanium-germanium phosphates by the TiP method.

Product	Moles of Ti /mol	Volume of $TiCl_4$ /ml	Volume of 1 M $TiCl_4$ acetic acid solution /ml*	Moles of Ge /mol	Mass of GeO_2 /g
$Ti_{0.9}Ge_{0.1}(HPO_4)_2.H_2O$	2.49×10^{-2}	2.74	24.90	0.28×10^{-2}	0.29
$Ti_{0.8}Ge_{0.2}(HPO_4)_2.H_2O$	2.21×10^{-2}	2.43	22.10	0.55×10^{-2}	0.58
$Ti_{0.7}Ge_{0.3}(HPO_4)_2.H_2O$	1.93×10^{-2}	2.12	19.30	0.83×10^{-2}	0.87
$Ti_{0.6}Ge_{0.4}(HPO_4)_2.H_2O$	1.67×10^{-2}	1.83	16.70	1.11×10^{-2}	1.16
$Ti_{0.5}Ge_{0.5}(HPO_4)_2.H_2O$	1.39×10^{-2}	1.52	13.90	1.39×10^{-2}	1.45
$Ti_{0.4}Ge_{0.6}(HPO_4)_2.H_2O$	1.11×10^{-2}	1.22	11.10	1.67×10^{-2}	1.75
$Ti_{0.3}Ge_{0.7}(HPO_4)_2.H_2O$	0.83×10^{-2}	0.91	8.30	1.93×10^{-2}	2.03
$Ti_{0.2}Ge_{0.8}(HPO_4)_2.H_2O$	0.55×10^{-2}	0.60	5.50	2.21×10^{-2}	2.32
$Ti_{0.1}Ge_{0.9}(HPO_4)_2.H_2O$	0.28×10^{-2}	0.30	2.80	2.49×10^{-1}	2.60

**Note this is the total volume of 1 M $TiCl_4$ acetic acid solution used. The volume of 1 M acetic acid is the difference between this value and the volume of $TiCl_4$ used.*

α-GeP Based Method

Due to problems with synthesising the germanium rich compounds a second method based on that reported by Losilla *et al.*[8] and used for the preparation of the germanium-zirconium phosphates was employed. This involved the immediate heating of the precursors; titanium tetrachloride and germanium dioxide (see Table 2.5 for the relevant quantities) in an autoclave at 125 °C with phosphoric acid for one week.

Table 2.5: Quantities of reagents used for the preparation of titanium-germanium phosphates by the GeP method.

Product	Moles of Ti /mol	Volume of $TiCl_4$ /ml	Moles of Ge /mol	Mass of GeO_2 /g
$Ti_{0.9}Ge_{0.1}(HPO_4)_2.H_2O$	2.49×10^{-2}	2.74	0.28×10^{-2}	0.29
$Ti_{0.8}Ge_{0.2}(HPO_4)_2.H_2O$	2.21×10^{-2}	2.43	0.55×10^{-2}	0.58
$Ti_{0.7}Ge_{0.3}(HPO_4)_2.H_2O$	1.93×10^{-2}	2.12	0.83×10^{-2}	0.87
$Ti_{0.6}Ge_{0.4}(HPO_4)_2.H_2O$	1.67×10^{-2}	1.83	1.11×10^{-2}	1.16
$Ti_{0.5}Ge_{0.5}(HPO_4)_2.H_2O$	1.39×10^{-2}	1.52	1.39×10^{-2}	1.45
$Ti_{0.4}Ge_{0.6}(HPO_4)_2.H_2O$	1.11×10^{-2}	1.22	1.67×10^{-2}	1.75
$Ti_{0.3}Ge_{0.7}(HPO_4)_2.H_2O$	0.83×10^{-2}	0.91	1.93×10^{-2}	2.03
$Ti_{0.2}Ge_{0.8}(HPO_4)_2.H_2O$	0.55×10^{-2}	0.60	2.21×10^{-2}	2.32
$Ti_{0.1}Ge_{0.9}(HPO_4)_2.H_2O$	0.28×10^{-2}	0.30	2.49×10^{-2}	2.60

2.2.1.4 Tin Phosphate Systems

α-Tin phosphate proved extremely difficult to synthesise in any useable quantity. A method reported by Varshney *et al.*[9] was trialled and found to give only amorphous products. A second method involving the heating of tin chloride ($SnCl_4.5H_2O$) with phosphoric acid in an autoclave produced crystalline tin phosphate in small quantities. Investigation into various temperatures and experimental durations gave the optimum conditions to be heating 10 g tin chloride ($SnCl_4.5H_2O$) in 30 ml phosphoric acid (12 M) for one week at 150 °C in a 50 ml autoclave.

$Ti_xSn_{1-x}(HPO_4)_2.H_2O$ for $0 \leq x \leq 1$

The experimental procedure used was similar to that previously reported by Trobajo *et al.*[10]. Stoichiometric quantities of tin tetrachloride ($SnCl_4$) and titanium tetrachloride ($TiCl_4$) as indicated in Table 2.6, were heated to 150 °C with 30 ml H_3PO_4 (17 M) in an autoclave for one week to give the phosphates.

Table 2.6: Quantities of reagents used for the titanium-tin phosphates preparations.

Product	Moles of Ti /mol	Volume of $TiCl_4$ /ml	Moles of Sn /mol	Volume of $SnCl_4$ / ml
$Ti_{0.9}Sn_{0.1}(HPO_4)_2.H_2O$	3.88×10^{-2}	4.26	0.43×10^{-2}	0.50
$Ti_{0.8}Sn_{0.2}(HPO_4)_2.H_2O$	3.44×10^{-2}	3.78	0.86×10^{-2}	1.00
$Ti_{0.7}Sn_{0.3}(HPO_4)_2.H_2O$	3.01×10^{-2}	3.31	1.29×10^{-2}	1.50
$Ti_{0.6}Sn_{0.4}(HPO_4)_2.H_2O$	2.58×10^{-2}	2.84	1.72×10^{-2}	2.00
$Ti_{0.5}Sn_{0.5}(HPO_4)_2.H_2O$	2.15×10^{-2}	2.36	2.15×10^{-2}	2.50
$Ti_{0.4}Sn_{0.6}(HPO_4)_2.H_2O$	1.72×10^{-2}	1.89	2.58×10^{-2}	3.00
$Ti_{0.3}Sn_{0.7}(HPO_4)_2.H_2O$	1.29×10^{-2}	1.42	3.01×10^{-2}	3.50
$Ti_{0.2}Sn_{0.8}(HPO_4)_2.H_2O$	0.86×10^{-2}	0.95	3.44×10^{-2}	4.00
$Ti_{0.1}Sn_{0.9}(HPO_4)_2.H_2O$	0.43×10^{-2}	0.47	3.88×10^{-2}	4.50

$Zr_xSn_{1-x}(HPO_4)_2.H_2O$ for $0 \leq x \leq 1$

Stoichiometric amounts of zirconyl chloride ($ZrOCl_2.8H_2O$) and tin chloride ($SnCl_4.5H_2O$) as indicated in Table 2.7, were ground together in a pestle and mortar. The homogenous mix was heated to 200 °C in a hydrothermal bomb for one week in 30 ml H_3PO_4 (12 M). The end products were collected via centrifugation.

Table 2.7: Quantities of reagents used for the zirconium-tin phosphates preparations.

Product	Moles of Zr /mol	Mass of $ZrOCl_2.8H_2O$ /g	Moles of Sn /mol	Mass of $SnCl_4.5H_2O$ /g
$Zr_{0.9}Sn_{0.1}(HPO_4)_2.H_2O$	2.96×10^{-2}	9.54	0.33×10^{-2}	1.15
$Zr_{0.8}Sn_{0.2}(HPO_4)_2.H_2O$	2.61×10^{-2}	8.41	0.65×10^{-2}	2.29
$Zr_{0.7}Sn_{0.3}(HPO_4)_2.H_2O$	2.26×10^{-2}	7.29	0.97×10^{-2}	3.40
$Zr_{0.6}Sn_{0.4}(HPO_4)_2.H_2O$	1.92×10^{-2}	6.19	1.28×10^{-2}	4.49
$Zr_{0.5}Sn_{0.5}(HPO_4)_2.H_2O$	1.59×10^{-2}	5.12	1.59×10^{-2}	5.57
$Zr_{0.4}Sn_{0.6}(HPO_4)_2.H_2O$	1.26×10^{-2}	4.06	1.89×10^{-2}	6.62
$Zr_{0.3}Sn_{0.7}(HPO_4)_2.H_2O$	0.94×10^{-2}	3.02	2.18×10^{-2}	7.66
$Zr_{0.2}Sn_{0.8}(HPO_4)_2.H_2O$	0.62×10^{-2}	1.99	2.47×10^{-2}	8.67
$Zr_{0.1}Sn_{0.9}(HPO_4)_2.H_2O$	0.31×10^{-2}	0.99	2.76×10^{-2}	9.68

2.2.2 Ion Exchange Reactions

The basic ion exchange reactions used in this work were carried out using an aqueous method. In this technique typically 1 g of metal phosphate was stirred overnight in a 250 ml aqueous solution containing the desired cation. The solution was either a nitrate, acetate, hydroxide or chloride and the cations of interest included strontium, cobalt, cesium and sodium. The products were collected by either filtration or centrifugation.

In some cases extended durations or increased temperatures and volumes were attempted to try to increase or force the exchange. These variations are discussed in more detail in chapter 4.

2.3 Crystallography

2.3.1 Crystal Structure

Crystals are solids in which the constituent atoms, molecules or ions are packed in a regular order in three dimensional space. In an ideal crystal, the arrangement of the atoms can be represented by a repeating unit known as the *unit cell*. The unit cell can be defined as the smallest repeating unit which shows the full symmetry of the crystal structure and from which the entire crystal structure can be generated through translation. The unit cell is described by six parameters, three axes (*a, b, c*) and the angles between them (*α, β, γ*). These are known as the lattice parameters. There are seven crystal systems derived from having one or more relationship between the lattice parameters, for example in cubic *a* = *b* = *c* and all angles are 90°. The introduction of body and face centering produces the fourteen lattice types known as the *Bravais Lattices* (Figure 2.1). The Bravais lattices describe the geometrical arrangement of the lattice points and therefore the translational symmetry of the crystal. Each crystal system is governed by the presence or absence of symmetry.

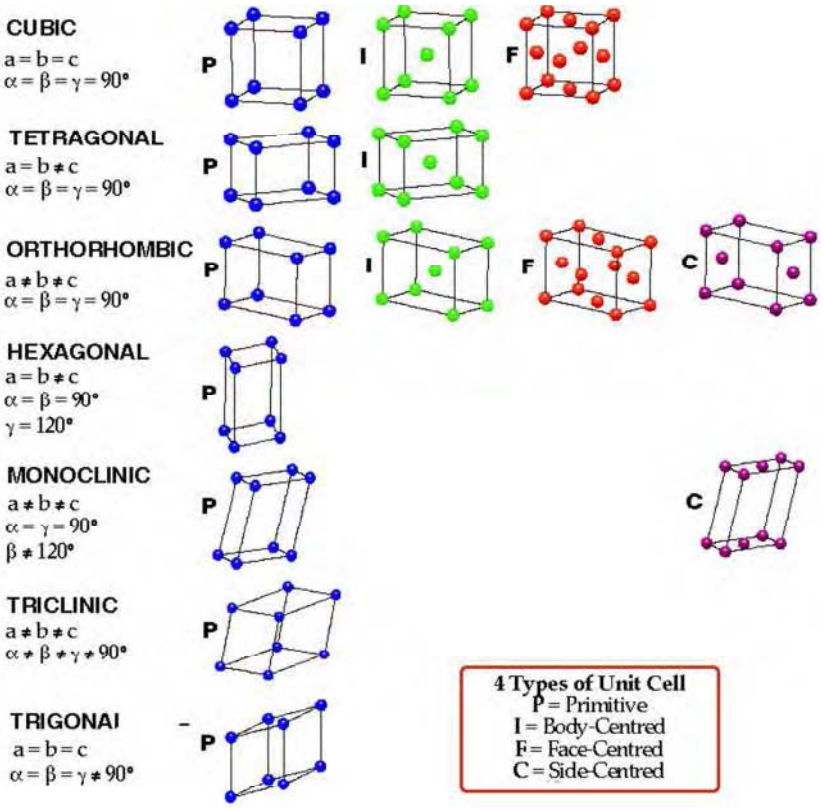

Figure 2.1: Bravais Lattices. Adapted from reference[11]

Crystal structures are described according to their internal symmetry, their lattice parameters and the atomic positions of any atoms within the unit cell. The atomic positions are expressed as fractional coordinates in each direction along the unit cell. The arrangement of these atoms can give rise to *screw axes* and *glide planes*. A glide plane is a symmetry operation describing a reflection in a plane followed by a translation parallel to that plane. A screw axis describes a rotation about an axis followed by a translation along the direction of that axis. The combination of the 14 Bravais lattices with all possible symmetry elements in three dimensional space gives rise to the 230 *space groups.* The space group completely describes the symmetry of a crystal system.

2.3.2 Lattice Planes and Miller Indices

Crystals can be described in terms of sets of lattice planes. Each set of lattice planes must be arranged parallel and equally spaced throughout the structure with one member of the family passing through the origin of the unit cell. The planes cut through the three axis of the unit cell and these intersections can be described as fractions of the cell edge. The reciprocal of these intercepts are used to label the lattice planes and are known as the *Miller indices*. Each plane is therefore described in three dimensions by the three integers *h*, *k* and *l*, conventionally written as (*hkl*). Crystallographic planes parallel to one of the unit cell faces are defined by the type (*h*00), (0*k*0) or (00*l*). Some examples are shown in Figure 2.2.

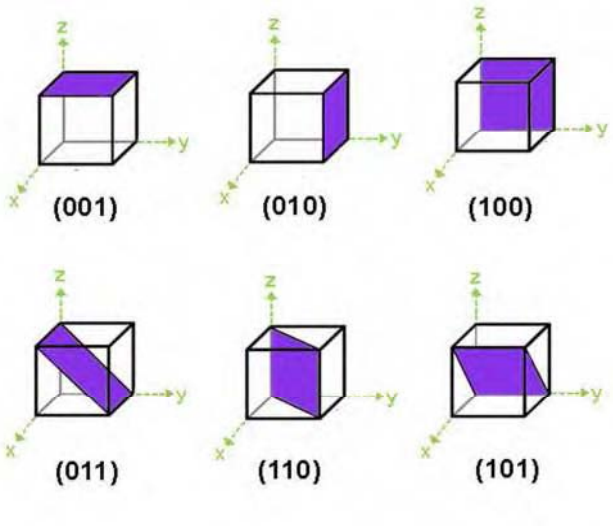

Figure 2.2: Examples of some Miller indices representations.

The perpendicular distance between any pair of adjacent planes is the interplanar *d*-spacing denoted (d_{hkl}).

2.4 X-Ray Diffraction

2.4.1 Fundamentals of X-ray Diffraction

X-ray diffraction is the principal technique used to characterise crystalline materials. Each crystalline solid has its own characteristic X-ray powder pattern which may be used as a "fingerprint" for its identification by comparing it to database standards or by comparison to the simulated patterns of a known crystal structure. X-ray crystallography can also be used to determine the structural parameters, e.g. bond angles and distances, unit cell size etc of a particular material. In this body of work X-ray powder diffraction has been used to identify and check the purity of phases formed, to identify successful ion exchange and for structural characterisation.

The technique has been widely discussed elsewhere[12,13] but the basic principles are outlined here. In order to probe a crystal structure X-rays are used as they have wavelengths comparable to periodic distances in crystals (~1 Å). Powder X-ray diffraction is essentially the study of the pattern generated from radiation diffracted by a polycrystalline material, based on the premise that all atoms within a crystal are located in regularly spaced discrete planes that can diffract an X-ray beam passing through it. When an incident X-ray beam strikes a plane some of the X-rays are reflected back at the angle of incidence while others pass through and can be reflected by subsequent planes. Bragg's law is used to describe the interference of waves of radiation reflected from these planes. To understand Bragg's law once must consider two parallel X-rays incident at an angle of θ upon two parallel planes, A and B as illustrated in Figure 2.3.

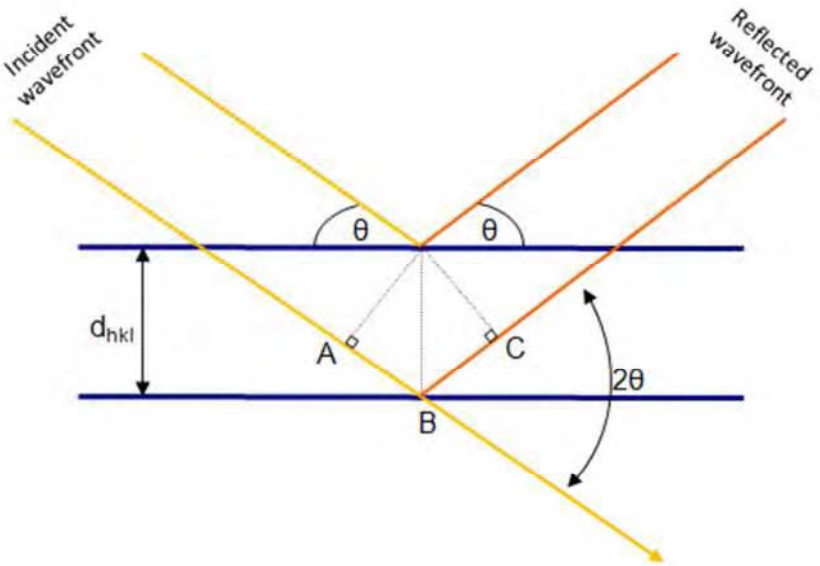

Figure 2.3: Derivation of Braggs Law

Using geometry:

$$sin\theta = \frac{AB}{d_{hkl}} \equiv \frac{BC}{d_{hkl}}$$

Therefore the path difference between the reflected X-rays is given by:

$$AB + BC = 2d_{hkl} \sin\theta$$

If the path difference of the scattered X-rays is a whole number of wavelengths, *n*, then the two reflected beams are in phase, therefore Bragg's law (Equation 2.1) is satisfied and constructive interference occurs.

$$n\lambda = 2d_{hkl}\, sin\,\theta$$

Equation 2.1: Bragg's Law

This produces a peak in the intensity of the reflected X-rays detected for each value of 2θ at which constructive interference occurs. Destructive interference results from all non integer values of *n*.

The basic requirements for powder X-ray diffraction are a source of X-rays, a finely ground powder sample and a moveable detector positioned at a defined geometry relative to the sample and source. A monochromatic source of X-rays strike the powder sample, which is ideally made up of randomly orientated lattice planes, at a defined angle θ .The intensity of the scattered radiation at an angle 2θ is measured by the detector. Angles corresponding to the *d*-spacings of lattice planes obeying Bragg's law will have greater intensity.

One of the most common types of detector used in powder X-ray diffraction experiments is a scintillation counter. This is a point detector as it only collects data at a single 2θ angle at a time. The X-rays hit the phosphorescent screen and emit photons which are detected and amplified. The signal obtained is directly proportional to the amount of X-rays hitting the screen. Position sensitive detectors can also be used; they are able to collect data over a range of 2θ angles.

In an ideal sample the crystallites should be arranged in every possible orientation so that all possible angles of the lattice planes are present. The X-ray beam is therefore diffracted at all possible angles giving a 3-dimensional cone of diffraction for each lattice spacing in the crystal. Each cone is represented by a peak in the 1-dimensional X-ray diffraction pattern, which in turn corresponds to lattice planes with known (*hkl*) values. There is a large amount of data contained in the produced powder diffraction pattern , and each pattern can be viewed in terms of four components; background, peak shape, peak position and peak

intensity, as illustrated in Figure 2.4, which summarises the parameters that affect each of these.

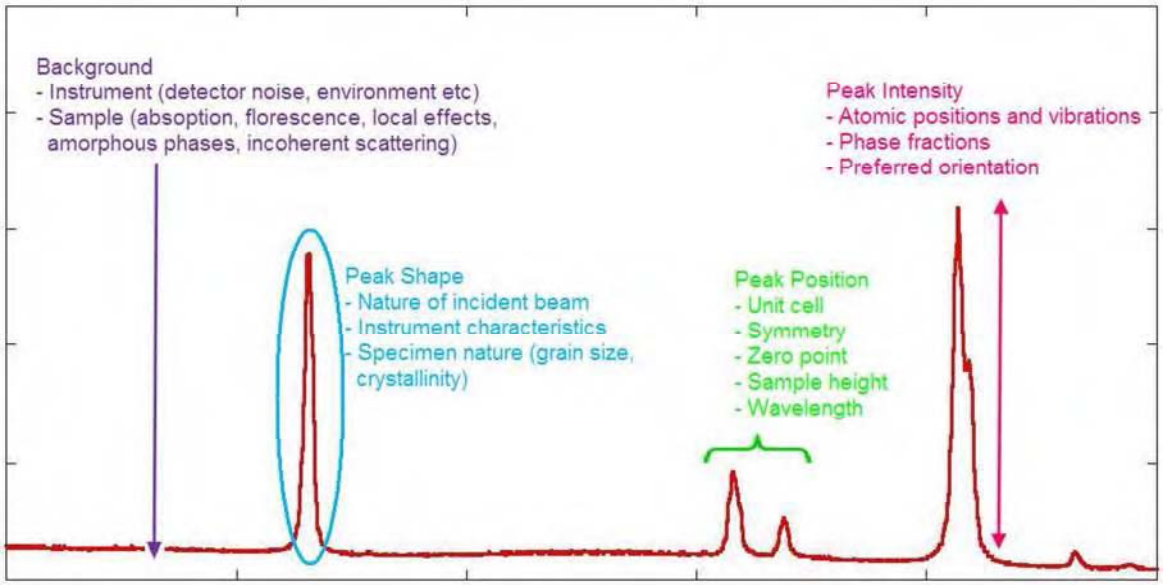

Figure 2.4: The contribution of different parameters to the powder diffraction pattern.

2.4.2 Generation of X-rays

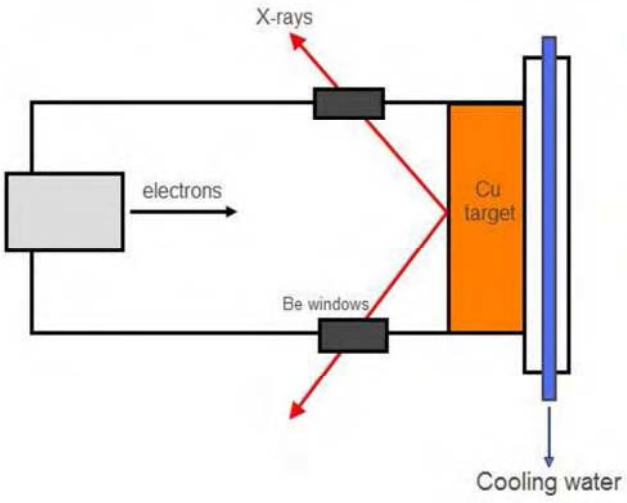

Figure 2.5: Schematic illustration of a laboratory X-ray tube.

The X-rays used in laboratory based diffraction experiments are typically produced in an X-ray tube (Figure 2.5), which is an evacuated chamber where electrons are generated from heating a tungsten filament. The electrons, accelerated through a voltage (typically ~ 40 kV), collide with a metal target, often copper or molybdenum. The incident beam ionises the electrons from the inner 1*s* orbital (*K* shell) of the metal target resulting in vacancies. These vacancies are filled by electrons in higher energy levels and consequently X-rays are emitted. This is depicted in Figure 2.6. These transitions have fixed wavelengths depending on the metal and the orbitals involved. For copper the X-rays generated in the transition between $2p \rightarrow 1s$ orbitals, known as K_α, have a wavelength of 1.5418 Å and those from the $3p \rightarrow 1s$ transition, called K_β, have a wavelength of 1.3922 Å. The K_α is the most intense as this transition occurs more frequently and is therefore the one commonly used in diffraction. K_α is in fact a doublet comprised of $K_{\alpha1}$ = 1.54051 Å and $K_{\alpha2}$ = 1.5433 Å, due to the small difference in energy arising from the two possible spin states of the 2*p* electron.

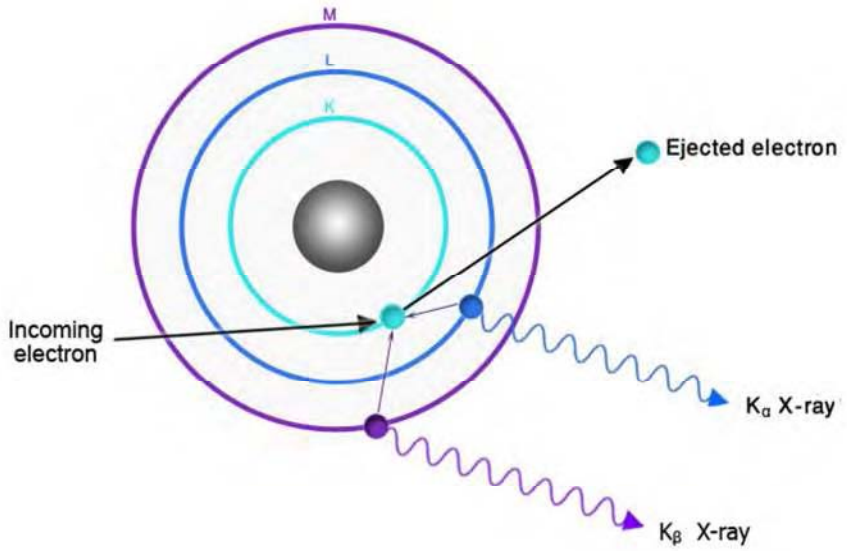

Figure 2.6: Generation of X-rays

Once generated, the X-rays leave the X-ray tube through beryllium windows. As the amount of X-rays absorbed depends on the atomic weight of the element, beryllium, having an atomic number of 4, is one of the most suitable elements to use. The resultant X-ray beam consists of both discrete wavelength radiation characteristic of the metal target as well as a continuous background spectrum (white radiation) predominantly caused by Bremsstrahlung. Bremsstrahlung arises from the deceleration of the electrons as they contact the metal target when some of their lost energy is converted into electromagnetic radiation. It displays a continuous spectrum as not every electron will decelerate in the same manner. As a monochromatic source of X-rays is required for diffraction, all other radiation has to be filtered out. A thin metal foil, e.g. nickel, can be employed to filter out the K_β radiation leaving only the K_α component. Alternatively monochromators can be used. Crystal monochromators are single crystals, typically made from silicon, quartz or germanium that are set at a specific orientation so that the desired wavelength of the radiation can be achieved by satisfying Bragg's condition (Equation 2.1). In contrast to conventional monochromator crystals Göebel mirrors are curved multilayer crystals consisting of alternating strongly and weakly scattering materials, typically including combinations of W-Si and Ni-C. The mirror reflects only the radiation at a wavelength governed by the multilayer spacing and produces a parallel focused X-ray beam. The degree of 'monochromation' obtained is insufficient to differentiate between Cu $K_{\alpha1}$ and $K_{\alpha2}$ radiation.

2.4.3 X-ray Intensity

It is important to gain an understanding of the factors that affect the intensity of the reflections in order to utilise the information contained within an X-ray diffraction pattern. The intensity I_{hkl} of a diffracted X-ray beam can be expressed as:

$$I_{hkl} = K{F_{hkl}}^2 \, mALP$$

K = proportionality constant.

$\boldsymbol{F_{hkl}}$ = structure factor

m = multiplicity factor

A = absorption factor

L = Lorentz factor

P = polarization factor

Equation 2.2: Formula for the intensity of an X-ray beam

The factors from the formula will be discussed in turn:

The Multiplicity Factor

The multiplicity factor accounts for the number of planes which contribute towards the same observed Bragg peak.

The Absorption Factor

The absorption factor accounts for the proportion of the incident and diffracted X-rays absorbed by the sample. The amount absorbed depends on the sample composition (linear absorption coefficient, μ) and the thickness of the sample, x. The decrease in the intensity due to absorption can be modelled by the equation:

$$I = I_0 exp(-\mu x)$$

Equation 2.3: Equation for the reduction in intensity due to absorption. I_0 = incident intensity, I = the reduced intensity after passing through the sample.

The absorption factor is also dependant on the diffraction angle used, θ, which gives rise to the following two equations:

For powder transmission mode diffraction:

$$A_x = \frac{exp[-\mu(1 - sec\theta)]}{sec\theta}$$

For powder reflectance mode diffraction:

$$A_x = \frac{\sin\theta}{2\mu}$$

The Lorentz factor

The Lorentz factor essentially corrects for the geometry of the diffractometer. It provides the intensity variation with diffraction angle depending upon the geometrical alignment of the experimental setup. Equation 2.4 can used to model this but not when either synchrotron sources or monochromators are used as the equations for the Lorentz factor are diffractometer specific.

$$L_x = \frac{1}{2\sin\theta}$$

Equation 2.4: The Lorentz factor

The Polarisation factor

The polarisation factor accounts for the polarisation of the X-ray beam. The X-rays interact with the sample most strongly when their electric field vector is aligned either parallel or anti parallel to the sample. It is at its weakest when perpendicular. The equations used to model this are diffractometer specific. An example equation to model this is given in Equation 2.5 however this equation cannot be used for synchrotron sources or when monochromators are utilized.

$$P_x = \frac{1 + \cos^2\theta}{2}$$

Equation 2.5: The Polarisation factor

The Structure factor

The structure factor is the most important factor affecting the intensity of the diffracted peaks. It provides the summation of the scattering power from the individual atoms within the unit cell. It can be expressed mathematically as:

$$F_{(hkl)} = \sum_{n} f_n \, P_n exp[2\pi i(hx_n + \ ky_n + \ lz_n)] exp\left[-\frac{B_n \sin^2\theta}{\lambda^2}\right]$$

f_n = atomic scattering factor (corrected for real and imaginary terms) of the n^{th} atom type.

p_n = the site occupancy of the n^{th} atomic site. It accounts for either atoms in special positions, atomic disorder or both.

x_n, y_n and z_n = the fractional coordinates of the n^{th} atom

h, k and l = the miller indices of the k^{th} reflection.

B is proportional to the root mean square oscillations of the atoms and is temperature dependent.

The thermal factor is given by the second term in the equation, and takes into account the reduction of intensity by thermal vibrations of the n^{th} atom.

Equation 2.6: The structure factor

2.4.4 Laboratory Equipment

Laboratory powder X-ray diffraction data were collected on a Bruker D8 diffractometer in transmission mode (Figure 2.7). A copper X-ray source was monochromated by a germanium

crystal monochromoater to give only Cu $K_{\alpha 1}$ radiation at a wavelength of 1.5406 Å. Samples were prepared for analysis by grinding in a pestle and mortar, mounting onto Scotch™ '*Magic Tape'* and fixing to plastic XRD discs. The magic tape gives negligible scattering in comparison to the crystalline samples. The samples were rotated about a fixed position throughout data collection. Data were collected via a position sensitive detector with a 3° window. The detector rotates about the sample and produces a diffraction pattern electronically.

A Bruker D8 diffractometer set up in reflection mode (Figure 2.7) equipped with an MRI temperature stage was used for the variable temperate XRD analysis. Variable temperature measurements were carried out on the samples over a temperature range of 25 – 900 °C. This diffractometer was also equipped with a germanium crystal primary beam monochromator supplying radiation at a wavelength of 1.5406 Å. The X-ray source and detector move through a range of θ around a rotating sample.

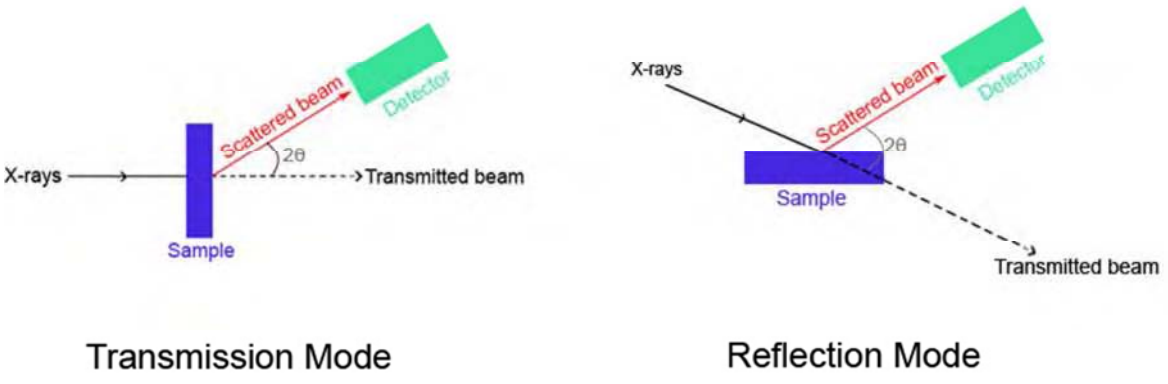

Figure 2.7: Comparison of the transmission and reflection XRD modes.

2.4.5 Synchrotron Sources

Synchrotron sources can be employed to obtain data of much higher quality than that produced from general laboratory diffractometers. A synchrotron is essentially a particle accelerator where charged particles such as electrons are accelerated in a circular orbit at relativistic speeds. First electrons are generated and injected into a booster ring via a linear accelerator. From here the electrons move into the storage ring, where they are deflected by magnetic fields to produce radiation which is drawn off through tangential beam lines (see Figure 2.8). Suitable monochromators are employed to select specific wavelengths from the wide range generated. Insertion devises, e.g. wigglers and undulators, are used within the storage ring to give the synchrotron radiation specific enhanced properties.

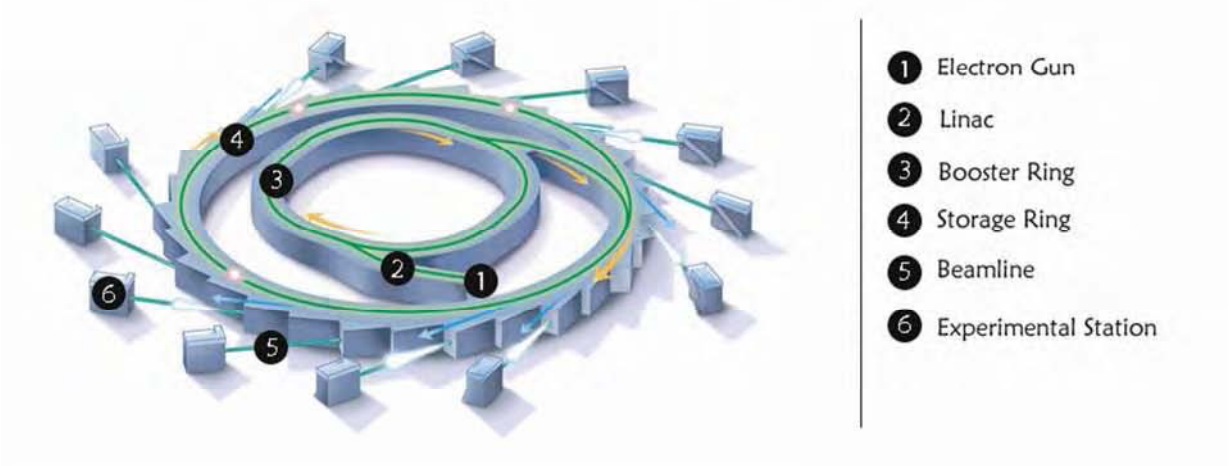

Figure 2.8: Schematic diagram of a synchrotron source, adapted from Ref[14]

There are many advantages of synchrotron radiation, foremost is that the beams produced are of very high intensity, several orders of magnitude greater than conventional sources. The beams produced are also tunable, highly collimated and offer a high degree of polarization.

High quality data for structural refinement work in this project was collected at station I11, at the Diamond facility, UK. The station utilises a heavy duty diffractometer equipped with 5 sets of multi-analysing crystal (MAC) arrays leading to a total of 45 MAC channels as shown in Figure 2.9. Automatic sample changing was made possible with the use of a robotic arm and a 200 specimen carousel.

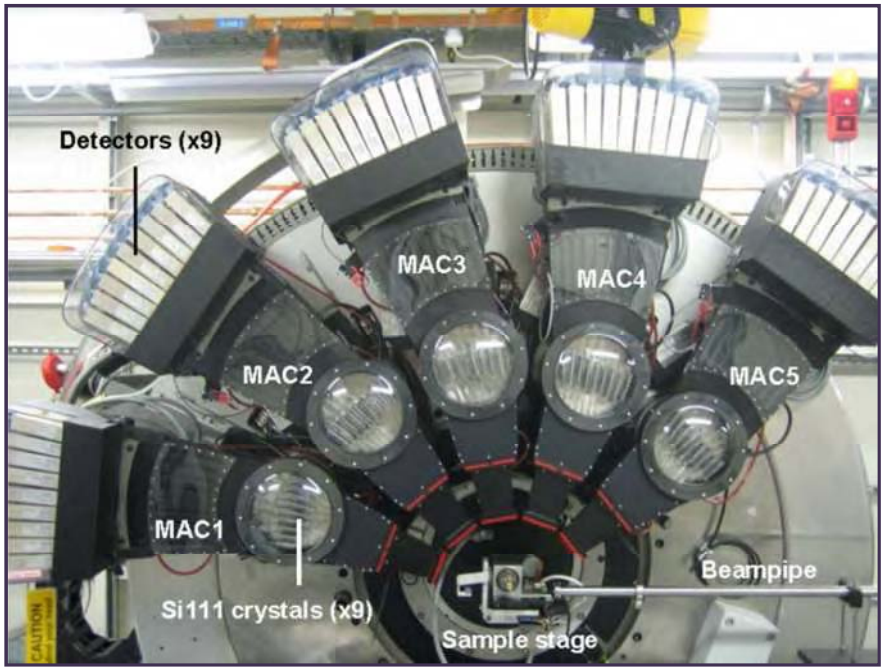

Figure 2.9: Five MAC arms each with nine Si(111) analysing crystals and nine detectors[15].

Samples were packed into glass capillaries of 0.5 mm diameter and sealed. The sealed capillaries were fixed onto magnetic holders and pre-aligned before mounting onto a sample spinner, thus improving the randomisation of the grain orientations and reducing any preferred orientation effects. The exact wavelength of the radiation used was determined from silicon standards, but was typically set at ca. 0.83 Å.

2.5 Rietveld Refinements

The Rietveld method[16,17] is a 'whole-pattern-fitting structural refinement' technique widely employed to refine crystal structures from diffraction data. In the Rietveld method, least squares refinements are carried out until the best fit is obtained between the entire observed powder diffraction pattern and the entire calculated pattern. The calculated pattern is obtained using a structural model that describes the unit cell size and shape as well as the atomic positions, occupancies and thermal motions of the atoms present. This is combined with various experimental parameters that describe the peak shapes and background. The function being minimized in the refinements is the residual S_y, summed over all data points.

$$S_y = \sum_i w_i (y_i - y_{ci})^2$$

Equation 2.7: The residual S_y. w_i = weighting factor, $1/y_i$, y_i = observed intensity at the *i*th step, y_{ci} = calculated intensity at the *i*th step

The intensities of the peaks in the calculated pattern, y_{ci}, are calculated from Equation 2.8, which is based upon both the structure factor $|F_K|^2$ and contributions from the background y_{bi}.

$$y_{ci} = S \sum_{K} L_K |F_k|^2 \emptyset(2\theta_i - 2\theta_K) P_K A + y_{bi}$$

S is the scale factor

K represents the miller indices (*hkl*) for a Bragg reflection

L_K contains the Lorentz, polarisation and multiplicity factors

F_K is the structure factor for the Kth Bragg reflection

Φ is the reflection profile function

ϑ_i is the 2θ position of the ith profile point in the diffraction pattern

ϑ_K is the calculated (ideal) 2θ position of the Kth reflection.

P_K is the preferred orientation function

A is the absorption factor

y_{bi} is the background intensity at the ith step

Equation 2.8: Equation for the calculated intensities of the Rietveld model.

The least squares minimisation procedure acts to reduce the difference between the observed and the calculated patterns by minimising the difference between y_i and y_{ci}. It achieves this by simultaneously refining a number of different parameters that contribute to y_{ci}. These include both sample specific parameters such as atomic coordinates, temperature factors, lattice parameters and fractional site occupancies as well as experimental factors such as zero point, background and absorption. The contributions of various parameters to a diffraction pattern have already been summarised in Section 2.4.1. Given the nature of the technique the correct choice of starting model is essential and thus approximate structural models are required for all phases present in the sample being analysed.

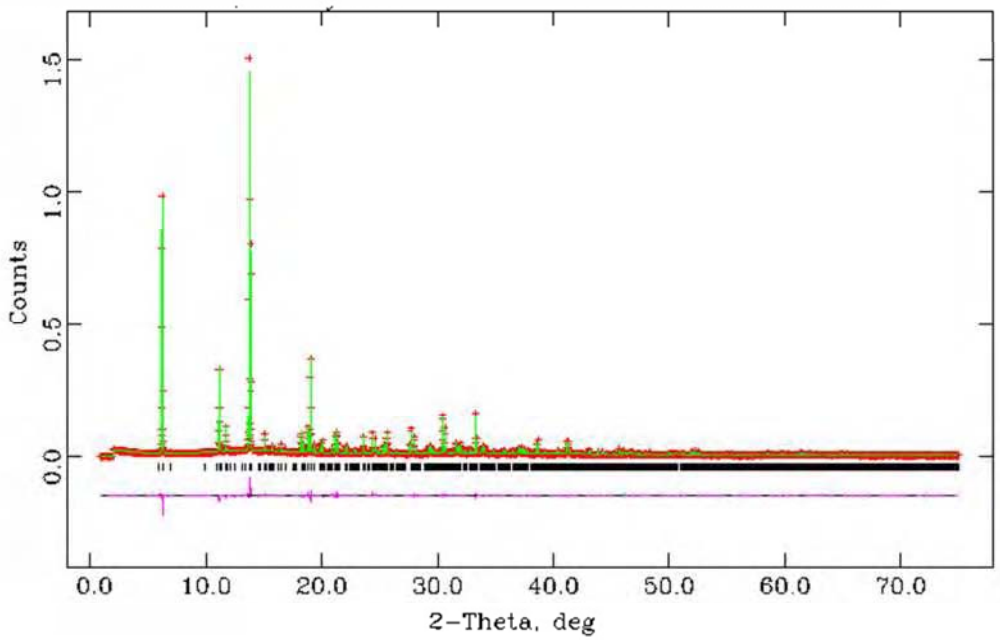

Figure 2.10: An example Rietveld refinement plot. The observed and calculated intensities are shown in red and green respectively. The difference between them is shown underneath in pink whilst the black tick marks indicate the peaks associated with the phase.

Refinement progress can be easily followed by examination of the observed, calculated and difference plots, an example is shown in Figure 2.10. In addition to this, there are many numerical terms that reflect the progress of the refinement. The most meaningful of these, from a mathematical point of view, is the weighted profile *R*-value (R_{wp}), defined by Equation 2.9, as the numerator is the residual *S* being minimized.

$$R_{wp} = \left\{\frac{\sum w_i(y_i - y_{ci})^2}{\sum w_i(y_i)^2}\right\}^{1/2}$$

Equation 2.9: The weighted profile

Ideally the final R_{wp} value should approach R_{exp}, the statistically expected *R* value:

$$R_{exp} = \left[\frac{N-P}{\sum_i^N w_i y_i(obs)^2}\right]^{1/2}$$

Equation 2.10: The expected *R* value. *N* is the number of observations and *P* the number of parameters.

The 'goodness of fit' indicator χ^2, expressed in Equation 2.11 gives the ratio between these two values and is the value usually quoted in literature to reflect the success of the refinement - ideally this should equal 1.

$$\chi^2 = \left(\frac{R_{wp}}{R_e}\right)^2$$

Equation 2.11: The goodness of fit indicator

Another commonly used structural agreement factor is R_F^2:

$$R_F{}^2 = \frac{\sum\left|F_{obs}^2 - F_{calc}^2\right|}{\sum\left|F_{obs}^2\right|}$$

Equation 2.12: The structural agreement factor R_F^2

The value R_F^2 is similar to that reported for single crystal refinements. It compares the observed and calculated intensity at the positions of Bragg reflections predicted from the unit cell of the structure and as such is biased towards the structural model.

As well as these and other numerical indicators[18] the calculated atomic bond distances, angles and fractional occupancies should be sensible and the latter consistent with the

chemical composition of the sample, if the refinement has been successful. It is important not to rely solely on the numerical values of fit when assessing the success of a refinement as they can be influenced by non-model related effects. R_{wp} for example is vulnerable to giving high values if the background is inadequately described or if some peaks are not accounted for. Conversely, artificially low values can be given if there is a high well-fitted background, as a significant part of the intensity is accounted for by the background function. It is therefore imperative to use both the graphical and the numerical data together with the calculated structure values in the assessment of the refinement.

All Rietveld refinements in this work were performed using the EXPGUI GSAS software suite[1].

2.6. Pair Distribution Function (PDF) Analysis

2.6.1. Introduction

PDF analysis is a method which can extract structure related information from powder diffraction data. Diffraction intensity consists of two parts; Bragg scattering and diffuse scattering. Bragg scattering contains information about the long range average structure of the material. The diffuse scattering contains information about the local atomic arrangements, disorder or two body correlations, such as chemical short range order or correlated motion. In the Rietveld method the diffuse scattering is discarded as part of the background, so the aperiodic (disorder) information is lost. The PDF method utilises both the Bragg and the diffuse scattering, so it provides information about both the long and short

range atomic ordering in a given material[19]. Structural information is provided as distances between atoms in the structure. The PDF method was traditionally applied to glasses, liquids and amorphous materials[20] where no crystalline order is present and so traditional crystallographic methods were of little use. However PDFs are used increasingly for structural analysis of local order in crystalline materials[21].

The PDF, *G*(r) is a real space function giving the probability of finding pairs of atoms separated by distance *r* in a given material. It is defined as:

$$G(r) = 4\pi r[\rho(r) - \rho_0]$$

Equation 2.13: The pair distribution function. ρ(r) is the microscopic pair density, ρ_0 is the average number density and *r* the radial distance.

The PDF, *G*(*r*) is obtained by Fourier transform of the normalised scattering intensity *S*(*Q*):

$$G(r) = \frac{2}{\pi}\int_0^\infty Q[S(Q) - 1]\sin(Qr)\,dQ$$

Equation 2.14: Equation for the Fourier transform of *S*(*Q*) to get *G*(*r*). *Q* is the scattering vector. For elastic scattering $Q = 4\pi r \sin(\theta)/\lambda$ where 2θ is the scattering angle and λ the wavelength of the radiation used.

S(*Q*) is a continuous function of intensity vs *Q* which converges to unity at high *Q* as shown in Figure 2.11. It is defined as:

$$S(Q) = \frac{IQ - \sum c_i |f_i(Q)|^2}{|\sum c_i f_i(Q)|^2} + 1$$

Equation 2.15: The normalised scattering intensity. *I*(*Q*) is the corrected measured scattered intensity normalised by the flux and number of atoms in the sample, c_i is the atomic concentration and f_i the X-ray atomic factor.

Corrections for background, Compton scattering, absorption, atomic scattering factors, detector dead time, diffraction geometry and polarisation are applied to the raw data and then normalised with respect to the number of atoms in the sample to obtain *S*(*Q*). Further corrections for oblique incidence angle dependence and the detector energy dependence are also required when using an image plate area detector[22,23]. The true background intensity has to be independently measured by carrying out a measurement without the sample.

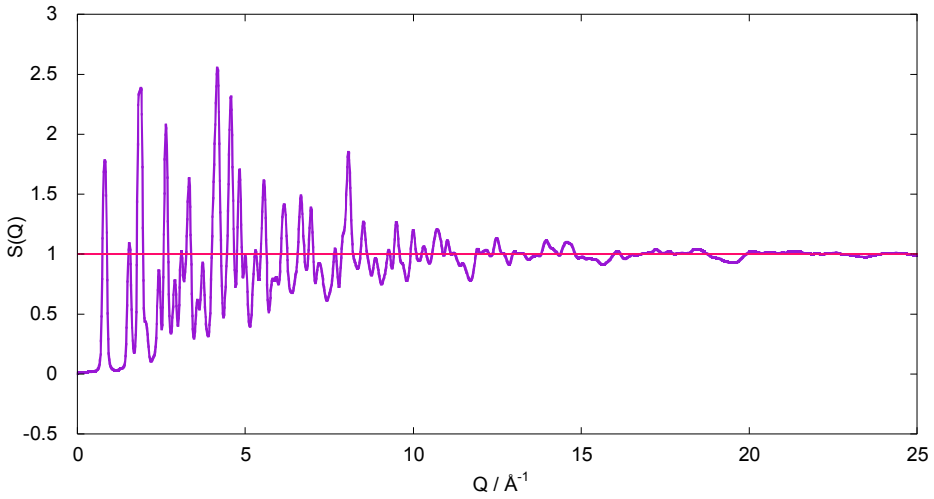

Figure 2.11: An example plot of the normalised scattering intensity.

PDF patterns can be determined experimentally by diffraction measurements over a wide range in momentum transfer *Q*, using X-rays, neutrons, electrons or even by EXAFS. Programs like PDFgetX2[2] can be used to apply the necessary corrections to the data and to perform the Fourier transform to obtain the PDF. The PDF pattern consists of a series of peaks as shown in Figure 2.12. Study of this can tell us about both the local structure (low r region) and average structure (high *r* region). The peak positions give the distances of atom pairs in real space. Peak width analysis provides information about correlated motion[24] and the coordination number of the atom pair can be obtained through integration of the peak intensity.

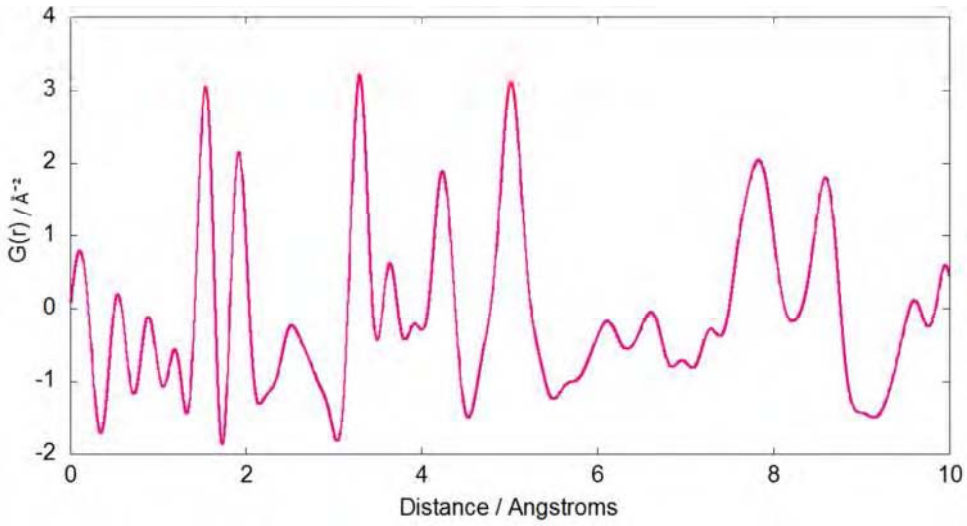

Figure 2.12: An example PDF pattern.

Requirements for obtaining a good PDF include high *Q* resolution, good counting statistics at high *Q*, low instrument background and a high Q_{max}. The Fourier transform in Equation 2.14 ideally requires the data to be measured up to *Q* infinity which is impossible. The cut-off of *Q* has a detrimental effect on the real space resolution of the PDF and the termination at a

value of Q_{max} will cause so called termination ripples in the PDF. Extending Q_{max} lowers this effect. As $Q = 4\pi r \sin(\theta)/\lambda$ (for elastic scattering) and since sinθ ≤ 1, the experimentally accessible range for Q is limited to < 4π/λ. Copper K_α sources used in laboratory X-ray facilities are limited to a Q range of about 8 $Å^{-1}$. However recent advances using molybdenum and silver tubes in laboratory equipment have yielded Q ranges of 14 $Å^{-1}$ and 16 $Å^{-1}$ respectively[25]. Ideally for PDF analysis a Q range of at least 20-30 $Å^{-1}$ is required so synchrotron and pulsed neutron sources are employed.

2.6.2 Data Collection

The data in this project was collected at Station 11-ID-B, Advanced Photon Source, Argonne National Lab., USA, using λ=0.137024 Å and a GE amorphous Si detector. The use of the 2d detector allowed for rapid acquisition PDF experiments in which the data is collected in a single shot reducing the data collection time from 8 hours to a matter of seconds[22].

The samples were packed in kapton capillaries to minimise the background. Data from empty kapton capillaries were also collected and subtracted from subsequent measurements, to give more accurate results. FIT2D[26] was employed to integrate the data and PDFgetX2[2] to process it.

2.6.3. PDF Structure Refinement

Full profile refinement of the PDF based on a structural model can be carried out using full profile least squares fitting using programs such as PDFFit[27] or PDFGui[3]. In order to fit an

experimental PDF one needs to calculate a PDF from a structural model. This can be done using the relationship:

$$G_{calc}(r) = \frac{1}{r}\sum_{i}\sum_{j}\left[\frac{b_i b_j}{\langle b\rangle^2}\delta(r - r_{ij})\right] - 4\pi r\rho_0$$

Equation 2.16: Equation to calculate a PDF for a structural model, summed goes over all pairs of atoms *i* and *j* within the model separated by r_{ij} .The scattering power of atom *i* is b_i. In the case of neutron scattering b_i is simply the scattering length, for X-rays it is the atomic form factor evaluated at a defined value of *Q* (set by the command X-ray). The default value is *Q* = 0 in which case b_i is just the number of electrons of atom *i*.

Once the calculated and experimental PDFs are obtained an approach similar to the Rietveld method (Section 2.5) is followed. Structural parameters in the model such as atomic positions, thermal factors and occupancies are varied in such a way as to improve the agreement between the calculated and the experimental PDF.

The PDF peak width contains contributions from thermal and zero point displacements as well as static disorder. For small distances, the motion of two atoms can be strongly correlated leading to a sharpening of the first peak(s) in the observed PDF. The program PDFGUi[3] offers two mechanisms to account for this. The first is to sharpen the peaks at low distance using the parameters *rcut* and *sratio*. *sratio* defines the low to high distance PDF peak ratio from which peaks below the defined value of *rcut* are sharpened. Alternatively refinement of the delta terms; *delta1* and *delta2* can be employed. In PDF the peak width is defined as:

$$\sigma_{ij} = \sigma'_{ij}\sqrt{1 - \frac{\sigma_1}{r_{ij}} - \frac{\sigma_2}{{r_{ij}}^2} + {Q_{broad}}^2 {r_{ij}}^2}$$

Equation 2.17: PDF peak widths where σ'_{ij} is the peak width without correlated motion, $\frac{\sigma_1}{r_{ij}}$ (delta1) and $\frac{\sigma_2}{{r_{ij}}^2}$ (delta2) are terms to correct for correlated motion.

The two terms are highly correlated so they must not be refined together; *delta1* describes the high temperature behaviour and *delta2* the low temperature behaviour. The final term in the equation deals with the effects of peak broadening as a result of the *Q*-resolution of the diffractometer. This is only significant at large distance ranges and can be accounted for using the *Qbroad* parameter in the PDFGUI[3] program. Limited *Q* resolution can also result in exponential dampening of the PDF peaks. The parameter *Qdamp* can be used to model this.

A scale factor must also be refined to deal with the relative peak intensities. It keeps the overall ratio between the intensities of the peaks the same, relative to the total pattern intensity.

The success of the refinement can be followed both visually by the fit as illustrated in Figure 2.13 and by the numerical goodness of fit indicator, the weighted profile agreement factor R_{wp}:

$$R_{wp} = \left\{\frac{\sum_i w(r_i)\,[G_{obs}(r_i) - N_m G_{calc}(r_i)]^2}{\sum_i w(r_i)[G_{obs}(r_i)]^2}\right\}^{\frac{1}{2}}$$

Equation 2.18: The weighted profile agreement factor. $G_{obs}(r)$ and $G_{calc}(r)$ are the measured and model PDFs and $w(r)$ is the weighting factor.

As the points in the PDF are statistically correlated there is not the same statistical significance as crystallographic R_{wp} factors.

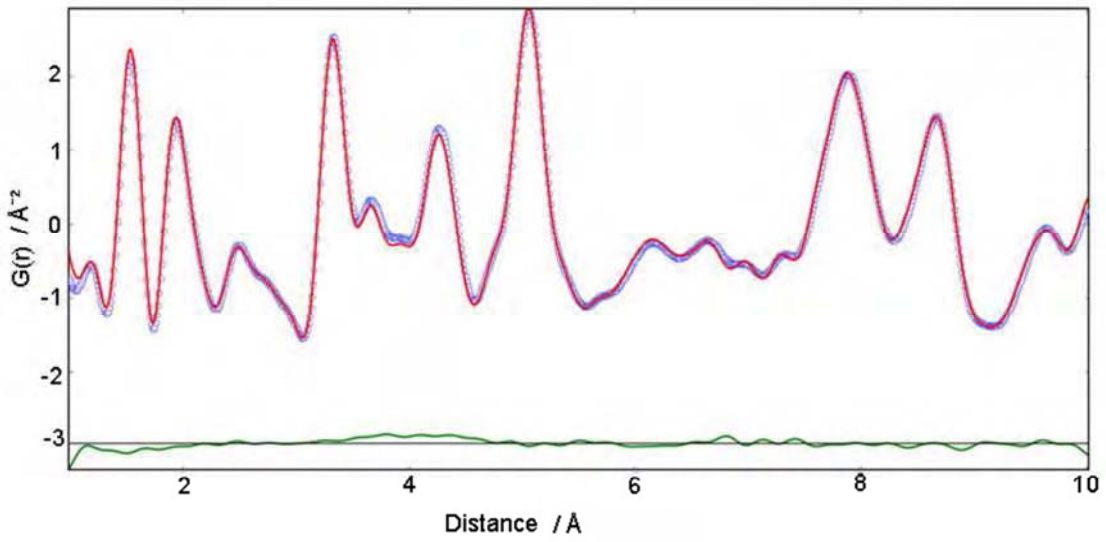

Figure 2.13: An example PDF refinement fit. The red line is the PDF from the model, the blue line is the PDF from the data and the green line is the difference between the two.

All PDF refinements in this work were conducted with the PDFGUI[3] program.

The benefits of the PDF refinement method compared to the traditionally used Rietveld method are that it can be used to study amorphous and poorly crystalline samples where XRD yields little or no information. It can also be employed to investigate short range ordering, local defects, stacking faults in layered structures and metal ordering in mixed metal systems etc. However given the nature of the PDF technique whereby both the Bragg and diffuse scattering is considered, the refinement results for a given crystalline phase are not expected to be as reliable as those values obtained from a corresponding Rietveld refinement. The presence of any amorphous and/or impurity phases would affect the values

obtained, for example, if amorphous SnO_2 was also present in a product containing crystalline TiO_2, there would be a significant amount of peak overlap due to the two phases and the values obtained from the refinement of TiO_2 would be altered by the data from the amorphous SnO_2.This is less likely to be a problem in a Rietveld refinement where only the Bragg peaks from the crystalline phase are considered. In addition to this, it should also be noted that the XRD data used in a Rietveld fit contains a lot more data points than the corresponding PDF used for the PDF refinements (150 sharp peaks in an XRD pattern cf. 20 broad peaks in a PDF) and consequently this will also have a detrimental effect on the reliability of the PDF results compared with those from a Rietveld fit.

2.7 Thermogravimetric Analysis + Mass Spectroscopy (TGA-MS)

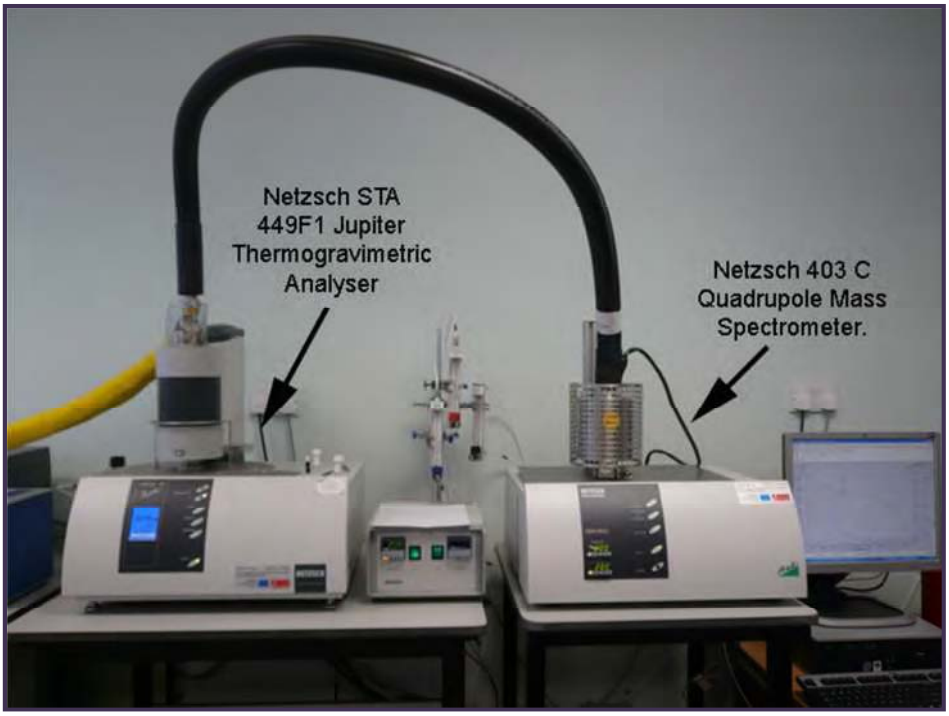

Figure 2.14: In-House TGA-MS Equipment

Thermogravimetric analysis monitors the change in mass of a sample as a function of temperature and/or time within a controlled atmosphere. Any changes in the mass may indicate the loss of some species, e.g. water, from the sample. However, many thermal changes in materials (e.g. phase transitions) do not involve a change of mass and so differential thermal analysis (DTA) can be carried out at the same time.

In DTA the temperature of the sample is compared with that of a thermally inert reference material (typically Al_2O_3). Until a thermal event occurs there should be no discernable difference between the temperature of the sample and that of the reference. When the temperature of the sample falls behind that of the reference material an endothermic event is recorded and is displayed as a 'dip' in the DTA curve. If the temperature of the sample advances that of the inert reference an exothermic event is recorded which is displayed as a 'peak'.

Any gases evolved from the sample are transferred to the Quadrupole Mass Spectrometer (QMS) whereby they are converted into positively charged ions by an ion source. The different ions are detected according to their M/Z ratio which allows for qualitative analysis of the gases and therefore the thermal reactions occurring.

In this work TGA-MS was used to monitor the decomposition of the metal phosphates whilst detecting the gases evolved. Small amounts of sample (~50 mg) were heated over a temperature range of 30 – 800 °C at a rate of 10 °C/min in a nitrogen atmosphere. The experiments were undertaken on a Netzsch STA 449F1 Jupiter (TGA) and Netzsch 403 C (QMS) as shown in Figure 2.14.

2.8 X-ray Fluorescence (XRF)

2.8.1 Basics of XRF

X-ray fluorescence (XRF) is an emission technique that provides both qualitative and quantitative elemental analysis of a sample. In XRF the sample is bombarded with high energy X-rays which result in electrons being ejected from the inner shells (typically *K* and *L*). The vacancies created render the atoms unstable and so outer shell electrons fill these 'holes'. The excess energy from these transitions is released in the form of a photon (X-ray fluorescence) as depicted in Figure 2.15. The energy of the photon corresponds to the difference in energy between the initial and final states of the transferred electron and is therefore characteristic of the element present.

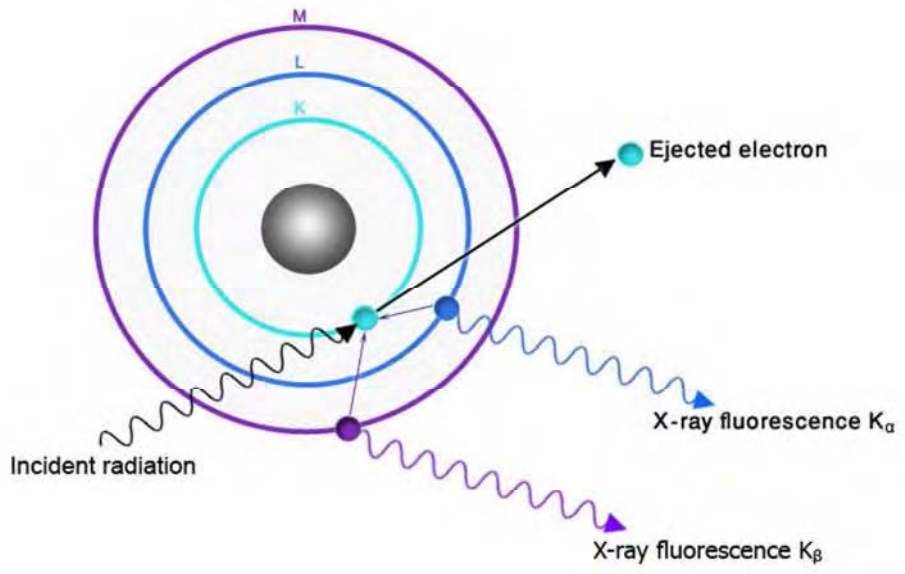

Figure 2.15: Principle of XRF

The fluorescent radiation can be analyzed either by sorting the energies of the photons (energy-dispersive analysis) or by separating the wavelengths of the radiation (wavelength-dispersive analysis). A typical X-ray spectrum will display multiple peaks of different

intensities. From the spectral peak positions the elements present can be identified and from their intensities a quantitative analysis made.

The Auger Effect

Sometimes, as the atom returns to its stable condition, instead of emitting a characteristic X-ray the excess energy may be used to reorganise the electron distribution within the atom leading to the ejection of electron(s) from the outer shell. This is known as the 'Auger effect'[28] and the ejected electrons; Auger electrons. An important consequence of this effect is that the number of photons produced from an atom is lower than expected. This effect is more prevalent with the low Z elements as their electrons are more loosely bound and their characteristic X-rays more readily absorbed.

2.8.2 Instrumentation

The use of a primary X-ray beam to excite fluorescent radiation from the sample was first proposed by Glocker and Schreiber[29] in 1928 to overcome the limitations arising from the use of direct electron excitation e.g. sample volatility and poor conduction. X-ray tubes are now commonly used as the primary source of X-rays, the details of which were discussed in Section 2.4.2. For routine XRF the provision of a tube giving high spectral output over a wide wavelength range is required. From this point of view a middle order atomic number anode (e.g. rhodium) is desirable as the electron back scatter is only moderate.

The fluorescence process is inefficient, and the fluorescent radiation much weaker than the primary beam. Furthermore, radiation from lighter elements is of low energy and has low penetrating power, so is severely attenuated when the beam passes through air for any distance. For high-performance analysis, the X-ray tube to sample to detector path is maintained under high vacuum and consequently most of the working parts of the instrument are located in a large vacuum chamber.

The fluorescent radiation from the sample passes through a mask to cut out any unwanted signals, namely those from the sample holder. A collimator is employed to improve the resolution. Possible detectors include gas filled proportional counters and scintillation counters. The gas proportional counter comprises a cylindrical metallic tube in the middle of which the counting wire is mounted. This tube is filled with a suitable gas which becomes ionised when the fluorescent photons penetrate the detector. The resultant positive ions move to the cathode (the metallic tube), and the free electrons to the anode (the wire) due to the potential difference maintained. The electrons reaching the anode produce a current. The number of electron-ion pairs created is proportional to the energy of the photon. There are two models of gas proportional counters: the *flow counter* and the sealed *proportional counter*. The flow counter is connected to a continuous supply of counting gas and can be equipped with very thin entrance windows rendering it suitable for light elements. Conversely the proportional counter has a closed volume and requires a thick window normally made of beryllium which prevents the measurement of very light elements (beryllium to sodium).

The scintillation counter utilises a two step process; firstly the X-ray energy is converted into a lower energy state by use of a phosphor and secondly the conversion of this longer

wavelength radiation into volts by a photomultiplier. The phosphors used in XRF comprise a sodium iodide crystal in which thallium atoms are homogeneously distributed. The fluorescent energy absorbed by the phosphor causes excitation of the atoms that result in emission of radiation e.g. a 'flash' of light which strikes a photocathode. A photomultiplier converts this energy into a current which can be used to produce a voltage. The height of the pulse of voltage produced is proportional to the energy of the detected X-ray quantum.

In this work, measurements were performed on a Bruker S8 high end wavelength dispersive X-ray fluorescence (WDXRF) spectrometer. Spectra plus software version 2.0 was used for the analysis. The set up of the S8 machine is shown in Figure 2.16. It features two detectors which can be used individually or in tandem. For light elements the proportional counter is used and the scintillation counter for the heavier elements.

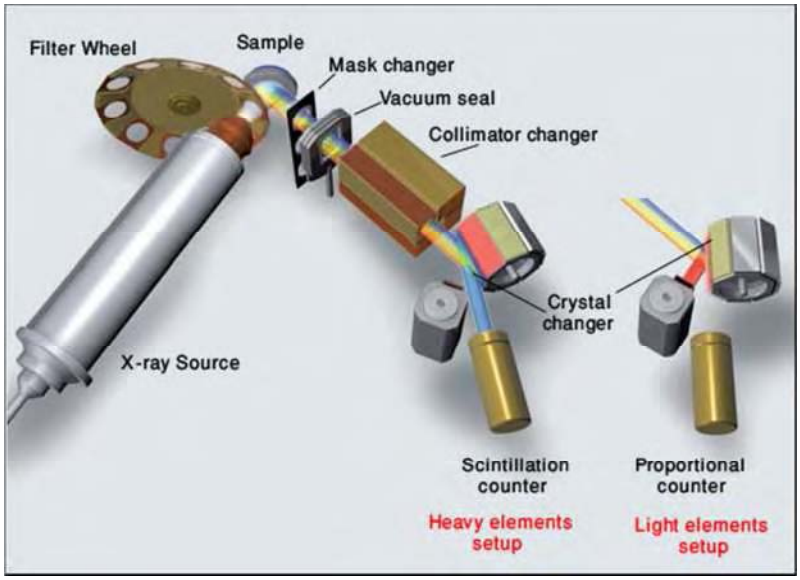

Figure 2.16: Experimental set-up of the Bruker S8 adapted from ref[30]

2.8.3 Matrix Effects

A certain degree of spread is seen in the count data due to random errors associated with each reading, the three most important sources of random error are counting statistics, generator and X-ray tube stability and other equipment errors.

Residual systematic errors due to the sample are called matrix effects. These fit into two broad categories, elemental interactions and physical effects. These can be further broken down to give the four basic types of matrix effect which will be discussed separately below. It should be noted that one or more of these effects can occur simultaneously. Both internal and external standards can be employed to help reduce these effects.

2.8.3.1 Elemental interactions

Absorption

Any element in the matrix can absorb or scatter the fluorescence from the element of interest. Due to this the number of fluorescent photons leaving the sample will be significantly less than the number initially produced. As most of the excited atoms of the element lie deep within the sample matrix, the fluorescent radiation must travel through the volume of the matrix in order to leave the sample to be detected. Consequently the contribution of the outer layers of the sample will be greater than that of the inner layers. Figure 2.17 illustrates the effect of absorption on the calibration. One way to overcome this is by manually altering the matrix e.g. with the detection of a heavy element in water (as per curve 4 in Figure 2.17), the water being light will give a very high background due to scattering of the primary beam photons by the sample surface. Adding aluminium oxide alters the matrix and reduces the background thereby lowering the effect.

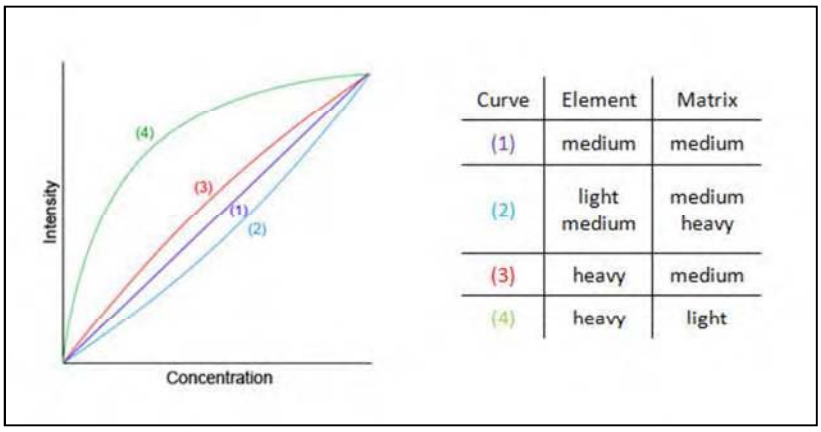

Curve	Element	Matrix
(1)	medium	medium
(2)	light medium	medium heavy
(3)	heavy	medium
(4)	heavy	light

Figure 2.17: Effects of absorption on calibrations.

Enhancement

The fluorescent X-rays from one element can further excite other elements in the matrix, thereby enhancing the signal. Consequently the number of characteristic photons actually measured is in excess of that predicted due to normal excitation by the primary radiation.

2.8.3.2 Physical effects

Particle size and surface effects

The volume of sample which contributes to the measured fluorescent radiation is dependent upon the effective penetration depth of the measured wavelength. It is therefore imperative to have a completely homogeneous sample with a smooth flat surface. Compositional variations in depth lead to results that are not representative of the whole sample. One of the best ways to overcome this effect is though the use of fused beads (see section 2.8.4).

Effects due to the chemical state

The wavelength of the fluorescence detected is dependent upon the chemical state of the element in question. Changes in electron density due to valence or co-ordination are associated with the outermost orbitals. Whilst these are not generally featured in XRF they can be and so significant wavelength shifts due to such variations in chemical composition can be seen. If an element is present in the matrix in two different oxidation states then two peaks will be seen in the spectrum corresponding to two wavelengths.

2.8.4 Sample Preparation

XRF can be carried out on samples in various forms, including liquids, pressed pellets and fused beads. The quality of the sample preparation is very important and ideal samples (and standards) should be reproducible and representative of the whole material. Samples and standards must also cover the same irradiated area and be free from surface contamination.

Liquid samples

Analysing samples in liquid form can overcome many of the matrix effects. However support film and solvent choice can introduce further problems. The use of a liquid sample holder and helium atmosphere is required.

This preparation method was used in this work to monitor the metal concentrations during synthesis of the mixed metal phosphates. Mylar® polyester film was used as the support film

and care was taken to ensure that no 'sagging' occurred therefore avoiding errors from a non flat sample surface.

Pressed Pellets

The quickest and simplest method of preparation for powder samples is to press them directly into pellets of constant density, with or without the use of a binder. Compression of the powder in a pellet die yields a dense flat surface that provides good analytical accuracy and sensitivity. Choice of binding agent must be made with care; it must be free from significant contaminant elements and have low absorption. It must also be stable under vacuum and irradiation conditions. Of the large number of binding agents available, the most useful are wax and ethyl cellulose.

Certain matrix effects can be prevalent when using pressed pellets as a homogeneous sample can be hard to obtain. For example when a powder is pressed into a pellet, the finer particles concentrate at the surface and the heavier at the bottom. This can lead to a non-representative sample surface and therefore inaccurate results.

In this work powder samples were pressed into 10 mm pellets using a Graseby Specac pellet press. 500 mg of sample were combined with 100 mg of wax binder as the pellets without binder were brittle and prone to chipping.

Fused beads

This method is employed when it is difficult to obtain a homogenous mixture, when segregation occurs and also to significantly minimise matrix effects - all of which are problems encountered with pressing pellets. The fusion procedure consists of heating a mixture of powdered sample with flux at high temperatures (800 to 1250 °C) in an inert heat resistant crucible until the flux melts and the sample dissolves in it yielding a homogeneous melt. Upon cooling a fused glass like bead is obtained. These beads can be stored in desiccators for long periods of time and be reused. The elements within the sample become oxidised into their most stable form. For borate fusions to be successful, the sample when fused must be in the form of an oxidised, inorganic compound.

Standard crucibles are made from platinum, often with the addition of small amounts of gold to prevent wetting from the borate fusion mixture and to reduce wastage and aid cleaning. The flux acts as a matrix and is typically either lithium tetraborate ($Li_2B_4O_7$, mp 920 °C), or a mixture of that and lithium metaborate ($LiBO_4$, mp 845 °C). Lithium tetraborate is better for basic oxides and the mixture for acidic oxides. Non-wetting agents, which are iodides or bromides, can be added in small quantities to a fusion to increase the surface tension of the melt so that the molten flux does not stick to the crucible. The quantity added is important as too much or too little can affect the bead shape. Through trial and error the following procedure was found to be most suitable for the samples used in this work. A 10:1 ratio of flux (3.5 g) to sample (0.35 g) was ground together in a mortar and pestle and heated in a crucible (95% platinium 5% gold) for 6 minutes at 1250 °C. After this time approximately 15 mg of ammonium iodide was added as a non wetting agent before it was placed back in the oven for a further 6 minutes. When removed the mixture was swirled to

eliminate air bubbles, re-heated for 30 seconds and taken out to cool. This method produced 28 mm beads of 3-4 mm thickness which was ideal.

2.8.5 Calibrations

By use of a range of standards a calibration curve can be constructed in which the peak response of a characteristic line is correlated with the concentration of the element present. For obvious reasons, the calibration standards must be indicative of the samples to be measured and prepared in the same way.

Calibration of the mixed zirconium-titanium phosphates

Zirconium and titanium oxide mixed in various stoichiometric amounts were used to make the standards for the calibration of this series. Calibrations with zirconium are always difficult for a number of reasons. Firstly, no zirconium compound is ever completely free of hafnium and secondly the melting point of zirconium oxide is very high and exceeds the operating temperature of the ovens. Due to this zirconium oxide cannot be used to form calibration standards via the fusion method. The nitrates and chlorides are not considered pure enough and so the fused bead method was not possible for this series of compounds. Instead the calibration had to be done using pressed pellets.

The original calibration did not produce as good a calibration curve as expected. To address this it was found that better results were obtained when the oxides had been heat treated to remove water prior to pelletizing to remove added matrix effects from unknown water

quantities present. Also ensuring that the ratios of zirconium to titanium within the standards were not in a basic mathematical sequence prevented the calibration from being mathematically biased.

The final calibration used for this series had standard deviations for the titanium and zirconium of 1.68 % and 3.19 % respectively. The calibrations curves are shown below in Figures 2.18 and 2.19.

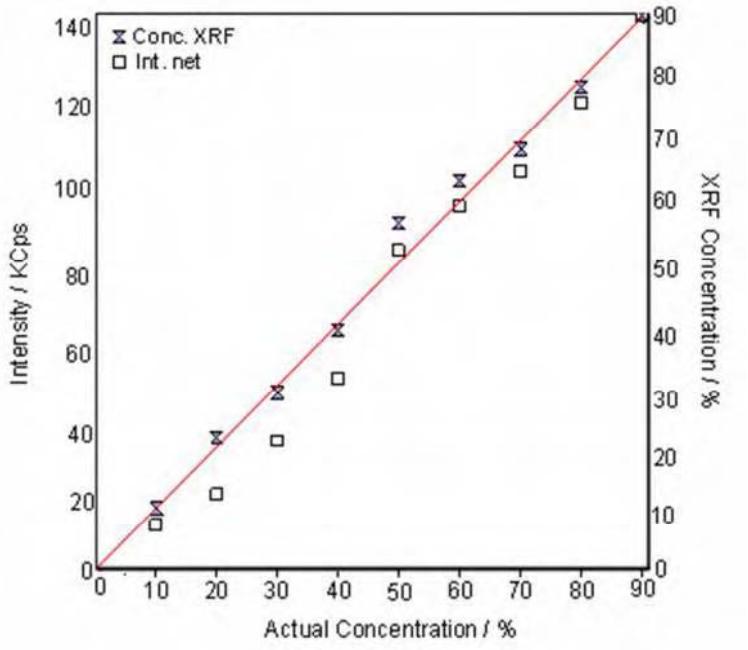

Figure 2.18: Pressed pellet XRF calibration curve for titanium.

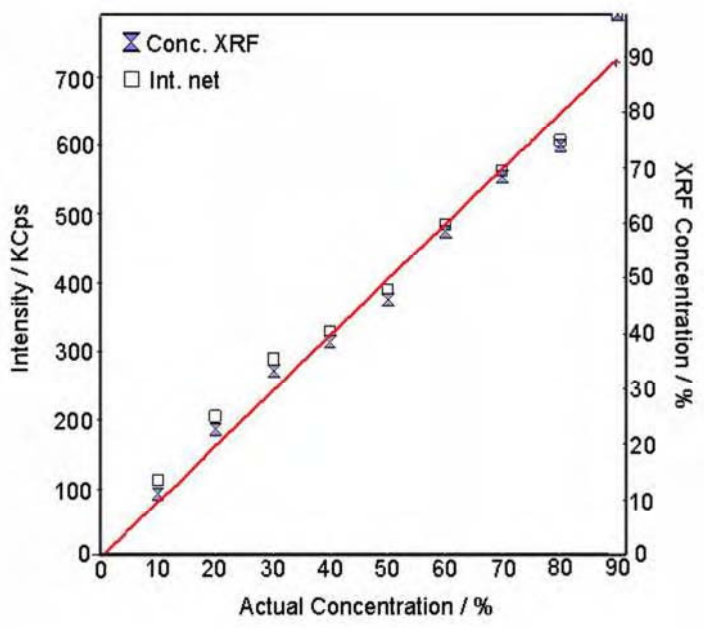

Figure 2.19: Pressed pellet XRF calibration curve for zirconium.

Calibration of the mixed germanium titanium phosphates

With this series of compounds it was possible to produce fused bead calibration standards from a mixture of titanium and germanium oxide. The final calibration gave standard deviations of 2.97 % for titanium and 1.46 % for germanium. The calibration curves are illustrated in Figures 2.20 and 2.21.

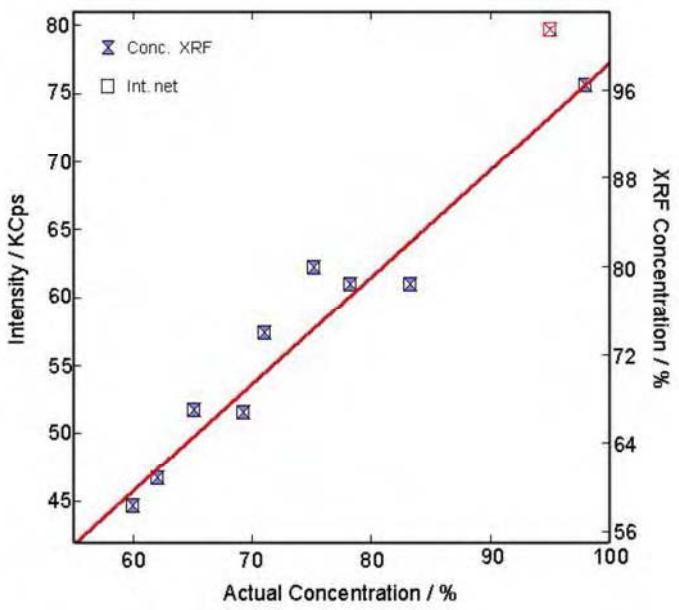

Figure 2.20: Fused bead XRF calibration curve for titanium.

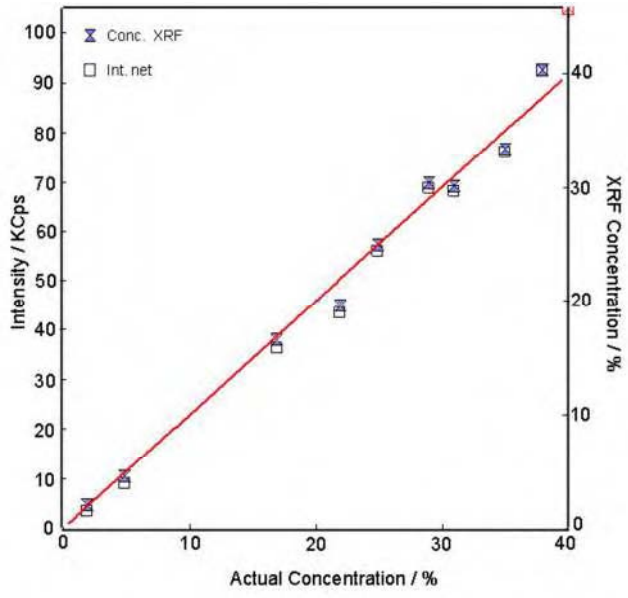

Figure 2.21: Fused bead XRF calibration curve for germanium.

2.9 Leaching Experiments

2.9.1 Sample Preparation

The samples used in the leaching experiments were ground using a pestle and mortar, manually sieved through a 75 µm sieve and weighed to ensure a known maximum surface area. By modelling the particles as tetrahedra the surface area of the samples could be calculated using Equation 2.19:

$$SA = \frac{862.2}{d \times 10000} m$$

Equation 2.19: Calculation for the sample surface area. SA = sample surface area (m^2), *d* = density of the sample (g cm^{-3}), *m* = mass of the sample (g).

2.9.2 Soxhlet Extraction

Leach testing was carried out using a Soxhlet process whereby the sample is constantly exposed to distilled water at temperatures close to 100 °C. Soxhlet extraction was originally designed for the determination of fat in milk[31] but it remains one of the most accepted leaching techniques used[32]. It has been used in this work to ascertain the leach rate of selected ion-exchanged materials. In this process a known amount of sample was placed in a cellulose extraction thimble positioned inside the main chamber of the Soxhlet extractor. The Soxhlet extractor was connected to both a round bottomed flask containing the extraction solvent which in this case was the leachate, 100 ml of deionised water, and to a condenser, as shown in Figure 2.22. The solvent was heated to reflux causing it to vapourise

and condense back into the main Soxhlet chamber onto the sample. The chamber automatically emptied by the siphon side arm when almost full, siphoning the solvent and any extract back into the round bottomed flask.

The leach tests were run for 1, 3, 7 and 14 days, after which the leachates were re-measured to ensure a constant volume of 100 ml. The leachate samples including a blank sample were sent to Stephen Baker at the University of Birmingham for Inductively Coupled Plasma Atomic Emission Spectroscopy (ICP-AES) analysis. A brief description of ICP-AES can be found in Section 2.10. The solid samples recovered were analysed by X-ray diffraction.

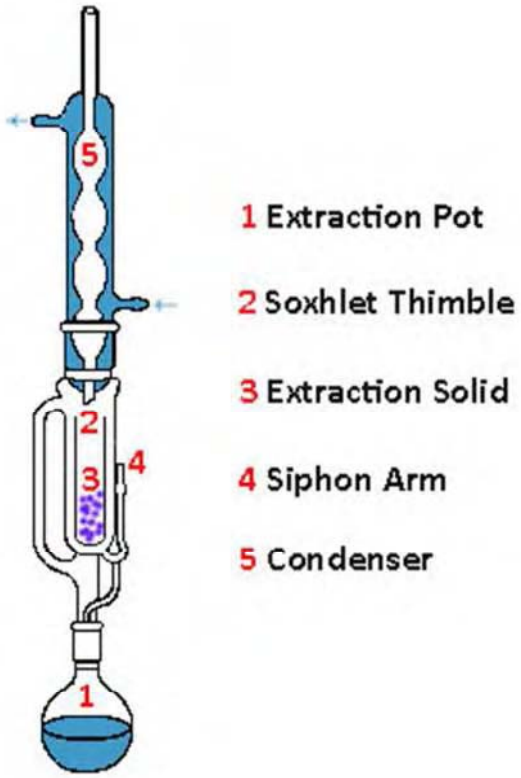

Figure 2.22: Schematic diagram of a Soxhlet Extraction

2.9.3 Leach Rate Calculations

Leach rates were calculated using the following formula[33]:

$$LR_t = \frac{[X]_t \times 10^{-3} \times V}{SA \times t} \times N_f$$

$\boldsymbol{LR_t}$ = Leach rate at time *t* (g m^{-2} d^{-1})

$\boldsymbol{[X]_t}$ = Concentration of ion of interest (strontium) in the leachate at time *t* (mg l^{-1})

V = Volume of leachate (l)

SA = Surface area of the solid sample (m^2)

t = Time (d)

$\boldsymbol{N_f}$ = Normalisation factor (dimensionless)

Equation 2.20: Leach rate calculation

The factor 10^{-3} is included to convert the concentration from mg l^{-1} to g l^{-1}. The normalisation factor (N_f) allows for the fact that the different samples contain different proportions of analyte. It is calculated by dividing 100 by the mass percentage of analyte in the sample.

2.9.4 Errors

The total error in the leach rates reported need to be assessed and can be calculated from the errors associated with the constituent terms in Equation 2.19. These are summarised below:

Analyte concentration – the error in the concentration is from the ICP analysis, this can be taken as worst case of ±10% relative error.

Leachate volume – 100 ml of water was pipetted using a 25 ml volume pipette accurate to ±0.05 ml, giving an error of 0.2/100 = ±0.2%.

After the experiments 20 ml of leachates were sampled with a 10 ml pipette (accurate to ±0.05 ml) giving an error of 0.1/20 = ±0.5%.

Surface area – The samples were weighed on a balance which reports to four decimal places with an error of ±0.00005 g. This gives an error of ±0.02% for a 0.3000 g sample.

Time – The error in the duration of the experiment can be estimated to 1 hour which gives errors of ±4.17%, ±1.39%, ±0.60% and ±0.30% for the 1, 3, 7 and 14 day durations respectively.

The total relative errors of the leach rates obtained in each experiment will be provided in the relevant section. They are simply the sum of the above errors together with the errors in concentration from the ICP analysis which, as previously mentioned, are individual to each result.

By far the biggest source of error in the leach rate values will be due to the surface area calculations. As the samples were only sieved through a 75 µm sieve, the minimum particle

size is unknown and in reality the actual size of some the particles could be considerably less than 75 µm. This results in a large error that cannot be calculated as it will vary with the particle size. For more accurate results the samples should be sieved through a 50 µm sieve as well, so that the known particle sizes are between 75 µm and 50 µm.

2.10 Inductively Coupled Plasma Atomic Emission Spectroscopy (ICP-AES)

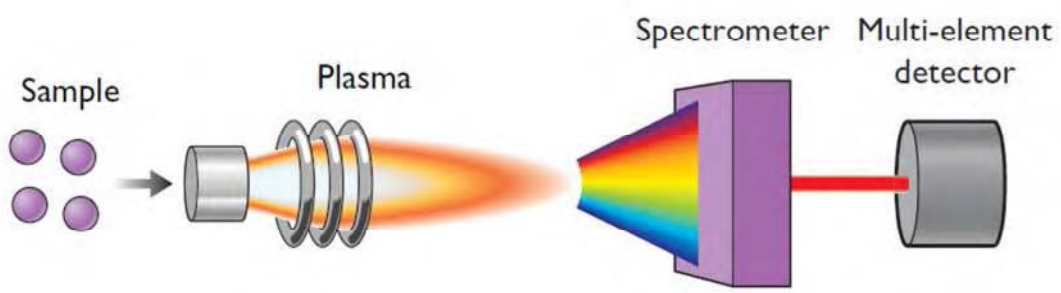

Figure 2.23: Schematic of an ICP-AES adapted from reference[34]

ICP-AES is an analytical technique used for the detection of trace metals in solution. Figure 2.23 provides an overview of the process. Liquid samples are transformed into aerosols by a nebuliser and the subsequent droplets are separated by size. The smaller droplets (1-10 µm) are transferred via the argon flow into the plasma (ionised argon) operating at typically 7000-8000 K. The aerosol particles are ionised once they enter the inert gas plasma. When these excited atoms or ions return to their ground state they emit electromagnetic radiation at wavelengths characteristic of the element present. The emitted light is measured by optical spectrometry. The intensity of the radiation is proportional to the element

concentration. Detection limits typically range from parts per million (ppm) to parts per billion (ppb).

In this thesis single element ICP-AES was used to analyse the sodium or strontium concentrations in the leachates.

2.11 References

(1) Jones, R. H., Thomas, J. M., Huo, Q., Xu, R., Hursthouse, M. B., Chen, J, *J. Chem. Soc., Chem. Commin,* **1520** (1991)
(2) Qui, X., Thompson, W., Billinge, S., J., L. *J. Appli. Cryst***. 37**, 678 (2004)
(3) Farrow, C. L., Juhas, P., Liu, J. W. *J. Phys.: Condense. Matter.* **19**, 1-7 (2007)
(4) Clearfield, A., Frianeza, T. N. *J. Inorg. Nucl. Chem.* **40**, 1925-1932 (1978)
(5) Farfan-Torres, E. M., SHam, E. L., Martinez-Lara, M., Jimenez-Lopez, A. *Mat. Res. Bull*. **27**, 1255-1262 (1992)
(6) Thakkar, R., Chudasama, U. *J. Sci. Ind. Res.* **68**, 312-318 (2009)
(7) Capitani, D., Casciola, M., Donnadio, A., Vivani, R. *Inorg. Chem.* **49**, 9409-9415 (2010)
(8) Losilla, E. R., Cabeza, A., Bruque, S., Aranda, M. A. G., Sanz, J., Iglesias, J. E., Alonso, J. A. *J. Solid State Chem.* **156**, 213-219 (2001)
(9) Varshney, K. G., Rafiquee, M. Z. A, Somya, A. *Coll. Surfaces A*. **301**, 224-228 (2007)
(10) Trobajo, C., Rodriguez, M. L., Suarez, M., Garcia, J. R., Rodriguez, J., Parra, J. B., Salvado, M. A., Pertierra, P., Garcia-Granda, S. *J. Mat. Res.* **13,** 754-759 (1998)
(11) http://oeis.org/A004030.
(12) West, A. R. *Solid State Chemistry and its Applications*; J. Wiley and sons; Chichester, (1984)
(13) A. K. Cheetham, P. D. *Solid State Chemistry Techniques*; Oxford University Press; Oxford, (1990)
(14) http://www.signaltec.com/gemeinsam/links/links_txt.htm.
(15) Thompson, S. P., Parker, J. E., Potter, J., Hill, T. P., Birt, A., Cobb, T. M., Yuan, Y., Tang, C. C., *Rev. Sci. Instr.* **80**, 075107 (2009)
(16) Rietveld, H. M. *Acta. Cryst.* **22**, 151 (1967)
(17) Rietveld, H. M. *J. Appl. Cryst.* **2**, 65-71 (1969)
(18) Young, R. A. *The Rietveld Method*; Oxford University Press: Oxford, (2002)
(19) Proffen, T., Petkov, V., Billinge, S. J. L., Vogt, T., *Z. Kristallogr.* **217**, 47 (2002)
(20) Warren, B. E. *X-ray Diffraction*; Dover: New York, (1990)
(21) Egami, T., Billinge, S. J. L. *Underneath the Bragg Peaks: Structural Analysis of Complex Materials*; Elsevier Ltd: Oxford; Vol. 7. (2003)
(22) Chupas, P. J., Qiu, X., Hanson, J. C., Lee, P. L., Grey, C. P., Billinge, S. J., L. *J. Appl. Cryst.* **36**, 1342-1347 (2003)
(23) Ito, M., Amemiya, Y. *Nucl. Instrum. Methods A*, **310,** 369-372 (1991)

(24) Jeong, I. K., Proffen, T., Mohiuddin-Jacobs, F., Billinge, S. J. L. *J. Phys. Chem. A*, **103**, 921-924 (1999)
(25) http://www.panalytical.com/index.cfm?pid=1196.
(26) Hammersley, A. P. *Syn. Rad. News*. **2**, 24 (1989)
(27) Proffen, T., Billinge, S. J. L. *J. Appli. Cryst*. **32**, 572-575 (1999)
(28) Burhop, E. H. S. *The Auger Effect*; University Press: Cambridge (1952)
(29) Glocker, R., Schrieber, H. *Ann. Physic.* **85**, 1089 (1928)
(30) www.bruker-axs.com.
(31) Soxhlet, F. *Dinglers' Polyt. J.* **232** (1879)
(32) Luque de Castro, M. D., Garcia-Ayuso, L. E. *Anal. Chim. Acta*. **369**, 1-10 (1998)
(33) Sheppard, G. P., Ph.D thesis 'Immobilisation of Iodine in Condensed Zeolite Systems' Univeristy of Birmingham (2009)
(34) http://www.innovationservices.philips.com/.

Chapter 3: Synthesis and Characterisation of Mixed Metal Phosphates

3.1 Mixed Zr/Ti Phosphates

3.1.1 Introduction

It was of interest to attempt the preparation of mixed zirconium-titanium phosphates for two main reasons. The first was to determine whether the ion exchange properties could be altered and controlled in this manner. By changing the average metal radii through doping zirconium for titanium, subtle changes in the structure may occur that alter the bonding environment between the layers where entering radionuclides reside, thus modifying the ion exchange capabilities. The second was to stabilise the titanium-rich samples as it is known that its phosphates groups are more readily hydrolysed[1].

The first reported attempt to prepare a few mixed zirconium-titanium phosphates was by Clearfield and Frianeza[1] via precipitation of the metals from solutions with phosphoric acid and refluxing of the amorphous solids in concentrated phosphoric acid. It was reported that 20% metal substitution of both end members was possible but that attempts to achieve 33% resulted in two phase products. Later Farfán-Torres *et al*.[2] attempted to prepare mixed zirconium-titanium phosphates by sol-gel processing, using zirconium and titanium isopropoxide as precursors, which were hydrolysed with phosphoric acid to form amorphous solids that were then crystallised via reflux in phosphoric acid. From their findings they believed the solubility limit for α-TiP to be 2:1 giving a hexagonal distribution of the metal atoms within the plane. The solubility limit at the α-ZrP end of the series was found to be

slightly lower at 3:1. An alternative sol-gel method was used by Thakkar and Chudasama[3] to attempt the synthesis of $Ti_{0.5}Zr_{0.5}(HPO_4)_2.H_2O$. The authors believed the product obtained to be $Zr_{0.51}Ti_{0.49}(H_2PO_4).0.5H_2O$, however close examination of the XRD data provided suggests a two phase nature to the product. A third preparative method has been reported involving slow phosphoric acid precipitation of the fluorocomplexes of zirconium and titanium formed in HF aqueous solution followed by crystallisation by refluxing in 12 M phosphoric acid[4]. These previous studies had either limited or unproven success at synthesising the full range of solid solutions and often led to poorly crystalline solids. No reason has yet been given for a miscibility gap. It has also been hypothesised that the structures change with the changing metal ratios, however no structural refinements have been carried out on any of the products to prove this.

In this work, attempts at the synthesis of mixed zirconium-titanium phosphates of composition $Ti_xZr_{1-x}(HPO_4)_2.H_2O$ where x = 0-1 by an alternative hydrothermal crystallisation route have been made. The crystal structures of the single phase products have been determined by Rietveld refinements allowing an investigation into the structural changes caused by the varying metal ratios. Pair distribution function analysis has also been employed to determine the metal ordering within these systems and attempts have been made to quantify the reasons behind the solubility gap observed.

3.1.2 Results and Discussion

3.1.2.1 X-Ray Diffraction (XRD) Analysis

The $Ti_xZr_{1-x}(HPO_4)_2.H_2O$ series was synthesised by hydrothermal methods as outlined in Section 2.2.1.1 and analysed by laboratory XRD to check for confirmation of structure type

and purity. Based on the in-house XRD analysis all of the products were obtained as crystalline materials. The purity of the end members α-TiP and α-ZrP was confirmed by matching patterns to the ICDD PDFs (International Centre for Diffraction Data Powder Diffraction File) 80-1067 and 71-1529, respectively, as shown in Figures 3.1 and 3.2.

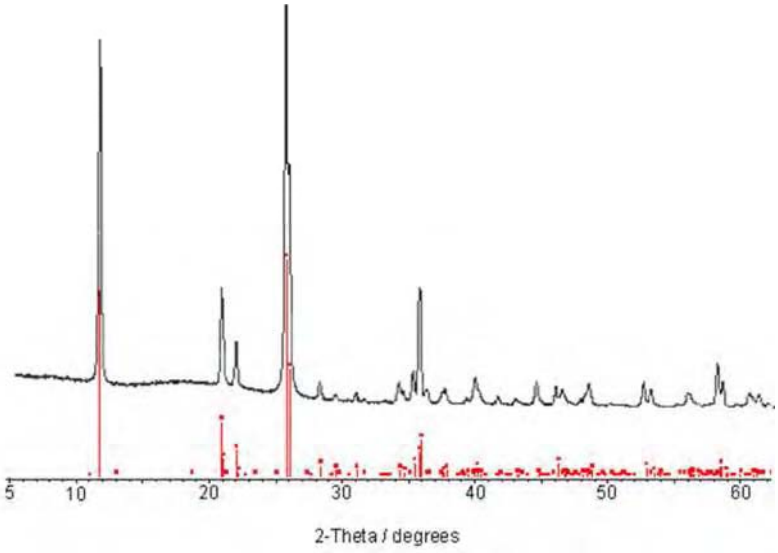

Figure 3.1: Laboratory XRD Pattern of α-TiP. The Red Lines are the indexed peaks from the ICDD PDF 80-1067.

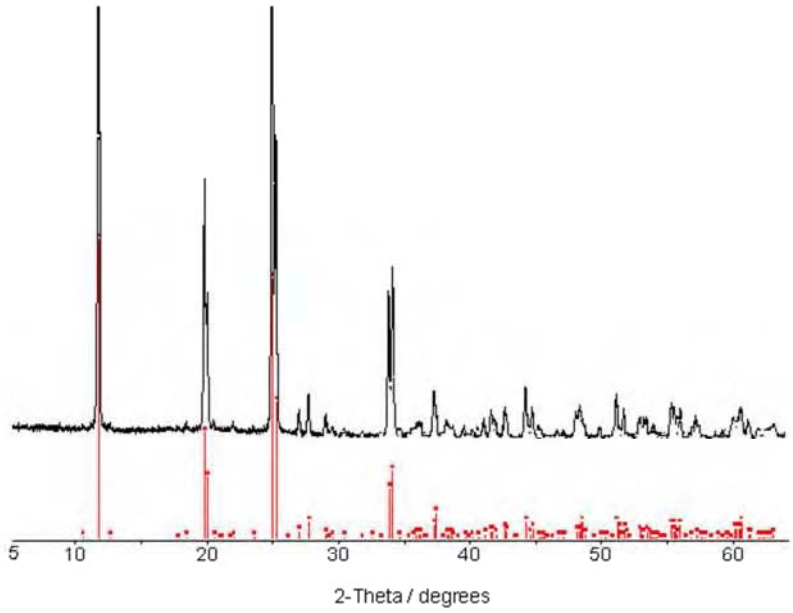

Figure 3.2: Laboratory XRD Pattern of α-ZrP. The Red Lines are the indexed peaks from the ICDD PDF 71-1529.

Comparison of the data obtained for the mixed Zr/Ti series as well as the pure α-TiP and α-ZrP end members are shown in Figure 3.3. It can be seen that many of the XRD patterns of the coprecipitates are similar to those of the end members. The products with up to 30% Zr (nominally $Ti_{0.9}Zr_{0.1}(HPO_4)_2.H_2O$, $Ti_{0.8}Zr_{0.2}(HPO_4)_2.H_2O$, and $Ti_{0.7}Zr_{0.3}(HPO_4)_2.H_2O$) gave patterns similar to α-TiP and vice versa for the 90% Zr product ($Ti_{0.1}Zr_{0.9}(HPO_4)_2.H_2O$) and α-ZrP as expected from similar findings by Clearfield and Frianeza[1]. The patterns of the other coprecipitates (nominally $Ti_{0.6}Zr_{0.4}(HPO_4)_2.H_2O$, $Ti_{0.5}Zr_{0.5}(HPO_4)_2.H_2O$, $Ti_{0.4}Zr_{0.6}(HPO_4)_2.H_2O$, $Ti_{0.3}Zr_{0.7}(HPO_4)_2.H_2O$ and $Ti_{0.2}Zr_{0.8}(HPO_4)_2.H_2O$) contain both more and broader peaks suggesting a two phase nature.

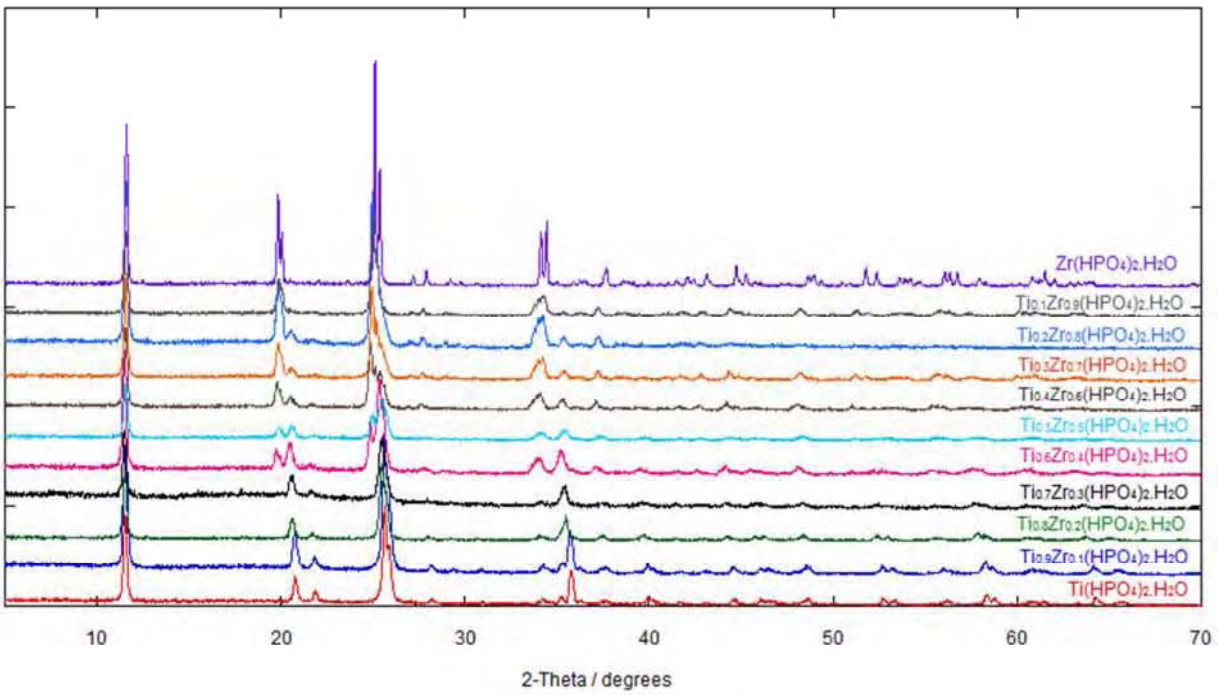

Figure 3.3: Overlaid laboratory XRD scans of the Zr/Ti phosphates.

Synchrotron data

Synchrotron X-ray powder diffraction data sets were collected on all samples to obtain Rietveld quality data. For the mixed members, it was important to determine whether they were single or two phase products before the refinements were undertaken. A visual inspection of the synchrotron XRD patterns in the 2θ region of 10-15° (Figure 3.4) suggested that the products $Ti_{0.6}Zr_{0.4}(HPO_4)_2.H_2O$, $Ti_{0.5}Zr_{0.5}(HPO_4)_2.H_2O$, $Ti_{0.4}Zr_{0.6}(HPO_4)_2.H_2O$, $Ti_{0.3}Zr_{0.7}(HPO_4)_2.H_2O$ and $Ti_{0.2}Zr_{0.8}(HPO_4)_2.H_2O$ were two phase as peaks correlating to both titanium-rich and zirconium-rich phosphates were clearly visible. It was also clear that two partially substituted phases were present rather than a mixture of the pure end members.

It should also be noted that in all of the two-phase systems there is a much larger amorphous component in the powder diffraction patterns, the consequence of this will be discussed in more detail later in this work.

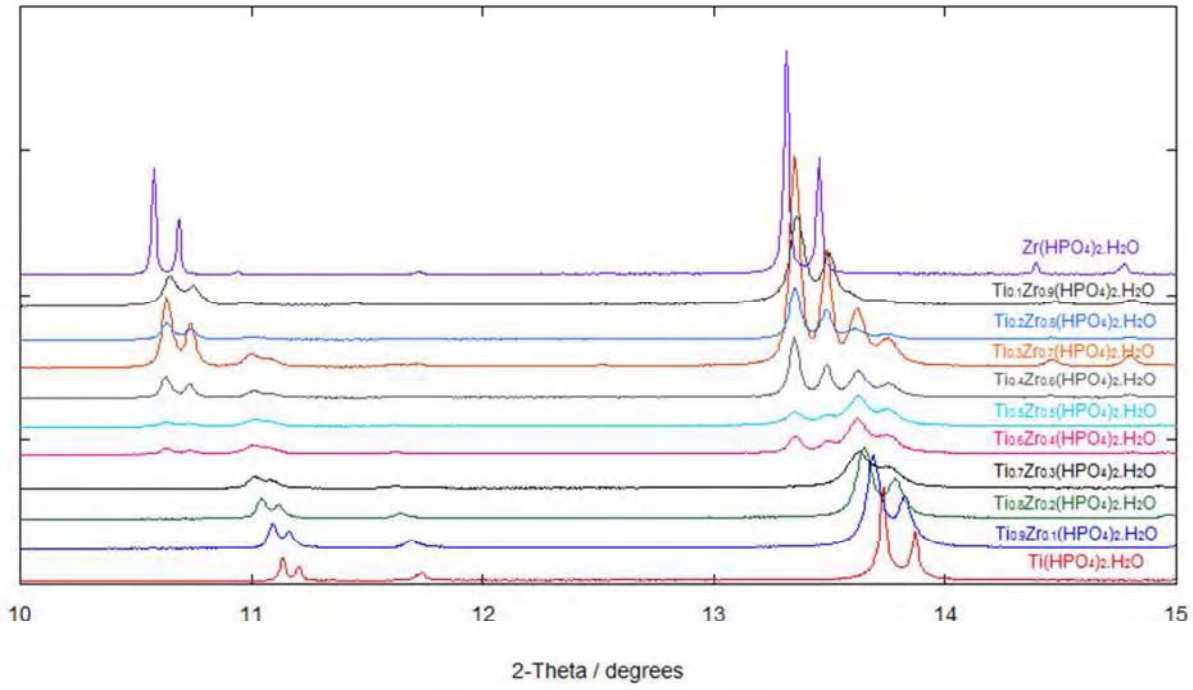

Figure 3.4: Synchrotron X-ray powder diffraction patterns in the 2θ region 10 – 15 °

3.1.2.2 X-Ray Fluorescence (XRF) Results

The bulk elemental compositions of the mixed metal samples as determined by XRF are shown in Table 3.1. These results were calibrated against a series of zirconium and titanium oxide wax pellets as outlined in Section 2.8.5. Good agreement is seen between the expected and the actual Zr/Ti ratios in the products that appeared to be single phase by XRD. The samples in the middle of the solid solution (ca. 60-20 nominal % Ti) appeared to have approximately the same bulk composition irrespective of the starting Zr/Ti ratios; in all cases the solid is titanium-rich relative to the expected ratio. This suggests some aspect of the solution chemistry influences the products that form, irrespective of whether or not the

structure type is able to accommodate a full solid solution between the end member compositions.

Table 3.1: Chemical compositions of the mixed zirconium-titanium phosphates as determined by XRF*.

Nominal Formula	Observed Mass %Ti (relative)	Observed Mass %Zr (relative)	Measured Formula
$Ti_{0.9}Zr_{0.1}(HPO_4)_2.H_2O$	32.8	8.3	$Ti_{0.88}Zr_{0.12}(HPO_4)_2.H_2O$
$Ti_{0.8}Zr_{0.2}(HPO_4)_2.H_2O$	27.3	17.5	$Ti_{0.75}Zr_{0.25}(HPO_4)_2.H_2O$
$Ti_{0.7}Zr_{0.3}(HPO_4)_2.H_2O$	24.3	22.3	$Ti_{0.68}Zr_{0.32}(HPO_4)_2.H_2O$
$Ti_{0.6}Zr_{0.4}(HPO_4)_2.H_2O$	21.9	34.0	$Ti_{0.55}Zr_{0.45}(HPO_4)_2.H_2O$
$Ti_{0.5}Zr_{0.5}(HPO_4)_2.H_2O$	21.9	35.9	$Ti_{0.53}Zr_{0.47}(HPO_4)_2.H_2O$
$Ti_{0.4}Zr_{0.6}(HPO_4)_2.H_2O$	21.9	45.2	$Ti_{0.48}Zr_{0.52}(HPO_4)_2.H_2O$
$Ti_{0.3}Zr_{0.7}(HPO_4)_2.H_2O$	21.9	48.2	$Ti_{0.46}Zr_{0.54}(HPO_4)_2.H_2O$
$Ti_{0.2}Zr_{0.8}(HPO_4)_2.H_2O$	21.9	49.2	$Ti_{0.46}Zr_{0.54}(HPO_4)_2.H_2O$
$Ti_{0.1}Zr_{0.9}(HPO_4)_2.H_2O$	3.2	36.3	$Ti_{0.14}Zr_{0.86}(HPO_4)_2.H_2O$

* There is a 10% relative error associated with the XRF results.

3.1.2.3 Rietveld Structure Refinements

Rietveld profile analysis was undertaken on all high resolution synchrotron X-ray powder diffraction patterns. Those samples deemed to be single phase (see Section 3.1.2.1) could be successfully refined as such starting from the structure for α-TiP as given by Salvado *et al.*[5] or from the structure for α-ZrP as given by Albertsson[6] using space group $P2_1/c$. For the mixed metal samples the compositions were allowed to refine starting from the values expected from the nominal compositions, but fractional occupancies were constrained to sum to 1. During the refinements the temperature factors of each discrete atom type were constrained to the same value, excluding that for the water oxygen, O(9), which was refined independently. A summary of key structural parameters is presented in Table 3.2, details of atomic coordinates and thermal parameters in Tables 3.3 – 3.8 and fits to the data shown in

Figures 3.5 – 3.10. The refined bond angles are summarised in Appendix 1 and the electronic crystallographic refinement files can be found in Appendix 3. The refined parameters for the end members are in excellent agreement with those found in the literature.[5,6]

Table 3.2: Structural parameters with estimated standard deviations for the single-phase members of the Zr/Ti series from the Rietveld refinements.

	α-TiP	$Ti_{0.9}Zr_{0.1}(HPO_4)_2.H_2O$	$Ti_{0.8}Zr_{0.2}(HPO_4)_2.H_2O$	$Ti_{0.7}Zr_{0.3}(HPO_4)_2.H_2O$	$Ti_{0.1}Zr_{0.9}(HPO_4)_2.H_2O$	α-ZrP
a/Å	8.63267(6)	8.65991(12)	8.69672(13)	8.7156(3)	8.9973(3)	9.06336(2)
b /Å	5.00672(3)	5.02351(6)	5.04765(7)	5.0582(1)	5.2465(1)	5.29060(1)
c /Å	16.1902(2)	16.2180(3)	16.2356(4)	16.2408(7)	16.2606(5)	16.24603(6)
β/deg	110.2065(6)	110.2554(9)	110.3460(9)	110.4008(18)	111.200(1)	111.4012(2)
V/Å^3	656.697(11)	661.903(19)	668.25(2)	671.07(4)	715.62(3)	717.16(3)
M-O(1)/ Å	1.944(9)	1.983(7)	1.998(9)	1.998(12)	2.119(13)	2.085(5)
M-O(2)/ Å	1.942(11)	1.960(8)	1.975(10)	1.937(16)	2.089(16)	2.090(6)
M-O(3)/ Å	1.913(11)	1.874(9)	1.960(10)	1.938(16)	1.980(16)	2.086(6)
M-O(5)/ Å	1.969(10)	1.978(8)	1.978(10)	1.937(15)	2.207(15)	2.084(6)
M-O(6)/ Å	1.941(11)	1.969(9)	1.987(11)	1.983(17)	2.084(17)	2.105(6)
M-O(7)/ Å	1.962(8)	1.988(7)	1.944(8)	1.952(11)	2.075(10)	2.090(5)
<M-O>/ Å	1.945	1.959	1.974	1.958	2.092	2.090
χ^2	3.000	3.095	2.393	2.091	4.225	2.844
R_p /%	4.93	4.52	3.90	3.98	4.34	5.51
R_{wp} /%	6.41	5.89	5.12	5.21	5.62	7.37
R_F^2/%	6.07	3.54	7.62	3.45	4.19	6.57

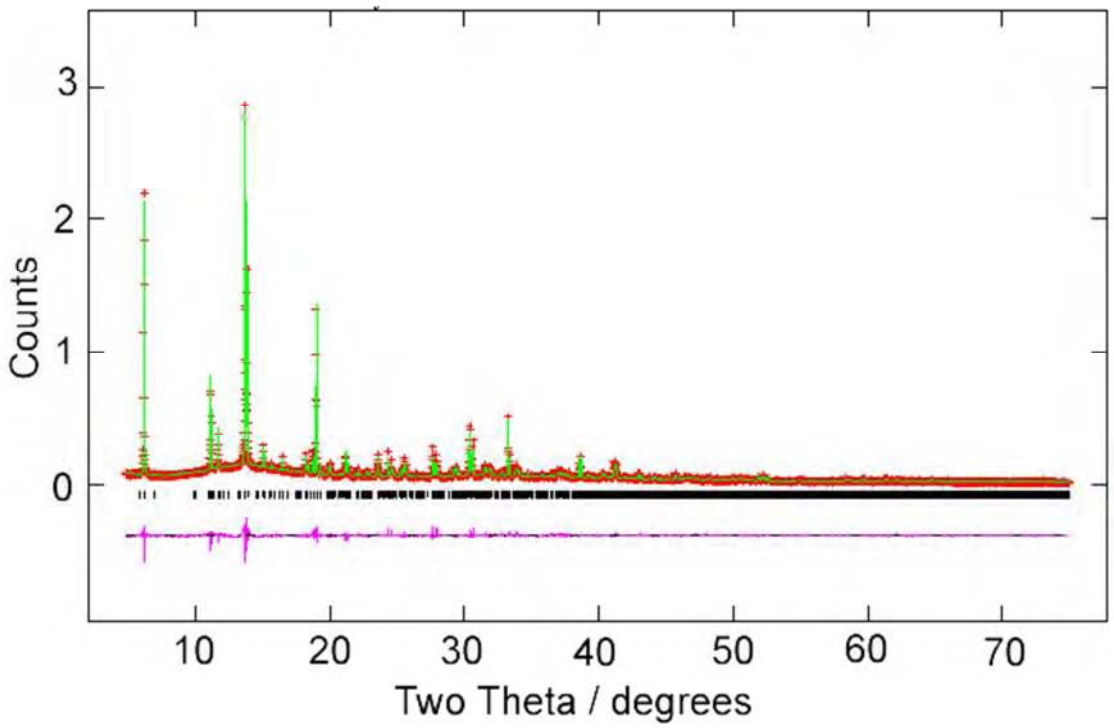

Figure 3.5: Final observed (red crosses), calculated (green line) and difference (bottom) X-ray diffraction profile with reflection positions noted as vertical tick marks for α-Ti$(HPO_4)_2.H_2O$

Table 3.3: Fractional atomic coordinates and isotropic thermal displacement parameters with estimated standard deviations for α-Ti$(HPO_4)_2.H_2O$ from the Rietveld refinement.

atom	*x*	*y*	*z*	U_{iso} (x10^2) Å^2
Ti	0.7594(3)	0.2518(13)	0.5120(2)	0.05(4)
P(1)	-0.0046(4)	0.7448(15)	0.6073(2)	0.27(7)
P(2)	0.4671(4)	0.2454(15)	0.5992(2)	0.27(7)
O(1)	0.1151(10)	0.8276(16)	0.5643(6)	0.49(9)
O(2)	-0.0640(11)	0.4681(17)	0.5903(8)	0.49(9)
O(3)	0.8570(11)	0.9581(16)	0.5876(7)	0.49(9)
O(4)	0.0967(7)	0.7694(22)	0.7093(5)	0.49(9)
O(5)	0.3273(10)	0.4249(16)	0.5580(6)	0.49(9)
O(6)	0.4169(11)	-0.0391(17)	0.5681(7)	0.49(9)
O(7)	0.6260(10)	0.3246(17)	0.5860(5)	0.49(9)
O(8)	0.5081(7)	0.2506(25)	0.7023(5)	0.49(9)
O(9)	0.2559(9)	0.2307(18)	0.7631(5)	0.21(2)

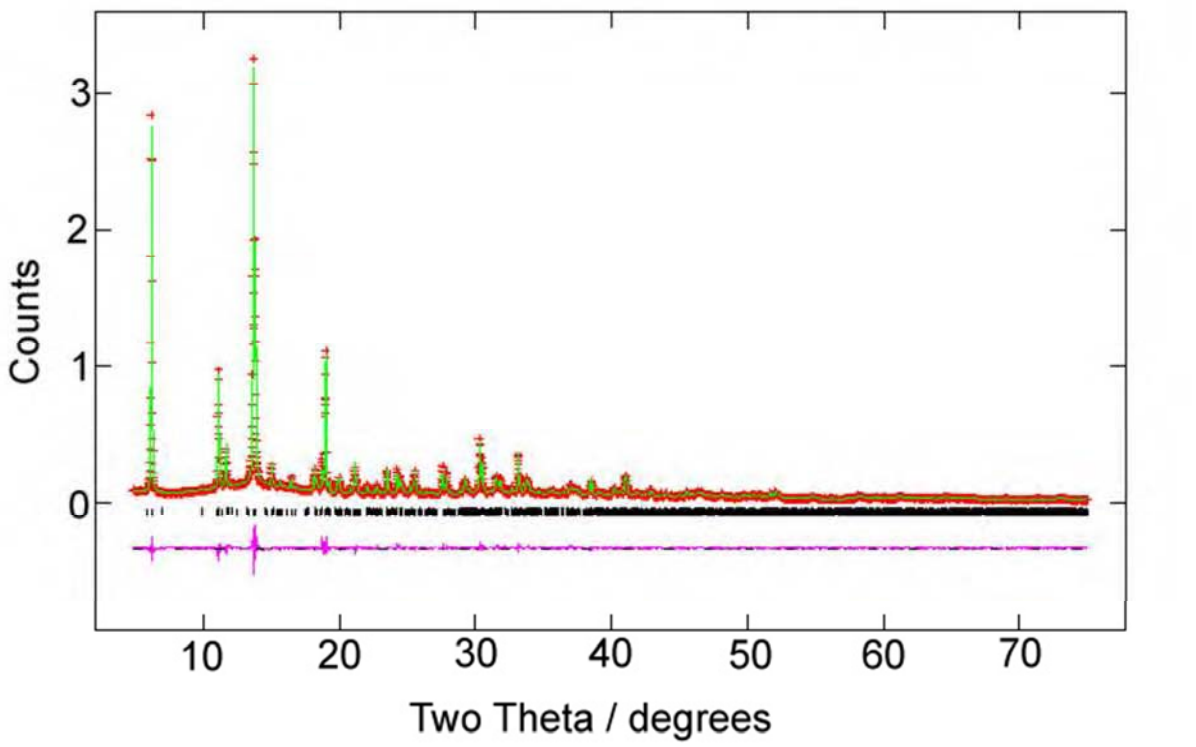

Figure 3.6: Final observed (red crosses), calculated (green line) and difference (bottom) X-ray diffraction profile with reflection positions noted as vertical tick marks for α-$Ti_{0.9}Zr_{0.1}(HPO_4)_2.H_2O$

Table 3.4: Fractional atomic coordinates and isotropic thermal displacement parameters with estimated standard deviations for α-$Ti_{0.9}Zr_{0.1}(HPO_4)_2.H_2O$ from the Rietveld refinement.

atom	*x*	*y*	*z*	U_{iso} (x10^2) Å^2	Fractional Occupancy
Ti	0.7591(2)	0.2459(9)	0.5126(1)	0.44(4)	0.911(4)
Zr	0.7591(2)	0.2459(9)	0.5126(1)	0.44(4)	0.089(4)
P(1)	-0.0040(3)	0.7356(10)	0.6081(2)	0.06(5)	
P(2)	0.4671(3)	0.2468(11)	0.5996(2)	0.06(5)	
O(1)	0.1155(8)	0.8252(14)	0.5668(5)	0.55(7)	
O(2)	-0.0684(9)	0.4739(15)	0.5909(6)	0.55(7)	
O(3)	0.8517(9)	0.9535(15)	0.5845(6)	0.55(7)	
O(4)	1.0983(6)	0.7763(18)	0.7092(4)	0.55(7)	
O(5)	0.3238(9)	0.4257(14)	0.5557(5)	0.55(7)	
O(6)	0.4193(9)	-0.0314(15)	0.5687(6)	0.55(7)	
O(7)	0.6265(8)	0.3342(14)	0.5874(4)	0.55(7)	
O(8)	0.5088(6)	0.2463(21)	0.7022(3)	0.55(7)	
O(9)	0.2559(8)	0.2325(18)	0.7631(4)	0.36(11)	

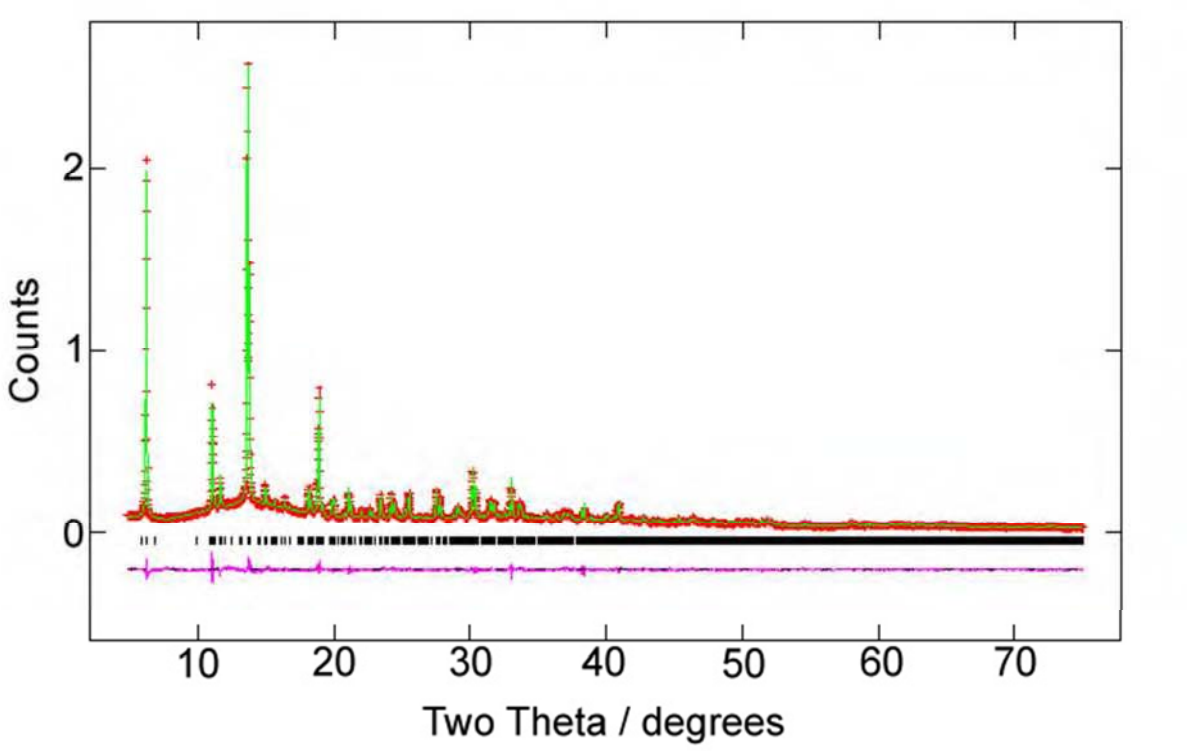

Figure 3.7: Final observed (red crosses), calculated (green line) and difference (bottom) X-ray diffraction profile with reflection positions noted as vertical tick marks for α-$Ti_{0.8}Zr_{0.2}(HPO_4)_2.H_2O$

Table 3.5: Fractional atomic coordinates and isotropic thermal displacement parameters with estimated standard deviations for α-$Ti_{0.8}Zr_{0.2}(HPO_4)_2.H_2O$ from the Rietveld refinement.

atom	*x*	*y*	*z*	U_{iso} (x10^2) Å^2	Fractional Occupancy
Ti	0.75906(27)	0.2483(10)	0.5124(2)	1.86(9)	0.862(4)
Zr	0.75906(27)	0.2483(10)	0.5124(2)	1.86(9)	0.138(4)
P(1)	-0.0037(4)	0.7436(15)	0.6092(2)	0.81(2)	
P(2)	0.4679(4)	0.2517(14)	0.5996(2)	0.81(2)	
O(1)	0.1132(11)	0.8204(17)	0.5666(6)	1.71(5)	
O(2)	-0.0656(11)	0.4688(18)	0.5935(7)	1.71(5)	
O(3)	0.8605(12)	0.9541(17)	0.5914(7)	1.71(5)	
O(4)	1.0959(8)	0.7180(23)	0.7083(5)	1.71(5)	
O(5)	0.3282(11)	0.4307(16)	0.5583(6)	1.71(5)	
O(6)	0.4191(12)	-0.0292(18)	0.5690(7)	1.71(5)	
O(7)	0.6325(11)	0.3307(17)	0.5870(5)	1.71(5)	
O(8)	0.5059(7)	0.2723(23)	0.7030(4)	1.71(5)	
O(9)	0.2579(11)	0.2298(25)	0.7625(5)	2.74(1)	

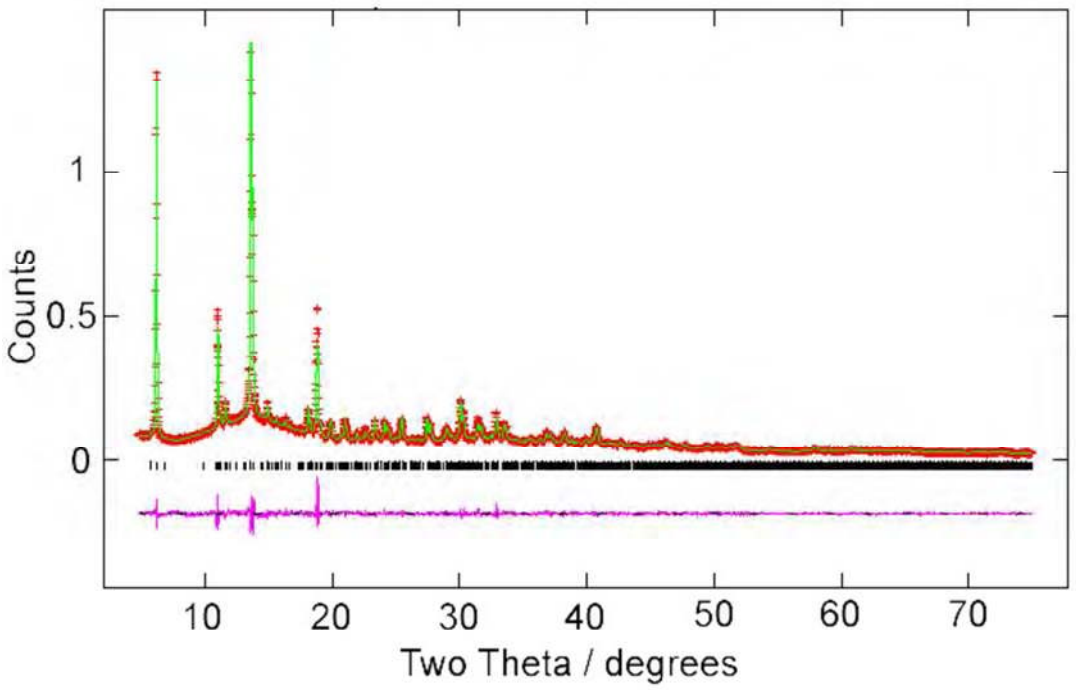

Figure 3.8: Final observed (red crosses), calculated (green line) and difference (bottom) X-ray diffraction profile with reflection positions noted as vertical tick marks for α-$Ti_{0.7}Zr_{0.3}(HPO_4)_2.H_2O$

Table 3.6: Fractional atomic coordinates and isotropic thermal displacement parameters with estimated standard deviations for α-$Ti_{0.7}Zr_{0.3}(HPO_4)_2.H_2O$ from the Rietveld refinement.

atom	*x*	*y*	*z*	U_{iso} (x10^2) Å^2	Fractional Occupancy
Ti	0.7576(3)	0.2527(12)	0.5126(2)	0.55(8)	0.779(6)
Zr	0.7576(3)	0.2527(12)	0.5126(2)	0.55(8)	0.221(6)
P(1)	-0.0040(6)	0.7479(21)	0.6083(3)	0.46(12)	
P(2)	0.4684(6)	0.2264(17)	0.6005(3)	0.46(12)	
O(1)	0.1110(15)	0.8123(28)	0.5645(8)	1.07(6)	
O(2)	-0.0665(18)	0.4650(27)	0.5905(9)	1.07(6)	
O(3)	0.8491(18)	0.9449(28)	0.5839(10)	1.07(6)	
O(4)	1.0967(10)	0.7516(49)	0.7072(6)	1.07(6)	
O(5)	0.3179(16)	0.4168(27)	0.5483(8)	1.07(6)	
O(6)	0.4094(18)	-0.0145(29)	0.5671(11)	1.07(6)	
O(7)	0.6287(15)	0.3342(27)	0.5865(6)	1.07(6)	
O(8)	0.5107(9)	0.2536(47)	0.7033(5)	1.07(6)	
O(9)	0.2529(16)	0.2250(39)	0.7609(7)	1.92(3)	

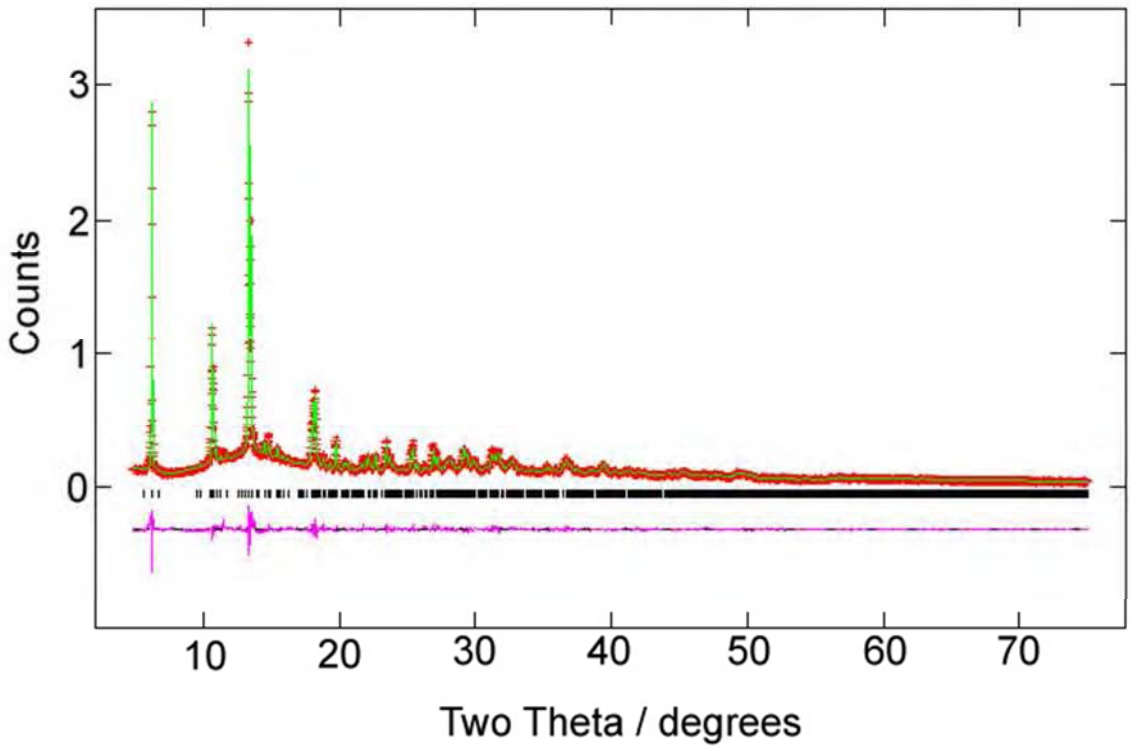

Figure 3.9: Final observed (red crosses), calculated (green line) and difference (bottom) X-ray diffraction profile with reflection positions noted as vertical tick marks for α-$Ti_{0.1}Zr_{0.9}(HPO_4)_2.H_2O$

Table 3.7: Fractional atomic coordinates and isotropic thermal displacement parameters with estimated standard deviations for α- $Ti_{0.1}Zr_{0.9}(HPO_4)_2.H_2O$ from the Rietveld refinement.

atom	*x*	*y*	*z*	U_{iso} (x10^2) Å^2	Fractional Occupancy
Ti	0.7597(3)	0.2518(10)	0.5144(1)	0.81(9)	0.299(8)
Zr	0.7597(3)	0.2518(10)	0.5144(1)	0.81(9)	0.701(8)
P(1)	-0.0062(7)	0.7291(20)	0.6136(3)	0.22(2)	
P(2)	0.4694(6)	0.2349(21)	0.1044(3)	0.22(2)	
O(1)	0.1073(16)	0.8316(24)	0.5663(8)	0.36(7)	
O(2)	0.9407(19)	0.4801(27)	0.5990(11)	0.36(7)	
O(3)	0.8698(19)	0.9666(29)	0.5923(11)	0.36(7)	
O(4)	0.1151(11)	0.7859(33)	0.7176(6)	0.36(7)	
O(5)	0.3429(19)	0.4125(27)	0.5682(9)	0.36(7)	
O(6)	0.4103(20)	-0.0128(28)	0.5722(10)	0.36(7)	
O(7)	0.6176(13)	0.2771(35)	0.5900(6)	0.36(7)	
O(8)	0.5116(10)	0.2462(48)	0.7075(6)	0.36(7)	
O(9)	0.2519(19)	0.2373(46)	0.7564(8)	3.26(13)	

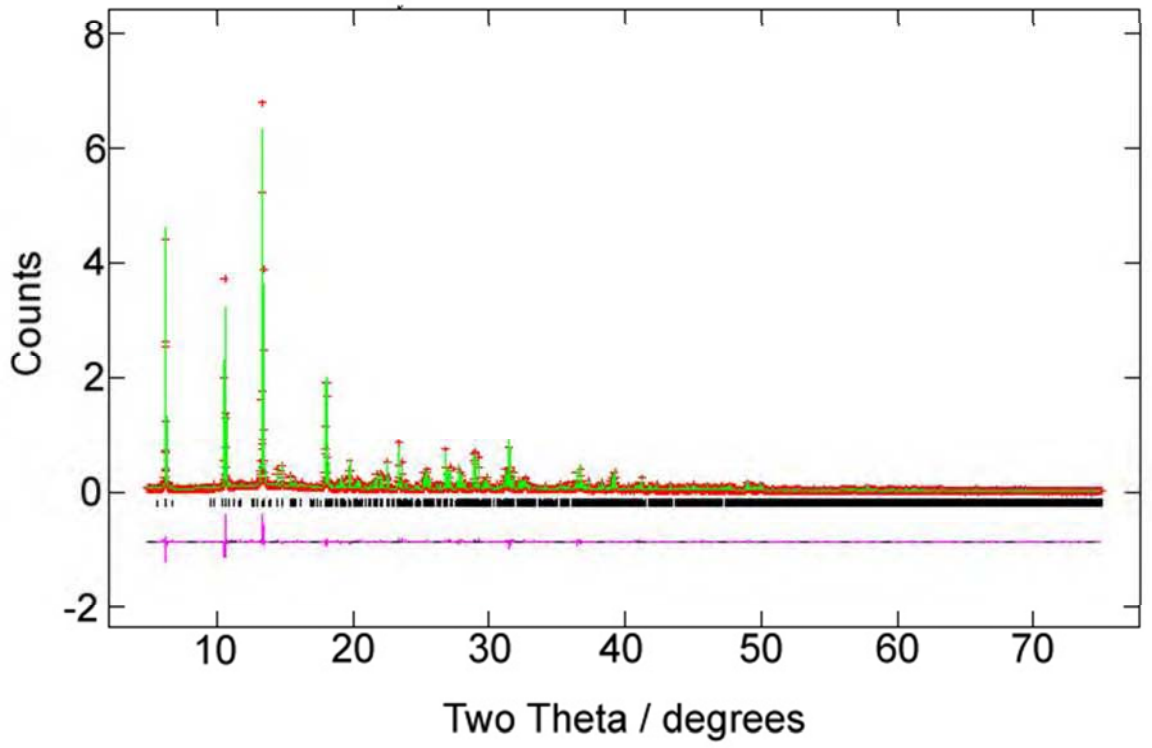

Figure 3.10: Final observed (red crosses), calculated (green line) and difference (bottom) X-ray diffraction profile with reflection positions noted as vertical tick marks for α-$Zr(HPO_4)_2.H_2O$

Table 3.8: Fractional atomic coordinates and isotropic thermal displacement parameters with estimated standard deviations for α- $Zr(HPO_4)_2.H_2O$ from the Rietveld refinement.

atom	*x*	*y*	*z*	U_{iso} (x10^2) Å^2
Zr	0.7612(1)	0.2531(4)	0.51476(5)	1.44(1)
P(1)	0.0007(2)	0.7483(10)	0.6141(1)	0.705(7)
P(2)	0.4697(2)	0.2580(9)	0.1038(1)	0.705(7)
O(1)	0.1057(6)	0.8018(10)	0.5646(3)	0.98(4)
O(2)	0.9364(7)	0.4870(11)	0.6001(4)	0.98(4)
O(3)	0.8715(7)	0.9471(10)	0.5944(4)	0.98(4)
O(4)	0.1049(5)	0.7743(13)	0.7146(3)	0.98(4)
O(5)	0.3460(7)	0.4324(10)	0.5606(4)	0.98(4)
O(6)	0.4147(7)	-0.0155(11)	0.5705(4)	0.98(4)
O(7)	0.6226(6)	0.3090(10)	0.5916(2)	0.98(4)
O(8)	0.5065(4)	0.2396(18)	0.7048(3)	0.98(4)
O(9)	0.2579(6)	0.2245(13)	0.7632(3)	1.75(9)

The samples with x = 0.4 - 0.8 gave complex patterns and had to be treated as two-phase mixtures. Given the similarities of the powder patterns of the two phases and therefore extreme overlap in each data set, it was not possible to refine the metal site occupancies and obtain sensible values. In all cases, based on the linear extrapolation of the unit cell values between the end members, one phase had a composition close to 14% Ti and the other approximately 68% Ti, therefore the compositions were fixed at these values and the phase fractions refined. From the scale factors for the two phase's useful estimates of the average compositions could be obtained. The results of the fits are summarised in Table 3.9 and a representative plot is shown in Figure 3.11. Further results and fits can be found in Appendix 2 and the crystallographic refinement files in Appendix 3.

Table 3.9: Structural parameters of the two phase products from the Rietveld refinements

	$Ti_{0.6}Zr_{0.4}(HPO_4)_2.H_2O$		$Ti_{0.5}Zr_{0.5}(HPO_4)_2.H_2O$		$Ti_{0.4}Zr_{0.6}(HPO_4)_2.H_2O$		$Ti_{0.3}Zr_{0.7}(HPO_4)_2.H_2O$		$Ti_{0.2}Zr_{0.8}(HPO_4)_2.H_2O$	
	Phase 1	Phase 2	Phase 1	Phase 2	Phase 1	Phase 2	Phase 1	Phase 2	Phase 1	Phase 2
Space group	$P2_1/c$	$P2_1/c$	$P2_1/c$	$P2_1/c$	$P2_1/c$	$P2_1/c$	$P2_1/c$	$P2_1/c$	$P2_1/c$	$P2_1/c$
a/Å	9.0091(6)	8.7150(4)	9.0168(8)	8.7161(6)	9.0207(2)	8.7190(5)	9.0161(2)	8.7238(6)	9.0198(2)	8.7354(12)
b /Å	5.2549(3)	5.06319(23)	5.2588(4)	5.0640(3)	5.26187(14)	5.06420(27)	5.25866(9)	5.0659(3)	5.2608(1)	5.0697(7)
c /Å	16.2444(10)	16.2424(10)	16.2482(16)	16.2451(15)	16.2561(4)	16.2533(11)	16.2597(3)	16.2485(8)	16.2661(4)	16.2756(17)
β/deg	111.273(3)	110.422(3)	111.285(5)	110.420(4)	111.274(1)	110.417(3)	111.265(9)	110.414(4)	111.268(1)	110.376(7)
V/Å^3	716.64(8)	671.66(6)	717.90(11)	671.97(9)	719.03(3)	672.58(7)	718.43(2)	672.98(7)	719.29(3)	675.50(13)
<M-O>/ Å	2.19	2.02	1.90	2.07	2.15	1.98	2.15	2.02	2.13	2.03
Ti Frac.	0.14	0.68	0.14	0.68	0.14	0.68	0.14	0.68	0.14	0.68
Zr Frac.	0.86	0.32	0.86	0.32	0.86	0.32	0.86	0.32	0.86	0.32
Weight frac.	21%	79%	23%	77%	55%	45%	64%	36%	72%	28%
Bulk comp-osition*	$Ti_{0.57}Zr_{0.43}(HPO_4)_2.H_2O$		$Ti_{0.56}Zr_{0.44}(HPO_4)_2.H_2O$		$Ti_{0.38}Zr_{0.62}(HPO_4)_2.H_2O$		$Ti_{0.33}Zr_{0.67}(HPO_4)_2.H_2O$		$Ti_{0.29}Zr_{0.71}(HPO_4)_2.H_2O$	

*Based on weight fractions of the two phases.

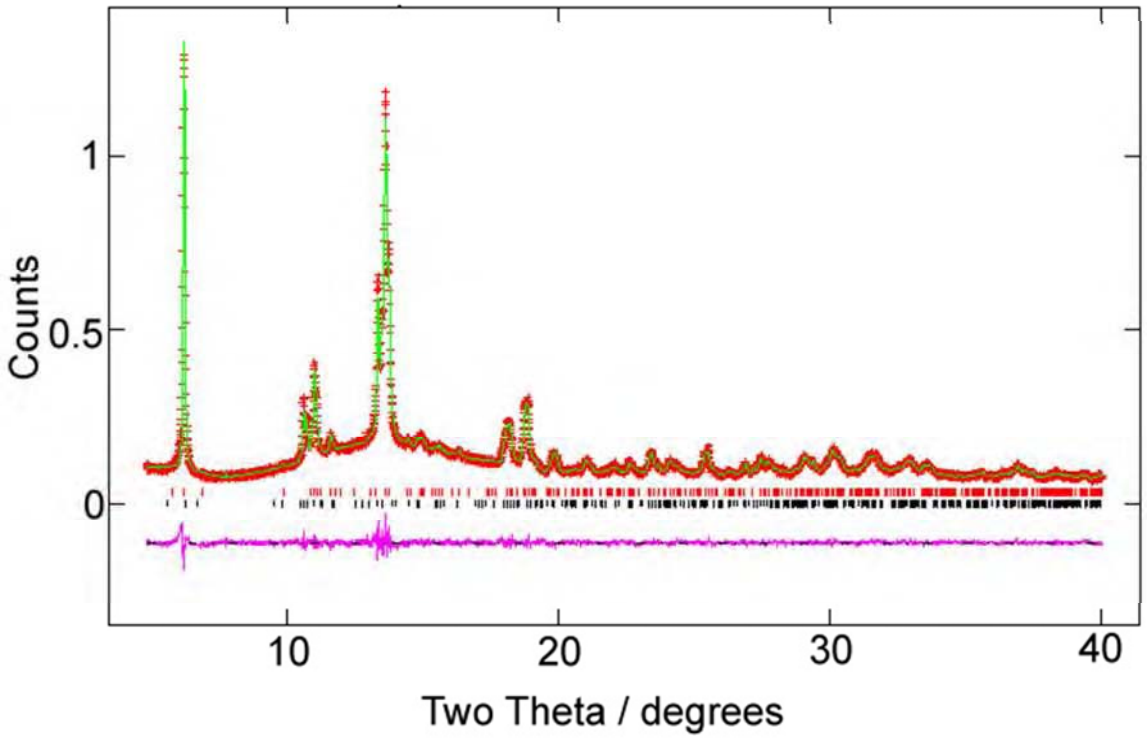

Figure 3.11: Final observed (red crosses), calculated (green line) and difference (bottom) X-ray diffraction profile for α-$Ti_{0.5}Zr_{0.5}(HPO_4)_2.H_2O$ with reflection positions noted as vertical tick marks (phase one shown in black and phase two in red).

Compositions of the two-phase products as determined from Rietveld are compared to those from XRF analyses in Table 3.10. The compositions of the crystalline components from the Rietveld analysis sum (based on weight fractions) to close to the expected ratios of titanium and zirconium. The XRF measurements however, show the bulk overall solid compositions in this range are nearly the same at ca. 50% titanium. This discrepancy must be due to the amorphous components which would seem to be zirconium-rich for the nominal 60% titanium system and titanium-rich for the other four. This will be discussed further in subsequent sections of this chapter.

Table 3.10: Comparison of compositions as determined from Rietveld and XRF analyses for the two-phase samples.

Nominal Product	Ti (Rietveld)	Zr (Rietveld)	Ti/Zr Ratio Rietveld	Ti/Zr Ratio XRF	Expected Ti/Zr Ratio
$Ti_{0.6}Zr_{0.4}(HPO_4)_2.H_2O$	0.567	0.433	1.31	1.22	1.50
$Ti_{0.5}Zr_{0.5}(HPO_4)_2.H_2O$	0.556	0.444	1.25	1.13	1.00
$Ti_{0.4}Zr_{0.6}(HPO_4)_2.H_2O$	0.383	0.617	0.62	0.92	0.67
$Ti_{0.3}Zr_{0.7}(HPO_4)_2.H_2O$	0.334	0.665	0.50	0.85	0.43
$Ti_{0.2}Zr_{0.8}(HPO_4)_2.H_2O$	0.291	0.709	0.41	0.85	0.25

3.1.2.4 Pair Distribution Function (PDF) Studies

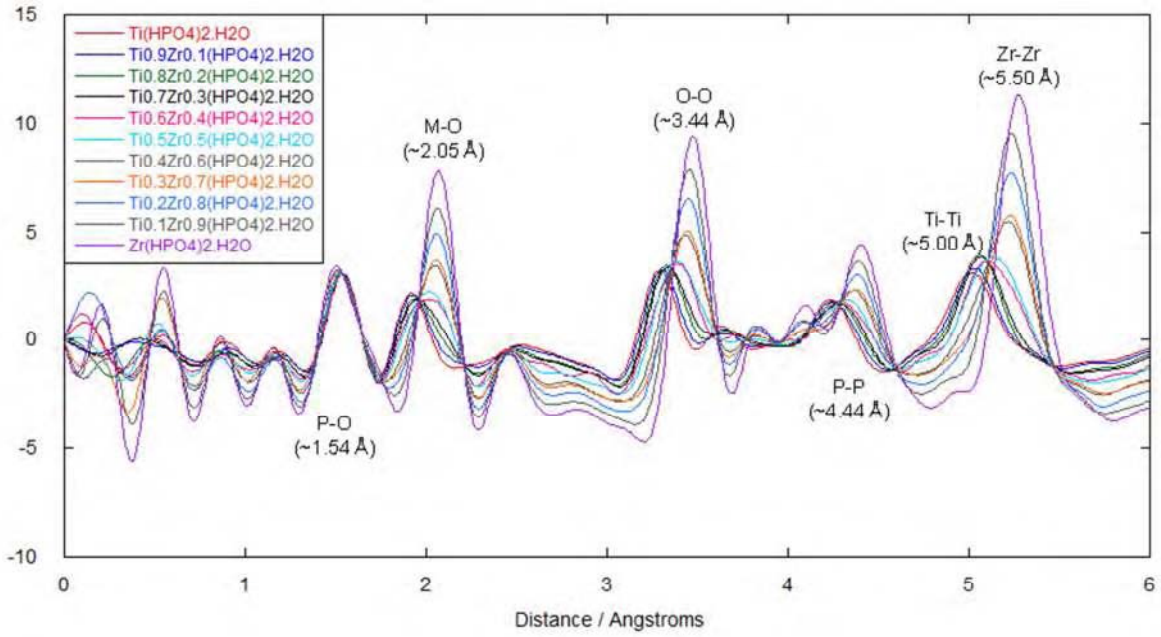

Figure 3.12: PDF patterns for the zirconium-titanium series.

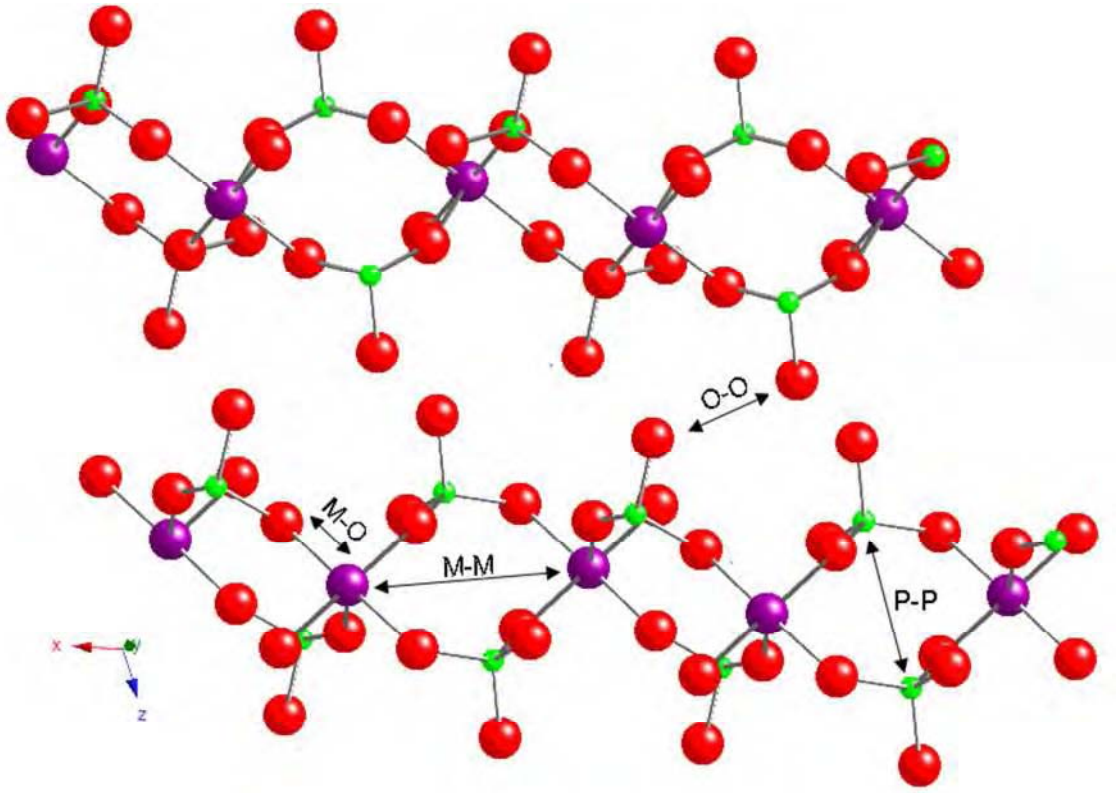

Figure 3.13: Examples of the metal - metal (M-M), phosphorus - phosphorus (P-P), oxygen -oxygen (O-O) and phosphorus - oxygen (P-O) distances highlighted in the PDFs. Note that the oxygen-oxygen distance is between hydroxyl oxygens on adjacent layers. The red spheres are the oxygen atoms, the green the phosphorus and the purple are the metal.

Pair distribution functions (PDFs) for the full zirconium-titanium series were produced from high energy total scattering data collected at the APS and processed using PDFGUI[7]. Figure 3.12 shows the overlaid PDF patterns for the full series in the low-r region. The intensities have been scaled on the phosphorus-oxygen peak height which must remain constant. Each peak represents different atomic distances present in the structure and so variation in bond lengths can be easily seen. By inspection, it is clear that the titanium based products have smaller intralayer interatomic distances, as shown by the oxygen-oxygen, phosphorus-phosphorus, metal-oxygen and metal-metal peaks at approximately 3.44, 4.44, 2.05 and

5.00-5.50 Å, respectively. These distances in reference to the layered structure are depicted in Figure 3.13. It is worth highlighting that these distances can be taken directly from the PDF patterns, i.e. no analysis of atomic coordinates or unit cell parameters were required. It is also interesting to observe that the M-O peak distances change little with doping, i.e. the titanium-rich samples all have an average distance similar to α-TiP and the zirconium-rich samples all have an average distance similar to α-ZrP. This is not as one would expect for a normal solid solution where a smoothly changing M-O distance would be predicted. Another aspect readily apparent upon close inspection of the intraplaner M-M peak, as shown in Figure 3.14, is that the systems that could be analysed using the Rietveld method have a single peak whereas the two-phase samples display the expected two peaks. This observation from the PDF patterns, in the absence of knowledge from the Rietveld analysis, could only be explained by phase segregation or a lowering of the crystallographic symmetry. Peak fitting, using Gaussian functions, of the metal-metal peaks were performed using the software Origin. The positions of the peaks represent the metal-metal distances for these materials. A clear linear trend is seen for the single phase zirconium-titanium phosphates as shown in Figure 3.15. The results for the two-phase phosphates reinforces the concept of the presence of two partially substituted phases; one titanium-rich and one zirconium-rich, however the exact values should be treated with caution owing to the large error bars associated with many of the data points.

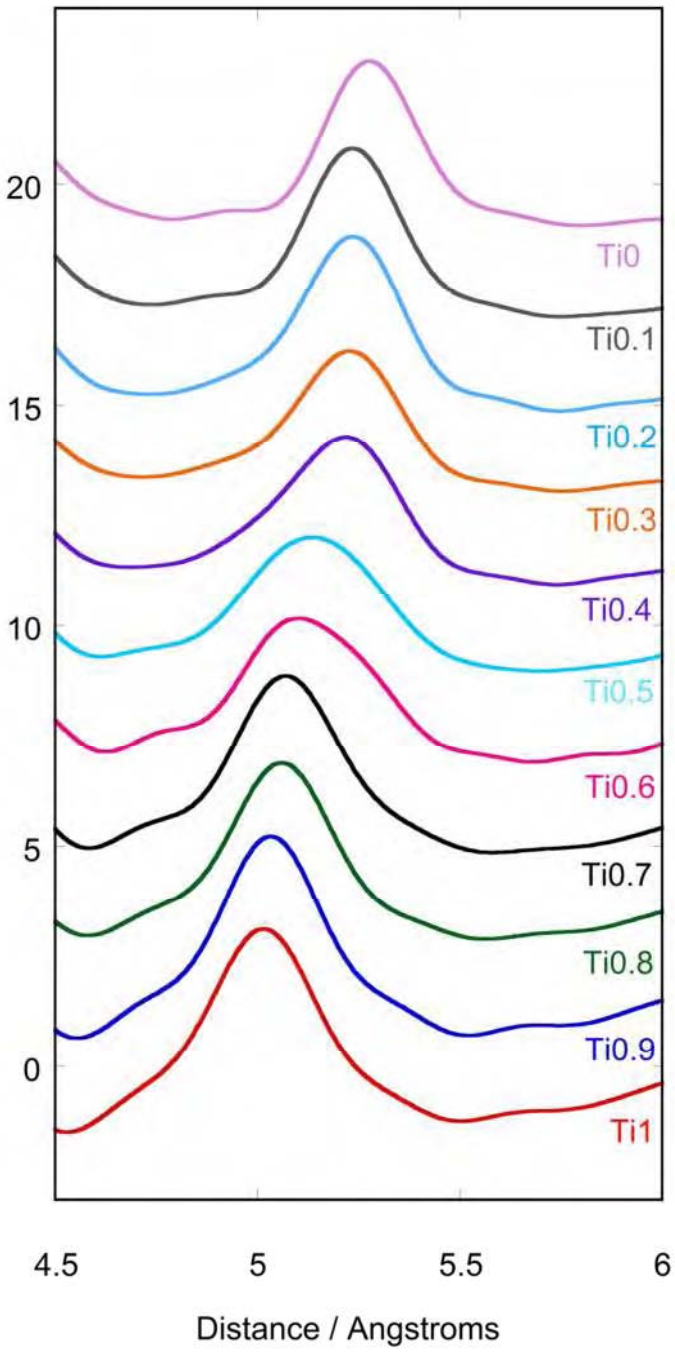

Figure 3.14: PDF patterns of the region where the metal-metal peaks are observed.

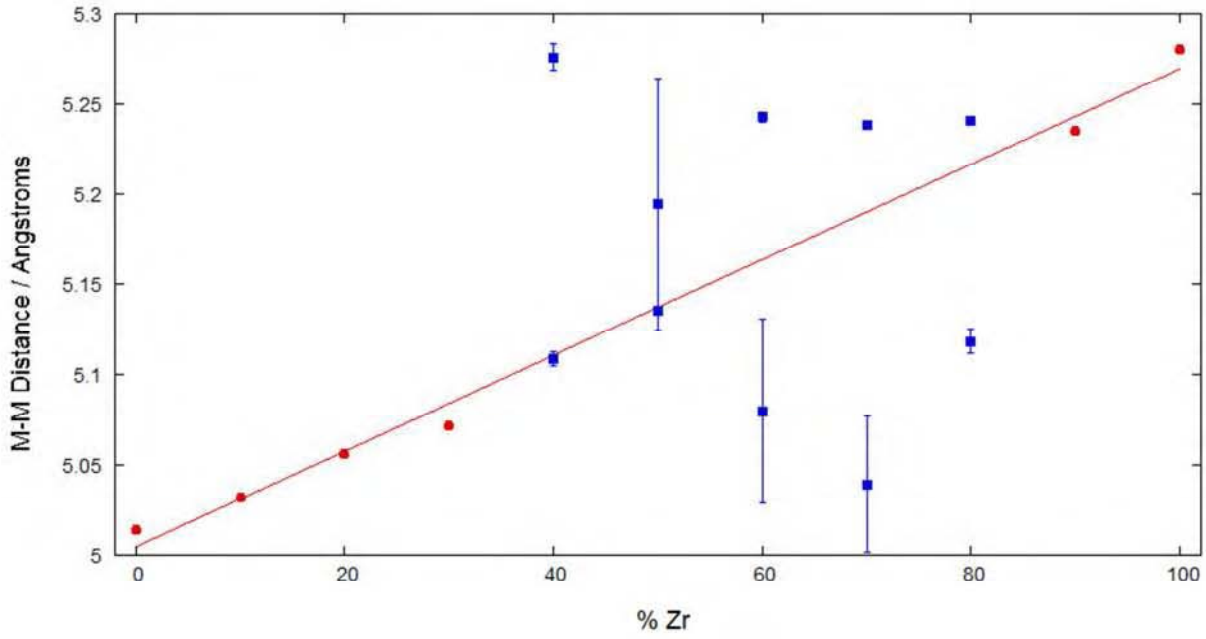

Figure 3.15: A graph of metal-metal distance versus composition as determined from peak fitting in Origin. The red circles are the data for the single phase phosphates and the blue squares the two phase phosphates; the red line indicates the best fit.

Variation in the peak intensity for the metal-oxygen and metal-metal peaks is readily explained by the different scattering powers of zirconium and titanium. Whilst the oxygen-oxygen and phosphorus-phosphorus peaks should be immune to this intensity effect they appear not to be, this is most likely due to other atomic distances that involve metal atoms occurring at similar distances. For example P-O-M-O distances can occur at approximately 3.39 Å (cf. oxygen-oxygen peak at 3.44 Å) and O-P-O-M distances at 4.36 Å (cf. phosphorus-phosphorus peak at 4.44 Å).

A particular strength of the PDF method is that it should be more powerful than Rietveld analysis for determining the distribution of metals in solid solutions. There are three possible types of metal ordering within these systems: complete random disorder, local clustering

and phase segregation in large domains as depicted in Figure 3.16. PDF can distinguish between these by, for example, studying in detail the M-M peaks and in the case of clustering determine the length scale. If the products were two-phase then one would expect to see two separate peaks in the region of 5 Å, reflecting the presence of both Zr-Zr and Ti-Ti distances. Single phase products with no metal ordering are expected to display a single peak varying in distance throughout the series, but a clustering of metal atoms is expected to produce at least three peaks (representing Zr-Zr, Ti-Ti and Zr-Ti distances). An inspection of the metal-meal peak region in the PDF patterns for the whole series (refer back to Figure 3.14), is indicative that the solid solutions with x = 0.1, 0.2, 0.3 and 0.9 have a random distribution of the metal atoms within the layers, rather than clustering. This is evident from the presence of one peak with a smoothly changing M-M distance. These findings are in contrast to those reported by Farfan-Torres *et al*.[2] where it was indicated that there was a hexagonal distribution of the metal atoms within the planes of the solid solutions formed. The only evidence given to support this hypothesis was the metal ratios of the products believed from XRD to be single phase. Rietveld refinements do not provide such information about the metal ordering within these systems.

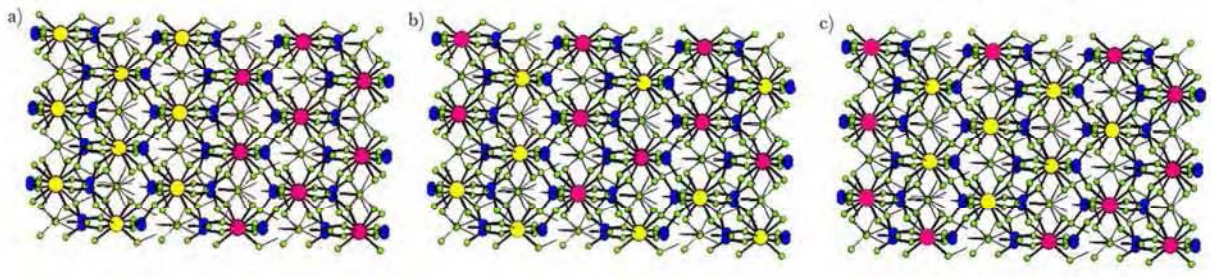

Figure 3.16: Possible metal distributions: (a) phase segregation, (b) random disorder and (c) clustering where Ti atoms are pink and Zr are yellow.

For the *x* = 0.4, 0.5, 0.6, 0.7 and 0.8 products the M-M peaks appear to consist of two overlapping peaks which is in keeping with the two-phase nature of these products as seen from the Rietveld refinements.

3.1.2.5 PDF Structure Refinement

All of the PDF refinements for the single phase materials were modelled using PDFGUI[7], following the method outlined in Section 2.6.3. The starting models were as noted for the Rietveld work (see Section 3.1.2.3) and the metal fractions refined. The fits were excellent, with R_{wp} values of 0.084, 0.058, 0.061, 0.108 and 0.065 for *x* = 0, 0.1, 0.2, 0.3, 0.9 and 1, respectively. A summary of unit cell parameters and metal-oxygen bond distances are given along with a comparison to those derived from the Rietveld refinements in Table 3.11. Fits to the data and crystallographic details can be found in Tables 3.12 – 3.17 and Figures 3.17 – 3.22. The crystallographic refinement files can be found in Appendix 4. Even though these materials are crystallographically relatively complex compared with other systems studied using PDF in the literature, the correspondence of refined unit cells and atomic parameters with the more conventional Rietveld analysis are very good.

No accurate estimated standard deviations could be calculated for the derived parameters as an area detector was employed to collect the data and the integration software FIT2D[8] does not produce estimated standard deviations on the individual data points.

Table 3.11: Comparison of refined unit cell parameters and metal-oxygen distances for the single-phase members of the series, PDF derived numbers are in normal font and those from Rietveld analysis are shown in italics for comparison. The esd's on the numbers from the PDF analysis are undetermined as esd's on the individual data points are unknown.

	α- TiP	α- $Ti_{0.9}Zr_{0.1}(HPO_4)_2.H_2O$	α- $Ti_{0.8}Zr_{0.2}(HPO_4)_2.H_2O$	α- $Ti_{0.7}Zr_{0.3}(HPO_4)_2.H_2O$	α- $Ti_{0.1}Zr_{0.9}(HPO_4)_2.H_2O$	α- ZrP
a/Å	8.628	8.662	8.659	8.763	9.186	9.107
	8.63267(6)	*8.65991(12)*	*8.69672(13)*	*8.7156(3)*	*9.0048(2)*	*9.06336(2)*
b/Å	5.008	5.027	5.081	5.073	5.167	5.276
	5.00672(3)	*5.02351(6)*	*5.04765(7)*	*5.0582 (1)*	*5.2513(1)*	*5.29060(1)*
c/Å	16.11	16.12	16.16	16.26	16.21	16.26
	16.19025(24)	*16.21800(34)*	*16.23560(35)*	*16.2408(7)*	*16.2680(5)*	*16.24603(6)*
β/°	110.26	110.34	109.85	110.69	111.63	111.42
	110.2065(6)	*110.2554(9)*	*110.3460(9)*	*110.4008(18)*	*111.2093(13)*	*111.40120(2)*
V /Å^3	652.91	658.08	668.84	676.42	715.07	727.31
	656.697(11)	*661.90(2)*	*668.25(2)*	*671.07(4)*	*718.82(14)*	*717.16(3)*
M-O(1)/ Å	2.014	1.854	2.046	1.948	1.918	2.240
	1.944(9)	*1.983(7)*	*1.998(9)*	*1.998(12)*	*2.119(13)*	*2.083(5)*
M-O(2)/ Å	1.913	2.002	2.097	1.939	2.472	1.985
	1.942(11)	*1.960(8)*	*1.975(10)*	*1.937(16)*	*2.089(16)*	*2.090(6)*
M-O(3)/ Å	1.899	1.961	1.853	1.929	2.092	2.100
	1.913(11)	*1.874(9)*	*1.960(10)*	*1.938(16)*	*1.980(16)*	*2.086(6)*
M-O(5)/ Å	1.918	2.095	1.986	2.117	2.009	2.082
	1.969(10)	*1.978(8)*	*1.978(10)*	*1.937(15)*	*2.207(15)*	*2.084(6)*
M-O(6)/ Å	2.024	1.907	1.924	2.041	2.093	2.096
	1.941(11)	*1.969(9)*	*1.987(11)*	*1.983(17)*	*2.084(17)*	*2.105(6)*
M-O(7)/ Å	1.875	1.931	1.956	2.126	2.126	2.009
	1.962(8)	*1.988(7)*	*1.944(8)*	*1.952(11)*	*2.075(10)*	*2.090(5)*
<M-O>/ Å	1.940	1.958	1.977	2.017	2.118	2.085
	1.945	1.959	1.974	1.958	2.092	2.090

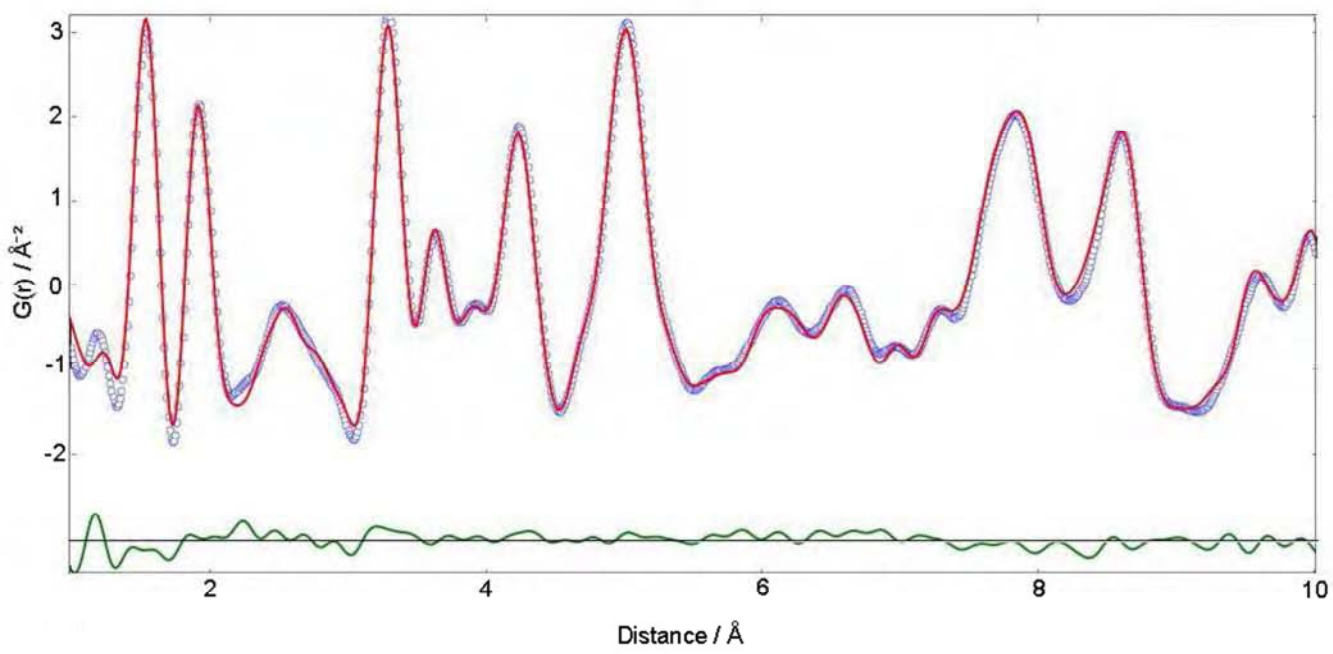

Figure 3.17: Final observed (blue), calculated (red), and difference (green) PDF profiles for α-$Ti(HPO_4)_2.H_2O$.

Table 3.12: Fractional atomic and isotropic displacement parameters for α-$Ti(HPO_4)_2.H_2O$ from the PDF refinement.

atom	*x*	*y*	*z*	U_{iso} (x10^2) Å^2
Ti	0.7623	0.2559	0.5134	0.04
P(1)	0.9963	0.7459	0.6099	0.06
P(2)	0.4739	0.2313	0.5978	0.06
O(1)	0.0854	0.8389	0.5527	0.09
O(2)	0.9506	0.4405	0.5914	0.09
O(3)	0.8509	0.9498	0.5833	0.09
O(4)	0.0917	0.7634	0.7114	0.09
O(5)	0.3186	0.4317	0.5572	0.09
O(6)	0.4268	0.9460	0.5748	0.09
O(7)	0.6335	0.2917	0.5857	0.09
O(8)	0.4907	0.2557	0.6957	0.09
O(9)	0.2232	0.1537	0.7499	0.32

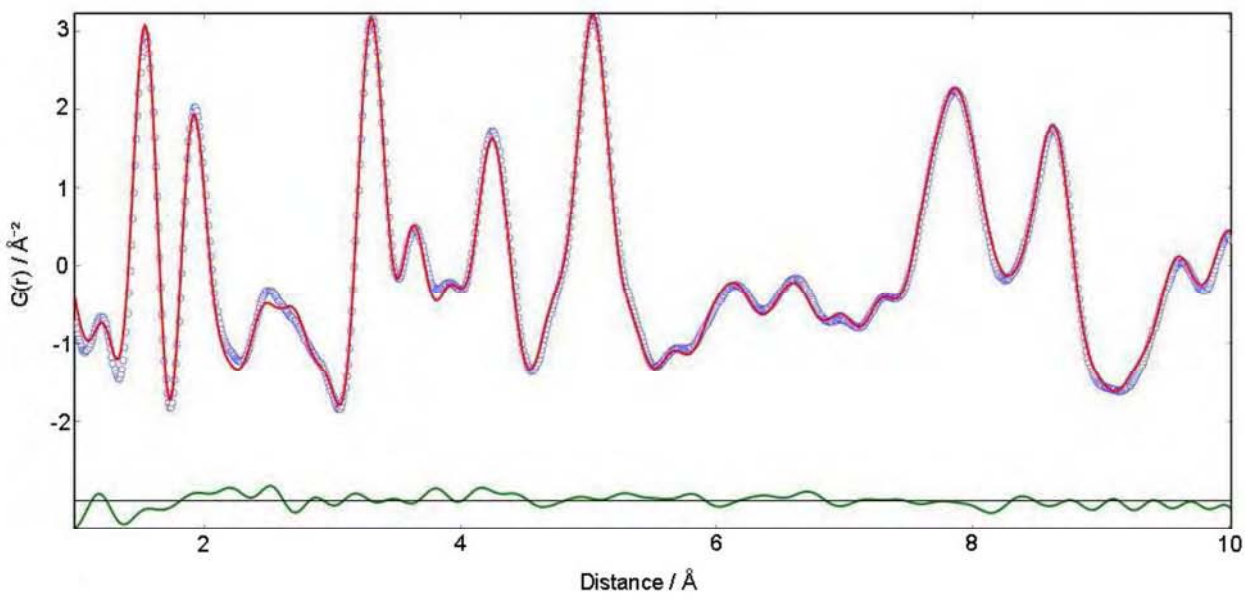

Figure 3.18: Final observed (blue), calculated (red), and difference (green) PDF profiles for α-$Ti_{0.9}Zr_{0.1}(HPO_4)_2.H_2O$.

Table 3.13: Fractional atomic and isotropic displacement parameters for α-$Ti_{0.9}Zr_{0.1}(HPO_4)_2.H_2O$ from the PDF refinement.

atom	*x*	*y*	*z*	U_{iso} (x10^2) Å^2	Fractional Occupancy
Ti	0.7635	0.2622	0.5142	0.04	0.9552
Zr	0.7635	0.2622	0.5142	0.04	0.0448
P(1)	0.0051	0.7474	0.6123	0.02	
P(2)	0.4682	0.2378	0.5955	0.02	
O(1)	0.0995	0.8297	0.5479	0.01	
O(2)	0.9469	0.4395	0.6105	0.01	
O(3)	0.8521	0.9350	0.5791	0.01	
O(4)	0.0962	0.7898	0.7101	0.01	
O(5)	0.3262	0.4112	0.5693	0.01	
O(6)	0.4000	0.9628	0.5641	0.01	
O(7)	0.6268	0.3399	0.5838	0.01	
O(8)	0.5032	0.2603	0.6950	0.01	
O(9)	0.2560	0.1812	0.7447	0.15	

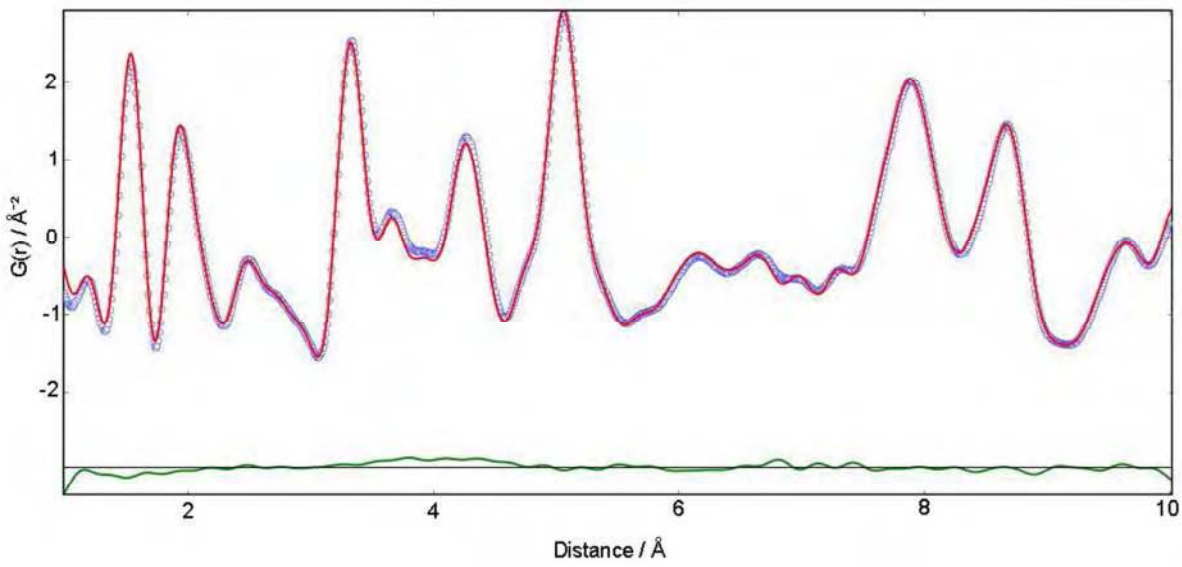

Figure 3.19: Final observed (blue), calculated (red), and difference (green) PDF profiles for α-$Ti_{0.8}Zr_{0.2}(HPO_4)_2.H_2O$.

Table 3.14: Fractional atomic and isotropic displacement parameters for α-$Ti_{0.8}Zr_{0.2}(HPO_4)_2.H_2O$ from the PDF refinement.

atom	*x*	*y*	*z*	U_{iso} (x10^4) Å^2	Fractional Occupancy
Ti	0.7621	0.2440	0.5122	0.20	0.840
Zr	0.7591	0.2483	0.5126	0.20	0.160
P(1)	0.0060	0.7670	0.6150	0.06	
P(2)	0.4720	0.2536	0.6017	0.06	
O(1)	0.1003	0.8940	0.5594	0.07	
O(2)	0.9438	0.4809	0.5991	0.07	
O(3)	0.8495	0.9400	0.5736	0.07	
O(4)	0.0886	0.7321	0.2099	0.07	
O(5)	0.3293	0.4371	0.5585	0.07	
O(6)	0.3877	0.9555	0.5824	0.07	
O(7)	0.6243	0.3247	0.5830	0.07	
O(8)	0.5053	0.1947	0.7017	0.07	
O(9)	0.2462	0.1866	0.7459	0.07	

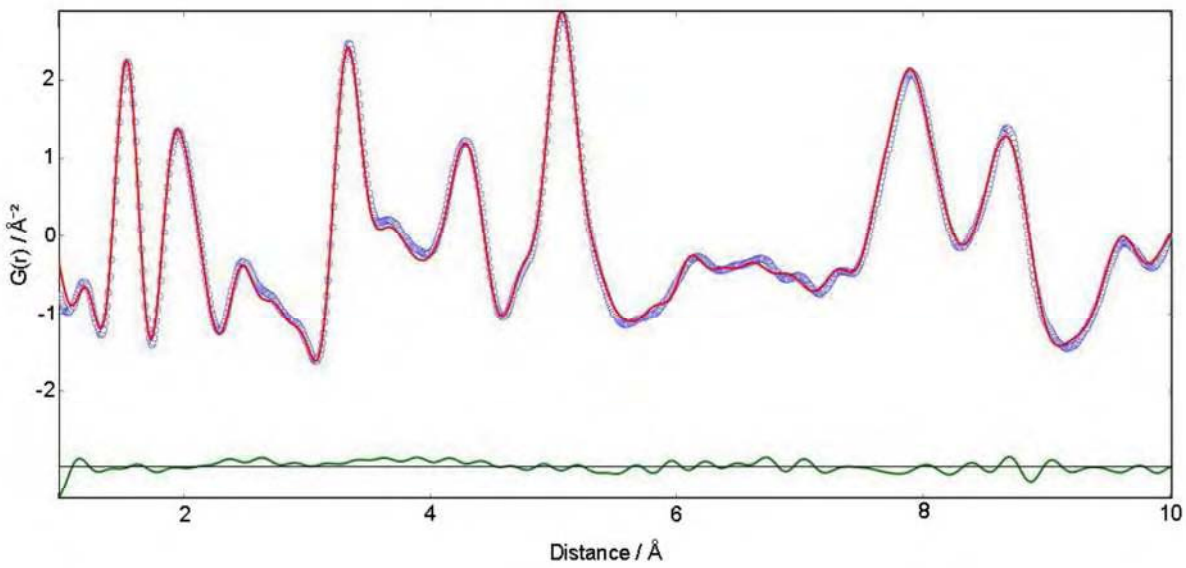

Figure 3.20: Final observed (blue), calculated (red), and difference (green) PDF profiles for α-$Ti_{0.7}Zr_{0.3}(HPO_4)_2.H_2O$.

Table 3.15: Fractional atomic and isotropic displacement parameters for α-$Ti_{0.7}Zr_{0.3}(HPO_4)_2.H_2O$ from the PDF refinement.

atom	*x*	*y*	*z*	U_{iso} (x10^2) Å^2	Fractional Occupancy
Ti	0.7679	0.2443	0.5177	0.02	0.80
Zr	0.7679	0.2443	0.5177	0.02	0.20
P(1)	0.0005	0.7380	0.6145	0.05	
P(2)	0.4668	0.2654	0.5934	0.05	
O(1)	0.1147	0.8438	0.5604	0.04	
O(2)	0.9101	0.4581	0.6129	0.04	
O(3)	0.8760	0.9559	0.5931	0.04	
O(4)	0.1107	0.7196	0.7098	0.04	
O(5)	0.3187	0.4372	0.5707	0.04	
O(6)	0.4125	0.9748	0.5697	0.04	
O(7)	0.6368	0.3528	0.6003	0.04	
O(8)	0.4858	0.2270	0.7100	0.04	
O(9)	0.2624	0.2204	0.7620	0.04	

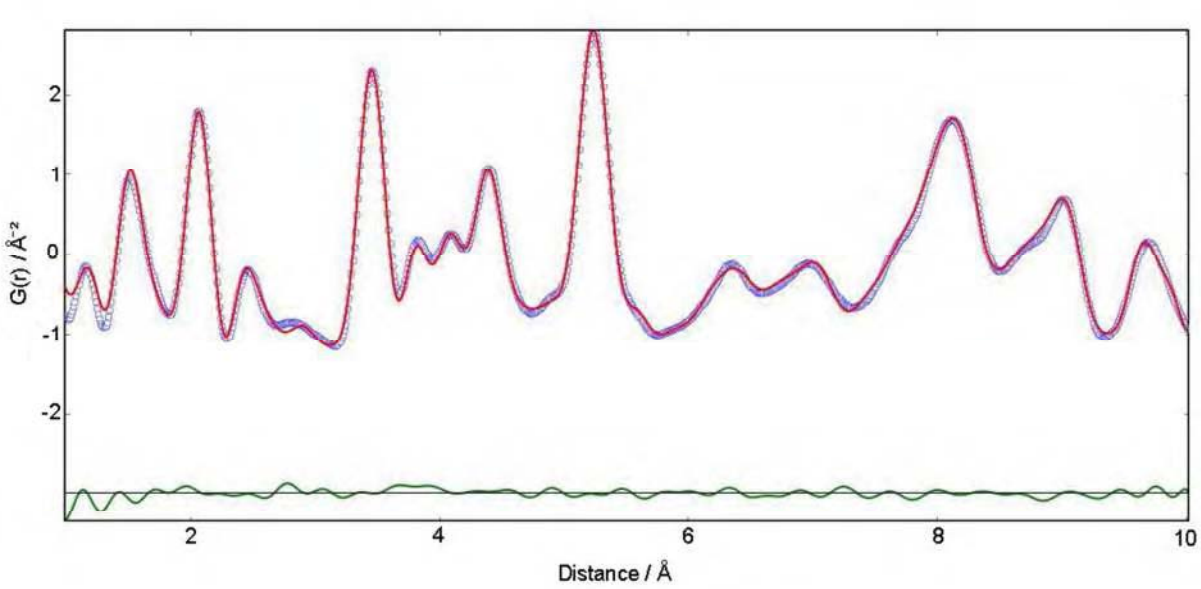

Figure 3.21: Final observed (blue), calculated (red), and difference (green) PDF profiles for α-$Ti_{0.1}Zr_{0.9}(HPO_4)_2.H_2O$.

Table 3.16: Fractional atomic and isotropic displacement parameters for α-$Ti_{0.1}Zr_{0.9}(HPO_4)_2.H_2O$ from the PDF refinement.

atom	*x*	*y*	*z*	U_{iso} (x10^2) Å^2	Fractional Occupancy
Ti	0.75814	0.22361	0.50529	0.308524	0.22
Zr	0.75814	0.22361	0.50529	0.308524	0.78
P(1)	-0.03275	0.72619	0.62711	0.00009	
P(2)	0.48268	0.25693	0.60543	0.00009	
O(1)	0.12003	0.83285	0.56479	0.00001	
O(2)	0.93500	0.50659	0.62224	0.00001	
O(3)	0.83558	0.92263	0.59587	0.00001	
O(4)	0.10452	0.76334	0.70526	0.00001	
O(5)	0.33905	0.44735	0.56109	0.00001	
O(6)	0.40982	0.00975	0.58075	0.00001	
O(7)	0.61668	0.34763	0.57871	0.00001	
O(8)	0.50162	0.21400	0.71070	0.00001	
O(9)	0.32298	0.21090	0.76064	0.00035	

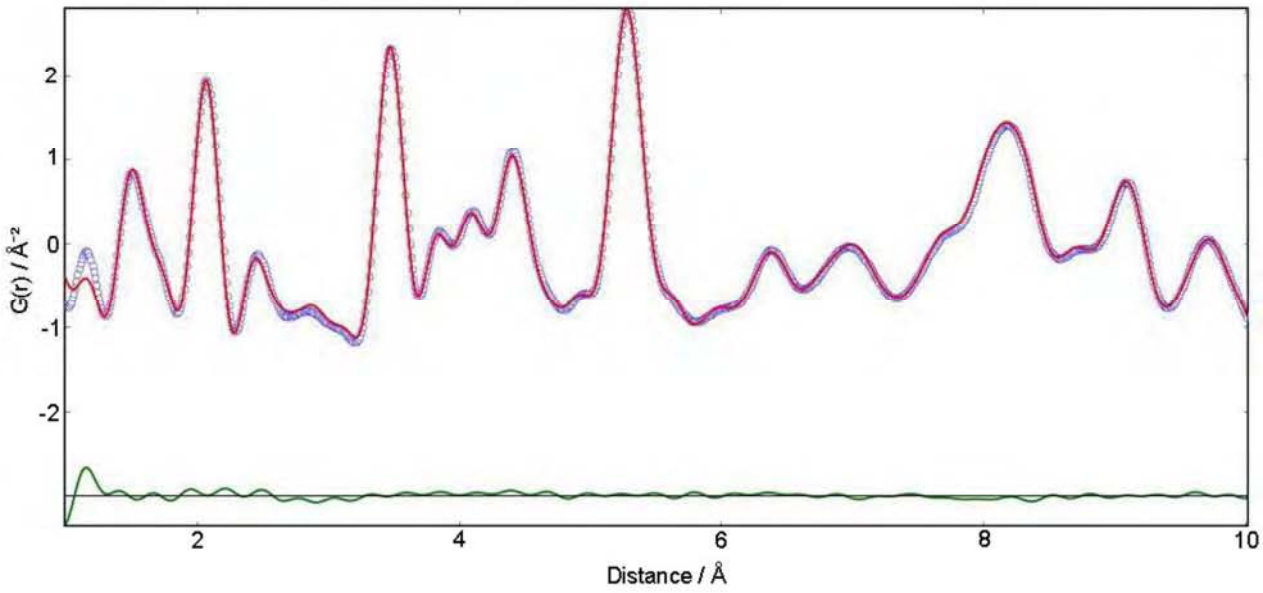

Figure 3.22: Final observed (blue), calculated (red), and difference (green) PDF profiles for α-$Zr(HPO_4)_2.H_2O$.

Table 3.17: Fractional atomic and isotropic displacement parameters for α-$Zr(HPO_4)_2.H_2O$ from the PDF refinement.

atom	*x*	*y*	*z*	U_{iso} (x10^2) Å^2
Zr	0.7575	0.2556	0.5151	0.022
P(2)	0.0048	0.7390	0.6093	0.030
P(3)	0.4767	0.2563	0.6118	0.030
O(1)	0.1063	0.9125	0.5617	0.004
O(2)	0.8995	0.4977	0.6013	0.004
O(3)	0.8560	0.9628	0.6061	0.004
O(4)	0.1137	0.7672	0.7036	0.004
O(5)	0.3464	0.4179	0.5534	0.004
O(6)	0.4197	0.9670	0.5746	0.004
O(7)	0.6213	0.2976	0.5875	0.004
O(8)	0.5049	0.2684	0.7067	0.004
O(9)	0.2633	0.2019	0.7745	0.001

3.1.2.6 Comparison of Refinement Methods

Both PDF and Rietveld methods have been used to successfully refine the structural models of the single phase mixed zirconium-titanium phosphates. For the end members, α-ZrP and α-TiP, the values and parameters obtained from both techniques compare well with literature values (Tables 3.18 and 3.19). There is also good agreement between the values obtained for the mixed metal phosphates from both techniques as shown in Table 3.11. There is no literature data for comparison. Due to the nature of the PDF method, which gives real space information regarding neighbouring atoms, one may expect that the PDF refinements would provide more accurate average bond distances whereas a Rietveld analysis would be better employed in the determination of accurate unit cell parameters.

However for these crystalline systems the values obtained from the Rietveld refinements are believed to be more reliable than those obtained from the PDF refinements for the reasons outlined in section 2.6.3. Firstly, the data obtained from the PDF refinements may include a contribution from amorphous phases that may be present in the products, therefore lowering the reliability of the results. This is less of a problem in the Rietveld refinements where the information from any amorphous phases present would be modelled within the background, and therefore should not contribute to the data within the Bragg peaks. In addition to this one must also consider the information loss associated in going from 100+ sharp peaks in the XRD patterns to only ~20 broad peaks in the PDF patterns used for the PDF refinements.

Table 3.18: Comparison of the refinement parameters for α-TiP to those in the literature[5].

	Rietveld	PDF	Literature[5]
a / Å	8.63267(6)	8.628	8.6110(3)
b / Å	5.00672(3)	5.008	4.9963(2)
c / Å	16.19025(24)	16.11	16.1507(7)
β /°	110.2065(6)	110.26	110.206(3)
Cell Volume / Å^3	656.70(1)	652.91	-
<M-O> / Å	1.945	1.940	1.946

Table 3.19: Comparison of the refinement parameters for α-ZrP to those in the literature[6].

	Rietveld	PDF	Literature[6]
a / Å	9.06336(2)	9.107	9.0610(10)
b / Å	5.29060(1)	5.276	5.2873(7)
c / Å	16.2460(6)	16.26	16.2481(31)
β /°	111.4012(2)	111.42	111.41(1)
Cell Volume / Å^3	717.16(3)	727.31	724.70
<M-O> / Å	2.090	2.085	-

3.1.2.7 Unit Cell Variations

Various plots for selected unit cell parameters and mean metal-oxygen distances for the single phase mixed metal phosphates, as obtained from the Rietveld and PDF refinements, are shown in Figure 3.23. The Rietveld data is shown as red circles and the PDF as blue squares. The variation in the monoclinic angle is not shown, but it is clear from the data in

Table 3.11 that it varies in a similar, yet much less dramatic fashion. As expected, all of these parameters increase with the content of the larger zirconium ion. The fact that the *a*- and *b*-axes are much more sensitive to the metal content is readily explained by the layers and more of the M-O bonds being in the *a,b*-plane. Nearly all of the volume expansion when moving from titanium to zirconium is due to these as the interplanar spacing, approximately along the *c*-axis, is the same for both end members at 7.56 Å. In the graphs there are two lines plotted. One of these connects the average values of the end members and therefore if the mixed samples obeyed Vegard's Law one would expect their values to fall on that line. In each graph a second line is drawn based on a least-squares fit to the four points for the titanium end member samples.

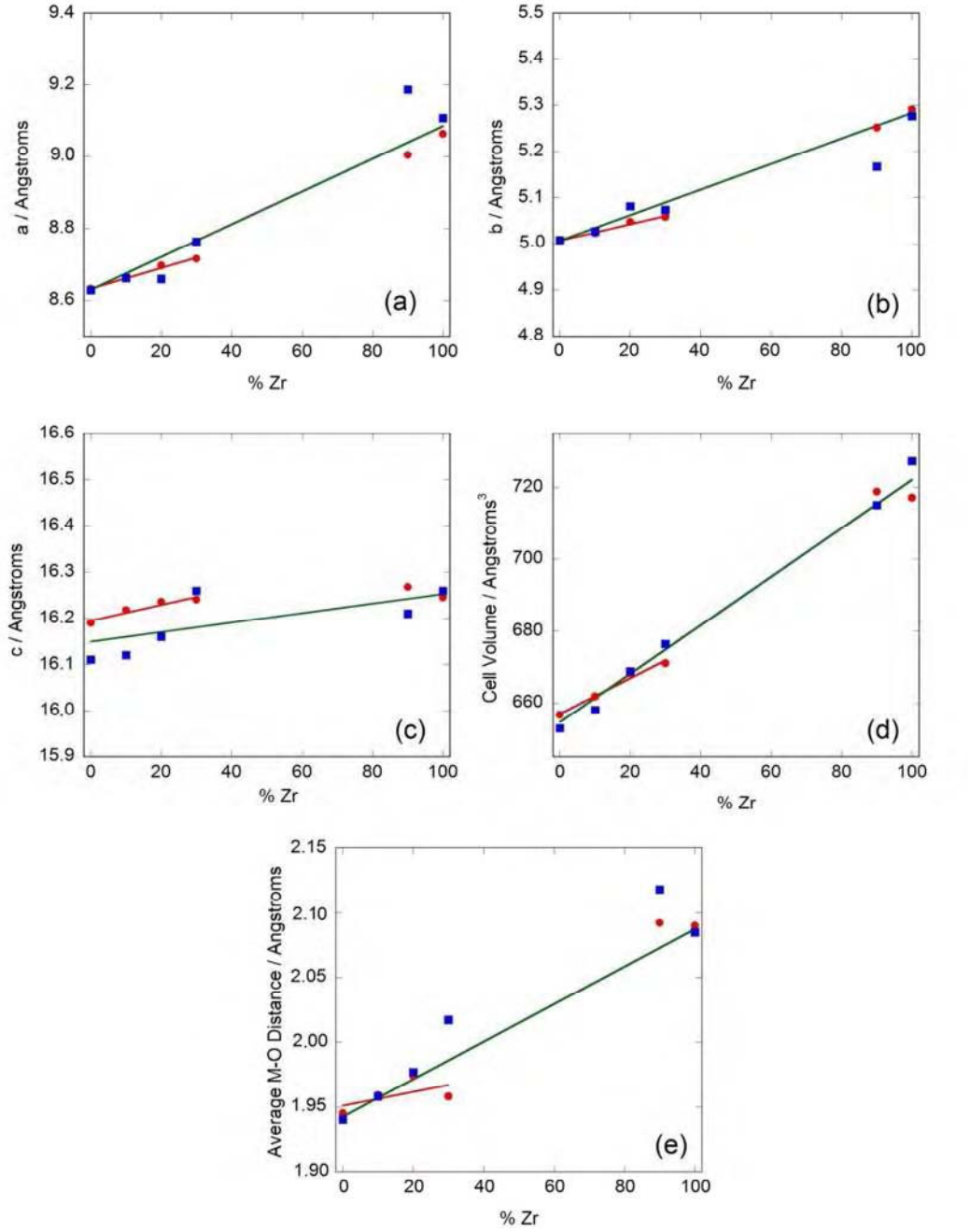

Figure 3.23: Unit cell parameters for: (a) *a*-axis; (b) *b*-axis; (c) *c*-axis; (d) volume and (e) mean M-O distance versus %Zr for the single-phase compositions in the Zr/Ti series. Red circles are data from the Rietveld refinements and blue squares from the PDF fits. The green lines connect the average values from the end members and the red lines are best fits for the Rietveld points at the titanium rich end.

These all have a smaller gradient than expected. In fact it appears that they change little with metal doping in spite of the rather large differences in the ionic radii of Ti^{4+} and Zr^{4+}, 74.5 and 86 pm, respectively. This may be a significant indicator that the introduction of the larger zirconium ion strains the system and may be an underlying feature preventing the formation of the full range of solid solutions.

3.1.2.8 Other Synthetic Methods

Variations of the hydrothermal method used as well as other synthetic methods were investigated to see if solid solutions of the zirconium-titanium series could be produced. It was also of interest to see if alternative methods held any advantage over the hydrothermal route used e.g. avoiding the potential hydrolysis of $TiCl_4$ when in contact with water.

A series of variations on the hydrothermal route used to produce the phosphates were conducted to investigate the effects of temperature, duration etc on the synthesis of $Ti_{0.5}Zr_{0.5}(HPO_4)_2.H_2O$. These included:

- An increase in oven temperature from 150 °C to 200 °C.
- Extended duration of the autoclave step from one week to two weeks.
- A change in the acid used to make the $TiCl_4$ solutions from acetic acid to hydrochloric.
- A 'one-pot' synthesis whereby all reagents were placed directly in the bomb, omitting the 24 hour stirring step.

The powder XRD patterns of the products obtained from these investigations are shown in Figure 3.24 along with the original $Ti_{0.5}Zr_{0.5}(HPO_4)_2.H_2O$ product. The one pot method and the increased duration of two weeks had a detrimental effect on the product crystallinity.

The increased temperature on the other hand produced a more crystalline product as shown by the sharper more intense peaks. Upon close inspection of the patterns, particularly around 20 -30 ° 2θ it is evident that all the products remain two phase.

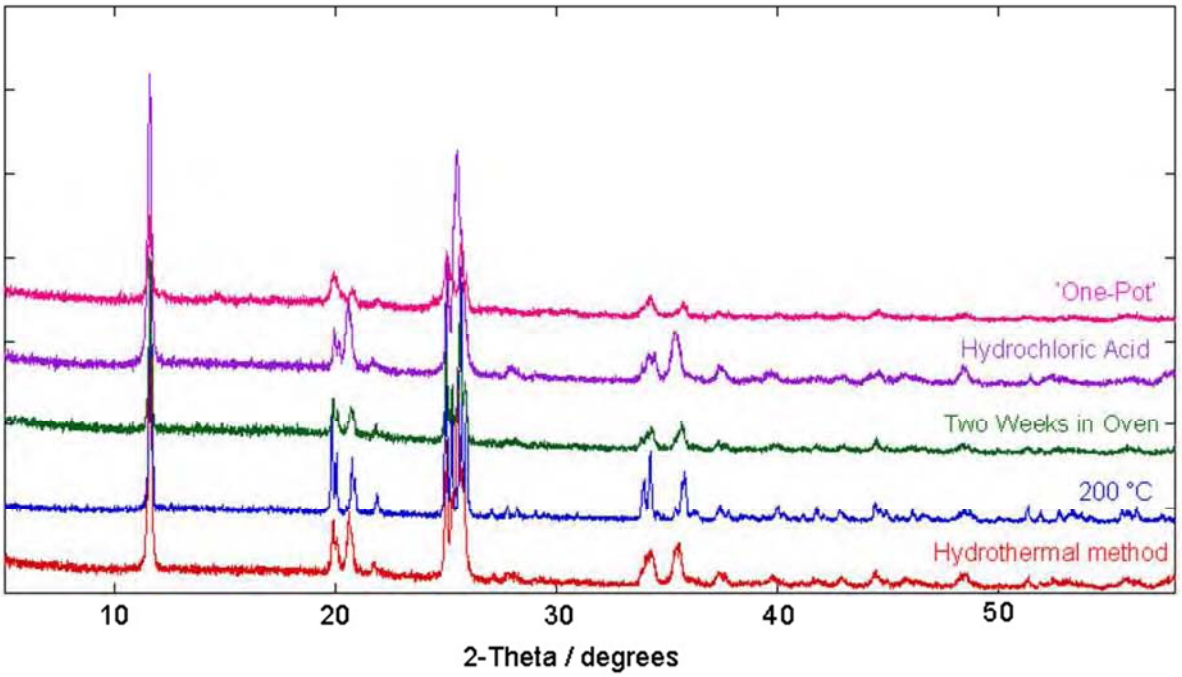

Figure 3.24: Laboratory powder XRD patterns of the $Ti_{0.5}Zr_{0.5}(HPO_4)_2.H_2O$ products obtained from the variations of the hydrothermal method.

Various alternative methods found in the literature were also investigated for the synthesis of $Ti_{0.5}Zr_{0.5}(HPO_4)_2.H_2O$. These included two sol gel methods, based on those reported by Farfan-Torres *et al.*[2] and by Thakkar and Chudasama[3] and an oxalic acid method reported by Capitani *et al.*[9]. The powder XRD patterns of the products are compared in Figure 3.25. The crystallinity of the product obtained from the oxalic acid method was severely reduced. In the literature report only pure α-ZrP was synthesised to a high degree of crystallinity[9]. The other two products, obtained from the two different sol gel methods, showed evidence of being two phase. The $Ti_{0.5}Zr_{0.5}(HPO_4)_2.H_2O$ products synthesised by these methods in the

literature were reported as being single phase[2,3], however close inspection of the XRD patterns published is suggestive of a two phase nature.

Variation in the peak height ratios of the products suggest differing ratios of the two phases are obtained via each method. In addition to this no increased yields were obtained.

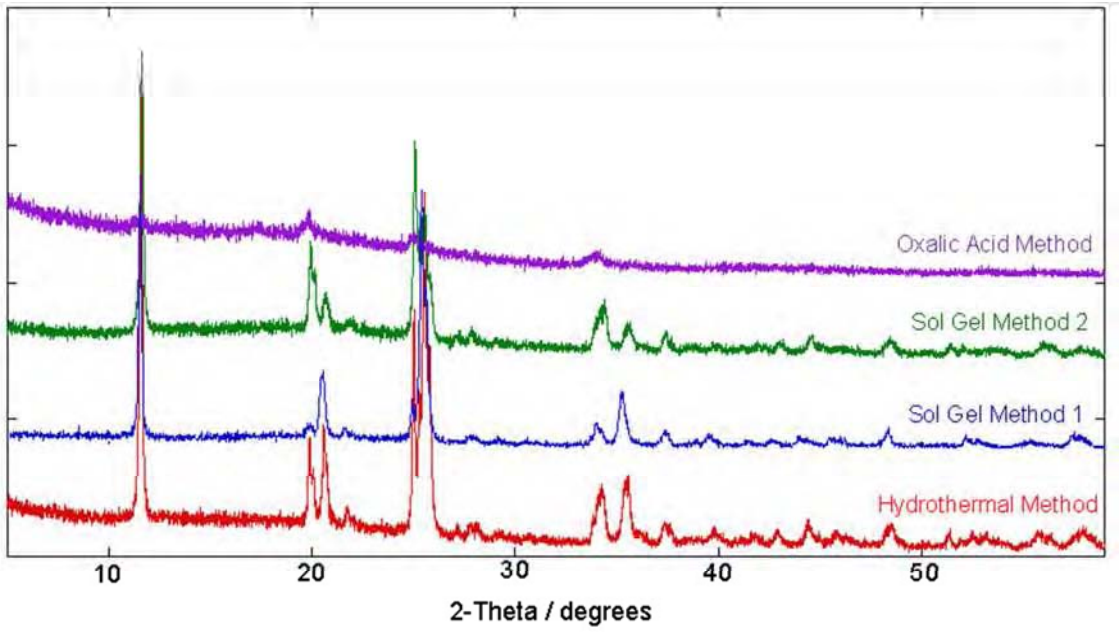

Figure 3.25: Laboratory powder XRD patterns of the $Ti_{0.5}Zr_{0.5}(HPO_4)_2.H_2O$ products synthesised by the different literature methods: Sol gel 1 (Farfan-Torres *et al.*[2]), Sol gel 2 (Thakkar and Chudasama[3]) and Oxalic Acid method[9]

Silicon Substitution

The ability of α-TiP to withstand a larger % of zirconium than α-ZrP could titanium was unexpected due to the smaller unit cell size of α-TiP and the larger incoming ion, zirconium. One rationalisation for this might be that the swelling of the α-TiP structure needed to accommodate zirconium is energetically easier than the twisting deformations of the bonds required in the α-ZrP structure to accommodate the smaller titanium. To investigate this further, $Ti_{1-x}Zr_x(H_{1-x}P_{1-x}Si_xO_4)_2.H_2O$ systems were prepared with the view that replacing some

of the phosphorus with smaller silicon may allow for greater substitution of the second metal. The *x* = 0.25, 0.5 and 0.75 phosphates were synthesised by a method outlined in Section 2.2.1.1. The presence of silicon was confirmed by XRF measurements but much smaller amounts were found than expected (Table 3.20). Investigation into the unit cell parameters of these products would need to be undertaken to establish whether the silicon present had been substituted for phosphorus or whether it was surface absorbed. However, from the XRD analyses of the products (shown in Figure 3.25) it was evident that two phase products had been synthesised. Consequently no further work was carried out on this system, but variations on the method/precursors used may be of interest for future study.

Table 3.20: Comparison of the Si:P Ratios in the $Ti_{1-x}Zr_x(H_{1-x}P_{1-x}Si_xO_4)_2.H_2O$ products

Product	Si : P Molar Ratio	
	Nominal	XRF
$Ti_{0.75}Zr_{0.25}(H_{0.75}P_{0.75}Si_{0.25}O_4)_2.H_2O$	0.33	0.08
$Ti_{0.5}Zr_{0.5}(H_{0.5}P_{0.5}Si_{0.5}O_4)_2.H_2O$	1.00	0.25
$Ti_{0.25}Zr_{0.75}(H_{0.25}P_{0.25}Si_{0.75}O_4)_2.H_2O$	3.00	0.19

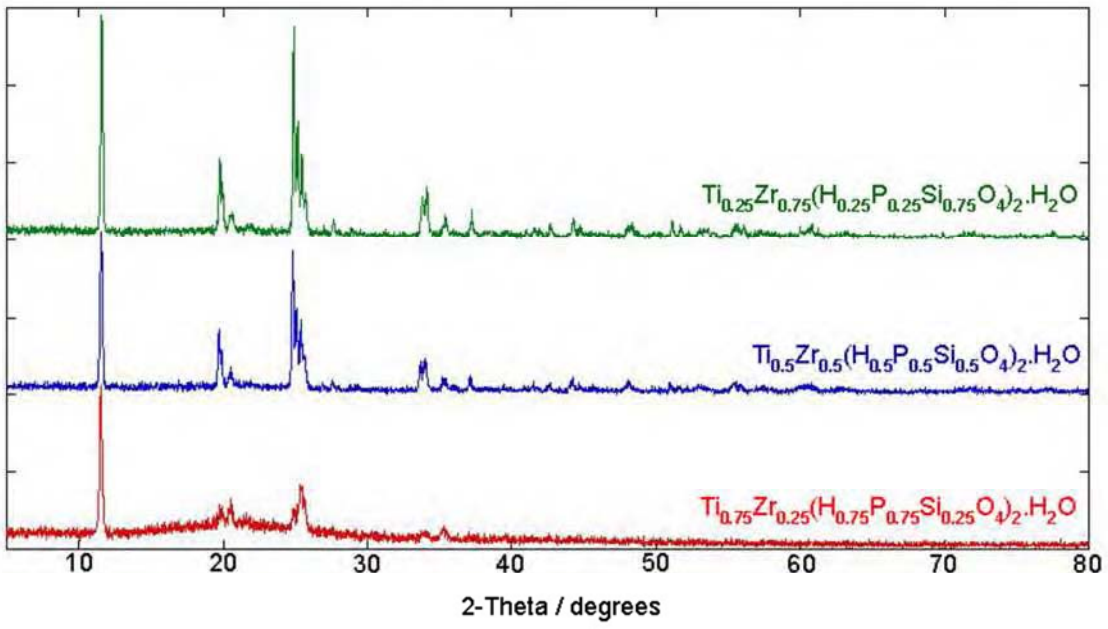

Figure 3.26: Laboratory powder XRD patterns of the $Ti_{1-x}Zr_x(H_{1-x}P_{1-x}Si_xO_4)_2.H_2O$ series.

3.1.2.9 Limits of the Solid Solution

The findings in this section support the idea that the saturation point of zirconium within α-TiP is around 30 % and titanium in α-ZrP is around 10 % even though the end members are isostructural. This differs slightly from previous findings[2] where it was believed that both unit cells could withstand 25 % metal substitution but not 33 %.

The average metal-oxygen distance does not vary too much from the end member values when the second metal is accommodated. It may be that the unit cells cannot withstand the alterations required in the *a*- and *b*- directions to accommodate more of the second metal. The strain arising from the lack of flexibility within the octahedral coordination environment plays an important part in frustrating the formation of solids with the intermediate compositions. It was also noted that in all of the two-phase systems there was a much larger amorphous component in the powder diffraction patterns, also indicative of a frustrated system and perhaps one that is unable to crystallise under the relatively mild conditions employed. These amorphous components were thought to cause the discrepancy in the compositions obtained from the Rietveld and XRF analyses, where, in general the bulk solids were titanium rich. To investigate this further XRF measurements were obtained at various stages throughout the synthesis of $Ti_{0.5}Zr_{0.5}(HPO_4)_2.H_2O$. The molar ratio of titanium to zirconium in the filtrate was found to be 0.6 which was less than the starting value of 1.0 and showed that there was an excess of zirconium remaining in solution. Indeed both the crude and crystalline products obtained were titanium rich with ratios of 1.2 and 1.1 respectively.

The full answer may therefore be more complicated than just lattice strain, and involve aspects of the solution chemistry, nature of the amorphous pre-cursor(s) from which the

layered phosphates crystallise and relative rates of crystallisation under the mild hydrothermal conditions employed.

3.1.2.10 Global Instability Index (GII)

The global instability index (GII) is derived from the bond valence model and represents the instability of a given structure[10]. The bond valence model provides a useful and quantitative description of inorganic bonding in ionic solids. In this model, the sum of the bond valences calculated from the experimental structural data for each ion in the structure is compared with its nominal valence. The bond valence (S_{ij}) is given by Equation 3.1:

$$S_{ij} = exp\left[\left(R_o - R_{ij}\right)\Big/_B\right]$$

R_o is the characteristic bond distance for the cation-anion pair

R_{ij} is the experimentally determined bond length of the cation-anion pair.

B is taken to be a universal constant[11] equal to 0.37 Å

Equation 3.1: The bond valence equation

The valence sum rule establishes that the sum of the bond valence ($\Sigma_j S_{ij}$) around an ion must be equal to the formal valence (V_i) of that ion. The deviation between these can be attributed to the instability of the structure. The root mean square of the bond valence sum deviations for all the atoms present in the asymmetric unit is a measure of the extent to

which the valence sum rule is violated over the whole structure. It is known as the global instability index[10] and is given by Equation 3.2:

$$GII = \sqrt{\frac{\sum_{i=1}^{N}\left(\sum_j S_{ij} - V_i\right)^2}{N}}$$

$\mathbf{S_{ij}}$ is the bond valence between two atoms i and j.

V is the formal valence

N is the number of atoms

Equation 3.2: Global Instability Index

For unstrained systems the GII is typically below 0.1 valence units (v.u.) and may reach 0.2 v.u. in structures with lattice-induced strain. GII values greater than 0.2 v.u. indicate the presence of intrinsic stains large enough to cause instability at room temperature, potentially leading to a collapse in the structure or phase transformation.

The GII values for the single phase mixed zirconium-titanium phosphates were calculated using the bond lengths obtained from the Rietveld refinements and R_o values found in the literature[12]. For the mixed systems the values were weighted according to their Zr/Ti ratio. The results of the GII calculation, shown in Figure 3.27, provide clear evidence of instabilities in the crystal structures. The α-TiP , $Ti_{0.9}Zr_{0.1}(HPO_4)_2.H_2O$, $Ti_{0.8}Zr_{0.2}(HPO_4)_2.H_2O$ and α-ZrP products have GII values of less than 0.2 v.u (0.128, 0.120, 0.197 and 0.141 v.u. respectively) indicating structures with lattice induced strains. The products, $Ti_{0.7}Zr_{0.3}(HPO_4)_2.H_2O$ and $Ti_{0.1}Zr_{0.9}(HPO_4)_2.H_2O$ however, have much higher GII values of 0.305 and 0.482 v.u. The effect

of further metal substitution at either compositional end should give even higher values which justify the non-existence of them. Instead two less strained phases form.

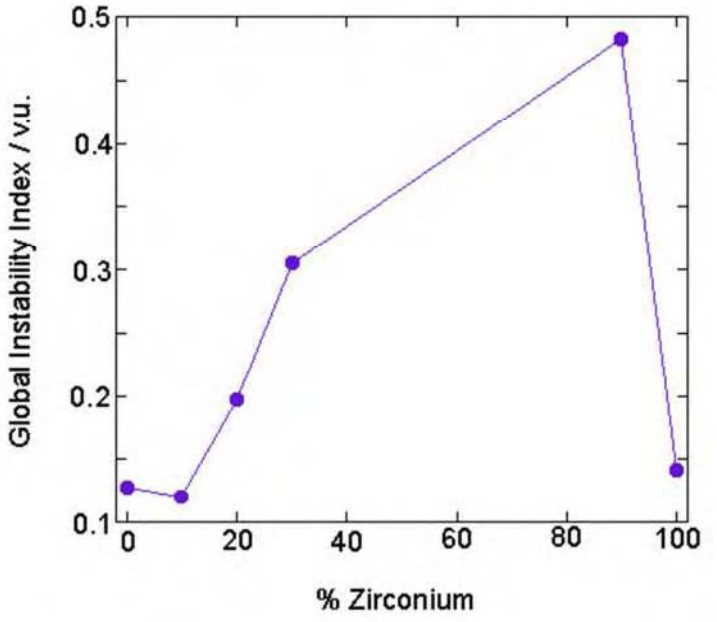

Figure 3.27: The Global Instability Index of the single phase zirconium-titanium series

It is interesting to note that the GII values obtained for the zirconium rich phosphates are higher than their titanium rich counterparts. Indeed it would appear that α-ZrP is a more strained structure and the effect of the addition of titanium is more detrimental to the stability of the structure compared to the addition of zirconium into α-TiP. This readily explains why titanium phosphate has been shown to undergo a 30% metal substitution whereas α-ZrP could only withstand 10%.

3.1.2.11 Thermal Studies

The thermal behaviours of α-TiP and α-ZrP have been widely reported in the literature[1,9,13-16]. Work reported on the mixed zirconium-titanium phosphates found them to exhibit the same thermal behaviour as the end members they were compositionally closest to[1,2,17]. The

thermal studies carried out in this work are in accordance with these reports. The single phase products were analysed by TGA/DTA with mass spectrometry and variable temperature XRD.

Table 3.21: Comparison of the % weight loss from TGA

Product	% Weight Loss during dehydration		% Weight Loss during condensation	
	Theoretical	TGA	Theoretical	TGA
α-TiP	7.0	7.2	7.5	7.4
$Ti_{0.9}Zr_{0.1}(HPO_4)_2.H_2O$	6.9	7.2	7.3	6.9
$Ti_{0.8}Zr_{0.2}(HPO_4)_2.H_2O$	6.8	7.0	7.3	6.6
$Ti_{0.7}Zr_{0.3}(HPO_4)_2.H_2O$	6.6	6.9	7.1	6.7
$Ti_{0.1}Zr_{0.9}(HPO_4)_2.H_2O$	6.1	6.9	6.5	6.2
α-ZrP	6.0	10.8	6.4	4.7

Weight loss curves as determined thermogravimetrically for the series indicate that the products contained approximately two molecules of water (Figure 3.28) per formula unit. One mole is lost at 100 - 200 °C and a second above 400 °C. The two processes represent the loss of the water of crystallisation at low temperatures and condensation of the monohydrogenphosphate groups to form pyrophosphates at the higher temperature. Comparison of the weight loss data with the theoretical values is presented in Table 3.21. The agreement between these is generally good. However the results obtained for α-ZrP were unexpected as they differ from the rest of the series and consequently the experiment was re-run but the same profiles were obtained on a second sample. Given the quality of the Rietveld refinement of this product these 'anomalous' results are unlikely to be due to structural/compositional problems within the sample. The high water loss at low temperatures associated with the additional events in the mass spectrometry and DTA traces can be attributed to a large quantity of surface water present on the sample. In

keeping with previous work on α-ZrP[9,16,18-20] the shape of the TGA trace and the lower than expected water loss associated with the condensation of the phosphates is hypothesised to be as a result of the preparative conditions used. The dehydration kinetics of α-ZrP have been found to be dependent upon the degree of crystallinity of the sample and therefore upon the preparative conditions[9,16,21]. More crystalline samples, like the one in this work, generally undergo slower and partial dehydrations, with condensations proceeding in two stages. It has been shown[16] that as dehydration occurs some of the interlayer water that resides in the inner most part of the microcrystals can remain entrapped. The loss of this water is then delayed until higher temperatures and can in some cases overlap with the loss of the condensation water resulting in less separated thermal events. No clear DTA signal is observed during the condensation, this is presumably because the water loss is spread out so the DTA signal for this event is too broad and weak to be seen.

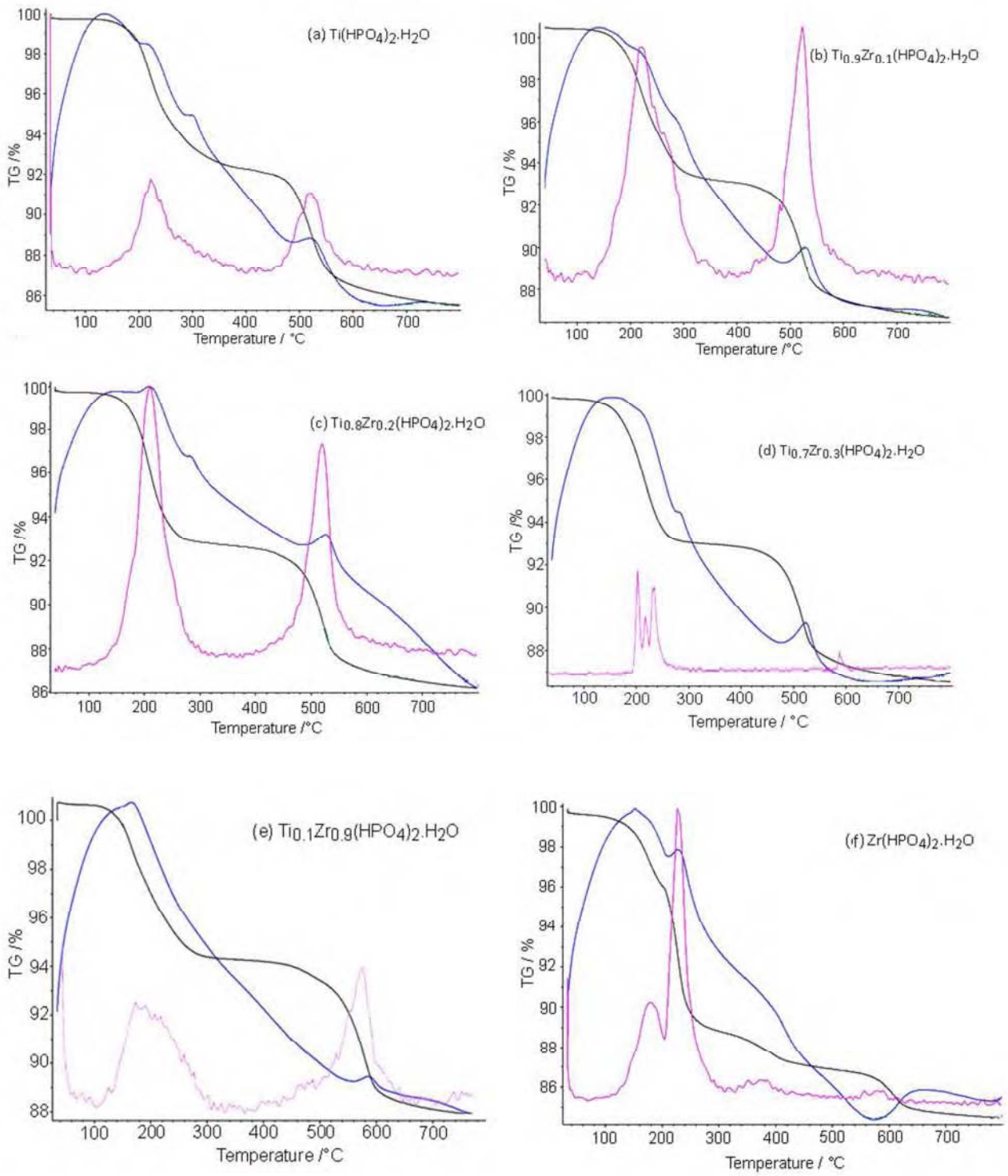

Figure 3.28: TGA traces (black) showing the dehydration pathways of the mixed zirconium-titanium phosphates. The DTA curves are shown in blue and the pink trace represents the mass spectrometry results for H_2O.

The in-situ laboratory XRD patterns of α-TiP recorded as a function of temperature are shown in Figure 3.29. The others can be found in Appendix 3. A reduction in the *d*-spacing of the first crystalline peak (002) is observed upon heating until it disappears at ~700 °C. This signifies a reduction in the interlayer spacing as the layers in the structure collapse down on each other when the water molecules are lost. Three different crystalline phases are shown to occur at 200, 225, and 750 °C (Figure 3.30). The phases at 200 °C and 750 °C are confirmed from ICDD PDFs 00-032-1369 and 00-038-1468 to be ζ-$Ti(HPO_4)_2$ and cubic titanium pyrophosphate, TiP_2O_7 arising from the water losses seen in the TGA. The phase at 225 °C arises from a phase change without accompanying mass loss to give η-$Ti(HPO_4)_2$[14]. Given the high crystallinity of this product attempts were made to isolate it for further analysis. Unfortunately, as shown in Figure 3.31, upon cooling the product neither remained nor reverted back to the lower temperature phases. Instead a less crystalline pattern was obtained.

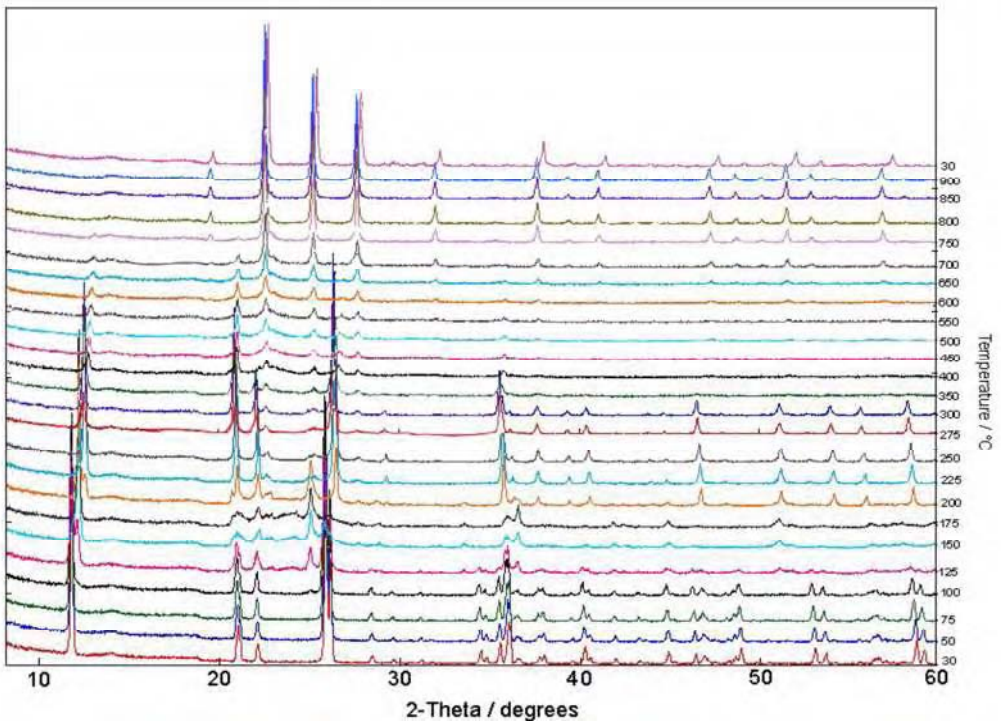

Figure 3.29: The in-situ laboratory XRD patterns of α-TiP recorded as a function of temperature

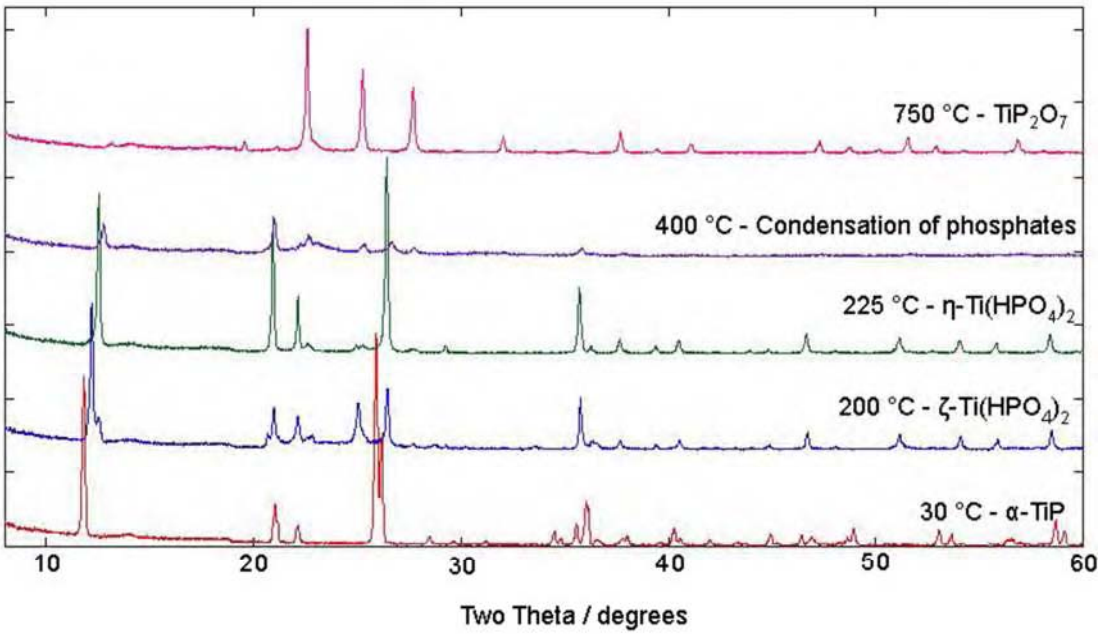

Fig 3.30: The high temperature phases of α-TiP

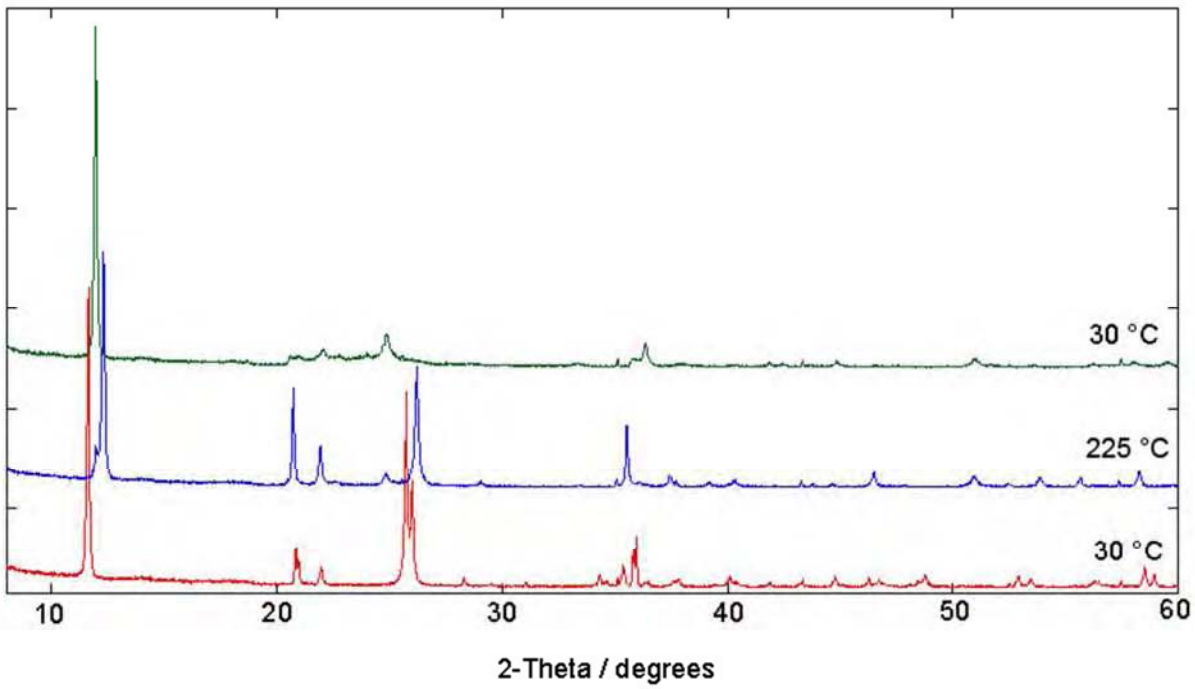

Fig 3.31: XRD patterns showing the attempted isolation of the η-$Ti(HPO_4)_2$

The thermal behaviour of the other single phase products can be interpreted in the same manner. Two dehydrated phases are obtained at lower temperatures. Condensation of the phosphates occurs at elevated temperatures to give the layered pyrophosphates which are generally less crystalline. Further heating above 700 °C yields the cubic pyrophosphates which remain upon cooling. From this the general trend below can be deduced. The relevant temperatures for each product are noted in Table 3.22. The reasons for the anomalous temperatures found for α-ZrP have been discussed however the lower temperatures for water loss infer weaker hydrogen bonding of the water molecules in ZrP.

$$\alpha\text{-}M(HPO_4)_2.H_2O \xrightarrow{T1} \zeta\text{-}M(HPO_4)_2 \xrightarrow{T2} \eta\text{-}M(HPO_4)_2 \xrightarrow{T3} \text{layered } M_2P_2O_7 \xrightarrow{T4} \text{cubic } M_2P_2O_7$$

Table 3.22: Phase change temperatures for the single phase zirconium-titanium phosphates.

Product	T1	T2	T3	T4
α-TiP	200 °C	225 °C	400 °C	750 °C
$Ti_{0.9}Zr_{0.1}(HPO_4)_2.H_2O$	225 °C	250 °C	400 °C	850 °C
$Ti_{0.8}Zr_{0.2}(HPO_4)_2.H_2O$	225 °C	300 °C	400 °C	800 °C
$Ti_{0.7}Zr_{0.3}(HPO_4)_2.H_2O$	225 °C	400 °C	450 °C	850 °C
$Ti_{0.1}Zr_{0.9}(HPO_4)_2.H_2O$	175 °C	250 °C	400 °C	800 °C
α-ZrP	175 °C	400 °C	500 °C	700 °C

3.2 Mixed Ge/Ti Phosphates

3.2.1 Introduction

One factor thought to be preventing the formation of the full solid solution in the zirconium-titanium series was the size difference between the two metals involved. The ionic radii of Ti^{4+}, Zr^{4+} and Ge^{4+} are given as 60.5, 72 and 53 pm respectively[22]. For this reason a series of mixed titanium-germanium phosphates were investigated. The hope was that this smaller difference in metal size could allow for greater substitution and hopefully the full solid solution. There are no literature reports on any work for this series

Most of the early attempts to synthesise germanium phosphate resulted in products that were poorly crystalline and later shown to be impure[23-27]. La Ginestra *et al.*[28] reported optimum conditions to prepare pure crystalline germanium phosphate by refluxing germanium tetrachloride in phosphoric acid in a 1:10 molar ratio. Patrono *et al.*[19] attempted to shorten the preparation time with the use of a hydrothermal treatment. The amorphous product was heated with phosphoric acid in a sealed glass tube for varying durations at various temperatures. Due to the increased propensity for hydrolysis of α-GeP, $GeOHPO_4$ was always formed instead. More recently Romano *et al.*[29] overcame the problems of hydrolysis by using softer conditions and longer durations in their multistep reactions of germanium dioxide and phosphoric acid to yield germanium phosphate with a high degree of purity. A shorter hydrothermal method to give high quality pure α-GeP was reported by Losilla *et al.*[30] which involved heating germanium dioxide in phosphoric acid for 7 days at 125 °C.

The method outlined by Losilla *et al.*[30] was used in this work for the synthesis of germanium phosphate. The $Ti_xGe_{1-x}(HPO_4)_2.H_2O$ series where $x = 0 – 1$ was synthesised using both this

method (*GeP method*) and the hydrothermal method used in the synthesis of the zirconium-titanium phosphates (*TiP method*).

3.2.2 Results and Discussion

3.2.2.1 X-ray Diffraction Analysis

Figure 3.32 shows the powder XRD pattern of phase pure α-GeP with a match to the peaks searched in the ICDD PDF number 00-037-0278. Full details of the refinement are shown later within this chapter.

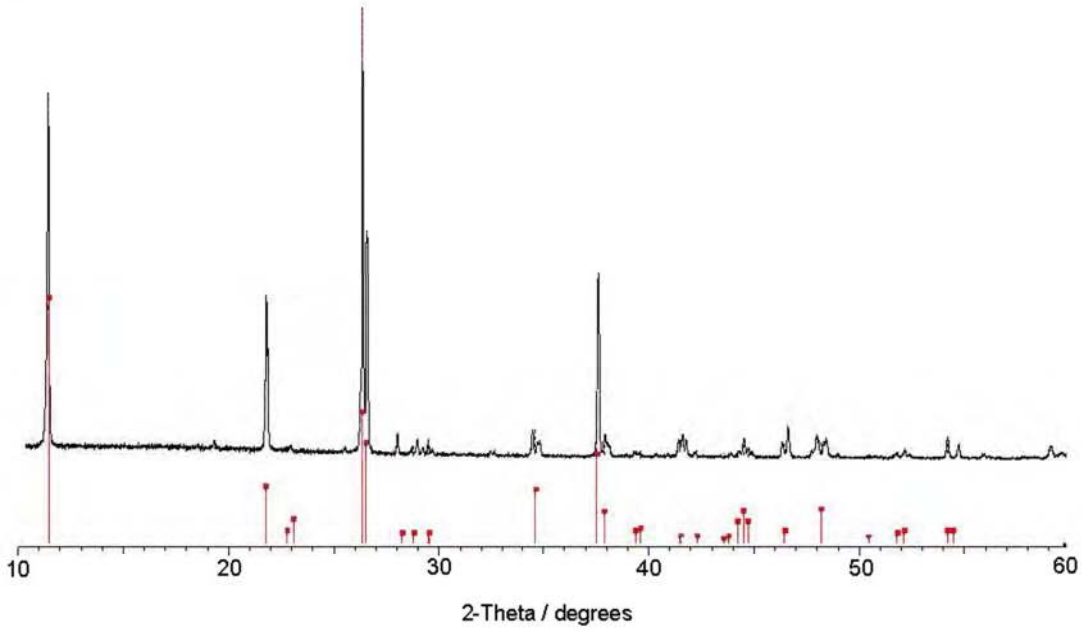

Figure 3.32: Laboratory XRD pattern of GeP. The Red Lines are those reported in ICDD PDF 00-037-0278.

Examination of the powder XRD patterns of the '*TiP method*' samples, Figure 3.33, shows the products with 50% or more germanium contain two phases. The pattern for the $Ti_{0.1}Ge_{0.9}(HPO_4)_2.H_2O$ product has been omitted as only GeO_2 or amorphous products could be synthesised. The crystallinity of the products decreases rapidly with increasing germanium content.

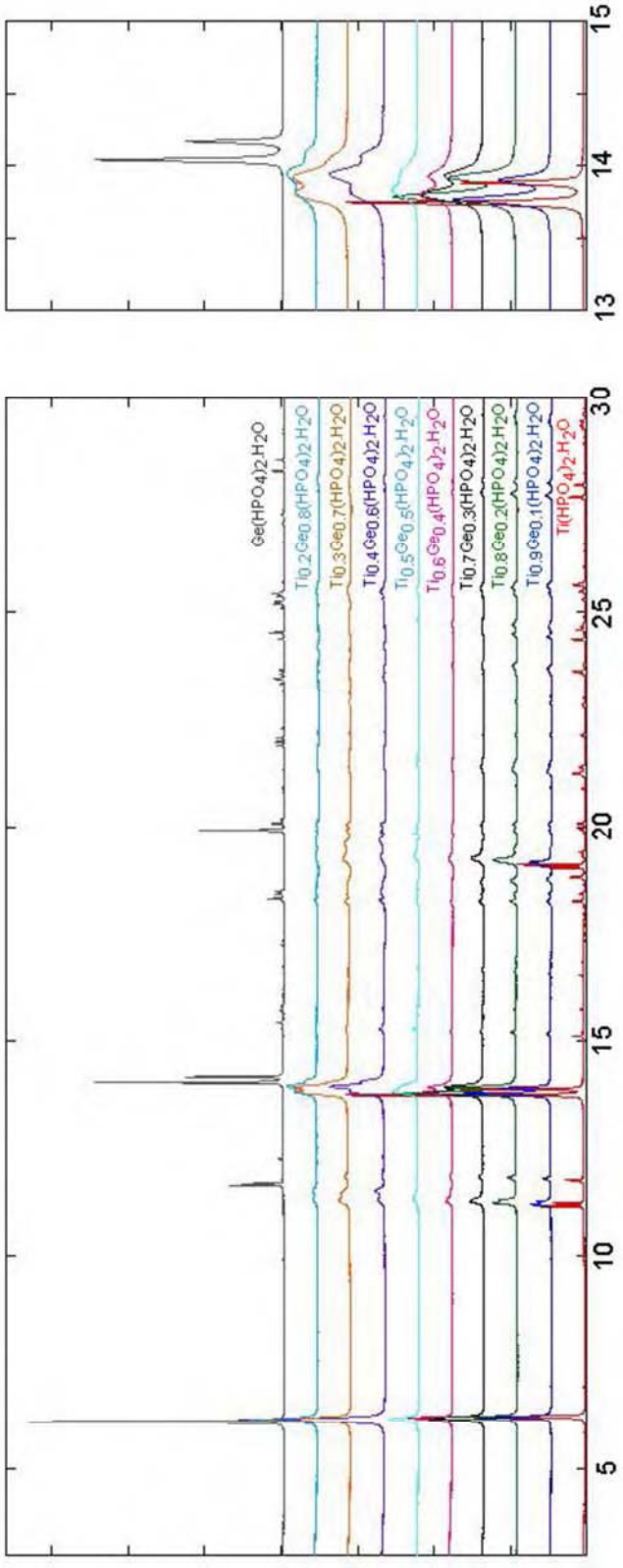

Figure 3.33: Overlaid laboratory XRD scans of the Ge/Ti phosphates synthesised by the '*TiP method*'.

The synthesis of the germanium-rich products was more successful using the '*GeP method*'. From the XRD patterns in Figure 3.34, it can be seen that the products with 30 - 70% titanium contain both more and broader peaks suggesting a two phase nature. Again the crystallinity of the coprecipitates is reduced.

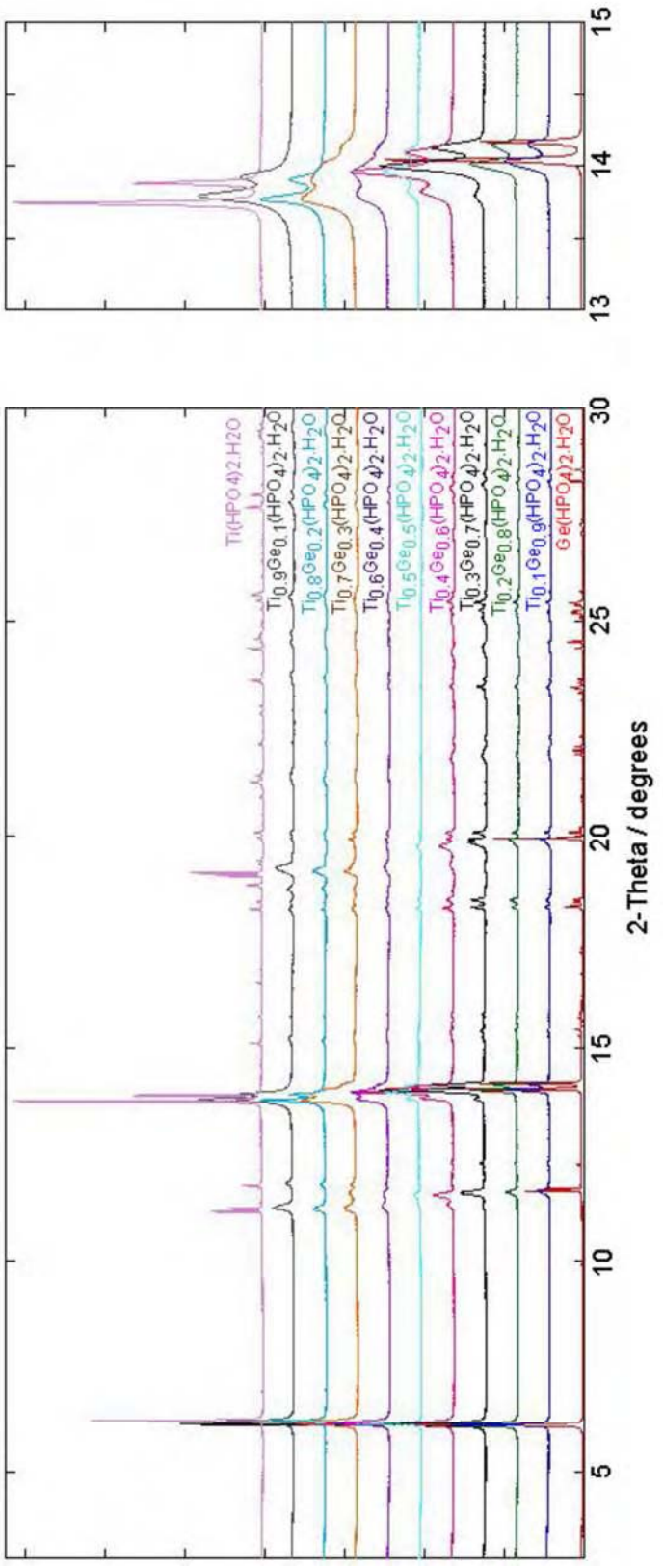

Figure 3.34: Overlaid laboratory XRD scans of the Ge/Ti phosphates synthesised by the *'GeP method'*.

3.2.2.2 X-ray Fluorescence Analysis

Table 3.23 shows the bulk compositions of the samples as determined from calibrated XRF measurements. The samples were run as fused beads. Refer to Section 2.8.5 for more information on the calibration used.

Table 3.23: Chemical compositions of the mixed titanium-germanium phosphates as determined by XRF.

Nominal Composition	XRF Measured Formula	
	TiP method samples	GeP method samples
$Ti_{0.9}Ge_{0.1}(HPO_4)_2.H_2O$	$Ti_{0.92}Ge_{0.08}(HPO_4)_2.H_2O$	$Ti_{0.87}Ge_{0.13}(HPO_4)_2.H_2O$
$Ti_{0.8}Ge_{0.2}(HPO_4)_2.H_2O$	$Ti_{0.86}Ge_{0.14}(HPO_4)_2.H_2O$	$Ti_{0.92}Ge_{0.08}(HPO_4)_2.H_2O$
$Ti_{0.7}Ge_{0.3}(HPO_4)_2.H_2O$	$Ti_{0.80}Ge_{0.20}(HPO_4)_2.H_2O$	$Ti_{0.75}Ge_{0.25}(HPO_4)_2.H_2O$
$Ti_{0.6}Ge_{0.4}(HPO_4)_2.H_2O$	$Ti_{0.72}Ge_{0.28}(HPO_4)_2.H_2O$	$Ti_{0.64}Ge_{0.36}(HPO_4)_2.H_2O$
$Ti_{0.5}Ge_{0.5}(HPO_4)_2.H_2O$	$Ti_{0.66}Ge_{0.34}(HPO_4)_2.H_2O$	$Ti_{0.47}Ge_{0.53}(HPO_4)_2.H_2O$
$Ti_{0.4}Ge_{0.6}(HPO_4)_2.H_2O$	$Ti_{0.59}Ge_{0.41}(HPO_4)_2.H_2O$	$Ti_{0.48}Ge_{0.52}(HPO_4)_2.H_2O$
$Ti_{0.3}Ge_{0.7}(HPO_4)_2.H_2O$	$Ti_{0.57}Ge_{0.43}(HPO_4)_2.H_2O$	$Ti_{0.26}Ge_{0.74}(HPO_4)_2.H_2O$
$Ti_{0.2}Ge_{0.8}(HPO_4)_2.H_2O$	$Ti_{0.61}Ge_{0.39}(HPO_4)_2.H_2O$	$Ti_{0.19}Ge_{0.81}(HPO_4)_2.H_2O$
$Ti_{0.1}Ge_{0.9}(HPO_4)_2.H_2O$	Unable to synthesise	$Ti_{0.15}Ge_{0.85}(HPO_4)_2.H_2O$

All samples prepared by the '*TiP method*' were titanium-rich relative to the expected ratios. The samples believed to be two-phase from XRD analysis (ca. 50-10 nominal % titanium) have approximately the same bulk composition, as was seen with the mixed titanium-zirconium phosphates. Again this suggests that aspects of the solution chemistry prevents the formation of these products. XRF measurements were taken throughout the synthesis of a $Ti_{0.4}Ge_{0.6}(HPO_4)_2.H_2O$ sample. From the values obtained in Table 3.24, it is clearly apparent that germanium remains in solution.

Table 3.24: Germanium/titanium molar ratios determined by XRF measurements at various stages in the synthesis of $Ti_{0.4}Ge_{0.6}(HPO_4)_2.H_2O$.

	Germanium/titanium molar ratio
At the start of the experiment	1.50
Liquid filtrate of the final product	3.80
Final product	0.69

Better agreement is seen between the nominal and measured compositions of the samples obtained from the '*GeP method*'. The samples in the middle of the solid solution (ca. 70-30 nominal % Ti) gave varied compositions close to the expected, rather than the same titanium-rich compositions seen previously. Whilst this method prevents germanium from remaining in solution, it is still not effective for the synthesis of the full solid solution.

3.2.2.3 Rietveld Refinements

Rietveld profile analysis was undertaken on all of the mixed germanium-titanium products using high resolution synchrotron X-ray data collected at station I11 (high resolution powder diffraction) at the Diamond Light Source facility in the UK. The samples deemed to be single phase were successfully analysed as such starting from the structure for α-TiP given by Salvado *et al*.[5] for the titanium rich samples or the structure of α-GeP as reported by Peters and Evans[31] for the germanium rich samples, both using space group $P2_1/c$. For the mixed metal samples the compositions were allowed to refine starting from the values expected from the nominal compositions, but fractional occupancies were constrained to sum to 1. During the refinements the temperature factors of each discrete atom type were constrained to the same value, excluding that for the water oxygen, O(9), which was refined independently. Key structural parameters showing the success of the refinements is

presented in Table 3.25. Refined parameters for α-GeP from previous literature work[31] are given in italics below. Good agreement is seen. For the sake of comparability, the refined parameters for α-TiP as determined in Section 3.1.2.3 have also been included. Refined atomic coordinates and thermal parameters for each single phase product are shown in Tables 3.27 – 3.34 along with the fits to the data in Figures 3.35 – 3.43. The refined bond angles are summarised in Appendix 1 and the crystallographic refinement files can be found in Appendix 3.

From XRD analysis $Ti_{0.9}Ge_{0.1}(HPO_4)_2.H_2O$ and $Ti_{0.8}Ge_{0.2}(HPO_4)_2.H_2O$ appeared to have been successfully synthesised by both the *GeP* and *TiP methods*. Consequently the samples from both methods were analysed. As can be seen in Table 3.25 the structures of the products do not vary significantly with the synthetic method used and only small difference in the refined values are observed.

Table 3.25: Structural parameters with estimated standard deviations for the single-phase members of the Ge/Ti series from the Rietveld refinements. The literature values for α-GeP[28] are shown in italics.

	α-TiP	$Ti_{0.9}Ge_{0.1}(HPO_4)_2.H_2O$		$Ti_{0.8}Ge_{0.2}(HPO_4)_2.H_2O$		$Ti_{0.7}Ge_{0.3}(HPO_4)_2.H_2O$	$Ti_{0.6}Ge_{0.4}(HPO_4)_2.H_2O$	$Ti_{0.2}Ge_{0.8}(HPO_4)_2.H_2O$	$Ti_{0.1}Ge_{0.9}(HPO_4)_2.H_2O$	GeP
		TiP method	GeP method	TiP method	GeP method	TiP method	TiP method	GeP method	GeP method	
a/Å	8.63267(6)	8.60359(9)	8.5655(2)	8.5789(1)	8.5931(2)	8.5562(3)	8.5262(4)	8.3181(2)	8.3070(4)	8.28465(2) *8.2920(2)*
b/Å	5.00672(3)	4.98759(5)	4.9660(1)	4.97082(8)	4.98176(9)	4.9586(1)	4.9526(2)	4.8025(1)	4.7981(2)	4.78345(1) *4.7880(1)*
c/Å	16.1902(2)	16.2163(2)	16.2311(5)	16.2384(3)	16.2113(4)	16.2667(6)	16.2717(10)	16.3817(3)	16.3858(4)	16.40369(4) *16.4058(3)*
β/deg	110.2065(6)	110.0941 (6)	110.0017(14)	109.9950(9)	110.082(1)	109.9197(17)	109.9218(26)	109.0648(12)	109.046(1)	108.9576(1) *108.985(1)*
V/Å^3	656.697(11)	653.501(13)	648.758(30)	650.737(20)	651.793(24)	648.86(4)	645.99(6)	618.51(2)	617.35(4)	614.805(2)
M-O(1)/ Å	1.944(9)	1.940(6)	1.842(7)	1.973(8)	1.933(8)	1.929(9)	1.945(14)	1.879(14)	1.816(17)	1.870(4) *1.86(1)*
M-O(2)/ Å	1.942(11)	1.969(7)	1.921(9)	1.891(9)	1.906(9)	1.970(9)	2.048(13)	2.008(15)	1.944(19)	1.877(5) *1.90(1)*
M-O(3)/ Å	1.913(11)	1.936(7)	1.868(10)	1.966(9)	1.873(10)	1.910(11)	1.943(16)	1.739(14)	1.804(19)	1.863(5) *1.88(1)*
M-O(5)/ Å	1.969(10)	1.922(7)	2.067(9)	1.910(9)	2.050(11)	1.952(11)	1.882(17)	1.853(15)	1.876(19)	1.879(5) *1.86(1)*
M-O(6)/ Å	1.941(11)	1.943(7)	1.838(9)	1.968(9)	1.874(10)	1.971(12)	1.930(17)	1.852(15)	1.916 (19)	1.885(5) *1.92(1)*
M-O(7)/ Å	1.962(8)	1.953(6)	1.964(7)	1.880(7)	1.951(7)	2.011(8)	2.068(12)	1.909(13)	1.869(16)	1.881(4) *1.87(1)*
<M-O>/ Å	1.945	1.944	1.917	1.93	1.931	1.958	1.969	1.873	1.87	1.876 *1.88*
χ^2	3.00	4.17	5.69	6.56	3.74	5.34	4.96	6.26	7.27	3.35
R_p/%	4.93	4.84	4.26	5.25	4.01	5.40	4.84	5.09	5.27	4.30
R_{wp}/%	6.41	6.22	5.62	6.43	5.43	6.57	6.62	7.59	8.38	5.58
R_F^2/%	6.07	6.64	3.26	6.06	4.44	5.88	10.42	7.11	9.22	5.59

α-GeP:

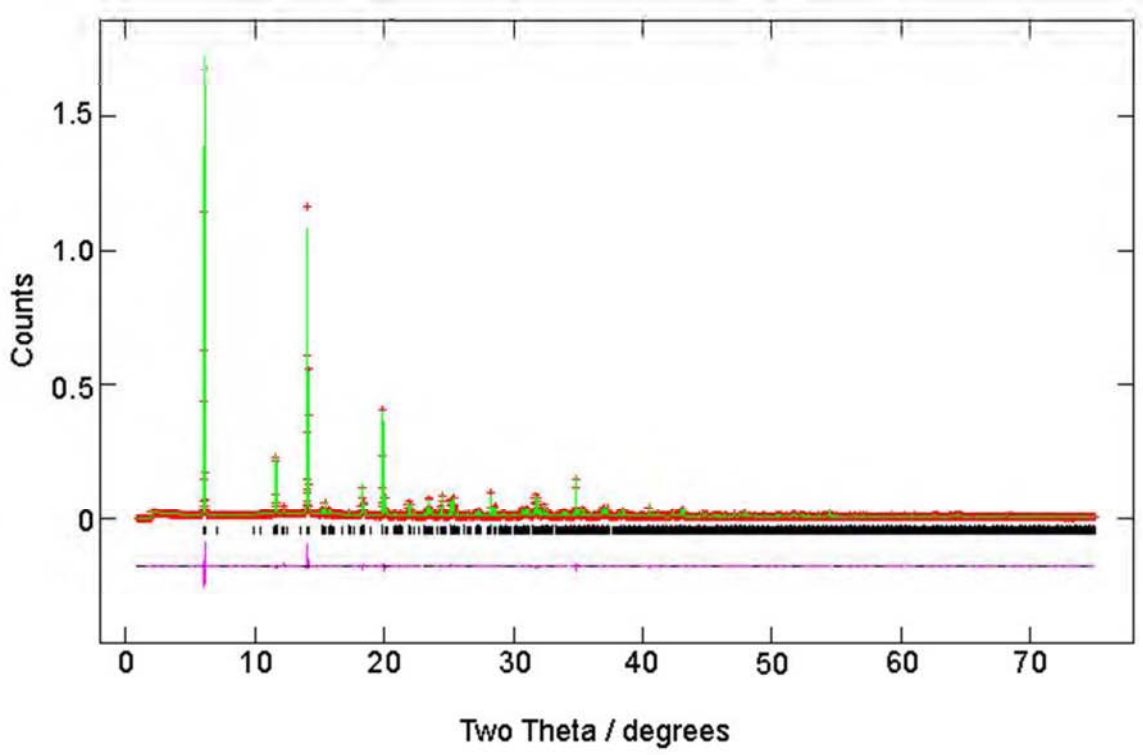

Figure3.35: Final observed (red crosses), calculated (green line) and difference (bottom) X-ray diffraction profile with reflection positions noted as vertical tick marks for α-GeP.

Table 3.26: Fractional atomic coordinates and isotropic thermal displacement parameters with estimated standard deviations for α-GeP from the Rietveld refinement.

atom	*x*	*y*	*z*	U_{iso} (x10^2) Å^2
Ge	0.7560(1)	0.2503(5)	0.50931(4)	0.91(2)
P(1)	-0.0080(2)	0.7523(9)	0.60162(9)	0.76(2)
P(2)	0.4671(2)	0.24561(9)	0.09528(9)	0.76(2)
O(1)	0.1188(6)	0.8565(9)	0.56225(2)	0.88(3)
O(2)	0.9430(6)	0.4496(10)	0.5820(3)	0.88(3)
O(3)	0.8370(6)	0.9454(9)	0.5817(4)	0.88(3)
O(4)	0.0814(4)	0.7577(16)	0.7031(2)	0.88(3)
O(5)	0.3147(6)	0.0730(9)	0.0581(3)	0.88(3)
O(6)	0.4312(6)	0.5544(10)	0.0653(3)	0.88(3)
O(7)	0.5139(4)	0.2597(16)	0.1962(2)	0.88(3)
O(8)	0.3727(5)	0.8560(9)	0.9202(2)	0.88(3)
O(9)	0.2539(6)	0.2753(13)	0.2589(3)	1.41(9)

$Ti_{0.1}Ge_{0.9}(HPO_4)_2.H_2O$ (GeP method):

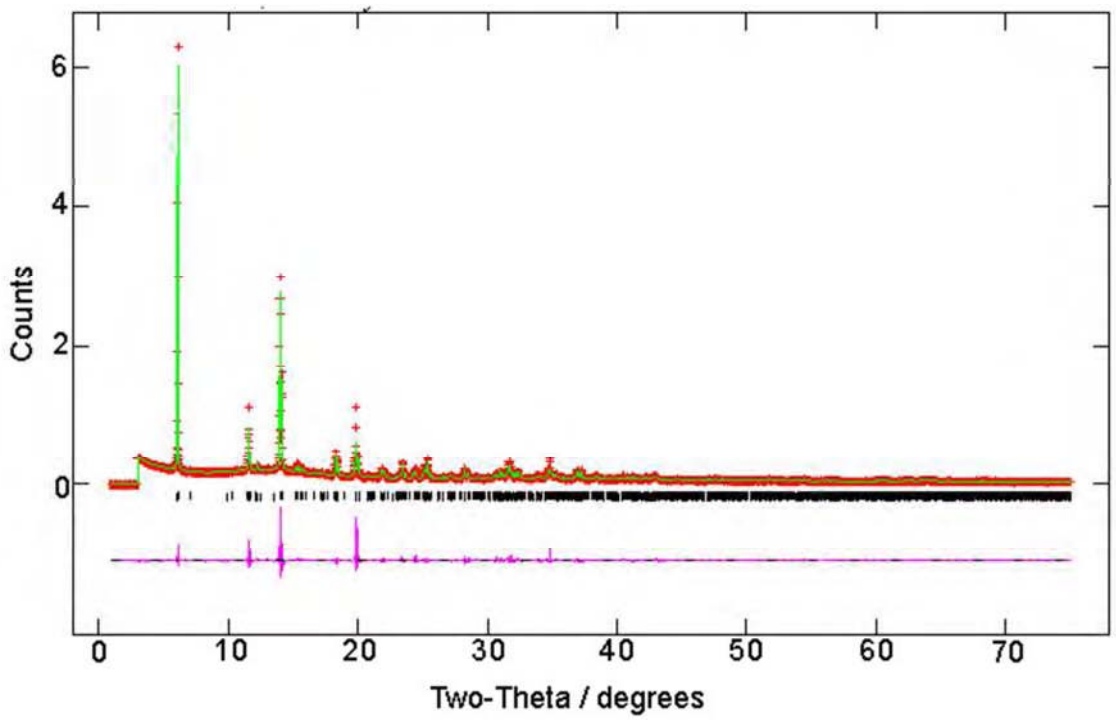

Figure 3.36: Final observed (red crosses), calculated (green line) and difference (bottom) X-ray diffraction profile with reflection positions noted as vertical tick marks for α-$Ti_{0.1}Ge_{0.9}(HPO_4)_2.H_2O$.

Table 3.27: Fractional atomic coordinates and isotropic thermal displacement parameters with estimated standard deviations for α-$Ti_{0.1}Ge_{0.9}(HPO_4)_2.H_2O$ from the Rietveld refinement.

atom	*x*	*y*	*z*	U_{iso} (x10^2) Å^2	Fractional Occupancy
Ti	0.7542(5)	0.2475(18)	0.5091(2)	0.48(5)	0.241(2)
Ge	0.7542(5)	0.2475(18)	0.5091(2)	0.48(5)	0.759(2)
P(1)	-0.0037(10)	0.749(4)	0.6015(4)	2.28(10)	
P(2)	0.4731(9)	0.246(4)	0.0959(4)	2.28(10)	
O(1)	0.1127(22)	0.861(4)	0.5538(9)	1.34(11)	
O(2)	0.9570(25)	0.445(4)	0.5784(11)	1.34(11)	
O(3)	0.8301(26)	0.939(4)	0.5731(9)	1.34(11)	
O(4)	0.0757(16)	0.741(9)	0.7062(6)	1.34(11)	
O(5)	0.3121(25)	0.082(4)	0.0518(9)	1.34(11)	
O(6)	0.4292(26)	0.539(4)	0.0682(10)	1.34(11)	
O(7)	0.4922(17)	0.304(4)	0.1931(7)	1.34(11)	
O(8)	0.3765(22)	0.853(4)	0.9224(7)	1.34(11)	
O(9)	0.2507(30)	0.227(5)	0.2601(10)	1.83(9)	

$Ti_{0.2}Ge_{0.8}(HPO_4)_2.H_2O$ (GeP Method):

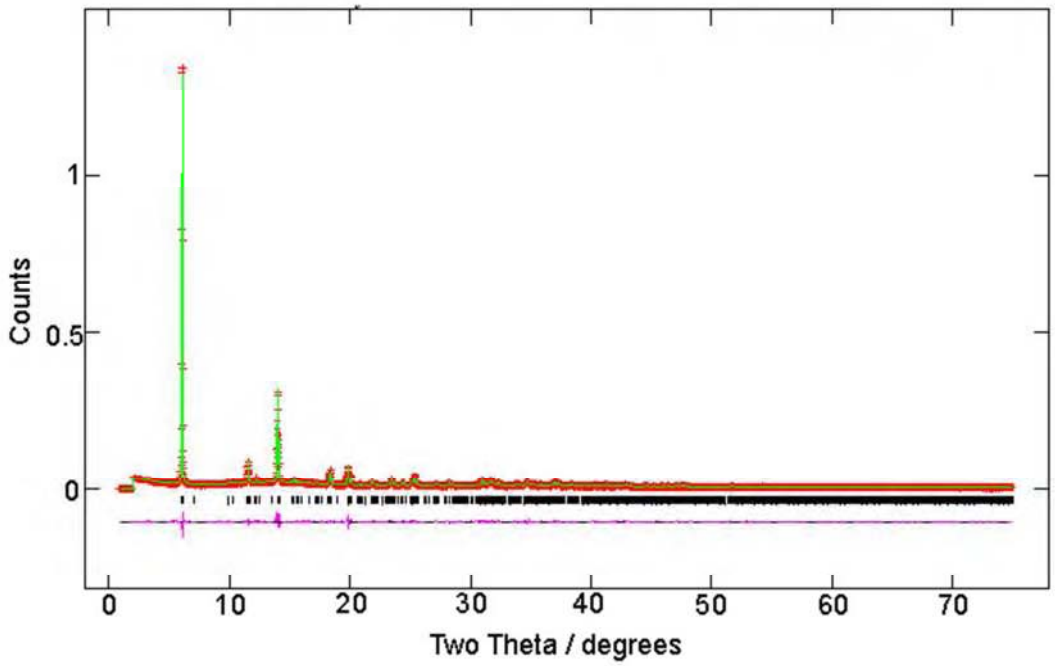

Figure 3.37: Final observed (red crosses), calculated (green line) and difference (bottom) X-ray diffraction profile with reflection positions noted as vertical tick marks for α-$Ti_{0.2}Ge_{0.8}(HPO_4)_2.H_2O$.

Table3.28: Fractional atomic coordinates and isotropic thermal displacement parameters with estimated standard deviations for α-$Ti_{0.2}Ge_{0.8}(HPO_4)_2.H_2O$ from the Rietveld refinement.

atom	*x*	*y*	*z*	U_{iso} (x10^2) Å^2	Fractional Occupancy
Ti	0.7536(5)	0.2503(15)	0.5090(1)	1.78(8)	0.179(6)
Ge	0.7536(5)	0.2503(15)	0.5090(1)	1.78(8)	0.821(6)
P(1)	-0.0065(8)	0.7517(33)	0.6019(3)	0.39(7)	
P(2)	0.4680(6)	0.2532(30)	0.0960(3)	0.39(7)	
O(1)	0.1172(18)	0.8515(30)	0.5614(6)	0.29(10)	
O(2)	0.9595(20)	0.4524(31)	0.5849(8)	0.29(10)	
O(3)	0.8437(21)	0.9791(32)	0.5794(7)	0.29(10)	
O(4)	0.0718(14)	0.7396(62)	0.7049(5)	0.29(10)	
O(5)	0.3163(20)	0.0703(31)	0.0562(6)	0.29(10)	
O(6)	0.4323(21)	0.5825(32)	0.0708(6)	0.29(10)	
O(7)	0.4770(15)	0.3186(28)	0.1929(5)	0.29(10)	
O(8)	0.3766(18)	0.8532(34)	0.9190(5)	0.29(10)	
O(9)	0.2418(21)	0.2556(59)	0.2607(7)	0.37(22)	

$Ti_{0.6}Ge_{0.4}(HPO_4)_2.H_2O$ (TiP method):

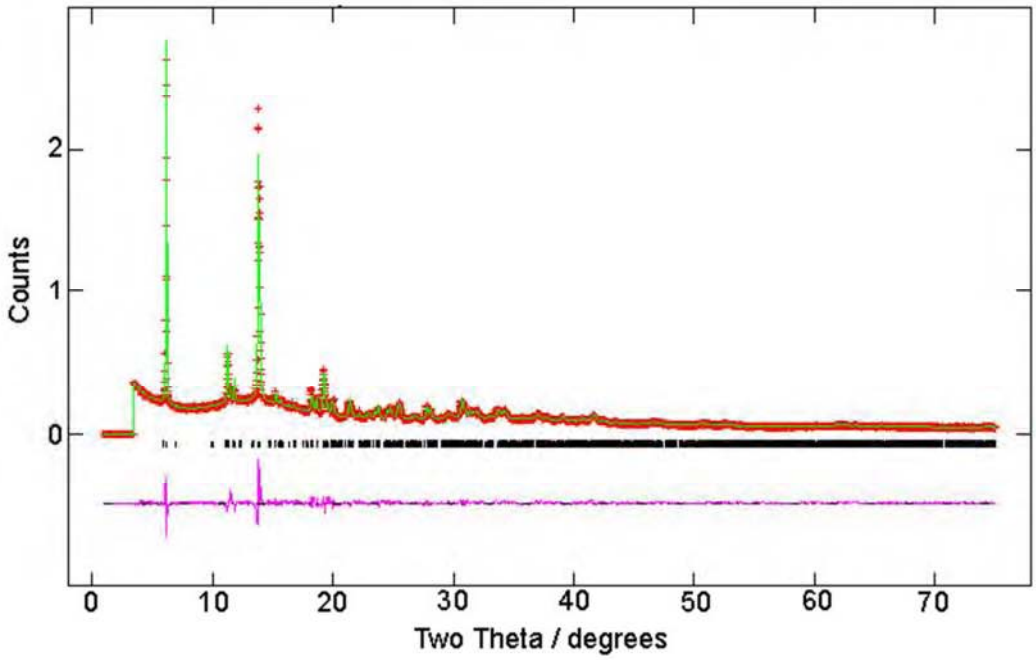

Figure 3.38: Final observed (red crosses), calculated (green line) and difference (bottom) X-ray diffraction profile with reflection positions noted as vertical tick marks for α-$Ti_{0.6}Ge_{0.4}(HPO_4)_2.H_2O$.

Table 3.29: Fractional atomic coordinates and isotropic thermal displacement parameters with estimated standard deviations for α-$Ti_{0.6}Ge_{0.4}(HPO_4)_2.H_2O$ from the Rietveld refinement.

atom	*x*	*y*	*z*	U_{iso} (x10^2) Å^2	Fractional Occupancy
Ti	0.7580(6)	0.2475(17)	0.5073(3)	1.44(9)	0.181(18)
Ge	0.7580(6)	0.2475(17)	0.5073(3)	1.44(9)	0.819(18)
P(1)	-0.0078(8)	0.7373(22)	0.6078(4)	1.60(10)	
P(2)	0.4626(8)	0.2439(23)	0.5974(4)	1.60(10)	
O(1)	0.1092(17)	0.8391(26)	0.5654(8)	0.27(4)	
O(2)	-0.0320(16)	0.3956(25)	0.6006(9)	0.27(4)	
O(3)	0.8538(20)	0.9544(29)	0.5883(10)	0.27(4)	
O(4)	0.1220(14)	0.6990(28)	0.7022(7)	0.27(4)	
O(5)	0.3133(17)	0.4313(30)	0.5563(9)	0.27(4)	
O(6)	0.4053(17)	-0.0028(33)	0.5671(10)	0.27(4)	
O(7)	0.6292(16)	0.3116(30)	0.5928(7)	0.27(4)	
O(8)	0.5208(12)	0.2499(46)	0.6996(5)	0.27(4)	
O(9)	0.2775(16)	0.2074(28)	0.7682(6)	0.13(11)	

$Ti_{0.7}Ge_{0.3}(HPO_4)_2.H_2O$ (TiP method):

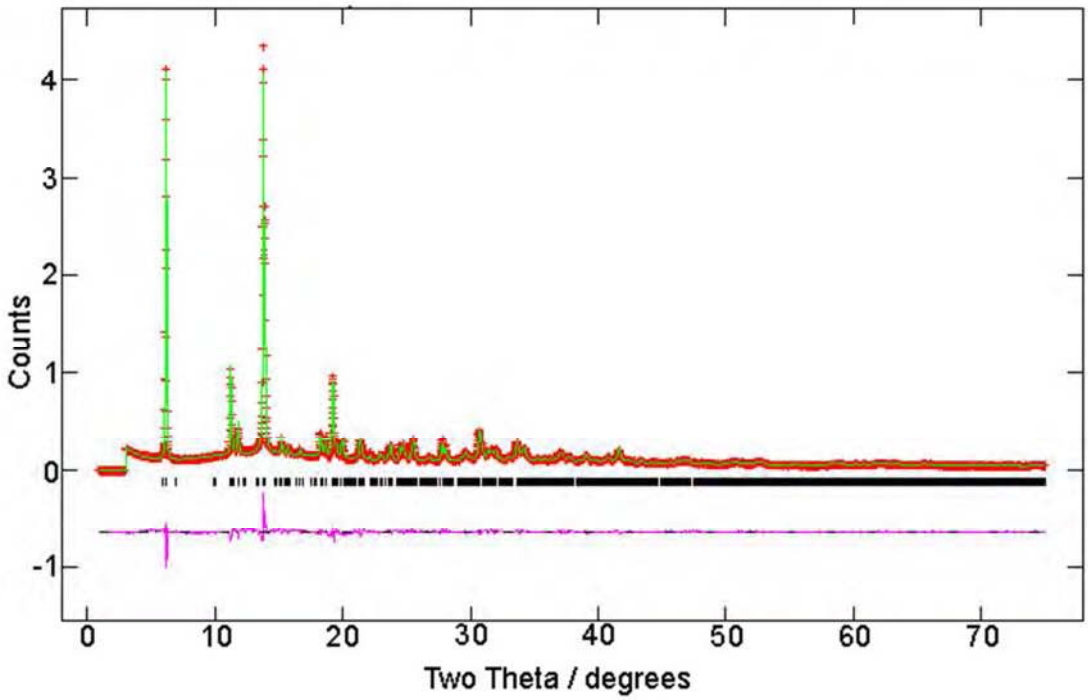

Figure 3.39: Final observed (red crosses), calculated (green line) and difference (bottom) X-ray diffraction profile with reflection positions noted as vertical tick marks for α-$Ti_{0.7}Ge_{0.3}(HPO_4)_2.H_2O$.

Table 3.30: Fractional atomic coordinates and isotropic thermal displacement parameters with estimated standard deviations for α-$Ti_{0.7}Ge_{0.3}(HPO_4)_2.H_2O$ from the Rietveld refinement.

atom	*x*	*y*	*z*	U_{iso} (x10^2) Å^2	Fractional Occupancy
Ti	0.7576(1)	0.2445(11)	0.5107(2)	0.56(6)	0.828(9)
Ge	0.7576(1)	0.2445(11)	0.5107(2)	0.56(6)	0.172(9)
P(1)	-0.0016(4)	0.7356(16)	0.6087(2)	0.46(6)	
P(2)	0.4660(5)	0.2506(16)	0.5979(2)	0.46(6)	
O(1)	0.1109(11)	0.8472(17)	0.5609(6)	0.06(4)	
O(2)	-0.0468(11)	0.4295(17)	0.5919(6)	0.06(4)	
O(3)	0.8533(13)	0.9490(19)	0.5849(7)	0.06(4)	
O(4)	0.1005(8)	0.7209(25)	0.7039(4)	0.06(4)	
O(5)	0.3190(11)	0.4316(20)	0.5598(6)	0.06(4)	
O(6)	0.4056(11)	0.0044(20)	0.5677(7)	0.06(4)	
O(7)	0.6281(11)	0.3188(19)	0.5907(4)	0.06(4)	
O(8)	0.5079(7)	0.2508(37)	0.6987(4)	0.06(4)	
O(9)	0.2683(12)	0.2207(31)	0.7649(5)	1.75(25)	

$Ti_{0.8}Ge_{0.2}(HPO_4)_2.H_2O$ (TiP method):

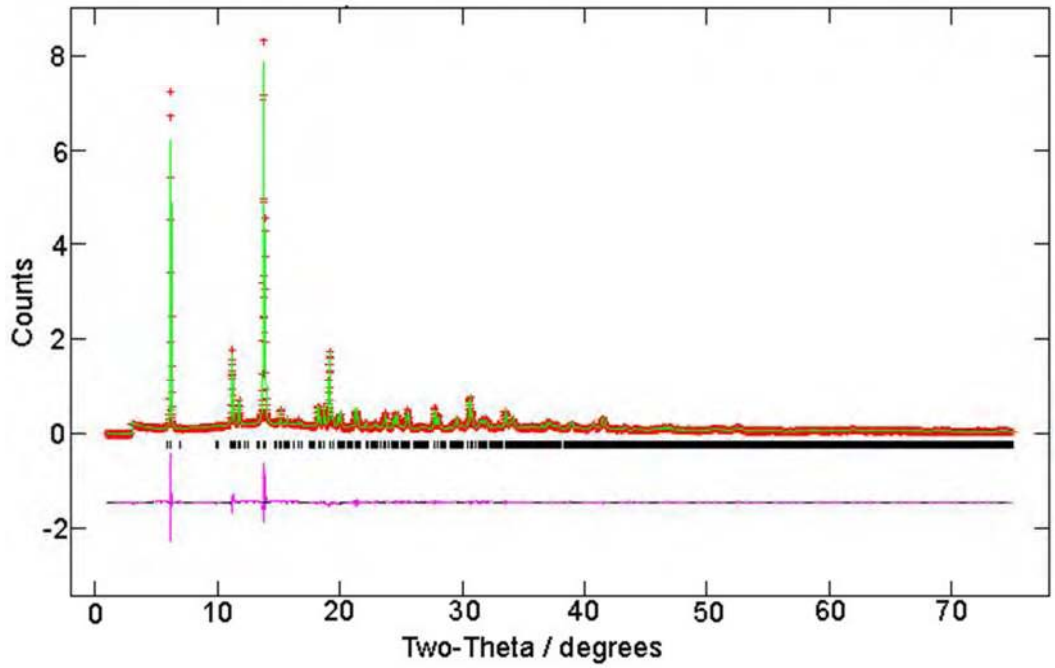

Figure 3.40: Final observed (red crosses), calculated (green line) and difference (bottom) X-ray diffraction profile with reflection positions noted as vertical tick marks for α-$Ti_{0.8}Ge_{0.2}(HPO_4)_2.H_2O$.

Table3.31: Fractional atomic coordinates and isotropic thermal displacement parameters with estimated standard deviations for α-$Ti_{0.8}Ge_{0.2}(HPO_4)_2.H_2O$ from the Rietveld refinement.

atom	*x*	*y*	*z*	U_{iso} (x10^2) Å^2	Fractional Occupancy
Ti	0.7569(3)	0.2546(10)	0.5114(1)	0.38(4)	0.878(5)
Ge	0.7569(3)	0.2546(10)	0.5114(1)	0.38(4)	0.122(5)
P(1)	-0.0019(3)	0.7479(14)	0.6086(2)	0.55(4)	
P(2)	0.4645(3)	0.2425(13)	0.5977(2)	0.55(4)	
O(1)	0.1104(9)	0.8421(15)	0.5624(5)	0.60(5)	
O(2)	-0.0664(10)	0.4562(16)	0.5886(5)	0.60(5)	
O(3)	0.8591(10)	0.9468(16)	0.5864(6)	0.60(5)	
O(4)	0.0946(7)	0.7622(25)	0.7076(3)	0.60(5)	
O(5)	0.3210(9)	0.4322(17)	0.5587(5)	0.60(5)	
O(6)	0.4216(10)	-0.0258(17)	0.5647(6)	0.60(5)	
O(7)	0.6323(9)	0.3211(16)	0.5846(4)	0.60(5)	
O(8)	0.5048(6)	0.2629(25)	0.6991(3)	0.60(5)	
O(9)	0.2618(8)	0.2118(14)	0.7670(3)	1.84(11)	

$Ti_{0.8}Ge_{0.2}(HPO_4)_2.H_2O$ (GeP method):

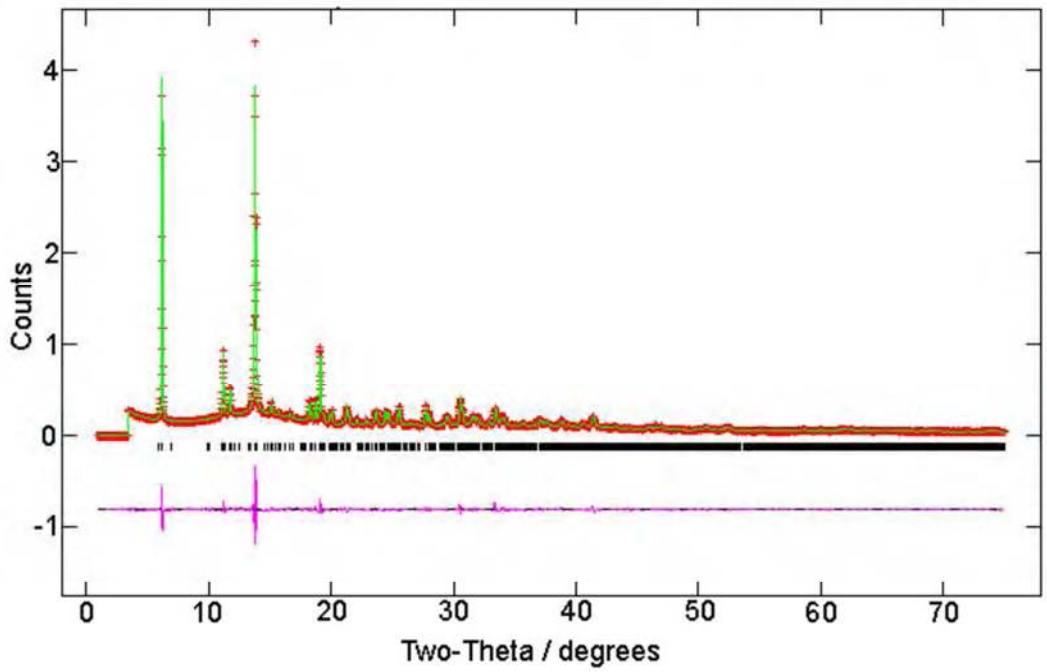

Figure 3.41: Final observed (red crosses), calculated (green line) and difference (bottom) X-ray diffraction profile with reflection positions noted as vertical tick marks for α-$Ti_{0.8}Ge_{0.2}(HPO_4)_2.H_2O$.

Table 3.32: Fractional atomic coordinates and isotropic thermal displacement parameters with estimated standard deviations for α-$Ti_{0.8}Ge_{0.2}(HPO_4)_2.H_2O$ from the Rietveld refinement.

atom	*x*	*y*	*z*	U_{iso} (x10^2) Å^2	Fractional Occupancy
Ti	0.7586(3)	0.2465(12)	0.5121(2)	0.89(3)	0.869(7)
Ge	0.7586(3)	0.2465(12)	0.5121(2)	0.89(3)	0.131(7)
P(1)	-0.0030(4)	0.7479(17)	0.6078(2)	0.51(5)	
P(2)	0.4648(4)	0.2447(16)	0.5968(2)	0.51(5)	
O(1)	0.1143(9)	0.8150(17)	0.5640(5)	0.04(2)	
O(2)	-0.0751(12)	0.4816(18)	0.5842(6)	0.04(2)	
O(3)	0.8454(11)	0.9565(17)	0.5874(7)	0.04(2)	
O(4)	0.0949(7)	0.7536(34)	0.7064(4)	0.04(2)	
O(5)	0.3238(11)	0.4019(17)	0.5542(5)	0.04(2)	
O(6)	0.4212(11)	-0.0612(17)	0.5665(6)	0.04(2)	
O(7)	0.6246(9)	0.3222(18)	0.5851(4)	0.04(2)	
O(8)	0.5104(6)	0.2525(30)	0.7027(3)	0.04(2)	
O(9)	0.2496(11)	0.2297(28)	0.7618(5)	1.16(6)	

$Ti_{0.9}Ge_{0.1}(HPO_4)_2.H_2O$ (TiP method):

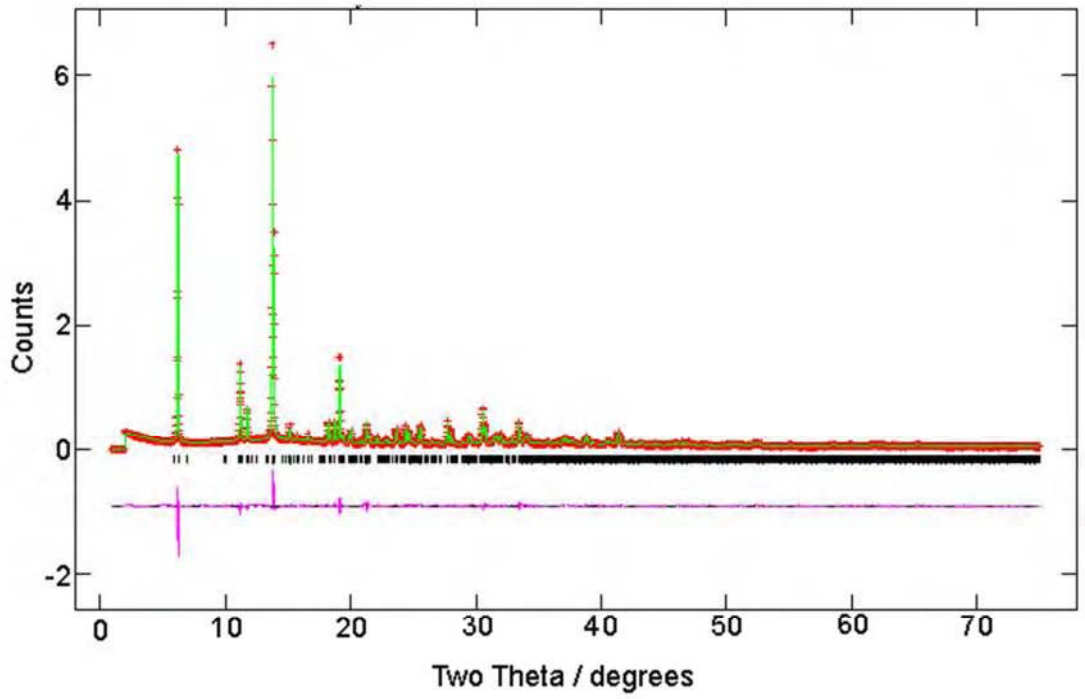

Figure 3.42: Final observed (red crosses), calculated (green line) and difference (bottom) X-ray diffraction profile with reflection positions noted as vertical tick marks for α-$Ti_{0.9}Ge_{0.1}(HPO_4)_2.H_2O$.

Table 3.33 Fractional atomic coordinates and isotropic thermal displacement parameters with estimated standard deviations for α-$Ti_{0.9}Ge_{0.1}(HPO_4)_2.H_2O$ from the Rietveld refinement.

atom	*x*	*y*	*z*	U_{iso} (x10^2) Å^2	Fractional Occupancy
Ti	0.7581(2)	0.2545(8)	0.5111(1)	1.28(3)	0.952(5)
Ge	0.7581(2)	0.2545(8)	0.5111(1)	1.28(3)	0.048(5)
P(1)	-0.0044(3)	0.7494(11)	0.6083(2)	1.13(3)	
P(2)	0.4654(3)	0.2430(10)	0.5988(2)	1.13(3)	
O(1)	0.1122(7)	0.8319(11)	0.5624(4)	1.51(4)	
O(2)	-0.0626(8)	0.4723(13)	0.5916(4)	1.51(4)	
O(3)	0.8532(7)	0.9566(13)	0.5886(4)	1.51(4)	
O(4)	0.0928(5)	0.7690(18)	0.7083(3)	1.51(4)	
O(5)	0.3250(7)	0.4019(17)	0.5542(5)	1.51(4)	
O(6)	0.4206(8)	-0.0377(13)	0.5659(4)	1.51(4)	
O(7)	0.6308(7)	0.3274(12)	0.5878(3)	1.51(4)	
O(8)	0.5062(5)	0.2477(20)	0.6995(3)	1.51(4)	
O(9)	0.2584(7)	0.2321(18)	0.7657(4)	2.38(14)	

$Ti_{0.9}Ge_{0.1}(HPO_4)_2.H_2O$ (GeP method):

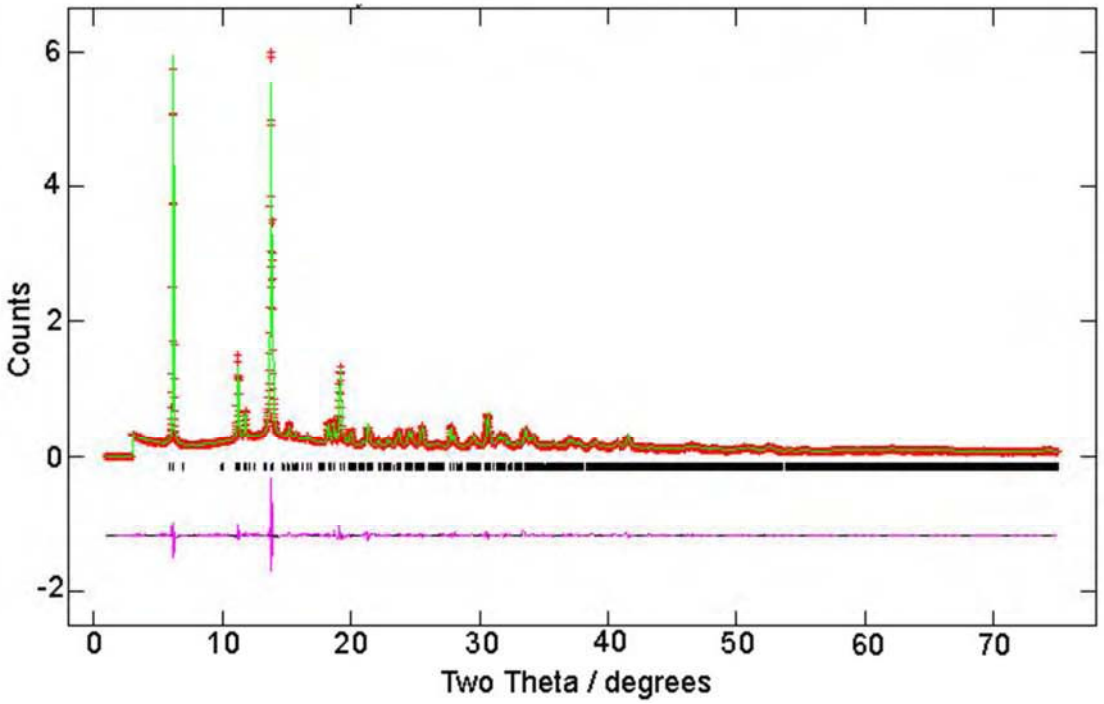

Figure 3.43: Final observed (red crosses), calculated (green line) and difference (bottom) X-ray diffraction profile with reflection positions noted as vertical tick marks for α-$Ti_{0.9}Ge_{0.1}(HPO_4)_2.H_2O$.

Table3.34: Fractional atomic coordinates and isotropic thermal displacement parameters with estimated standard deviations for α-$Ti_{0.9}Ge_{0.1}(HPO_4)_2.H_2O$ from the Rietveld refinement.

atom	*x*	*y*	*z*	U_{iso} (x10^2) Å^2	Fractional Occupancy
Ti	0.7580(3)	0.2482(10)	0.5115(1)	0.03(5)	0.922(6)
Ge	0.7580(3)	0.2482(10)	0.5115(1)	0.03(5)	0.078(6)
P(1)	-0.0014(4)	0.7529(15)	0.6075(2)	0.97(5)	
P(2)	0.4654(3)	0.2430(10)	0.5988(2)	0.97(5)	
O(1)	0.1231(8)	0.8125(16)	0.5622(5)	0.07(2)	
O(2)	-0.0710(10)	0.4771(17)	0.5861(6)	0.07(2)	
O(3)	0.8440(11)	0.9561(16)	0.5857(6)	0.07(2)	
O(4)	0.0943(7)	0.7549(29)	0.7068(4)	0.07(2)	
O(5)	0.3238(10)	0.3981(16)	0.5567(5)	0.07(2)	
O(6)	0.4193(10)	-0.0688(15)	0.5661(6)	0.07(2)	
O(7)	0.6162(8)	0.3167(18)	0.5822(4)	0.07(2)	
O(8)	0.5076(6)	0.2644(23)	0.7018(3)	0.07(2)	
O(9)	0.2503(8)	0.2145(15)	0.7661(4)	0.36(4)	

The quality of these refinements is not as good as those on the mixed zirconium-titanium series (Section 3.1.2.3). The quality of some of the XRD data obtained is too poor to get a good fit; this is in spite of multiple synchrotron scans summed together and is due to the poorly crystalline samples. As can be seen in Figures 3.35 to 3.43, the majority of the refinements suffer from intensity issues in the two most intense peaks at approximately 8 and 15° 2θ, which could not be rectified in spite of allowances made for preferred orientation effects. Issues were also seen with some of the metal-oxygen and phosphorus-oxygen bond lengths, specifically with O(8) atoms. Attempts were made to constrain these bond lengths and atom positions to more sensible values but this forced other bond lengths to become unrealistic and did not solve the issue. Consequently the constraints were removed. The oxygen atoms causing the problems, the hydroxyl oxygens, are fundamentally involved in the corrugation of the layers within the alpha structure type. The layers within α-GeP are considerably more corrugated than those within α-TiP and it appears that due to this the system struggles to accommodate the second metal. A review of the layer corrugation in these mixed metal systems will be presented later in this chapter.

Refinements of the two-phase products were attempted. Given the similarities of the powder patterns of the two phases and therefore extreme overlap in each data set, it was not possible to refine the metal site occupancies and obtain sensible values. In all cases, based on the linear extrapolation of the unit cell values between the end members, one phase had a composition close to 19% Ti and the other 72% Ti, therefore the compositions were fixed at these values and the phase fractions refined. The results are summarised in Table 3.35. Further results and fits can be found in Appendix 2 and the crystallographic refinement files in Appendix 3. The bulk compositions obtained from the XRF studies have

also been included to allow comparison to those obtained from the scale factors within the refinements. There is little agreement between the compositional results except for the $Ti_{0.3}Ge_{0.7}(HPO_4)_2.H_2O$ products and $Ti_{0.5}Ge_{0.5}(HPO_4)_2.H_2O$ synthesised by the '*GeP method*' which compare well. The Rietveld refinements show the bulk overall solid compositions are nearly the same at ca. 45% titanium for most of the products. In general this is less titanium than the XRF results. However from the structural data obtained the products consist of different phases and indicate that titanium rich amorphous components are present in these products.

Table 3.35: Structural parameters for the two phase products from the Rietveld refinements.

	$Ti_{0.7}Ge_{0.3}(HPO_4)_2.H_2O$ (GeP method)		$Ti_{0.6}Ge_{0.4}(HPO_4)_2.H_2O$ (GeP method)		$Ti_{0.5}Ge_{0.5}(HPO_4)_2.H_2O$ (GeP method)		$Ti_{0.5}Ge_{0.5}(HPO_4)_2.H_2O$ (TiP method)		$Ti_{0.4}Ge_{0.6}(HPO_4)_2.H_2O$ (GeP method)		$Ti_{0.4}Ge_{0.6}(HPO_4)_2.H_2O$ (TiP method)		$Ti_{0.3}Ge_{0.7}(HPO_4)_2.H_2O$ (GeP method)		$Ti_{0.3}Ge_{0.7}(HPO_4)_2.H_2O$ (TiP method)		$Ti_{0.2}Ge_{0.8}(HPO_4)_2.H_2O$ (TiP method)	
	Phase 1	Phase 2	Phase 1	Phase 2	Phase 1	Phase 2	Phase 1	Phase 2	Phase 1	Phase 2	Phase 1	Phase 2	Phase 1	Phase 2	Phase 1	Phase 2	Phase 1	Phase 2
a/Å	8.5097(16)	8.3597(26)	8.5292(7)	8.3853(8)	8.550(4)	8.3623(5)	8.5587(6)	8.344(4)	8.5139(7)	8.3648(4)	8.5139(7)	8.3772(5)	8.5113(3)	8.3221(4)	8.5316(4)	8.3805(4)	8.5053(7)	8.3688(6)
b /Å	4.9501(8)	4.8511(15)	4.9600(3)	4.7956(4)	4.9336(22)	4.7879(3)	4.9221(3)	4.8668(29)	4.9467(4)	4.8086(3)	4.9520(3)	4.8457(3)	4.9657(2)	4.8064(2)	4.9558(2)	4.8320(23)	4.9490(3)	4.8480(3)
c /Å	16.2916 (31)	16.3440(4)	16.2542(14)	16.4396(15)	16.257(5)	16.3987(12)	16.2744(14)	16.426(8)	16.2416(19)	16.4000(11)	16.3036(11)	16.3414(9)	16.4629(5)	16.3679(6)	16.2649(9)	16.2400(6)	16.2864(13)	16.3437(11)
β/deg	109.935(10)	109.166(19)	109.952(5)	110.140(6)	110.001(7)	110.276(4)	109.929(5)	110.324(15)	109.908(6)	110.479(4)	110.004(6)	109.3064(32)	110.333(2)	109.093(2)	109.9089(30)	109.100(4)	109.925(5)	109.317(4)
V/Å^3	645.14(20)	626.06(32)	646.36(9)	620.66(10)	644.0(5)	615.88(7)	644.52(9)	624.5(6)	643.16(11)	617.96(7)	645.91(8)	625.73(24)	652.45(4)	618.69(4)	646.60(5)	621.80(5)	644.50(8)	625.76(7)
<M-O>/ Å	2.01	1.86	2.00	1.85	1.95	1.80	2.01	1.87	1.90	1.78	1.90	1.88	1.96	1.88	2.03	1.90	1.93	1.85
Ti Frac.	0.72	0.19	0.72	0.19	0.72	0.19	0.72	0.19	0.72	0.19	0.72	0.19	0.72	0.19	0.72	0.19	0.72	0.19
Ge Frac.	0.28	0.81	0.28	0.81	0.28	0.81	0.28	0.81	0.28	0.81	0.28	0.81	0.28	0.81	0.28	0.81	0.28	0.81
Weight frac.	52%	48%	62%	38%	43%	57%	53%	47%	49%	51%	50%	50%	14%	86%	66%	34%	53%	47%
GSAS Bulk comp.	$Ti_{0.47}Ge_{0.53}(HPO_4)_2.H_2O$		$Ti_{0.52}Ge_{0.48}(HPO_4)_2.H_2O$		$Ti_{0.42}Ge_{0.58}(HPO_4)_2.H_2O$		$Ti_{0.47}Ge_{0.53}(HPO_4)_2.H_2O$		$Ti_{0.45}Ge_{0.55}(HPO_4)_2.H_2O$		$Ti_{0.45}Ge_{0.15}(HPO_4)_2.H_2O$		$Ti_{0.26}Ge_{0.74}(HPO_4)_2.H_2O$		$Ti_{0.54}Ge_{0.46}(HPO_4)_2.H_2O$		$Ti_{0.47}Ge_{0.53}(HPO_4)_2.H_2O$	
XRF Bulk comp.	$Ti_{0.75}Ge_{0.25}(HPO_4)_2.H_2O$		$Ti_{0.64}Ge_{0.36}(HPO_4)_2.H_2O$		$Ti_{0.47}Ge_{0.53}(HPO_4)_2.H_2O$		$Ti_{0.66}Ge_{0.34}(HPO_4)_2.H_2O$		$Ti_{0.48}Ge_{0.52}(HPO_4)_2.H_2O$		$Ti_{0.59}Ge_{0.41}(HPO_4)_2.H_2O$		$Ti_{0.26}Ge_{0.74}(HPO_4)_2.H_2O$		$Ti_{0.57}Ge_{0.43}(HPO_4)_2.H_2O$		$Ti_{0.61}Ge_{0.39}(HPO_4)_2.H_2O$	

3.2.2.4 Pair Distribution Function (PDF) Analysis

The overlaid PDF patterns of the mixed germanium-titanium phosphates in the low-r region are displayed in Figure 3.44. By inspection, it is clear that the germanium-rich products have smaller intralayer interatomic distances as shown by the oxygen-oxygen, phosphorus-phosphorus, metal-oxygen and metal-metal peaks at approximately 3.20, 4.20, 1.80 and 4.80-5.00 Å respectively. Refer back to Figure 3.13 for a pictorial description of these distances in relation to the layered structure. In all cases as the titanium content of the product increases so does the distance. The rationalisation for the variation in peak heights in Section 3.1.2.4 for the zirconium-titanium phosphates apply for this system as well. A close up of the metal-metal peak region is shown in Figure 3.45. The patterns confirm the products to be solid solutions with no metal ordering. Exceptions should be noted for $Ti_{0.7}Ge_{0.3}(HPO_4)_2.H_2O$ and $Ti_{0.6}Ge_{0.4}(HPO_4)_2.H_2O$ synthesised from the '*TiP method*' whose patterns in this region show a more complicated structure that may allude to the presence of a second phase. From the PDF data alone it is unclear whether this is a germanium-titanium phase or an impurity. Re-examination of the Rietveld refinement plots (Figures 3.38 and 3.39) show no evidence of a second crystalline germanium-titanium phase, however for both products a high background is observed around 15° 2θ. This is indicative of the presence of amorphous phases, which, given the high titanium bulk compositions for these products, are believed to be titanium based impurities. As with the Rietveld refinements little difference is seen between the patterns of the $Ti_{0.9}Ge_{0.1}(HPO_4)_2.H_2O$ and $Ti_{0.8}Ge_{0.2}(HPO_4)_2.H_2O$ products synthesised by the two different methods.

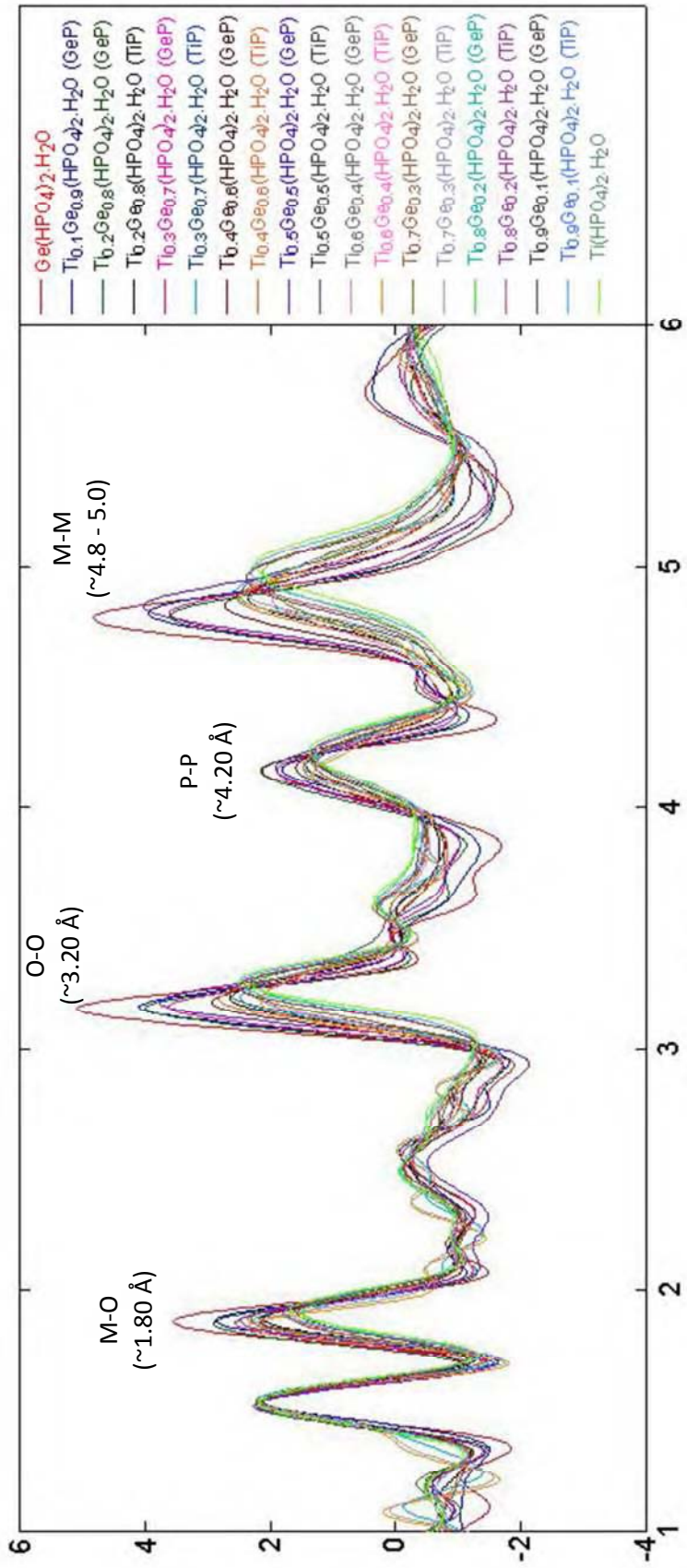

Figure 3.44: Overlaid PDF patterns of the Ge/Ti phosphates scaled on the phosphorus-oxygen peak height.

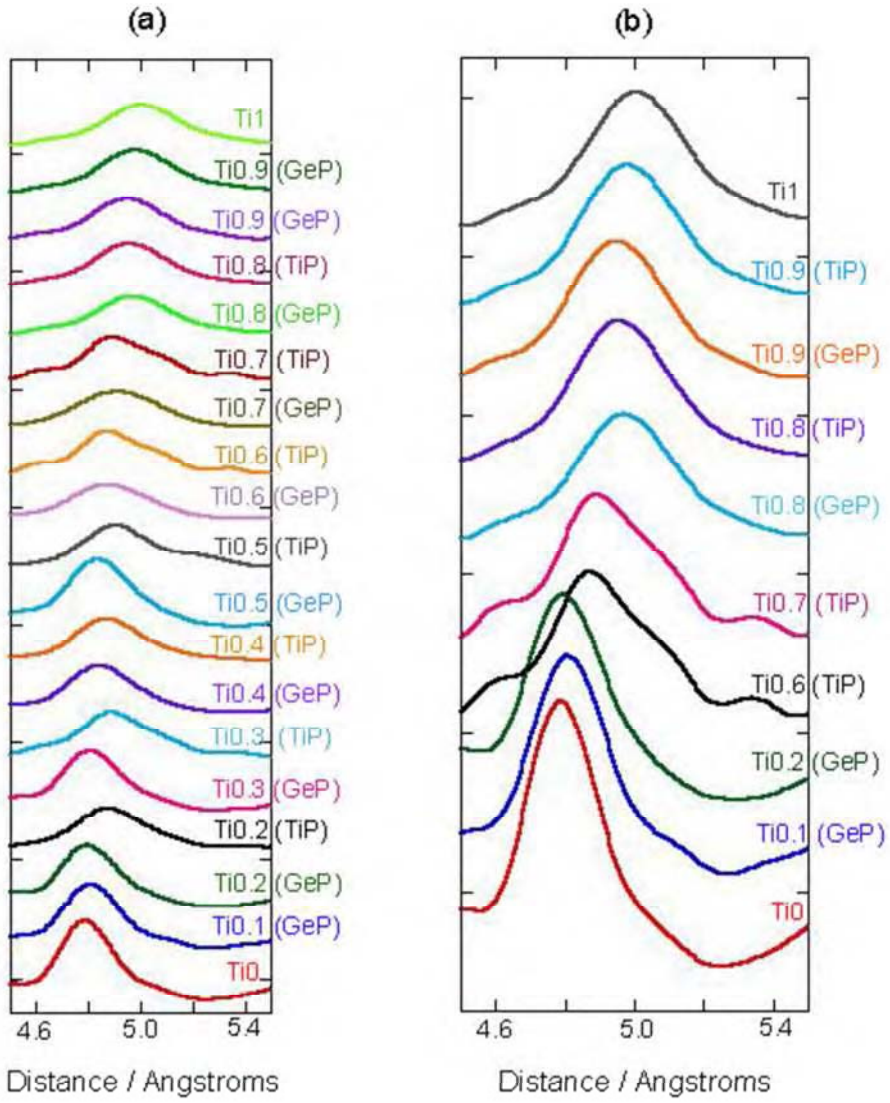

Figure 3.45: PDF patterns of the (a) whole series, (b) single phase products in the region where the metal-metal peaks are observed. The synthetic method is noted in brackets.

The presence of two overlapping metal-metal peaks seen in the patterns of the other products confirms the previously determined two-phase nature.

3.2.2.5 PDF Refinements

The PDFs for the single phase materials were modelled using PDFGUI[7], following the method outlined in Section 2.6.3. The starting models were as noted for the Rietveld work (Section 3.2.2.3) and the metal fractions refined. The refinements converged readily and gave good fits as shown by the R_{wp} values indicated in the refinement summary table (Table 3.36). Good agreement can be seen between the parameters obtained here and those included from the Rietveld refinements. Fits to the data and crystallographic details can be found in Tables 3.37 – 3.45 and Figures 3.46 – 3.54. The crystallographic refinement files can be found in Appendix 4. Again no estimated standard deviations are reported due to the issues with the integration software discussed previously. The fits of the $Ti_{0.6}Ge_{0.4}(HPO_4)_2.H_2O$ and $Ti_{0.7}Ge_{0.3}(HPO_4)_2.H_2O$ products were not as successful with R_{wp} values close to 0.2. This can be attributed to the presence of impurities that were not accounted for in the refinements.

Table 3.36: Comparison of the refinement parameters for the single-phase members of the series, PDF derived numbers are in normal font and those from Rietveld analysis are shown in italics for comparison. The esd's on the numbers from the PDF analysis are undetermined as esd's on the individual data points are unknown.

	$Ti_{0.9}Ge_{0.1}(HPO_4)_2.H_2O$		$Ti_{0.8}Ge_{0.2}(HPO_4)_2.H_2O$		$Ti_{0.7}Ge_{0.3}(HPO_4)_2.H_2O$	$Ti_{0.6}Ge_{0.4}(HPO_4)_2.H_2O$	$Ti_{0.2}Ge_{0.8}(HPO_4)_2.H_2O$	$Ti_{0.1}Ge_{0.9}(HPO_4)_2.H_2O$	$Ge(HPO_4)_2.H_2O$
	TiP Meth	GeP Meth	TiP Meth	GeP Meth					
a/Å	8.5809 *8.60359(9)*	8.52416 *8.56546(21)*	8.5548 *8.5789(1)*	8.55839 *8.59311(17)*	8.5221 *8.5562(3)*	8.6021 *8.5262(4)*	8.31176 *8.31806(20)*	8.28474 *8.3070(4)*	8.24097 *8.28464(1)*
b /Å	4.9724 *4.98759(5)*	4.95768 *4.96596(10)*	4.9513 *4.97082(8)*	4.97182 *4.98176(9)*	4.9342 *4.9586(1)*	4.8977 *4.9526(2)*	4.80859 *4.80246(10)*	4.80052 *4.7981(2)*	4.77694 *4.78345(1)*
c /Å	16.2076 *16.2163(2)*	16.103 *16.2311(5)*	16.1008 *16.2384(3)*	16.0617 *16.2113(4)*	16.2072 *16.2667(6)*	16.193 *16.2717(10)*	16.3531 *16.38171(30)*	16.2806 *16.3858(4)*	16.3634 *16.40369(4)*
β/deg	110.309 *110.0941(6)*	109.596 *110.0017(14)*	109.556 *109.9950(9)*	109.744 *110.0821(12)*	109.892 *109.9197(17)*	110.186 *109.9218(26)*	109.528 *109.0648(12)*	109.032 *109.046(1)*	108.799 *108.9576(1)*
V/Å^3	648.545 *653.501(13)*	641.1 *648.758(30)*	642.643 *650.737(20)*	643.259 *651.793(24)*	640.853 *648.86(4)*	640.32 *645.99 (6)*	616.005 *618.508(23)*	612.102 *617.35(4)*	609.807 *614.8052(24)*
M-O(1)/ Å	1.9267 *1.940(6)*	1.92714 *1.842(7)*	1.9273 *1.973(8)*	1.87495 *1.933(8)*	2.092 *1.929(9)*	2.0769 *1.945(14)*	1.90518 *1.879(14)*	1.89142 *1.816(17)*	1.87279 *1.870(4)*
M-O(2)/ Å	1.9910 *1.969(7)*	1.90591 *1.921(9)*	2.0399 *1.891(9)*	1.94587 *1.906(9)*	1.954 *1.970(9)*	1.8791 *2.048(13)*	1.81427 *2.008(15)*	1.84113 *1.944(19)*	1.93295 *1.877(5)*
M-O(3)/ Å	1.9568 *1.936(7)*	1.83393 *1.868(10)*	1.8767 *1.966(9)*	1.92585 *1.873(10)*	1.842 *1.910(11)*	1.9201 *1.943(16)*	1.83089 *1.739(14)*	1.8696 *1.804(19)*	1.83066 *1.863(5)*
M-O(5)/ Å	1.8741 *1.922(7)*	1.97993 *2.067(9)*	1.9007 *1.910(9)*	2.0000 *2.050(11)*	1.892 *1.952(11)*	1.8357 *1.882(17)*	1.89329 *1.853(15)*	1.8555 *1.876(19)*	1.82642 *1.879(5)*
M-O(6)/ Å	1.8724 *1.943(7)*	1.89716 *1.838(9)*	1.9583 *1.968(9)*	1.85585 *1.874(10)*	1.858 *1.971(12)*	1.9664 *1.930(17)*	1.95052 *1.852(15)*	1.9502 *1.916 (19)*	1.85232 *1.885(5)*
M-O(7)/ Å	2.1564 *1.953(6)*	2.01306 *1.964(7)*	1.8743 *1.880(7)*	2.14641 *1.951(7)*	1.949 *2.011(8)*	1.8777 *2.068(12)*	1.87574 *1.909(13)*	1.93913 *1.869(16)*	1.9198 *1.881(4)*
<M-O>/ Å	1.963 *1.944*	1.9262 *1.917*	1.93 *1.93*	1.958 *1.931*	1.931 *1.958*	1.926 *1.969*	1.878315 *1.873*	1.89 *1.87*	1.87249 *1.8758*
R_{wp}	0.098	0.109	0.087	0.087	0.190	0.178	0.106	0.14	0.14

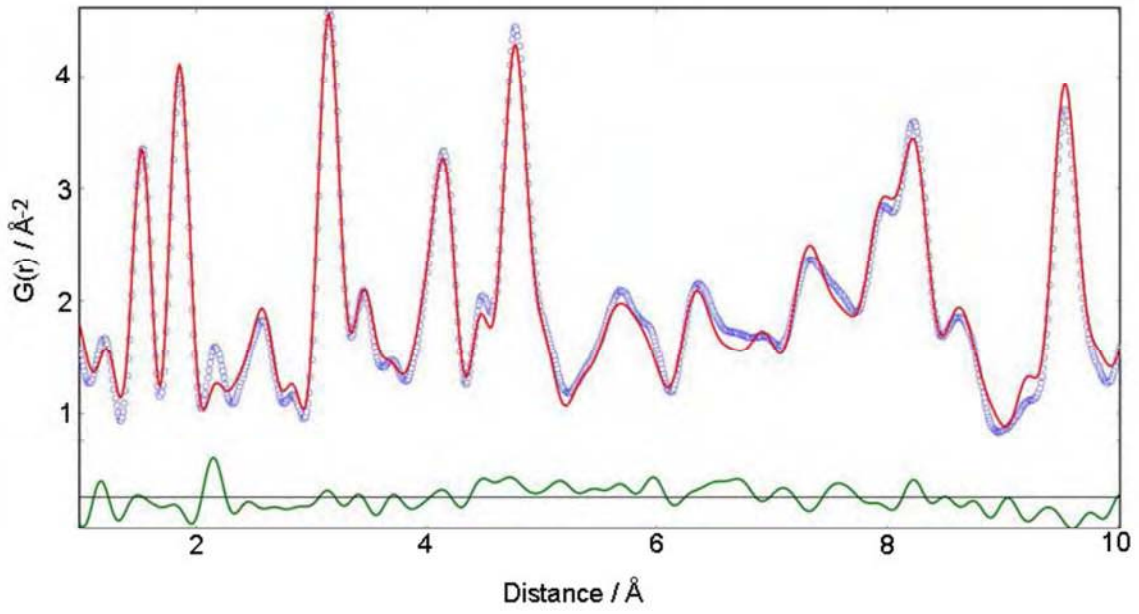

Figure 3.46: Final observed (blue), calculated (red), and difference (green) PDF profiles for α-$Ge(HPO_4)_2.H_2O$.

Table 3.37: Fractional atomic and isotropic displacement parameters for α-$Ge(HPO_4)_2.H_2O$ from the PDF refinement.

atom	*x*	*y*	*z*	U_{iso} (x10^2) Å^2
Ge	0.7537	0.2571	0.5074	0.23
P(1)	0.9938	0.7470	0.6024	0.25
P(2)	0.4652	0.2635	0.0941	0.25
O(1)	0.1084	0.8672	0.5566	0.27
O(2)	0.9448	0.4243	0.5956	0.27
O(3)	0.8552	0.9438	0.5664	0.27
O(4)	0.0702	0.7264	0.7019	0.27
O(5)	0.3150	0.0443	0.0698	0.27
O(6)	0.4276	0.5592	0.0668	0.27
O(7)	0.6335	0.2917	0.5857	0.27
O(8)	0.2104	0.1931	0.2653	0.49

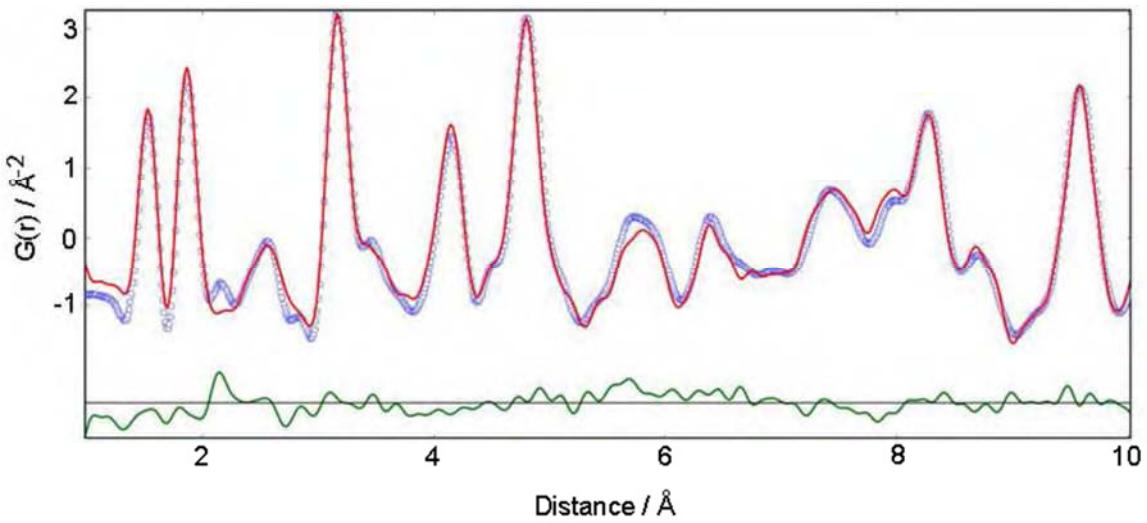

Figure 3.47: Final observed (blue), calculated (red), and difference (green) PDF profiles for α-$Ge_{0.9}Ti_{0.1}(HPO_4)_2.H_2O$ (GeP method).

Table 3.38: Fractional atomic and isotropic displacement parameters for α-$Ge_{0.9}Ti_{0.1}(HPO_4)_2.H_2O$ (GeP method) from the PDF refinement.

Atom	*x*	*y*	*z*	U_{iso} (x10^2) Å^2	Fractional Occupancy
Ti	0.7592	0.2517	0.5078	0.20	0.3206
Ge	0.7592	0.2517	0.5078	0.20	0.6794
P(1)	0.9948	0.7431	0.6054	0.20	
P(2)	0.4692	0.2647	0.0967	0.20	
O(1)	0.1142	0.8866	0.5613	0.19	
O(2)	0.9342	0.4376	0.5887	0.19	
O(3)	0.8323	0.9390	0.5787	0.19	
O(4)	0.0502	0.7028	0.7013	0.19	
O(5)	0.3163	0.0850	0.0496	0.19	
O(6)	0.4580	0.6362	0.0759	0.19	
O(7)	0.5373	0.2946	0.1995	0.19	
O(8)	0.3792	0.8320	0.9193	0.19	
O(9)	0.2688	0.1540	0.2406	0.16	

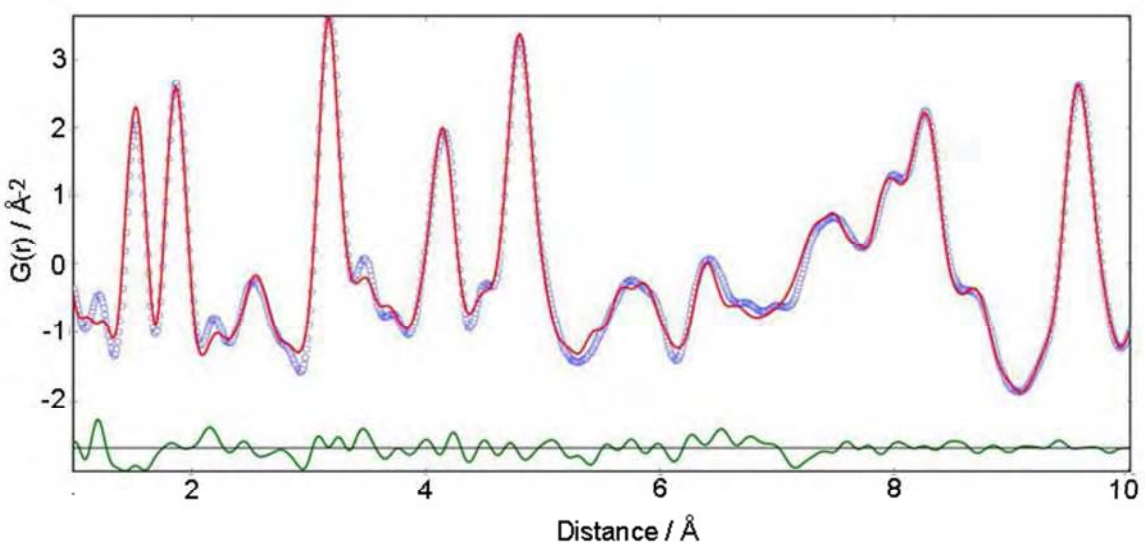

Figure 3.48: Final observed (blue), calculated (red), and difference (green) PDF profiles for α-$Ge_{0.8}Ti_{0.2}(HPO_4)_2.H_2O$ (GeP method).

Table 3.39: Fractional atomic and isotropic displacement parameters for α-$Ge_{0.8}Ti_{0.2}(HPO_4)_2.H_2O$ (GeP method) from the PDF refinement.

Atom	*x*	*y*	*z*	U_{iso} (x10^2) Å^2	Fractional Occupancy
Ti	0.7568	0.2595	0.5113	0.33	0.8000
Ge	0.7568	0.2595	0.5113	0.33	0.2000
P(1)	0.9959	0.7626	0.6003	0.37	
P(2)	0.4695	0.2661	0.0968	0.37	
O(1)	0.1341	0.8787	0.5660	0.39	
O(2)	0.9467	0.4297	0.5826	0.39	
O(3)	0.8228	0.9231	0.5644	0.39	
O(4)	0.0707	0.7348	0.7018	0.39	
O(5)	0.3076	0.1183	0.0360	0.39	
O(6)	0.4155	0.5487	0.0778	0.39	
O(7)	0.4999	0.2759	0.1915	0.39	
O(8)	0.3797	0.8510	0.9216	0.39	
O(9)	0.2712	0.1543	0.2624	0.59	

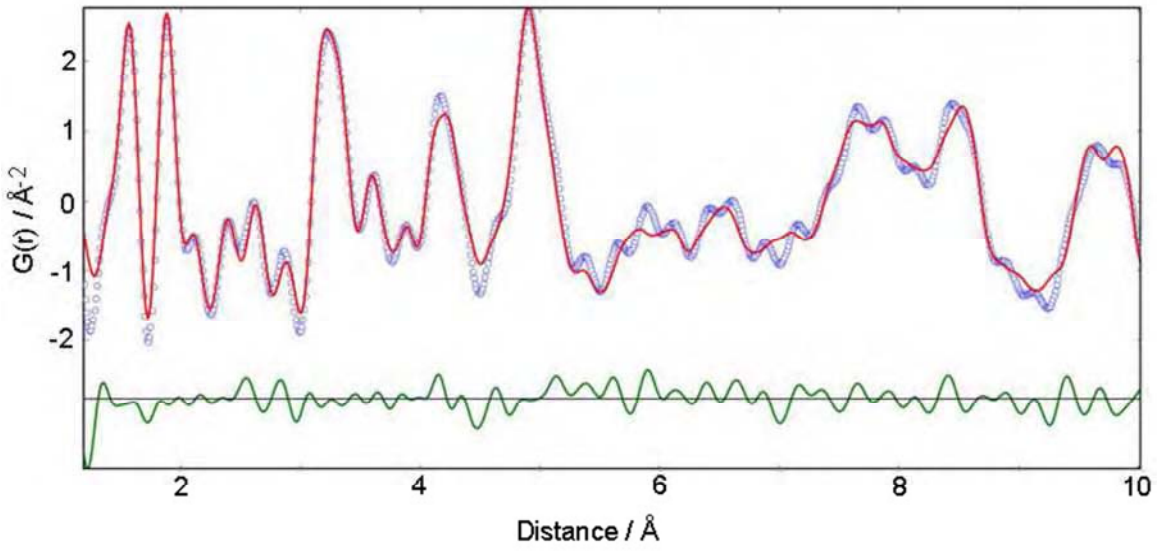

Figure 3.49: Final observed (blue), calculated (red), and difference (green) PDF profiles for α-$Ge_{0.4}Ti_{0.6}(HPO_4)_2.H_2O$ (TiP method).

Table 3.40: Fractional atomic and isotropic displacement parameters for α-$Ge_{0.4}Ti_{0.6}(HPO_4)_2.H_2O$ (TiP method) from the PDF refinement.

Atom	*x*	*y*	*z*	U_{iso} (x10^2) Å^2	Fractional Occupancy
Ti	0.7585	0.2474	0.5114	0.79	0.5257
Ge	0.7585	0.2474	0.5114	0.79	0.4743
P(1)	0.9989	0.7422	0.6083	0.50	
P(2)	0.4756	0.2742	0.5929	0.50	
O(1)	0.0605	0.8315	0.5433	0.30	
O(2)	0.9446	0.4372	0.5850	0.30	
O(3)	0.8544	0.9374	0.5836	0.30	
O(4)	0.1079	0.6876	0.7098	0.30	
O(5)	0.2993	0.4140	0.5383	0.30	
O(6)	0.4244	0.9621	0.5712	0.30	
O(7)	0.6414	0.3264	0.5873	0.30	
O(8)	0.5149	0.2666	0.6922	0.30	
O(9)	0.2953	0.2915	0.7653	0.43	

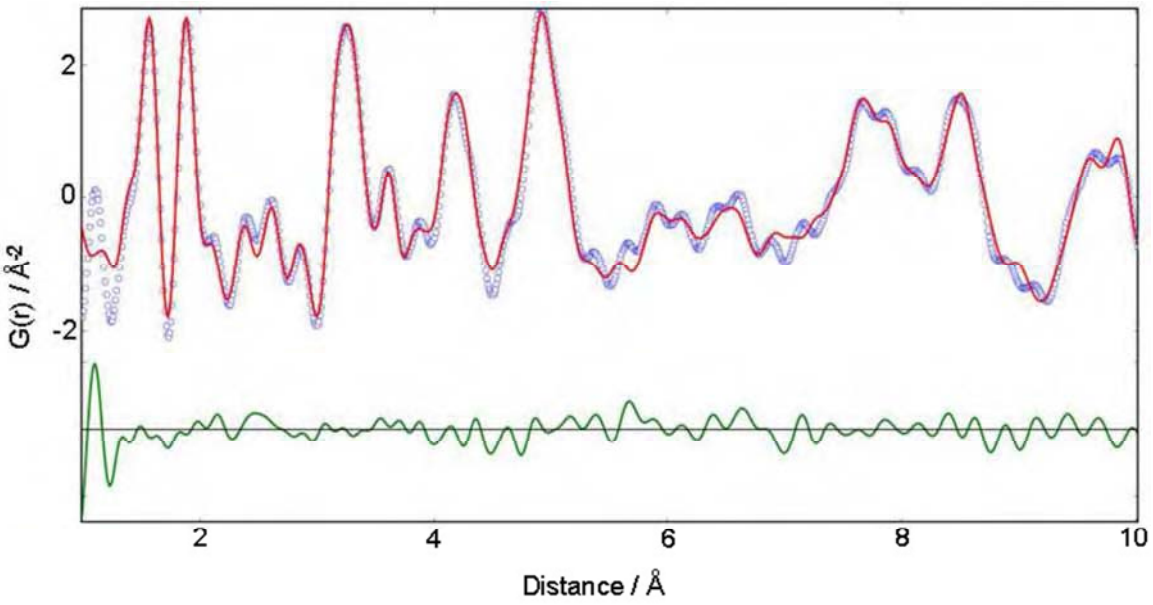

Figure 3.50: Final observed (blue), calculated (red), and difference (green) PDF profiles for α-$Ge_{0.3}Ti_{0.7}(HPO_4)_2.H_2O$ (TiP method).

Table 3.41: Fractional atomic and isotropic displacement parameters for α-$Ge_{0.3}Ti_{0.7}(HPO_4)_2.H_2O$ (TiP method) from the PDF refinement.

Atom	*x*	*y*	*z*	U_{iso} (x10^2) Å^2	Fractional Occupancy
Ti	0.7567	0.2381	0.5099	0.83	0.5921
Ge	0.7567	0.2381	0.5099	0.83	0.4079
P(1)	0.9943	0.7563	0.6034	0.48	
P(2)	0.4791	0.2655	0.6000	0.48	
O(1)	0.1022	0.8790	0.5675	0.26	
O(2)	0.9441	0.4414	0.5894	0.26	
O(3)	0.8452	0.9332	0.5746	0.26	
O(4)	0.1023	0.7338	0.7058	0.26	
O(5)	0.3134	0.4484	0.5602	0.26	
O(6)	0.4147	-0.0032	0.5500	0.26	
O(7)	0.6570	0.3156	0.5992	0.26	
O(8)	0.5030	0.2869	0.6953	0.26	
O(9)	0.2813	0.2673	0.7650	0.13	

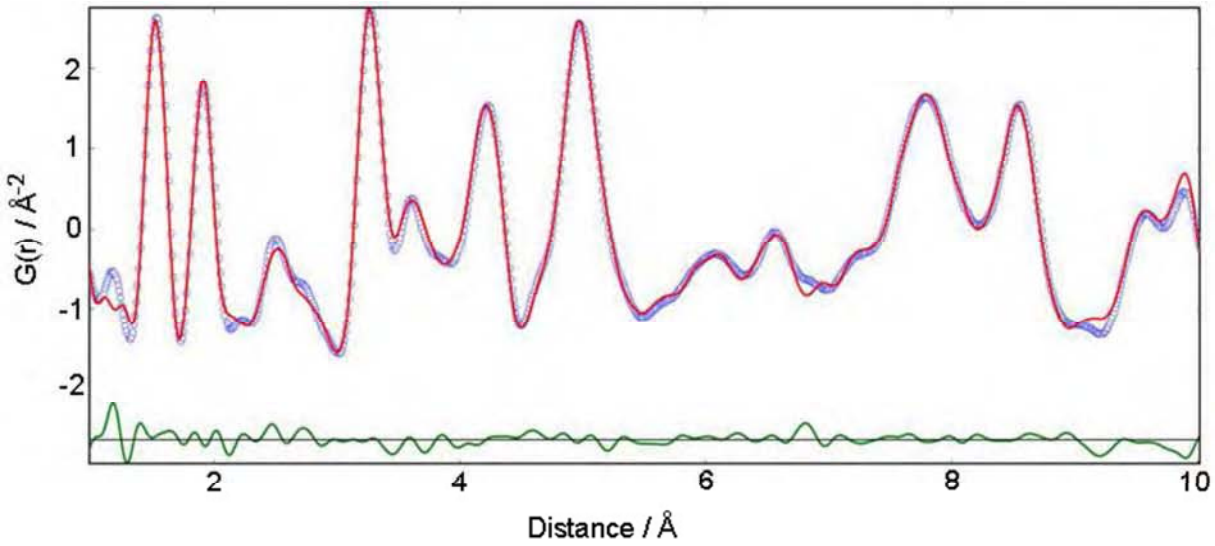

Figure 3.51: Final observed (blue), calculated (red), and difference (green) PDF profiles for α-$Ge_{0.2}Ti_{0.8}(HPO_4)_2.H_2O$ (GeP method).

Table 3.42: Fractional atomic and isotropic displacement parameters for α-$Ge_{0.2}Ti_{0.8}(HPO_4)_2.H_2O$ (GeP method) from the PDF refinement.

Atom	*x*	*y*	*z*	U_{iso} (x10^2) Å^2	Fractional Occupancy
Ti	0.7637	0.2541	0.5121	0.31	0.8208
Ge	0.7637	0.2541	0.5121	0.31	0.1792
P(1)	0.9994	0.7472	0.6082	0.50	
P(2)	0.4596	0.2318	0.5968	0.50	
O(1)	0.1073	0.8157	0.5594	0.55	
O(2)	0.9453	0.4529	0.5957	0.55	
O(3)	0.8415	0.9380	0.5834	0.55	
O(4)	0.0941	0.7673	0.7112	0.55	
O(5)	0.3145	0.4275	0.5672	0.55	
O(6)	0.4083	0.9626	0.5564	0.55	
O(7)	0.6071	0.3020	0.5910	0.55	
O(8)	0.5031	0.2205	0.7029	0.55	
O(9)	0.2769	0.2893	0.7700	0.93	

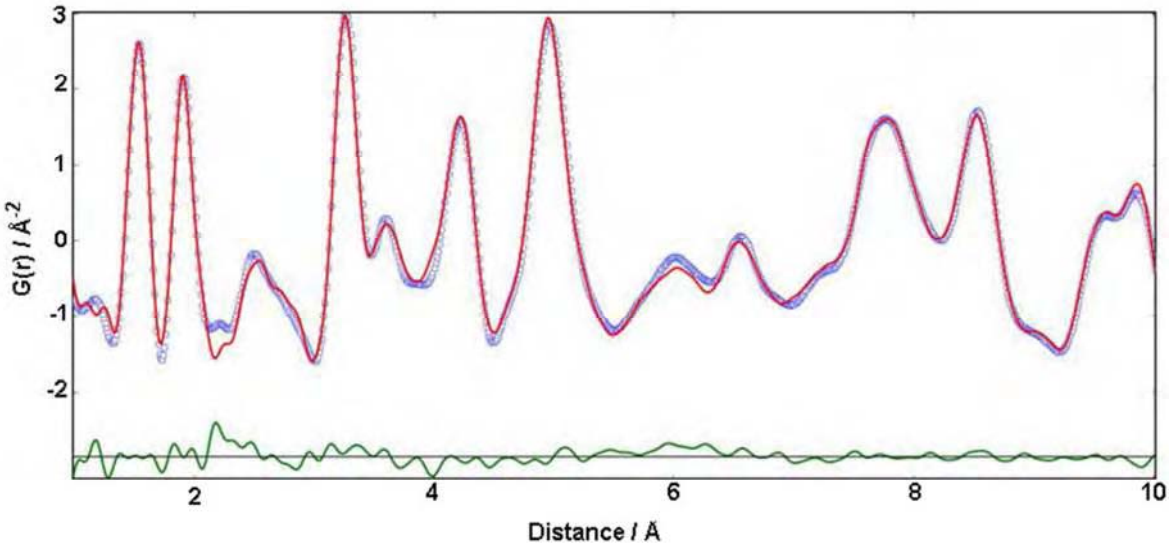

Figure 3.52: Final observed (blue), calculated (red), and difference (green) PDF profiles for α-$Ge_{0.2}Ti_{0.8}(HPO_4)_2.H_2O$ (TiP method).

Table 3.43: Fractional atomic and isotropic displacement parameters for α-$Ge_{0.2}Ti_{0.8}(HPO_4)_2.H_2O$ (TiP method) from the PDF refinement.

Atom	*x*	*y*	*z*	U_{iso} (x10^2) Å^2	Fractional Occupancy
Ti	0.7617	0.2460	0.5109	0.41	0.6923
Ge	0.7617	0.2460	0.5109	0.41	0.3076
P(1)	0.9935	0.7424	0.6070	0.67	
P(2)	0.4676	0.2452	0.6005	0.67	
O(1)	0.0925	0.8270	0.5553	0.62	
O(2)	0.9476	0.4436	0.6047	0.62	
O(3)	0.8539	0.9703	0.5926	0.62	
O(4)	0.0789	0.7398	0.7105	0.62	
O(5)	0.3126	0.4391	0.5587	0.62	
O(6)	0.4258	0.9630	0.5655	0.62	
O(7)	0.6132	0.3321	0.5701	0.62	
O(8)	0.5136	0.2860	0.6951	0.62	
O(9)	0.2719	0.3081	0.7721	0.72	

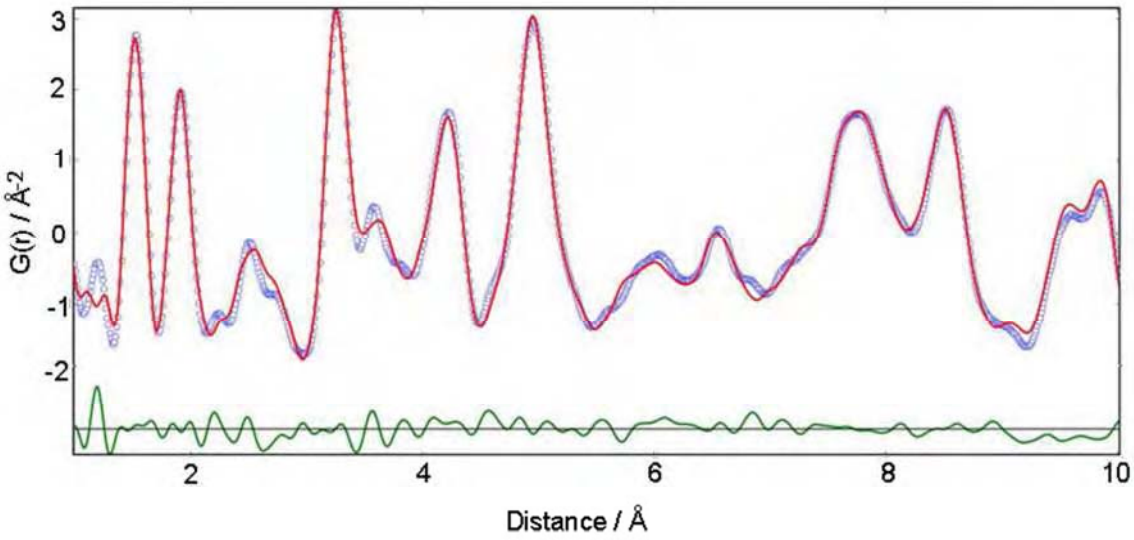

Figure 3.53: Final observed (blue), calculated (red), and difference (green) PDF profiles for α-$Ge_{0.1}Ti_{0.9}(HPO_4)_2.H_2O$ (GeP method).

Table 3.44: Fractional atomic and isotropic displacement parameters for α-$Ge_{0.1}Ti_{0.9}(HPO_4)_2.H_2O$ (GeP method) from the PDF refinement.

Atom	*x*	*y*	*z*	U_{iso} (x10^2) Å^2	Fractional Occupancy
Ti	0.7609	0.2552	0.5119	0.42	0.8006
Ge	0.7609	0.2552	0.5119	0.42	0.1994
P(1)	0.9969	0.7514	0.6083	0.43	
P(2)	0.4664	0.2420	0.5974	0.43	
O(1)	0.0939	0.8275	0.5542	0.91	
O(2)	0.9456	0.4413	0.5926	0.91	
O(3)	0.8359	0.9383	0.5692	0.91	
O(4)	0.0889	0.7705	0.7068	0.91	
O(5)	0.3126	0.4357	0.5708	0.91	
O(6)	0.4130	0.9562	0.5654	0.91	
O(7)	0.6185	0.3333	0.5866	0.91	
O(8)	0.5105	0.1850	0.6932	0.91	
O(9)	0.2872	0.3239	0.7701	0.39	

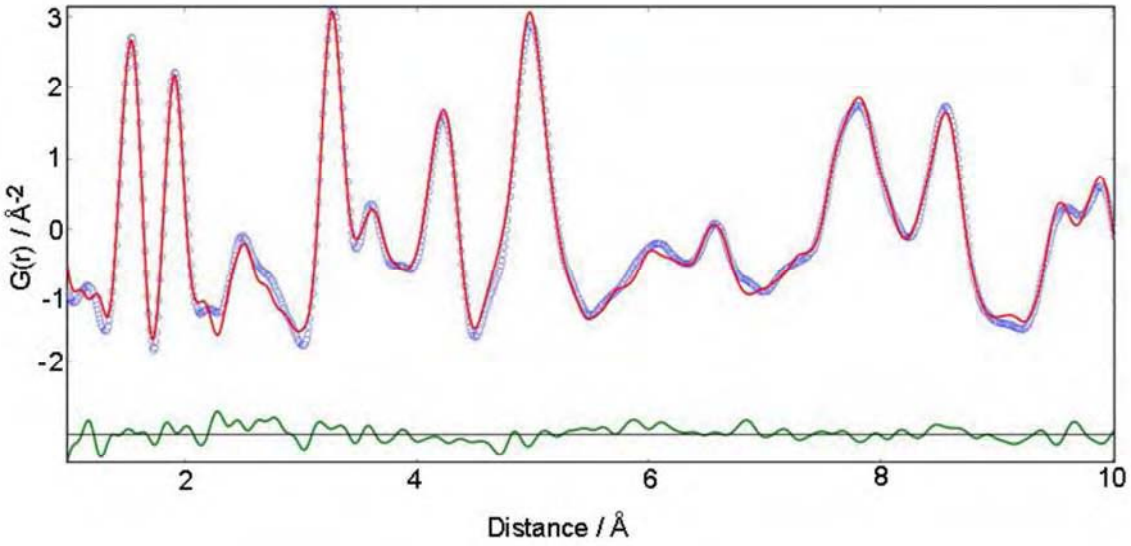

Figure 3.54: Final observed (blue), calculated (red), and difference (green) PDF profiles for α-$Ge_{0.1}Ti_{0.9}(HPO_4)_2.H_2O$ (TiP method).

Table 3.45: Fractional atomic and isotropic displacement parameters for α-$Ge_{0.1}Ti_{0.9}(HPO_4)_2.H_2O$ (TiP method) from the PDF refinement.

atom	*x*	*y*	*z*	U_{iso} (x10^2) Å^2	Fractional Occupancy
Ti	0.7612	0.2516	0.5101	0.43	0.5416
Ge	0.7612	0.2516	0.5101	0.43	0.4584
P(1)	0.9965	0.7543	0.6069	0.40	
P(2)	0.4667	0.2436	0.5990	0.40	
O(1)	0.1066	0.8310	0.5614	0.46	
O(2)	0.9333	0.4658	0.6007	0.46	
O(3)	0.8462	0.9390	0.5857	0.46	
O(4)	0.0801	0.7828	0.7113	0.46	
O(5)	0.3159	0.4591	0.5675	0.46	
O(6)	0.4144	0.9650	0.5585	0.46	
O(7)	0.6169	0.3551	0.5911	0.46	
O(8)	0.5106	0.2262	0.7023	0.46	
O(9)	0.2967	0.2827	0.7651	0.90	

3.2.2.6 Unit Cell Variations

Various plots for selected unit cell parameters and mean metal-oxygen distances for the single phase mixed metal phosphates are shown in Figure 3.55. The Rietveld data is shown as red circles and the PDF as blue squares. Average values for $Ti_{0.9}Ge_{0.1}(HPO_4)_2.H_2O$ and $Ti_{0.8}Ge_{0.2}(HPO_4)_2.H_2O$ have been plotted owing to the similarity of the structures shown by the other characterisation techniques. As expected all of the parameters, excluding the *c*-axis, decrease with the content of the smaller germanium ion. The increase in the *c* parameter is readily explained by the larger interplaner spacing of α-GeP (7.60 Å compared with 7.56 Å for α-TiP) which is approximately along the *c*-axis.

The graphs feature two lines. One of these connects the average values of the end members and therefore if the samples obeyed Vegard's Law one would expect the values to fall on that line. The second line is based on a least-squares fit to the five points for the titanium rich samples. These generally have a smaller gradient than expected. For the metal-oxygen distance this line is in contrast to that of the end member average which is indicative of a frustrated system and one that cannot withstand any further metal substitution.

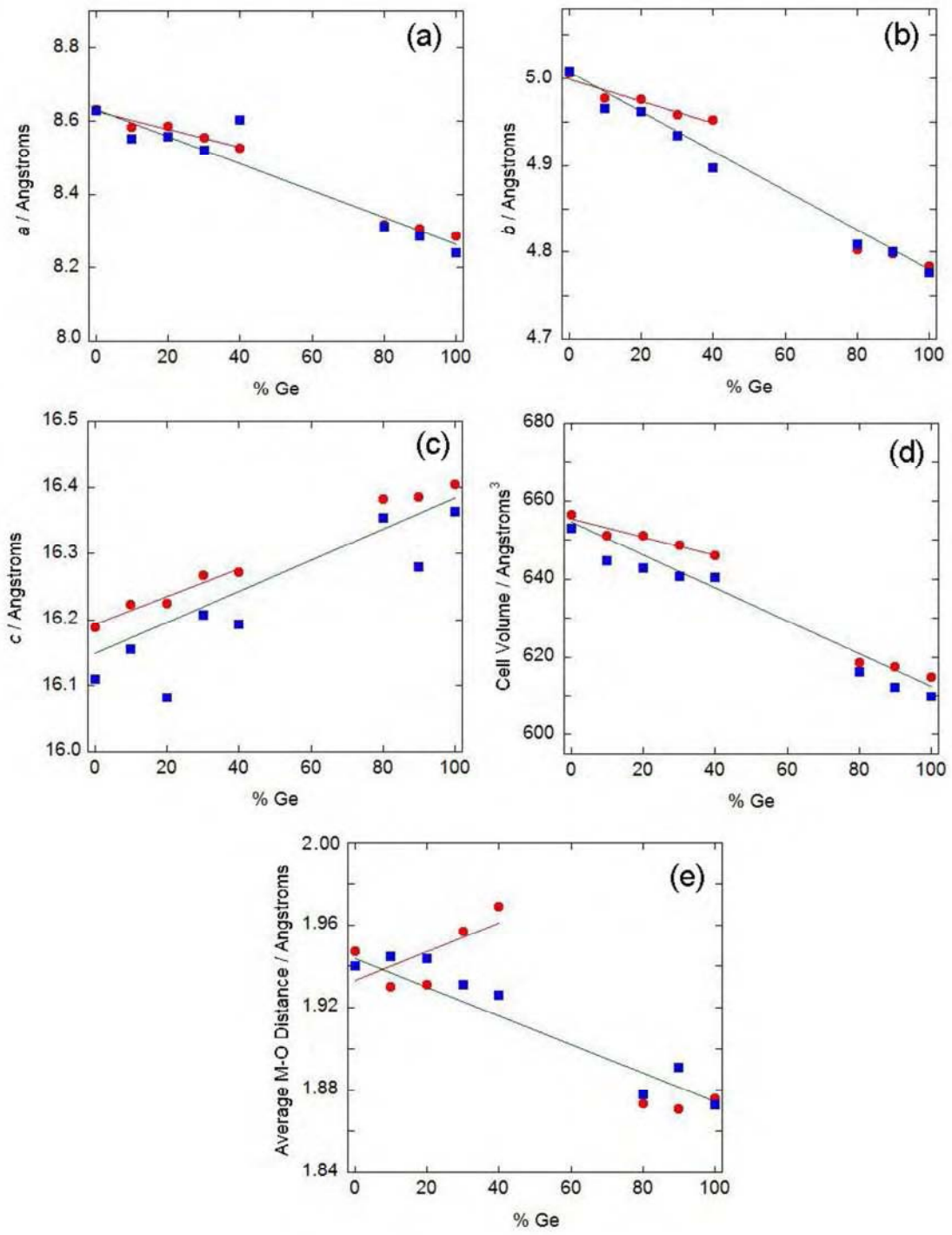

Figure 3.55: Unit cell parameters for: (a) *a*-axis; (b) *b*-axis; (c) *c*-axis; (d) volume and (e) mean M-O distance versus %Ge for the single-phase compositions in the Ti/Ge series. Red circles are data from the Rietveld refinements and blue squares from the PDF fits. The green lines connect the average values from the end members and the red lines are best fits for the Rietveld points at the titanium rich end.

3.2.2.7 Global Instability Index (GII)

The Global instability index (GII) values for the single phase mixed titanium-germanium phosphates are summarised in Figure 3.56. Calculations were made using the bond lengths obtained from the Rietveld refinements and R_o values found in the literature[12].For the mixed metal products the values used were weighted according to their Ge/Ti ratios. Average values for $Ti_{0.9}Ge_{0.1}(HPO_4)_2.H_2O$ and $Ti_{0.8}Ge_{0.2}(HPO_4)_2.H_2O$ have been plotted.

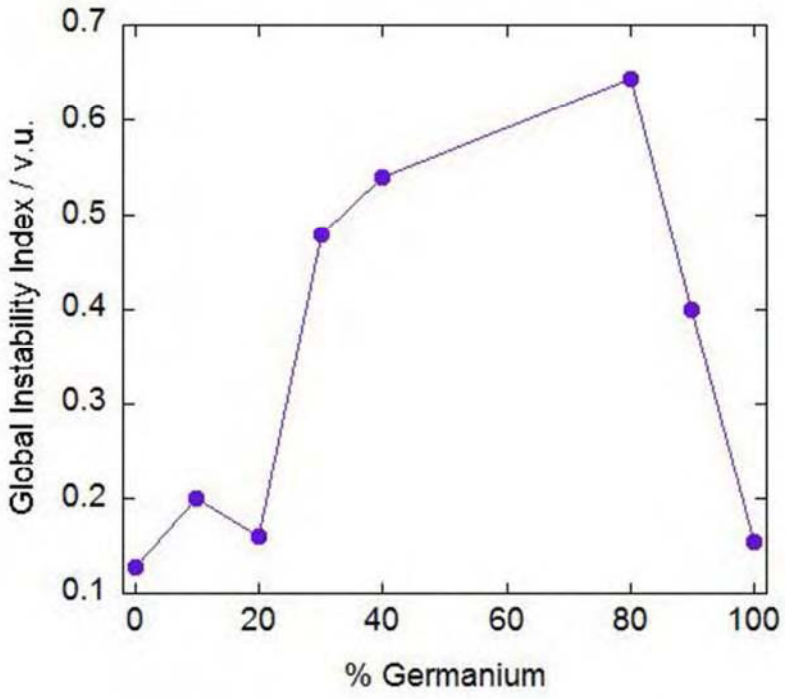

Figure 3.56: The Global Instability Index of the single phase titanium-zirconium series.

Increased metal doping results in high GII values which is indicative of highly strained structures. The effect of further metal substitution would yield very unstable structures and so consequently they do not form. Instead, two lesser substituted products are obtained.

3.2.2.8 Limits of the Solid Solutions

These findings show that the α-TiP structure is able to accommodate up to 20% germanium. Substitution of 30-40% germanium was also found possible but the products obtained were not phase pure. This is a higher level of substitution than was seen in the titanium-zirconium series. Clearly the smaller size difference between titanium and germanium does allow for greater metal substitution as envisaged, but still not the full solid solution. From the GII values obtained it appears that the structure lacks the flexibility required to allow further metal substitution without introducing strain that cannot be relieved by the mild conditions employed. In addition to this the XRF results suggest complex solution chemistry prevents gel precursors with all ranges of compositions from forming. The use of the '*GeP method'* in the synthesis of these materials has been shown to alleviate some of these problems; however the materials contain higher water levels which affect their thermal trends (to be discussed in the following section).

The α-GeP structure cannot withstand more than 20% titanium substitution in spite of the smaller metal size difference. This metal doping is only possible with the use of the *'GeP method'* which has also been shown to alleviate some of the solution chemistry issues thought to be affecting the formation of these mixed metal systems. The reasons for the low levels of doping in α-GeP must therefore be attributed to the increased corrugation of the layers within the α-GeP structure compared with those in α-TiP. As a result of this the unit cell struggles to accommodate titanium and the strains accumulate until the structure is no longer stable and is unable to form. Any attempts to 'force' higher amounts of substitution within these systems by the employment of high temperature / harsher experimental

conditions are unlikely to be successful owing to the low stability of the germanium products which already struggle to form at temperatures above 125 °C.

3.2.2.9 Thermal Analysis

Thermogravimetric experiments in conjunction with variable temperature (VT) XRD were performed on α-GeP to assess the water content and to analyse the thermal behaviour. The TGA/DTA trace is depicted in Figure 3.57 whilst the VT XRD patterns are shown in Figure 3.58. The results obtained are similar to those for the titanium-zirconium phosphates discussed previously and are in complete agreement with those published previously for α-GeP[28]. It can be seen from Figure 3.58 that the high temperature phases of α-GeP are of lower crystallinity than those observed previously for the titanium-zirconium phosphates.

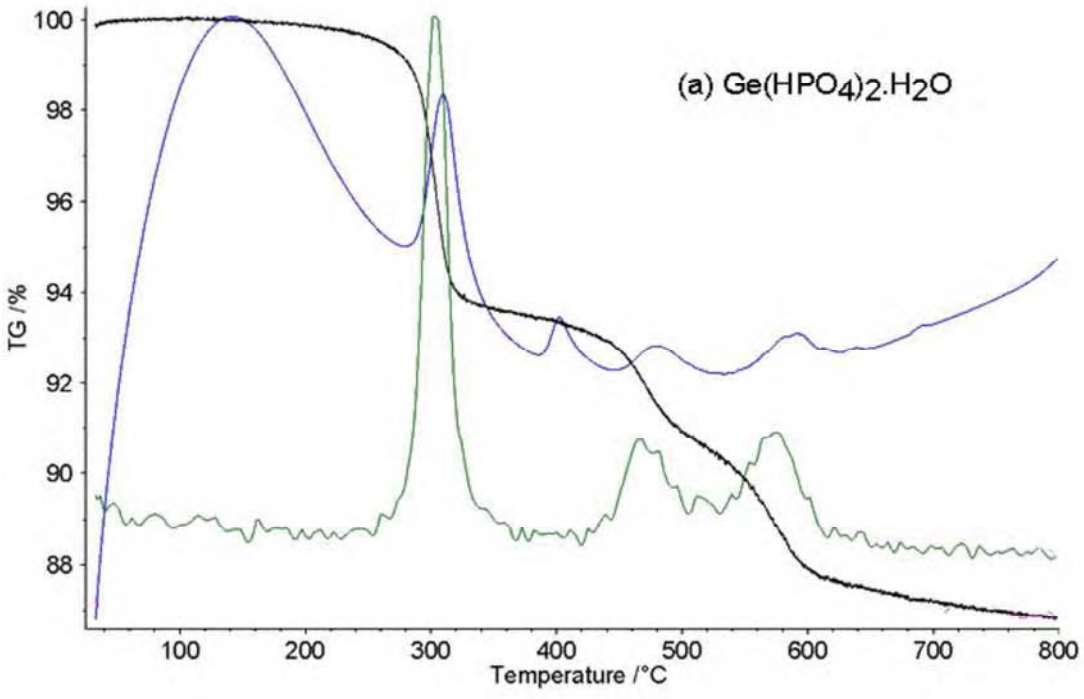

Figure 3.57: TGA/DTA traces of α-GeP. The TGA line is shown in black, the DTA curve in blue and the mass spectrometry traces for mass 18 (H_2O) is shown in green.

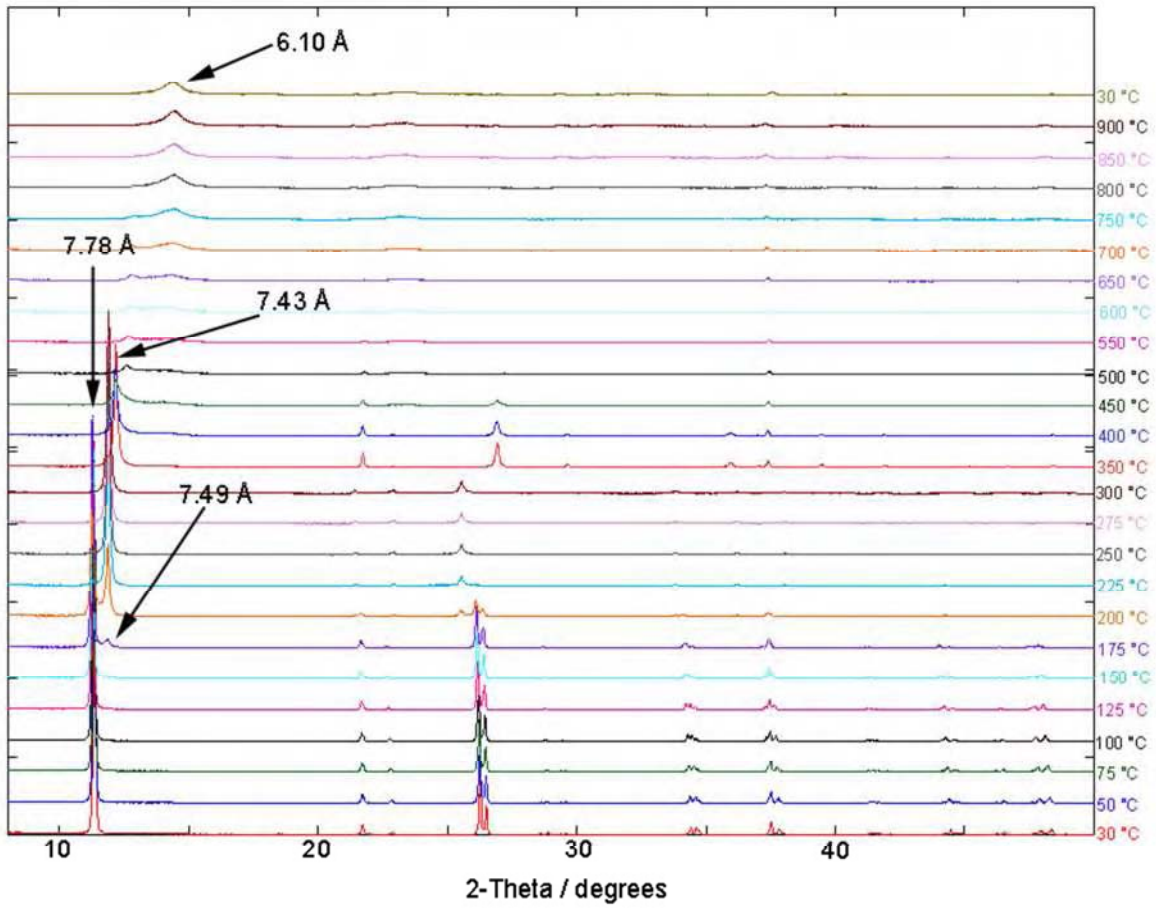

Figure 3.58: Variable temperature XRD patterns of α-$Ge(HPO_4)_2.H_2O$. The interlayer spacing (derived from the d-spacing's of the first peak) of the four crystalline decomposition products: α-$Ge(HPO_4)_2.H_2O$ (7.78 Å), ζ-$Ge(HPO_4)_2$ (7.49 Å), η-$Ge(HPO_4)_2$ (7.43 Å) and GeP_2O_7 (6.10 Å) are denoted.

Table 3.46: Comparison of the % weight loss from TGA

Product	% Weight loss from dehydration		% Weight loss from condensation	
	Theoretical	TGA	Theoretical	TGA
$Ge(HPO_4)_2.H_2O$	6.4	6.5	6.4	6.5

Comparison of the weight loss data to the theoretical values presented in Table 3.46 shows excellent agreement and confirms the presence of two molecules of water. The thermal

behaviour of α-GeP over the temperature range studied is summarised in Table 3.47. Dehydration (T1) begins around 175 °C and results in the formation of ζ-$Ge(HPO_4)_2$ with an interlayer spacing of 7.49 Å. $Ge(HPO_4)_2$ undergoes an endothermic phase change (T2) around 400°C to give η-$Ge(HPO_4)_2$, with an interlayer spacing of 7.43 Å. Finally at temperatures above 450 °C condensation of the phosphate groups occur to give the pyrophosphate. This final water loss occurs via two stages, which is in keeping with other reports[28] and common for highly crystalline samples[20].

$$\alpha\text{-}M(HPO_4)_2.H_2O \xrightarrow{T1} \zeta\text{-}M(HPO_4)_2 \xrightarrow{T2} \eta\text{-}M(HPO_4)_2 \xrightarrow{T3} \text{layered } M_2P_2O_7 \xrightarrow{T4} \text{cubic } M_2P_2O_7$$

Table 3.47: Starting phase change temperatures for α-GeP.

Product	T1	T2	T3	T4
$Ge(HPO_4)_2.H_2O$	200 °C	400 °C	450 °C	800 °C

Thermal analysis of the mixed germanium-titanium phosphates was also undertaken and found to vary according to the preparation method used. This is not unexpected due to similar other findings in the literature[9,16,19]. In light of this, separate discussion is given for the mixed metal phosphates synthesised from the *'TiP'* and the '*GeP*' methods.

Mixed germanium-titanium phosphates synthesised from the 'TiP Method':

The TGA/DTA traces are depicted in Figure 3.59 and a comparison of the weight loss data to the theoretical values is presented in Table 3.48. The VT XRD patterns are provided in Appendix 3.

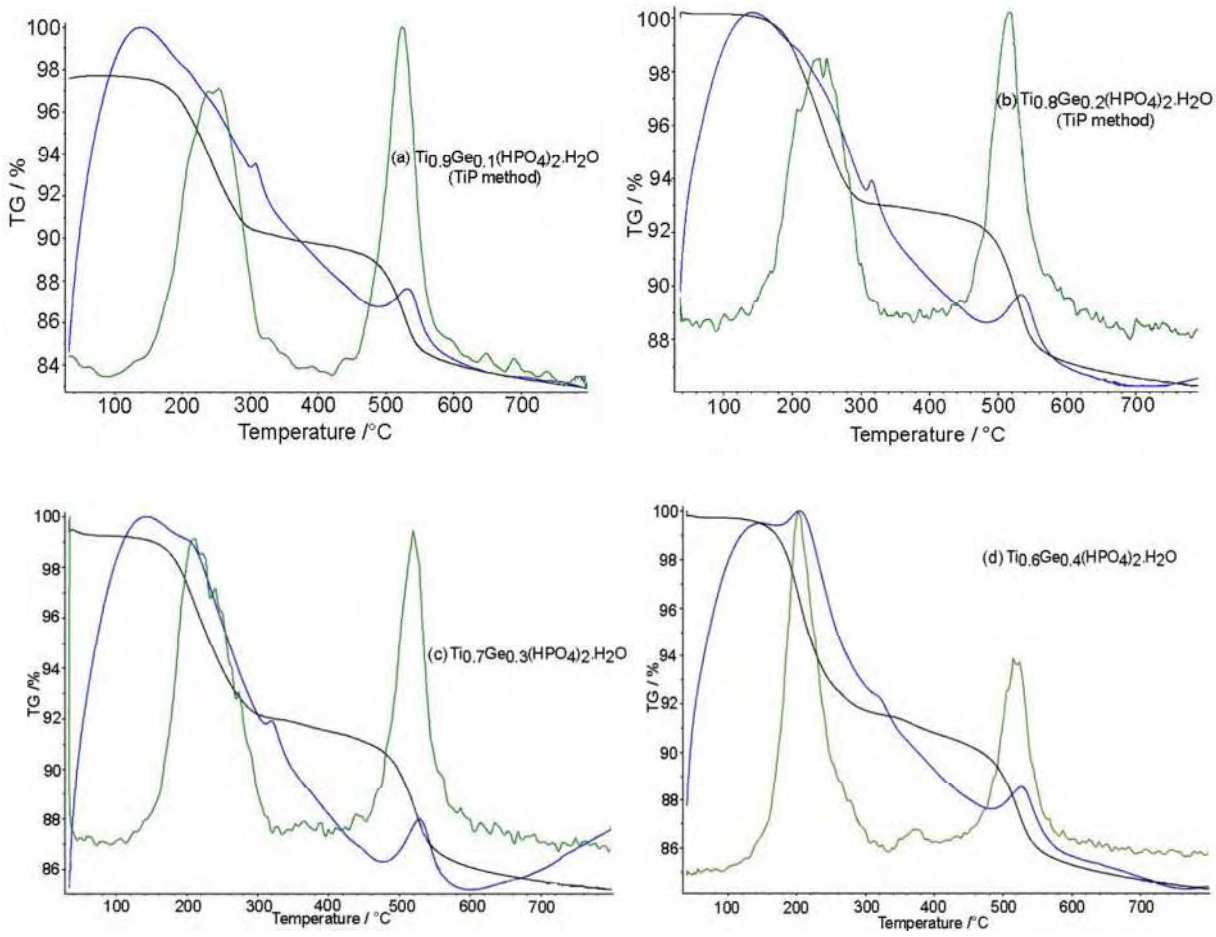

Figure 3.59: TGA/DTA traces of mixed germanium-titanium phosphates synthesised by the '*TiP method*'. The TGA line is shown in black, the DTA curve in blue and the mass spectrometry traces for mass 18 (H_2O) is shown in green.

Table 3.48: Comparison of the % weight loss from TGA.

Product	% Weight loss from dehydration		% Weight loss from condensation	
	Theoretical	TGA	Theoretical	TGA
$Ti_{0.9}Ge_{0.1}(HPO_4)_2.H_2O$	6.9	7.8	7.4	7.0
$Ti_{0.8}Ge_{0.2}(HPO_4)_2.H_2O$	6.9	7.1	7.4	6.9
$Ti_{0.7}Ge_{0.3}(HPO_4)_2.H_2O$	6.8	7.4	7.3	6.9
$Ti_{0.6}Ge_{0.4}(HPO_4)_2.H_2O$	6.7	8.2	7.2	7.2

The products are confirmed to have two molecules of water present. Examination of the TGA/DTA traces and VT XRD data shows the titanium-rich phosphates undergo the same high temperature transitions as α-TiP - with similar thermal kinetics as discussed in previous sections of this chapter. The temperatures at which the following transitions occur are shown in Table 3.49.

$$\alpha\text{-}M(HPO_4)_2.H_2O \xrightarrow{T1} \zeta\text{-}M(HPO_4)_2 \xrightarrow{T2} \eta\text{-}M(HPO_4)_2 \xrightarrow{T3} \text{layered } M_2P_2O_7 \xrightarrow{T4} \text{cubic } M_2P_2O_7$$

Table 3.49: Starting phase change temperatures for the single phase germanium-titanium phosphates synthesised by the '*TiP method*'.

Product	T1	T2	T3	T4
$Ti_{0.9}Ge_{0.1}(HPO_4)_2.H_2O$ (TiP method)	125	250	450	700
$Ti_{0.8}Ge_{0.2}(HPO_4)_2.H_2O$ (TiP method)	150	250	400	800
$Ti_{0.7}Ge_{0.3}(HPO_4)_2.H_2O$ (TiP method)	175	250	425	800
$Ti_{0.6}Ge_{0.4}(HPO_4)_2.H_2O$ (TiP method)	150	250	400	800

It is worth noting that for the $Ti_{0.7}Ge_{0.3}(HPO_4)_2.H_2O$ and $Ti_{0.6}Ge_{0.4}(HPO_4)_2.H_2O$ products there is no evidence of a second germanium-titanium phase observed in either the TGA/DTA or

the VT XRD data. This provides further support for the presence of amorphous impurities observed in the PDF studies for these two products.

Mixed germanium-titanium phosphates synthesised from the 'GeP Method':

The TGA/DTA traces are depicted in Figure 3.60 and the VT XRD patterns are provided in Appendix 3.

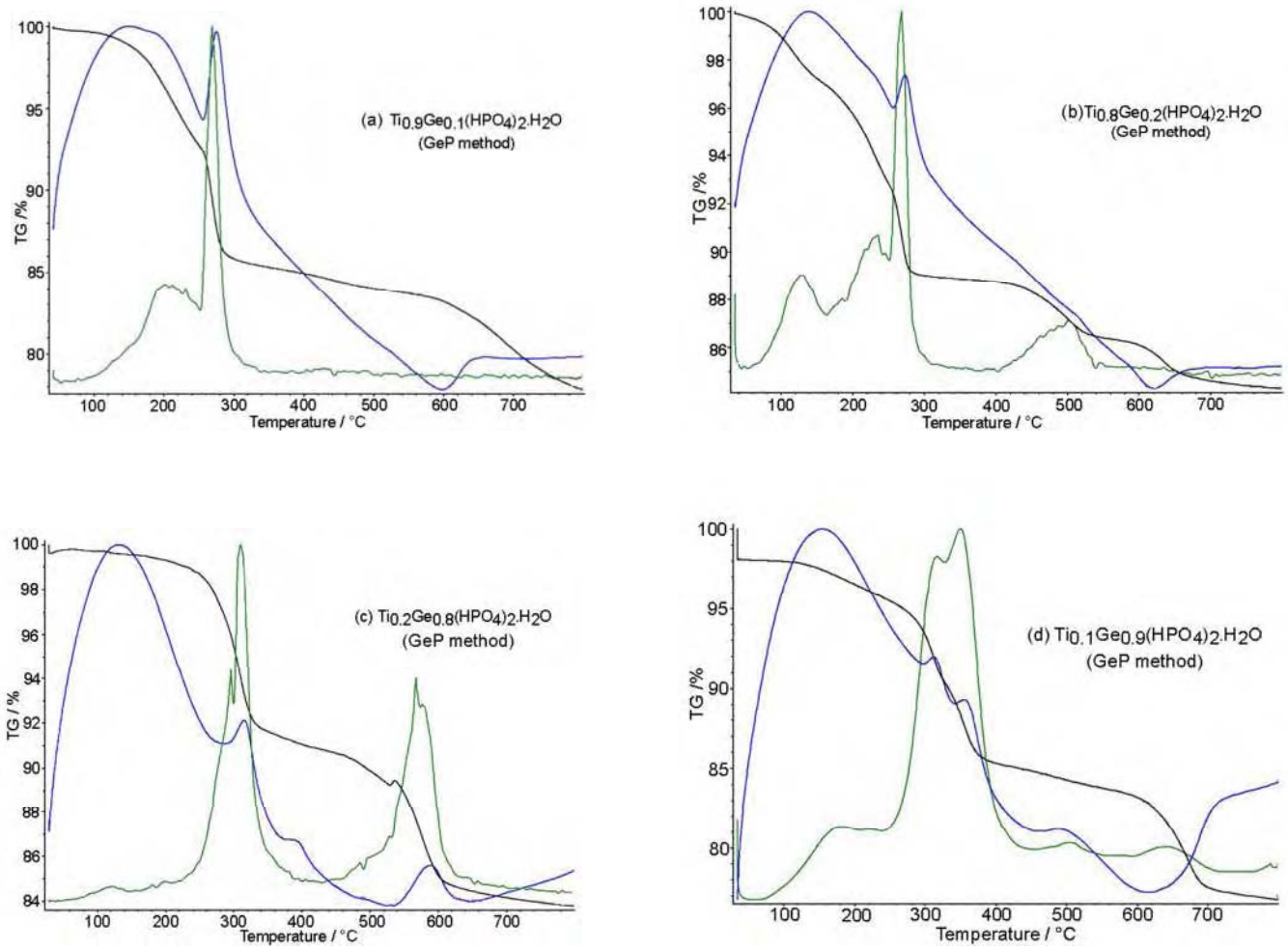

Figure 3.60: TGA/DTA traces of mixed germanium-titanium phosphates synthesised by the '*TiP method*'. The TGA line is shown in black, the DTA curve in blue and the mass spectrometry traces for mass 18 (H_2O) is shown in green.

The TGA traces of these products are more complicated than the others featured in this chapter. The products generally show the two water losses to occur in stages, which as discussed previously for α-GeP is not uncommon for these phosphates. It can also be observed that the onset of pyrophosphate formation at around 550 °C is generally not accompanied by the expected endothermic peak in the DTA curve. Only for $Ti_{0.2}Ge_{0.8}(HPO_4)_2.H_2O$ is this present. The DTA traces for the other products display 'dips' representing exothermic events. The reasons for this are not yet fully understood but may be attributed to the subtle differences in the structure, hydration and crystallite size arising from the preparation method which affects the thermal kinetics of these materials. There is no indication of additional phases present in these products that could have conflicting thermal events at these temperatures.

A summary of the thermal behaviour of these products is provided in Table 3.50.

$$\alpha\text{-}M(HPO_4)_2.H_2O \xrightarrow{T1} \zeta\text{-}M(HPO_4)_2 \xrightarrow{T2} \eta\text{-}M(HPO_4)_2 \xrightarrow{T3} \text{layered } M_2P_2O_7 \xrightarrow{T4} \text{cubic } M_2P_2O_7$$

Table 3.50: Starting phase change temperatures for the single phase germanium-titanium phosphates synthesised by the '*GeP method*'.

Product	T1	T2	T3	T4
$Ti_{0.9}Ge_{0.1}(HPO_4)_2.H_2O$ (GeP method)	125	225	500	700
$Ti_{0.8}Ge_{0.2}(HPO_4)_2.H_2O$ (GeP method)	125	275	400	700
$Ti_{0.2}Ge_{0.8}(HPO_4)_2.H_2O$ (GeP method)	160	350	500	800
$Ti_{0.1}Ge_{0.9}(HPO_4)_2.H_2O$ (GeP method)	130	350	500	750

Table 3.51: Comparison of the % weight loss from TGA.

Product	% Weight loss from dehydration		% Weight loss from condensation	
	Theoretical	TGA	Theoretical	TGA
$Ti_{0.9}Ge_{0.1}(HPO_4)_2.H_2O$ (GeP method)	6.9	14.0	7.4	7.8
$Ti_{0.8}Ge_{0.2}(HPO_4)_2.H_2O$ (GeP method)	6.9	11.1	7.4	4.8
$Ti_{0.2}Ge_{0.8}(HPO_4)_2.H_2O$ (GeP method)	6.5	8.7	6.9	7.0
$Ti_{0.1}Ge_{0.9}(HPO_4)_2.H_2O$ (GeP method)	6.4	14.1	6.9	6.9

From the weight loss data provided in Table 3.51, it can be seen that the products undergo higher weight losses at low temperatures compared with the theoretical values. This is consistent with the products initially having more than one mole of water and could help to explain the differences observed between the thermal properties of these materials with those of the same nominal compositions synthesised through the '*TiP method*'. It is worth noting however, that the X-ray diffraction data and subsequent structural refinements showed no evidence of these products being gamma phosphates of the type $M(HPO_4)_2.2H_2O$, instead it appears that they are alpha phosphates containing slightly higher water contents than expected. Better agreement is seen between the theoretical and the observed weight losses for the second step. There is however one anomalous result for $Ti_{0.8}Ge_{0.2}(HPO_4)_2.H_2O$ which shows a mass loss of only 4.8 %, corresponding to only 0.65 moles of water rather than 1 as expected. The reasons for this can be explained by examination of the VT XRD patterns given in Figure 3.61. Peaks corresponding to the crystalline cubic pyrophosphate are observed from 175 °C in addition to the other expected phases. The low stability of this product results in the condensation of some of the phosphate groups at similar temperatures to the dehydration of the crystalline water. The same low temperature pyrophosphate formation is observed for the other titanium-rich

phosphate $Ti_{0.9}Ge_{0.1}(HPO_4)_2.H_2O$ synthesised by this method. Owing to the low crystallinity of the high temperature germanium phases it remains unclear if this also occurs in the germanium-rich phosphates. These results indicate that more stable germanium-titanium phosphates are obtained from the '*TiP method*'.

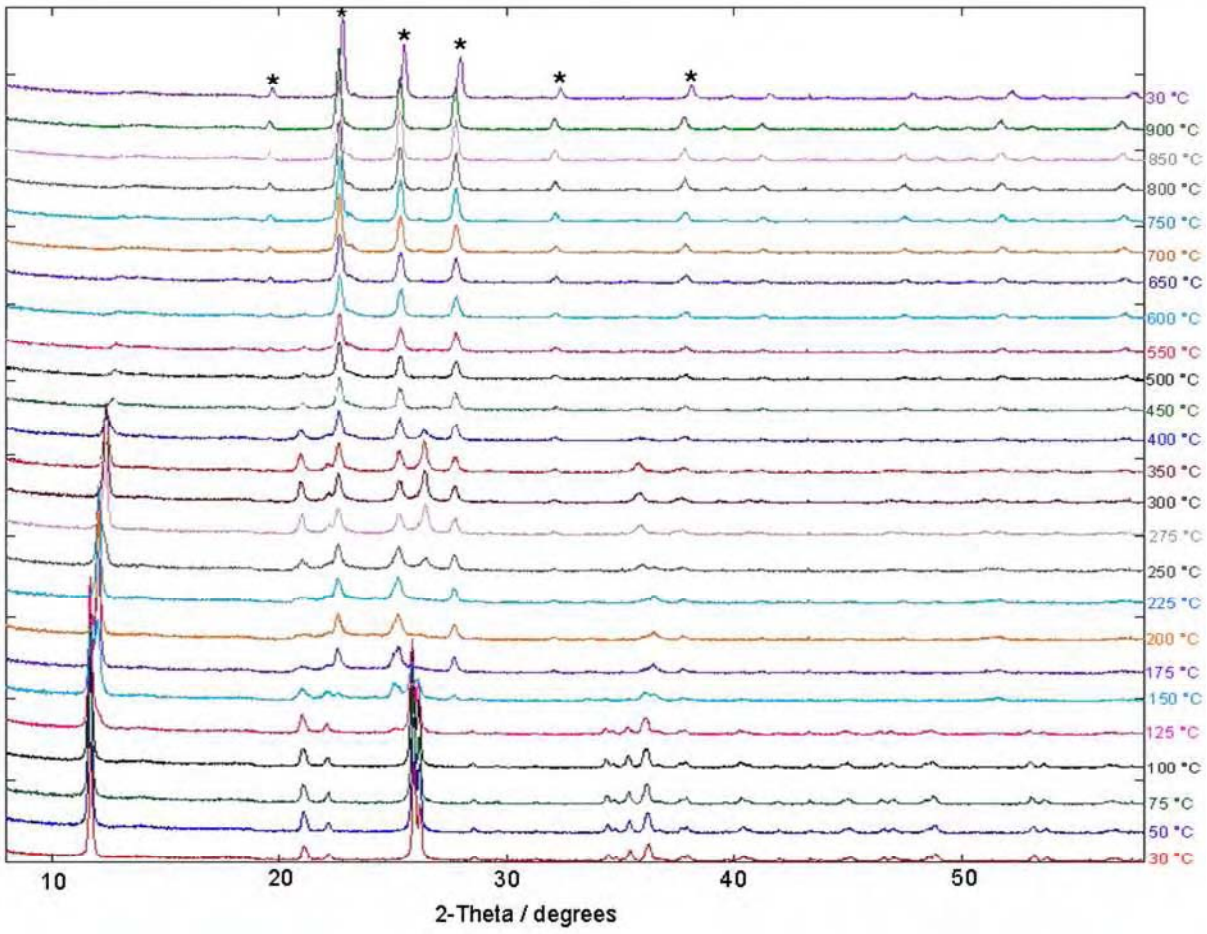

Figure 3.61: Variable temperature XRD patterns of $Ti_{0.8}Ge_{0.2}(HPO_4)_2.H_2O$. The asterisks correspond to peaks characteristic of cubic pyrophosphates.

3.3 Mixed Ge/Zr Phosphates

3.3.1 Introduction

A study into mixed germanium-zirconium phosphates was undertaken by Galli *et al.*[32] in the mid 1980s. The phosphates were prepared by refluxing stoichiometric amounts of germanium and zirconium chloride in phosphoric acid. X-ray diffraction showed the products obtained to be poorly crystalline but isostructural to the end members with interlayer distances intermediate between 7.56 Å (for α-ZrP) and 7.75 Å (for α-GeP). It should be noted that the XRD patterns were not published and so cannot be analysed further. Thermal analysis was used to distinguish between the mono- and bi-phasic nature of the systems. They concluded that solid solutions of up to 20% germanium within the α-ZrP matrix was possible but that systems with greater than 35% germanium were two phase.

In this work attempts were made at the synthesis of a series of mixed germanium-zirconium phosphates of composition $Ge_xZr_{1-x}(HPO_4)_2.H_2O$ where x = 0 - 1 using the method outlined by Losilla *et al.*[30] (the *GeP method* in the previous section). This method was shown to have more success in forming the mixed germanium titanium phosphates and so it was of interest to see if this method could also be used in the synthesis of this system.

3.3.2 Results and Discussion

3.3.2.1 Characterisation

Characterisation of the germanium-zirconium products by XRF (Table 3.52) and XRD (Figure 3.62) showed the majority of the products were two-phase materials, mainly consisting of a pure end member and a low doped phosphate. Details of the Rietveld refinements of these two phase products are shown in Table 3.53.

Table 3.52: Chemical compositions of the mixed germanium-zirconium phosphates as determined by XRF.

Nominal Formula	Observed Mass %Ge (relative)	Observed Mass %Zr (relative)	Measured Formula
$Ge_{0.9}Zr_{0.1}(HPO_4)_2.H_2O$	22.0	1.5	$Ge_{0.95}Zr_{0.05}(HPO_4)_2.H_2O$
$Ge_{0.8}Zr_{0.2}(HPO_4)_2.H_2O$	20.5	5.6	$Ge_{0.82}Zr_{0.18}(HPO_4)_2.H_2O$
$Ge_{0.7}Zr_{0.3}(HPO_4)_2.H_2O$	16.3	10.5	$Ge_{0.66}Zr_{0.34}(HPO_4)_2.H_2O$
$Ge_{0.6}Zr_{0.4}(HPO_4)_2.H_2O$	14.2	12.9	$Ge_{0.58}Zr_{0.42}(HPO_4)_2.H_2O$
$Ge_{0.5}Zr_{0.5}(HPO_4)_2.H_2O$	19.0	12.7	$Ge_{0.65}Zr_{0.35}(HPO_4)_2.H_2O$
$Ge_{0.4}Zr_{0.6}(HPO_4)_2.H_2O$	11.4	25.8	$Ge_{0.36}Zr_{0.64}(HPO_4)_2.H_2O$
$Ge_{0.3}Zr_{0.7}(HPO_4)_2.H_2O$	10.0	28.5	$Ge_{0.31}Zr_{0.69}(HPO_4)_2.H_2O$
$Ge_{0.2}Zr_{0.8}(HPO_4)_2.H_2O$	0.0	66.0	$Zr(HPO_4)_2.H_2O$
$Ge_{0.1}Zr_{0.9}(HPO_4)_2.H_2O$	0.0	64.5	$Zr(HPO_4)_2.H_2O$

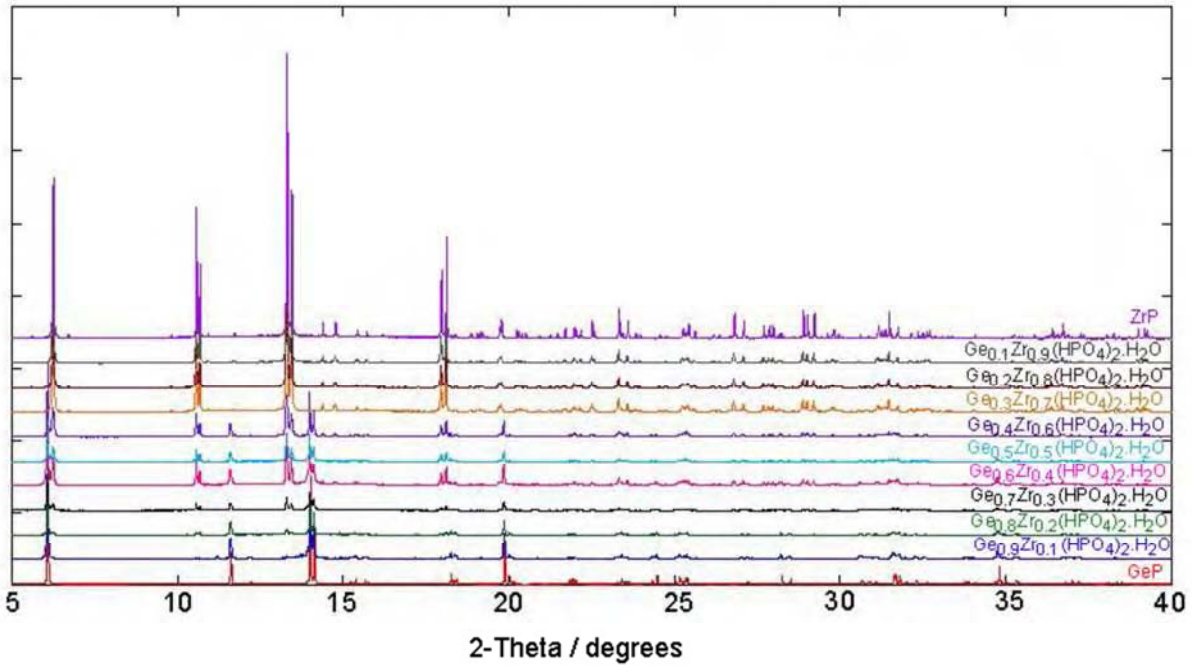

Figure 3.62: Overlaid synchrotron XRD patterns of the mixed germanium-zirconium phosphates.

Table 3.53: Structural parameters for the two phase products from the Rietveld refinements

	$Ge_{0.8}Zr_{0.2}(HPO_4)_2.H_2O$		$Ge_{0.7}Zr_{0.3}(HPO_4)_2.H_2O$		$Ge_{0.6}Zr_{0.4}(HPO_4)_2.H_2O$		$Ge_{0.5}Zr_{0.5}(HPO_4)_2.H_2O$		$Ge_{0.4}Zr_{0.6}(HPO_4)_2.H_2O$	
	Phase 1	Phase 2	Phase 1	Phase 2	Phase 1	Phase 2	Phase 1	Phase 2	Phase 1	Phase 2
Space group	$P2_1/c$	$P2_1/c$	$P2_1/c$	$P2_1/c$	$P2_1/c$	$P2_1/c$	$P2_1/c$	$P2_1/c$	$P2_1/c$	$P2_1/c$
a/Å	8.2940(1)	9.0627(6)	8.2961(3)	9.0616(2)	9.0596(8)	8.2962(2)	9.0593(1)	8.2965(1)	9.0604(8)	8.2961(8)
b /Å	4.7889(7)	5.2918(3)	4.7911(1)	5.2895(1)	5.2879(5)	4.7919(1)	5.2878(6)	4.7907(7)	5.2882(4)	4.7904(5)
c /Å	16.4181(3)	16.2747(14)	16.4383(7)	16.2584(7)	16.2537(2)	16.4503(6)	16.2530(3)	16.4262(4)	16.2508(2)	16.4188(2)
β/deg	108.9837(8)	111.413(5)	109.011(2)	111.391(2)	111.385(6)	108.987(2)	111.391(9)	108.991(1)	111.393(8)	108.989(7)
V/Å^3	616.64(2)	726.63(9)	617.74(4)	725.60(4)	725.04(1)	618.40(3)	724.94(2)	617.34(2)	724.98(1)	617.04(1)
<M-O> / Å	1.89	2.11	1.87	2.20	2.05	1.88	2.05	1.87	2.06	1.86
Zr Frac.	0.10	1	0.10	0.92	0.30	0	0.04	0	0.25	0
Ge Frac.	0.90	0	0.90	0.08	0.70	1	0.96	1	0.75	1
Weight frac.	83%	17%	67%	33%	44%	56%	53%	47%	63%	37%

From the XRD patterns in Figure 3.62, it can be seen that the products with up to 30% germanium (nominally $Ge_{0.1}Zr_{0.9}(HPO_4)_2.H_2O$, $Ge_{0.2}Zr_{0.8}(HPO_4)_2.H_2O$, and $Ge_{0.3}Zr_{0.7}(HPO_4)_2.H_2O$) gave patterns similar to α-ZrP and vice versa for the 90% germanium product ($Ge_{0.9}Zr_{0.1}(HPO_4)_2.H_2O$) and α-GeP. The same trend is mirrored in the PDF patterns shown in Figure 3.63, where no graduation of metal-metal distance is observed.

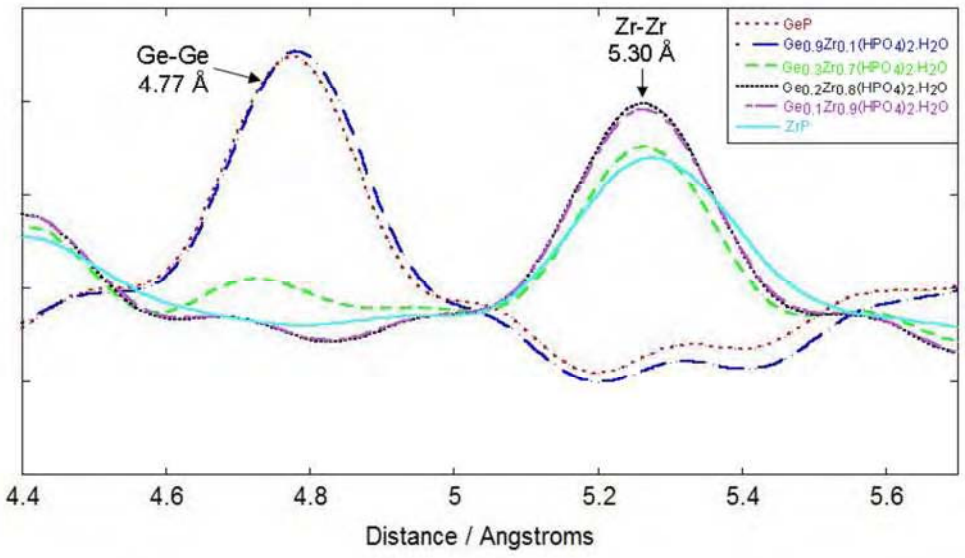

Figure 3.63: Overlaid PDF patterns of selected germanium-zirconium phosphates in the metal-metal peak region.

The bulk elemental compositions of these products as determined by XRF were given in Table 3.52. The two most zirconium rich products, $Ge_{0.1}Zr_{0.9}(HPO_4)_2.H_2O$ and $Ge_{0.2}Zr_{0.8}(HPO_4)_2.H_2O$ were shown to contain no germanium and consequently were refined as pure α-ZrP. For the $Ge_{0.3}Zr_{0.7}(HPO_4)_2.H_2O$ and $Ge_{0.9}Zr_{0.1}(HPO_4)_2.H_2O$ products the Ge/Zr ratios determined from the XRF studies were very close to those expected. Single phase Rietveld refinements were performed on these products and the fits, including selected refinement parameters, are shown in Figures 3.64 and 3.65. The R_{wp} value for the $Ge_{0.9}Zr_{0.1}(HPO_4)_2.H_2O$ product was very high and close visual inspection of the plot, as shown in the insert in Figure 3.65 highlighted the presence of multiple phases. Some of the low intensity peaks could be attributed to the presence of α-ZrP but the additional peaks (marked with asterisks) are as yet unidentified. Whilst the peaks appear mid way between the (112) and (20-4) reflections for $Ge_{0.9}Zr_{0.1}(HPO_4)_2.H_2O$ and α-ZrP it seems unlikely that they were due to a heavily substituted phase as no other evidence of such phases could be found in any of the other products. The addition of α-ZrP as a second phase in the

refinement caused significant divergence of the calculations. Even with fixing the second phase the refinement was unstable. The data was not of a high enough quality to allow for a three phase refinement, especially considering the similarity of the unit cells of the phases and therefore extreme overlap of many peaks.

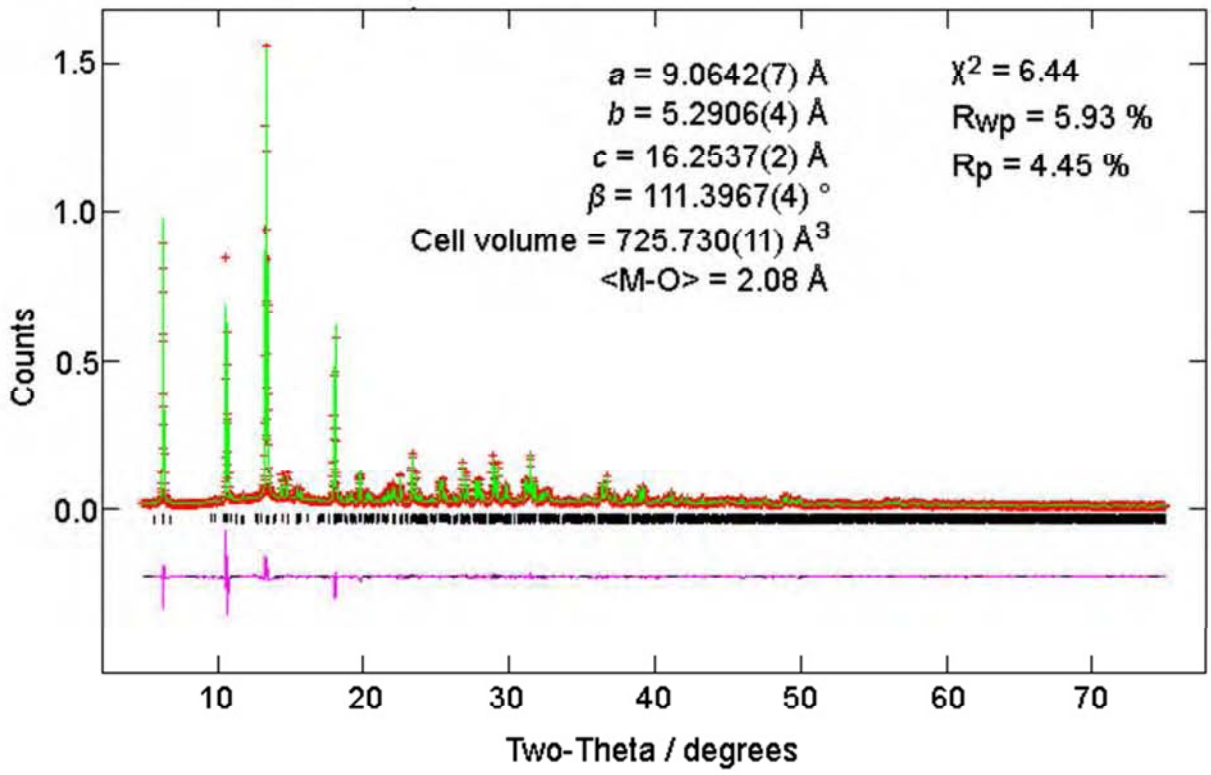

Figure 3.64: Final observed (red crosses), calculated (green line) and difference (bottom) X-ray diffraction profile with reflection positions noted as vertical tick marks for α- $Ge_{0.3}Zr_{0.7}(HPO_4)_2.H_2O$.

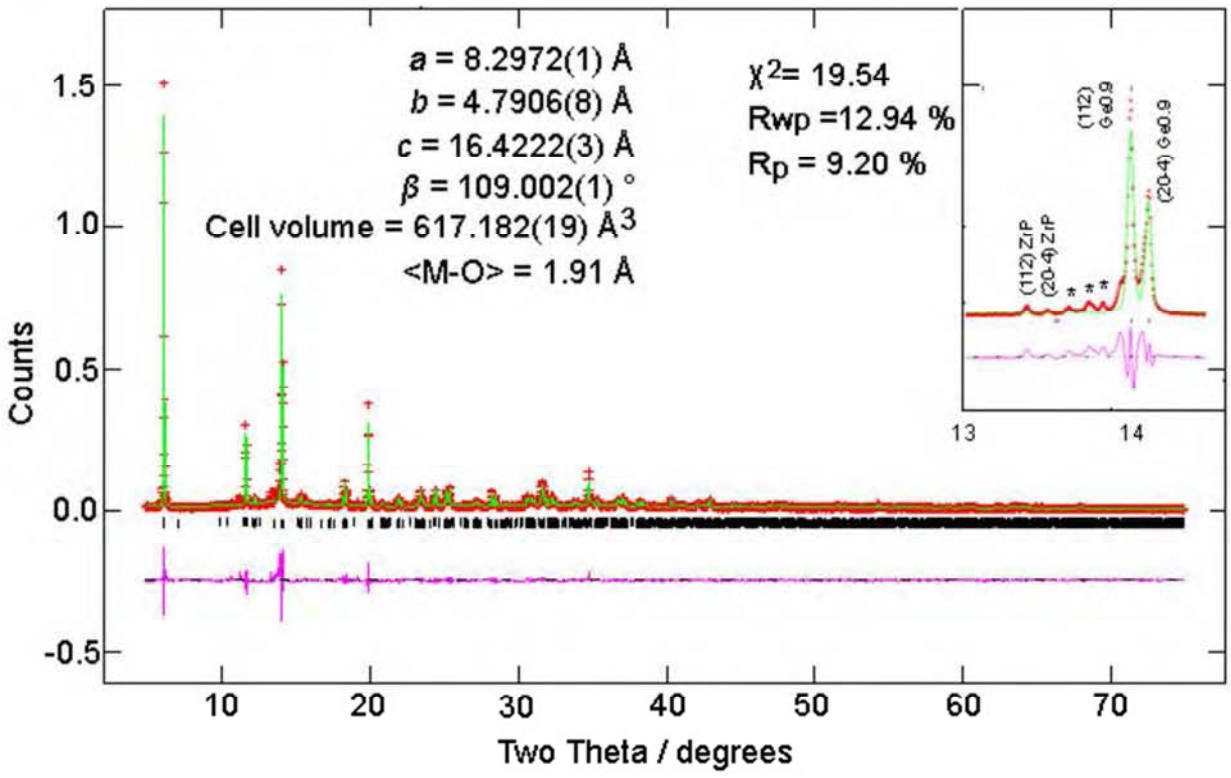

Figure 3.65: Final observed (red crosses), calculated (green line) and difference (bottom) X-ray diffraction profile with reflection positions noted as vertical tick marks for α- $Ge_{0.9}Zr_{0.1}(HPO_4)_2.H_2O$. An enlargement of part of the plot is shown in the insert; the peaks marked with an asterisk belong to the unknown phase.

3.3.2.2 Synthetic Success

Only 30% doping of germanium within α-ZrP was found to give a single phase product in this work. Although this is higher than the 20% doping reported by Galli *et al.*[32] the 20 and 10 % germanium products did not form and only α-ZrP could be recovered. The reasons for this are not yet fully understood but the experiments could be repeated to establish the reproducibility of these results. To ascertain if this was as a result of the synthetic method, $Ge_{0.2}Zr_{0.8}(HPO_4)_2.H_2O$ was synthesised by the same method used to make α-ZrP[1]. The XRD pattern obtained (Figure 3.66) in conjunction with the XRF results found the product to be α-ZrP.

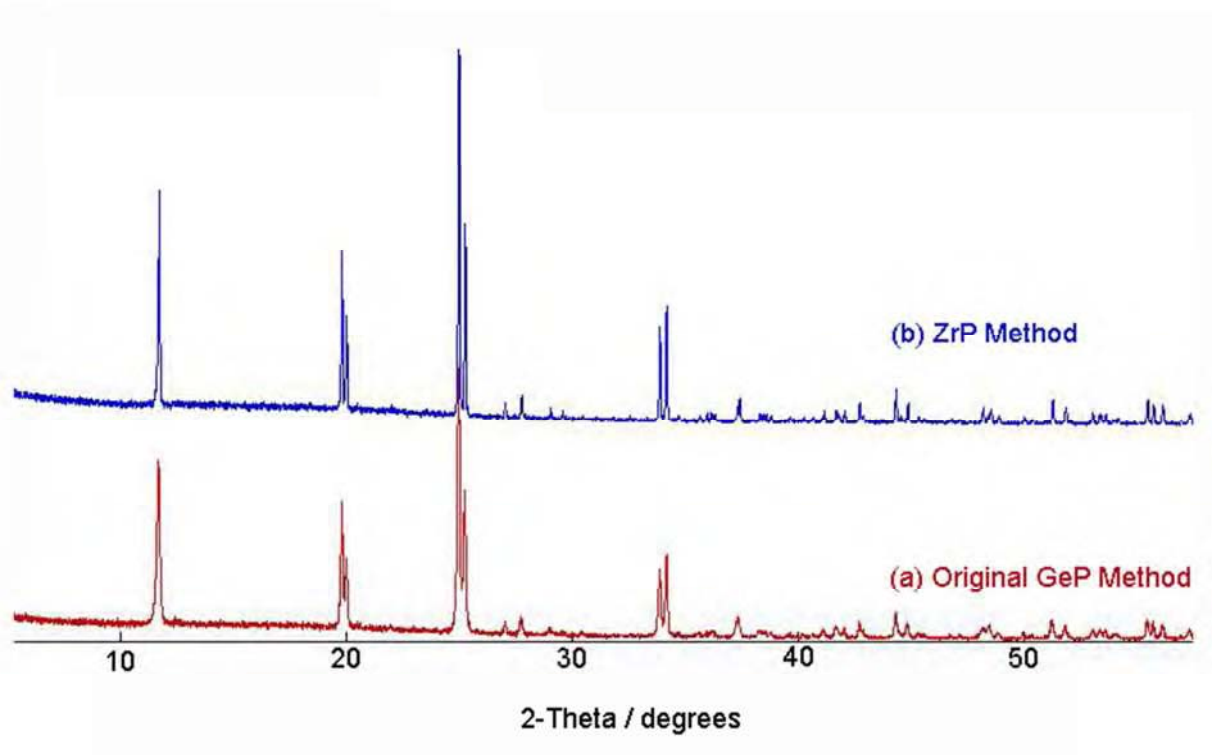

Figure 3.66: Comparison of the XRD patterns of $Ge_{0.2}Zr_{0.8}(HPO_4)_2.H_2O$ synthesised by (a) the original method (b) the α-ZrP method[33]

Adaptations of the synthetic method used by Galli *et al.*[32] could be investigated as future work for the synthesis of this system. However as stated previously the layers within α-GeP are highly corrugated. In contrast to this the layers within α-ZrP are the least corrugated of any of the known alpha-metal phosphates[34]. As a result of this it is unlikely that the full solid solution of this system can be synthesised, especially given that those within the Zr-Ti and Ti-Ge systems could not be, even though there was more similarity in the structure type.

3.4 Mixed Tin Systems

3.4.1 Introduction

Tin phosphate, α-SnP, is an ion exchange material with a wide range of useful separation applications notably in the processing of radioactive effluents and in water purification[35]. In general there are two possible methods for the synthesis of α-SnP; a reflux method described by Costantino and Gasperoni[36] or by hydrothermal treatment.

Costantino and Gasperoni[36] synthesised crystalline α-SnP by refluxing anhydrous tin chloride in a solution of phosphoric and nitric acid (with a P:Sn ratio of 30) for 100 hours. Previous attempts at refluxing amorphous stannic phosphate for 200 hours were found to be unsuccessful[36]. A similar method but with longer refluxing time was employed by Bihari Sadu *et al.*[37] for the formation of α-SnP as part of their investigation into its cation exchange and sorption properties. The products obtained from these conventional refluxing methods were shown to have low crystallinity. In attempts to combat this and to reduce the preparation time, Patrono *et al.*[19] investigated the use of hydrothermal treatment. They reported that the use of higher temperatures lead to highly crystalline but less hydrated phases even though the alpha structure type was preserved. Hydrothermal treatments were also used by Bruque *et al.* [34] whereby tin chloride in phosphoric acid was heated to 150 °C in an autoclave for 7 days. The crystalline structure of the product was refined in the *C*2/*c* space group which is the isomorphic *C*-centred supergroup of $P2_1/n$ more commonly used in alpha phosphates. Anistropic lorentzian peak broadening was found in the refinements originating from small particles with anisotropic shape. These microparticles were shown to be much longer in the *ab* plane than along the *c* axis with rough dimensions of 700 Å x 100 Å.

In addition to these, alternative methods for the synthesis of α-SnP have also been reported by Thind and Ganghi[38] and by Varshney *et al.*[39]. In the former, α-SnP was prepared by mixing tin tetrachloride with ammonium dihydrogen phosphate and using either hydrochloric acid or an alkali to adjust the pH to 1. The crude gel was treated with nitric acid and dried to afford the final product. In the latter, α-SnP was prepared by the dropwise addition of tin chloride to phosphoric acid to give a slurry that was left to stand overnight, filtered and washed until pH 4.

In an investigation into mixed titanium-tin systems carried out by Trobajo *et al.*[40], the phosphates were synthesised from chloride precursors using similar conditions used to form γ-TiP. From the XRD and differential scanning calorimetry analysis of the products they reported that 75% isomorphic substitution of tin by titanium in α-SnP was possible. Higher substitution resulted in a mixture of products containing the alpha, gamma and beta forms. The same method was used in the formation of tin-titanium phosphates that were loaded with vanadium oxide for the use in the oxidative dehydrogenation of ethane[41].

Mixed zirconium-tin[42] phosphates with compositions of $Zr_{0.79}Sn_{0.21}(HPO_4)_2.H_2O$, $Zr_{0.54}Sn_{0.46}(HPO_4)_2.H_2O$ and $Zr_{0.31}Sn_{0.69}(HPO_4)_2.H_2O$ were synthesised by an adapted version of the Costantino and Gasperoni method[36] which involved the coprecipitation of the tin and zirconium chlorides in phosphoric and nitric acid to afford the crude products that were later refluxed. It was believed that all three products were recovered as solid solutions.[42]

3.4.2 Synthesis and Optimisation of Tin Phosphate (α-SnP)

In this report α-SnP was first synthesised according to the method outlined by Bruque *et al.*[34]. $SnCl_4.5H_2O$ in 12 M phosphoric acid was heated for 7 days at 150 °C. Following these procedures, crystalline α-SnP was synthesised, however only a 6% yield was obtained. Investigations into the effect of temperature on the yield offered no improvements. The results of this study are summarised in Table 3.54 and in Figure 3.67.

Table 3.54: Summary of the results obtained by following Bruque's[34] synthesis with variation in reaction temperature.

Sample ID	Temperature / °C	Product Yield	XRD result
ZS6	100	0 %	No product obtained.
ZS18	140	54.6 %*	Poorly crystalline α-SnP
ZS2	150	6.37 %	α-SnP
ZS4	200	6.88 %	α-SnP

* Only a 'wet' waxy product could be isolated.

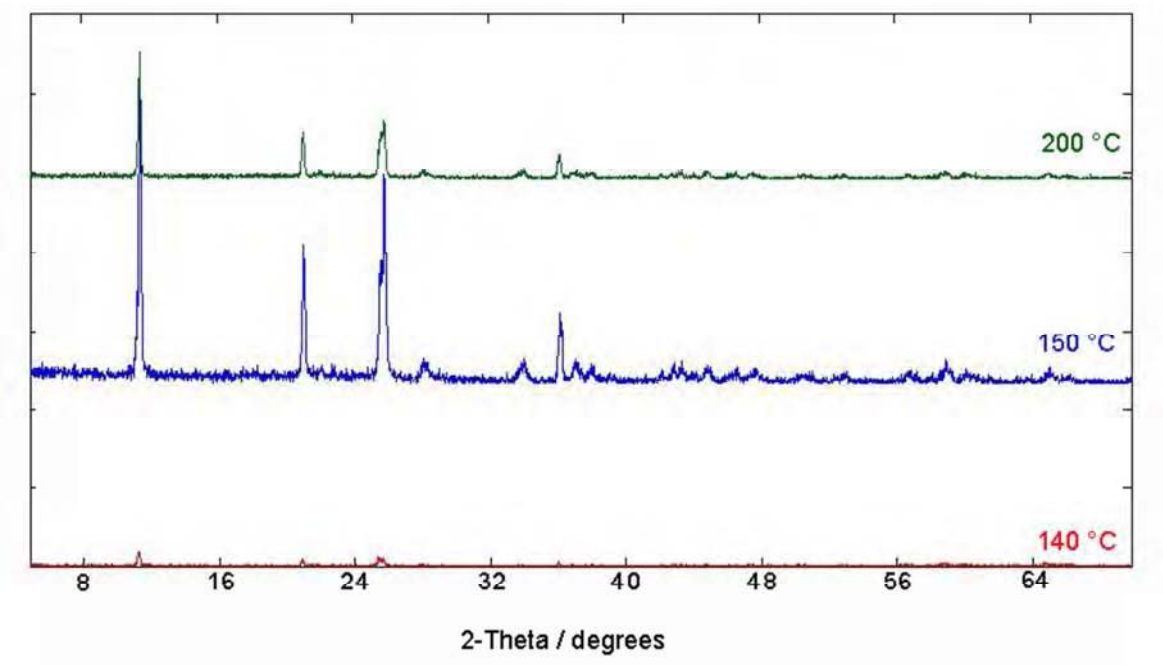

Figure 3.67: PXRD patterns for hydrothermally synthesised α-SnP. Reaction temperature is varied from 140-200 °C, inclusive.

Attempts were also made to synthesise α-SnP by Varshney's method[39] but this led to amorphous products.

3.4.3 Rietveld Refinement of Tin Phosphate (α-SnP)

A Rietveld refinement was carried out from an overnight laboratory XRD scan of the α-SnP product synthesised at 150 °C as this was the most crystalline. The calculated pattern was based on that reported by Bruque *et al.*[34]. A summary of the refined parameters compared to those in the literature are displayed in Table 3.55. The refinement fit and crystallographic details are shown in Figure 3.68 and Table 3.56. There are some discrepancies in the fit due to the poor quality of the data and the poor peak resolution. The refinement is also hindered by the heavy tin which limits the precision in the atomic parameters for the lighter atoms such as oxygen. The key point from the refinement is that no additional crystalline phases are shown to be present. The formation and presence of other tin phases such as tin oxide could have been a factor in the low yields of α-SnP obtained. The powder XRD pattern does display a high background which may infer the presence of amorphous products instead.

Table 3.55: Comparison of refined crystal parameters of α-SnP to those in the Literature.

	a / Å	*b* / Å	*c* / Å	*β* /°	*V* /Å^3	<M-O> /Å
α-SnP	8.6107(6)	4.9672(3)	15.8895(12)	99.725(4)	669.84(8)	2.04
Literature[34]	8.6115(3)	4.9643(5)	15.8605(16)	100.03(1)	667.6(1)	2.03

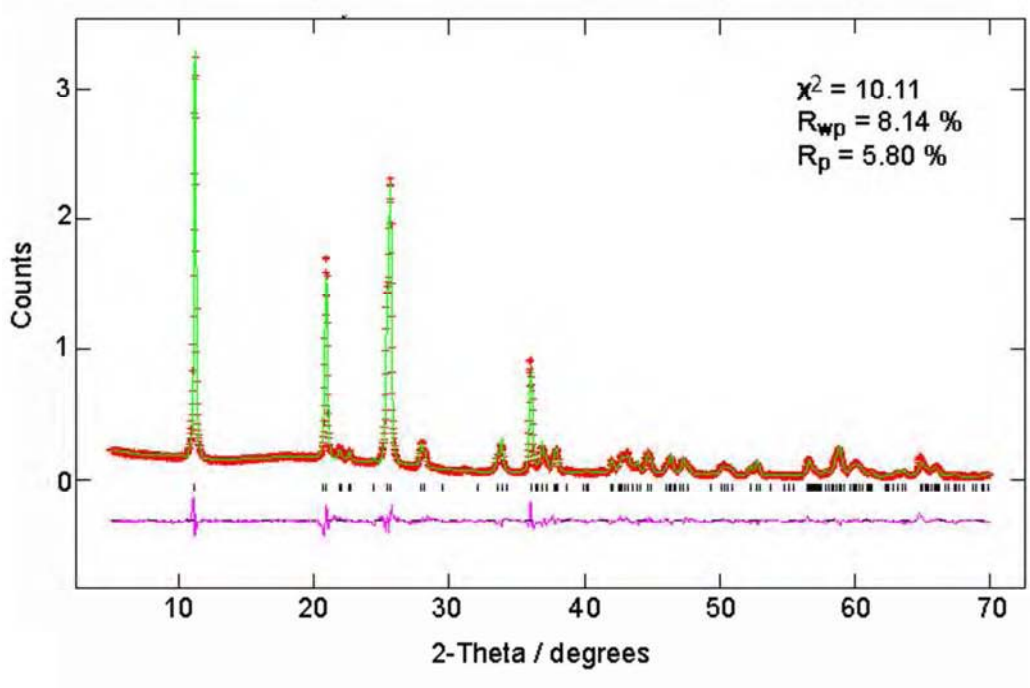

Figure 3.68: Final observed (red crosses), calculated (green line) and difference (bottom) X-ray diffraction profile with reflection positions noted as vertical tick marks for α-$Sn(HPO_4)_2.H_2O$.

Table 3.56: Refined fractional atomic coordinates and isotropic thermal displacement parameters with estimated standard deviations for α-$Sn(HPO_4)_2.H_2O$.

atom	*x*	*y*	*z*	U_{iso} (x10^2) Å^2
Sn	0.2500	0.2500	0.5000	3.68(14)
P	0.3859(11)	0.762(6)	0.3963(4)	4.99(28)
O(1)	0.5535(24)	0.720(5)	0.4219(10)	7.08(33)
O(2)	0.3794(29)	0.462(5)	0.4225(13)	7.08(33)
O(3)	0.2792(30)	0.909(5)	0.4254(13)	7.08(33)
O(4)	0.3666(21)	0.778(7)	0.3031(10)	7.08(33)
O(5)	0.0000	0.744(14)	0.25000	7.08(33)

3.4.4 Mixed Tin-Titanium Phosphates

A series of mixed tin-titanium phosphates of composition $Sn_xTi_{1-x}(HPO_4)_2.H_2O$ where *x* = 0-1 were prepared using a hydrothermal version of the method reported by Trobajo *et al.*[40]. Figure 3.69 shows the laboratory XRD patterns of the products obtained. The products with up to 30% tin display XRD patterns similar to that for α-TiP whilst those of the remaining

products are more closely matched to that of α-SnP. Peak graduation can be seen throughout the series, especially in the first peak (002) but peak broadening is also observed for the products in the middle of the compositional range. The XRD analysis shows no signs of any additional beta or gamma phases present as seen in previous literature studies of tin-titanium phosphates[40].

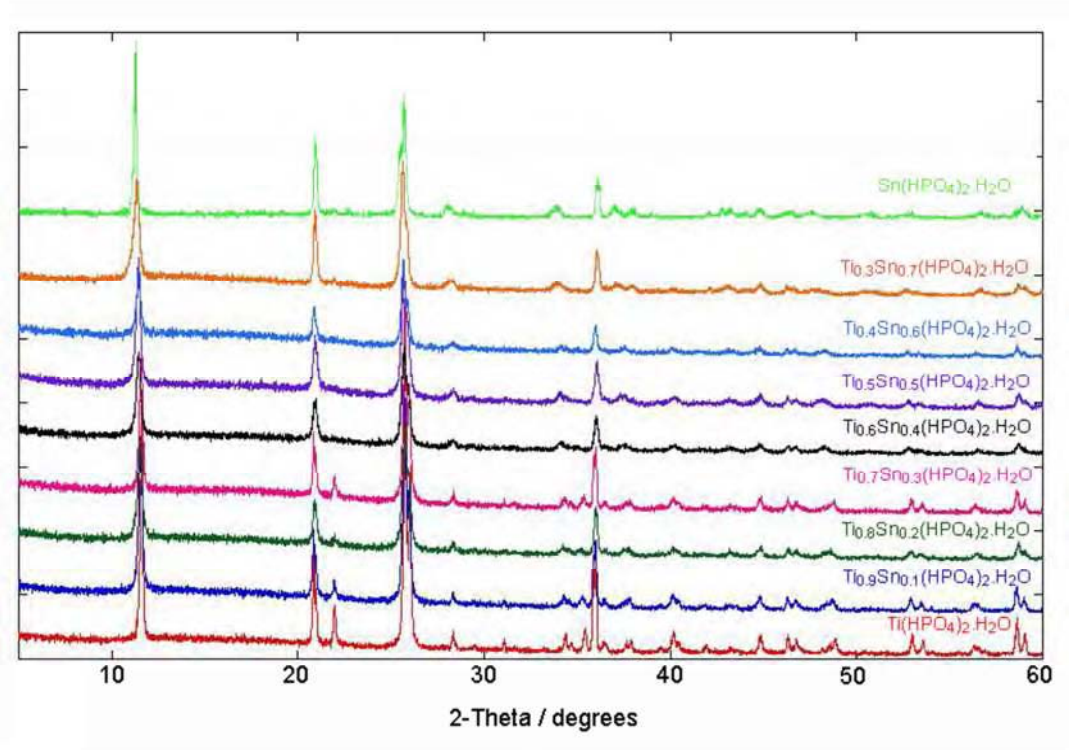

Figure 3.69: Overlaid laboratory XRD scans of the Sn/Ti phosphates.

The Sn / Ti ratios were investigated by XRF. The samples were run as pressed pellets as tin compounds are incompatible with the platinum crucible used for fusing. A summary of the compositional results are displayed in Table 3.57. In general these results show excellent agreement with the nominal compositions and confirm the products to be mixed metal species. Exceptions are noted for the $Sn_{0.3}Ti_{0.7}(HPO_4)_2.H_2O$ and $Sn_{0.6}Ti_{0.4}(HPO_4)_2.H_2O$ products

which have less tin than expected. This is not surprising given the synthetic difficulties with this system. In order to ascertain the true nature of the products, structural refinements need to be carried out and for this higher quality XRD data is required.

Table 3.57: Compositions of the Sn/Ti products as determined from XRF.

Nominal		Measured	
Composition	Sn/Ti molar ratio	Sn/Ti molar ratio	Composition
$Sn_{0.1}Ti_{0.9}(HPO_4)_2.H_2O$	0.11	0.12	$Sn_{0.11}Ti_{0.89}(HPO_4)_2.H_2O$
$Sn_{0.2}Ti_{0.8}(HPO_4)_2.H_2O$	0.25	0.28	$Sn_{0.22}Ti_{0.78}(HPO_4)_2.H_2O$
$Sn_{0.3}Ti_{0.7}(HPO_4)_2.H_2O$	0.43	008	$Sn_{0.07}Ti_{0.93}(HPO_4)_2.H_2O$
$Sn_{0.4}Ti_{0.6}(HPO_4)_2.H_2O$	0.67	0.69	$Sn_{0.41}Ti_{0.59}(HPO_4)_2.H_2O$
$Sn_{0.5}Ti_{0.5}(HPO_4)_2.H_2O$	1.00	0.89	$Sn_{0.47}Ti_{0.53}(HPO_4)_2.H_2O$
$Sn_{0.6}Ti_{0.4}(HPO_4)_2.H_2O$	1.50	0.45	$Sn_{0.31}Ti_{0.69}(HPO_4)_2.H_2O$
$Sn_{0.7}Ti_{0.3}(HPO_4)_2.H_2O$	2.33	2.70	$Sn_{0.73}Ti_{0.27}(HPO_4)_2.H_2O$

The preparations were not easily reproducible and often two or three attempts were required to obtain a product. $Sn_{0.8}Ti_{0.2}(HPO_4)_2.H_2O$ and $Sn_{0.9}Ti_{0.1}(HPO_4)_2.H_2O$ could not be synthesised at all. For the other products only small yields were obtained. From the erosion of foil and metal spatulas used it was thought that HCl gas was evolved during synthesis. In an effort to explore whether adjusting the pH of the synthesis solution either by replacing the lost HCl or by the addition of alkali, as previously reported necessary in the synthesis of α-SnP[38], could lead to the formation of a product, the pH of the solutions were monitored. For the preparations that resulted in products, the pH of the synthesis solution remained at 2 throughout whilst those that did not fell to 0. This is something that could be further investigated. However owing to the difficulties in forming several of the products within this

series as well the pure tin end member, no further characterisation nor ion exchange was carried out. With the small quantities obtained and the lack of reproducibility, this series was deemed to be a non-viable option for industrial application.

3.4.5 Mixed Tin-Zirconium Phosphates

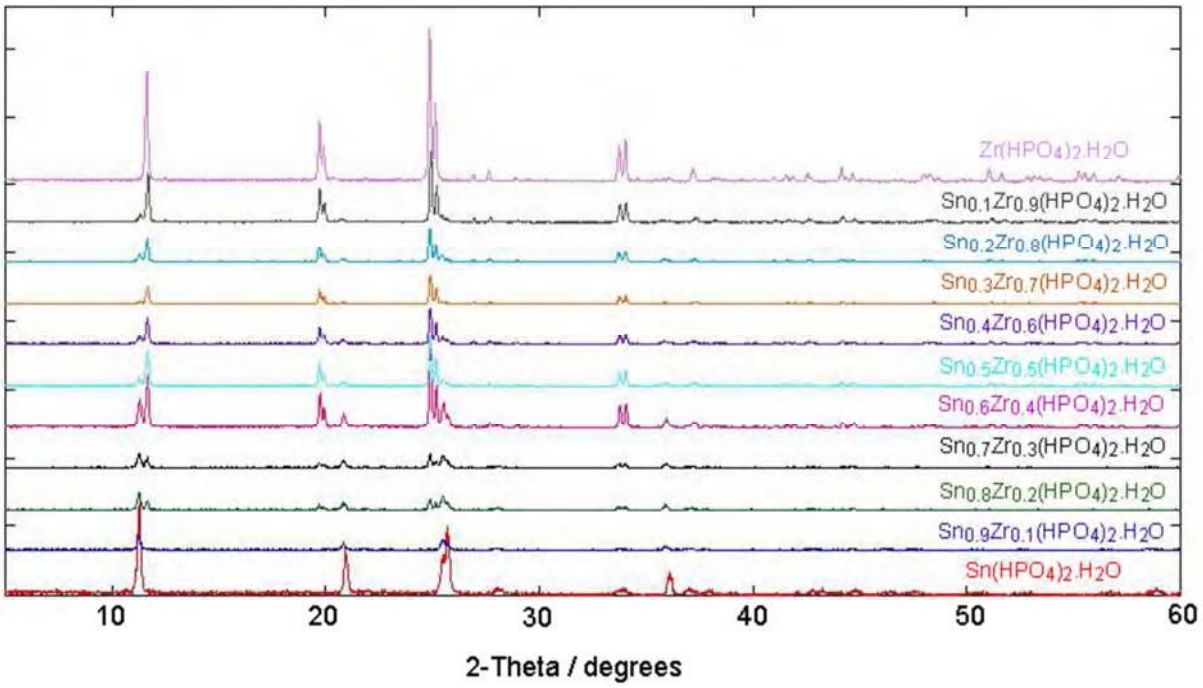

Figure 3.70: Overlaid XRD patterns of the mixed tin-zirconium phosphates

Previous work in the Hriljac group[43] found that mixed tin-zirconium phosphates could be synthesised if tin and zirconium chloride were ground together in a pestle and mortar before any hydrothermal treatment takes place. This same procedure was used in this work to synthesise a range of mixed tin-zirconium phosphates of composition $Sn_xZr_{1-x}(HPO_4)_2.H_2O$ where x = 0 - 1. Initial characterisation of the products was undertaken by XRD and the resultant patterns can be seen in Figure 3.70. There was no evidence of any solid solutions within the series as the presence of two phases was observed in all of the co precipitate

patterns excluding that of $Sn_{0.9}Zr_{0.1}(HPO_4)_2.H_2O$ which resembles less crystalline α-SnP. Following this attempts were made to limit the exposure time of the tin precursor to the atmosphere during the grinding stage. It was hypothesised that this exposure could lead to the formation of tin oxides and hydroxides thereby lowering the amount of tin available for phosphate formation. No difference in the XRD patterns for the new products were seen and so work on this system was discontinued.

3.5 Corrugation of the Layers

Corrugation of the layers in the alpha structure occurs when the metal atoms within the layers approach each other due to coupled polyhedral rotations, thus pushing the phosphate groups into the interlayer space (Figure 3.71). In essence the P-OH bonds (those involving O8 in Figure 3.71) become increasingly perpendicular to the *ab*-plane of the layers as the corrugation increases.

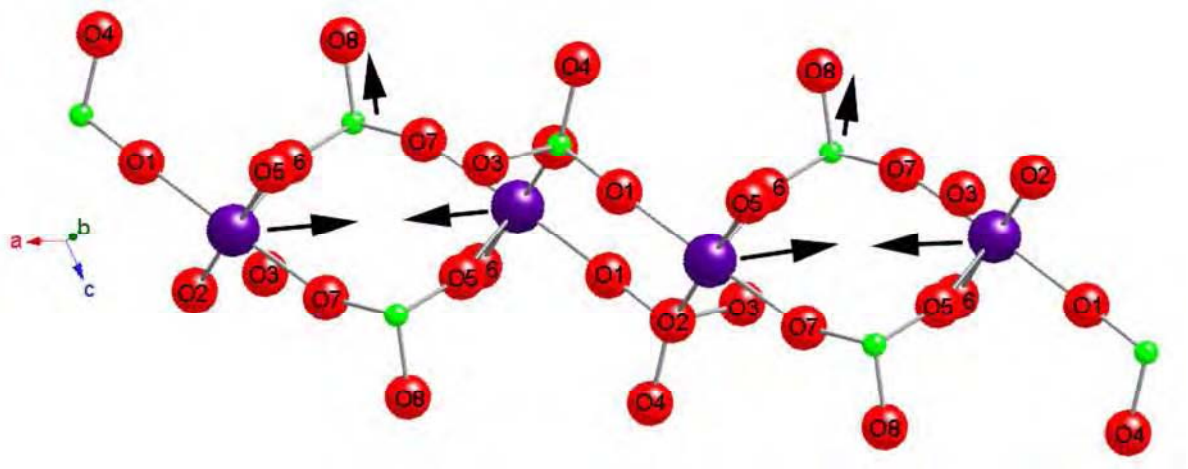

Figure 3.71: Structural representation of the corrugation of the layers. Metal atoms (purple), phosphorus atoms (green) and oxygen atoms (red). The black arrows denote the direction of movement of the atoms upon corrugation.

Bruque *et al.*[34] found a correlation between the displacement of the metal atoms from the plane to the average M-O-P angle which can be used to quantify this corrugation: the smaller the M-O-P angle, the greater the corrugation. Figure 3.72 shows the average M-O-P angle of the end member phosphates synthesised in this work.

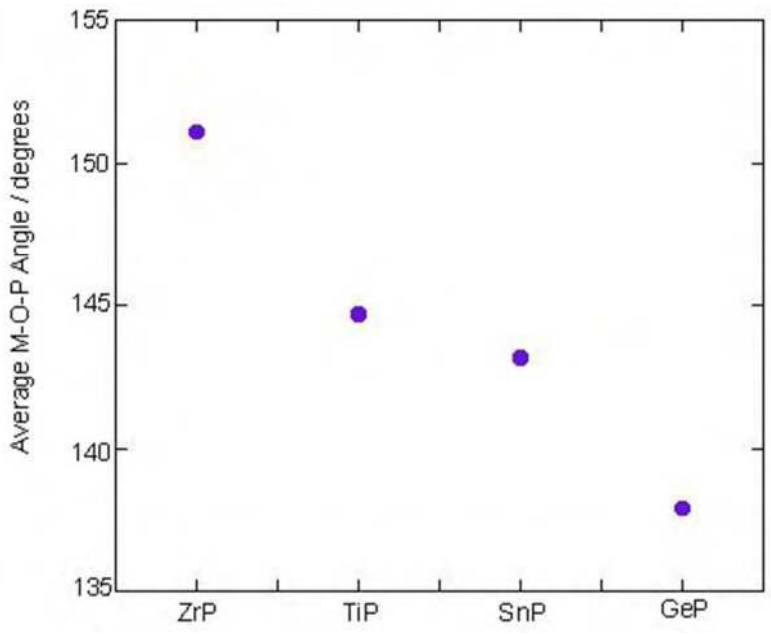

Figure 3.72: The trend in the average M-O-P angle of the metal phosphates.

The trend in the corrugation of the layers is shown to be in the order of α-ZrP << α-TiP < α-SnP << α-GeP which is in agreement with previous findings[31,34]. It has been speculated that the driving force for this corrugation is to enhance the fit of the interlayer water through cooperative rotations that optimise the hydrogen bonding interactions[31]. A correlation between the degree of corrugation and the electronegativity of the metal species present has been postulated[31]. The group 14 metals Ge, Sn and Pb with Pauling electronegatives of 2.01, 1.96 and 2.33, respectively, form polar covalent bonds to the oxygen atoms. Compared to the group 4 metals Ti, Hf and Zr (with Pauling electronegativities of 1.54, 1.30 and 1.33), which form more ionic bonds, the oxygen atoms in the group 14 metal phosphates carry a

lower real charge which allows the *ab*-plane to contract and simultaneously leads to greater corrugation of the layers.

These results help us to ascertain why solid solutions could not be formed in many of the mixed metal systems investigated. The difference in the degree of 'corrugation' of the end member structures is a significant factor in why solid solutions cannot form. When there is a large difference, as in the case of zirconium-germanium phosphates, the structures of the mixed metal species become increasingly strained as they try to accommodate the large differences and so solid solutions do not form. Based on the trend displayed in Figure 3.72 it would appear that mixed titanium-tin phosphates would be the most likely to form solid solutions. The work on titanium-tin phosphates in this thesis was halted due to the synthetic problems associated with tin phosphate. However further investigation into alternative synthetic procedures which overcome these issues may be beneficial.

3.6 Conclusions

In this chapter it has been demonstrated that zirconium and titanium phosphates form solid solutions with each other but, in keeping with previous reports, there is a miscibility gap. We have also shown the first evidence of mixed germanium-titanium phosphates. Again a miscibility gap is present in this series, but higher levels of substitution were possible. The reason for this is most likely due to the greater similarity in structure type and metal radii. The solid solutions from both series behave like the end member they are compositionally closest to. PDF analysis indicated there was no metal ordering within these compounds, which is in contrast to previous findings on the mixed zirconium-titanium phosphates.

The structures of the co-precipitates have been refined using both Rietveld and PDF methods. Given the complexity of the systems the refinements were generally successful and the results from both methods compared well. Rietveld refinements undertaken on the two-phase products determined the presence of two partially substituted phases. Reasonable fits were achieved in spite of the poor quality data obtained for some of the products.

Our work has also shed some light on the reasons for the miscibility gap seen in these mixed metal phosphates. Firstly the structures appear to lack the flexibility required to accommodate more of the second metal, particularly when there is a large difference in metal size and/or degree of corrugation in the layers. The effect of layer corrugation results in significant strains within the structures upon substitution. The GII's highlighted the points at which these strain became too much and the products could not form. In addition to this we believe that some aspects of solution chemistry also play a role in the lack of formation of the full solid solutions.

The formation of coprecipitates in the mixed zirconium-germanium and tin systems were unsuccessful. The synthetic problems associated with tin could not be improved through variation of the reaction temperature.

3.7 Further Work

Zirconium-titanium phosphates

- An expansion of the work using silicon to alter the size of the unit cell.

- Further structural analysis of the decomposition products of the single phase phosphates.

Titanium-germanium phosphates

- Further analysis of the decomposition products of the single phase phosphates. Notably further investigation into the additional partially dehydrated crystalline phase observed ~ 175 °C.

Zirconium – germanium phosphates

- Investigate the Galli[32] synthetic method and whether the reflux step can be replaced by hydrothermal treatment.
- Collect higher quality XRD data on the $Ge_{0.9}Zr_{0.1}(HPO_4)_2.H_2O$ product to allow for structural refinement and identify the third phase present.

Tin systems

- Investigate the method published by Bagnasco *et al.*[42] and whether the reflux step can be substituted for more hydrothermal methods.
- pH controlled synthesis of tin-titanium phosphates.
- Obtain higher quality XRD data of the tin-titanium phosphates to allow structural characterisation.

In addition to the above it would be interesting to see if tin-germanium solid solutions could be synthesised. The series was not studied in this work owing to the difficulties with synthesising α-SnP. However a previous literature report on this system by La Ginestra *et al.*[44] lead to the formation of solid solutions for all compositions studied. Their results

indicated that these phosphates could only be synthesised by reflux methods owing to the hydrolysability of germanium phosphate.

To extend the investigation we would also like to explore the feasibility of synthesising other mixed metal phosphates containing lead and hafnium. The structures of both lead phosphate (α-PbP) and hafnium phosphate (α-HfP) have been solved previously by Bruque *et al.*[34] and Nakai *et al.*[45]. Both were found to be isostructural to α-ZrP. α-PbP has been shown to be as 'corrugated 'as α-GeP, making mixed lead-germanium phosphates the most likely to form.

3.8 References

(1) Clearfield, A., Frianeza, T. N. *J. Inorg. Nucl. Chem.* **40**, 1925-1932 (1978).
(2) Farfan-Torres, E. M., Sham, E. L., Martinez-Lara, M., Jimenez-Lopez, A. *Mat. Res. Bull*, **27**, 1255-1262 (1992).
(3) Thakkar, R., Chudasama, U. *J. Sci. Ind. Res.* **68**, 312-318 (2009).
(4) Szirtes, L., Poko, Z., Shakshooki, S. K., Ahmed, M., Dehair, A., Benhamed, A. *J. Therm. Anal.*, **35**, 895-902 (1989).
(5) Salvado, M. A., Pertierra, P., Garcia-Granda, S., Garcia, J. R., Rodriguez, J., Fernandez-Diaz, M. T. *Acta. Cryst.* **B52**, 896-898 (1996).
(6) Albertsson, J., Oskarsson, A., Tellgren, R., Thomas, J. O. *J. Phys. Chem.* **81**, 1574-1578 (1977).
(7) Farrow, C. L., Juhas, P., Liu, J. W. *J. Phys.: Condense. Matter***. 19**, 1-7 (2007).
(8) Hammersley, A. P. *Syn. Rad. News*, **2**, 24 (1989).
(9) Capitani, D., Casciola, M., Donnadio, A., Vivani, R. *Inorg. Chem.* **49**, 9409-9415 (2010).
(10) Salinas-Sanhez, A., Garcia-Munoz, J. L., Rodrigues-Carvajal, J., Saez-Puche, R., Martinez, J. L. *J. Solid State Chem.*, **100**, 201-211 (1992).
(11) Brown, I. D., Altermatt, D *Acta. Cryst.* **B41**, 244-247 (1985).
(12) Brese, N. E., O'Keefe, M. *Acta. Cryst.* **B47**, 192-197 (1991).
(13) Trobajo, C., Khainakov, A., Espina, Aranzazu, Garcia, J. R. *Chem. Mater.* **12**, 1787-1790 (2000).
(14) Slade, R. C. T., Knowles, J. A., Jones, D. J., Roziere, J. *Solid State Ionics*, **96**, 9 - 19 (1997).
(15) Satya Kishore, M., Pralong, V., Caignaert, V., Varadaraju, U. V., Raveau, B. *J. Power Sources*, **169**, 355-360 (2007).
(16) La Ginestra, A., Patrono, P. *Mat. Chem. Phys.* **17**, 161-179 (1987).
(17) Thakkar, R., Chudasama, U. *J. Hazard. Mat.* **172**, 129-137 (2009).
(18) Burnell, V. A., Msci Thesis ' The synthesis and ion exchange of mixed Zr/Ti phosphates' University of Birmingham, (2007).

(19) Patrono, P., La Ginestra, A., Ferragina, C., Massucci, M. A., Frezza, A., Vecchio, S. *J. Therm. Anal.* **38**, 2603-2612 (1992).
(20) Costantino, U., La Ginestra, A. *Thermochim. Acta*, **58**, 179-189 (1982).
(21) La Ginestra, A., Ferragina, C., Massucci, M. A., Tomassini, N. *Thermal Analsis, Proc. IV ICTA*, Budapest, **1**, 631 (1973).
(22) Shannon, R. D., Prewitt, C. T. *Acta. Cryst.* **B25**, 925-946 (1969).
(23) Winkler, V. A., Thilo, E. *Z. anorg. allg. chem.* **364**, 92-112 (1966).
(24) Everest, D. A. *J. Chem. Soc.*, 4117 - 4120 (1953).
(25) Avduevskaya, K. A., Tananaev, I. V. *Russ. J. Inorg. Chem.* 527(1963).
(26) Avduevskaya, K. A., Tananaev, I. V. *Russ. J. Inorg. Chem.* (1965**)**.
(27) Lelong, B. *Ann. Chim.* **9** (1964).
(28) La Ginestra, A., Galli, P., Berardelli, M. L. *J. Chem. Soc. Dalton Trans.* 527-531 (1984).
(29) Romano, R., Ruiz, A. I., Alves, O. L. *J. Solid State Chem.* **177**, 1520-1528 (2004).
(30) Losilla, E. R., Cabeza, A., Bruque, S., Aranda, M. A. G., Sanz, J., Iglesias, J. E., Alonso, J. A. *J. Solid State Chem.* **156**, 213-219 (2001).
(31) Peters, L., Evans, J. S. O. *Journal of Solid State Chemistry*, **180**, 2363-2370 (2007).
(32) Galli, P., La Ginestra, A., Berardelli, M. L., Massucci, M. A., Patrono, P. *Thermo. Acta*, **92**, 615-618 (1985).
(33) Bereznitski, Y., Jaroniec, M., Bortun, A. I., Poojary, D. M., Clearfield, A. *J. Coll. Inter. Sci,* **191**, 442-448 (1997).
(34) Bruque, S., Aranda, M. A. G., Losilla, E. R., Olivera-Pastor, P., Maireles-Torres, P. *Inorg. Chem.*, **34**, 893-899 (1995).
(35) Rodriguez-Castellon, E., Rodriguez-Garcia, A., Bruque, S. *Mater. Res. Bull.*, **20**, 115 (1985).
(36) Costantino, U., Gasperoni, A *J. Chromatog.* **51**, 289-296 (1970).
(37) Sahu, B. B., Mishra, H. K., Parida, K *J. Coll. Inter. Sci,* **225**, 511-519 (2000).
(38) Thind, P. S., Ghandhi, J. S. *J. Solid State Chem.* **60**, 165-171 (1985).
(39) Varshney, K. G., Rafiquee, M. Z. A., Somya, A. *Coll. Surfaces A*, **301**, 224-228 (2007).
(40) Trobajo, C., Rodriguez, M. L., Suarez, M., Garcia, J. R., Rodriguez, J., Parra, J. B., Salvado, M. A., Pertierra, P., Garcia-Granda, S. *J. Mat. Res.* **13**, 754-759 (1998).
(41) Anillo, A., Rodriguez, M. L., Llavona, R., Rodriguez, J., Martinez-huerta, M. V., Banares, M. A., Fierro, J. L. G. *Inter. J. Inorg. Mat.* **2**, 177-185 (2000).
(42) Bagnasco, G., Ciambelli, P., Frezza, A., Galli, P., La Ginestra, A. *App. Cryst.* **68**, 55-68 (1991).
(43) Beattie, M., Msci Thesis 'Synthesis of mixed zirconium tin layered phosphates' University of Birmingham, (2008).
(44) La Ginestra, A., Patrono, P., Frezza, A., Mancini, C., Massucci, M. A., Vecchio *J. Therm. Anal.* **40**, 1223-1232 (1993).
(45) Nakai, I., Imai, K., Kawashima, T., Ohsumi, K., Izumi, F., Tomita, I. *Anal. Sci.* **6**, 689-693 (1990).

Chapter 4: Ion Exchange Studies

4.1 Ion Exchange in the Titanium-Zirconium Series

4.1.1 Introduction

In this chapter the ion exchange behaviour of the titanium-zirconium phosphates towards cations of interest to the nuclear industry (Cs^{+}, Sr^{2+}, Co^{2+}) and sodium are investigated. Successful trapping of these cations could offer a relevant form of nuclear waste immobilisation. A detailed discussion on the ion exchange behaviour of α-TiP and α-ZrP was presented in Chapter 1. A review of the literature shows little work on the exchange of cobalt[1], caesium[2-6] or strontium[6-9] for the crystalline alpha phosphates, with no reported structures for exchange products.

In the first instance, room temperature ion exchanges were carried out on α-TiP. The exchanges that appeared successful were then also attempted on the single phase mixed titanium-zirconium phosphates and α-ZrP.

There are a few reports in the literature of the ion exchange of mixed titanium-zirconium phosphates, both in the crystalline[10,11] and amorphous forms[12-15]. The amorphous phases often exhibit different - and sometimes better - ion exchange behaviour than their single metal counterparts[12,15]. There are differing reports on the exchange behaviour of the crystalline phases and this may be as a result of different starting materials as no structural work was carried out on them. Sodium ion exchange studies[10,11] showed them to exhibit behaviour similar to the end member they were compositionally closest to and produced phases isomorphous to those obtained from their single metal counterparts. In contrast to

these findings Yazawa *et al.*[16] did not observe the intermediate monosodium phase in the sodium exchange of titanium-rich phosphates. This was unlike α-TiP, and in contrast to the zirconium-rich phosphates. Instead they reported the formation of two disodium phases with interlayer spacings of 9.9 Å and 8.4 Å. It is possible that the 8.4 Å phase was misinterpreted and was actually a monosodium phase given that the corresponding monosodium α-TiP phase has the same interlayer spacing[17]. There are no literature reports on the ion exchange of these mixed metal phosphates with strontium, cobalt or caesium.

4.1.2 Results and Discussion

4.1.2.1 α-TiP Strontium Ion Exchange

Samples of α-TiP were treated with strontium solutions at room temperature overnight. In each experiment the mass of α-TiP and the volume of exchange solution were kept constant at 1 g and 0.25 dm^3. The solid samples recovered were analysed using PXRD. Any samples which showed evidence of exchange were further analysed by XRF. During the exchange process the interlayer distance expands or contracts thereby enabling the process to be followed qualitatively by XRD. Successful exchange is expected to show a shifting of the first peak (d_{002}) in the XRD pattern to lower/higher 2θ values reflecting an increase/decrease in the interlayer spacing to accommodate the incoming ion. PXRD patterns from the strontium nitrate, chloride, acetate and hydroxide exchanges are given in Figures 4.1 to 4.4.

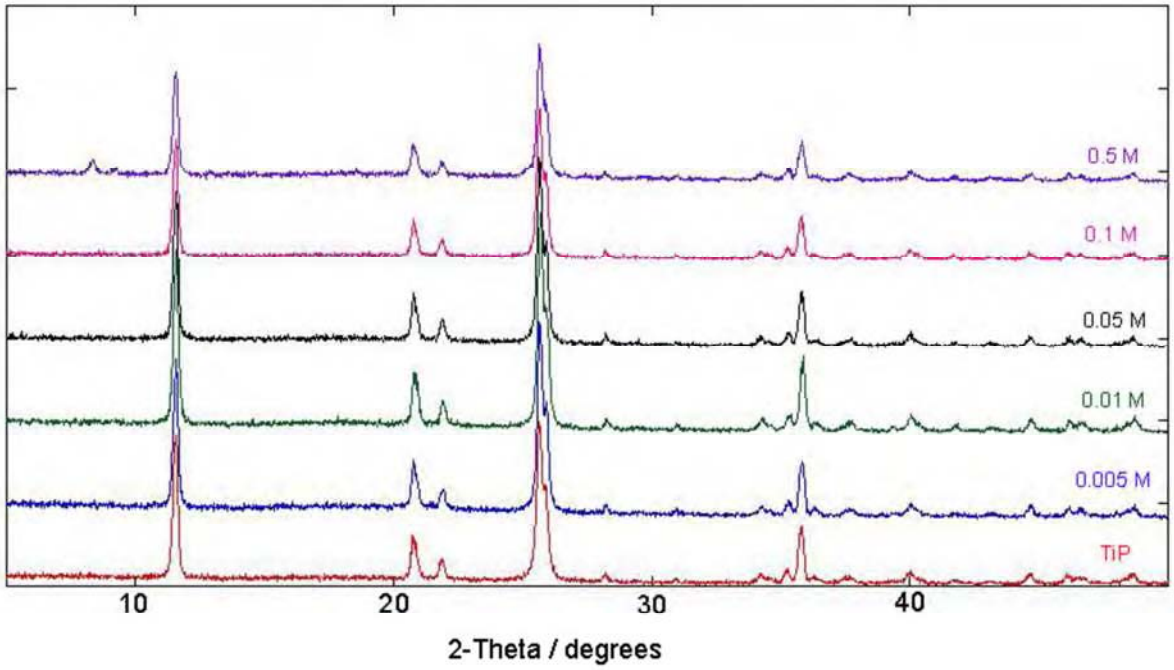

Figure 4.1: Laboratory PXRD patterns of α-TiP treated with strontium acetate solutions of differing concentrations.

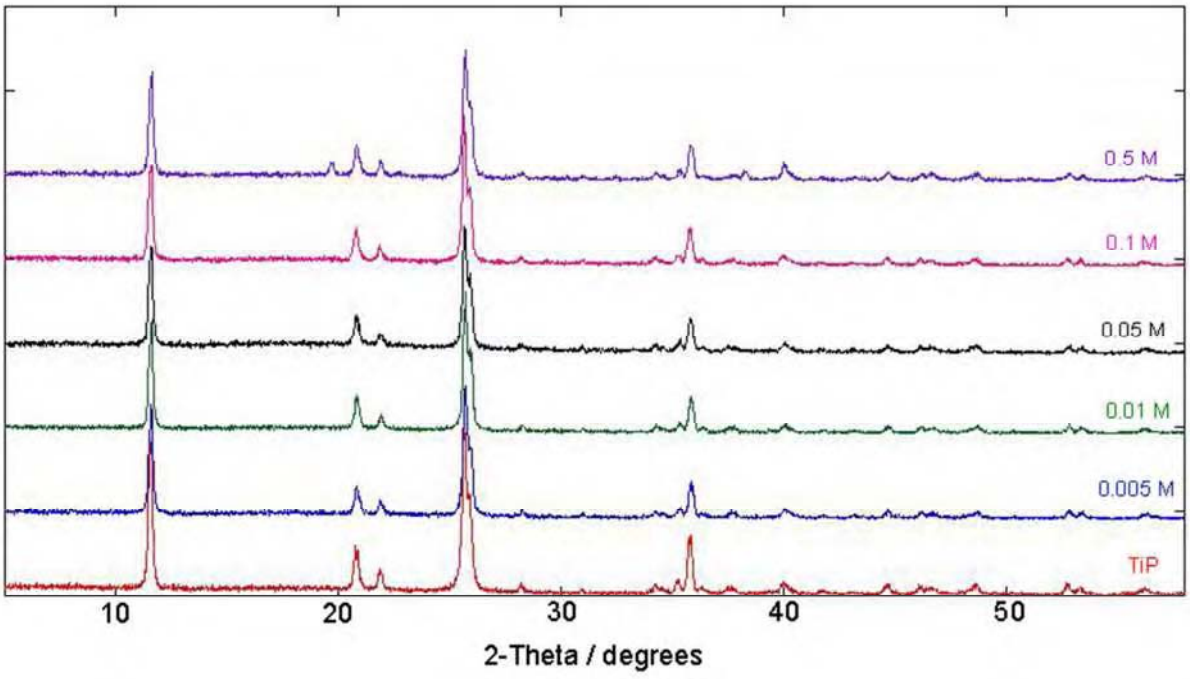

Figure 4.2: Laboratory PXRD patterns of α-TiP treated with strontium nitrate solutions of differing concentrations.

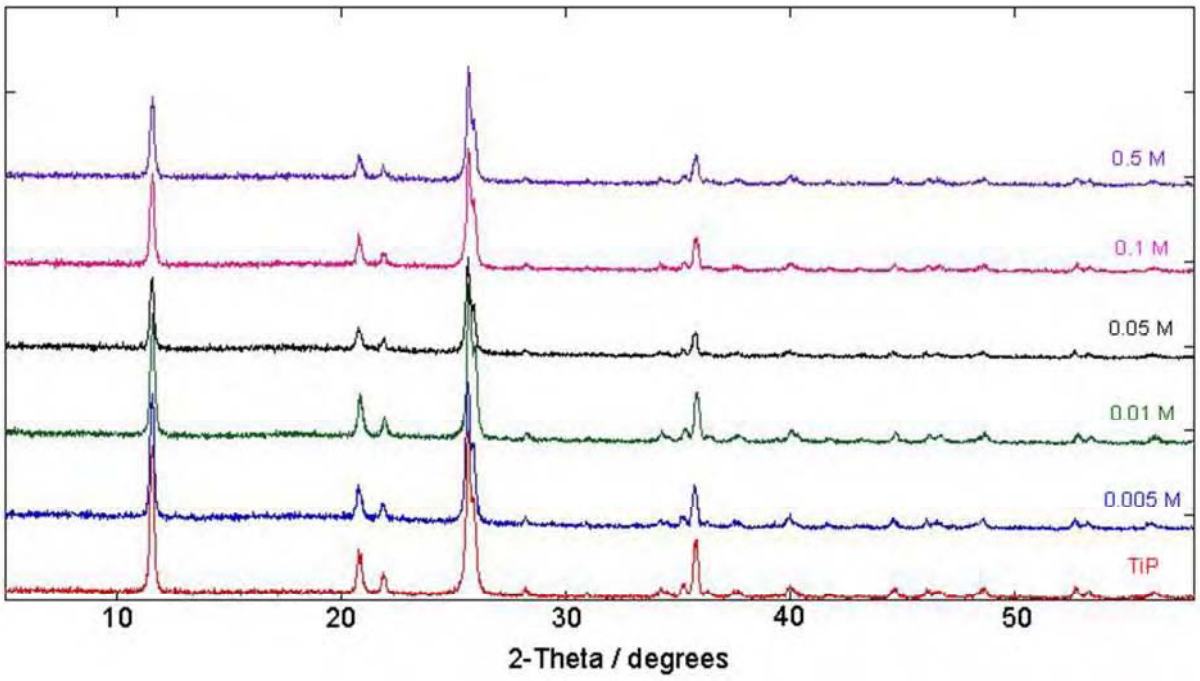

Figure 4.3: Laboratory PXRD patterns of α-TiP treated with strontium chloride solutions of differing concentrations.

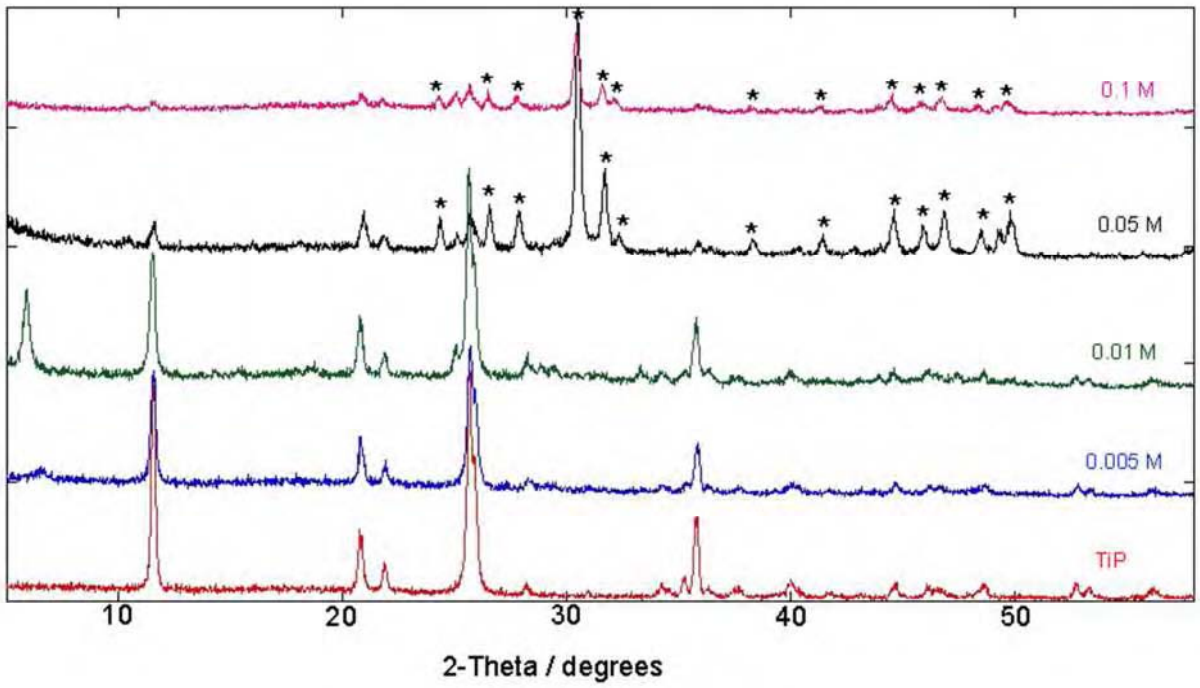

Figure 4.4: Laboratory PXRD patterns of α-TiP treated with strontium hydroxide solutions of differing concentrations. The asterisks denote characteristic $Sr_5(PO_4)_3OH$ peaks (PDF 70-1511).

We do not observe any clear evidence of ion exchange with the strontium chloride or nitrate solutions. The small additional peak at ~19° 2θ for the 0.5 M strontium nitrate exchange was deemed to be from an impurity due to the lack of significant changes in nearly all of the other peaks. Similarly another small peak was observed in the 0.5 M strontium acetate exchange at ~8° 2θ. XRF analysis gave a Ti/Sr molar ratio of 5.88 (compared to a ratio of 1 for complete H^{+}-Sr^{2+} exchange). Subsequent PDF analysis showed no significant alteration in the PDF pattern compared to that of α-TiP and there was no sign of any peaks corresponding to Sr-O or Sr-Sr distances expected for strontium exchange (Figure 4.5) indicating that these results were due to an impurity rather than exchange.

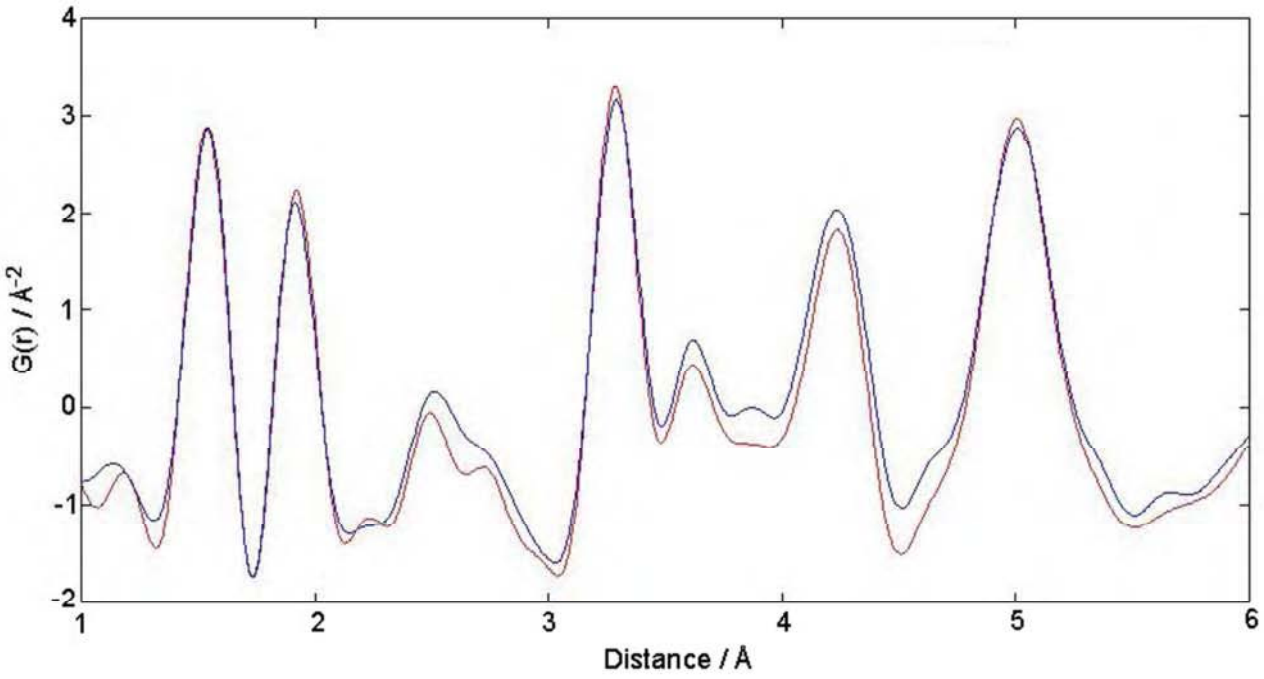

Figure 4.5: Comparison of the PDFs of α-TiP(red) and the product from the TiP ion exchanged with 0.5 M strontium acetate (blue).

Strontium hydroxide exchange gave mixed results. At concentrations at and above 0.05 M $Sr_5(PO_4)_3(OH)$ was formed as shown by the peaks marked with an asterisk in Figure 4.4. At lower concentrations a new peak was observed at ~ 6° 2θ along with minor alterations in the patterns at higher 2θ values. For the 0.01 M product, XRF analysis gave a strontium to titanium ratio of 0.5:1 rather than the 1:1 expected for full exchange. It was not possible to identify this phase using the search and match facility of the powder diffraction file. Attempts at further exchange of this product (under identical conditions) resulted in the eventual loss of α-TiP but with a reduction in the product crystallinity, see Figure 4.6. Due to the small yields obtained it was not possible to get XRF data on these products.

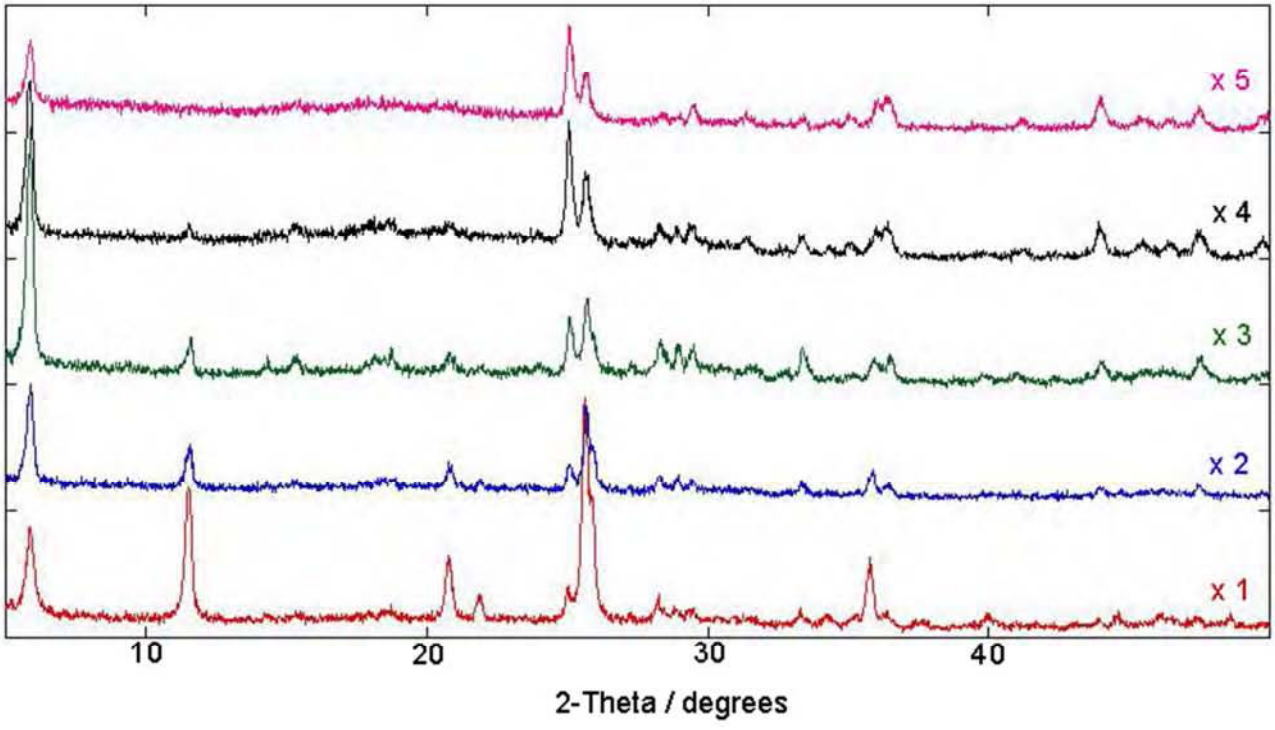

Figure 4.6: Laboratory PXRD patterns of the repeat 0.01 M strontium hydroxide ion exchanges.

In the initial exchange there were 0.0025 moles of strontium present compared with 0.0039 moles of α-TiP. As there are two exchangeable protons per titanium, one mole of strontium could be exchanged per mole of α-TiP. Using this knowledge the volume of solution was increased 4-fold to 1L and the exchange was re-attempted both overnight and over a four day duration. Neither resulted in full exchange (see Figure 4.7) and the longer duration had a detrimental effect on the product crystallinity. Increasing the temperature of exchange (Figure 4.8) led to the formation of strontium hydroxide phosphate ($Sr_5(PO_4)_3(OH)$) instead.

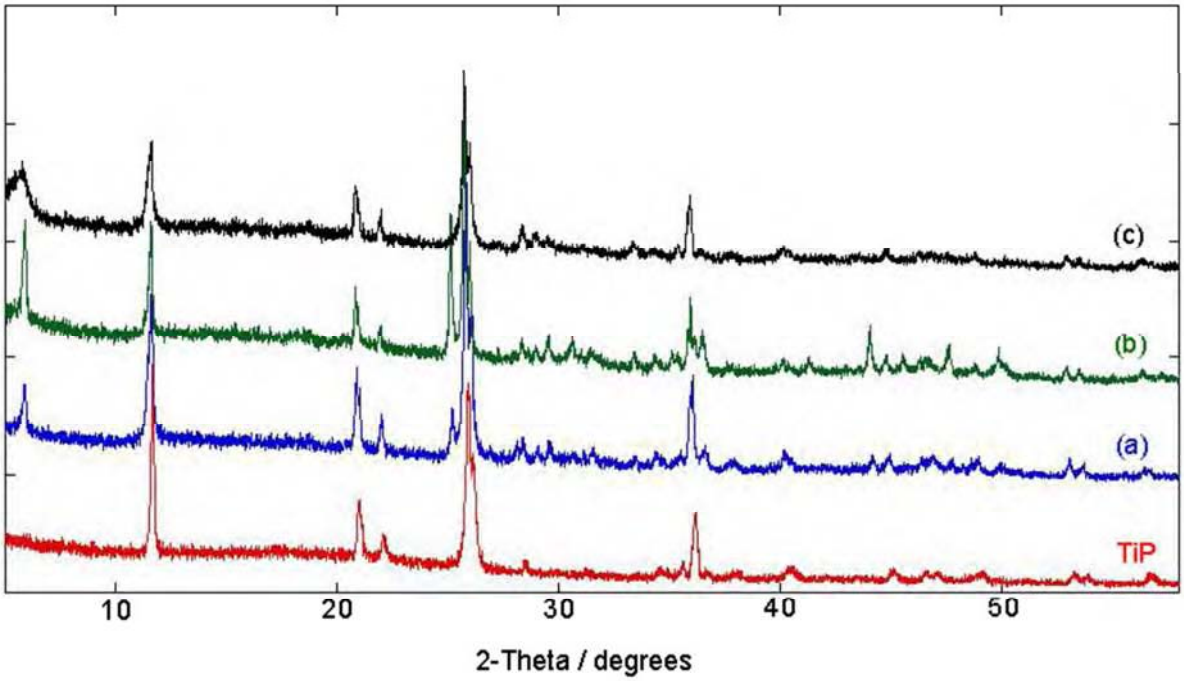

Figure 4.7: Laboratory PXRD patterns of 1 g of α-TiP treated with (a) 250 ml of 0.01 M strontium hydroxide solution overnight (b) 1L of the same overnight (c) 1L of the same for four days.

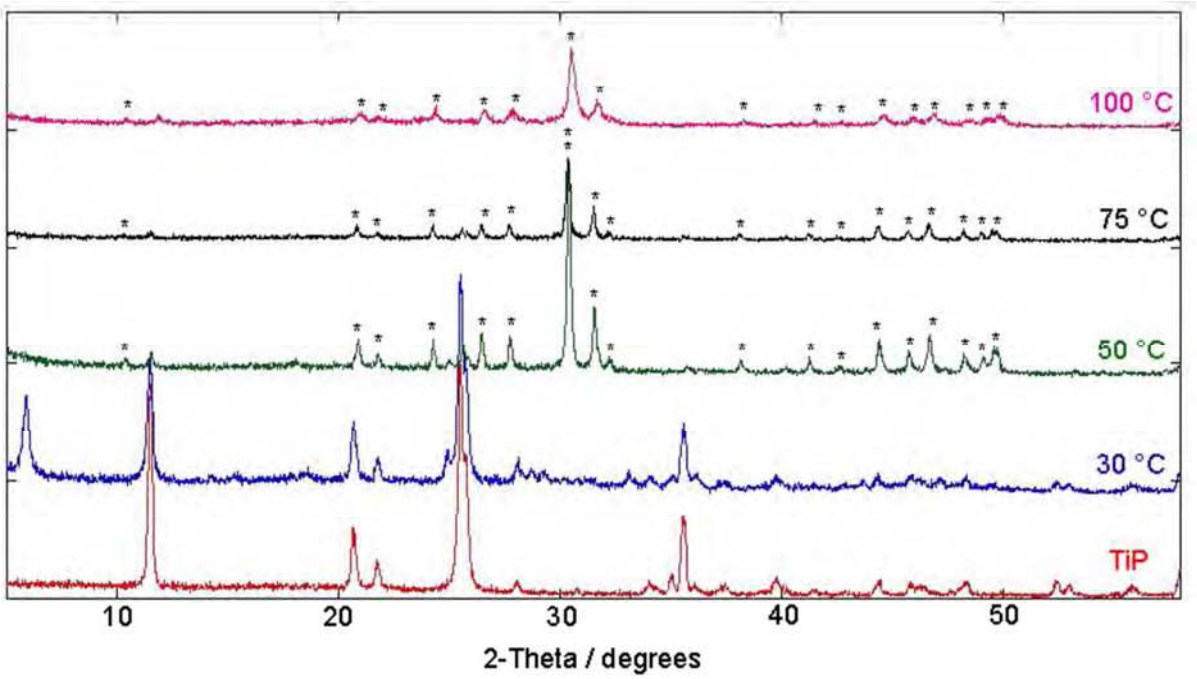

Figure 4.8: The effect of temperature on the ion exchange of α-TiP with 0.01 M strontium hydroxide solution. The asterisks denote characteristic $Sr_5(PO_4)_3OH$ peaks (PDF 70-1511).

Differential PDFs were used to investigate any structural changes occurring upon exchange as well as to identify any new features due to the presence of strontium. In this technique a reference pattern of the starting material is subtracted from the PDF of the exchanged α-TiP so as to isolate only the new information that has occurred from the ion exchange. In theory this should provide a snapshot of the interlayer region. Study of the differential PDF given in Figure 4.9 shows that the starting material and the strontium exchanged product have similar structures and that new, strong peaks consistent with Sr-O and Sr-Sr distances are present in the exchanged product.

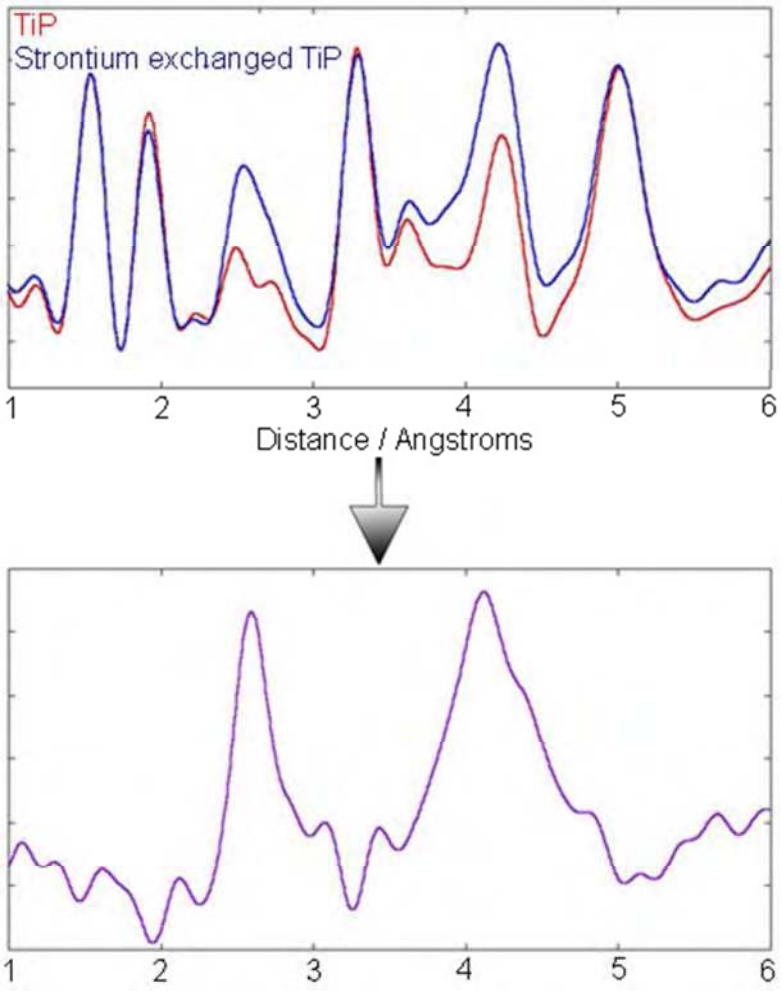

Figure 4.9: Differential PDFs of strontium exchanged α-TiP

Analysis of the long *r* metal-metal distances was undertaken to establish whether the layers either shifted or were spread further apart/contracted upon exchange. No significant variations in the distances were observed (see Figure 4.10), indicating that neither situation had occurred. An increase or decrease in the interlayer spacing would result in an increase or decrease in *all* of the interlayer metal-metal distances. In contrast a shifting of the layers would result in a mixture, with some interlayer metal-metal distances being increased and others decreased. A schematic of these scenarios is presented in Figure 4.11.

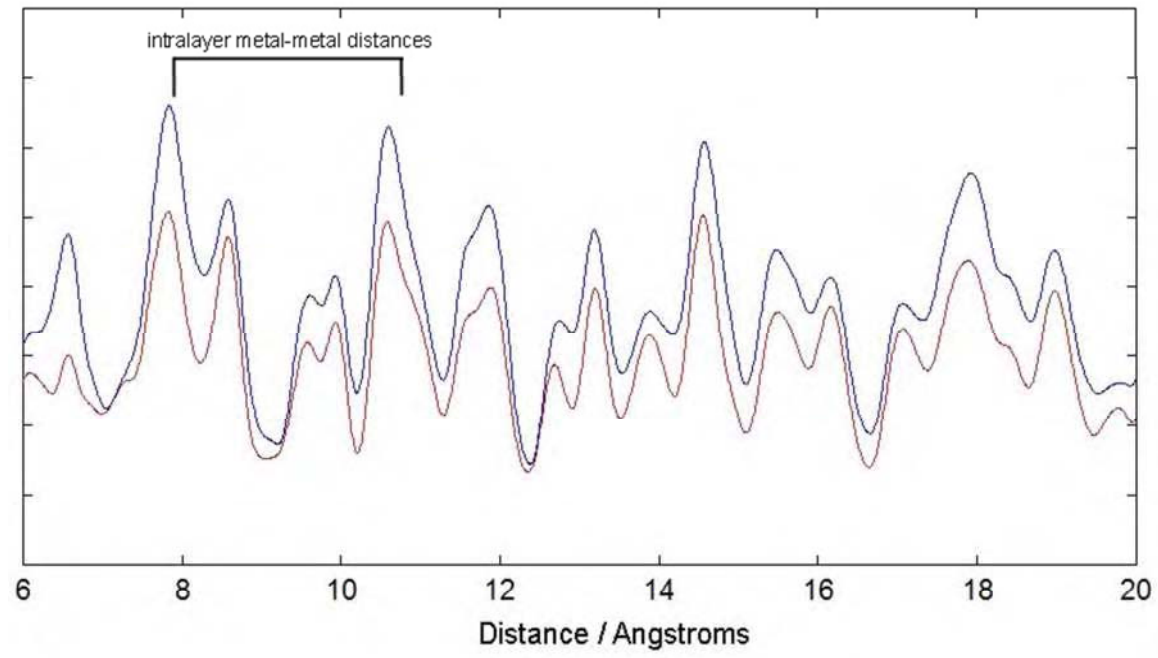

Figure 4.10: PDF patterns of α-TiP (red) and strontium exchanged TiP (blue) in the long *r* region.

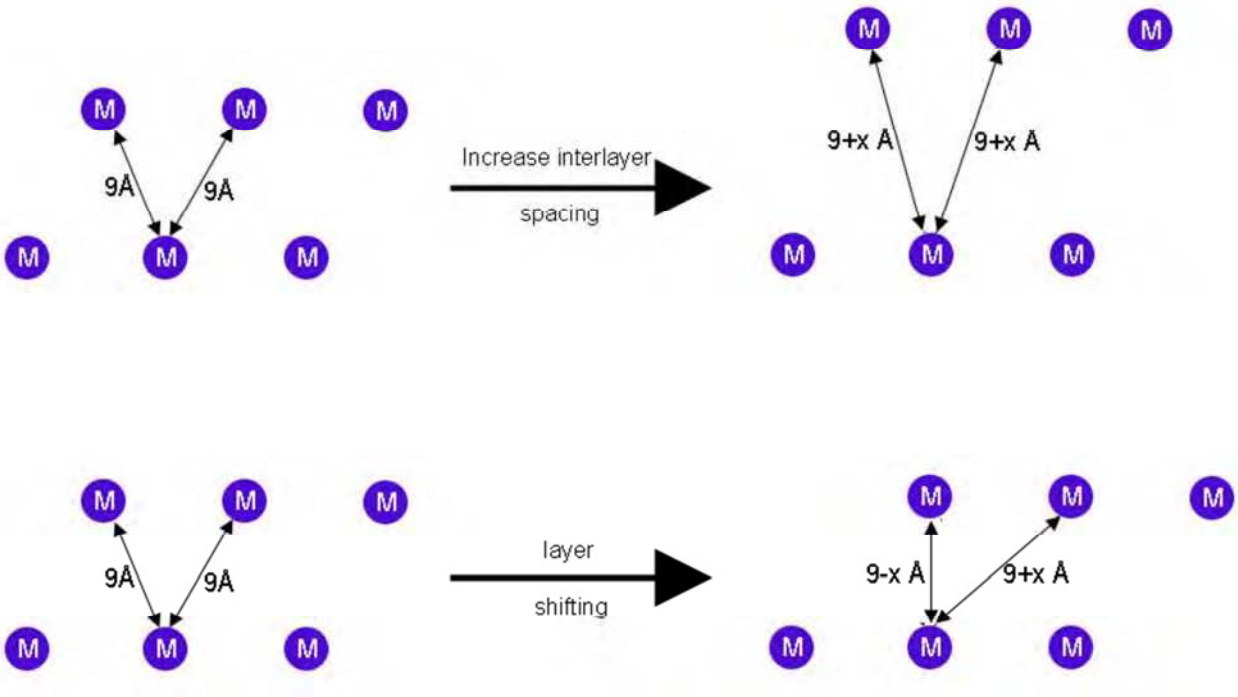

Figure 4.11: Schematic representation of the effects of layer shifting and expansion on the interlayer metal-metal distances. The values used are not to scale.

Thermogravimetric analysis (Figure 4.12) in conjunction with variable temperature XRD (Figure 4.13) showed that the exchanged product undergoes similar dehydration and decomposition pathways as α-TiP with no variation in the initial level of hydration. Strontium titanium phosphate was identified as a decomposition product that crystallised out with titanium pyrophosphate at temperatures above 700 °C. Attempts were made to synthesise $SrTi_4(PO_4)_6$ to enable a study into its stability and leach testing however no pure crystalline products could be obtained.

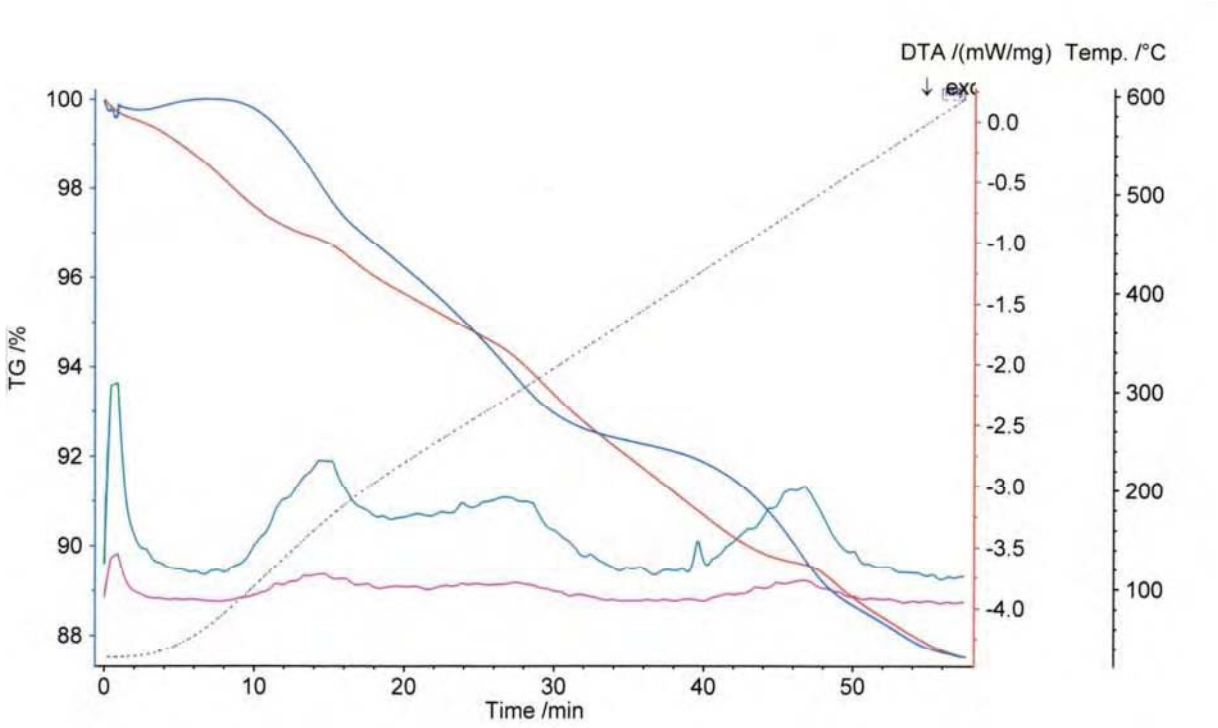

Figure 4.12: Thermogravimetric analysis of strontium exchanged α-TiP. The TGA trace is shown in blue, the DTA in red and the mass spectrometry traces for H_2O and OH^+ in green-blue and pink respectively. The temperature trace is shown as a dotted line.

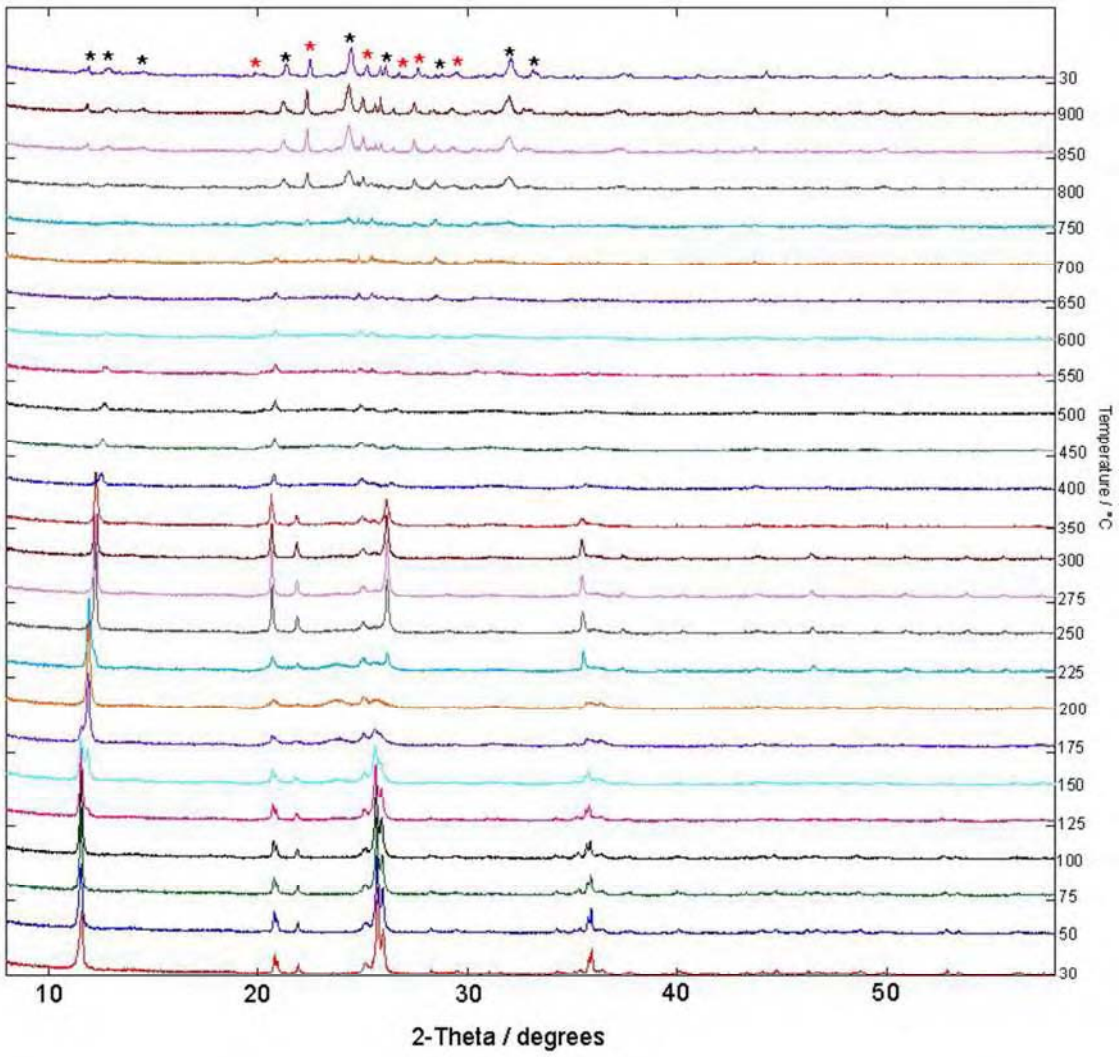

Figure 4.13: Laboratory PXRD patterns of strontium exchanged α-TiP as a function of temperature. $SrTi_4(PO_4)_6$ peaks are marked with black asterisks (04-002-6467) and those for TiP_2O_7 with red asterisks (00-038-1468).

The solid state ^{31}P NMR spectra of both the parent phase (α-TiP) and the exchanged product are compared in Figure 4.14. The two peaks in the parent material are due to the two crystallographically non-equivalent phosphorus environments[18] of α-TiP[19-21]. As the two spectra are almost identical it suggests that the product is not ion exchanged. Instead it seems more likely that an impurity is present, which is responsible for the low angle peak in the XRD pattern and extra features in the PDFs. The ^{31}P NMR results indicate that this impurity is not a phosphate but no identifications could be made.

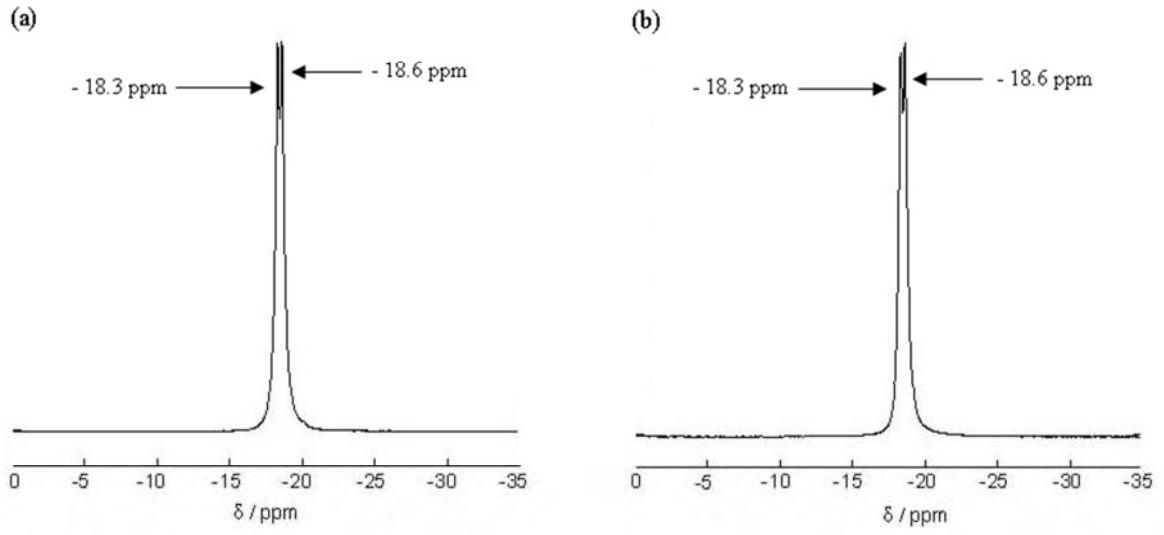

Figure 4.14: ^{31}P NMR spectra of (a) α-TiP (b) strontium exchanged α-TiP

In addition to this, Raman spectra of both the parent phase and the strontium-exchanged product were collected on a Renishaw in-Via Raman microscope. The results obtained are given in Figure 4.15. The spectra obtained for the strontium-exchanged TiP product is practically indistinguishable from that of the parent phase α-TiP. Once again this confirms that no exchange occurred. Both spectra are almost identical to those reported in the literature for α-TiP[22,23] .

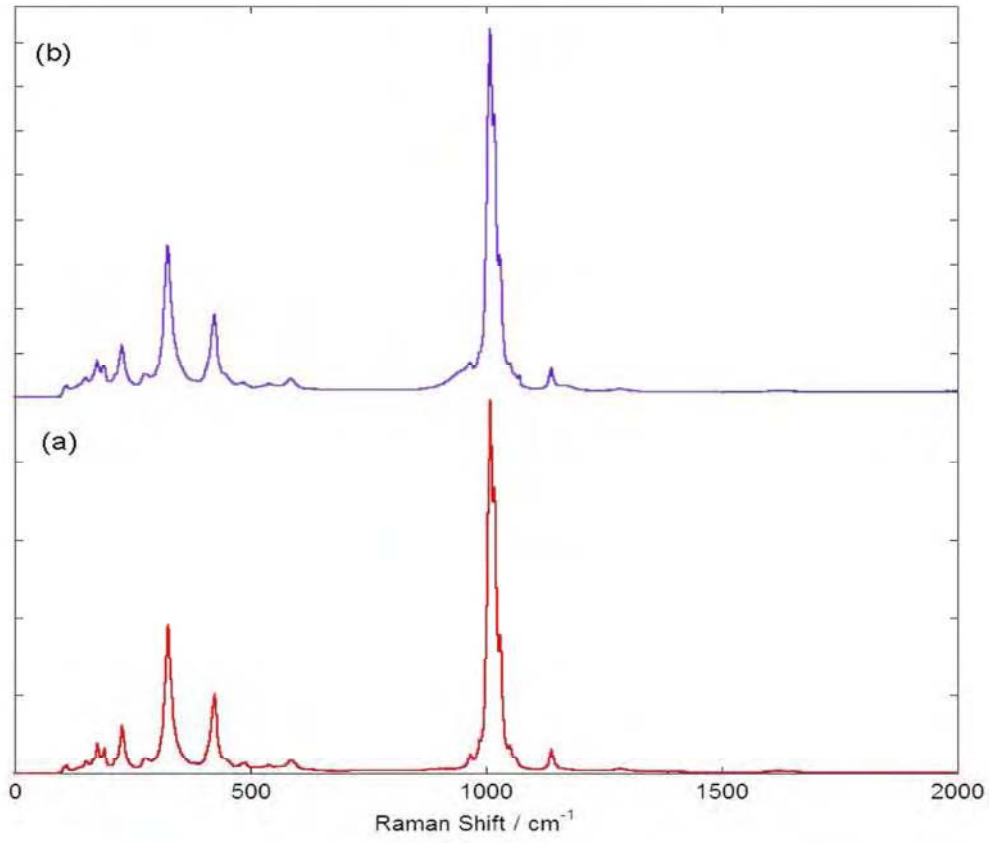

Figure 4.15: Raman spectra of (a) unexchanged α-TiP (b) strontium exchanged TiP

SEM EDX analysis was used for further analysis. As can be seen from the SEM micrographs in Figure 4.16 the product consists of two morphologies; plates and flakes. Given the small size of the particles present and the bi-phasic nature of the sample, it was not possible to select individual grains / phases for EDX analysis. Instead areas of the sample dominated by one phase type were selected for analysis and the results are also given in Figure 4.16. Care must be taken when interpreting these results as they do not provide accurate compositional information for either phase and can only be used as a rough guide. As the area actually analysed was bigger than that selected due to the interaction of the incident beam with the sample, the presence of the other phase nearby/underneath would have affected the

results. However, lower strontium contents were found in areas containing predominantly plate-like particles which would indicate that these are α-TiP. This is consistent with previous morphological findings for α-TiP[24-27]. It is therefore assumed that the flake-like particles are the impurity phase and is supported by the higher strontium contents seen in these areas. No further compositional information for this phase can be obtained from these results for reasons already stated.

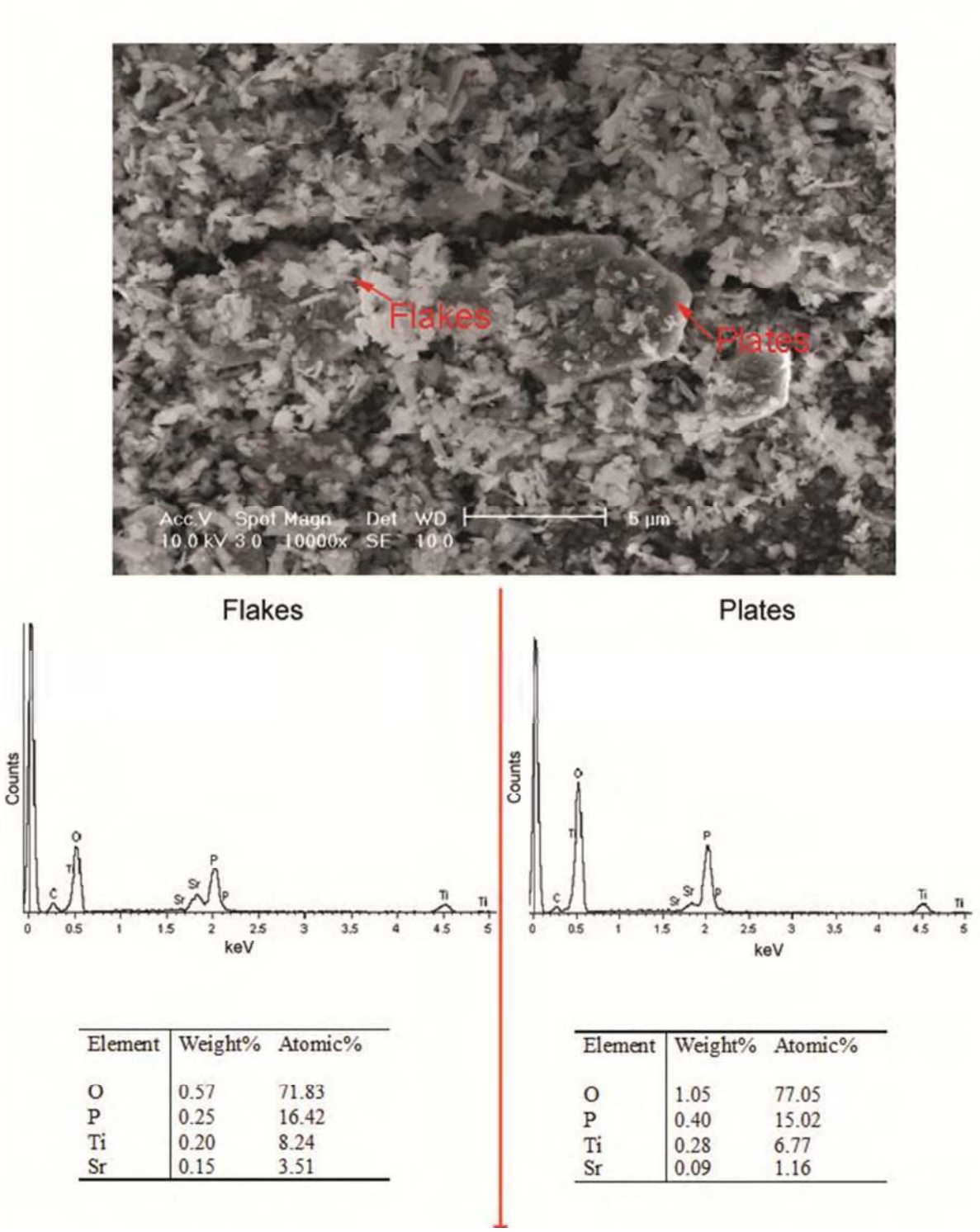

Element	Weight%	Atomic%
O	0.57	71.83
P	0.25	16.42
Ti	0.20	8.24
Sr	0.15	3.51

Element	Weight%	Atomic%
O	1.05	77.05
P	0.40	15.02
Ti	0.28	6.77
Sr	0.09	1.16

Figure 4.16: SEM/EDX results for the 0.01 M strontium hydroxide ion exchanged α-TiP product

In order to assess the reproducibility of these results, the same experiment was repeated several times. Figure 4.17 displays the PXRD patterns of the products obtained. It is clear to

see that the 'impurity' peak at ~ 8° 2θ was present in most, but not all, of the PXRD patterns. The products that displayed this peak were checked by XRF (pressed pellet rather than fused bead method) and gave between 0.47 and 0.53 moles of strontium per mole of titanium in all cases. The consistency in the strontium content is due to the fact that the same experimental conditions were used each time and so the impurity was always forming under identical conditions.

Peak broadening was also observed for some of the samples and in addition to this the peak at ~31° 2θ was absent from some of the patterns displayed in Figure 4.17. In conclusion it can be stated that these results show a low level of reproducibility for this experiment.

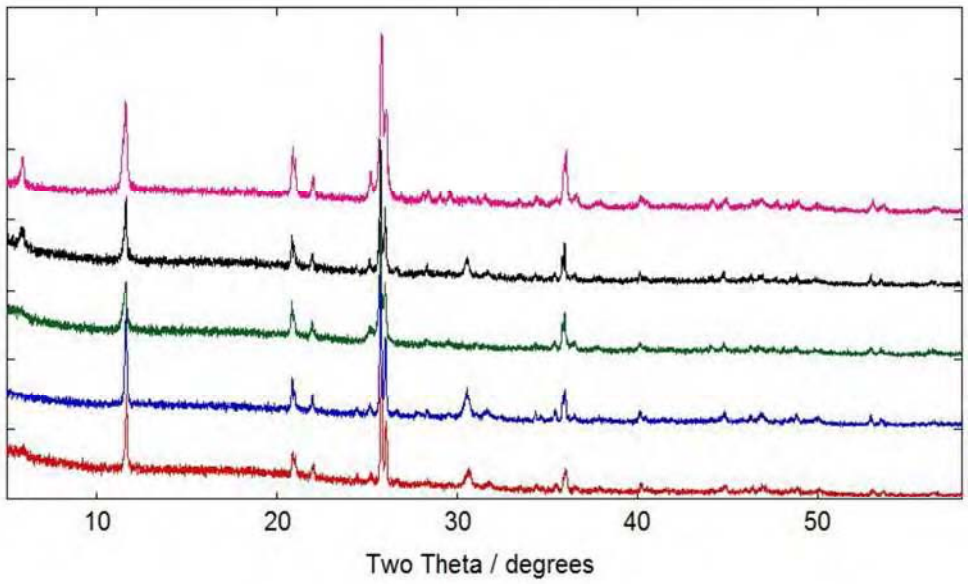

Figure 4.17: Laboratory XRD patterns of products obtained from the strontium hydroxide exchanges of α-TiP.

Previous ion exchange studies on layered phosphates of this type have found that high pH solutions are often required to swell the layers apart to allow for exchange[28,29]. In light of this, pH controlled exchanges using 0.01 M strontium chloride and hydroxide solutions

(maintaining an overall volume of 250 ml) were attempted on α-TiP, but no exchanges were observed (Figure 4.18).

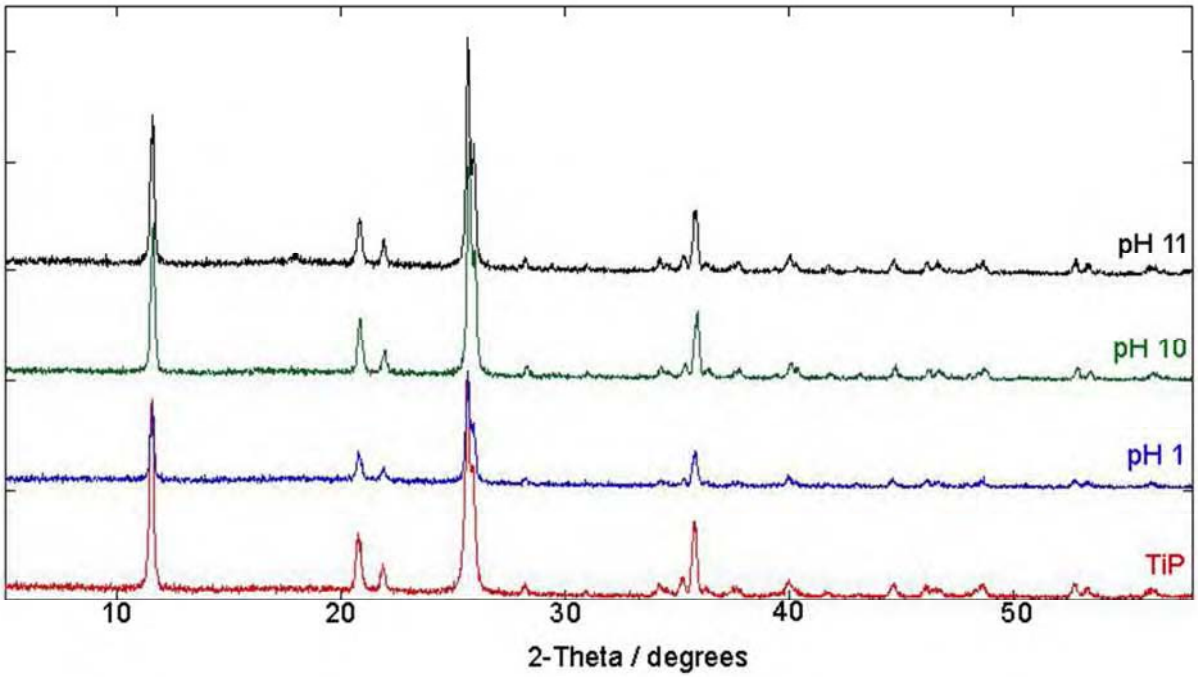

Figure 4.18: Laboratory PXRD patterns of α-TiP treated with pH controlled strontium solutions.

4.1.2.2 Mixed Metal Titanium-Zirconium Phosphate Strontium Ion Exchange

As the 0.01 M strontium hydroxide exchange of α-TiP was originally thought to have been successful, the same exchange was carried out on the single phase mixed titanium-zirconium phosphates. The resultant PXRD patterns of the solid products recovered are shown in Figure 4.19.

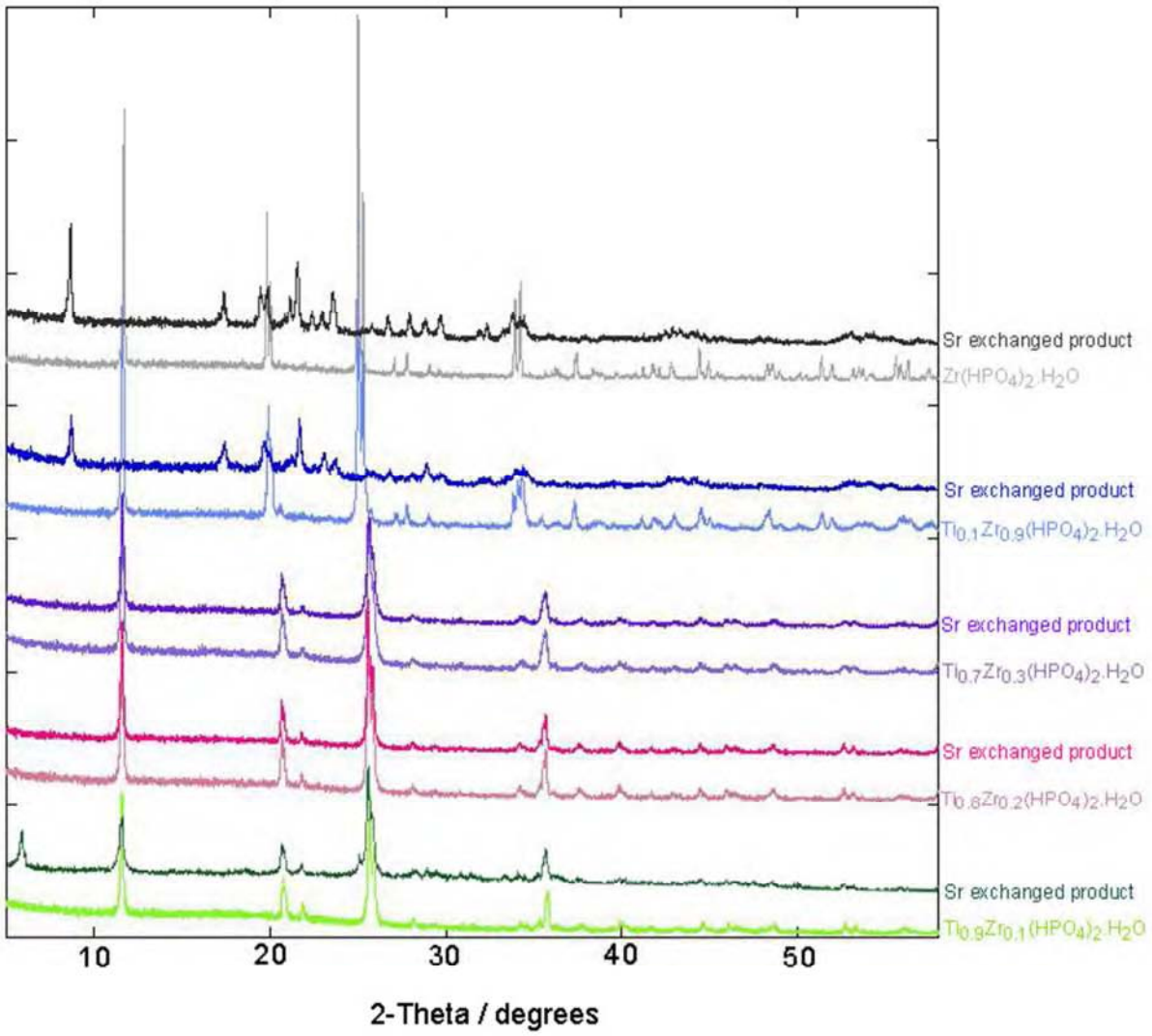

Figure 4.19: Laboratory PXRD patterns of the single phase phosphates (lighter colours) compared to the strontium hydroxide products (darker coloured).

There is no evidence of ion exchange in any of the patterns for the titanium-rich coprecipitates. The peak observed in the α-TiP exchanged product attributed to an unknown strontium impurity is also present in the pattern of exchanged $Ti_{0.9}Zr_{0.1}(HPO_4)_2.H_2O$. Similarly the Sr:Ti ratio obtained for this product by XRF analysis was also 0.5:1. This impurity does not appear to be present in the patterns of the $Ti_{0.8}Zr_{0.2}(HPO_4)_2.H_2O$ and $Ti_{0.7}Zr_{0.3}(HPO_4)_2.H_2O$ exchanged products. The reasons for this are not yet understood.

In contrast, at the other end of the series, exchange with $Ti_{0.1}Zr_{0.9}(HPO_4)_2.H_2O$ and α-ZrP appears to have been successful. The peaks observed for the α-ZrP product correspond to those seen for other strontium exchanged α-ZrP phases reported in the literature (see Table 4.1). In further support of this, the XRF data for both products gave approx. 0.5 moles of strontium per mole of metal. The absence of other characteristic peaks is probably as a result of the lowered crystallinity of the product and the poor quality data. Given the similarity in the XRD patterns, the $Ti_{0.1}Zr_{0.9}(HPO_4)_2.H_2O$ product is assumed to be isomorphous to that from α-ZrP. Further investigation of these products, accompanied by higher resolution XRD data, is discussed in Chapter 5. The leach testing of these products is addressed in Chapter 6.

Table 4.1: PXRD data for the strontium α-ZrP product compared with known phases found in the literature.

Strontium exchanged ZrP *d* (Å)	$ZrHSr_{0.5}(PO_4)_2.3.6H_2O$[30] *d* (Å)	$ZrSr_{0.45\text{-}0.55}H_{1.1\text{-}0.9}(PO_4)_2.3.5H_2O$[8] *d* (Å)
10.2	10.2	10.2
-	6.60 (vw)	6.64
5.09	5.10	5.10
4.57	4.56	4.57
4.48	4.46	4.46
4.22	-	4.25
4.13	4.11	4.12
3.97	3.96	3.97
3.87	-	-
3.77	3.75	3.76
-	3.65 (vm)	-
3.48	3.52	3.51
3.34	3.32	3.33
3.20	3.19	3.19
3.10	-	3.09
3.00	3.00	3.00

4.1.2.3 α-TiP Cobalt Ion Exchange

Samples of α-TiP were treated with cobalt solutions at room temperature overnight. The PXRD patterns of the solid products recovered from the cobalt nitrate, acetate, chloride and hydroxide exchanges are given in Figures 4.20 to 4.23.

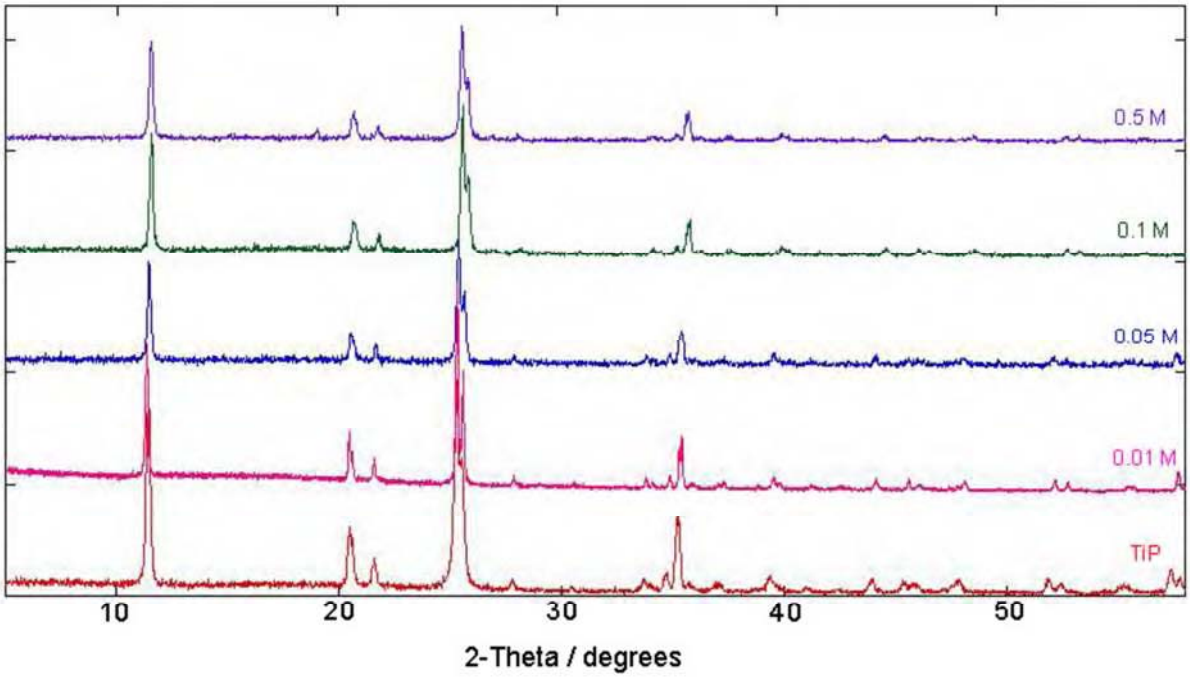

Figure 4.20: Laboratory PXRD patterns of α-TiP treated with cobalt nitrate solutions of differing concentrations.

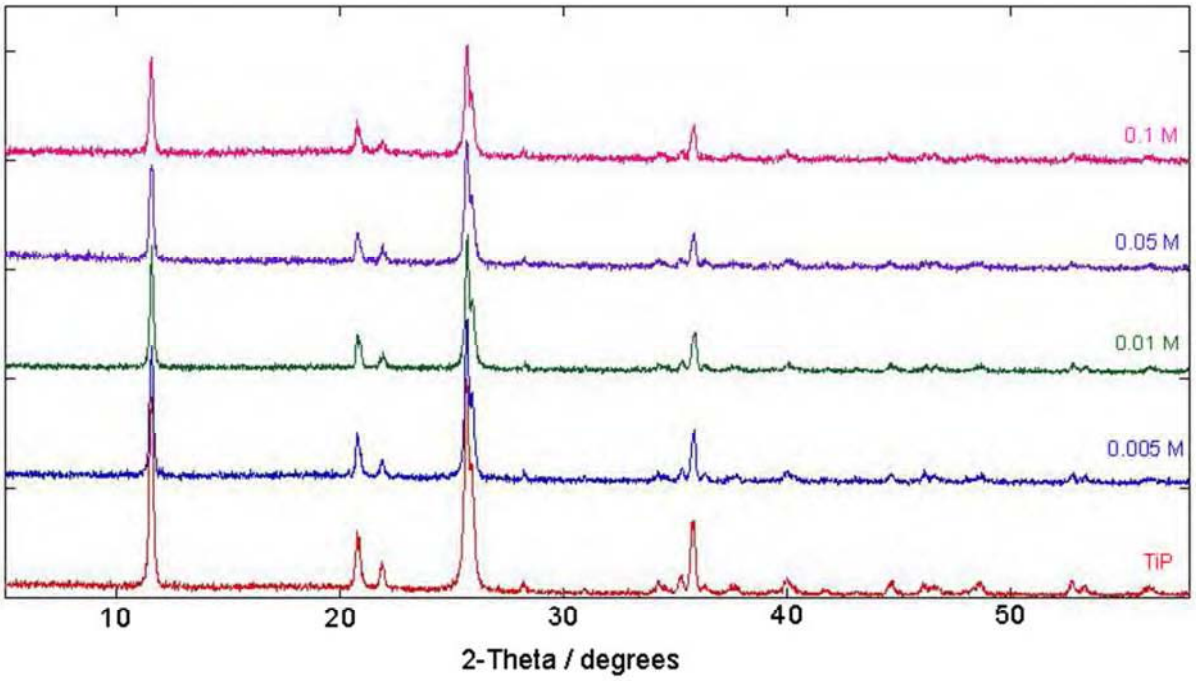

Figure 4.21: Laboratory PXRD patterns of α-TiP treated with cobalt acetate solutions of differing concentrations.

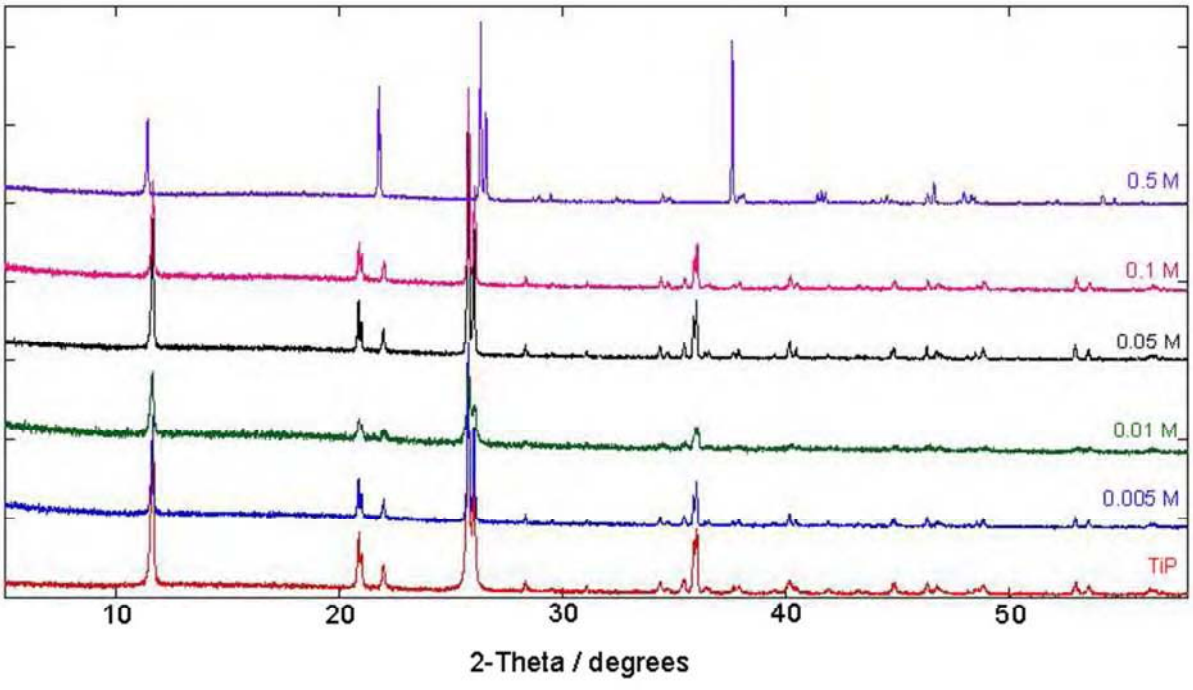

Figure 4.22: Laboratory PXRD patterns of α-TiP treated with cobalt chloride solutions of differing concentrations.

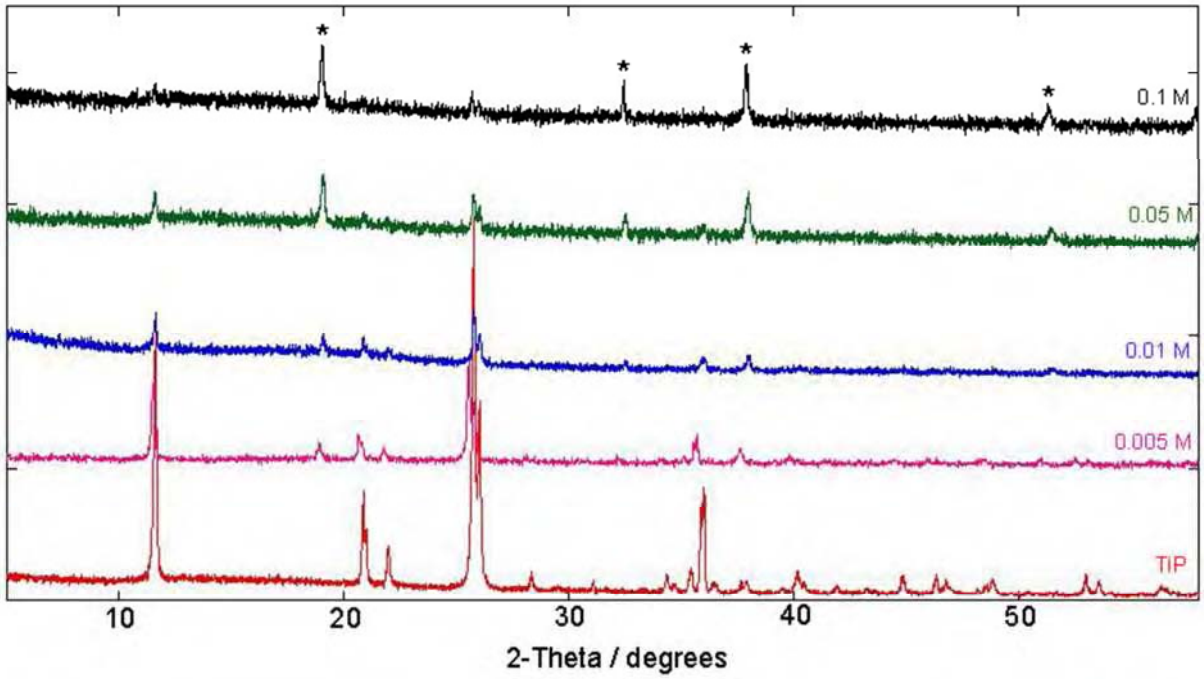

Figure 4.23: Laboratory PXRD patterns of α-TiP treated with cobalt hydroxide solutions of differing concentrations. The asterisk denote the peaks for β-$Co(OH)_2$ (JCPDS ICDD 30-443).

No evidence of ion exchange was observed from the cobalt nitrate, acetate or hydroxide exchanges. Contact with sodium hydroxide leads to a reduction in the crystallinity of α-TiP and higher concentrations resulted in the formation of β-$Co(OH)_2$. The 0.5 M cobalt chloride exchanged product gave an entirely new pattern with no evidence of the parent compound. No identification could be made from the XRD data and so further analysis of this product is recommended for future work. The experiment should also be reattempted to assess the reproducibility of this result.

High temperature cobalt hydroxide exchanges were performed in order to investigate whether the increased energy could facilitate exchange. Samples of α-TiP were treated with 0.01 M cobalt hydroxide solutions at temperatures of 50 and 75 °C. An experiment at 100 °C in a hydrothermal bomb was also attempted. From the PXRD patterns given in Figure 4.24 it

is clear that the higher temperatures lead to a loss in the crystallinity of the products, but there is still no clear evidence of exchange. As the patterns show a large amorphous component some exchange may have occurred which resulted in amorphous products. Unfortunately the quantities obtained were not sufficient for further analysis. Ideally crystalline exchange products are preferred as they are more likely to securely entrap the exchanged cations for longer durations.

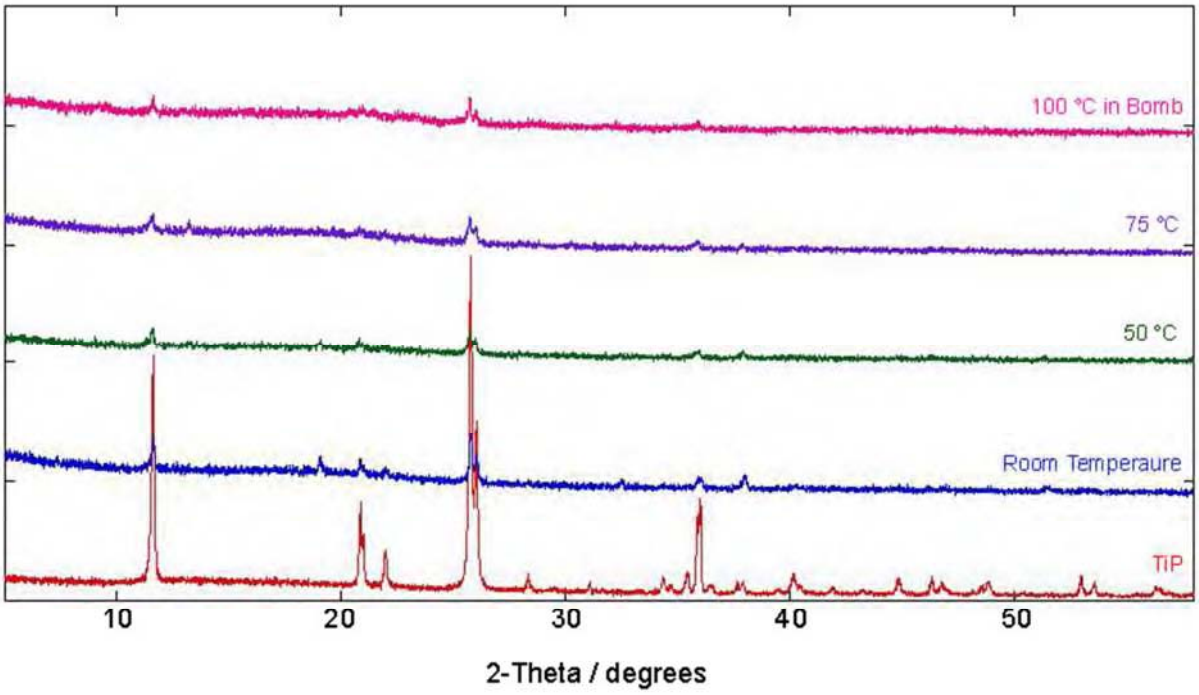

Figure 4.24: The effect of temperature on cobalt ion exchange of α-TiP.

Room temperature cobalt ion exchanges were also attempted on the strontium exchanged α-ZrP compound discussed previously. It was of interest to see if cobalt could be exchanged once the layers were already spread apart by the presence of strontium, or whether the strontium exchanged product was stable upon exposure to cobalt sources. The PXRD patterns of the strontium exchanged α-ZrP cobalt exchanges are given in Figure 4.25. There

are no visible differences in the patterns aside from the loss of crystallinity. This would suggest that no cobalt has been exchanged and that strontium exchanged α-ZrP has remained, albeit with some structural deformation. It would be of use to further analyse these reactions by XRF to establish if any strontium ions were lost. This was not investigated due to the poor yields and reproducibility of the products. The new peak observed in the pattern of the cobalt hydroxide product is in-keeping with the presence of β-$Co(OH)_2$ as seen in the exchanges with α-TiP.

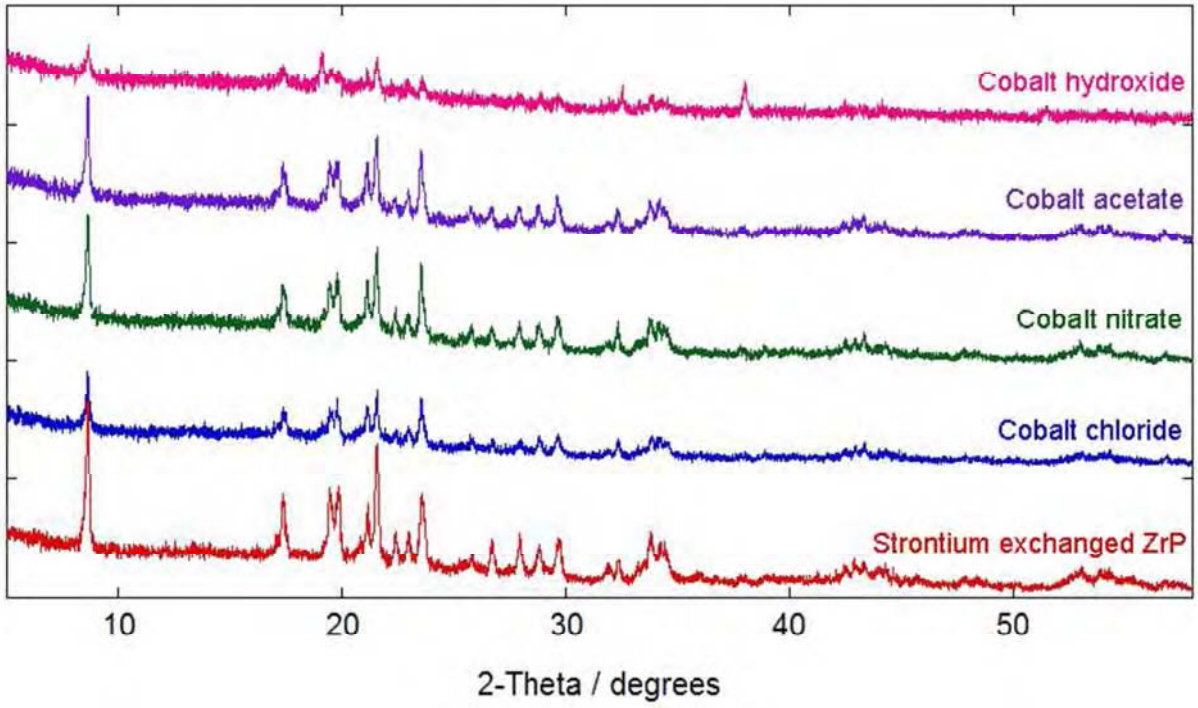

Figure 4.25: Laboratory PXRD patterns of strontium exchanged α-ZrP treated with cobalt solutions overnight.

4.1.2.4 α-TiP Caesium Ion Exchange

Samples of α-TiP were treated with caesium solutions at room temperature overnight and the solid products recovered were analysed by PXRD.

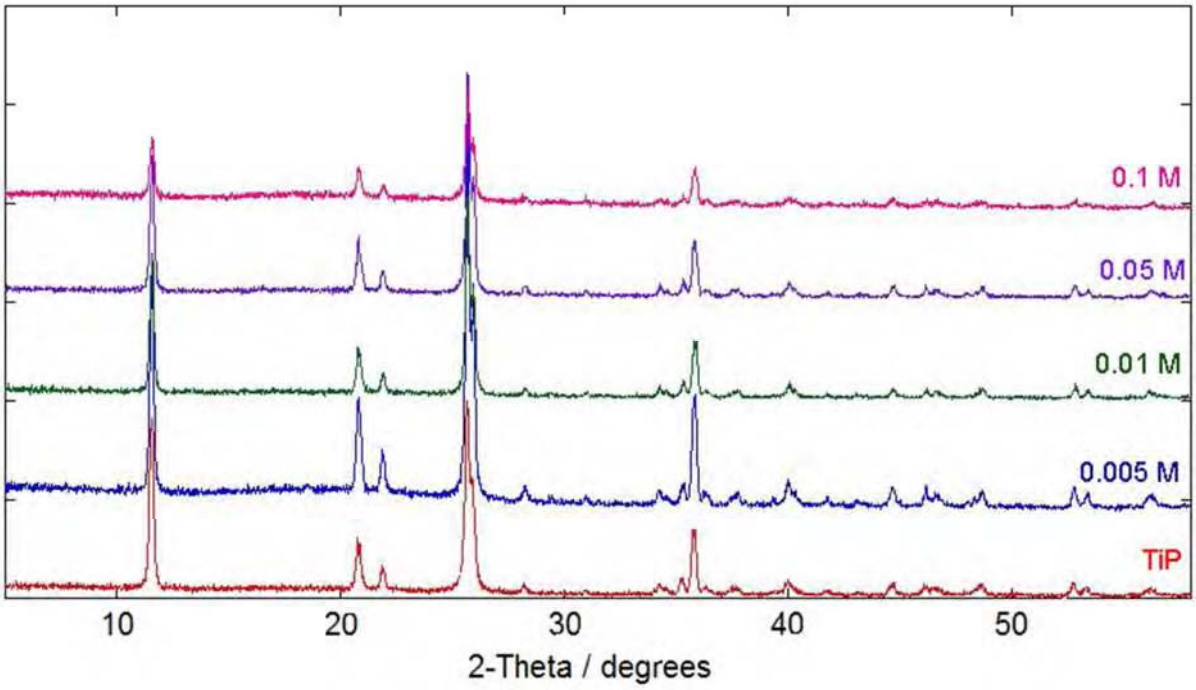

Figure 4.26: Laboratory PXRD patterns of α-TiP treated with caesium acetate solutions.

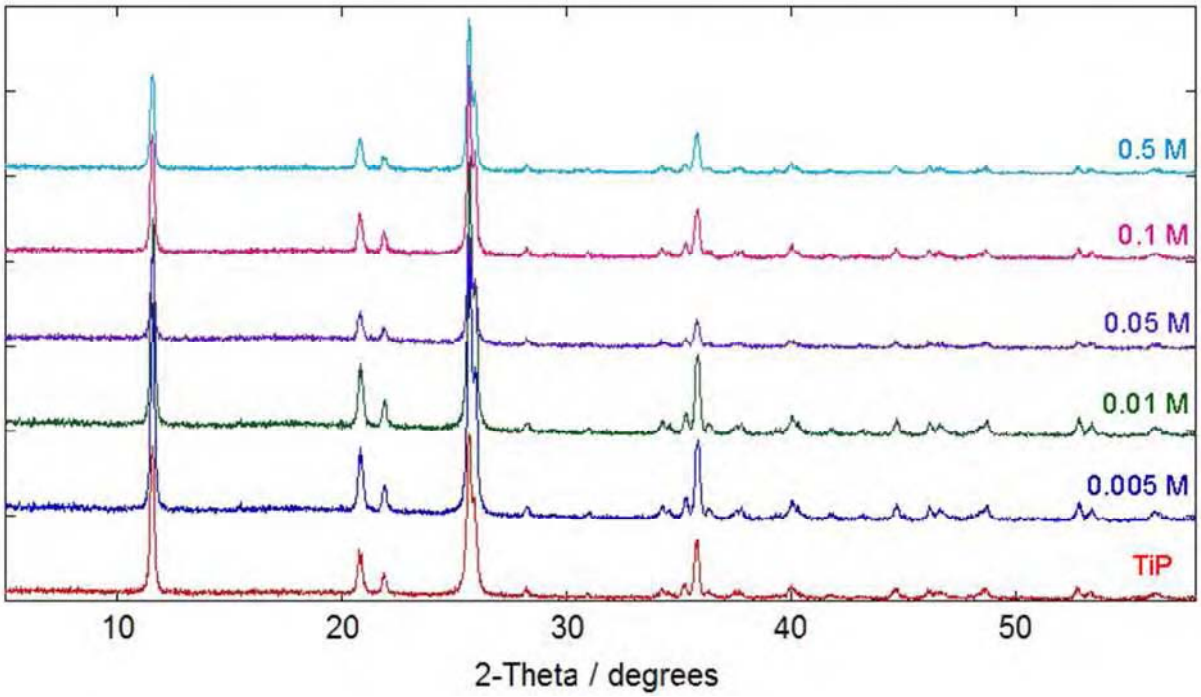

Figure 4.27: Laboratory PXRD patterns of α-TiP treated with caesium chloride solutions.

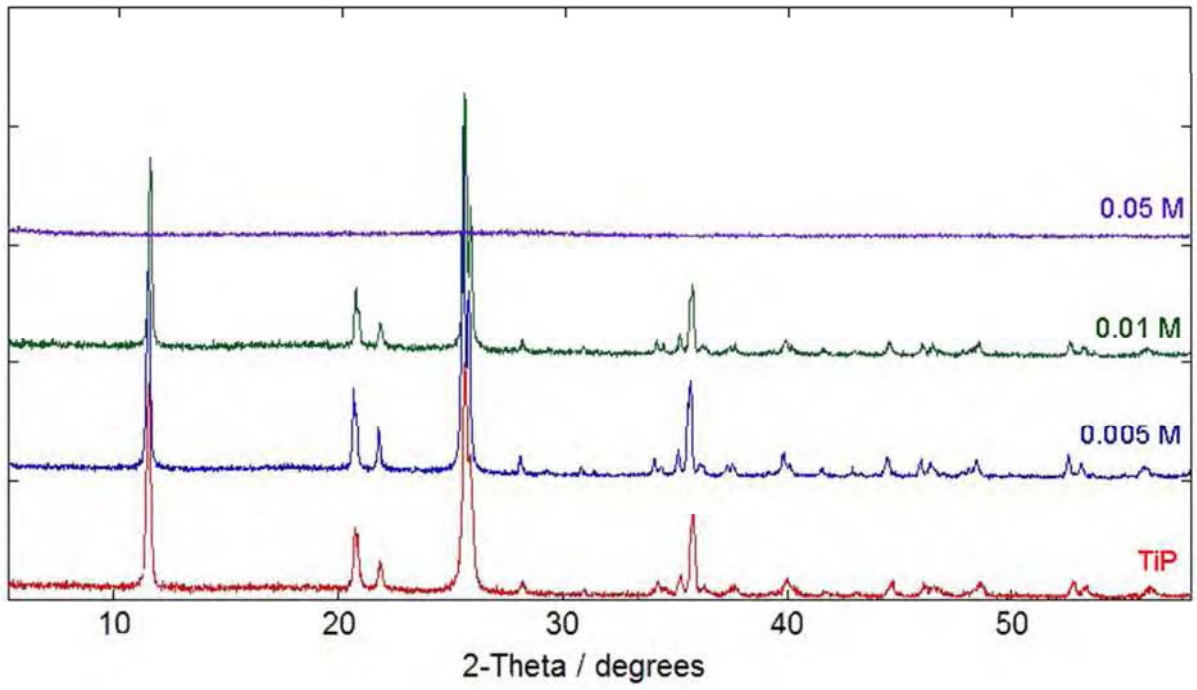

Figure 4.28: Laboratory PXRD patterns of α-TiP treated with caesium hydroxide solutions.

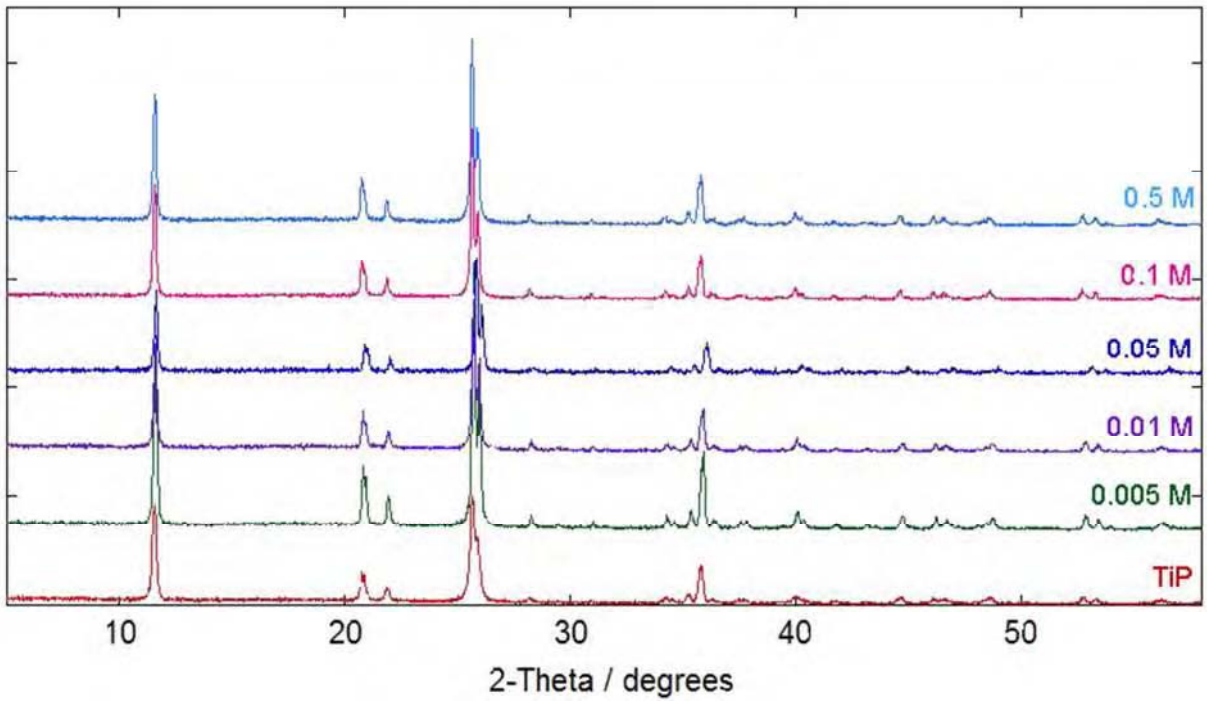

Figure 4.29: Laboratory PXRD patterns of α-TiP treated with caesium nitrate solutions.

As shown in Figures 4.26 – 4.29, there is no evidence of caesium exchange in any of the PXRD patterns. Exposure to 0.05 M sodium hydroxide solution resulted in a fully amorphous product. XRF analysis determined very low caesium amounts in this product, consistent with surface adsorbed caesium. No solid products were obtained when higher concentrations were used.

These results show ion exchange with caesium under these conditions is unsuccessful - possibly owing to the larger size of the caesium ions. In light of this, exchanges with low concentrated caesium hydroxide solutions were attempted at higher temperatures. The PXRD patterns of the products recovered are displayed in Figure 4.30. In both cases no exchange appears to have taken place. One sample of α-TiP was also hydrothermally treated with caesium hydroxide at temperatures of 100 °C overnight, however no solid product could be recovered. Another method to encourage caesium ion exchange in α-TiP that could be investigated in a future study is by pH control of the solutions used. Higher pH's can help to swell the layers apart which facilitates exchange of larger cations[28].

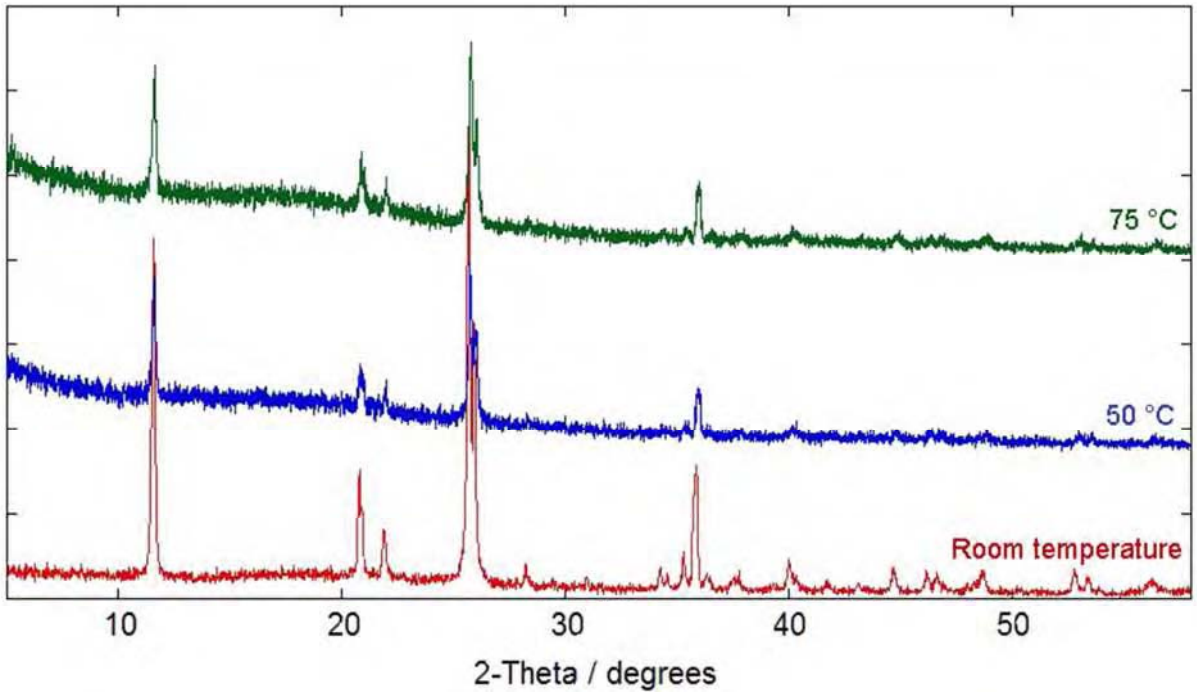

Figure 4.30: The effect of temperature on caesium ion exchange of α-TiP.

As per the cobalt exchanges it was of interest to see if caesium could be exchanged once the layers were already spread apart by the presence of strontium, and whether the strontium exchanged product was stable upon exposure to caesium. For these reasons, room temperature ion exchanges using 0.01 M caesium solutions were attempted on strontium exchanged α-ZrP. The PXRD patterns of the products are shown in Figure 4.31.

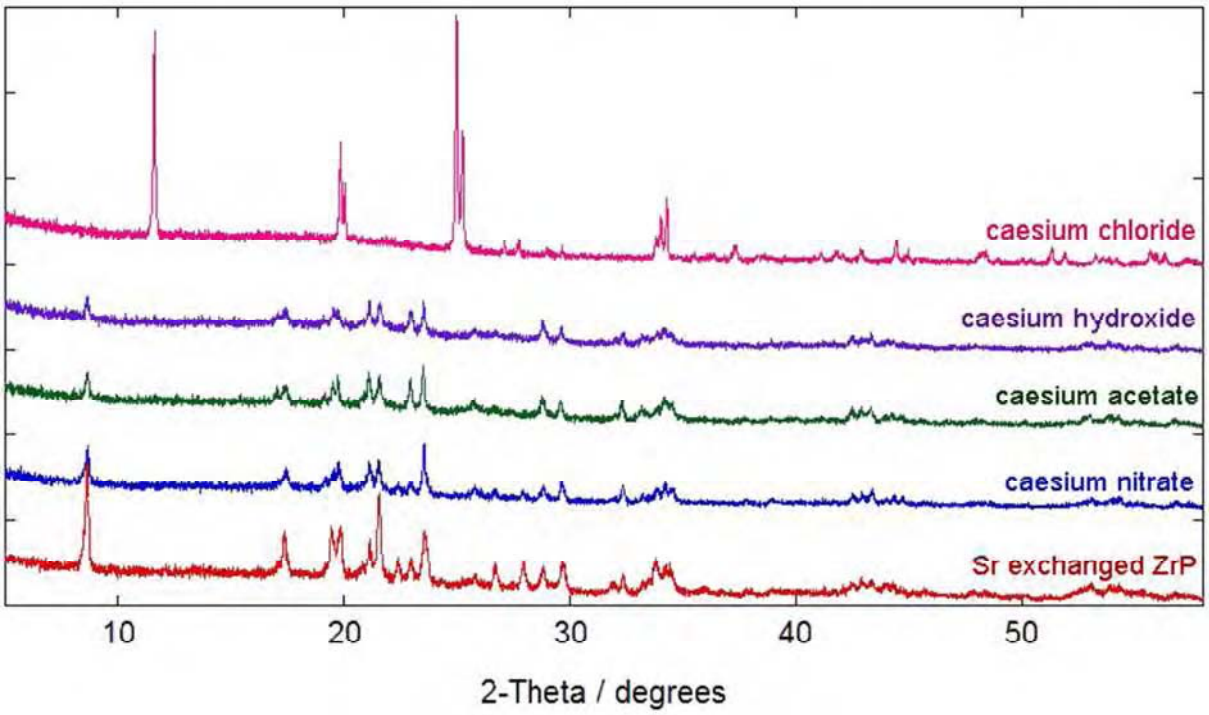

Figure 4.31: Laboratory PXRD patterns of strontium exchanged α-ZrP treated with caesium solutions overnight.

These results show that caesium could not be exchanged despite the increased interlayer spacing of strontium α-ZrP. Interestingly the pattern given for the exchange with caesium chloride matches up to that of α-ZrP suggesting that back exchange occurs in this solution. Further work is required to confirm this e.g. analysis of the exchange solutions to determine the strontium and caesium contents and the reproducibility of this result should be determined by repeating the experiment.

4.1.2.5 α-TiP Sodium Ion Exchange

A common method used to ion exchange large cations is to use a step-wise process whereby the material is first exchanged with a smaller cation e.g. sodium. This spreads the layers

apart, which in theory makes it easier for the larger ion to be exchanged in a second step. For this reason samples of α-TiP were treated with sodium chloride, nitrate, hydroxide and acetate solutions at room temperature overnight. All solid samples recovered were analysed using PXRD and those which showed evidence of exchange were further analysed by XRF.

No evidence of exchange was seen in any of the products from the exchanges with the sodium nitrate or chloride solutions as shown in Figures 4.32- 4.33. No solid products could be recovered when higher concentrations of these solutions were used.

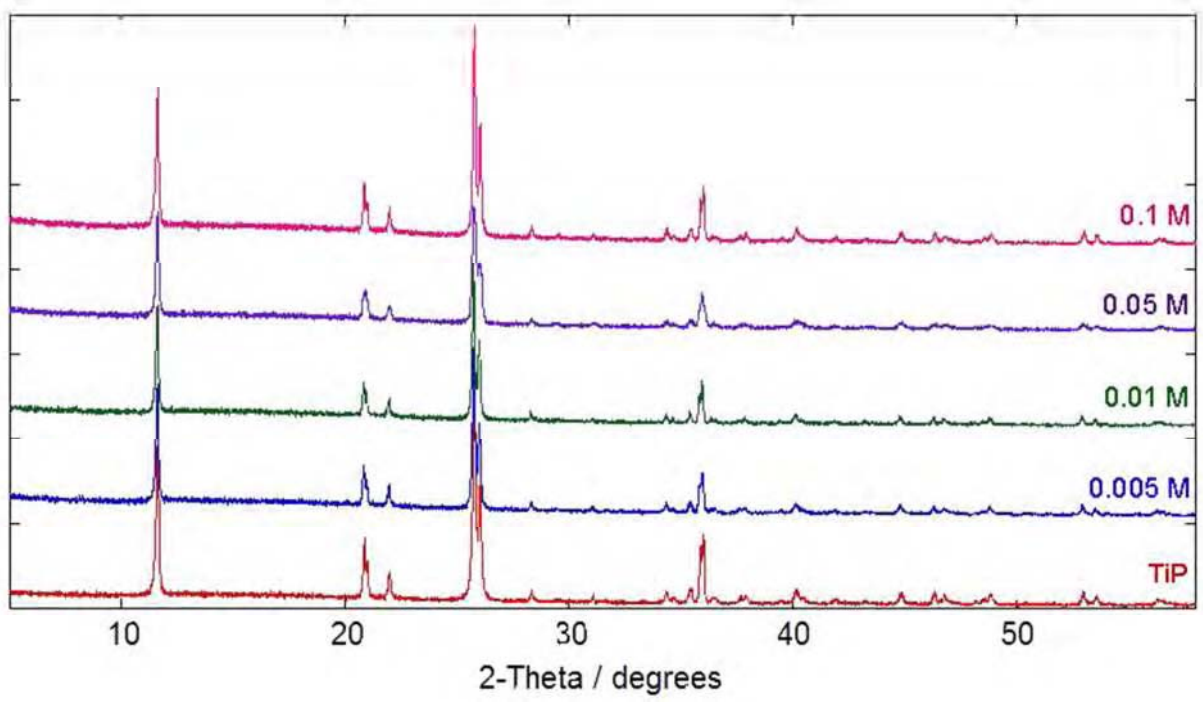

Figure 4.32: Laboratory PXRD patterns of α-TiP treated with sodium chloride solutions.

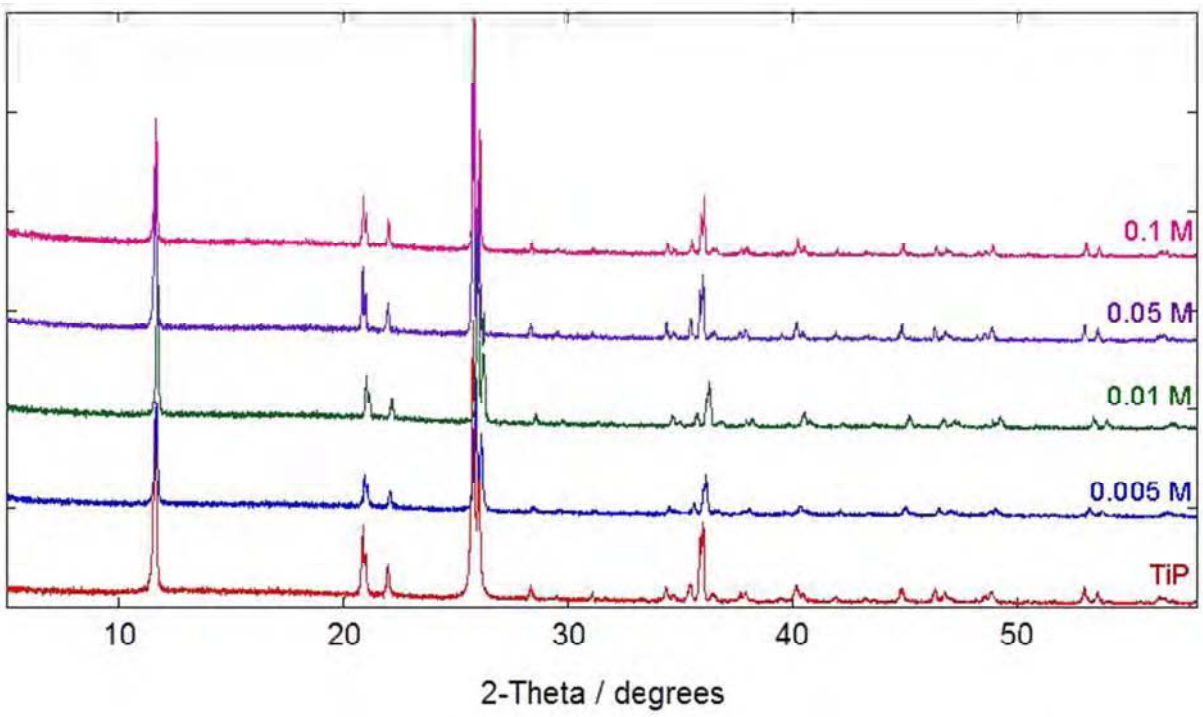

Figure 4.33: Laboratory PXRD patterns of α-TiP treated with sodium nitrate solutions.

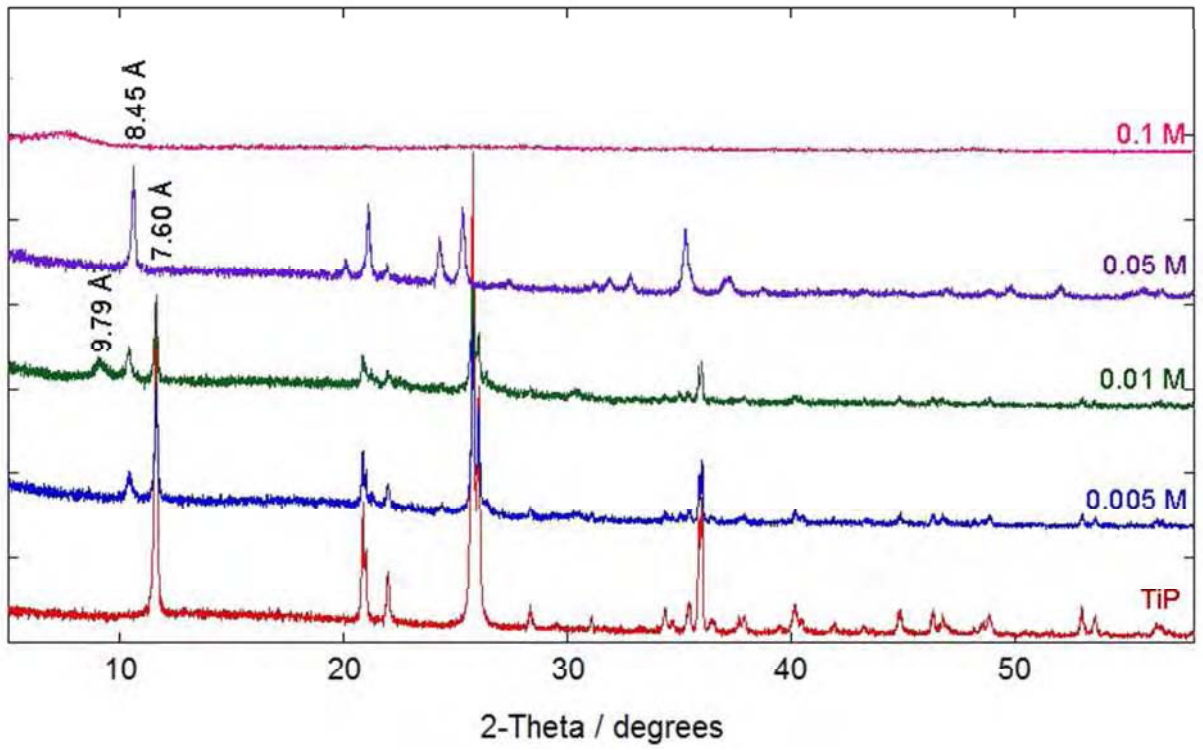

Figure 4.34: Laboratory PXRD patterns of α-TiP treated with sodium hydroxide solutions.

The PXRD patterns of the products obtained from the exchanges with sodium hydroxide are shown in Figure 4.34. Given the amorphous nature of the product it appears that the 0.1 M solution is too concentrated for α-TiP. The patterns for the other hydroxide exchanged products show the emergence of new phases with interlayer spacings of 8.45 Å and 9.79 Å corresponding to the half and fully exchanged phases; $TiHNa(PO_4)_2.H_2O$[17] and $TiNa_2(PO_4)_2.3H_2O$[17]. In accordance with previous reports[10,17], these two phases coexsist with the unexchanged starting material. The exception to this is the product from the 0.05M exchange where only peaks for the half exchanged phase are observed. Exchange with the 0.01 M solution is the only one to result in the formation of some of the fully exchanged phase. XRF analysis showed 0.74 moles of sodium per mole of titanium in this product compared with 0.32 moles of sodium per mole of titanium for the 0.005 M product. This is consistent with the additional fully exchanged phase observed in this product. The yield of the 0.05 M exchange product was not sufficient for XRF analysis.

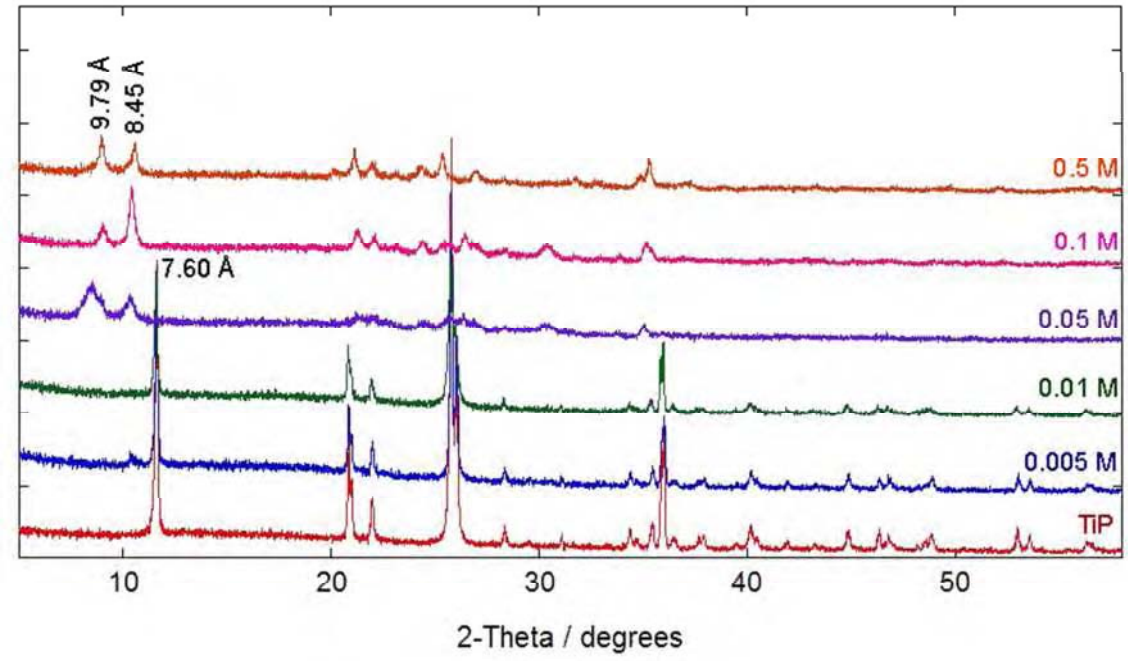

Figure 4.35: Laboratory PXRD patterns of α-TiP treated with sodium acetate solutions.

The PXRD patterns of the products obtained from the exchanges with sodium acetate are shown in Figure 4.35, exchange did not occur when less concentrated sodium acetate solutions were used. For the higher concentration solutions, peaks corresponding to both the half and fully exchanged phases are observed. Unlike sodium hydroxide exchange, there is no evidence of any unexchanged starting material seen in these products. This is reflected in the XRF results which show the presence of significantly higher amounts of sodium (1.19 moles of sodium per titanium cf. 0.74 moles sodium per titanium in the 0.01M sodium hydroxide product). In addition to this the products appear to be more crystalline than those obtained from the hydroxide exchanges (Figure 4.36). In keeping with previous reports[8] these results indicate higher exchange when acetate solutions are employed. Acetate ions can neutralise most of the protons which helps to facilitate exchange[8].

Although sodium exchange was possible using the higher pH solutions, the fully exchanged phase was never obtained as a pure product. Further attempts using greater pH control or higher sodium levels may be required. The reduction in crystal quality in addition to the multiple phase nature of these products makes detailed structural investigations difficult. However further characterisation of these phases is presented in Chapter 5 of this thesis.

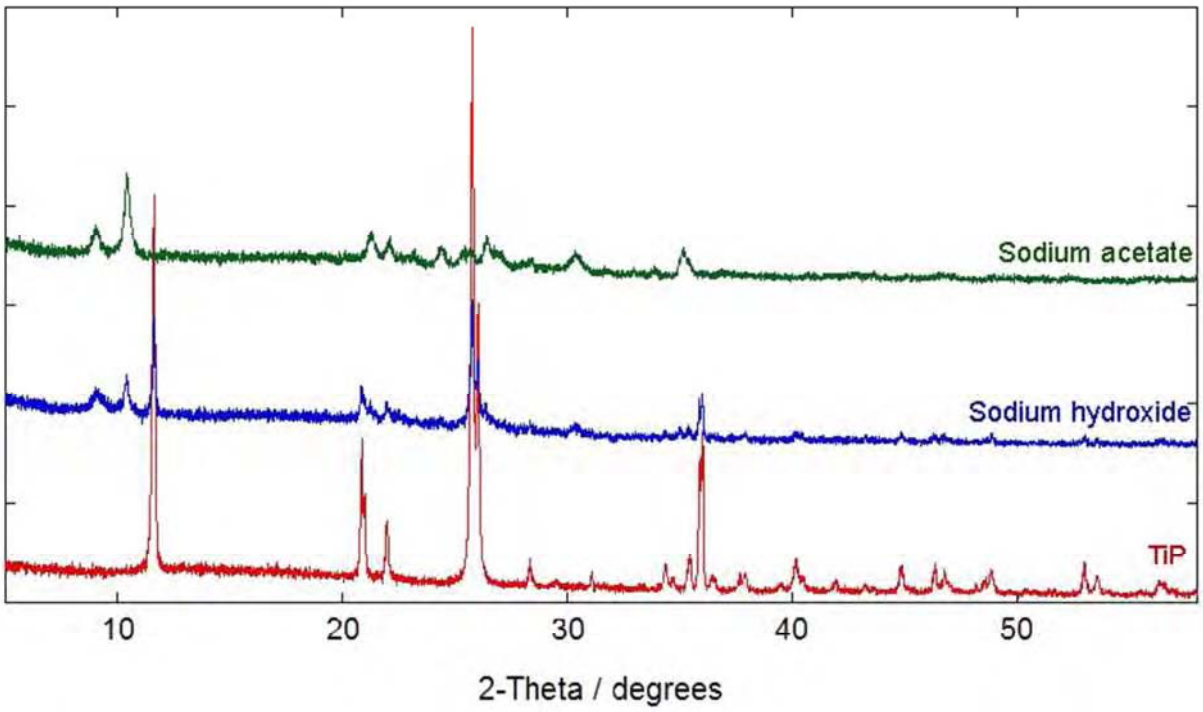

Figure 4.36: Comparison of the sodium exchanged α-TiP products.

4.1.2.6 Mixed Metal Titanium-Zirconium Phosphate Sodium Ion Exchange

The single phase mixed titanium-zirconium phosphates were treated with 0.01 M sodium hydroxide solutions. The PXRD patterns of the products and those from the Ti and Zr end members are given in Figure 4.37. The interlayer spacing of the products based on the first peaks in the pattern are given in Table 4.2 and the sodium contents as determined from XRF analysis are given in Table 4.3.

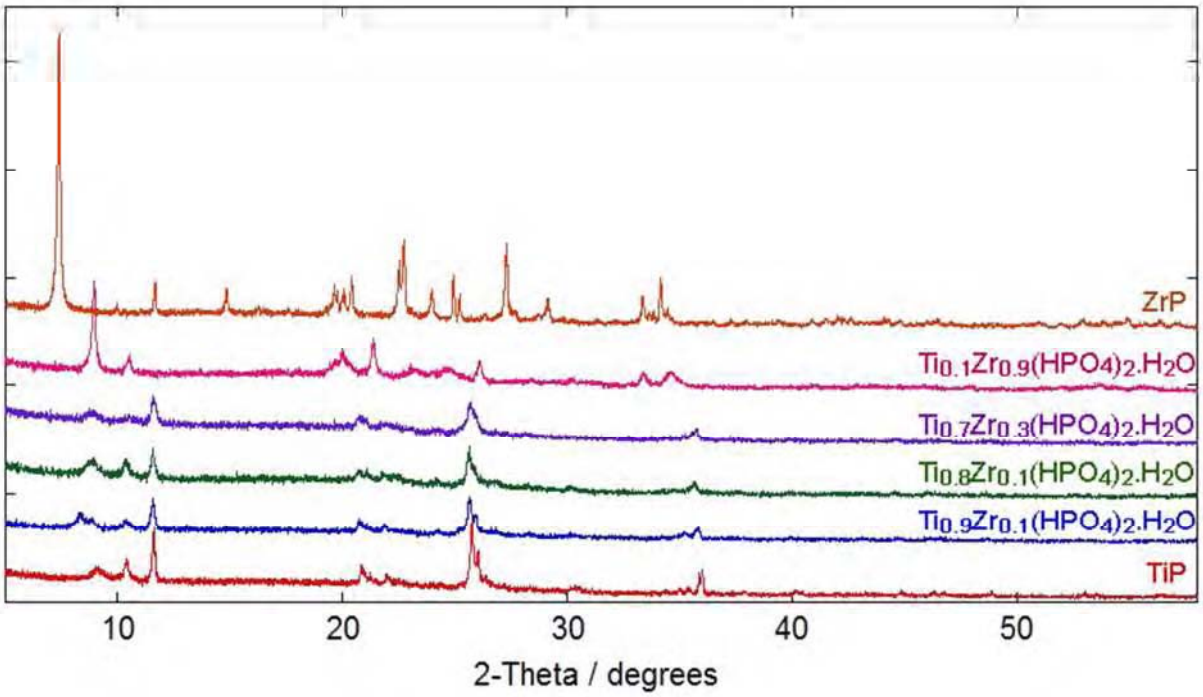

Figure 4.37: PXRD patterns of the titanium-zirconium phosphates ion exchanged with sodium hydroxide.

Table 4.2: Interlayer spacing of the phases obtained from the sodium hydroxide exchanged titanium-zirconium phosphates.

Starting Material	Interlayer Spacing of the Products /Å		
	Fully exchanged phase	Half exchanged phase	Unexchanged phase
$Ti(HPO_4)_2.H_2O$	9.8	8.5	7.6
$Ti_{0.9}Zr_{0.1}(HPO_4)_2.H_2O$	10.4	8.5	7.6
$Ti_{0.8}Zr_{0.2}(HPO_4)_2.H_2O$	10.0	8.5	7.6
$Ti_{0.7}Zr_{0.3}(HPO_4)_2.H_2O$	10.0	8.5	7.6
$Ti_{0.1}Zr_{0.9}(HPO_4)_2.H_2O$	10.0	8.4	-
$Zr(HPO_4)_2.H_2O$	-	11.9*	7.6

* this is a pentahydated species hence the larger d-spacing.

Table 4.3: XRF results for the sodium ion exchanged zirconium-titanium products.

Starting material	Moles of sodium per moles of metal in product	
	Hydroxide exchange	Acetate exchange
$Ti(HPO_4)_2.H_2O$	0.74	1.19
$Ti_{0.9}Zr_{0.1}(HPO_4)_2.H_2O$	0.86	0.96
$Ti_{0.8}Zr_{0.2}(HPO_4)_2.H_2O$	0.68	0.82
$Ti_{0.7}Zr_{0.3}(HPO_4)_2.H_2O$	0.62	1.86
$Ti_{0.1}Zr_{0.9}(HPO_4)_2.H_2O$	0.68	0.73
$Zr(HPO_4)_2.H_2O$	0.34	1.42

These results show the ion exchange behaviour of the mixed metal phosphates ($Ti_{0.9}Zr_{0.1}(HPO_4)_2.H_2O$, $Ti_{0.8}Zr_{0.2}(HPO_4)_2.H_2O$, $Ti_{0.7}Zr_{0.3}(HPO_4)_2.H_2O$ and $Ti_{0.1}Zr_{0.9}(HPO_4)_2.H_2O$) in sodium hydroxide solutions to be the same as α-TiP. All products except that from the exchange of $Ti_{0.1}Zr_{0.9}(HPO_4)_2.H_2O$ contain some unexchanged starting material. The XRD patterns also confirm the presence of half and fully exchanged sodium phases which in the absence of further structural information can be tentatively described as $Ti_xZr_{1-x}HNa(PO_4)_2.H_2O$ and $Ti_xZr_{1-x}Na_2(PO_4)_2.3H_2O$ based on those from α-TiP[17] and α-ZrP[31]. The products are also shown to have similar sodium contents to the α-TiP exchanged products. Although the presence of zirconium within the α-TiP framework is shown to have little effect, it should be noted that the quality of the patterns and degree of crystallinity is poor and that higher quality data is required for further analysis of all the exchanged products.

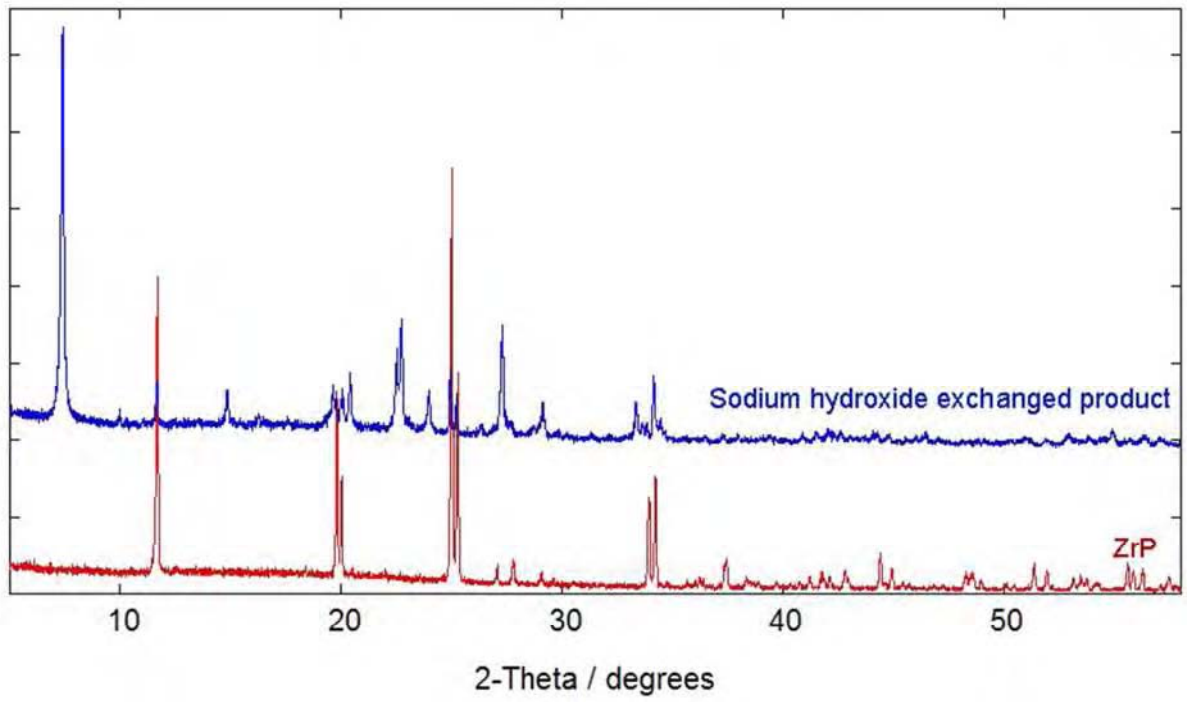

Figure 4.38: Laboratory PXRD pattern of the product obtained from the exchange of $Zr(HPO_4)_2.H_2O$.

The pattern obtained from the α-ZrP exchange is more crystalline and shows the presence of the half exchanged pentahydrate phase; $ZrHNa(PO_4)_2.5H_2O$[31] with an interlayer spacing of 11.9 Å. The extra water present in this species is responsible for the increased d-spacing of this phase compared to the other half exchanged phases discussed previously. The pattern also appears to contain some peaks corresponding to unexchanged α-ZrP (see Figure 4.38). The XRF results show a much lower sodium content than the other products which is in keeping with the absence of a fully exchanged phase. Based on previous work[16], higher loadings of sodium are required to obtain the fully exchanged phase ($ZrNa_2(PO_4)_2.3H_2O$). Unlike α-TiP and the mixed metal phosphates, the fully exchanged sodium phase of α-ZrP cannot be obtained from sodium hydroxide solutions under these conditions.

The effect of titanium within the α-ZrP framework appears to affect the degree of hydration of the phases formed. Rather than a pentahydrated half exchanged phase, as seen with α-

ZrP, $Ti_{0.1}Zr_{0.9}(HPO_4)_2.H_2O$ forms a half exchanged phase containing only one molecule of water as per α-TiP and the titanium-rich phosphates. The difference of four water molecules explains the large difference seen in the interlayer spacing of these two half exchanged phases: $ZrHNa(PO_4)_2.5H_2O$ (11.8 Å) and $Ti_{0.1}Zr_{0.9}HNa(PO_4)_2.H_2O$ (8.4 Å).

Sodium Acetate Solutions

The PXRD patterns of the products obtained from the exchanges with 0.1 M sodium acetate are given in Figure 4.39. The interlayer spacing of the products based on the first peaks in the patterns are given in Table 4.4 and the sodium contents as determined from XRF analysis were included in Table 4.3.

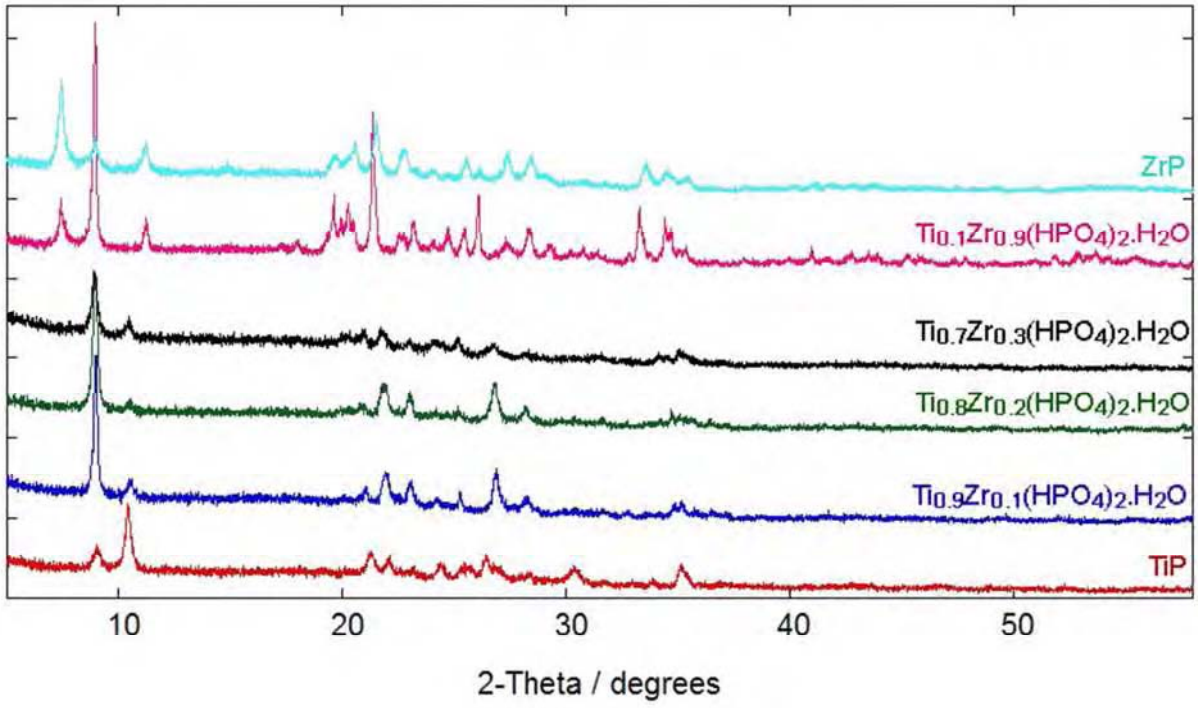

Figure 4.39: Laboratory PXRD patterns of the titanium-zirconium phosphates ion exchanged with sodium hydroxide.

Table 4.4: Interlayer spacing of the sodium acetate exchanged titanium-zirconium phosphates.

Starting Material	Interlayer Spacing of the Products /Å	
	Fully exchanged phases	Half exchanged phases
$Ti(HPO_4)_2.H_2O$	9.8	8.5
$Ti_{0.9}Zr_{0.1}(HPO_4)_2.H_2O$	9.8	8.5
$Ti_{0.8}Zr_{0.2}(HPO_4)_2.H_2O$	9.8	8.5
$Ti_{0.7}Zr_{0.3}(HPO_4)_2.H_2O$	9.8	8.5
$Ti_{0.1}Zr_{0.9}(HPO_4)_2.H_2O$	9.9	11.9* & 8.4
$Zr(HPO_4)_2.H_2O$	9.9	11.9* & 8.2

* pentahydrates hence larger interlayer spacings.

The patterns for the titanium-rich phosphates ($Ti_{0.9}Zr_{0.1}(HPO_4)_2.H_2O$, $Ti_{0.8}Zr_{0.2}(HPO_4)_2.H_2O$ and $Ti_{0.7}Zr_{0.3}(HPO_4)_2.H_2O$) closely resemble that obtained from the exchange with α-TiP. The patterns show no sign of any unexchanged starting materials, but evidence for both the half and fully exchanged phases are present. Variation of the peak intensities indicates a higher percentage of the fully exchanged phases when zirconium is present in the unit cell of the starting material. The variation in the sodium contents seen in the XRF results can only be explained by the bi-phasic nature of these products.

In contrast to the sodium hydroxide exchanges, the PXRD patterns obtained from the sodium acetate exchanges of the zirconium-rich products, $Ti_{0.1}Zr_{0.9}(HPO_4)_2.H_2O$ and α-ZrP, are very similar to each other. As per the titanium-rich phosphates, both products are shown to contain the mono and disodium phases with interlayer spacings of ~8.4 and 9.9 Å respectively. In addition to this, these products also contain a second half exchanged phase – the pentahydrated $MHNa(PO_4)_2.5H_2O$ with an interlayer spacing of 11.9 Å. As mentioned previously the increased d-spacing of this product results from the increased water content. The coexistence of exchanged phases with differing degrees of hydration is not uncommon for ZrP[16,31]. The additional presence of $ZrHNa(PO_4)_2.H_2O$ (8.2 Å) and $ZrNa_2(PO_4)_2.3H_2O$ (9.9 Å)

combined with the absence of unexchanged α-ZrP is reflected in the higher sodium content observed in this product compared with that from the sodium hydroxide exchange.

Based on these initial results the presence of titanium in α-ZrP does not appear to have a significant effect on the exchange behaviour under these conditions. The only noteworthy differences pertain to the lower sodium contents and crystallinity of the $Ti_{0.1}Zr_{0.9}(HPO_4)_2.H_2O$ product, however these observations may be explained by the differing quantities of the phases present. Higher quality data and further analysis of the products are required to investigate this further.

These results have demonstrated that α-TiP and α-ZrP exhibit slightly different ion exchange behaviour towards sodium acetate with different products forming. The mixed metal phosphates show ion exchange behaviour similar to the end member they are compositionally closest too.

4.1.2.7 Competitive Sodium Ion Exchange

As the PXRD patterns obtained from the sodium ion exchange of the zirconium-rich and titanium-rich phosphates were different it was possible to use XRD to study competitive sodium exchanges. Equal amounts of two phosphates e.g. α-TiP and α-ZrP, were treated with enough sodium solution to enable one full exchange. The solid products recovered were analysed by PXRD to determine if either phosphate had a stronger affinity for sodium.

4.1.2.7.1 α-TiP vs α-ZrP

The PXRD pattern of the product obtained when α-TiP and α-ZrP were exposed to a 0.01 M sodium hydroxide solution overnight is shown in Figure 4.40. For comparison the patterns of both pure and sodium exchanged α-TiP and α-ZrP are also shown. There is no evidence of either of the sodium-exchanged α-ZrP or α-TiP products within the pattern. Instead the product appears to be a mixture of the two starting materials. In support of this the XRF results indicated almost negligible quantities of sodium (0.03 moles per mole of metal). It is not fully understood why both phosphates readily ion exchange with sodium but not when in the presence of the other. As this result is so unexpected the experiment should be repeated to assess the reproducibility of this result before further conclusions are drawn.

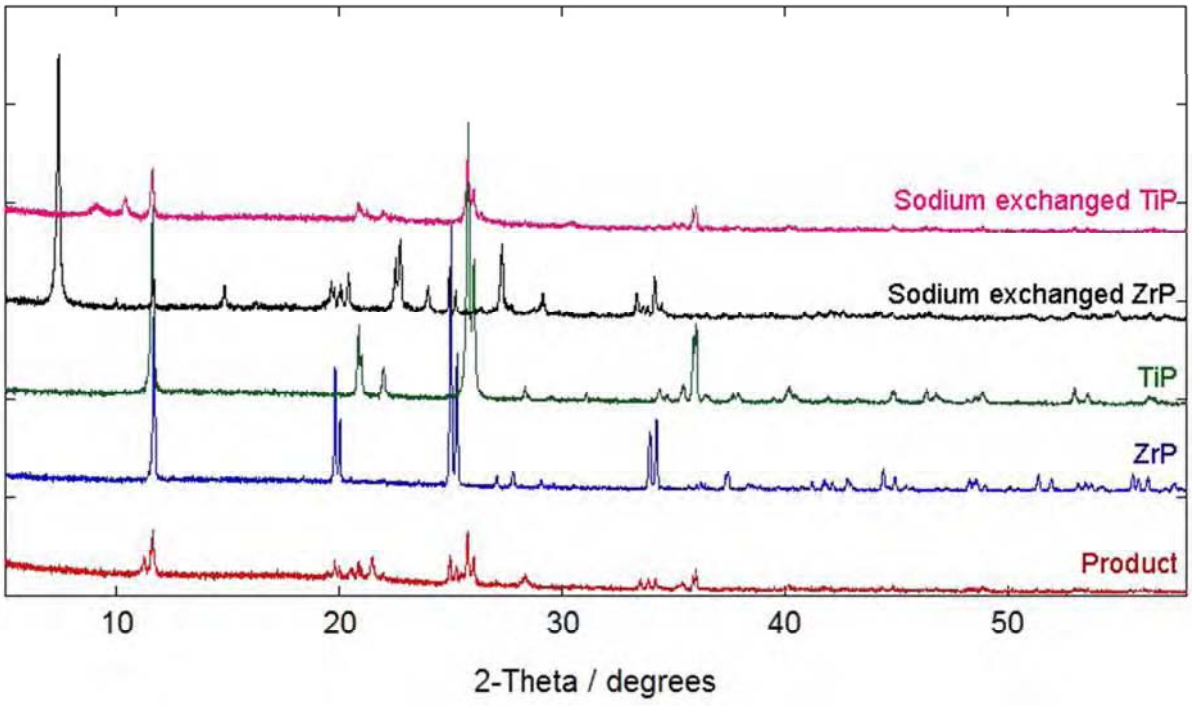

Figure 4.40: Laboratory PXRD results from the α-ZrP vs α-TiP competitive sodium exchange.

4.1.2.7.2 α-TiP vs α-$Ti_{0.1}Zr_{0.9}(HPO_4)_2.H_2O$

The same experiment was run using $Ti_{0.1}Zr_{0.9}(HPO_4)_2.H_2O$ instead of α-ZrP, to see if the presence of titanium within the α-ZrP framework would have an effect on its affinity for sodium ions. The PXRD pattern of the product obtained is presented in Figure 4.41. The results are not as easy to interpret given the low crystallinity of the product. There is no clear evidence of any peaks corresponding to α-TiP. The first peak displayed at ~ 7.5° 2θ corresponds to a phase with an interlayer spacing of 11.8 Å. This is consistent with the presence of half exchanged $Zr_{0.9}Ti_{0.1}HNa(PO_4)_2.5H_2O$. It remains unclear whether the other phases present are unexchanged $Ti_{0.1}Zr_{0.9}(HPO_4)_2.H_2O$ or sodium exchanged α-TiP phases. What is interesting to note is that the half exchanged phase of $Ti_{0.1}Zr_{0.9}(HPO_4)_2.H_2O$ was not observed when α-TiP was absent from the experiment. It therefore appears that the presence of α-TiP competing for the sodium ions results in a sodium deficiency for the formation of the fully exchanged phase that is normally obtained. The XRF results show the presence of 1.17 moles of sodium per metal in the product however there is not a significant reduction in the quantity of titanium compared with the starting materials. This further supports the idea of the presence of sodium exchanged α-TiP phases.

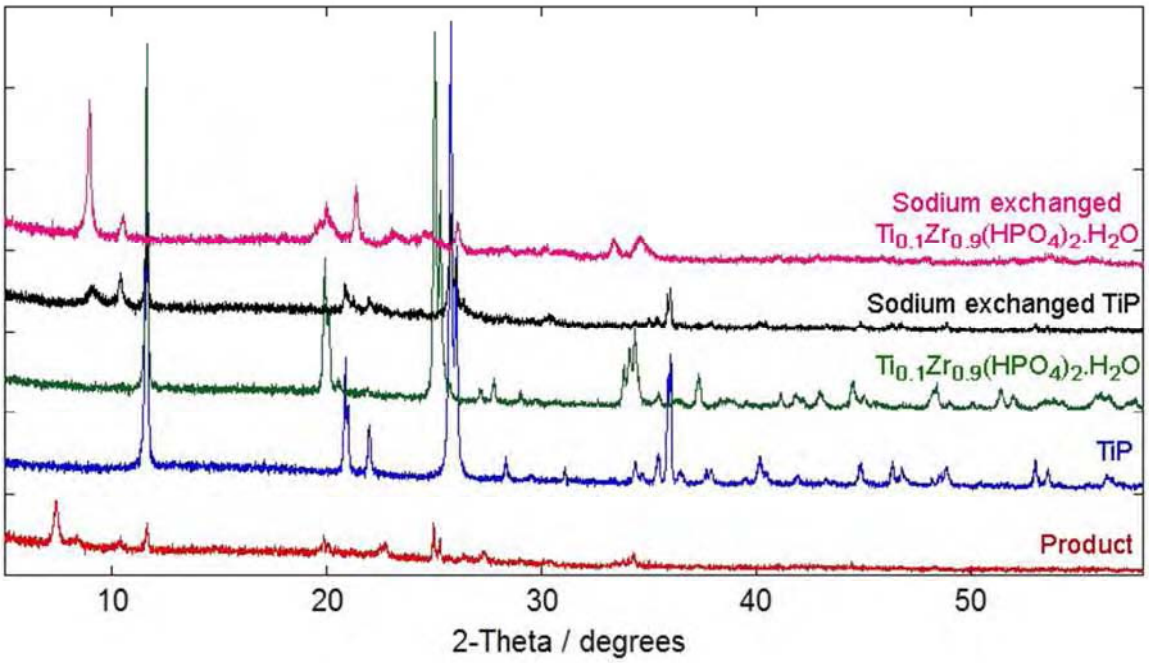

Figure 4.41: Laboratory PXRD results from the α-TiP vs α-$Ti_{0.1}Zr_{0.9}(HPO_4)_2.H_2O$ competitive sodium exchange.

4.1.2.7.3 α-ZrP vs α-$Ti_{0.7}Zr_{0.3}(HPO_4)_2.H_2O$

Similar experiments were run using samples of α-ZrP and $Ti_{0.7}Zr_{0.3}(HPO_4)_2.H_2O$ to see if the presence of zirconium in the α-TiP framework had any effect on the affinity for sodium. The PXRD pattern of the product obtained when the phosphates were treated with sodium hydroxide is shown in Figure 4.42. The results indicate that both α-ZrP and $Ti_{0.7}Zr_{0.3}(HPO_4)_2.H_2O$ underwent sodium ion exchange.

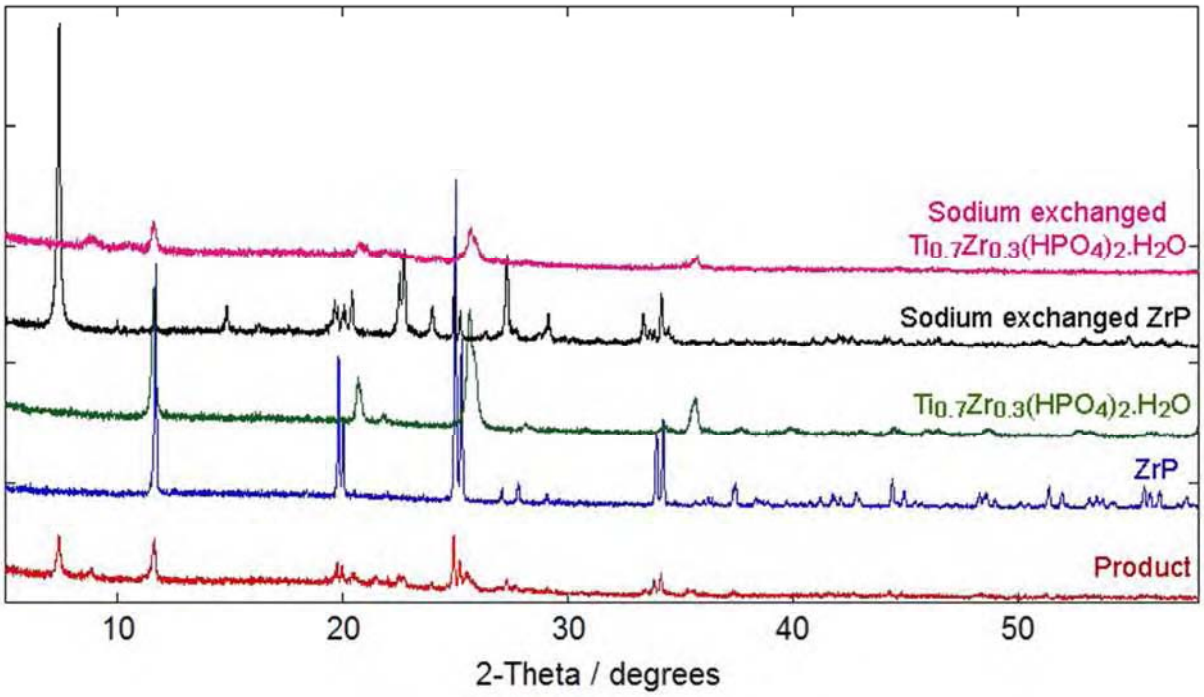

Figure 4.42: Laboratory PXRD results from the α-ZrP vs α-$Ti_{0.7}Zr_{0.3}(HPO_4)_2.H_2O$ competitive sodium hydroxide exchange.

The PXRD pattern of the product obtained when sodium acetate was used instead are shown in Figure 4.43. The results are slightly ambiguous given the low crystallinity of the product. There is no visual evidence of α-ZrP in the product but peaks corresponding to $Ti_{0.7}Zr_{0.3}(HPO_4)_2.H_2O$ are observed. It is therefore hypothesised that the product also contains some sodium exchanged α-ZrP, which would suggest that α-ZrP has the greater affinity for sodium in sodium acetate solutions. However this cannot be confirmed without further analysis.

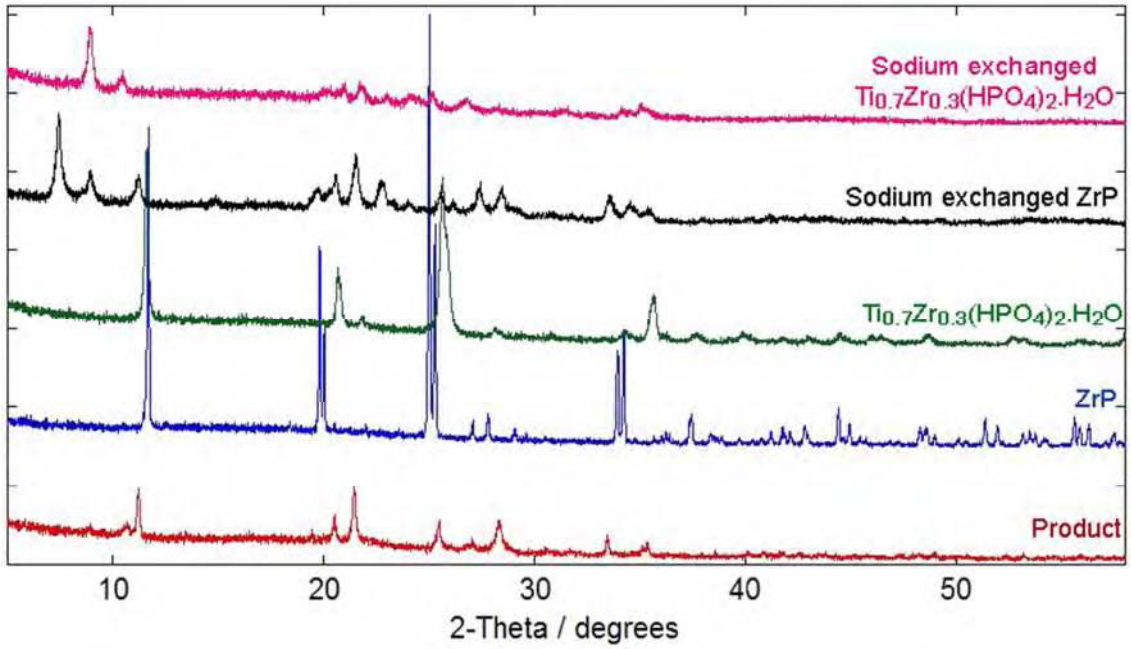

Figure 4.43: Laboratory PXRD results from the α-ZrP vs α-$Ti_{0.7}Zr_{0.3}(HPO_4)_2.H_2O$ competitive sodium acetate exchange.

4.1.2.8 Step-wise Ion Exchanges

In these studies, the sodium exchanged phosphates were treated with various caesium / cobalt 0.01 M solutions at room temperature overnight. It was hoped that the larger interlayer distances of the starting materials would lead to exchange of these cations. The solid products recovered were analysed by XRD and XRF.

4.1.2.8.1 Caesium Exchanges

Caesium exchanges on sodium-TiP

The experiments were run on sodium acetate exchanged α-TiP as this product was not believed to contain any unexchanged α-TiP.

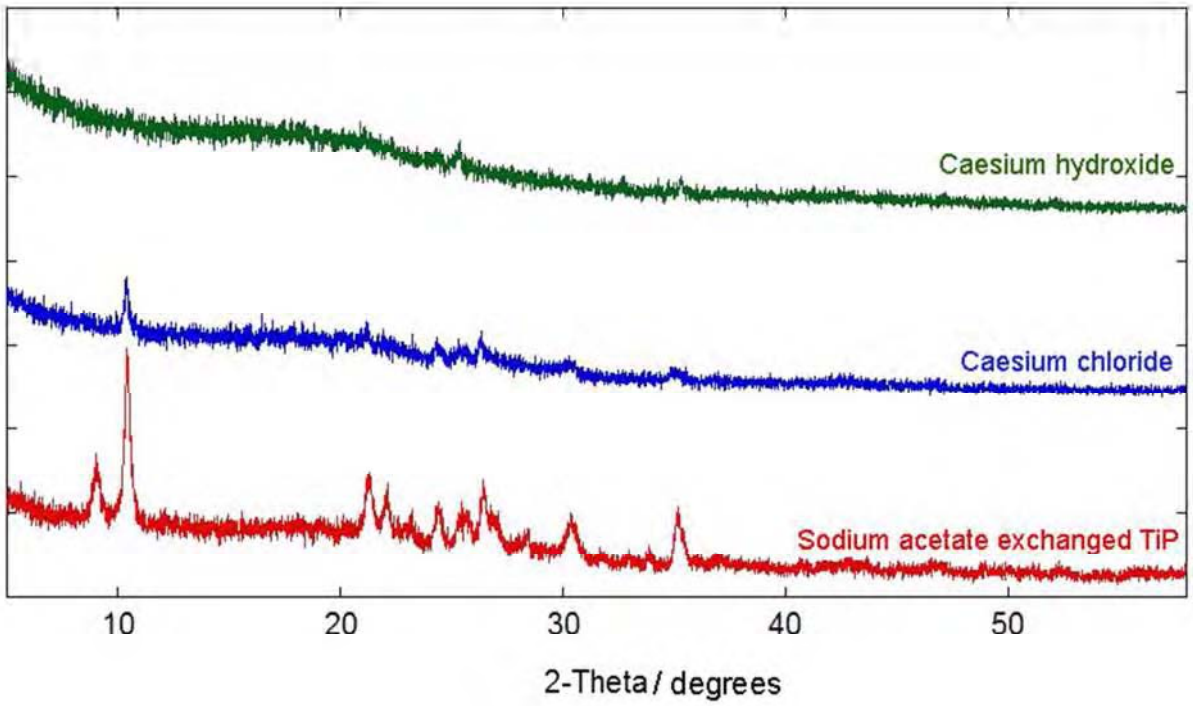

Figure 4.44: Laboratory PXRD patterns of the step wise caesium exchanges on sodium-acetate exchanged α-TiP.

The starting material was destroyed by both the caesium acetate and nitrate solutions which led to no solid products being obtained. The PXRD patterns of the products from the other exchanges are shown in Figure 4.44. Caesium chloride exchange does not appear to have been successful as the peaks present correspond to those in the starting material. As a high background is observed the presence of an additional amorphous product is likely. The product obtained from the exchange with caesium hydroxide was amorphous in nature and could not be analysed further from the XRD data. For both of these products, further investigation via PDF and/or XRF is required to determine if any caesium exchanged phases were obtained.

Caesium exchanges on sodium-ZrP

The PXRD patterns of the products obtained from the exchanges with sodium acetate-ZrP are given in Figure 4.45. Relevant XRF data is provided in Table 4.5.

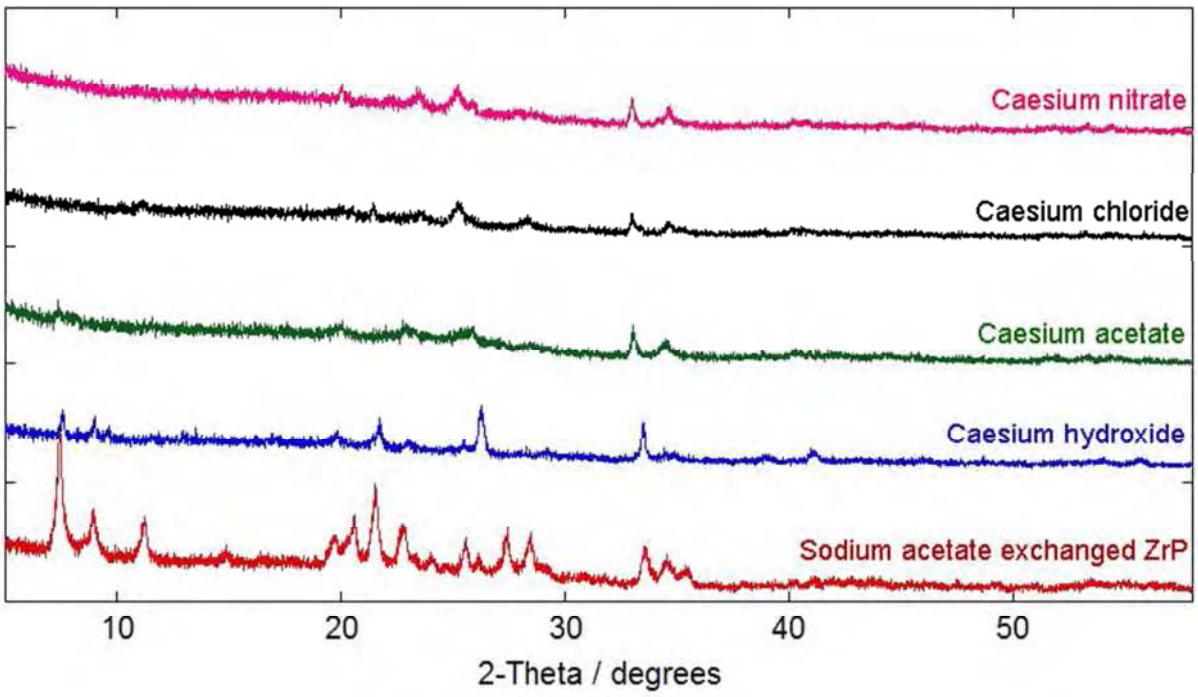

Figure 4.45: Laboratory PXRD patterns of the step wise caesium exchanges on sodium-acetate exchanged ZrP.

Table 4.5: XRF results of the products obtained from the step wise caesium exchanges on sodium-acetate exchanged ZrP.

Exchange solution	Moles of sodium per metal in the starting material	Moles of sodium per metal in the product	Moles of caesium per metal in the product
Caesium hydroxide	1.42	0.44	0.85
Caesium nitrate	1.42	0.18	0.77
Caesium acetate	1.42	0.22	0.57

The exchanges appear to have been successful owing to the presence of caesium detected by the XRF measurements. However the poor quality of the XRD data renders further

characterisation difficult however similar patterns appear to have been obtained from the exchanges, along with significant lowering of the sodium contents.

These initial results suggest that caesium exchange maybe possible through this method and that sodium may leach back out when in contact with most caesium solutions. Sodium-ZrP appears to be a better 'stepping-stone' for caesium exchange than the strontium-ZrP discussed previously. These results cannot be compared to the caesium exchange of pure α-ZrP as this was not investigated in this work.

4.1.2.8.2 Cobalt Exchanges

Cobalt exchanges of sodium exchanged TiP

The PXRD patterns of the products obtained from the cobalt exchanges on sodium acetate-TiP are given in Figure 4.46. XRF data is provided in Table 4.6.

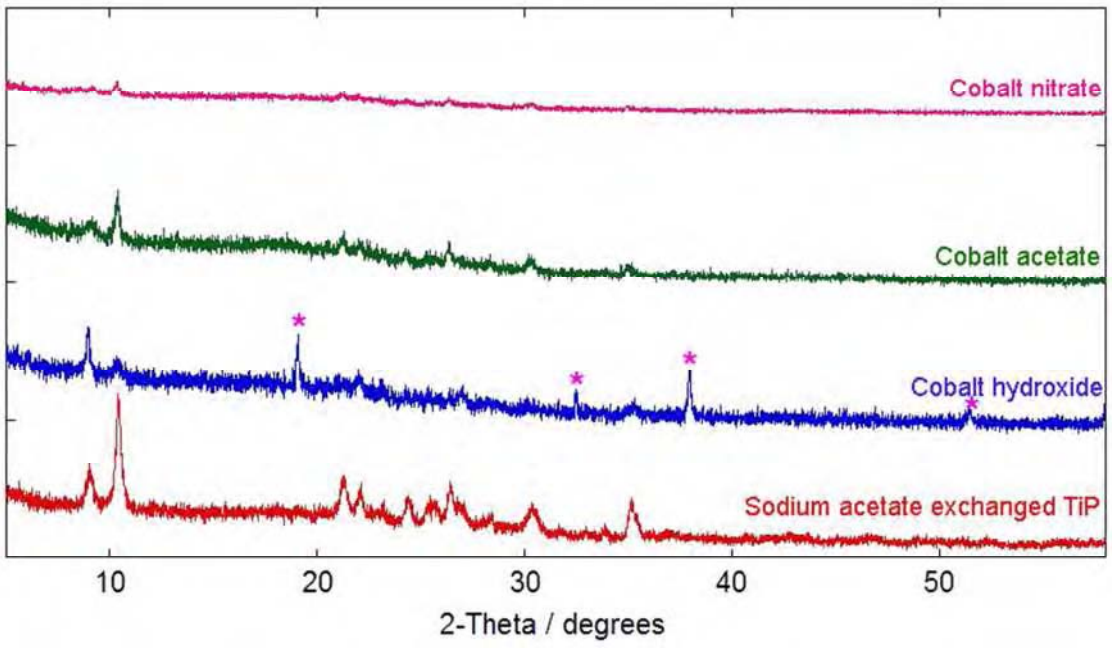

Figure 4.46: PXRD patterns of the step wise cobalt exchanges on sodium-acetate exchanged TiP. The asterisks denote peaks corresponding to β-$Co(OH)_2$ (JCPDS ICDD 30-443).

Table 4.6: XRF results from the cobalt exchanged products

Exchange solution	Moles of sodium per metal in the starting material	Moles of sodium per metal in the product	Moles of cobalt per metal in the product
Cobalt hydroxide	1.19	1.15	0.67

These results show that the cobalt exchanges were unsuccessful. The patterns correspond to less crystalline versions of the starting materials ($TiHNa(PO_4)_2.H_2O$ and $TiNa_2(PO_4)_2.3H_2O$). The cobalt hydroxide product contains β-$Co(OH)_2$ impurities which explains the large cobalt presence. The variation seen in the relative peak intensities of the exchanged products results from the two-phase starting material.

Cobalt exchanges of sodium exchanged ZrP

The PXRD patterns of the products obtained from the cobalt exchanges of sodium acetate exchanged ZrP are given in Figure 4.47. XRF data is provided in Table 4.7.

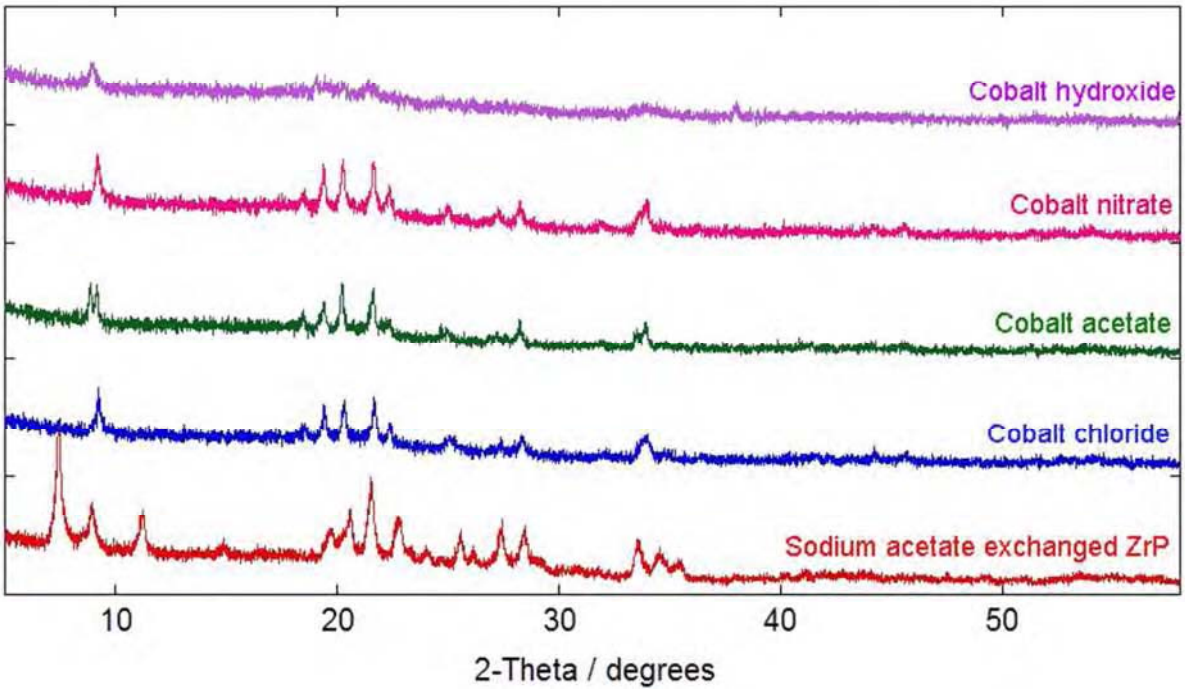

Figure 4.47: Laboratory PXRD patterns of the step wise cobalt exchanges on sodium-acetate exchanged ZrP.

Table 4.7: XRF results from the cobalt exchanged products

Exchange solution	Moles of sodium per metal in the starting material	Moles of sodium per metal in the product	Moles of cobalt per metal in the product
Cobalt hydroxide	1.19	0.61	0.62
Cobalt nitrate	1.19	0.70	0.35

The patterns produced resemble that of $ZrNa_2(PO_4)_2.3H_2O$ present in the starting material, regardless of the cobalt solution used. The absence of peaks corresponding to the other half exchanged phases in the starting material; $ZrHNa(PO_4)_2.5H_2O$ (interlayer spacing of 11.8 Å) and $ZrHNa(PO_4)_2.H_2O$ (interlayer spacing of 8.2 Å) suggests that cobalt exchange causes the breakdown of these phases to form cobalt based amorphous products. These results therefore show $ZrNa_2(PO_4)_2.3H_2O$ to be more stable towards cobalt than the half exchanged phases.

4.2 Ion Exchange of α-GeP and the Mixed Germanium-Titanium Phosphates

4.2.1 Introduction

The ion exchange of germanium phosphate and some germanium-titanium phosphates is investigated and the results analysed. There are no previous ion exchange reports for α-GeP.

4.2.2 Results and Discussion

4.2.2.1 α-GeP Strontium Ion Exchange

Samples of α-GeP were treated with various strontium solutions at room temperature overnight and the solid products recovered were analysed by XRD. Exchanges with strontium chloride, nitrate and acetate solutions were all unsuccessful as shown in Figures 4.48-4.50. In all cases no exchange was observed in the PXRD patterns of the products from the low

concentration solutions. Higher concentrations lead to either no solid products being formed or as with the acetate solutions, the formation of strontium phosphate.

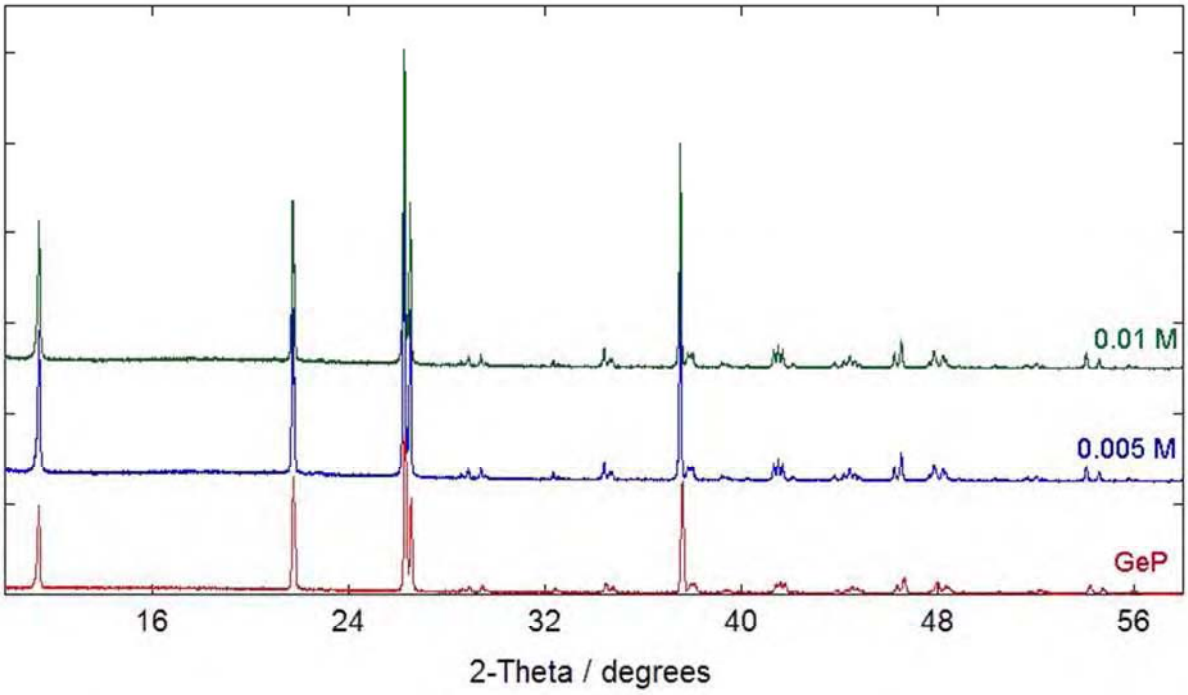

Figure 4.48: Laboratory PXRD patterns from the strontium chloride ion exchanges of α-GeP.

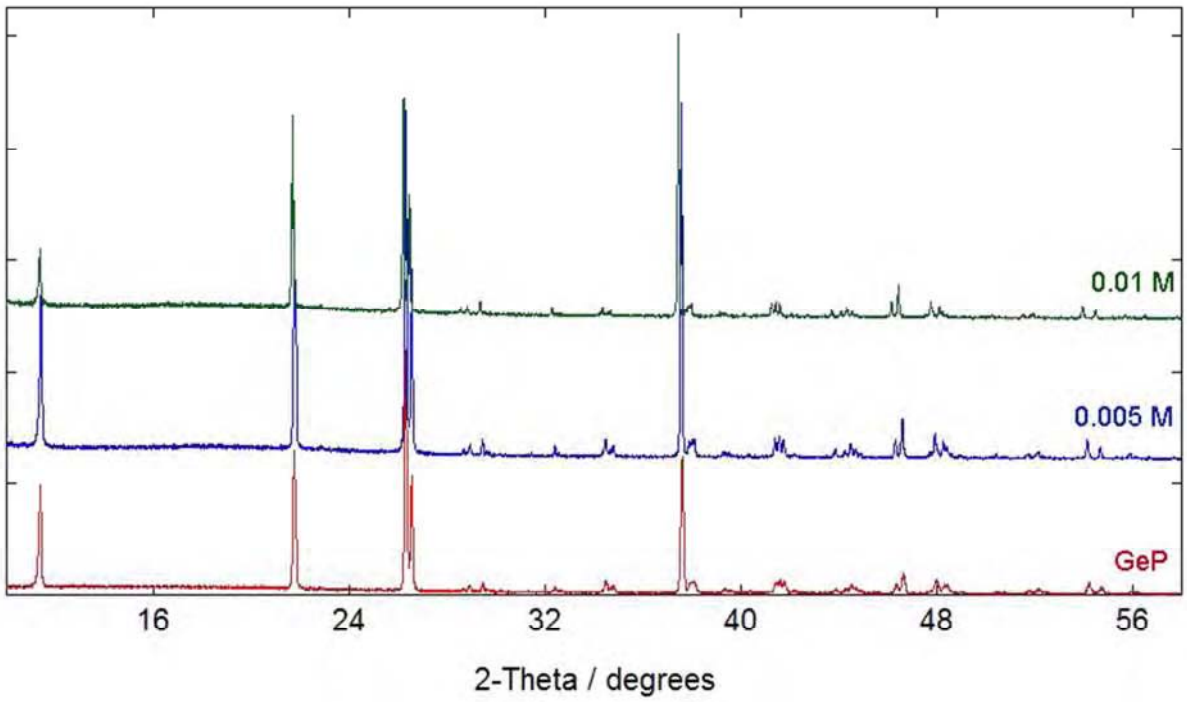

Figure 4.49: Laboratory PXRD patterns from the strontium nitrate ion exchanges of α-GeP.

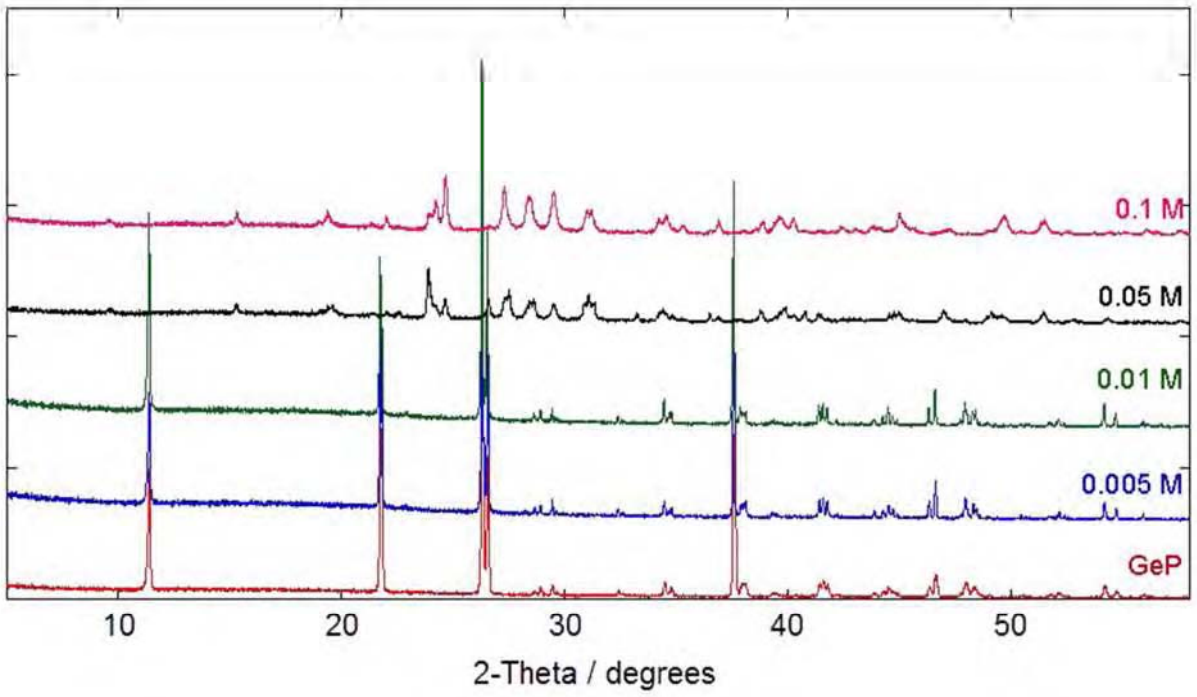

Figure 4.50: Laboratory PXRD patterns from the strontium acetate ion exchanges of α-GeP. The 0.1 M and 0.05 M patterns match to strontium phosphate.

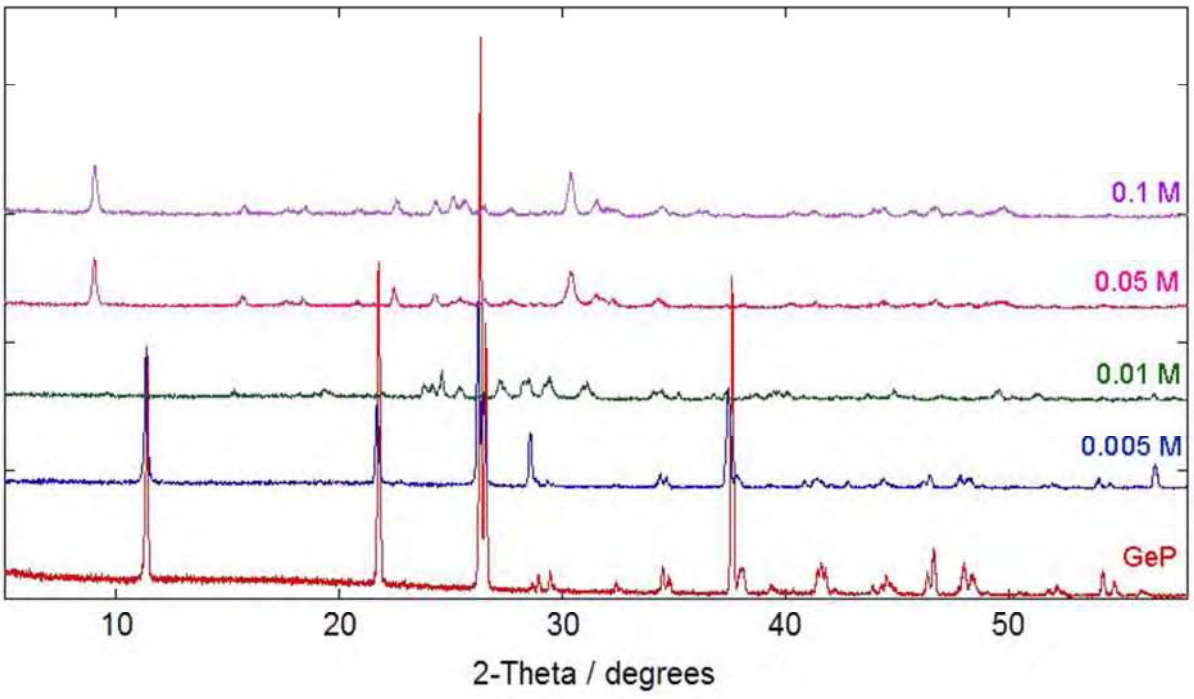

Figure 4.51: Laboratory PXRD patterns from the strontium hydroxide ion exchanges of α-GeP.

The PXRD patterns of the products obtained from the strontium hydroxide exchanges are given in Figure 4.51. Again no exchange is observed with 0.005 M solution; however different PXRD patterns are obtained from the other reactions. No peaks corresponding to the α-GeP starting material is present in the patterns and no identifications could be made using the search and match facilities of the PXRD database. The XRF results showed there to be 3.78 moles of strontium per germanium present in the 0.1 M product. This level is higher than that required for full exchange and alludes to the probability of an alternative product that is not strontium-GeP. In support of this the PDF pattern of the exchanged product bears no resemblance to that of the starting material (or general alpha phosphates) as demonstrated in Figure 4.52.

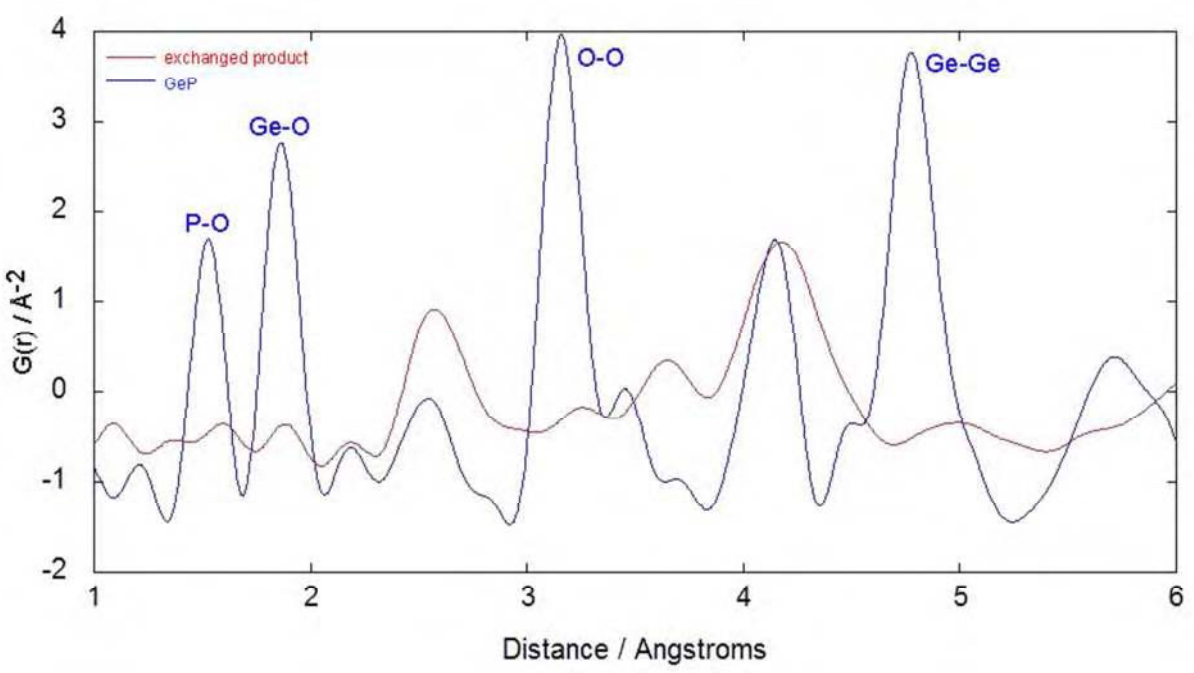

Figure 4.52: Comparison of the PDF patterns of GeP (blue) and the 0.1 M strontium hydroxide exchanged product (red).

The PDF pattern is fairly featureless and does not contain any of the expected peaks for phosphorus-oxygen, germanium-oxygen, oxygen-oxygen and germanium-germanium at the characteristic distances for α-GeP. The TGA trace of the exchanged product is also very different to that seen earlier for α-GeP (Chapter 3). As can be seen in Figure 4.53, the trace contains only one large mass loss of ~ 12 % corresponding to the loss of water over the temperature range 110-150 °C. These results suggest that this product is more likely a strontium-germanium phosphate borne out of the sample breakdown of α-GeP in the strontium solutions. In support of this, dissolving the product in water and heating overnight at 100 °C resulted in the formation of strontium phosphate as shown in Figure 4.54.

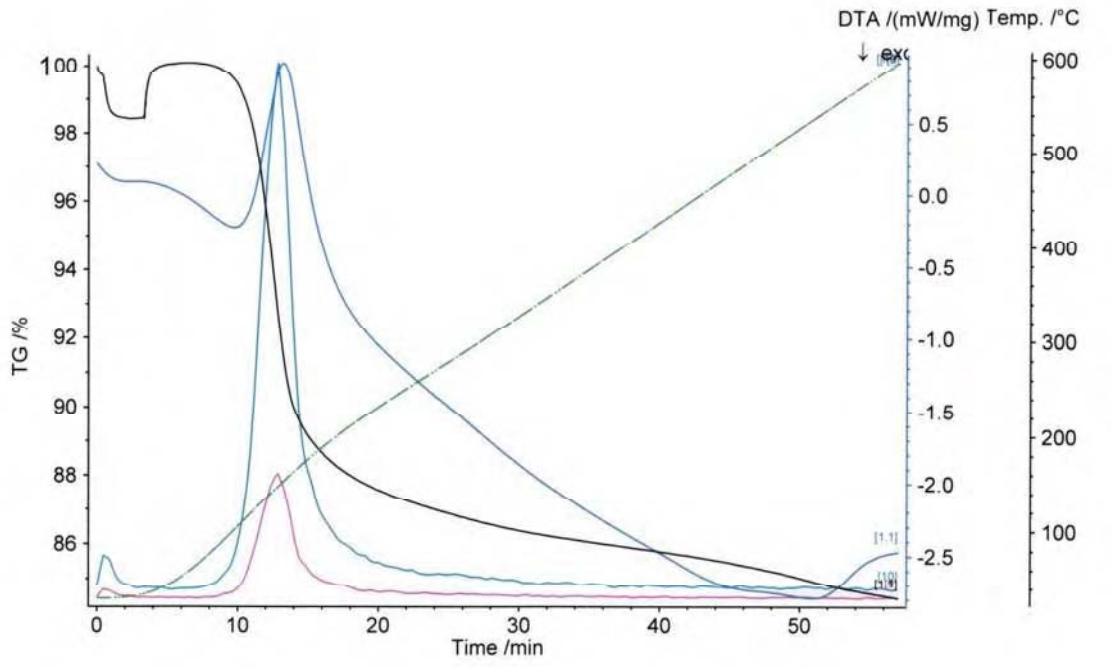

Figure 4.53: TGA trace for the 0.1 M strontium hydroxide exchanged GeP. The TGA trace is shown in black, the DTA in blue, the temperature in green and the mass spectrometry traces for H_2O and OH^+ in green-blue and pink respectively.

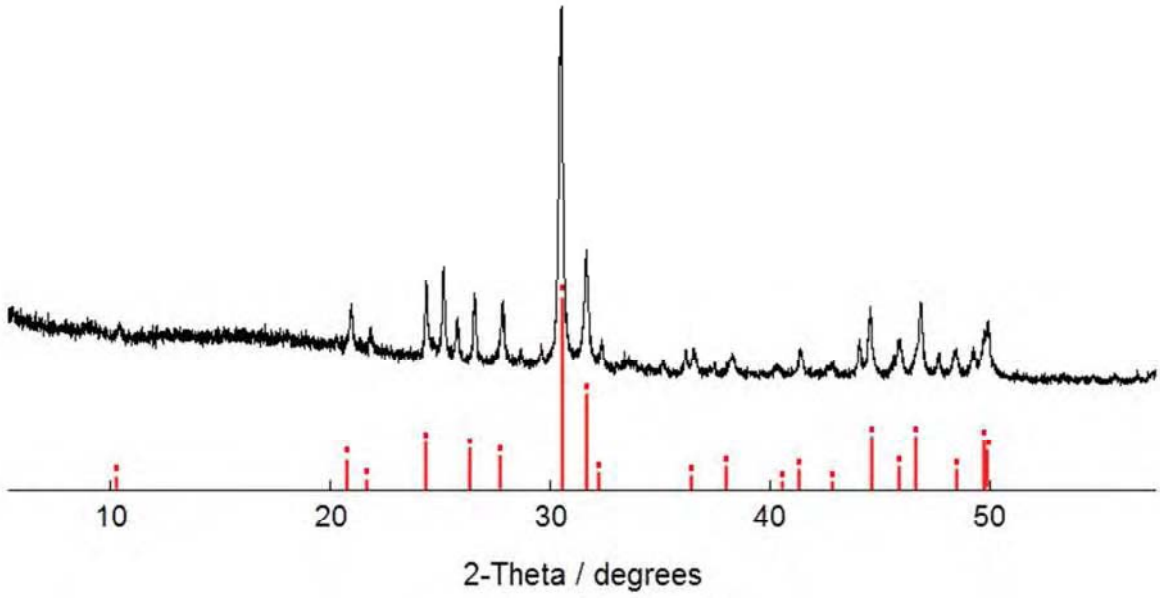

Figure 4.54: Laboratory PXRD pattern of the recrystalised 0.1 M strontium hydroxide exchanged GeP. The red lines are the indexed peaks from ICDD PDF 00-044-0654 for $Sr_{10}O(PO_4)_6$.

4.2.2.2 Strontium Ion Exchange in the Mixed Germanium-Titanium Phosphates

To investigate the effect of the second metal towards ion exchange, samples of $Ti_{0.1}Ge_{0.9}(HPO_4)_2.H_2O$ and $Ti_{0.9}Ge_{0.1}(HPO_4)_2.H_2O$ were treated with 0.01 M strontium hydroxide solutions overnight at room temperature. The PXRD pattern of the product obtained from the exchange of $Ti_{0.9}Ge_{0.1}(HPO_4)_2.H_2O$ is given in Figure 4.55.

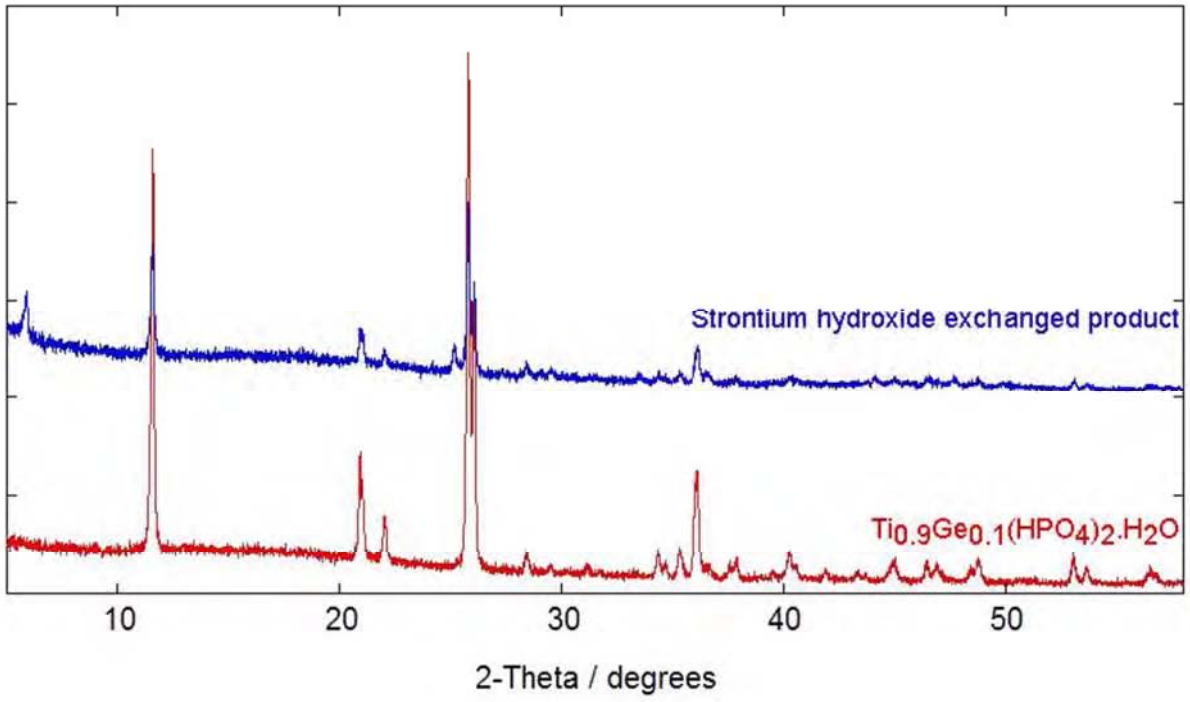

Figure 4.55: Laboratory PXRD pattern of the product obtained from the strontium hydroxide ion exchange of $Ti_{0.9}Ge_{0.1}(HPO_4)_2.H_2O$.

The pattern seen is as for the starting material, but features two additional peaks at ~ 6 and 25 ° 2θ, the first implying that the exchanged product has an interlayer spacing of 14.97 Å. The XRF data gave 0.56 moles of strontium for every mole of metal present. Further work is required to determine whether this is an exchanged product or whether it is the starting material with a similar impurity as was seen in the α-TiP ion exchange.

The PXRD pattern of the product obtained from the exchange of $Ti_{0.1}Ge_{0.9}(HPO_4)_2.H_2O$ is given in Figure 4.56. The pattern is the same as for the starting material which infers that no exchange occurred. This is unlike α-GeP where a strontium-germanium phosphate was believed to have been recovered. Consequently the presence of titanium in α-GeP does have an effect on its ion exchange behaviour and in this case it appears to render the phosphate

more stable towards strontium hydroxide solution. Further work should be carried out to assess the reproducibility of this result and also to determine whether the presence of titanium increases the stability of α-GeP at other concentrations and with other solutions.

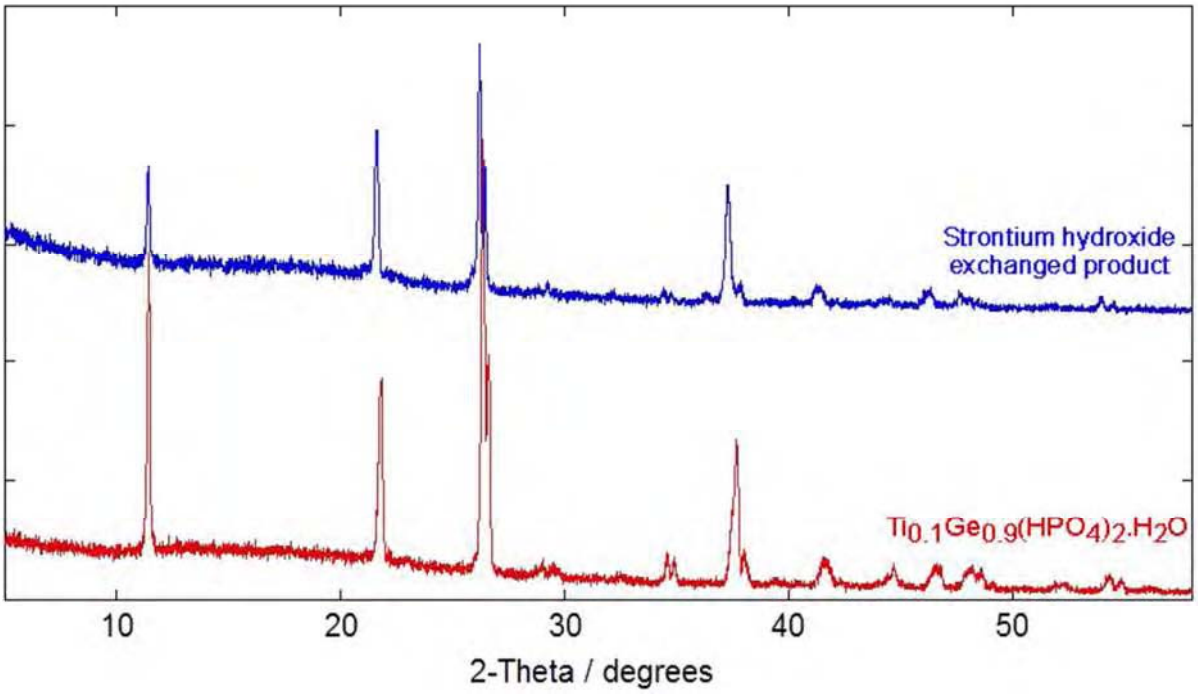

Figure 4.56: Laboratory PXRD pattern of the product obtained from the strontium hydroxide ion exchange of $Ti_{0.1}Ge_{0.9}(HPO_4)_2.H_2O$.

4.2.2.3 α-GeP Cobalt Ion Exchange

Cobalt ion exchanges were attempted on samples of α-GeP using nitrate, chloride, acetate and hydroxide solutions. Solid products were only obtained from the chloride exchanges, however the PXRD patterns (Figure 4.57) show no exchange occurred. There also does not appear to be any amorphous products present. These results suggest that α-GeP is unstable towards most cobalt solutions and that more forceful conditions would lead to further

sample breakdown. A more likely route to cobalt exchange is potentially through the 'step-wise' method.

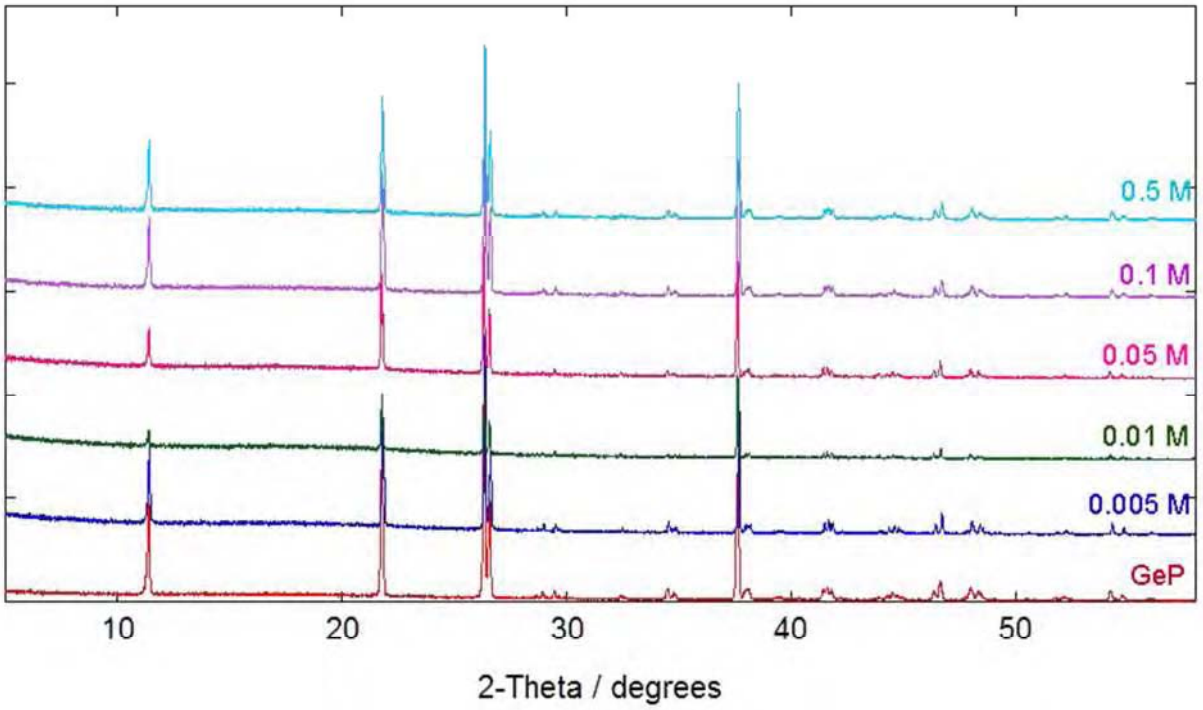

Figure 4.57: Laboratory PXRD patterns of the products obtained from the cobalt chloride ion exchanges.

4.2.2.4 α-GeP Caesium Ion Exchange

No solid products were recovered from the α-GeP exchanges with caesium nitrate or acetate solutions. With the chloride and hydroxide exchanges only the 0.005 M solutions resulted in a solid product. From the PXRD patterns of these, given in Figures 4.58 and 4.59, it is clear that no ion exchange took place. Again the solubility and low stability of α-GeP prevents the ion exchange under these conditions.

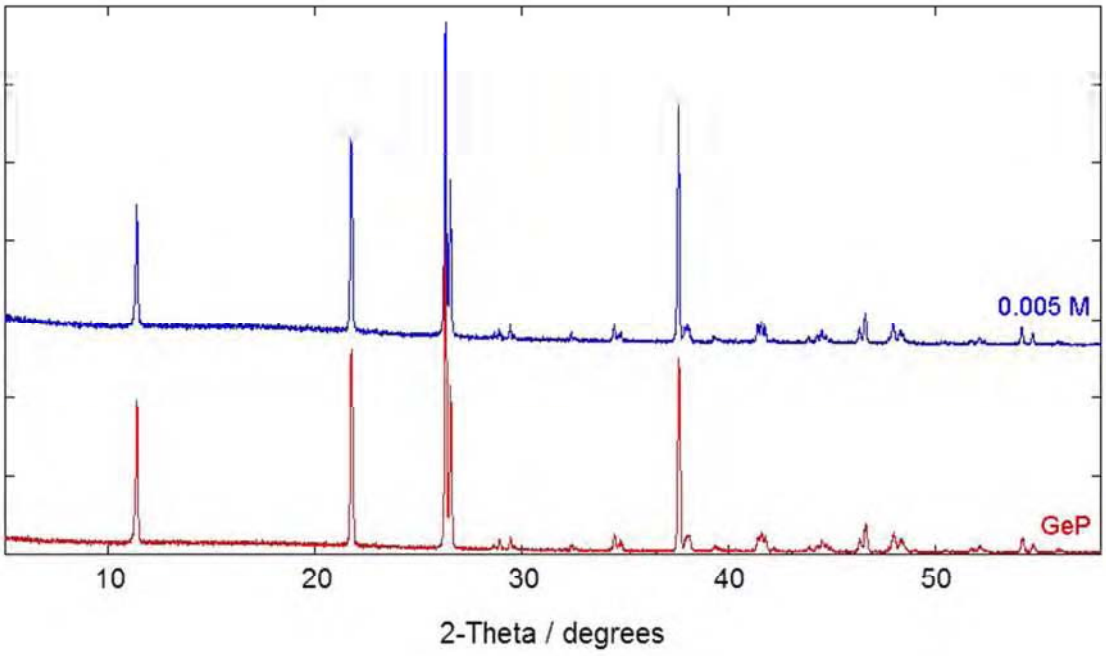

Figure 4.58: Laboratory PXRD patterns of the products obtained from the caesium chloride ion exchanges.

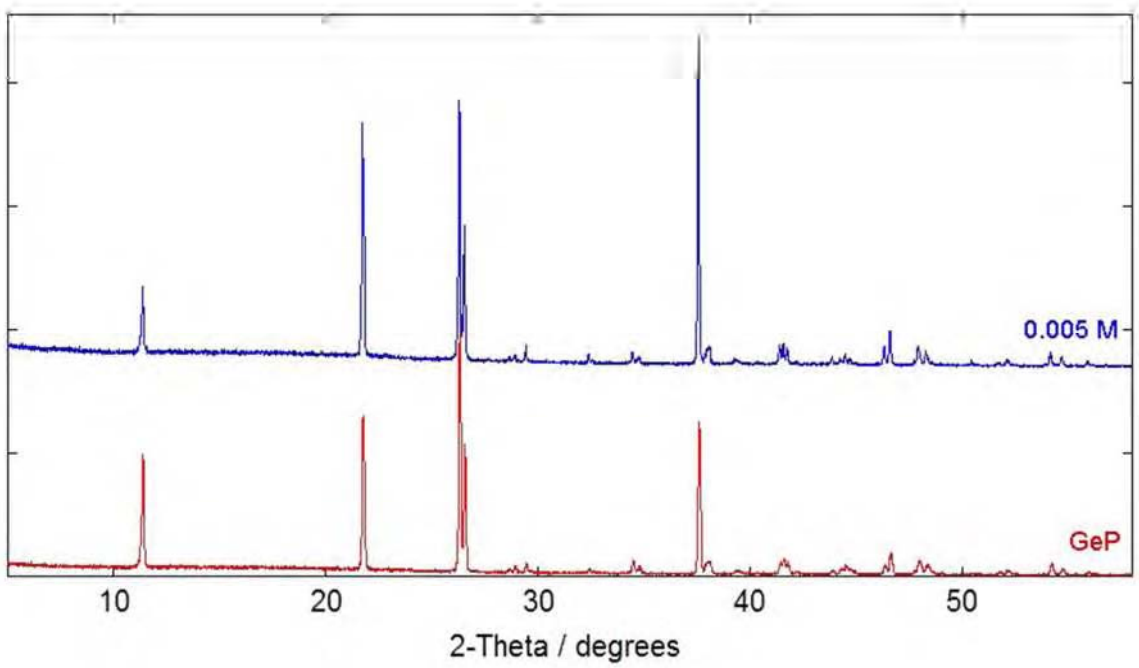

Figure 4.59: Laboratory PXRD patterns of the products obtained from the caesium hydroxide ion exchanges.

4.2.2.5 α-GeP Sodium Ion Exchange

The PXRD patterns of the solid products recovered from the ion exchanges of α-GeP with the sodium solutions are shown in Figures 4.60 – 4.63. Based on these results α-GeP is more stable towards sodium chloride solutions as high concentrations of the others lead to no products being recovered. There is no evidence of exchange in any of the PXRD patterns obtained.

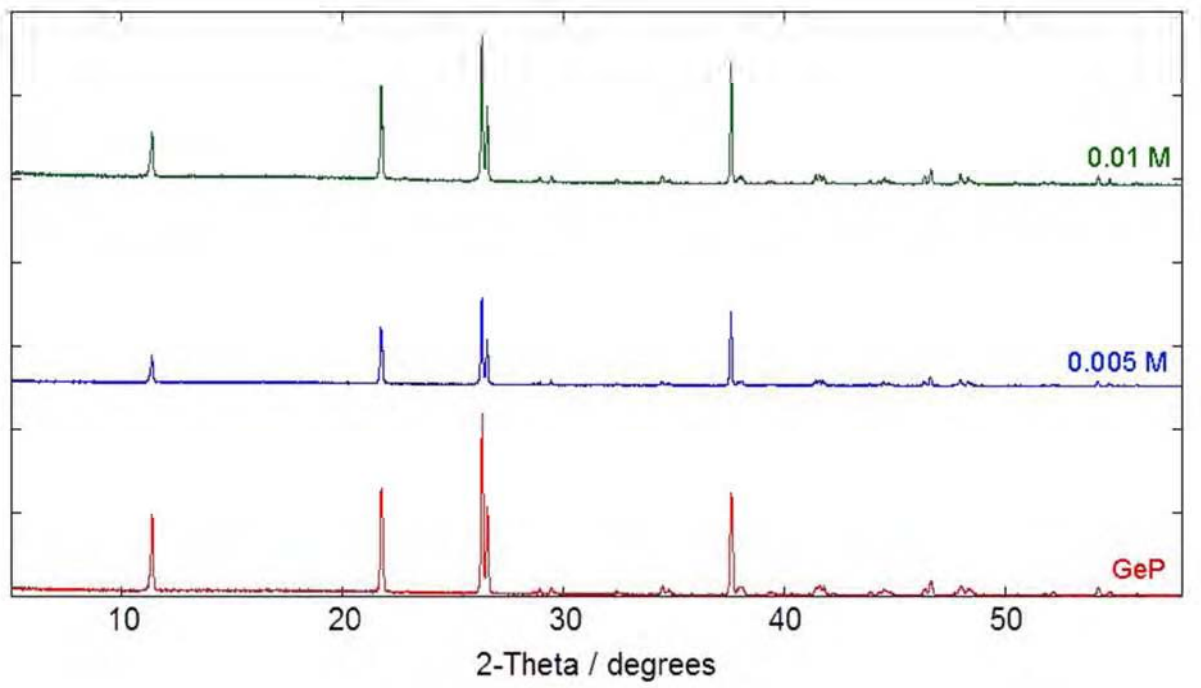

Figure 4.60: Laboratory PXRD patterns of the products obtained from the sodium hydroxide ion exchanges.

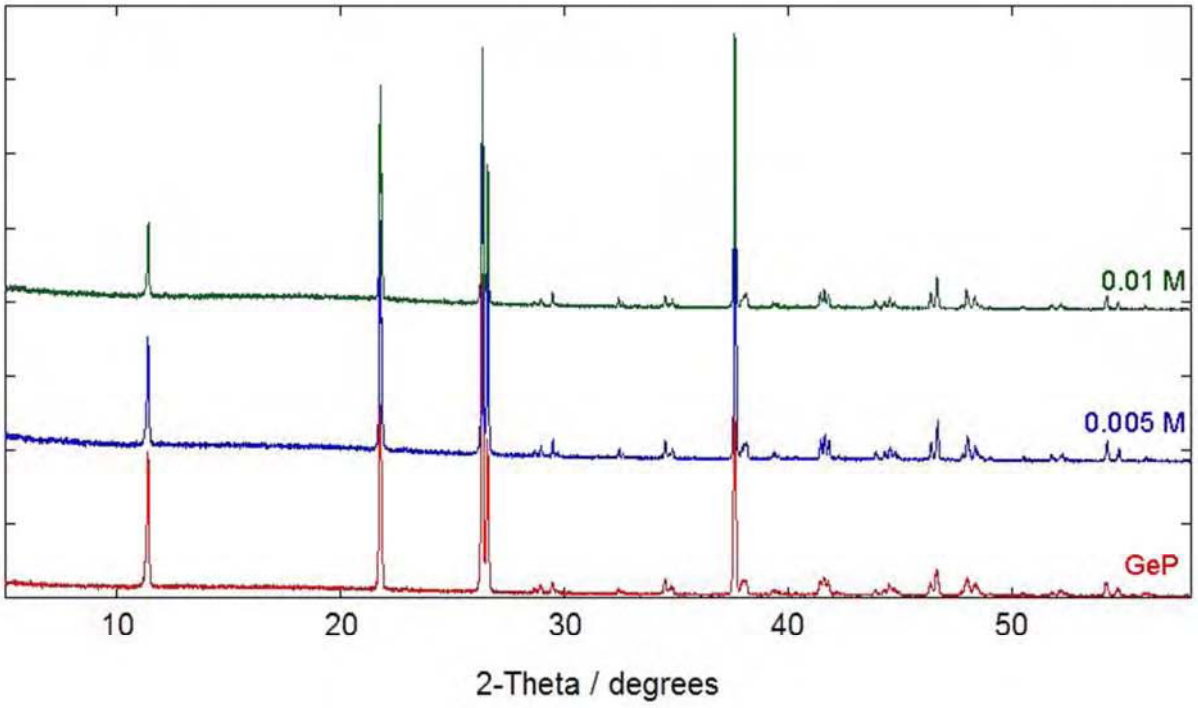

Figure 4.61: Laboratory PXRD patterns of the products obtained from the sodium acetate ion exchanges.

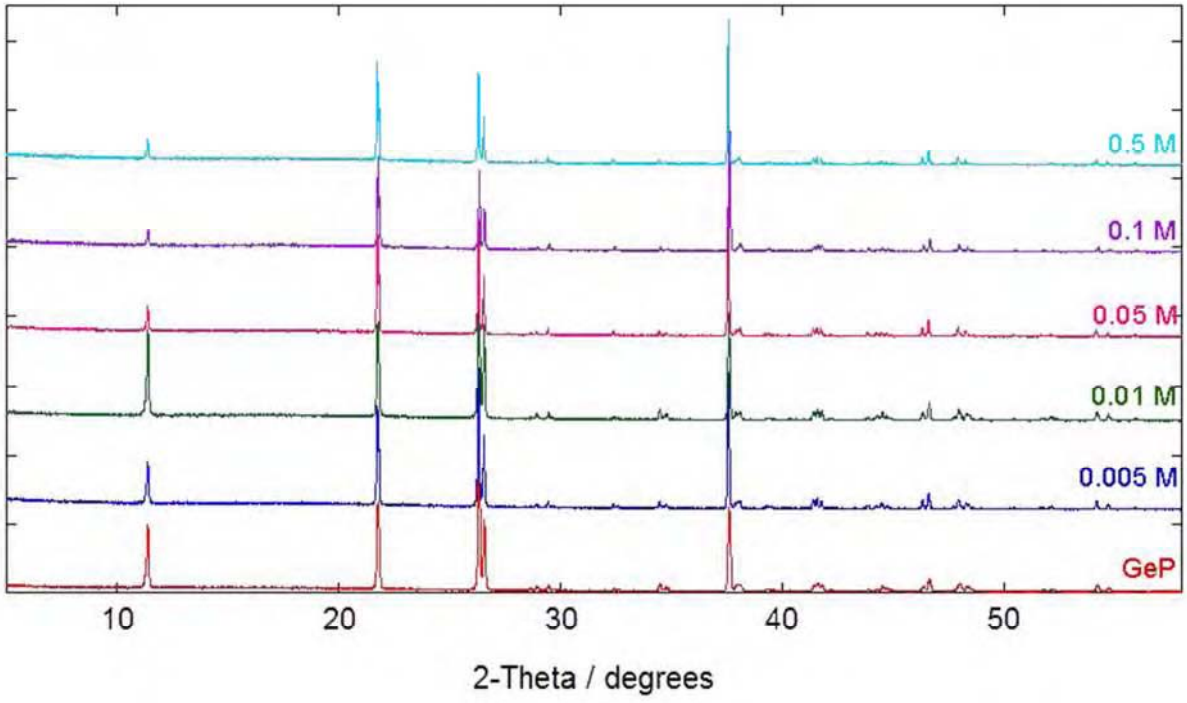

Figure 4.62: Laboratory PXRD patterns of the products obtained from the sodium chloride ion exchanges.

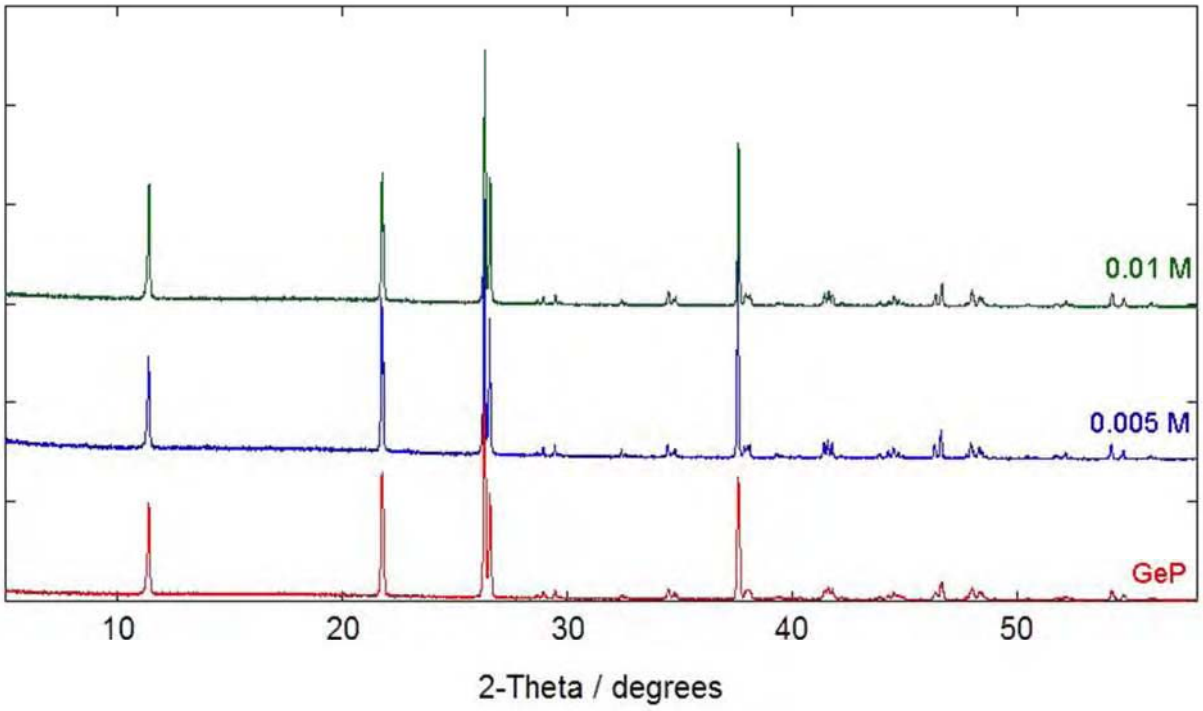

Figure 4.63: Laboratory PXRD patterns of the products obtained from the sodium nitrate ion exchanges.

4.2.2.6 Sodium Ion Exchange in the Mixed Germanium-Titanium Phosphates

Sodium ion exchanges were carried out on two of the mixed germanium-titanium phosphates to investigate the effect of the second metal towards ion exchange. The PXRD patterns of the products obtained from the sodium hydroxide exchanges of $Ti_{0.1}Ge_{0.9}(HPO_4)_2.H_2O$ and $Ti_{0.9}Ge_{0.1}(HPO_4)_2.H_2O$ are given in Figures 4.64 and 4.65.

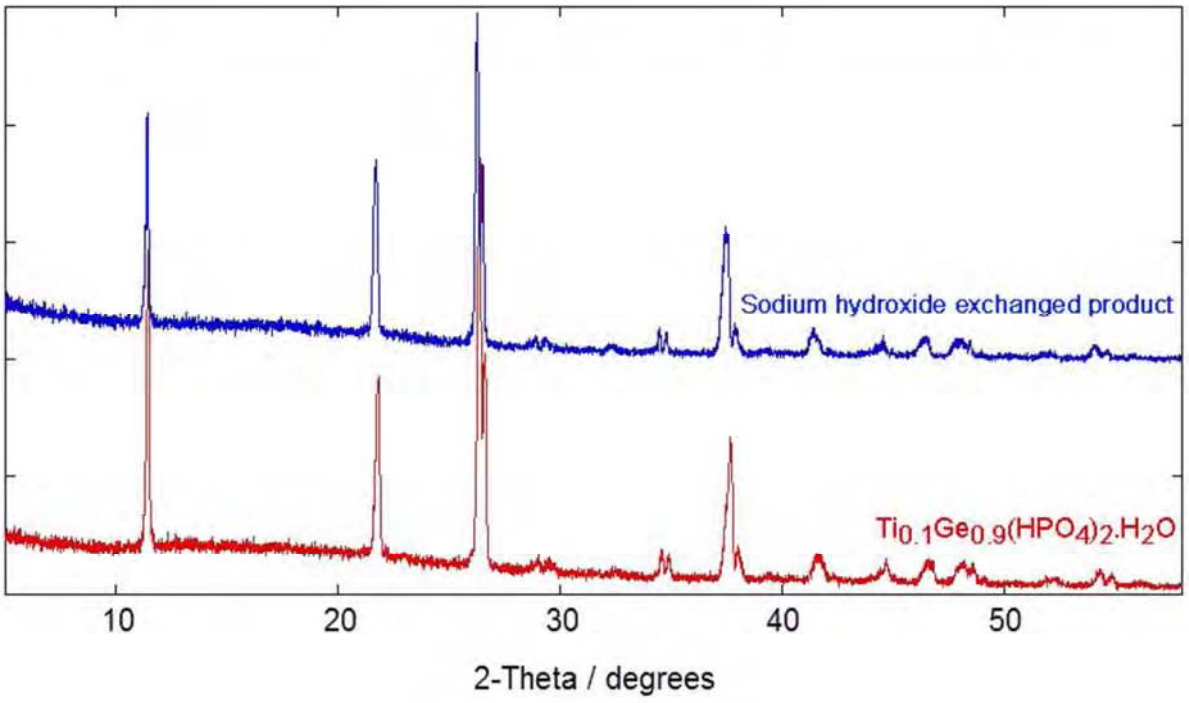

Figure 4.64: Laboratory PXRD pattern of the product obtained from the sodium hydroxide ion exchange of $Ti_{0.1}Ge_{0.9}(HPO_4)_2.H_2O$.

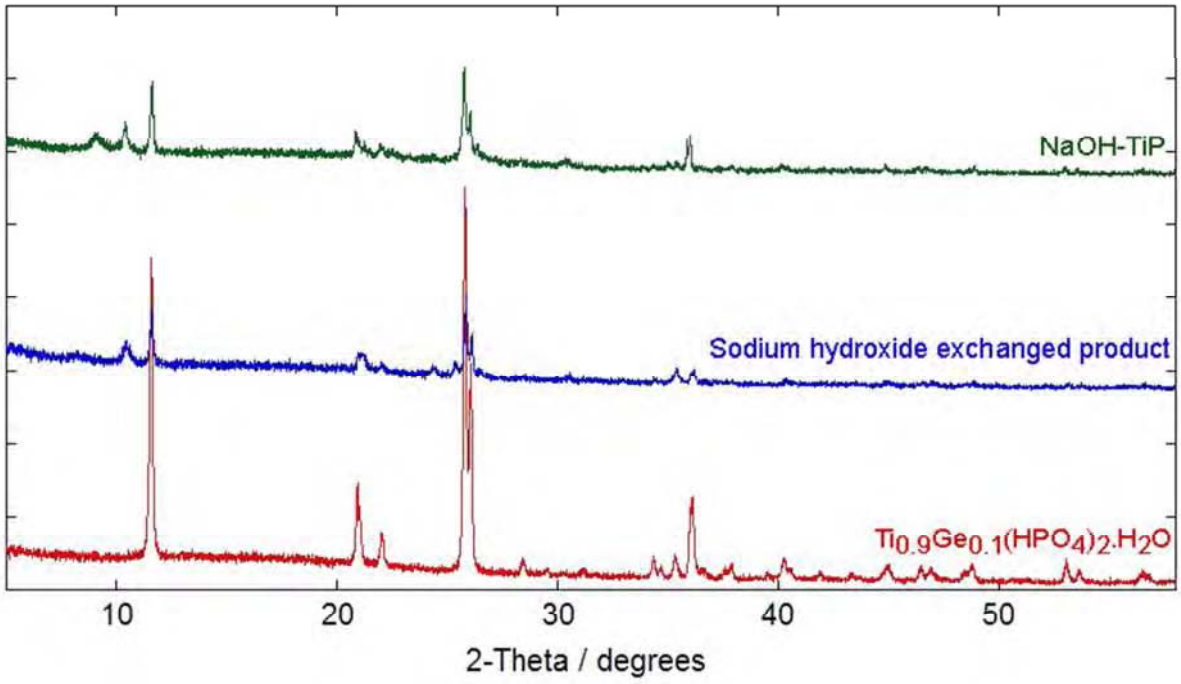

Figure 4.65: Laboratory PXRD pattern of the product obtained from the sodium hydroxide ion exchange of $Ti_{0.9}Ge_{0.1}(HPO_4)_2.H_2O$. The PXRD pattern of the α-TiP sodium hydroxide exchanged product is provided in green.

The presence of titanium within α-GeP is shown to have no effect on the sodium hydroxide ion exchange under these conditions. As seen with α-GeP, the exchange of $Ti_{0.1}Ge_{0.9}(HPO_4)_2.H_2O$ was unsuccessful.

Based on the XRD patterns, the exchange of $Ti_{0.9}Ge_{0.1}(HPO_4)_2.H_2O$ results in the formation of $Ti_{0.9}Ge_{0.1}HNa(PO_4)_2.H_2O$ with some unexchanged starting material. The presence of approximately 0.7 moles of sodium per mole of metal is confirmed from the XRF results. Consequently, the presence of germanium in α-TiP does have an effect on the sodium ion exchange behaviour as no fully exchanged sodium phase was formed.

The PXRD patterns of the products obtained from the sodium acetate exchanges are given in Figures 4.66 and 4.67.

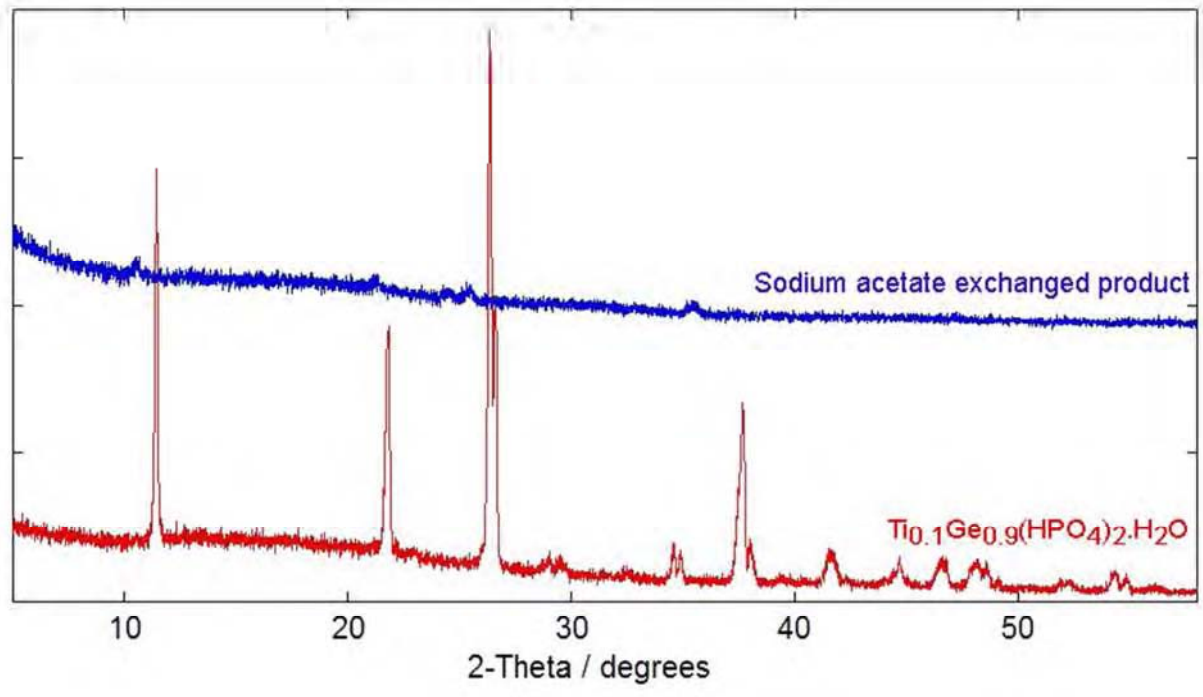

Figure 4.66: Laboratory PXRD pattern of the product obtained from the sodium acetate ion exchange of $Ti_{0.1}Ge_{0.9}(HPO_4)_2.H_2O$.

The pattern from the exchange of $Ti_{0.1}Ge_{0.9}(HPO_4)_2.H_2O$ is different to that of the starting material but the crystallinity of the product is so reduced that further characterisation by XRD is difficult. The same exchange of pure α-GeP resulted in no exchange, with the PXRD pattern of the product being identical to that of α-GeP and fairly crystalline. These results show that the presence of titanium in α-GeP has some effect on the sodium acetate ion exchange, but without further analysis it remains unclear how much.

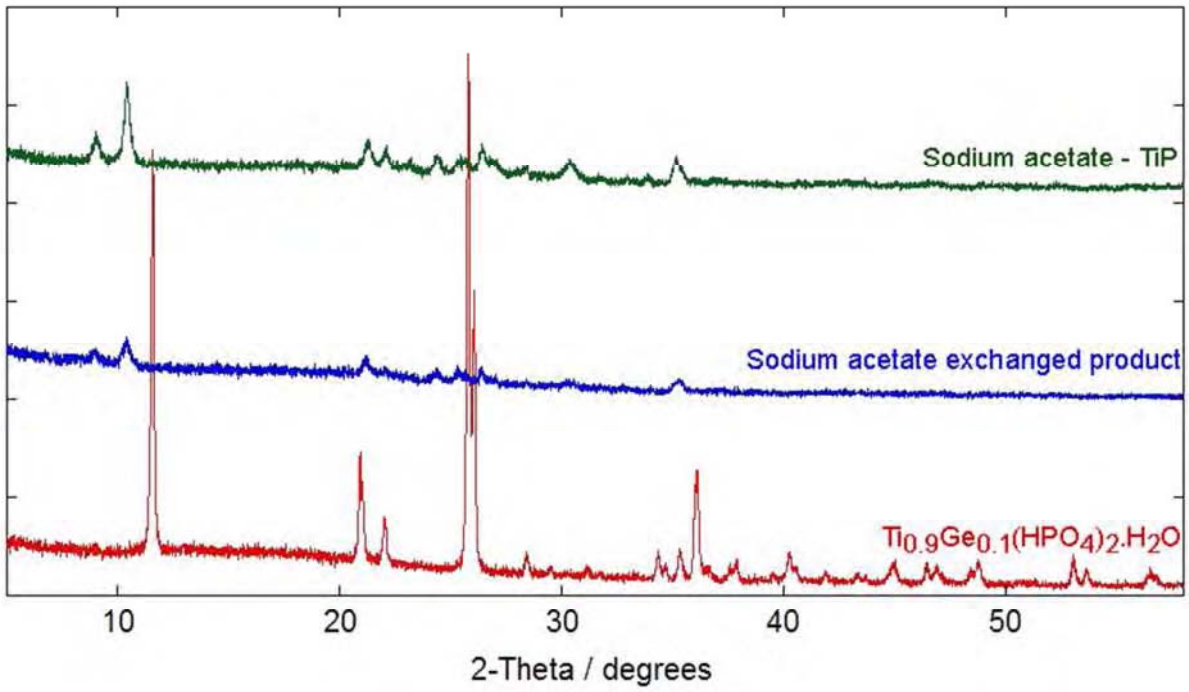

Figure 4.67: Laboratory PXRD pattern of the product obtained from the sodium acetate ion exchange of $Ti_{0.9}Ge_{0.1}(HPO_4)_2.H_2O$. The PXRD pattern of the α-TiP sodium acetate exchanged product is provided in green.

Based on the PXRD pattern in Figure 4.67, the presence of germanium in α-TiP does not have a significant effect on the sodium acetate ion exchange. The product obtained shows peaks corresponding to both half and fully exchanged sodium phases as per α-TiP. In addition to

this the XRF results show the same amount of sodium (ca. 1.2 moles per mole of metal) present in both products.

These results indicate that the titanium-rich mixed metal phosphates exhibit sodium ion exchange behaviour to α-TiP and that similar exchanged products are obtained. It is also observed that the exchange behaviour of α-GeP can be altered by the presence of titanium only when sodium acetate solutions are used.

4.3 Conclusions

Through the results discussed in this chapter the differences in the ion exchange behaviour of α-TiP and α-ZrP are apparent. In accordance with previous findings[10,11], the mixed metal phosphates generally exhibit ion exchange behaviour similar to the end member they are compositionally closest to.

Strontium ion exchange of α-TiP and the titanium rich phosphates was not achieved in this work in spite of varying the pH of the exchange solutions and the temperatures used. In contrast strontium was readily exchanged in α-ZrP and the zirconium rich phosphate. Based on the XRD data the products are believed to be similar to those reported in the literature[8,9,30]. Further work on these strontium phases is discussed in subsequent chapters.

Cobalt and caesium ion exchanges of α-TiP were unsuccessful even when more forceful conditions were employed, although a possible caesium-TiP phase may have been obtained through the step wise exchanges. The reasons for the lack of exchange are believed to be due to the size of the incoming cations. Further investigations into the pH of the solutions may be required to initiate the exchange of these ions.

The titanium-zirconium phosphates exhibited high affinity for sodium, especially when acetate solutions were used as per previous reports[8]. The half and fully exchanged sodium phases for both α-TiP and α-ZrP were obtained and will be subject to further investigation in the following chapters. In no case was a fully exchanged product obtained as a single phase material. Higher sodium levels in combination with other experimental factors may be required to achieve this. The XRD patterns of the α-TiP and α-ZrP sodium phases are very different with the α-ZrP ones being more crystalline. The structures of both $ZrHNa(PO_4)_2.5H_2O$ and $ZrNa_2(PO_4)_2.H_2O$ have been solved previously[31], whilst those for α-TiP are still unknown. These products are not very crystalline and the coexistence of other phases makes further structural investigations with XRD difficult.

Based on the XRD data the products from the exchanges with the coprecipitates are hypothesised to be isomorphous to those from their corresponding single metal counterparts. It has also been demonstrated that the presence of titanium in α-ZrP leads to the formation of products with different degrees of hydration compared with those obtained from pure α-ZrP. In contrast the presence of zirconium in α-TiP has not been shown to have a marked effect on its exchange behaviour.

Due to the high solubility and low stability of α-GeP, ion exchange was not possible with any of the cations investigated. Consequently the use of this material as an industrial ion exchanger is very limited. However these initial results have shown that the presence of a second metal, e.g. titanium, in α-GeP can alter its exchange behaviour.

4.4 Further Work

- Further analysis of the product obtained from the 0.5 M strontium acetate ion exchange of α-TiP to determine whether it is an exchanged phase.
- The pH dependency of exchange could be investigated to see if it helps to facilitate exchange of some of the ions that were not successfully exchanged in this work.
- Attempt to synthesise the fully exchanged sodium α-TiP and α-ZrP as single phase products.
- Further analysis of the 0.05 M sodium hydroxide exchanged TiP product to determine whether it is exclusively the half exchanged phase.
- Attempt to synthesise the fully exchanged strontium α-ZrP to enable structural characterisation.

4.5 References

(1) Parida, K. M., Sahu, B. B., Das, D. P. *J. Coll. Inter. Sci*, **270**, 436-445 (2004)
(2) Clearfield, A. *Ann. Rev. Mater. Sci.*, **14**, 205 (1984)
(3) Clearfield, A., Stynes, J. A. *J. Inorg. Nucl. Chem.*, **26**, 117-129 (1964)
(4) Alberti, G., Giammari, G., Grassini-Strazza, G. *J. Chromatog.*, **28,** 118-123 (1967)
(5) Alberti, G., Cardini-Galli, P., Costantino, U., Torracca, E *J. Inorg. Nucl. Chem.*, **29**, 571-578 (1967)
(6) Dyer, A., Leigh, D, Ocon, F. T. *J. Inorg. Nucl. Chem.*, **33**, 3141-3151 (1971)
(7) Clearfield, A., Nancollas, G. H., Blessing, R. H. In *Ion Exchange and Solvent Extraction*; Marcus, Y., SenGupta, A. K., Marinsky, J. A., Ed.; Dekker: New York; Vol. 5 (1973)
(8) Clearfield, A., Hagiwara, H *J. Inorg. Nucl. Chem.*, **40**, 907-914 (1978)
(9) Alberti, A., Costantino, U., Pelliccioni, M *J. Inorg. Nucl. Chem.*, **35**, 1327-1338 (1973)
(10) Clearfield, A., Frianeza, T. N. *J. Inorg. Nucl. Chem.*, **40**, 1925-1932 (1978)
(11) Tomita, I., Iwase, K., Saito, K., Sugiyama, Y. *Bull. Chem. Soc. Jap.*, **54**, 749-753 (1981)
(12) Shakshooki, S. K., Naqvi, N., Kowalczyk, J., Khalil, S., Rais, M., Tarish, F. *React. Poly.*, **7**, 221-226 (1988)
(13) Shakshooki, S. K., Szirtes, L., Yakovlev, Yu. V. *J. Radio. Nucl. Chem.*, **145**, 281-291 (1990)
(14) Thakkar, R., Chudasama, U. *J. Hazard. Mat.*, **172**, 129-137 (2009)
(15) Jignasa, A., Rakesh, T., Uma, C. *J. Chem. Sci.*, **118**, 185-189 (2006)
(16) Yazawa, Y., Eguchi, T., Takaguchi, K., Tomita, I. *Bull. Chem. Soc. Jap.*, **52**, 2923-2927 (1979)
(17) Suarez, M., Garcia, J. R., Rodriguez, J *J. Phys. Chem.*, **88**, 159-162 (1984)
(18) Romano, R., Ruiz, A. I., Alves, O. L. *J. Solid State Chem.*, **177**, 1520-1528 (2004)

(19) Nakayama, H., Eguchi, T., Nakamura, N., Yamaguchi, S., Danjyo, M., Tsuhako, M. *J. Mater. Chem*., **7**, 1063-1066 (1997)
(20) Salvado, M. A., Pertierra, P., Garcia-Granda, S., Garcia, J. R., Rodriguez, J., Fernandez-Diaz, M. T. *Acta. Cryst*., **B52**, 896-898 (1996)
(21) Norlund Christensen, A., Krogh Andersen, E., Krogh Andersen, I. G., Alberti, G., Nielsen, M., Lehmann, M. S. *Acta. Chem. Scan.*, **44**, 865-872 (1990)
(22) Slade, R. C. T., Knowles, J. A., Jones, D. J., Roziere, J. *Solid State Ionics*, **96**, 9-19 (1997)
(23) Schmutz, C., Barboux, P., Ribot, F., Taulelle, F., Verdaguer, M., Fernandez-Lorenzo, C. *J. Non-Cryst. Solids*, **170**, 250 - 262 (1994)
(24) Burnell, V. A., Msci Thesis 'The Synthesis and Ion-Exchange of Mixed Zr/Ti Phosphates' University of Birmingham (2007)
(25) Xu, J., Tang, Y., Zhang, H., Gao, Z. *J. Inc. Phen. Mol. Rec. Chem.*, **27**, 303-317 (1997)
(26) Capitani, D., Casciola, M., Donnadio, A., Vivani, R. *Inorg. Chem.*, **49**, 9409-9415 (2010)
(27) Satya Kishore, M., Pralong, V., Caignaert, V., Varadaraju, U. V., Raveau, B. *J. Power Sources*, **169**, 355-360 (2007)
(28) Albertsson, J., Oskarsson, A., Tellgren, R., Thomas, J. O. *J. Phys. Chem.*, **81**, 1574-1578 (1977)
(29) Tegehall, P.-E. *Acta. Chem. Scan.*, **A40**, 507-514 (1986)
(30) Alberti, G., Bertrami, R., Casciola, M., Costantino, U., Gupta, J. P. *J. Inorg. Nucl. Chem.*, **38**, 843-848 (1976)
(31) Alberti, G., Costantino, U., Allulli, S., Tomassini, N. *J. Inorg. Nucl. Chem.*, **40**, 1113-1117 (1978)

Chapter 5: Characterisation and Structure Solution of the Ion Exchanged Products

5.1 Introduction

A discussion on the ion exchange behaviour of α-TiP, α-GeP and some of the mixed metal phosphates was presented in Chapter 4. In this chapter the successfully exchanged products are subject to further characterisation and in some cases, attempts have been made to solve the structures.

5.2 Strontium ion exchanged ZrP – $ZrSr_{0.55}H_{0.9}(PO_4)_2.xH_2O$

5.2.1 Introduction

From the XRD and XRF data discussed in Chapter 4, this product was believed to be a half exchanged strontium phase similar to those reported in the literature[1,2]. To date, the structures of these strontium phases remain unknown and characterisation of them is limited to only XRD patterns.

5.2.2 Pair Distribution Function (PDF) Studies

PDF data of the exchanged product was obtained to identify any changes in the structure due to the incorporation of strontium. Figure 5.1 gives a comparison of the PDF of this product to that of the starting material α-ZrP in the low *r* region. In spite of the contrast between the XRD patterns (refer back to Figure 4.15 in Chapter 4), the PDFs are similar indicating that the exchanged structure is a modification of the parent α-ZrP as seen

previously with sodium exchanges[3]. The strontium exchanged product is shown to have longer zirconium-zirconium and oxygen-oxygen distances with smaller less defined differences seen in the positions of the other key peaks. Given the larger size of the strontium ion, an increase in these distances was expected. The oxygen-oxygen distance is an interlayer distance (refer back to Figure 3.13) and so the increase of approximately 0.5 Å infers a change in the layer arrangement of this compound either by a shifting of the layers relative to each other and/or an expansion of the interlayer distance. This is also mirrored in the significant changes in the long *r* region of the PDF pattern shown in Figure 5.2, whereby dramatic differences are observed for all the peaks present. An increase in the interlayer distance to accommodate the strontium ions is confirmed from the XRD data discussed previously. It remains unclear at this stage whether a layer shifting also accompanies the exchange process, as has been seen previously with the exchange of sodium[3].

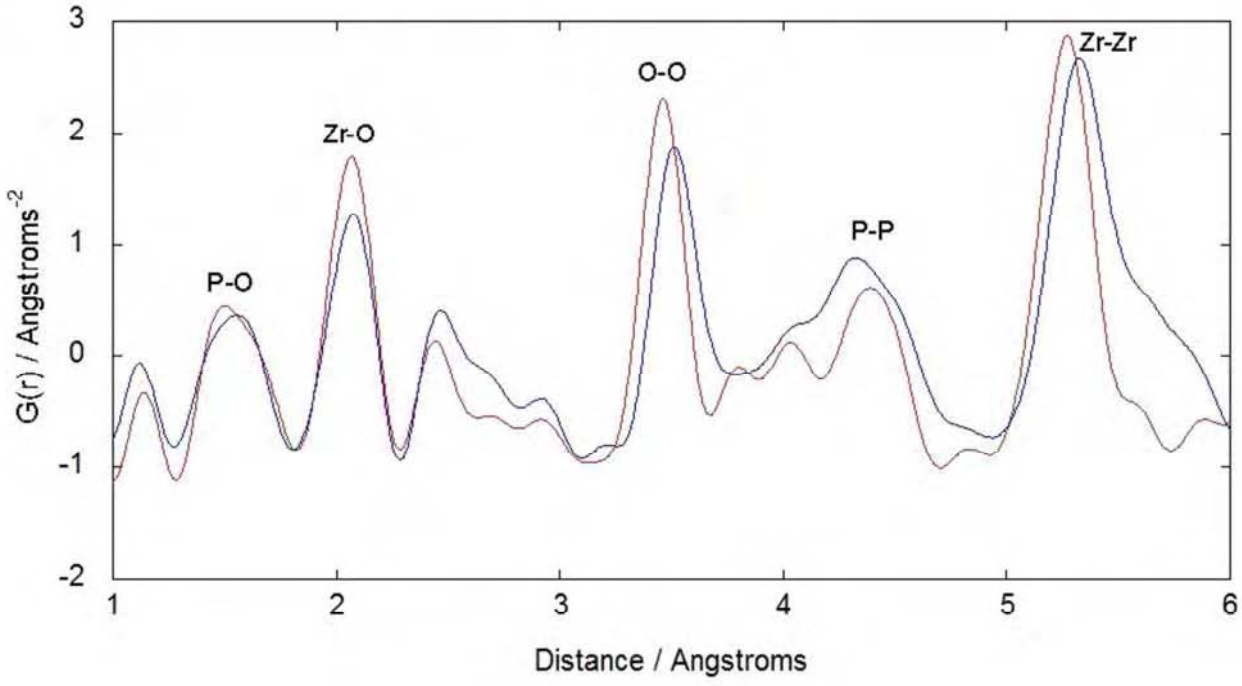

Figure 5.1: Comparison of the PDF patterns for strontium exchanged ZrP (Blue) and α-ZrP (red) in the low *r* region.

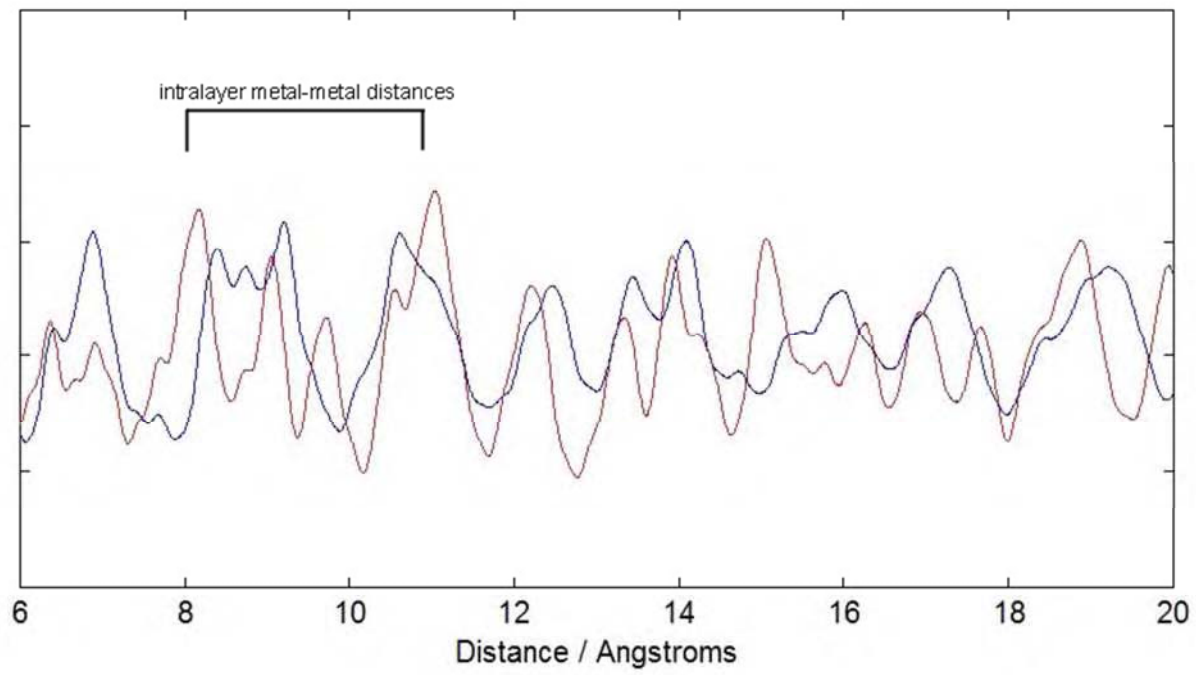

Figure 5.2: Comparison of the PDF patterns for strontium exchanged ZrP (Blue) and α-ZrP (red) in the long *r* region.

The differential PDF (in the low *r* region) is given in Figure 5.3. In addition to the increased distances already discussed, the differential PDF pattern shows some peaks around 2.5 and between 4-5 Å which are likely to be due to the presence of strontium-oxygen and strontium-strontium distances, these would not be unexpected at these values. The peak shown at ~5.75 Å corresponds to the shoulder seen in the zirconium-zirconium peak in Figure 5.1. Whilst no formal identification of the distance this represents has been made, it can be speculated that this either results from the presence of strontium within the unit cell, or it signifies phase segregation within the product.

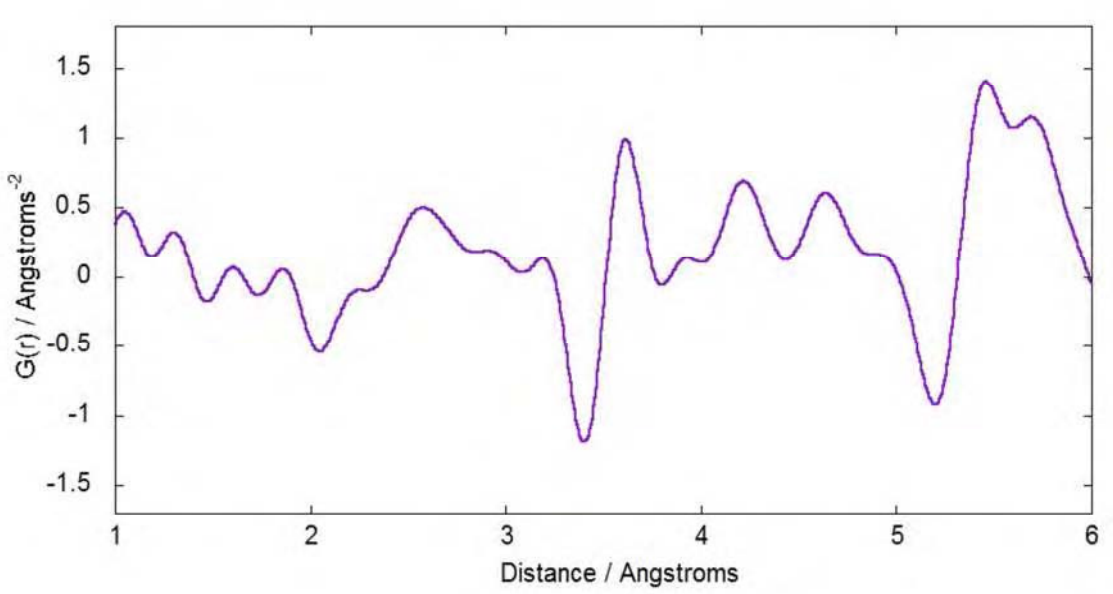

Figure 5.3: Differential PDF of strontium exchanged ZrP.

5.2.3 ^{31}P NMR Studies

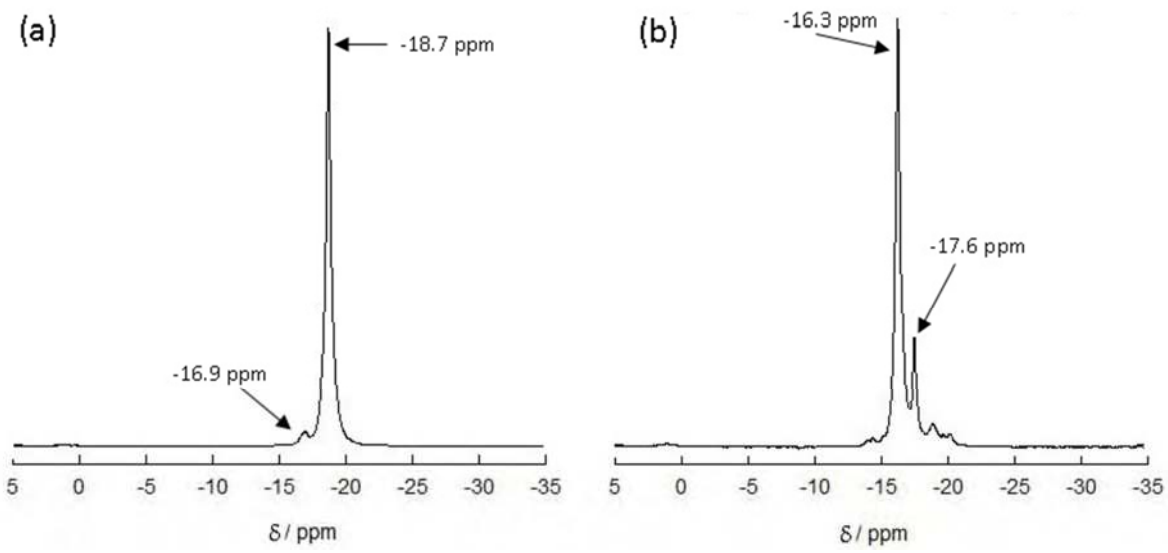

Figure 5.4: ^{31}P NMR spectra of (a) α-ZrP (b) strontium exchanged α-ZrP

Solid state ^{31}P NMR data was collected at The University of Warwick by Dr. John Hanna. The spectra of both the parent phase (α-ZrP) and the exchanged product are compared in Figure

5.4. The spectrum for the parent phase comprises a peak at ~ -18.7 ppm - characteristic of α-ZrP[4-6]. The small resonance at -16.9 ppm must arise from an impurity. The spectrum for the exchanged phase confirms that exchange has occurred but is more complicated and indicative of a multi-phase system. The main peaks at ~16.3 and ~-17.6 ppm can be attributed to strontium exchanged ZrP, and assigned to $(SrPO_4)^-$ and $(HPO_4)^{2-}$ units respectively, based on previous studies[4]. The non-equivalent intensities of these signals is consistent with more than 50% strontium exchange within the product. The other low intensity peaks probably arise from impurities and other phases present. These were not evident from the XRD data measured in this work, or from previous studies[1,2] of this product. However it should be noted that both the XRD pattern obtained in this work and those reported in the literature[1,2] are low quality and feature broad reflections which may conceal these additional phases/impurities.

5.2.4 SEM EDX

SEM EDX analysis was performed in order to assess the sample morphology of the phases present and composition using spot size 3 and a 10 kV accelerating voltage. A summary of compositional results are displayed in Figure 5.5 and Table 5.1. The results show three sample morphologies; plates, needles and blocks. Although attempts were made to obtain EDX data on the individual phases present, due to the large relative size of the electron beam it is highly likely that the area actually analysed contained grains of the other phases as well. Consequently, the values given serve only as a semi-quantitative indication into the differing strontium contents of the different phases present. Given the predominance of the plates it is assumed that these are the main strontium exchanged ZrP phase, which agrees well with previous findings[7-9] for layered metal phosphates. It is therefore assumed that the

needle and block like particles are responsible for the additional peaks observed in the ^{31}P NMR spectra. Unfortunately due to the mutli-phase nature of the sample no accurate compositional information on these phases could be obtained by this method.

Plate Particles

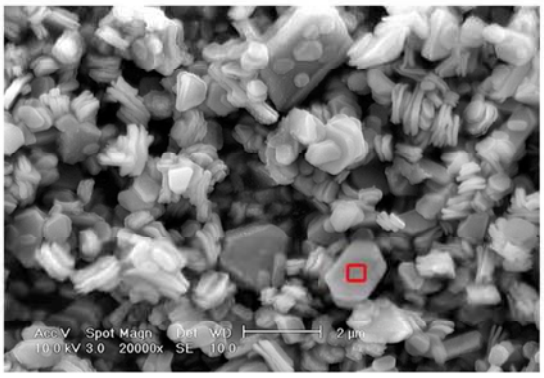

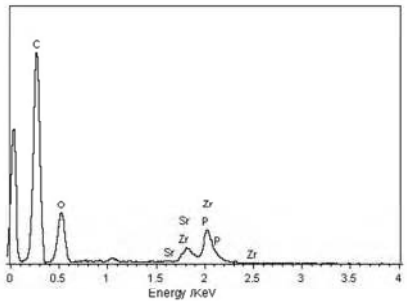

Needle Particles

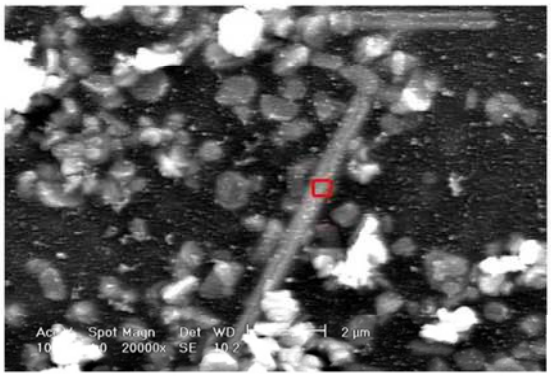

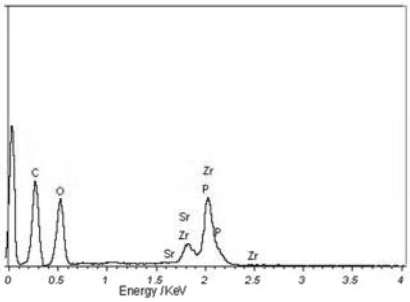

Block Particles

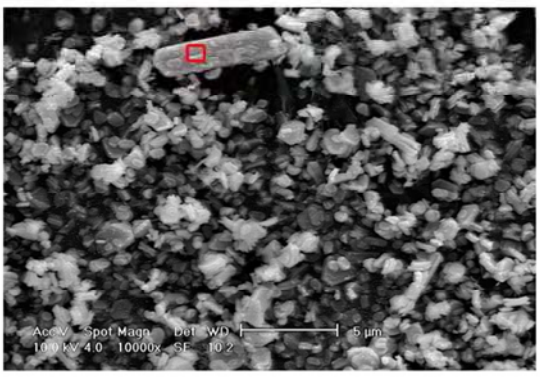

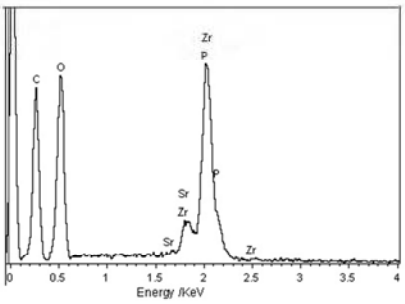

Figure 5.5: SEM images and EDX elemental analysis spectra for strontium-ZrP.

Table 5.1: SEM EDX data for strontium-ZrP

Plate Particles

Scan	SEM EDX Atomic %				Moles of Sr per mole of Zr
	O	P	Sr	Zr	
1	76.11	11.99	4.54	7.37	0.61
2	75.36	13.17	4.66	6.80	0.69
3	66.26	16.05	6.88	10.81	0.65
4	77.79	11.22	4.42	6.57	0.67
Average					0.65

Needle Particles

Scan	SEM EDX Atomic %				Moles of Sr per mole of Zr
	O	P	Sr	Zr	
1	71.41	15.57	4.11	8.91	0.46
2	74.33	13.07	4.16	8.45	0.49
Average					0.475

Block Particles

Scan	SEM EDX Atomic %				Moles of Sr per mole of Zr
	O	P	Sr	Zr	
1	72.38	15.72	2.48	9.41	0.26
2	73.13	14.41	2.89	9.57	0.30
Average					0.28

5.2.5 Thermal Analysis

TGA /DTA and VT XRD data obtained on the product are displayed in Figures 5.6 and 5.7. Figure 5.8 provides a summary of the main phase changes and high temperature products observed. The data obtained shows the product to undergo different thermal behaviour to the parent compound α-ZrP (discussed in Chapter 3).

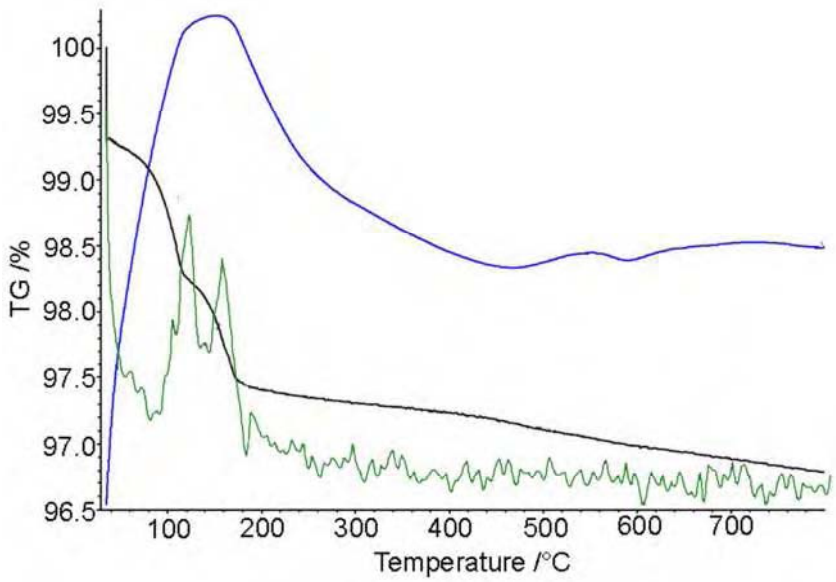

Figure 5.6: TGA trace (black) showing the decomposition pathway of strontium-ZrP. The DTA curve is shown in blue and the green trace represents the mass spectrometry results for H_2O.

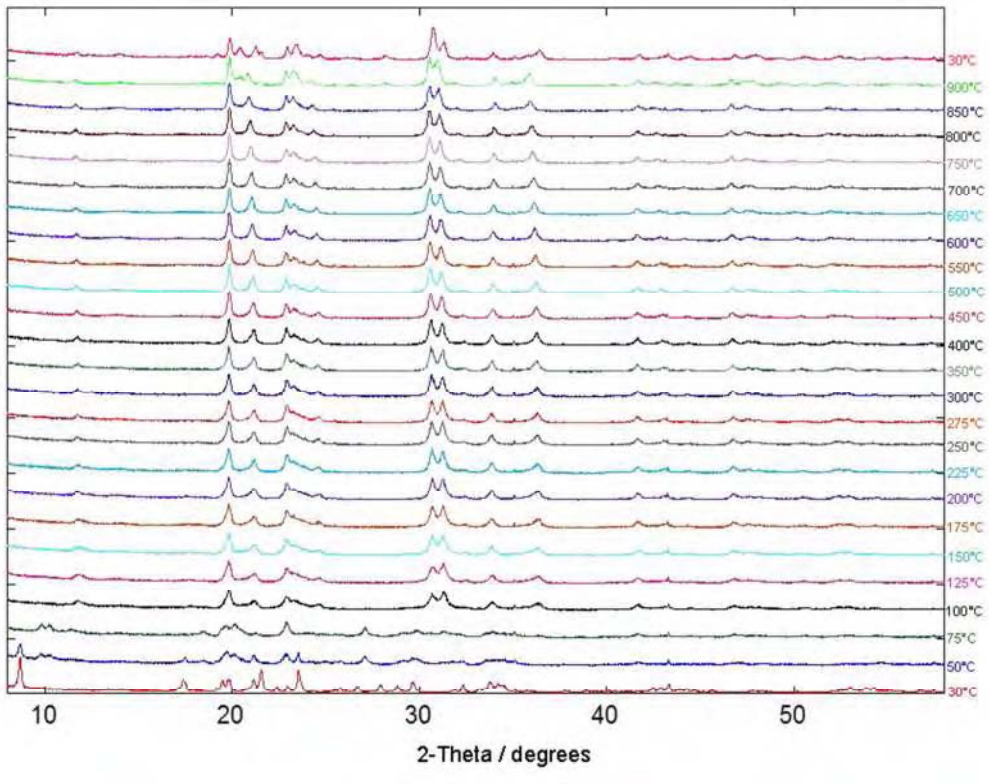

Figure 5.7: The in-situ XRD patterns of strontium-ZrP recorded as a function of temperature.

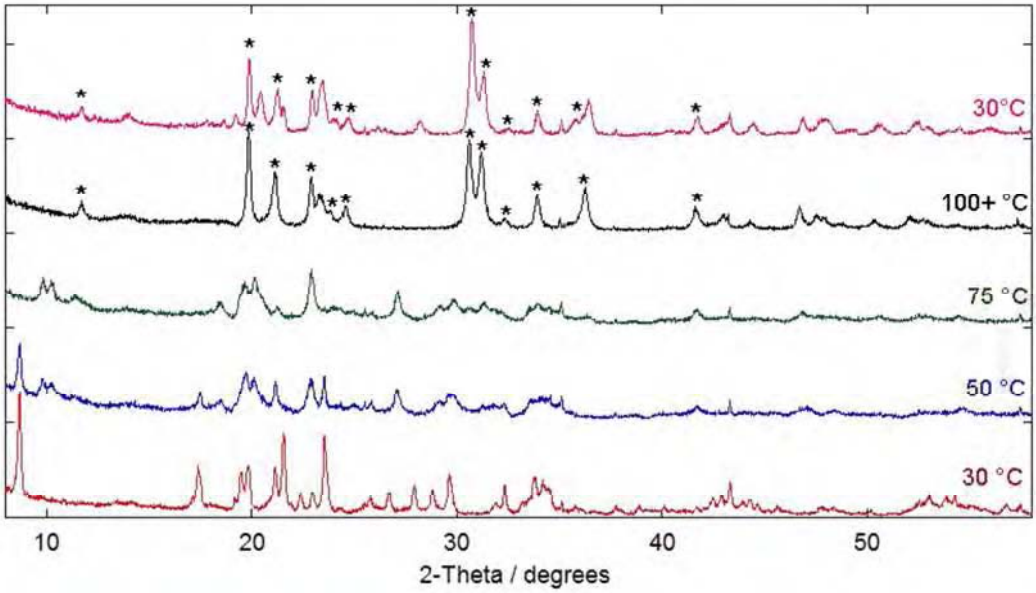

Figure 5.8: The high temperature phases of strontium-ZrP. The asterisks denote peaks reported in ICDD PDF 00-030-1317 for $Sr_{0.55}ZrH_{0.9}(PO_4)_2$.

A series of changes were observed in the XRD patterns when the sample was heated between 50 - 100 °C. In accordance with this the TGA trace shows a two-step water loss corresponding to 2 % weight loss in the product below 200 °C. This weight loss is much smaller than those typically seen for the dehydration of layered phosphates and therefore indicates lower levels of hydration within the product. Heating to 100 °C results in the formation of $Sr_{0.55}ZrH_{0.9}(PO_4)_2$ according to the peaks matched to ICDD PDF 00-030-1317. This phase remains upon heating to 900 °C and subsequent cooling back to room temperature. The presence of $Sr_{0.55}ZrH_{0.9}(PO_4)_2$ in the decomposition products indicates a high temperature stability for this compound.

No significant features are shown in the TGA trace between 200 - 800 °C. Instead a progressive and shallow weight loss is observed with no accompanying water loss. The lack of water is consistent with no condensation of the phosphate groups, as occurs in the parent

compound, and is consistent with the identification of a strontium metaphosphate in the XRD analysis. The small endothermic peak present at ~550 °C most likely results from phase changes occurring within the additional phases/impurities known to be present. Analysis of the XRD patterns indicates that the high temperature phases of these are in an amorphous form, given the lack of additional peaks and the higher background observed in the patterns. The additional low intensity peaks observed in the XRD pattern along with $Sr_{0.55}ZrH_{0.9}(PO_4)_2$ at temperatures at and above 900°C are believed to be a new phase crystallising out of the amorphous phases discussed previously. However due to the low intensity of these XRD peaks this additional phase(s) could not be identified by XRD.

5.2.6 Stability in Water

The stability of the strontium exchanged ZrP product in the presence of water was investigated by exposing the sample to water overnight at room temperature. The results were studied by XRD and are shown in Figure 5.9.

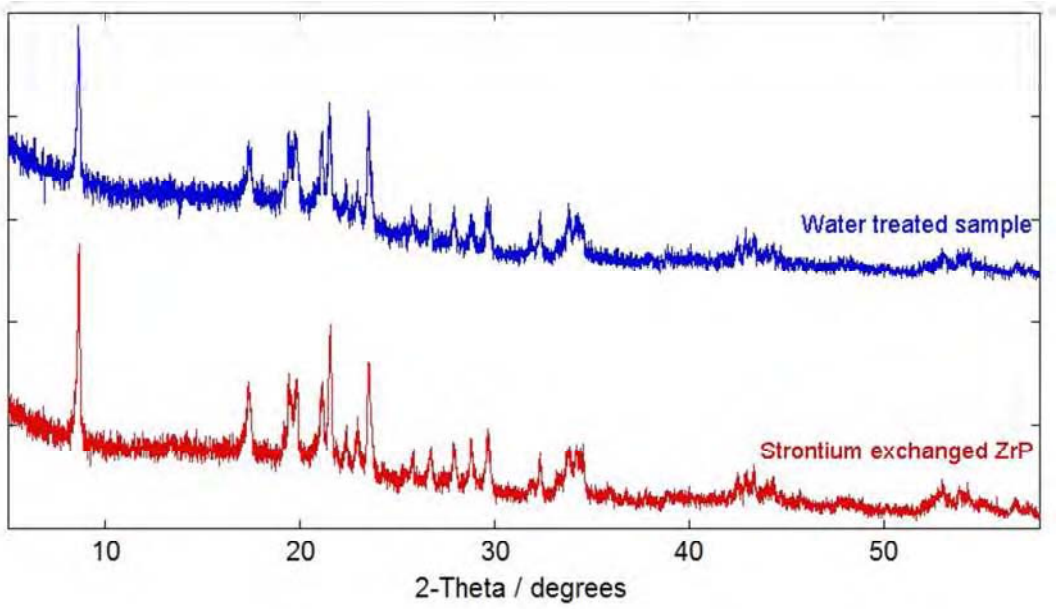

Figure 5.9: PXRD result of the water stability test.

The PXRD pattern indicated that the strontium exchanged product was stable towards water / hydrolysis as no change was observed between the two PXRD patterns. Hydrolysis of the exchanged product would produce a decrease in the intensity of the peaks as the percentage of amorphous material increases.

5.2.7 Variations in Exchange Conditions

Variation in the exchange method including; higher temperatures, longer durations and increased volumes of strontium solution (1 L compared to 250 ml) were attempted to see if either a single phase or a fully exchanged product could be synthesised. The PXRD patterns of the products obtained are displayed in Figure 5.10. The patterns of the products are all the same, but are different to that from the standard exchange. No identifications could be made from the PXRD data and the yields obtained were not sufficient for XRF analysis. A repeat exchange using the same conditions as the first exchange was also attempted on the strontium–ZrP sample. The pattern obtained, also given in Figure 5.10, is similar to that of the starting material; however additional peaks are also observed. The low crystallinity of this product makes further analysis difficult and again the yield obtained was not sufficient for XRF analysis. Given that the additional phases in the original exchange product, highlighted through the ^{31}P NMR and SEM/EDX analysis, were not obvious from the PXRD data, it would be worth investigating these products by the same techniques to see if they are also present here.

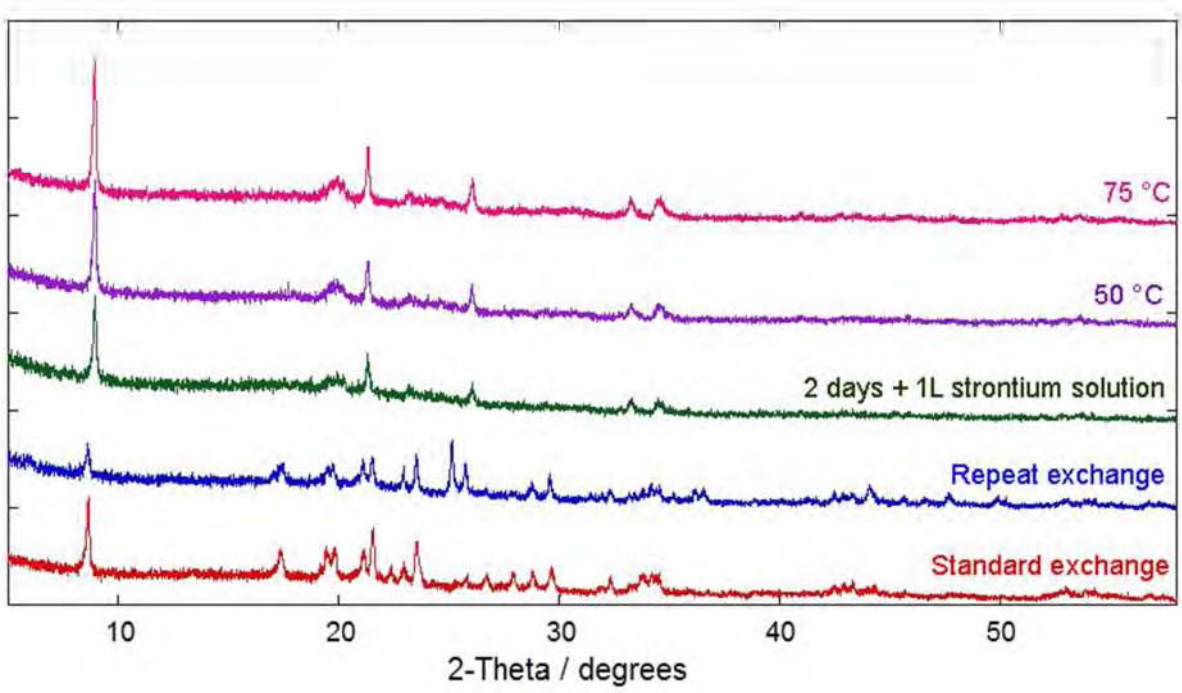

Figure 5.10: PXRD patterns obtained from variations to the strontium hydroxide ion exchange method of α-ZrP (1 g).

5.2.8 Indexing

Whilst the in-house PXRD data showed a good match to previously reported strontium-ZrP compounds[1,10], the presence of additional phases in these products was not obvious due to the low quality of the data. Higher quality data were required to enable indexing of the main product and so synchrotron PXRD scans were obtained. Scans on more than one batch of the sample were collected in the hope that peaks corresponding to different phases could be better identified. Figure 5.11 displays the synchrotron patterns obtained.

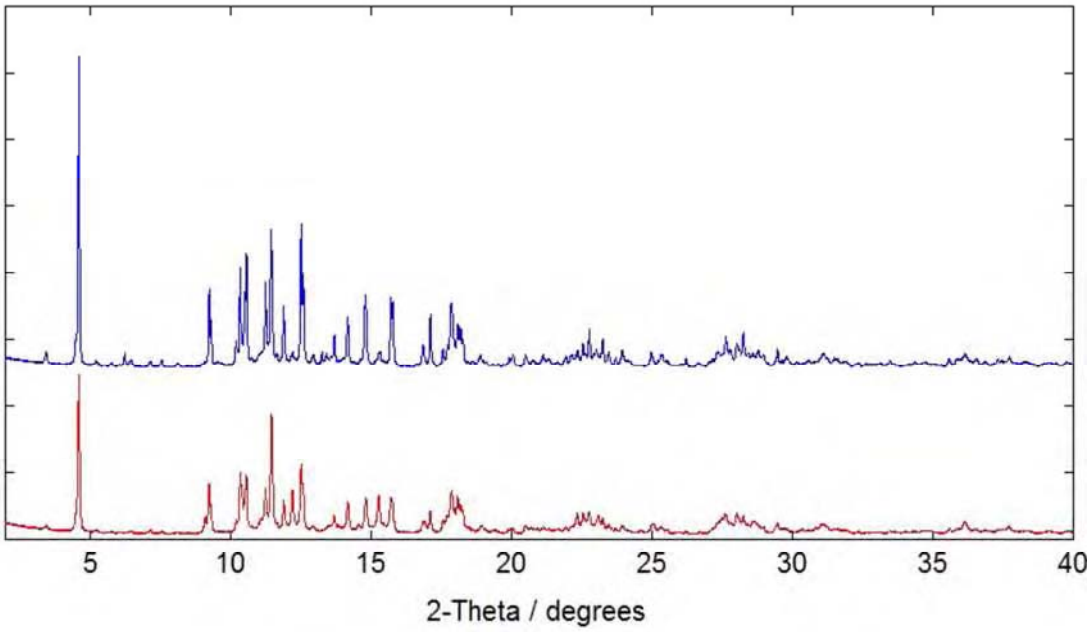

Figure 5.11: Synchrotron PXRD patterns of the two strontium-ZrP samples.

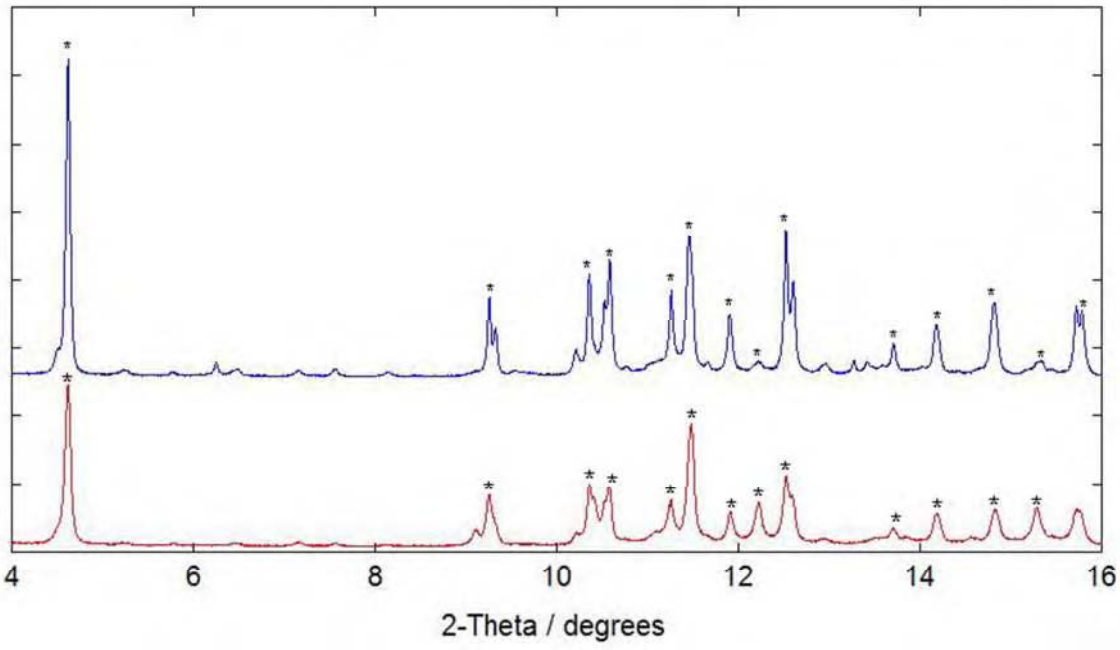

Figure 5.12: Close up of the synchrotron patterns, the peaks corresponding to previously reported strontium products[1,2] ($ZrSr_{0.4\text{-}0.55}H_{1.1\text{-}0.9}(PO_4)_2.3.5H_2O$)are marked with asterisks.

Whilst the patterns show fairly good correlation to each other, the relative intensities of the peaks varies, as does the extent of peak broadening. In addition to this some peaks are observed that are not present in both patterns. This is consistent with the multi-phase nature of the product and arises from different ratios of the phases present in the different batches. A close up of the scans is shown in Figure 5.12 and the peaks corresponding to previously reported strontium compounds ($ZrSr_{0.4\text{-}0.55}H_{1.1\text{-}0.9}(PO_4)_2.3.5H_2O$) are marked with asterisks. Using this peak list attempts were made to index this pattern using both CRYSFIRE[11] and DICVOL06[12] in all possible crystal systems. In addition to this indexing was also attempted by Dr Phil Chater of the School of Chemistry, The University of Birmingham, using the indexing routines of Topas[13]. The results from the indexing routines were analysed by both visual inspections of the calculated peak positions compared to observed peaks as well as by refining the given unit cells in a Le Bail fit. For these, the peak shape was fixed as artificially narrow, as unrestricted refinements in the presence of many peaks which did not match the given unit cell (i.e. potential peaks from other phases present) resulted in broadening of the peak shape to incorporate other peaks and minimise the R_{wp}. None of the results obtained were satisfactory.

A random unit cell search based on modifications of the parent α-ZrP unit cell was also tested using the lattice parameter search routine in Topas. This routine randomly selects starting values of unit cell constants (between given limits) and uses them as a starting point for a Le Bail refinement. The refinement continues after convergence with new, randomly selected unit cell constants, and the best results of the Le Bail refinements are retained. Peak shapes for the Le Bail fits were again kept artificially narrow to prevent miss-assignment of impurity peaks. Regions of the diffraction pattern identified as possibly

containing impurity peaks were excluded from the refinements. However, no results from the lattice parameter search were satisfactory.

In spite of the use of synchrotron sources, we were still unable to index this exchanged product. The main factors preventing this were the multi-phase nature of the product and an inability to determine which peaks correspond to which phase present. This was further complicated by the reduction in the crystallinity of the exchanged product compared with that of the starting material, α-ZrP. This is a common problem seen in exchanged α-ZrP samples. It has been reported that when the salt forms of α-ZrP are obtained the crystal quality is reduced to such an extent that detailed structural investigations are difficult, as it is almost impossible to obtain high quality XRD data required for crystal structure analysis[14,15]. In addition to this the presence of other phases / impurities adds further difficulty to the analysis.

The samples were viewed under both optical and polarising microscopes to see if crystals large enough for single crystal analysis could be isolated. Unfortunately no single crystals large enough to give a unit cell and space group were observed.

5.3 Strontium Ion Exchanged $Ti_{0.1}Zr_{0.9}(HPO_4)_2.H_2O$

As discussed in Chapter 4, the strontium exchanged $Ti_{0.1}Zr_{0.9}(HPO_4)_2.H_2O$ product gave an XRD pattern similar to that from the analogous exchange with α-ZrP. Although the crystallinity of the sample was reduced, the peaks also matched to those reported by Clearfield and Hagiwara[1] and Alberti *et. al.*[2] for half exchanged strontium-ZrP. In support of this XRF gave a bulk strontium to metal molar ratio of 0.5:1.

Recrystallisation of the product was attempted by heating in water for two days in an autoclave at 100 °C. From the PXRD pattern of the product, shown in Figure 5.13, this led to an increase in intensity of some peaks, however the recrystallisation process did not result in a highly crystalline product as was hoped.

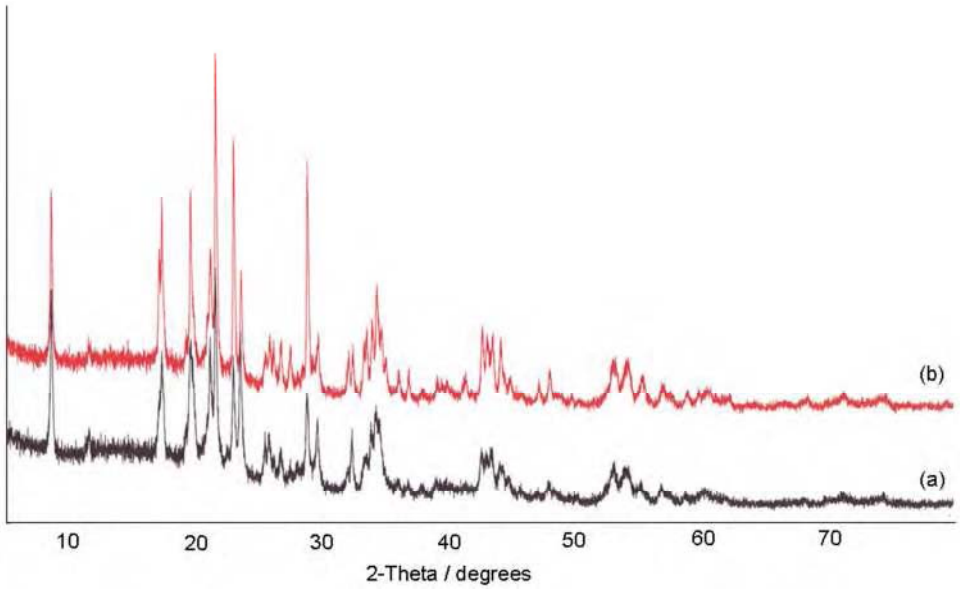

Figure 5.13: PXRD patterns of (a) strontium exchanged $Ti_{0.1}Zr_{0.9}(HPO_4)_2.H_2O$ (b) the recrystallised product.

Figure 5.14 compares a portion of the synchrotron scans of this product with that of the exchanged α-ZrP sample. Although the crystallinity of the $Ti_{0.1}Zr_{0.9}(HPO_4)_2.H_2O$ exchanged product is reduced, the similarity in the two patterns is evident, indicating that isomorphous products were formed from the two exchanges. It also appears highly likely that additional phases are present in the sample, however no ^{31}P NMR or SEM/EDX analysis was carried out to confirm this.

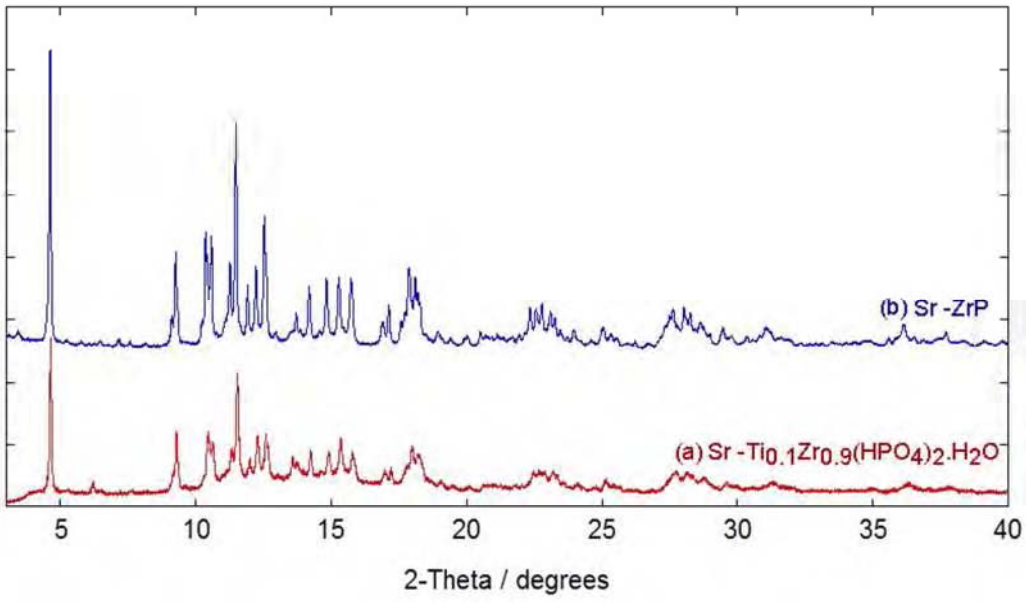

Figure 5.14: Comparison of the synchrotron PXRD scans of (a) strontium exchanged $Ti_{0.1}Zr_{0.9}(HPO_4)_2.H_2O$ (b) strontium exchanged ZrP.

Indexing of the product was attempted using DICVOL06[12], CRYSFIRE[11] and the indexing routines of Topas[13] however no satisfactory results were obtained. Given that the indexing of the more crystalline strontium exchanged α-ZrP product was unsuccessful it is not surprising that this product remains unindexed as well.

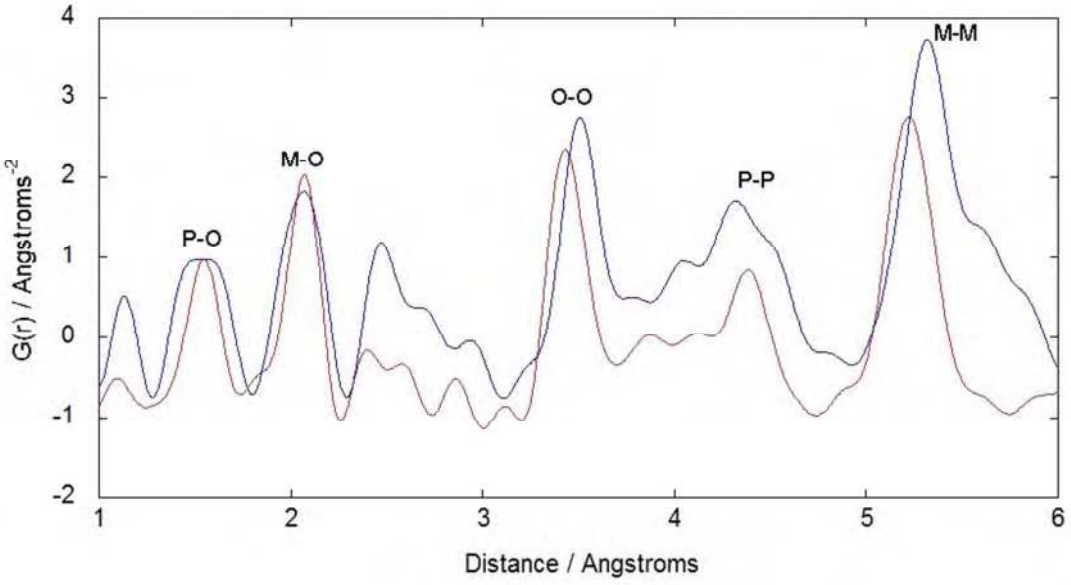

Figure 5.15: Comparison of the PDF patterns for strontium exchanged $Ti_{0.1}Zr_{0.9}(HPO_4)_2.H_2O$ (Blue) and $Ti_{0.1}Zr_{0.9}(HPO_4)_2.H_2O$ (red).

Figure 5.15 displays the PDF pattern of the strontium exchanged product. The PDF of the starting material $Ti_{0.1}Zr_{0.9}(HPO_4)_2.H_2O$ is also included for comparison. Strontium ion exchange is shown to have the same effect on the PDF pattern of $Ti_{0.1}Zr_{0.9}(HPO_4)_2.H_2O$ as it did α-ZrP, with increases in the metal-metal and oxygen-oxygen distances observed upon exchange. The peak broadening of the phosphorus-oxygen and metal-oxygen peaks in conjunction with the more complicated pattern seen in the metal-metal (5-6 Å) region may allude to the presence of additional phases.

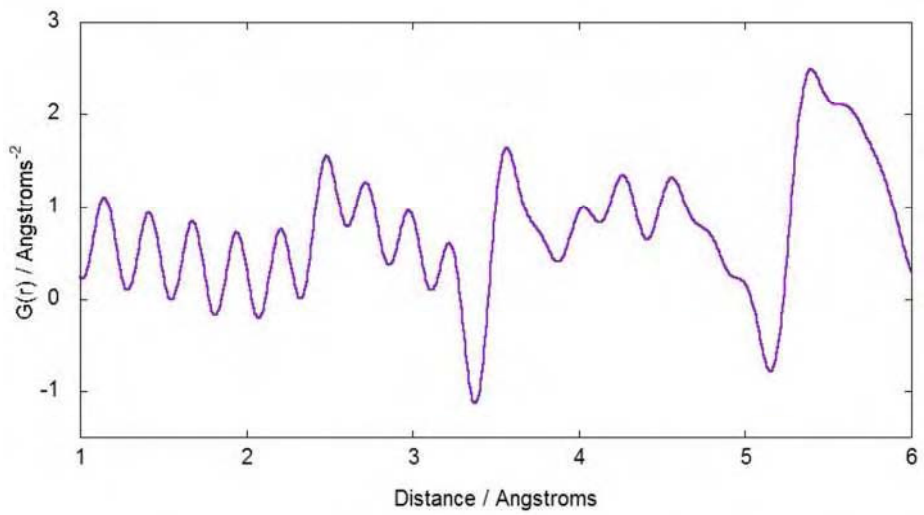

Figure 5.16: Differential PDF of strontium exchanged $Ti_{0.1}Zr_{0.9}(HPO_4)_2.H_2O$.

The differential PDF, displayed in Figure 5.16, is also very similar to that obtained from the α-ZrP exchange. Features in the pattern for the increased distances already discussed as well as for potential Sr-O and S-Sr distances at 2.5 and 4-5 Å respectively are observed.

5.4 Sodium Ion Exchanged TiP Phases

As discussed in Chapter 4, the half and fully exchanged sodium phases of α-TiP; $TiHNa(PO_4)_2.H_2O$ and $TiNa_2(PO_4)_2.3H_2O$ were obtained via exchange with sodium acetate (0.1

M) and hydroxide (0.01 M) solutions. Both phases were found to coexist and the product obtained from the hydroxide exchange also contained unexchanged starting material. The structures of both phases remain unknown and a review of the literature reveals very little characterisation of them has been undertaken.

5.4.1 ^{31}P NMR Studies

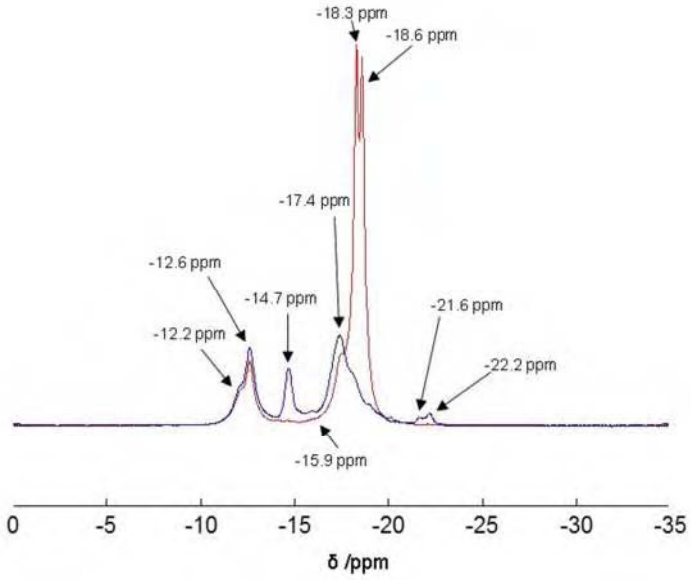

Figure 5.17: ^{31}P NMR spectra of sodium hydroxide exchanged TiP (red) and sodium acetate exchanged TiP (blue).

Solid state ^{31}P NMR data was collected at The University of Warwick by Dr. John Hanna. The spectra of both the sodium acetate and hydroxide exchanged α-TiP products are compared in Figure 5.17. The spectra obtained are consistent with the XRD results discussed previously for these products. The two peaks at -18.3 and -18.6 ppm in the spectrum of the hydroxide exchanged product correspond to those of unexchanged α-TiP, which from this data is confirmed to be the main phase present. As per the XRD data, the sodium acetate exchanged product is not shown to contain significant quantities of unexchanged α-TiP.

Additional peaks observed at -17.4, -12.6 and -12.2 ppm are present in both spectra and arise from the presence of the half and fully exchanged phases. Previous studies[16,17] show that deprotonation of the phosphate groups e.g. –P-OH becoming –P-O^-...X^+ leads to a downfield shift in the peaks seen in the NMR. Consequently, based on sodium-ZrP data reported previously[16,17] these are assigned to $(HPO_4)^{2-}$ for the -17.4 ppm peak and Na-PO_4 for those at -12.6 and -12.2 ppm. The presence of two peaks for the Na-PO_4 units indicates that the bonding environment of these units is different in the half and fully exchanged products. Again this is in agreement with previous findings for the zirconium analogues[16,17].

The spectrum for the sodium acetate exchanged product is more complicated and also features peaks at -14.7,-15.9, -21.6 and -22.2 ppm. These must correspond to other side products present, but no assignments could be made from the chemical shift data alone. Whilst peaks corresponding to anhydrous alpha phosphates are commonly observed at ~ -22 ppm[17] the lack of significant broadening of these peaks infers they are not due to anhydrous TiP, instead they may relate to a third sodium exchanged α-TiP phase. At this stage though, this is only conjecture.

5.4.2 PDF Studies

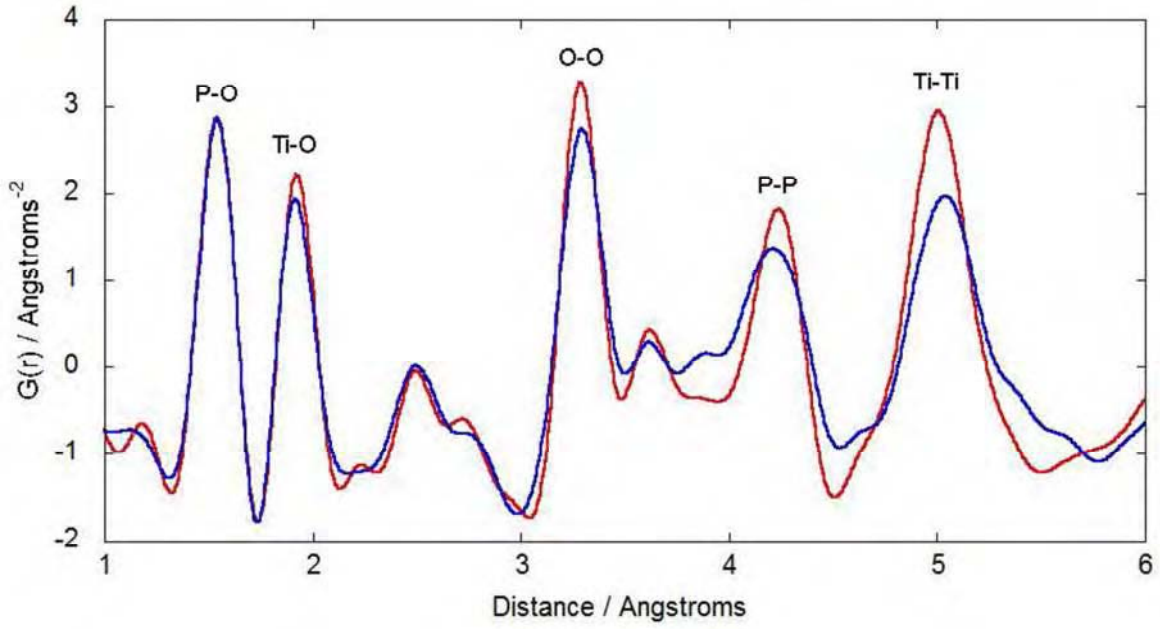

Figure 5.18: Comparison of the PDF patterns for sodium hydroxide exchanged TiP (Blue) and α-TiP (red).

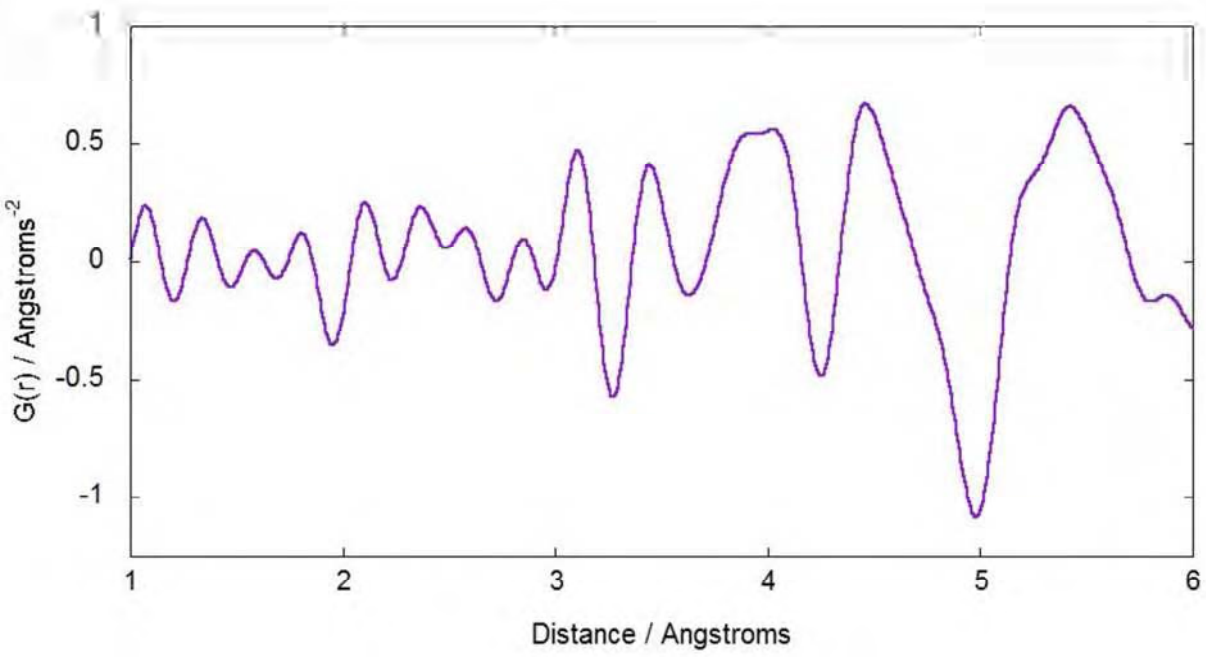

Figure 5.19: Differential PDF of sodium hydroxide exchanged TiP.

The PDF of the product obtained from the sodium hydroxide exchange is given in Figure 5.18. The PDF of the starting material α-TiP is also included for comparison. The differential PDF of the two is provided in Figure 5.19. The PDFs of the sodium exchanged and unexchanged TiP samples are very similar. This is consistent with both the XRD and the ^{31}P NMR data which showed that unexchanged α-TiP was the main phase present in this product. Variations are observed, mainly in the region between 3.4 - 5.8 Å. Whilst the main peaks in this region arise from the titanium-titanium and phosphorus- phosphorus distances within the structures, other distances resulting from the presence of sodium would be expected to occur here as well. From the structures of the zirconium analogues[3,18], possible distances expected for the half and fully exchanged phases include: sodium-sodium at 5-5.5 Å, phosphorus-sodium at 3.5-4 Å and titanium-sodium at 4-4.5 Å and 5-5.5 Å for the half and fully exchanged phases respectively. The increased complexity of the PDF for the exchanged product around this region infers the presence of such distances from the half and fully exchanged α-TiP phases known to be present. In addition to this, incorporation of sodium within the unit cell also leads to variations in the other non-sodium distances e.g. oxygen-oxygen and phosphorus-phosphorus, which can account for the small differences seen with these peaks. Further analysis of this data is hindered by the multiple phases present, and the predominance of unexchanged α-TiP within the sample renders analysis of the long *r* region of the PDFs to determine the layer movement in the exchanged phases almost impossible.

5.4.3 SEM EDX

Whilst SEM/EDX data was collected on both the sodium hydroxide and acetate exchanged α-TiP products, the usefulness of this technique was limited by the multi-phase nature of the products. A summary of compositional results are displayed in Figures 5.20 – 5.21 and Tables 5.2 – 5.3. Although some variation in the sample morphologies were observed in each product, the elemental compositions given by the EDX analysis were fairly consistent throughout the samples. The average sodium contents obtained via this method are compared with those obtained from the XRF studies in Table 5.4. It is important to note however that the EDX analysis is only a semi-quantitative method and that the results from the XRF data are more reliable. Although there are discrepancies between the values, both techniques show higher sodium levels in the sodium acetate exchanged α-TiP product. This again, is consistent with the absence of unexchanged α-TiP within this product, and may also be affected by the unidentified additional phases highlighted in the ^{31}P NMR studies.

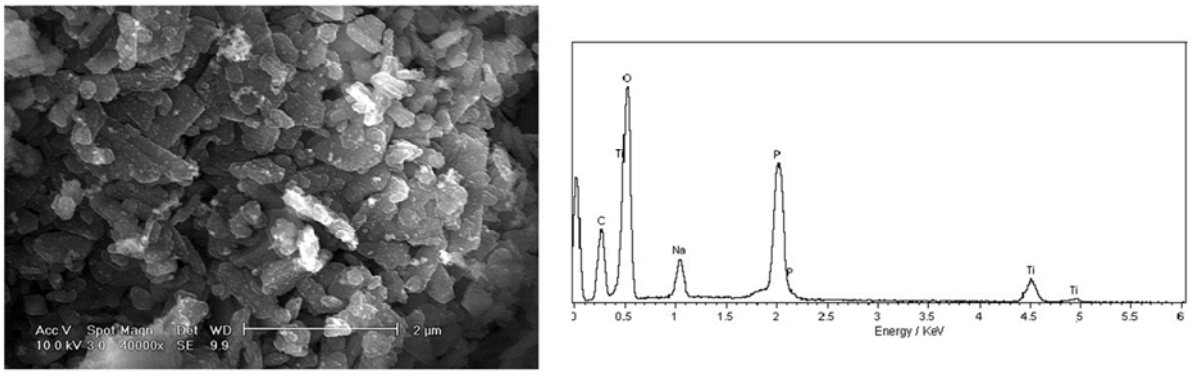

Figure 5.20: SEM images and EDX elemental analysis spectra for sodium hydroxide exchanged TiP.

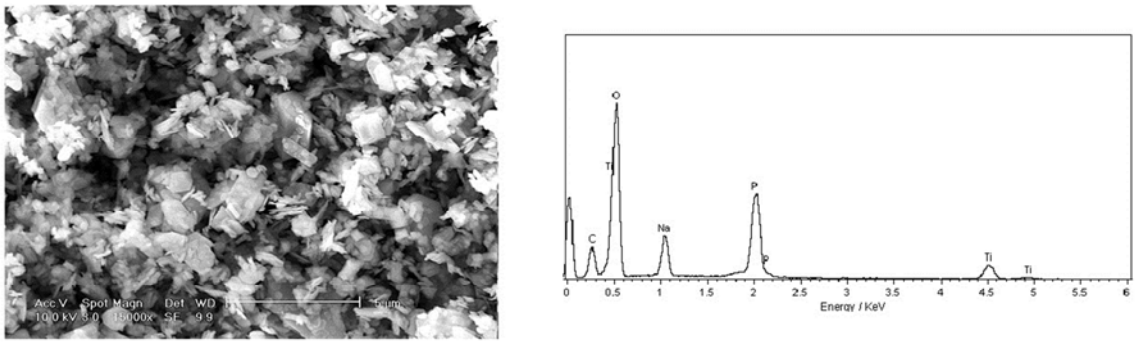

Figure 5.21: SEM images and EDX elemental analysis spectra for sodium acetate exchanged TiP.

Table 5.2: SEM EDX data for sodium hydroxide exchanged TiP.

Scan	SEM EDX Atomic %				Moles of Na per mole of Ti
	O	P	Na	Ti	
1	53.69	24.00	4.89	17.41	0.58
2	52.03	24.97	4.24	18.76	0.47
3	52.56	24.10	4.90	18.45	0.55
4	56.99	22.00	4.46	16.55	0.56
5	53.95	23.40	4.80	17.84	0.56
Average					0.54

Table 5.3: SEM EDX data for sodium acetate exchanged TiP.

Scan	SEM EDX Atomic %				Moles of Na per mole of Ti
	O	P	Na	Ti	
1	53.92	21.24	7.30	17.53	0.87
2	51.34	23.29	7.24	18.14	0.83
3	56.51	20.23	7.08	16.17	0.91
4	55.97	20.38	7.83	15.82	1.03
Average					0.91

Table 5.4: Comparison of the sodium contents given by the EDX and XRF techniques.

Product	Moles of sodium per moles of titanium	
	EDX	XRF
Sodium hydroxide exchanged TiP	0.54	0.74
Sodium acetate exchanged TiP	0.91	1.19

Based on the XRF results (Table 5.4) for the sodium acetate exchanged product, one can tentatively assume that this product consists of approximately 80% of the half exchanged phase and 20% of the fully exchanged phase. This is of course, only an approximation as the XRF results are uncalibrated and the presence of impurities may affect these values / ratios. Due to the presence of unexchanged starting material as well as the half and fully exchanged phases in the sodium hydroxide exchanged product, similar compositional assumptions cannot be made for this product.

5.4.4 Thermal Studies

The TGA /DTA and variable temperature XRD patterns obtained for the sodium acetate exchanged product are displayed in Figures 5.22 and 5.23.

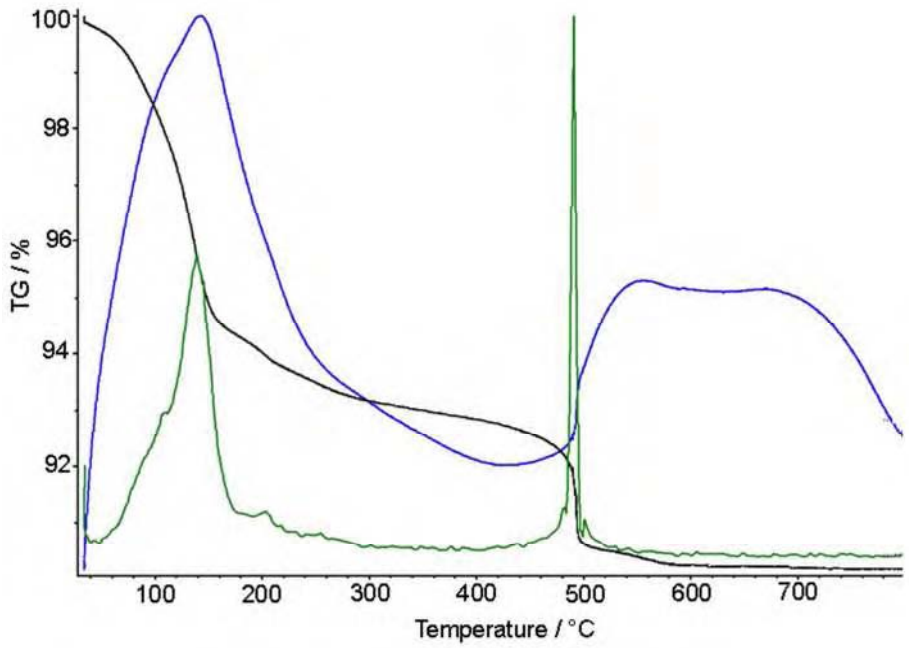

Figure 5.22: TGA trace (black) showing the decomposition pathway of sodium acetate-TiP. The DTA curve is shown in blue and the green trace represents the mass spectrometry results for H_2O.

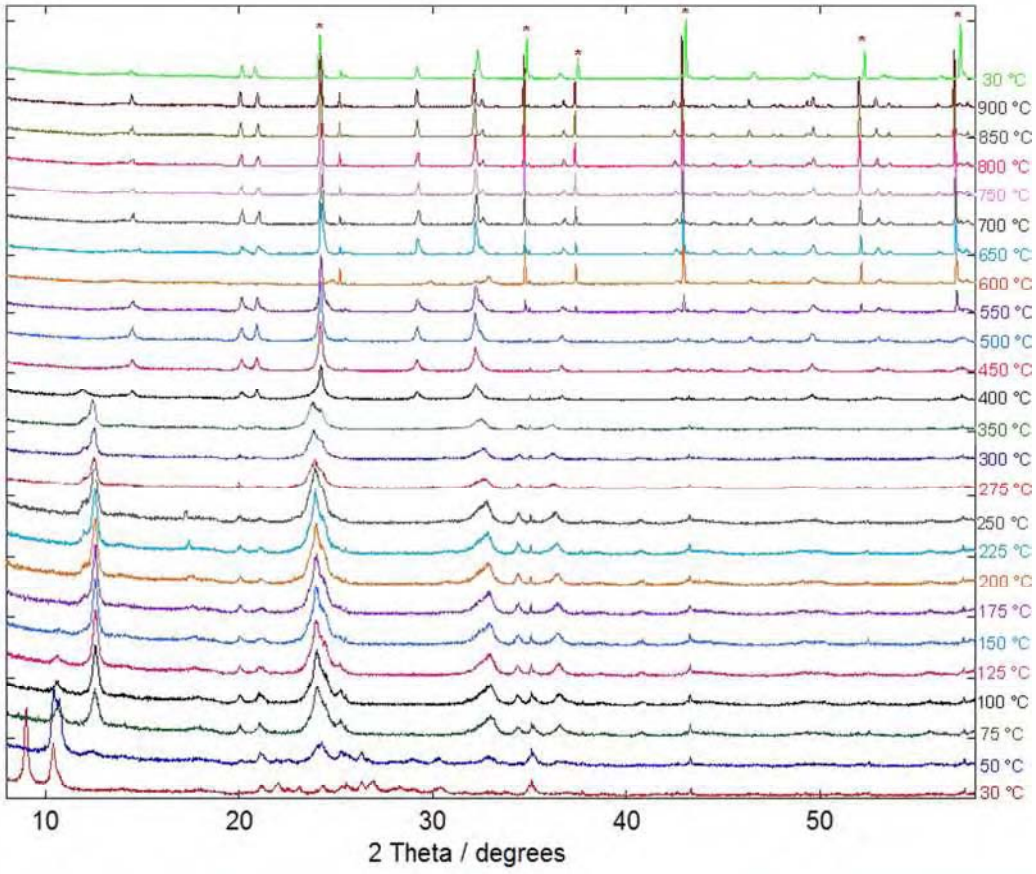

Figure 5.23: The in-situ PXRD patterns of sodium acetate-TiP recorded as a function of temperature. The sharp peaks marked with asterisks arise from the alumina sample holder used.

A review of the literature shows no previous work on the thermal behaviour of the sodium exchanged titanium phases, however the results obtained in this work are consistent with those for the analogous sodium-ZrP phases[19,20]. Low temperature heating of the product between 50-200 °C results in a 6.8 % weight loss due to the loss of the crystallisation water in both phases present to give the dehydrates $TiHNa(PO_4)_2$ and $TiNa_2(PO_4)_2$. These transitions are observed in the XRD data as variations in the pattern are seen within this temperature region. Heating to 50 °C results in the simultaneous loss of the peak at ~9 °2θ corresponding to $TiNa_2(PO_4)_2.3H_2O$ and the appearance of a new peak at ~12.5 ° 2θ thought to be due to the formation of $TiNa_2(PO_4)_2$. From the peak position this phase is believed to

have an interlayer spacing of 7 Å. The half exchanged phase is shown to be slightly more stable and is not fully dehydrated until heating above 150 °C.

A second water loss of only 2.1% occurs upon heating to 400 °C. This endothermic event is mirrored in the XRD data whereby a new pattern is observed. This pattern corresponds to that of $NaTi_2(PO_4)_3$ as demonstrated in Figure 5.24, originating from the following reaction:

$$2TiNa(PO_4)(HPO_4) \longrightarrow NaTi_2(PO_4)_3 + NaPO_3 + H_2O$$

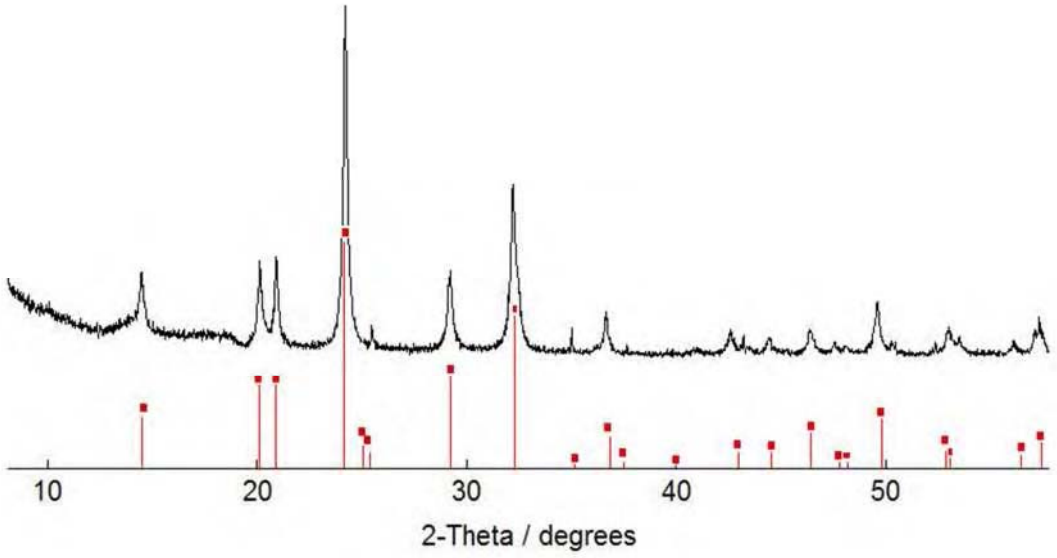

Figure 5.24: The PXRD pattern of obtained from heating above 400 °C. The red lines are the indexed peaks from the ICDD PDF 04-008-2019 for $NaTi_2(PO_4)_3$.

This is in keeping with previous reports on the decomposition of the half exchanged sodium α-ZrP phase[19,20]. As per these studies[20] the sodium metaphosphate product forms a glass which cannot be detected in the XRD patterns but which is responsible for the higher background observed at low angles.

Given the multiphase nature of the product it remains ambiguous whether the fully exchanged phase undergoes a similar reaction to give the same product. However it appears unlikely given that the zirconium analogue does not[19]. Instead the fully exchanged sodium-ZrP product has been shown only to undergo phase transitions at higher temperatures to give a further anhydrous phase[19]. If the titanium fully exchanged phase here behaves in a similar manner, it must be assumed that the anhydrous high temperature phase is not of sufficient crystallinity to be observed in the XRD patterns. In either case $NaTi_2(PO_4)_3$ remains upon heating to 900 °C and cooling back to room temperature. The sharp peaks seen in the patterns above 600 °C are from the alumina sample holder used and result from movement of the sample under testing. There is no evidence of any pyrophosphate formation in the high temperature PXRD patterns which confirms that this product contains no significant amount (if any) of unexchanged α-TiP. To enhance the investigation into the use of these exchanged phosphates for long term storage of cations, further investigation into this decomposition product would be prudent. This is especially true given the already well known properties of these $M(Ti,Zr)_2(PO_4)_3$ materials which have shown them to be suitable for the incorporation of radioactive nuclear waste over long time scales[21,22].

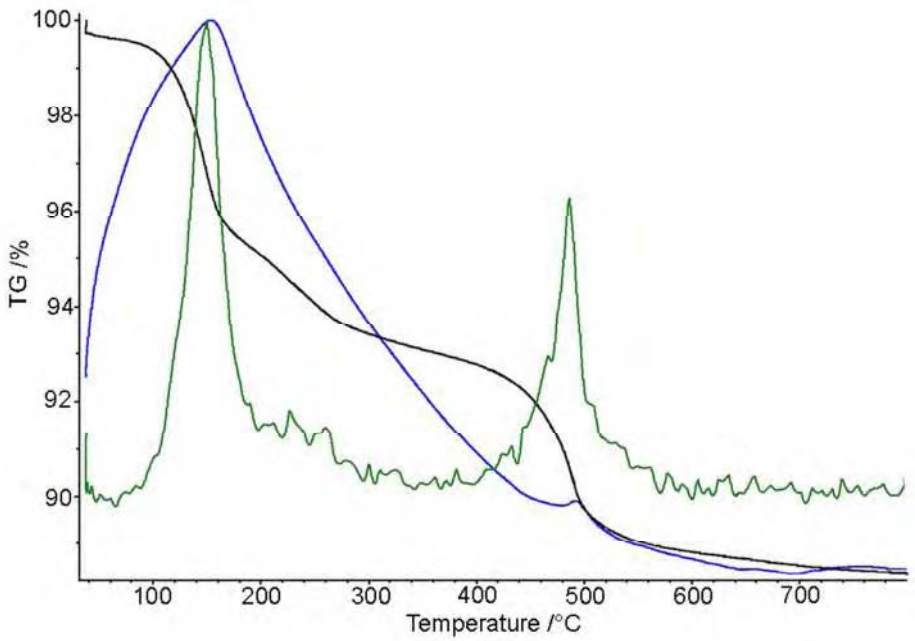

Figure 5.25: TGA trace (black) showing the decomposition pathway of sodium hydroxide-TiP. The DTA curve is shown in blue and the green trace represents the mass spectrometry results for H_2O.

TGA data was also obtained on the sodium hydroxide product and the results are shown in Figure 5.25. Variable temperature XRD patterns were not collected on this product as unexchanged α-TiP was shown to be the main phase present. Unsurprisingly the TGA curve is similar to that of α-TiP. A 6.8% weight loss is observed upon heating between 100-250 °C consistent with the loss of the crystallisation water. The second weight loss occurs upon heating above 350 °C and arises from the pyrophosphate formation. The weight loss for this transition is smaller than expected (4.3% cf. 7.4% for α-TiP) due to the presence of the additional sodium exchanged phases. Whilst the loss of water of crystallination in these exchanged phases as well as the formation of $NaTi_2(PO_4)_3$ contributes to the features in the TGA curve obtained, the results are dominated by the main α-TiP phase present.

5.4.5 Variations in Exchange Conditions

In an attempt to see if either the half or fully sodium exchanged TiP phase could be isolated, ion exchanges using 0.01 M sodium hydroxide solution were attempted at elevated temperatures. In addition to this the standard sodium-hydroxide product was subject to a second ion exchange under identical conditions. The PXRD patterns of the products obtained are displayed in Figure 5.26. The yields of the solid products recovered from the exchanges were insufficient for XRF analysis.

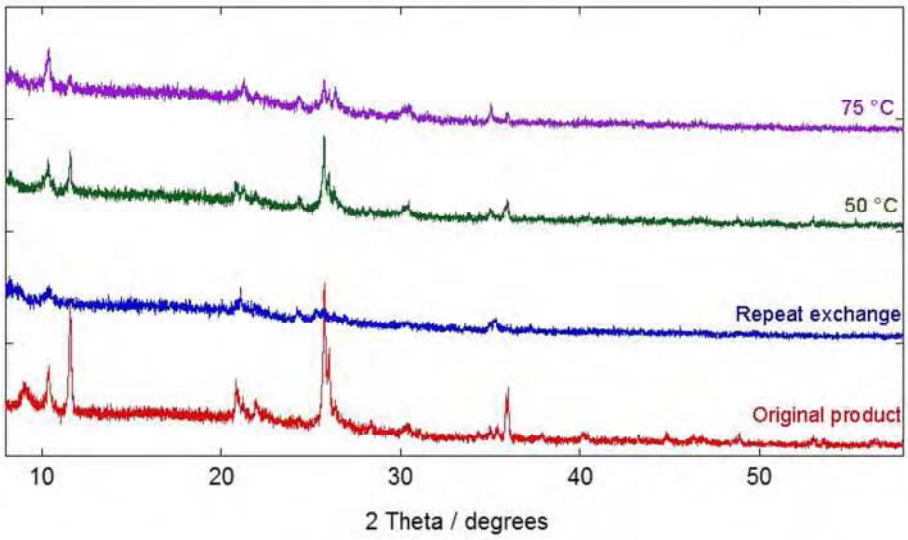

Figure 5.26: PXRD patterns obtained from the 'forced' sodium hydroxide ion exchanges of α-TiP.

All of the 'forced' exchanges resulted in products of low crystallinity, making further analysis difficult. Similarities in the patterns can be observed and the results indicate that the repeated exchange removes the unexchanged α-TiP present in the original product, by presumably providing enough sodium for all α-TiP to undergo either full or half exchange.

Similar experiments were also trialled on the sodium acetate exchanged product using variations in the temperature, duration and volume of sodium solution (1 L compared to 250 ml in the original exchange) used for exchange. The PXRD patterns of the products obtained

as well as that for a 'repeat exchange' are given in Figure 5.27. The crystallinity of the products is reduced and from the similarity in the PXRD patterns, the repeated exchange is not shown to have a significant effect on the product formed. The patterns indicate that longer durations/large volumes and elevated temperatures leads to less of the fully exchanged phase $TiNa_2(PO_4)_2.3H_2O$ as shown by the reduction in the peak at ~9 °2θ. This may therefore provide a useful route for isolating the half exchanged phase to allow for further analysis. Consequently these high temperature exchanged products and the effects of temperature and duration on the exchange process are recommended to be investigated as future work.

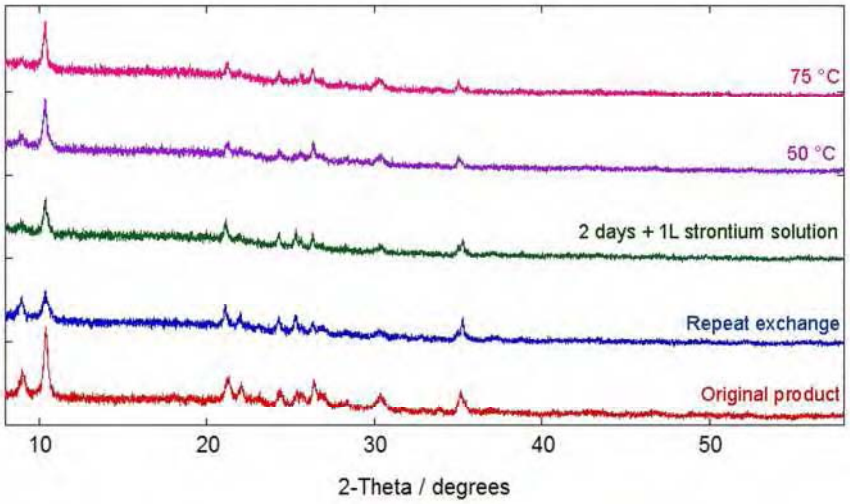

Figure 5.27: PXRD patterns obtained from the 'forced' sodium hydroxide ion exchanges of α-TiP.

5.4.6 Indexing

From the in-house XRD data alone it is clear that severe disordering of the crystal lattice occurs during the exchange leading to low intensity and broad reflections in the PXRD pattern. This is commonly found for sodium exchanged phosphates[23]. Although more accurate peak positions were obtained by using alumina standards, determination of the

structure was complicated by the low crystallinity and the fact that neither phase could be isolated from the other. Regardless, indexing of the half and fully exchanged phases from the sodium acetate product were attempted using DICVOL06[12] and CRYSFIRE[11] and the knowledge of the known zirconium analogue structures, however no satisfactory results were obtained. No attempts at indexing from the sodium hydroxide data were undertaken due to the predominance of unexchanged α-TiP in the product.

5.5 Conclusions

From the further characterisation performed in this work, $ZrSr_{0.55}H_{0.9}(PO_4)_2.xH_2O$ is believed to be the main phase obtained from the strontium hydroxide ion exchange of α-ZrP. Whilst this is in agreement with previous findings[1,2], the analysis here also confirmed the presence of additional phases that were not evident from the XRD patterns published previously. The presence of these minority phases in addition to the reduced crystal quality meant that the structure of this phase could not be identified. The same is true for the strontium exchanged $Zr_{0.9}Ti_{0.1}(HPO_4)_2.H_2O$ product believed to be the isomorphous $ZrSr_{0.55}H_{0.9}(PO_4)_2.xH_2O$ phase, given the similarity in the XRD, XRF and PDF data obtained.

Despite the attempts in this chapter, the crystal structures of both the half and fully exchanged sodium α-TiP phases $TiHNa(PO_4)_2.H_2O$[24] and $TiNa_2(PO_4)_2.3H_2O$[24] remain unknown. Whilst it is likely that these phases are isomorphous to the known α-ZrP phases[3,18] the low crystallinity of the products as well as the presence of additional phases meant that the indexing attempts gave unsatisfactory results. Investigation into the thermal behaviour of these products revealed that $NaTi_2(PO_4)_3$ is formed as a decomposition product of $TiHNa(PO_4)_2.H_2O$.

5.6 Further Work

- Further analysis of the $Zr_{0.9}Ti_{0.1}(HPO_4)_2.H_2O$ strontium product by SEM/EDX and ^{31}P NMR to determine if additional phases, like those found to be present in the α-ZrP exchanged product are also present.
- Obtain PDF data for sodium acetate exchanged α-TiP to establish any structural changes occurring from exchange. Any changes in the sodium hydroxide exchanged product were hard to indentify from the PDF data as the two phases of interest were only minority phases within this product.
- Further investigations into the effect of temperature during synthesis for isolation of the sodium-TiP phases.
- Investigate alternative ion exchange procedures in an attempt to synthesise phase pure products.
- To further characterise and obtain higher quality data on the product obtained from the 0.05 M sodium hydroxide exchange of α-TiP (discussed in Chapter 4). From the XRD data alone, it is possible that this product contains only the half exchanged phase, $TiHNa(PO_4)_2.H_2O$.

5.7 References

(1) Clearfield, A., Hagiwara, H *J. Inorg. Nucl. Chem.*, **40**, 907-914 (1978)
(2) Alberti, G., Bertrami, R., Casciola, M., Costantino, U., Gupta, J. P. *J. Inorg. Nucl. Chem.*, **38**, 843-848 (1976)
(3) Rudolf, P. R., Clearfield, A. *Inorg. Chem.*, **28**, 1706-1710 (1988)
(4) Nakayama, H., Eguchi, T., Nakamura, N., Yamaguchi, S., Danjyo, M., Tsuhako, M. *J. Mater. Chem*., **7**, 1063-1066 (1997)
(5) Clayden, N. J. *J. Chem. Soc. Dalton Trans.*, **8**, 1877-1881 (1987)
(6) Hayashi, A., Fujimoto, Y., Ogawa, Y., Nakayama, H., Tsuhako, M. *J. Coll. Inter. Sci.,* **283**, 57-63 (2005)
(7) Casciola, M., Donnadio, A., Montanari, F., Piaggio, P., Valentini, V. *J. Solid State Chem.*, **180**, 1198-1208 (2007)
(8) Capitani, D., Casciola, M., Donnadio, A., Vivani, R. *Inorg. Chem.*, **49**, 9409-9415 (2010)
(9) Burnell, V. A., Msci Thesis 'The Synthesis and Ion-Exchange of Mixed Zr/Ti Phosphates' University of Birmingham, (2007)
(10) Alberti, G., Costantino, U., Allulli, S., Tomassini, N. *J. Inorg. Nucl. Chem.*, **40**, 1113-1117 (1978)
(11) Shirley, R.; www.ccp14.ac.uk/CRYSFIRE
(12) Boultif, A., Louer, D. *J. Appl. Cryst.*, **37**, 724-731 (2004)
(13) Coelho, A. A. *J. Appl. Cryst.*, **36**, 86-95 (2003)
(14) Nilchi, A., Ghanadi Maragheh, M., Khanchi, A., Farajzadeh, M. A., Aghaei, A. A. *J. Radio. Nucl. Chem.*, **261**, 393-400 (2004)
(15) Clearfield, A., Costantino, U. *Layered Metal Phosphates and Their Intercalation Chemistry* in *Comprehensive Supermolecular Chemistry*; 1st ed.; Alberti, G., Bein, T., Ed.; Pergamon: New York; Vol. 7; 108-149 (1996)
(16) Nakayama, H. *Phosphorus Research Bulletin*, **23**, 1-9 (2009)
(17) MacLachlan, D. J., Morgan, K. R. *J. Phys. Chem.*, **94**, 7656-7661 (1990)
(18) Poojary, D. M., Clearfield, A. *Inorg. Chem.*, **33**, 3685-3688 (1994)
(19) Clearfield, A., Medina, A. S. *J. Inorg. Nucl. Chem.*, **32**, 2775-2780 (1970)
(20) Clearfield, A., Duax, W. L., Medina, A. S., Smith, G. D., Thomas, J. R. *J. Phys. Chem.*, **73**, 3424-3430 (1969)
(21) Liu, G. K., Luo, J. S., Loong, C. K., Abraham, M. M., Beitz, J. V., Bates, J. K *Mat. Res. Soc. Symp. Proc.*, **506**, 921 (1998)
(22) Rao, K. J., Sobha, K. S., Kumar, S. *Proc. Indian Acad. Sci.*, **113**, 497 (2001)
(23) Clearfield, A., Frianeza, T. N. *J. Inorg. Nucl. Chem.*, **40**, 1925-1932 (1978)
(24) Suarez, M., Garcia, J. R., Rodriguez, J *J. Phys. Chem.*, **88**, 159-162 (1984)

Chapter 6: Leach Testing of Ion Exchanged Products

6.1 Introduction

One of the main aims of this project was to develop ion exchange materials that could sequester cations of interest to the nuclear industry. For this reason it is imperative that the exchanged phases synthesised in this work are able to securely retain the exchanged cations over long durations of time. Both ^{90}Sr and ^{137}Cs are typical high level radioactive wastes generated from spent nuclear fuels in atomic power plants[1] with relatively long half-lives of approximately 30 years. Immobilisation methods must therefore produce compounds that are chemically and thermally stable with respect to the leachability of these cations over long time periods. Whilst direct assessment of the materials performance over time periods of these magnitudes is clearly impossible within the time frame of this project, attempts to mimic the effects of such durations have been undertaken through the use of accelerated leach tests involving higher temperatures. More information about the soxhlet method used for the leach tests was provided in the Experimental chapter.

A review of the literature reveals very little on leach testing of the salt forms of the alpha phosphates. A summary of some of the known materials already used for such applications was discussed in the introductory chapter of this thesis. Table 6.1, provides leach rate values for some of these commercial exchangers as well as for other materials currently under investigation for similar applications. Leach rate data for some commercially used products e.g. SrTreat®[2] and CsTreat®[3] were not available for comparison.

Table 6.1: Leach test data in the literature

Exchanger	Cation	Test Conditions*	Leach Rate / g m^{-2} day^{-1}	Reference
Borosilicate glass	Sr	Autoclave 90 °C for 30 days	$1 \times 10^{-3} – 3 \times 10^{-3}$	4,5
Aluminoborosilicate glass	Sr	Autoclave 70 °C for 7 days	1.8×10^{-1}	6
Phosphate glass	Sr	Autoclave 90 °C for 30 days	2×10^{-2}	5
Zirconium phosphate ceramic	Sr	Autoclave 70 - 90 °C for 28 days	2×10^{-2}	7,8
$SrZr_4(PO_4)_6$	Sr	Autoclave 160 °C for 24 hours	$0.2 \times 10^{-5} – 1 \times 10^{-3}$	1,9
$CsZr_2(PO_4)_3$	Cs	Soxhlet 1-7 days	$2 \times 10^{-2} – 1 \times 10^{-3}$	10
Synthetic tobermorite	Sr	Hespe method[11], 25°C for 0-120 days	$1 \times 10^{-2} – 1 \times 10^{1}$	12
$NaTh_2P_3O_{12}$	Na	Soxhlet 1-16 days	1.4×10^{-2}	13
$SrFeZrP_3O_{12}$	Sr	Soxhlet 1-16 days	2.2×10^{-4}	13
$Sr_3XP_3O_{12}$ where X = La, Y, Pr or Nd	Sr	Soxhlet 1-16 days	2×10^{-5} - 1.6×10^{-4}	13

*in all cases water was used as the leachate.

6.2 Strontium Ion Exchanged α-ZrP

Leach testing of the strontium exchanged α-ZrP sample was conducted over 1, 3, 7 and 14 days. Characterisation of this product discussed in the previous chapters of this thesis indicated that the main phase present was $ZrSr_{0.55}H_{0.9}(PO_4)_2.xH_2O$. The strontium contents of the leachates were determined from ICP analysis and the solid products recovered were analysed by XRD. The leach rates were calculated by the method outlined in section 2.7. It should also be noted that the real errors associated with the leach rates may be significantly higher than those quoted. There is expected to be a large unknown error in the leach rate values determined, due to issues arising from the calculations of the surface area as previously discussed in section 2.9.4.

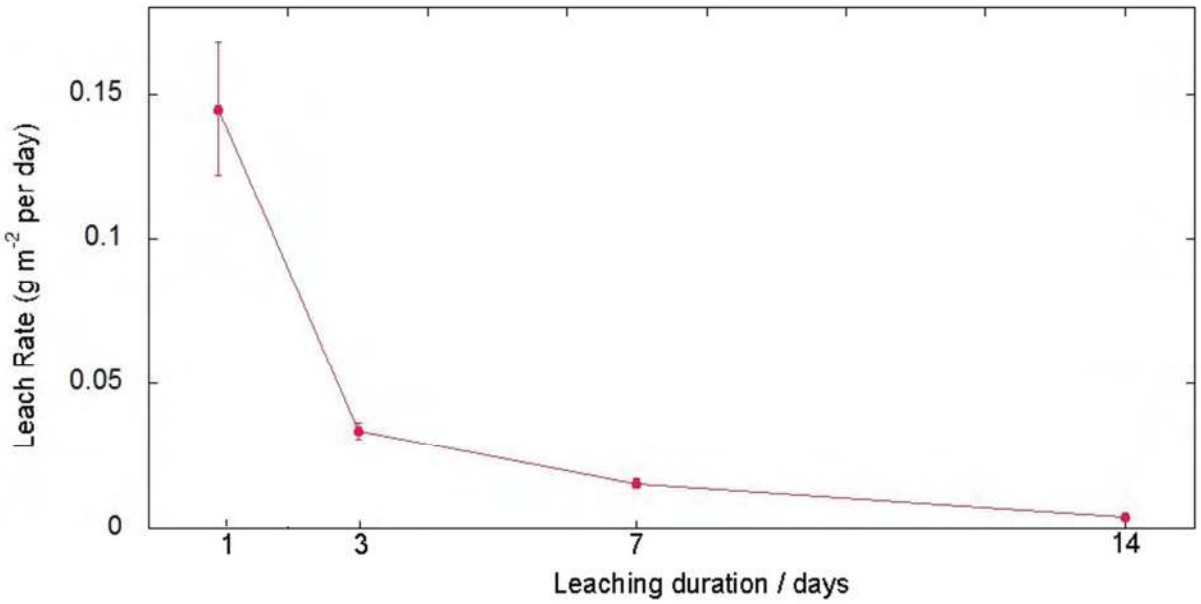

Figure 6.1: Strontium leach rates of strontium-ZrP.

Table 6.2: Leach rates of strontium-ZrP.

Number of days leached	Normalised leach rate ($g\ m^{-2}\ day^{-1}$)	± Error ($g\ m^{-2}\ day^{-1}$)
1	0.145	0.023
3	0.034	0.003
7	0.016	0.002
14	0.005	0.001

The results of the leach testing are given in Figure 6.1 and Table 6.2. The leach rate decreases sharply over time indicating that only surface adsorbed strontium is released upon initial exposure to water and that the material is able to retain the bulk exchanged strontium throughout these tests. Indeed, in all cases the normalised leach rates calculated correspond to the loss of less than 1% of the initial strontium content. In support of this no discernable

difference was observed between the PXRD patterns obtained before and after leaching (see Figure 6.2).

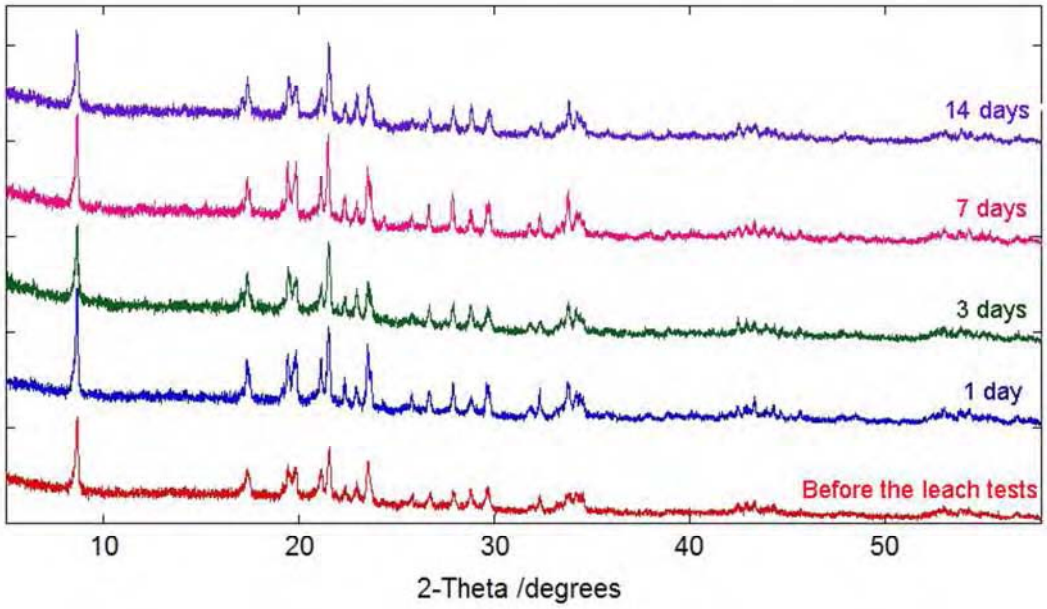

Figure 6.2: PXRD patterns of the samples before and after leaching.

The initially high leach rates may also be due in some parts to the samples not having been fully washed prior to leach testing. This may have resulted in the presence of very small particles on the sample which may greatly increase the surface area available for leaching and thus erroneously increasing the leach rates. It is also possible that the impurity/additional phases present in the sample are responsible for some or all of the strontium initially released.

The leach rates plateaux after 14 days to values of approximately 10^{-3} g m^{-2} day^{-1}. These results therefore show that $ZrSr_{0.55}H_{0.9}(PO_4)_2.xH_2O$ is able to retain strontium well - yielding similar leach rates to those reported in the literature for other materials under consideration

for similar applications, e.g. borosilicate glass[14] (10^{-3} g $m^{-2}day^{-1}$) and zirconium phosphate ceramics[10,15] (10^{-2} g $m^{-2}day^{-1}$) (see also Table 6.1).

6.3 Strontium Ion Exchanged $Zr_{0.9}Ti_{0.1}(HPO_4)_2.H_2O$

The results of the leach testing for strontium exchanged $Ti_{0.1}Zr_{0.9}(HPO_4)_2.H_2O$ are given in Figure 6.3 and Table 6.3. Characterisation carried out prior to leach testing indicated that this product was isomorphous to $ZrSr_{0.55}H_{0.9}(PO_4)_2.xH_2O$. It was therefore of interest to see if the presence of titanium within the framework would have an effect on the strontium leaching resistance. The surface area of the samples was calculated as per the method described in section 2.9 and due to the unknown errors in the particle size (see section 2.9.4); we envisage the real errors associated with the leach rates given to be much higher than those stated.

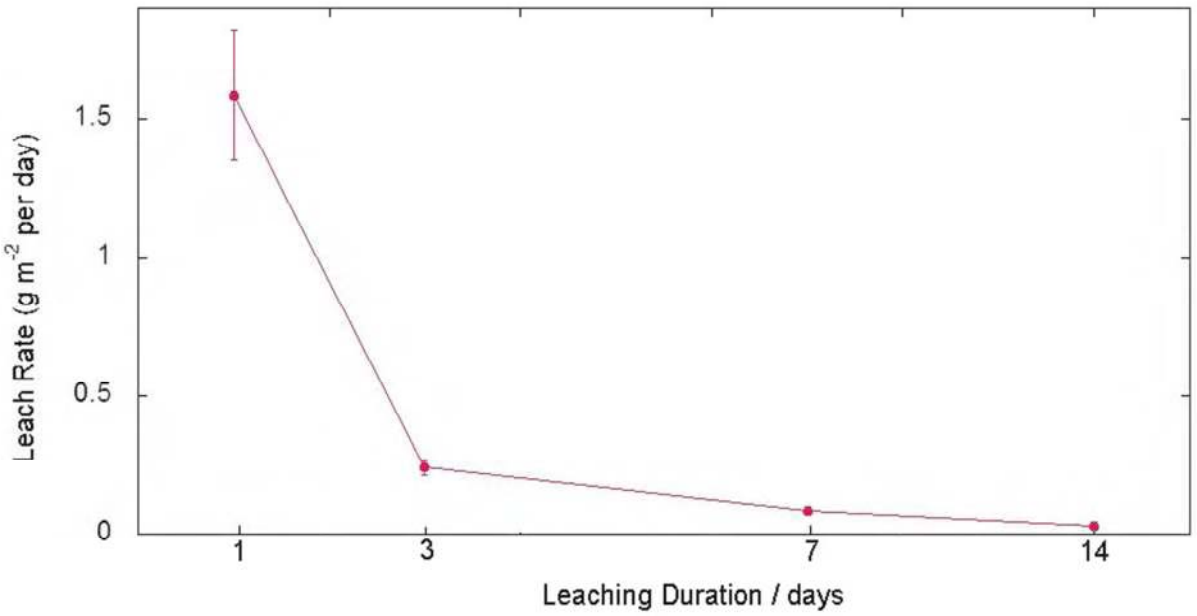

Figure 6.3: Strontium leach rates of strontium exchanged $Ti_{0.1}Zr_{0.9}(HPO_4)_2.H_2O$.

Table 6.3: Leach rates of strontium exchanged $Ti_{0.1}Zr_{0.9}(HPO_4)_2.H_2O$.

Number of days leached	Normalised leach rate ($g\ m^{-2}\ day^{-1}$)	± Error ($g\ m^{-2}\ day^{-1}$)
1	1.585	0.236
3	0.242	0.027
7	0.084	0.010
14	0.032	0.004

The results of the leaching experiments are similar to those obtained for the strontium exchanged ZrP product ($ZrSr_{0.55}H_{0.9}(PO_4)_2.xH_2O$) showing a sharp decrease in the leach rate between 1 and 3 days. The leach rates level off to a value of around 10^{-2} g m^{-2} day^{-1}, which is a magnitude of 10 higher than for $ZrSr_{0.55}H_{0.9}(PO_4)_2.xH_2O$. This could signify either a change in the particle size (therefore increasing the surface area) or a lowering of the chemical stability of the compound compared with $ZrSr_{0.55}H_{0.9}(PO_4)_2.xH_2O$. Given the similarity of XRD patterns collected before and after leaching (shown in Figure 6.4), it can be assumed that the crystal structure of the product is stable throughout the leaching process. In the absence of SEM data it is unclear whether a change in particle size is therefore responsible for the increased leach rates, but given the errors in particle size already discussed this seems the more plausible explanation. The presence of other minor phases in this product may also differ from those seen in $ZrSr_{0.55}H_{0.9}(PO_4)_2.xH_2O$ and could also be responsible for the higher levels of strontium lost. However this cannot be confirmed without further knowledge of the phases present before and after leach testing.

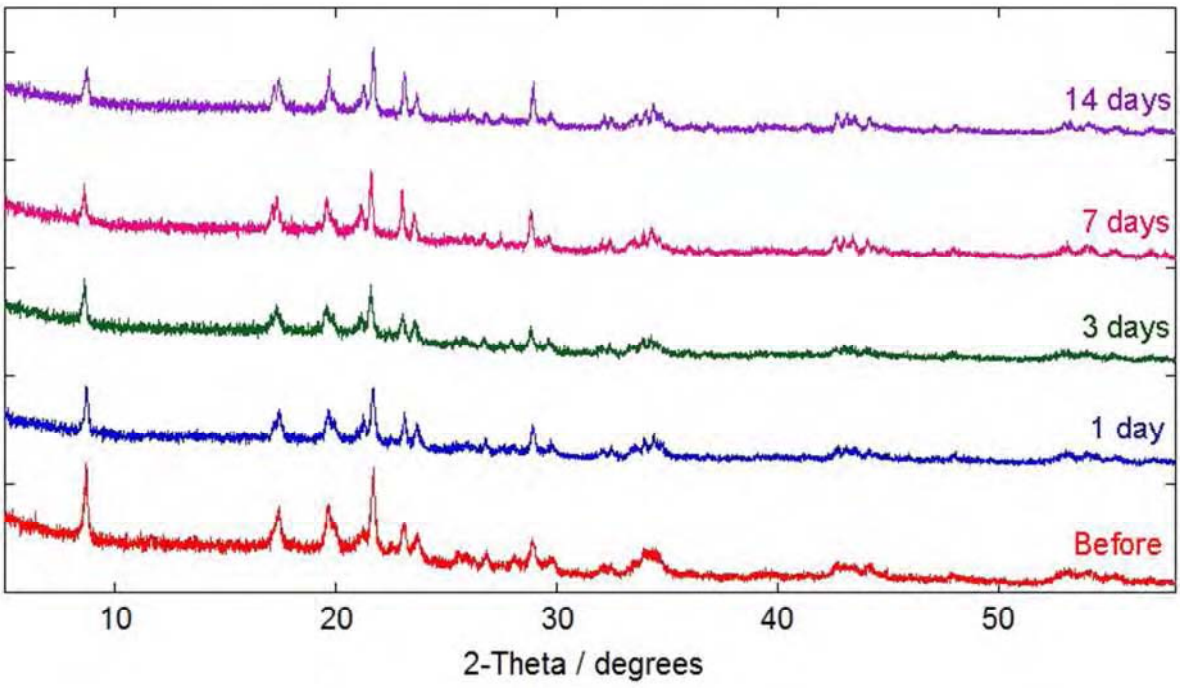

Figure 6.4: PXRD patterns of the strontium exchanged $Ti_{0.1}Zr_{0.9}(HPO_4)_2.H_2O$ samples before and after leaching.

6.4 Sodium Ion Exchanged α-TiP

Out of the two sodium exchanged α-TiP products, only the acetate exchanged product was selected for leach testing. This decision was based on the findings outlined in the previous chapters whereby unexchanged α-TiP was found to be the main phase present in sodium hydroxide exchanged TiP. In contrast, the acetate exchanged product was determined to consist of the half and fully exchanged phases $TiHNa(PO_4)_2.H_2O$ and $TiNa_2(PO_4)_2.3H_2O$ in addition to some minority phases that remain unidentified.

Due to the multiphase nature of the product under investigation, average values from the two phases were used in the calculations for determining the leach rates. The results given therefore provide only an overview of the strontium leaching resistance of this product rather than absolute values.

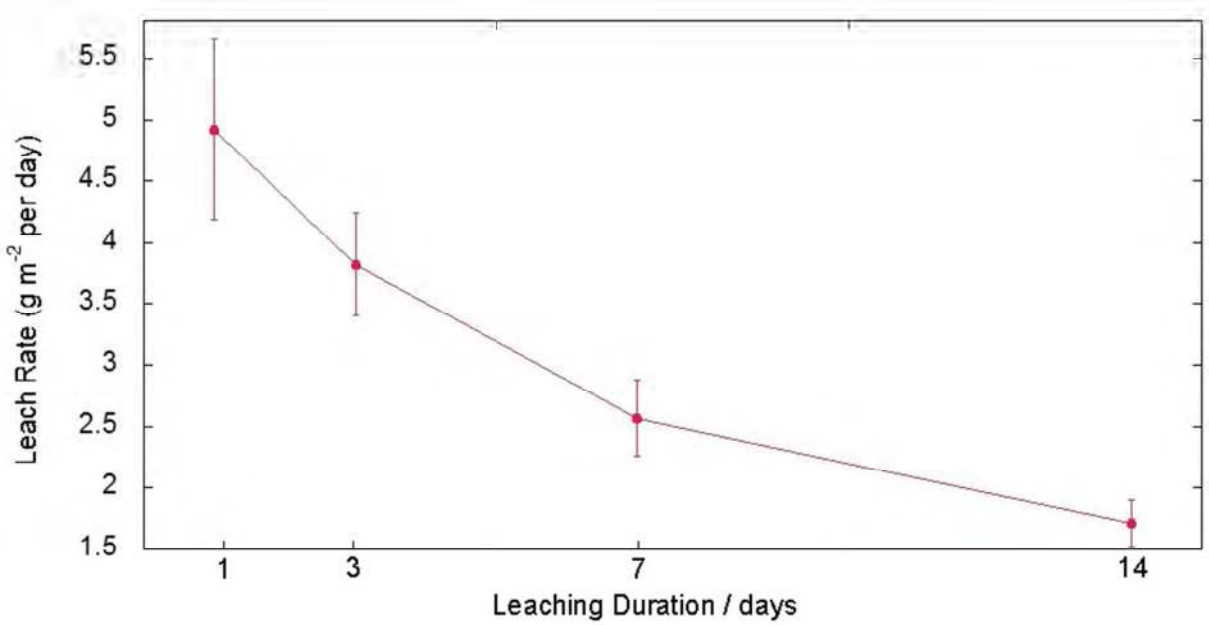

Figure 6.5: Sodium leach rates of sodium acetate-TiP

Table 6.4: Leach rates of sodium acetate-TiP

Number of days leached	Normalised leach rate ($g\ m^{-2}\ day^{-1}$)	± Error ($g\ m^{-2}\ day^{-1}$)
1	4.92	0.73
3	3.82	0.42
7	2.57	0.31
14	1.71	0.19

The results of the leach testing are given in Figure 6.5 and Table 6.4. Clearly, the leach rates obtained for this product are higher than those seen for the strontium exchanged products discussed previously. The values obtained are also higher than those observed for other sodium containing phases[13]. Again the leach rates decrease over time and plateau to values of ~ 1 g m^{-2} day^{-1} after 14 days. This suggests that there is some easily leachable phase(s) present that release sodium quickly at the beginning of the tests but that the bulk of the sample loses sodium at a slower rate.

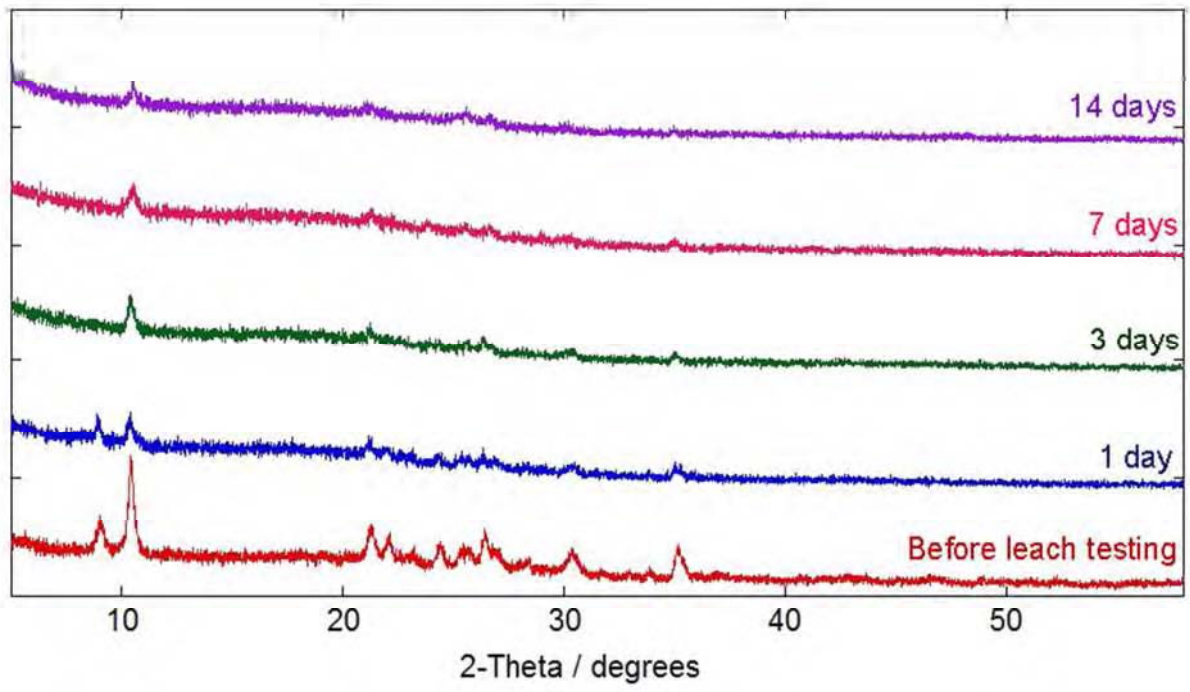

Figure 6.6: PXRD patterns of the sodium acetate-TiP samples before and after leaching.

PXRD patterns of the samples before and after leach testing are given in Figure 6.6. The effect of the leach tests is clearly visible within the patterns. The crystallinity of the samples is reduced even after only one day of testing. This is in keeping with the structural breakdown and sodium release indicated from the ICP results. It is interesting to note that the peak at ~9° 2θ, which corresponds to the fully exchanged phase $TiNa_2(PO_4)_2.3H_2O$ is not observed in the patterns collected after three or more days of leach testing. On the other hand the peak at ~10° 2θ corresponding to the half exchanged phase $TiHNa(PO_4)_2.H_2O$ is still observed in the patterns after 14 days, even though the intensity of it is severely reduced. These results in combination with the ICP/leach rates, suggest that the fully exchanged phase has a low stability and breaks down releasing sodium under these conditions. A lack of thermal stability was also observed in this phase from the TGA and variable temperature XRD work carried out and discussed previously. The half exchanged phase appears to exhibit

a higher sodium leaching resistance, however it also appears to undergo sample breakdown after prolonged periods of leach testing. In order to test this theory longer durations of leach testing could be carried out on this product as part of future work. Compositional analysis using XRF and probing of the phosphorus environments of the samples after leach testing with ^{31}P NMR spectroscopy could also be useful to ascertain the true extent of the sample degradation.

Whilst sodium in itself is not a problem in the nuclear industry and is therefore not an element requiring long term storage like ^{90}Sr or ^{137}Cs, these sodium exchanged phases were being investigated as a possible route to exchange of these problematic cations that proved harder to exchange in the pure phosphates. However, from these results, the sodium exchanged phases $TiHNa(PO_4)_2.H_2O$ and $TiNa_2(PO_4)_2.3H_2O$ do not appear to offer the long term stability and resistance towards leaching required for the end applications. Whilst increased sodium retention is unwanted due to the need to replace sodium with other cations , the extremely poor sodium retention and destruction of crystallinity seen in these studies indicate that exchange of larger cations into these systems would yield further damage and even lower cation retention.

6.5 Conclusions

Samples of strontium exchanged α-ZrP and $Zr_{0.9}Ti_{0.1}(HPO_4)_2.H_2O$ as well as sodium exchanged α-TiP were subject to accelerated leach tests to ascertain how easily sodium/strontium could be removed from the materials. This property is obviously vital for the use of these materials as long term stores for radioactive waste. The strontium samples were superior in cation retention compared with the sodium-TiP phases. The values of the

strontium leach rates for the strontium-ZrP samples were comparable to those reported for other materials considered suitable for these applications[10,14,15].

These initial results suggest that the presence of titanium within α-ZrP has a small but detrimental effect on the strontium leaching resistance, however further analysis is required to confirm this and determine the exact reason why.

The low stability and high leach rates found for the sodium-TiP phases hinder their further use. In contrast both the strontium samples display sufficiently low leach rates to be considered for further investigation into their use as strontium containing waste forms.

6.6 Further Work

- Further analysis of the leached samples by XRF and/or ^{31}P NMR spectroscopy to determine the effects of the leach tests and the extent of sample degradation.
- Leach testing for longer durations to identify if leaching continues at a steady rate.
- Leach testing of the products in different pH solutions to determine the effect of pH on cation retention.
- Leach testing of the decomposition products of these exchanged materials.
- If possible, leach testing of commercial samples e.g. SrTreat®[2] to allow for a direct comparison to the materials developed in this work.

6.7 References

(1) Nakayama, S., Itoh, K., *J. European. Cer. Soc.*, **23**, 1047-1052 (2003)
(2) Lehto, J., Brodkin, L., Harjula, R., In *Radioactive Waste Man. Env. Remediation*: ASME; 245-248 (1997)
(3) Harjula, A., Lehto, J., Saarinen, L., Paajanen, A., Tusa, E., In *Proc. of the Waste Management 96 Symposium*: Tucson, Arizona, USA; 17-38 (1996)
(4) Bernazikowski, T. A., Allender, J. S., Stone, J. A., Gordon, D. E., Gould, T. H. Jr., Westberry, C. F. III., *Am. Ceram. Soc. Bull.*, **62**, 1364-1390 (1983)
(5) Sales, B. C., Boatner, L. A., *Mater. Lett.*, **2**, 301-304 (1984)
(6) Audero, M. A., Bevilacqua, A. M., de Bernasconi, N. B. M., Russo, D. O., Sterba, M. E., *J. Nucl. Mater.*, **233**, 151-156 (1995)
(7) Scheetz, B. E., Agrawal, D. K., Breval, E., Roy, R., *Waste Management*, **14**, 489-505 (1994)
(8) Ishida, M., Kikuchi, K., Yanagi, T., Terai, R., *Nucl. Chem. Waste Management*, **6**, 127-131 (1986)
(9) Hashimoto, C., Nakajima, Y., Terada, T., Itoh, K., Nakayama, S., *J. Nucl. Mater.*, **408**, 231-235 (2011)
(10) Roy, R., Vance, E.R., Alamo, J., *Mat. Res. Bull.*, **17**, 585-589 (1982)
(11) Hespe, E. D., *Atomic Energy Rev.*, **9**, 195 (1971)
(12) Shrivastava, O. P., Shrivastava, R., *Bull. Mater. Sci.*, **23**, 515-520 (2000)
(13) Sugantha, M., Kumar, N. R. S., Varadaraju, U. V., *Waste Management*, **18**, 275-279 (1998)
(14) Kahl, L., *Nucl. Chem. Waste Management*, **2**, 143 (1981)
(15) Komarneni, S., Roy, R., *Mat. Res. Soc. Symp. Proc.*, **15**, 77 (1983)

Chapter 7: Summary

7.1 Mixed Metal Alpha Phosphates

The work in this thesis has shed further light on the structural chemistry and solid solution limits of an important class of ion-exchange materials with potential utility for nuclear waste clean-up. The synthesis of mixed metal phosphates was one of the principal aims of this thesis as outlined in Chapter 1. The properties and uses of both α-ZrP and α-TiP are already very well-known and documented[1-11], however the focus of this work was to investigate whether mixed metal phosphates of the alpha layer type *could* be synthesised and if so what effect the presence of the second metal had on the properties of the materials. For example, it was hypothesised that the ion-exchange capabilities could be altered through partial substitution of one metal for another within the alpha structure. Investigations into a number of mixed metal systems containing zirconium, titanium, germanium and/or tin, were conducted and the results presented in Chapter 3. The full solid solution could not be synthesised in any of the systems studied as all were found to have a miscibility gap. The reasons behind the miscibility gaps were probed and rationalised through structural changes determined from powder X-ray diffraction data and through the use of X-ray fluorescence. It was determined that the structures lack the flexibility required to accommodate higher levels of the second metal, particularity when there is a large difference in the metal radii and/or degree of corrugation within the layers. This layer corrugation can result in significant strains within the structures upon metal substitution and global instability index (GII) calculations were used to quantify these strains in order to determine the point at which the strains were too great to allow the product to form. In addition it would also appear that

some aspects of solution chemistry plays a role in the lack of formation of the full solid solutions by preventing gel precursors with all ranges of compositions from forming. To our knowledge this is the first detailed investigation into the factors preventing the formation of these mixed metal phosphate solid solutions.

A few literature reports on mixed titanium-zirconium phosphates already exist[6,12-14], however the products were poorly crystalline and the investigations were not thorough - with no structural analysis of the materials undertaken. In this thesis, for the first time, both traditional Rietveld and pair distribution function (PDF) analysis of powder X-ray diffraction data were used to characterise the structures of mixed titanium-zirconium phosphates and the results from the two methods were compared. A broad range of titanium-zirconium phosphate solid solutions were formed showing isomorphous substitution of titanium for zirconium in the α-TiP lattice and vice versa for titanium substitution in the α-ZrP lattice. The solid solutions behaved like the end member they are compositionally closest to, including the average metal-oxygen distance, which did not change in a linear fashion between end members indicating that the unit cells were unable to withstand major alterations in the *a*- and *b*- directions to accommodate more of the second metal. The PDF results showed there to be no metal ordering within these products which was in contrast to previous reports of a hexagonal metal distribution[12]. For both α-TiP and α-ZrP solubility is partial with the coexistence of two partially substituted phases observed in samples with nominal compositions between the solubility limits (products $Ti_{0.6}Zr_{0.4}(HPO_4)_2.H_2O$ to $Ti_{0.2}Zr_{0.8}(HPO_4)_2.H_2O$). The structures of these two phase products were also refined despite the complexity of these systems, as outlined in Section 3.1.2.3.

This thesis has also produced the first examples of mixed titanium-germanium phosphate solid solutions as presented in Chapter 3. Full characterisation of the products showed them to behave like the end member they were compositionally closest to and the PDF analysis showed no metal ordering within these compounds. Structural refinements using both Rietveld and PDF methods were again undertaken and the results were given in Chapter 3. As per the titanium-zirconium series, a miscibility gap was found even though higher levels of substitution were possible in this system with α-TiP able to accommodate 40% germanium substitution and α-GeP 20% titanium substitution (cf. 30% zirconium substitution in α-TiP and only 10% titanium substitution in α-ZrP). This is due to the greater similarity in the structure type, degree of layer corrugation and metal size. Rietveld refinements undertaken on the two phase products (nominally $Ti_{0.5}Ge_{0.5}(HPO_4)_2.H_2O$ – $Ti_{0.3}Ge_{0.7}(HPO_4)_2.H_2O$) determined the presence of two partially substituted phases and in spite of the poor quality data, reasonable fits were still achieved. Two different synthetic methods were employed for this series; one based upon the synthetic method used for α-TiP and the other for α-GeP. Whilst the use of the 'GeP method' allowed for the synthesis of the germanium-rich co-precipitates (which could not be formed using the 'TiP method'), all the products synthesised in this way were shown to contain more than one mole of water and consequently varied in their thermal behaviour compared with the products with the same nominal compositions obtained through the 'TiP method'. This was fully discussed in Section 3.2.2.9.

The mixed zirconium-germanium phosphates in this work were synthesised by a method based on that used for α-GeP rather than the method previously reported by Galli *et al.*[15] for this series. Their results showed that 20 % substitution of germanium in the α-ZrP matrix was

possible. In this work both X-ray diffraction and PDF methods demonstrated that almost all of the products synthesised were two phase and from the subsequent structural refinements these phases were in general found to be a pure end member phosphate and a slightly doped phase. Based on the XRF results the zirconium rich phosphates were found to contain no germanium and were successfully refined as pure α-ZrP. Only two of the products appeared to be solid solutions – $Ge_{0.3}Zr_{0.7}(HPO_4)_2.H_2O$ and $Ge_{0.9}Zr_{0.1}(HPO_4)_2.H_2O$ and they were refined as such using Rietveld methods. Closer inspection of the results of the refinement of $Ge_{0.9}Zr_{0.1}(HPO_4)_2.H_2O$ revealed the presence of potentially two additional phases but the data quality was not sufficient to allow for successful two or three phase refinements. The lack of co-precipitates formed in this series, compared with the others investigated, is believed to be due to the considerable differences in the end member structures. As discussed in Section 3.5, α-GeP is a highly corrugated structure whilst α-ZrP is the least corrugated of all the alpha phosphates. Therefore attempts to synthesise mixed germanium-zirconium phosphates results in the build-up of high levels of strain which cannot be overcome and prevents the formation of the solid solutions.

Based on previous reports in the literature of mixed tin-titanium[16] and tin-zirconium[17] phosphates, both series were investigated in this thesis and were discussed in Chapter 3. Whilst some success with the mixed zirconium-tin series was reported in the literature[17], the synthesis of this series in this work was unsuccessful without the formation of any solid solutions. This discrepancy may be due to the different synthetic methods used. For the mixed tin-titanium series both the XRD and XRF results obtained indicated that this series may have been successful, and in addition to this the XRD results showed no evidence of any beta or gamma phases that plagued this series in previous reports[16]. Due to the problems

with low levels of reproducibility and issues arising from the use of tin, this series was not further investigated in this thesis and so the highest level of metal substitution in this series remains unknown. Further characterisation of these phosphates could be conducted in future work to expand on the knowledge of these mixed metal phosphates.

7.2 Ion Exchange Experiments

One of the main reasons for synthesising the range of mixed metal phosphates was to see what affect the presence of the second metal had on the ion exchange behaviour. It was hoped that this property of these phosphates could be fine tuned by chemical control. It was therefore important to assess the ion exchange behaviour of the materials synthesised in this thesis to examine this and to determine their use as potential nuclear waste stores. Initially room temperature ion exchange experiments were performed on α-TiP using strontium, caesium and cobalt solutions (see Chapter 4). Any exchanges deemed successful were also conducted on the mixed titanium-zirconium phosphates as well as for pure α-ZrP. In accordance with previous findings[6,18], the mixed metal phosphates generally exhibited ion exchange behaviour similar to the end member they were compositionally closest to.

As outlined in Chapter 4, both the cobalt and caesium ion exchanges of α-TiP were unsuccessful, despite attempts to increase the temperature and duration of the experiment. We believe that in order to exchange these cations, even more forceful conditions – principally by exploiting the effects of increased pH towards exchange and /or stepwise exchanges with smaller cations first are required.

Room temperature strontium ion exchange was attempted on the titanium-zirconium series using 0.01 M strontium hydroxide solutions. We believe these to be the first attempts at

strontium ion exchange of mixed titanium-zirconium phosphates. For α-TiP and the titanium rich phosphates the exchanges were unsuccessful despite efforts to vary the temperature and pH of the exchange. In contrast the zirconium-rich coprecipitates, α-ZrP and $Zr_{0.9}Ti_{0.1}(HPO_4)_2.H_2O$ were found to readily exchange with strontium yielding the isomorphous strontium phases $Sr_{0.55}ZrH_{0.9}(PO_4)_2.xH_2O$ and $Sr_{0.55}Zr_{0.9}Ti_{0.1}H_{0.9}(PO_4)_2.xH_2O$. These products were further characterised using XRD, XRF, SEM/EDX, TGA and PDF methods as discussed in Chapter 5. In addition to this the thermal behaviour of the strontium-ZrP product ($Sr_{0.55}ZrH_{0.9}(PO_4)_2.xH_2O$) was probed using both TGA/DTA with mass spectrometry and variable temperature XRD, which identified $Sr_{0.55}ZrH_{0.9}(PO_4)_2$ as the main decomposition product.

Although the $Sr_{0.55}ZrH_{0.9}(PO_4)_2.xH_2O$ phase has been reported in the literature[19,20], the characterisation of the product undertaken in this work highlighted the presence of additional phase(s) that were not previously known. This was presumably due to the low quality data obtained and the lack of further characterisation undertaken. Although higher quality synchrotron XRD data were obtained on the strontium exchanged products in this work, the structures of both these strontium phases remains unknown due to the difficulties associated with the multi-phase nature of the products.

Attempts were made to increase the level of strontium exchanged in these products by employing higher temperatures and longer durations of exchange, however in general, this led only to a lowering of the crystallinity of the products, making further characterisation even more problematic. Leach testing of both strontium exchanged phases, $Sr_{0.55}ZrH_{0.9}(PO_4)_2.xH_2O$ and $Sr_{0.55}Zr_{0.9}Ti_{0.1}H_{0.9}(PO_4)_2.xH_2O$, were undertaken over a 1-14 day duration using the method outlined in Chapter 2. To our knowledge these leach tests are the

first known for any of the salt forms of alpha phosphates. The results given in Chapter 6 showed $Sr_{0.55}ZrH_{0.9}(PO_4)_2.xH_2O$ exhibited excellent strontium retention over the time periods investigated with leach rates comparable to other materials being proposed for real use e.g. borosilicate glass[21,22]. From these results, further study of this exchanged phase and its decomposition product ($Sr_{0.55}ZrH_{0.9}(PO_4)_2$) are encouraged. Whilst the structure remains unknown, this work has demonstrated that α-ZrP is able to ion exchange with strontium with relative ease and forms an exchanged phase that is able to retain strontium over long time durations. Higher strontium leach rates were observed for the $Sr_{0.55}Zr_{0.9}Ti_{0.1}H_{0.9}(PO_4)_2.xH_2O$ phase indicating that the presence of titanium within the product has a detrimental effect on the strontium retention.

Sodium ion exchange was also investigated as a possible route for the further exchange of larger cations (e.g. Co and Cs). All of the single phase titanium-zirconium phosphates tested exhibited a high affinity for sodium when sodium acetate (0.1 M) or hydroxide (0.01 M) solutions were employed. As per previous literature reports[19] a higher degree of exchange was found when the acetate solutions were used. Ion exchange of α-TiP with both sodium acetate (0.1 M) and hydroxide (0.01 M) solutions yielded the previously reported[23] half and fully exchanged sodium phases $TiHNa(PO_4)_2.H_2O$ and $TiNa_2(PO_4)_2.3H_2O$, which, in keeping with previous findings[6,23], were found to coexist within the products. Unexchanged starting material was also shown to be present and later determined to be the main phase present in the sodium hydroxide ion exchanged product. XRD analysis of these sodium phases showed that structural deformations occur upon exchange which results in poorly crystalline products/XRD patterns (see Chapter 5). This, in combination with the presence of additional

phases meant that neither the structure for $TiHNa(PO_4)_2.H_2O$ or $TiNa_2(PO_4)_2.3H_2O$ could be solved in this work. However further characterisation of the products by ^{31}P NMR, SEM and thermal methods, as presented in Chapter 5, have allowed for further understanding of the sodium phases and their thermal behaviour. As both of the sodium phases coexisted in the products obtained in this work, attempts were made to isolate one of the phases by varying the experimental conditions e.g. elevated temperatures or increased sodium content (see Section 5.4.5). Neither phase could be isolated when sodium hydroxide was used as the sodium source; however the XRD results indicated that when sodium acetate solutions were used instead, elevated temperatures may have led to the formation of the half exchanged phase exclusively. Based on these initial results, we would recommend further investigation into this method for the isolation of the sodium exchanged phases.

Based on the absence of unexchanged starting material, the sodium acetate exchanged product was selected for leach testing. As discussed in Chapter 6, the product was shown to have poor sodium retention with leach rates higher than those seen for the strontium-ZrP product. The XRD results demonstrated a structural breakdown of the fully exchanged phase $TiNa_2(PO_4)_2.3H_2O$ during the leaching procedure indicating a low stability of this phase. Whilst peaks corresponding to the half exchanged phase were still observed in the XRD pattern obtained after 14 days of leaching, the crystallinity was clearly reduced. The poor leach rates obtained and the destruction of the crystalline structures is a worrying indication into the limited use of these materials as 'stepping-stones' to the exchange of larger cations.

The known sodium exchanged ZrP phases $ZrHNa(PO_4)_2.5H_2O$[24], $ZrNa_2(PO_4)_2.3H_2O$ [25] and $ZrNa_2(PO_4)_2.H_2O$[24] were obtained in this work via the ion exchange of α-ZrP with sodium acetate (0.1 M) and hydroxide (0.01 M) solutions. Based on the XRD and XRF analysis, the

phases obtained from the sodium ion exchanges of the titanium-zirconium co-precipitates were hypothesised to be isomorphous to those from the corresponding exchanges of α-ZrP and α-TiP. Interestingly, when sodium hydroxide solutions were used for the exchanges, all of the mixed titanium-zirconium co-precipitates exhibited ion exchange behaviour like α-TiP leading to the formation of the $Ti_xZr_{1-x}HNa(PO_4)_2.H_2O$ and $Ti_xZr_{1-x}Na_2(PO_4)_2.3H_2O$ phases. Unlike α-ZrP there was no evidence of the pentahydrated $Ti_xZr_{1-x}HNa(PO_4)_2.5H_2O$ phase indicating that the presence of titanium in the α-ZrP unit cell affects the hydration levels of the phases formed. In contrast the presence of zirconium within α-TiP did not significantly affect the products formed under these exchange conditions. On the other hand, when sodium acetate solutions were used instead the co-precipitates exhibited the same exchange behaviour as the end member they were compositionally closest too – for the titanium-rich phosphates this lead to the formation of the $Ti_xZr_{1-x}HNa(PO_4)_2.H_2O$ and $Ti_xZr_{1-x}Na_2(PO_4)_2.3H_2O$ phases whilst $Ti_xZr_{1-x}HNa(PO_4)_2.5H_2O$ in addition to the $Ti_xZr_{1-x}HNa(PO_4)_2.H_2O$ and $Ti_xZr_{1-x}Na_2(PO_4)_2.3H_2O$ phases were obtained from the exchange of the zirconium-rich phosphates.

Cobalt and caesium step-wise ion exchanges were attempted on both the sodium exchanged ZrP and TiP products as well as on the strontium-ZrP product ($Sr_{0.55}ZrH_{0.9}(PO_4)_2.xH_2O$) to investigate whether the increased interlayer spacing of the starting materials could facilitate exchange. Even through this route cobalt could not be exchanged in any of the products investigated. No evidence of caesium exchange was observed for the strontium-ZrP or sodium-TiP products; however the initial results (featured in Chapter 4) indicate that some caesium may have been exchanged into the sodium-ZrP products.

This thesis has also produced the first reported attempts at the ion exchange of α-GeP (see Chapter 4). Ion exchanges with sodium, strontium, cobalt and caesium solutions were attempted with little success. The ease of hydrolysis and the low stability of α-GeP resulted in either complete destruction of the product or at best no sign of exchange in almost all of the exchanges attempted. This was in spite of attempts to force exchange using elevated temperatures and longer durations. The initial studies documented in this thesis indicate that the presence of titanium within the α-GeP unit cell (and vice versa) can affect the exchange behaviour of these materials with certain cations, however given the overall poor results obtained in this work the incorporation of germanium into other metal phosphates is not recommended to enhance the exchange behaviour of metal (IV) phosphates.

7.3 Summary of New and Original Work Reported in this Thesis

- A new hydrothermal crystallisation route was used for the synthesis of the mixed titanium-zirconium phosphates with considerable success.
- First structural analysis of mixed titanium-zirconium phosphates (both single and two phase products) from synchrotron X-ray diffraction data using Rietveld and PDF methods.
- First known attempts at the substitution of silicon for phosphorus in the mixed titanium-zirconium phosphates to allow for greater metal exchange.
- First reports of mixed germanium-titanium phosphates, their characterisation and structural investigations using both Rietveld and PDF methods.

- First proper investigation into the metal ordering within the titanium/zirconium and titanium/germanium systems. In contrast to previous reports[12], no metal ordering occurs in either series.
- First attempts to fully explain and quantify the miscibility gaps observed in the mixed metal systems by examination of the structure, XRF investigations throughout the synthetic procedure and from the calculation of the GII's of the products obtained.
- First attempted strontium ion exchange of mixed titanium-zirconium phosphates.
- First leach tests of the salt forms of the phosphates, including strontium-ZrP, strontium-$Zr_{0.9}Ti_{0.1}(HPO_4)_2.H_2O$ and the sodium exchanged TiP phases $TiNa_2(PO_4)_2.3H_2O$ and $TiHNa(PO_4)_2.H_2O$. This has allowed for a comparison of these materials to other known compounds of interest to the nuclear industry for similar applications.
- First attempts at the ion exchange of α-GeP with any cations. In this work exchange with sodium, strontium, caesium and cobalt were investigated.
- First attempted sodium and strontium ion exchange of mixed germanium-titanium phosphates.

7.4 References

(1) Clearfield, A., Stynes, J. A., *J. Inorg. Nucl. Chem*., **26**, 117-129 (1964)
(2) Alberti, G., Torracca, E., *J. Inorg. Nucl. Chem*., **30**, 317-318 (1968)
(3) Troup, J. M., Clearfield, A., *Inorg. Chem*., **16**, 3311-3313 (1977)
(4) Clearfield, A., Smith, G. D., *Inorg. Chem*., **8**, 431-436 (1969)
(5) Clearfield, A., *Mater. Chem. Phys*., **35**, 257-263 (1993)
(6) Clearfield, A., Frianeza, T. N., *J. Inorg. Nucl. Chem*., **40**, 1925-1932 (1978)
(7) Norlund Christensen, A., Krogh Andersen, E., Krogh Andersen, I. G., Alberti, G., Nielsen, M., Lehmann, M. S. *Acta. Chem. Scan*., **44**, 865-872 (1990)
(8) Clearfield, A., Nancollas, G. H., Blessing, R. H., *In Ion Exchange and Solvent Extraction*; Marcus, Y., SenGupta, A. K., Marinsky, J. A., Ed.; Dekker: New York; Vol. 5 (1973)

(9) Jia, K., Pan, B., Lv, L., Zhang, Q., Wang, X., Pan, B., Zhang, W., *J. Coll. Inter. Sci*, **331**, 453-457 (2009)
(10) Costantino, U., Gasperoni, A., *J. Chromatog*., **51**, 289-296 (1970)
(11) Hayashi, A., Fujimoto, Y., Ogawa, Y., Nakayama, H., Tsuhako, M., *J. Coll. Inter. Sci*., **283**, 57-63 (2005)
(12) Farfan-Torres, E. M., SHam, E. L., Martinez-Lara, M., Jimenez-Lopez, A., *Mat. Res. Bull.,* **27**, 1255-1262 (1992)
(13) Szirtes, L., Poko, Z., Shakshooki, S. K., Ahmed, M., Dehair, A., Benhamed, A., *J. Therm. Anal*., **35**, 895-902 (1989)
(14) Thakkar, R., Chudasama, U., *J. Sci. Ind. Res*., **68**, 312-318 (2009)
(15) Galli, P., La Ginestra, A., Berardelli, M. L., Massucci, M. A., Patrono, P., *Thermo. Acta,* **92**, 615-618 (1985)
(16) Trobajo, C., Rodriguez, M. L., Suarez, M., Garcia, J. R., Rodriguez, J., Parra, J. B., Salvado, M. A., Pertierra, P., Garcia-Granda, S., *J. Mat. Res*., **13**, 754-759 (1998)
(17) Bagnasco, G., Ciambelli, P., Frezza, A., Galli, P., La Ginestra, A., *App. Cryst*., **68**, 55-68 (1991)
(18) Tomita, I., Iwase, K., Saito, K., Sugiyama, Y., *Bull. Chem. Soc. Jap*., **54**, 749-753 (1981)
(19) Clearfield, A., Hagiwara, H., J*. Inorg. Nucl. Chem*., **40**, 907-914 (1978)
(20) Alberti, G., Bertrami, R., Casciola, M., Costantino, U., Gupta, J. P., *J. Inorg. Nucl. Chem*., **38**, 843-848 (1976)
(21) Bernazikowski, T. A., Allender, J. S., Stone, J. A., Gordon, D. E., Gould, T. H. Jr., Westberry, C. F. III, *Am. Ceram. Soc. Bull*., **62**, 1364-1390 (1983)
(22) Sales, B. C., Boatner, L. A., *Mater. Lett*., **2**, 301-304 (1984)
(23) Suarez, M., Garcia, J. R., Rodriguez, J., *J. Phys. Chem*., **88**, 159-162 (1984)
(24) Alberti, G., Costantino, U., Allulli, S., Tomassini, N., *J. Inorg. Nucl. Chem*., **40**, 1113-1117 (1978)
(25) Yazawa, Y., Eguchi, T., Takaguchi, K., Tomita, I., *Bull. Chem. Soc. Jap*., **52**, 2923-2927 (1979)

Appendices

(Appendices CD attached here)

Appendix 1: Bond Angle Data from the Rietveld Refinements

- *Single Phase Zr/Ti Phosphates.*

Table 1: Selected refined bond angles for α-TiP

Angle /°					
O4–Ti–O5	92.6(4)	O6–Ti–O9	94.4(4)	O5–P2–O7	107.4(7)
O4–Ti–O6	91.7(4)	O6–Ti–O10	88.5(4)	O6–P2–O7	105.6(6)
O4–Ti–O8	89.3(4)	O8–Ti–O9	90.7(4)		
O4–Ti–O9	86.8(4)	O8–Ti–O10	90.7(4)	O8–P3–O9	109.1(6)
O4–Ti–O10	177.9(5)	O9–Ti–O10	91.1(4)	O8–P3–O10	114.8(7)
O5–Ti–O6	86.4(4)			O8–P3–O11	108.5(6)
O5–Ti–O8	88.5(5)	O4–P2–O5	115.4(7)	O9–P3–O10	111.5(6)
O5–Ti–O9	179.0(6)	O4–P2–O6	108.8(7)	O9–P3–O11	107.4(7)
O5–Ti–O10	89.5(4)	O4–P2–O7	104.1(5)	O10–P3–O11	105.2(4)
O6–Ti–O8	174.9(5)	O5–P2–O6	114.6(5)		

Table 2: Selected refined bond angles for $Ti_{0.9}Zr_{0.1}(HPO_4)_2.H_2O$

Angle /°					
O4–M–O5	93.46(32)	O7–M–O10	93.14(34)	O6–P2–O8	111.4(5)
O4–M–O7	92.90(33)	O7–M–O11	90.48(32)	O7–P2–O8	105.6(5)
O5–M–O9	87.75(30)	O9–M–O10	91.90(33)		
O5–M–O10	86.89(31)	O9–M–O11	88.91(32)	O9–P3–O10	108.3(5)
O5–M–O11	176.6(4)	O9–M–O11	92.60(31)	O9–P3–O11	113.8(5)
O6–M–O7	89.40(35)			O9–P3–O12	110.6(5)
O6–M–O9	85.6(4)	O5–P2–O6	118.7(5)	O10–P3–O11	112.5(5)
O6–M–O10	177.4(4)	O5–P2–O7	107.1(5)	O10–P3–O12	106.8(6)
O6–M-O11	86.90(31)	O5–P2–O8	101.5(4)	O11–P3–O12	104.5(4)
O7–M–O9	175.0(4)	O6–P2–O7	111.4(5)		

Table 3: Selected refined bond angles for $Ti_{0.8}Zr_{0.2}(HPO_4)_2.H_2O$

Angle /°					
O5–M–O6	93.1(4)	O7–M–O10	94.7(4)	O6–P1–O8	98.0(7)
O5–M–O7	93.7(4)	O7–M–O11	88.7(4)	O7–P1–O8	111.7(6)
O5–M–O9	87.5(4)	O9–M–O10	91.0(4)		
O5–M–O10	87.4(4)	O9–M–O11	90.0(4)	O9–P2–O10	109.4(6)
O5–M–O11	177.5(5)	O10–M–O11	93.1(4)	O9–P2–O11	115.5(6)
O6–M–O7	85.6(4)			O9–P2–O12	106.0(6)
O6–M–O9	88.7(5)	O5–P1–O6	116.0(7)	O10–P2–O11	111.1(6)
O6–M–O10	179.384(5)	O5–P1–O7	110.0(7)	O10–P2–O12	109.8(7)
O6–M–O11	86.4(4)	O5–P1–O8	106.5(5)	O11–P2–O12	104.8(4)
O7–M–O9	174.2(5)	O6–P1–O7	113.9(6)		

Table 4: Selected refined bond angles for $Ti_{0.7}Zr_{0.3}(HPO_4)_2.H_2O$

Angle /°					
O5–M–O6	90.2(6)	O7–M–O10	87.6(6)	O6–P1–O8	104.2(11)
O5–M–O7	92.0(6)	O7–M–O11	90.5(6)	O7–P1–O8	112.1(9)
O5–M–O9	89.3(6)	O9–M–O10	98.6(6)		
O5–M–O10	86.6(5)	O9–M–O11	88.0(6)	O9–P2–O10	101.5(9)
O5–M–O11	177.2(8)	O10–M–O11	94.6(6)	O9–P2–O11	108.3(8)
O6–M–O7	89.3(6)			O9–P2–O12	110.6(8)
O6–M–O9	84.6(7)	O5–P1–O6	112.3(10)	O10–P2–O11	118.7(10)
O6–M–O10	175.5(7)	O5–P1–O7	112.2(10)	O10–P2–O12	114.5(11)
O6–M–O11	88.6(5)	O5–P1–O8	105.6(7)	O11–P2–O12	103.2(6)
O7–M–O9	173.8(7)	O6–P1–O7	110.2(9)		

Table 5: Selected refined bond angles for $Ti_{0.1}Zr_{0.9}(HPO_4)_2.H_2O$

Angle /°					
O5–M–O6	92.6(6)	O7–M–O10	93.0(7)	O6–P1–O8	113.6(10)
O5–M–O7	88.6(6)	O7–M–O12	86.7(7)	O7–P1–O8	103.0(9)
O5–M–O9	89.6(6)	O9–M–O10	91.5(6)		
O5–M–O10	84.2(5)	O9–M–O12	95.6(7)	O9–P2–O10	105.1(11)
O5–M-O12	171.4(8)	O10–M–O11	88.8(6)	O9–P2–O11	110.2(10)
O6–M–O7	85.5(5)			O9–P2–O12	127.0(11)
O6–M–O9	89.9(6)	O5–P1–O6	118.8(10)	O10–P2–O11	102.5(12)
O6–M–O10	176.5(7)	O5–P1–O7	98.6(8)	O10–P2–O12	102.0(11)
O6–M-O12	94.3(6)	O5–P1–O8	97.5(7)	O11–P2–O12	107.1(6)
O7–M–O9	175.0(7)	O6–P1–O7	121.4(10)		

Table 6: Selected refined bond angles for α-ZrP

Angle /°					
O4–Zr–O5	91.24(22)	O6–Zr–O9	91.21(24)	O5–P1–O7	107.2(4)
O4–Zr–O6	91.19(23)	O6–Zr–O11	89.77(22)	O6–P1–O7	106.5(4)
O4–Zr–O8	89.92(23)	O8–Zr–O9	90.67(23)		
O4–Zr–O9	88.84(22)	O8–Zr–O11	89.15(22)	O8–P2–O9	110.9(4)
O4–Zr–O11	178.57(22)	O9–Zr–O11	90.09(21)	O8–P2–O10	109.9(4)
O5–Zr–O6	88.39(21)			O8–P2–O11	110.5(4)
O5–Zr–O8	89.73(25)	O4–P1–O5	112.9(4)	O9–P2–O10	107.0(5)
O5–Zr–O9	179.591(2)	O4–P1–O6	110.6(4)	O9–P2–O11	111.7(4)
O5–Zr–O11	89.83(22)	O4–P1–O7	106.69(29)	O10–P2–O11	106.69(26)
O6–Zr–O8	177.84(28)	O5–P1–O6	112.51(33)		

- *Single Phase Ti/Ge Phosphates.*

Table 7: Selected refined bond angles for $Ti_{0.9}Ge_{0.1}(HPO_4)_2.H_2O$ (TiP method)

Angle /°					
O5–M–O6	92.6(3)	O7–M–O10	93.1(3)	O6–P1–O8	106.3(5)
O5–M–O7	91.4(3)	O7–M–O12	86.2(3)	O7–P1–O8	106.1(4)
O5–M–O9	89.7(3)	O9–M–O10	91.3(3)		
O5–M–O10	88.7(3)	O9–M–O12	92.7(7)	O9–P2–O10	111.2(4)
O5–M–O12	177.6(4)	O10–M–O11	91.1(3)	O9–P2–O11	114.6(4)
O6–M–O7	86.2(3)			O9–P2–O12	107.8(4)
O6–M–O9	89.4(3)	O5–P1–O6	114.4(4)	O10–P2–O11	110.2(4)
O6–M–O10	178.6(3)	O5–P1–O7	109.4(4)	O10–P2–O12	109.0(5)
O6–M–O12	87.6(3)	O5–P1–O8	106.8(3)	O11–P2–O12	103.5(3)
O7–M–O9	175.4(3)	O6–P1–O7	113.3(4)		

Table 8: Selected refined bond angles for $Ti_{0.9}Ge_{0.1}(HPO_4)_2.H_2O$ (GeP method)

Angle /°					
O5–M–O6	91.8(4)	O7–M–O10	96.6(4)	O6–P1–O8	105.0(7)
O5–M–O7	95.7(4)	O7–M–O12	88.0(4)	O7–P1–O8	109.7(6)
O5–M–O9	86.5(4)	O9–M–O10	90.8(4)		
O5–M–O10	89.0(3)	O9–M–O12	90.2(3)	O9–P2–O10	107.8(6)
O5–M–O12	175.5(4)	O10–M–O11	88.0(4)	O9–P2–O11	114.4(5)
O6–M–O7	89.6(4)			O9–P2–O12	105.8(5)
O6–M–O9	82.9(4)	O5–P1–O6	109.9(6)	O10–P2–O11	111.8(5)
O6–M–O10	173.7(5)	O5–P1–O7	116.9(5)	O10–P2–O12	112.3(5)
O6–M-O12	90.9(4)	O5–P1–O8	107.1(4)	O11–P2–O12	104.6(4)
O7–M–O9	172.3(4)	O6–P1–O7	107.6(5)		

Table 9: Selected refined bond angles for $Ti_{0.9}Ge_{0.2}(HPO_4)_2.H_2O$ (TiP method)

Angle /°					
O5–M–O6	91.9(3)	O7–M–O10	91.4(3)	O6–P1–O8	106.7(6)
O5–M–O7	87.6(3)	O7–M–O12	88.5(3)	O7–P1–O8	108.8(5)
O5–M–O9	89.6(3)	O9–M–O10	93.4(3)		
O5–M–O10	88.0(3)	O9–M–O12	94.3(3)	O9–P2–O10	110.8(5)
O5–M–O12	175.9(4)	O10–M–O11	90.6(3)	O9–P2–O11	116.2(5)
O6–M–O7	85.1(3)			O9–P2–O12	104.9(5)
O6–M–O9	90.1(4)	O5–P1–O6	116.0(5)	O10–P2–O11	107.9(5)
O6–M–O10	176.5(4)	O5–P1–O7	105.7(5)	O10–P2–O12	112.9(6)
O6–M–O12	89.3(3)	O5–P1–O8	107.7(4)	O11–P2–O12	104.1(3)
O7–M–O9	174.4(4)	O6–P1–O7	111.7(4)		

Table 10: Selected refined bond angles for $Ti_{0.8}Ge_{0.2}(HPO_4)_2.H_2O$ (GeP method)

Angle /°					
O5–M–O6	91.2(4)	O7–M–O10	96.5(4)	O6–P1–O8	108.8(8)
O5–M–O7	96.2(4)	O7–M–O12	86.4(4)	O7–P1–O8	108.7(6)
O5–M–O9	88.3(4)	O9–M–O10	90.4(4)		
O5–M–O10	90.2(4)	O9–M–O12	89.1(4)	O9–P2–O10	107.9(6)
O5–M–O12	177.3(5)	O10–M–O11	89.2(4)	O9–P2–O11	117.8(7)
O6–M–O7	91.7(4)			O9–P2–O12	111.0(6)
O6–M–O9	81.3(5)	O5–P1–O6	112.5(6)	O10–P2–O11	109.4(6)
O6–M–O10	171.5(6)	O5–P1–O7	113.4(6)	O10–P2–O12	107.0(7)
O6–M–O12	89.1(4)	O5–P1–O8	106.3(4)	O11–P2–O12	103.2(4)
O7–M–O9	171.8(4)	O6–P1–O7	106.9(6)		

Table 11: Selected refined bond angles for $Ti_{0.7}Ge_{0.3}(HPO_4)_2.H_2O$

Angle /°					
O5–M–O6	88.7(4)	O7–M–O10	88.9(5)	O6–P1–O8	99.0(7)
O5–M–O7	89.2(4)	O7–M–O12	86.8(4)	O7–P1–O8	114.9(6)
O5–M–O9	89.3(4)	O9–M–O10	96.5(4)		
O5–M–O10	83.8(4)	O9–M–O12	94.7(4)	O9–P2–O10	103.2(6)
O5–M–O12	176.0(5)	O10–M–O11	96.2(4)	O9–P2–O11	120.8(7)
O6–M–O7	81.6(4)			O9–P2–O12	107.1(7)
O6–M–O9	92.8(5)	O5–P1–O6	114.9(6)	O10–P2–O11	115.6(7)
O6–M–O10	168.0(5)	O5–P1–O7	102.5(6)	O10–P2–O12	107.9(8)
O6–M–O12	90.6(4)	O5–P1–O8	107.2(5)	O11–P2–O12	101.5(4)
O7–M–O9	174.2(5)	O6–P1–O7	118.3(6)		

Table 12: Selected refined bond angles for $Ti_{0.6}Ge_{0.4}(HPO_4)_2.H_2O$

Angle /°					
O5–M–O6	89.7(6)	O7–M–O10	88.8(7)	O6–P1–O8	88.4(9)
O5–M–O7	92.6(6)	O7–M–O12	81.1(7)	O7–P1–O8	121.8(9)
O5–M–O9	90.1(7)	O9–M–O10	99.4(6)		
O5–M–O10	85.3(6)	O9–M–O12	96.1(7)	O9–P2–O10	104.3(9)
O5–M–O12	173.7(8)	O10–M–O11	94.6(7)	O9–P2–O11	120.3(9)
O6–M–O7	73.2(5)			O9–P2–O12	111.2(11)
O6–M–O9	98.8(7)	O5–P1–O6	113.1(9)	O10–P2–O11	114.9(12)
O6–M–O10	161.2(7)	O5–P1–O7	105.6(9)	O10–P2–O12	111.4(11)
O6–M–O12	88.4(6)	O5–P1–O8	97.6(8)	O11–P2–O12	94.6(7)
O7–M–O9	171.5(8)	O6–P1–O7	126.6(9)		

Table 13: Selected refined bond angles for $Ti_{0.2}Ge_{0.8}(HPO_4)_2.H_2O$

Angle /°					
O5–M–O6	87.9(6)	O7–M–O10	102.6(7)	O6–P1–O8	98.5(13)
O5–M–O7	90.4(7)	O7–M–O12	89.4(7)	O7–P1–O8	106.7(10)
O5–M–O9	89.8(6)	O9–M–O10	85.6(7)		
O5–M–O10	88.0(7)	O9–M–O12	90.4(7)	O9–P2–O10	113.5(10)
O5–M–O12	179.739(3)	O10–M–O11	92.2(7)	O9–P2–O11	108.0(7)
O6–M–O7	81.8(6)			O9–P2–O12	112.5(11)
O6–M–O9	90.0(7)	O5–P1–O6	110.3(11)	O10–P2–O11	90.4(8)
O6–M–O10	174.0(7)	O5–P1–O7	106.6(11)	O10–P2–O12	112.7(11)
O6–M–O12	91.9(7)	O5–P1–O8	112.5(8)	O11–P2–O12	118.0(6)
O7–M–O9	171.8(8)	O6–P1–O7	122.1(10)		

Table 14: Selected refined bond angles for $Ti_{0.1}Ge_{0.9}(HPO_4)_2.H_2O$

Angle /°					
O5–M–O6	84.1(8)	O7–M–O10	90.2(9)	O6–P1–O8	104.1(16)
O5–M–O7	86.0(9)	O7–M–O12	92.2(7)	O7–P1–O8	108.9(11)
O5–M–O9	94.0(8)	O9–M–O10	93.8(9)		
O5–M–O10	88.3(8)	O9–M–O12	87.8(8)	O9–P2–O10	104.4(14)
O5–M–O12	177.7(8)	O10–M–O11	93.0(9)	O9–P2–O11	110.8(9)
O6–M–O7	89.2(8)			O9–P2–O12	114.6(14)
O6–M–O9	86.8(9)	O5–P1–O6	109.2(13)	O10–P2–O11	94.0(12)
O6–M–O10	172.5(11)	O5–P1–O7	106.7(14)	O10–P2–O12	113.2(15)
O6–M–O12	94.5(8)	O5–P1–O8	115.9(10)	O11–P2–O12	117.3(8)
O7–M–O9	176.0(11)	O6–P1–O7	112.3(13)		

Table 15: Selected refined bond angles for α-GeP

Angle /°					
O5–M–O6	91.6(2)	O7–M–O10	94.3(2)	O6–P1–O8	103.9(4)
O5–M–O7	91.7(2)	O7–M–O12	88.6(2)	O7–P1–O8	106.7(3)
O5–M–O9	89.2(2)	O9–M–O10	89.5(2)		
O5–M–O10	87.9(2)	O9–M–O12	90.5(2)	O9–P2–O10	111.8(3)
O5–M–O12	179.0(2)	O10–M–O11	91.1(2)	O9–P2–O11	108.8(3)
O6–M–O7	86.6(2)			O9–P2–O12	113.1(3)
O6–M–O9	89.6(2)	O5–P1–O6	114.1(3)	O10–P2–O11	106.7(4)
O6–M–O10	179.0(3)	O5–P1–O7	111.6(3)	O10–P2–O12	111.6(3)
O6–M–O12	89.3(2)	O5–P1–O8	107.2(2)	O11–P2–O12	104.4(2)
O7–M–O9	176.1(2)	O6–P1–O7	112.7(3)		

Appendix 2: Selected Rietveld Refinement Data for the Two Phase Phosphates

- *Titanium-Zirconium Phosphates*

$Ti_{0.6}Zr_{0.4}(HPO_4)_2.H_2O$:

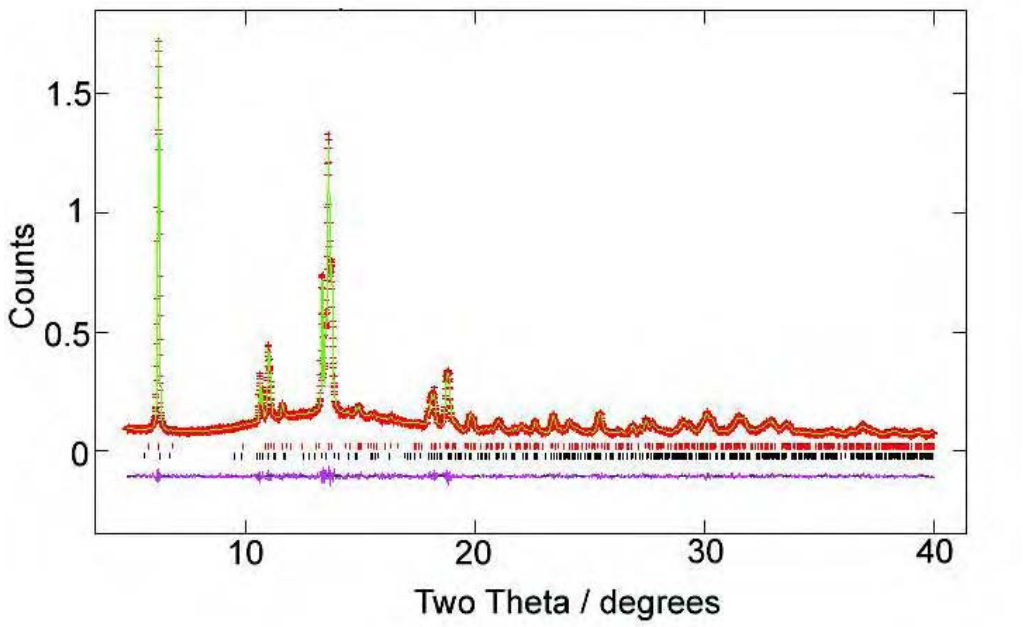

Figure 1: Refinement profile for $Ti_{0.6}Zr_{0.4}(HPO_4)_2.H_2O$. Vertical tick marks indicate allowed reflections for each phase. Phase 1 (red) and Phase 2 (black).

Table 1: Fractional atomic coordinates and isotropic thermal displacement parameters with estimated standard deviations for phase 1 from the Rietveld refinement.

atom	*x*	*y*	*z*	U_{iso} (x10^2) Å^2	Fractional Occupancy
Ti	0.769(1)	0.243(2)	0.5094(8)	4.11(33)	0.1400
Zr	0.769(1)	0.243(2)	0.5094(8)	4.11(33)	0.8600
P(1)	-0.018(2)	0.659(5)	0.6242(14)	0.56(2)	
P(2)	0.442(2)	0.248(6)	0.0939(15)	0.56(2)	
O(1)	0.048(4)	0.690(10)	0.5785(27)	2.99(1)	
O(2)	1.186(4)	0.456(6)	0.8351(31)	2.99(1)	
O(3)	0.883(5)	1.009(10)	0.5798(39)	2.99(1)	
O(4)	0.175(5)	0.897(7)	0.7112(27)	2.99(1)	
O(5)	0.380(6)	0.015(10)	0.0648(35)	2.99(1)	
O(6)	0.411(5)	0.564(8)	0.0897(31)	2.99(1)	
O(7)	0.521(5)	0.194(9)	0.1925(30)	2.99(1)	
O(8)	0.373(5)	0.760(11)	0.9288(27)	2.99(1)	
O(9)	0.283(5)	0.200(7)	0.2543(27)	0.15(14)	

Table 2: Fractional atomic coordinates and isotropic thermal displacement parameters with estimated standard deviations for phase 2 from the Rietveld refinement.

atom	*x*	*y*	*z*	U_{iso} (x10^2) Å^2	Fractional Occupancy
Ti	0.7372(6)	0.2375(11)	0.4858(3)	2.27(18)	0.6800
Zr	0.7372(6)	0.2375(11)	0.4858(3)	2.27(18)	0.3200
P(1)	-0.0341(10)	0.7238(25)	0.6022(5)	0.07(1)	
P(2)	0.4998(11)	0.2902(23)	0.6081(5)	0.07(1)	
O(1)	0.1074(19)	0.8145(32)	0.5827(9)	0.18(4)	
O(2)	-0.0785(23)	0.4548(34)	0.5746(15)	0.18(4)	
O(3)	0.8289(25)	0.9377(39)	0.5607(13)	0.18(4)	
O(4)	1.0130(14)	0.7605(42)	0.7131(9)	0.18(4)	
O(5)	0.3547(25)	0.4229(38)	0.5937(13)	0.18(4)	
O(6)	0.4498(21)	-0.0212(36)	0.5898(11)	0.18(4)	
O(7)	0.6094(22)	0.2157(35)	0.5630(12)	0.18(4)	
O(8)	0.6063(16)	0.3037(40)	0.7073(10)	0.18(4)	
O(9)	0.2358(23)	0.2797(37)	0.7343(10)	1.90(14)	

$Ti_{0.5}Zr_{0.5}(HPO_4)_2.H_2O$:

Table 3: Fractional atomic coordinates and isotropic thermal displacement parameters with estimated standard deviations for phase 1 from the Rietveld refinement.

atom	*x*	*y*	*z*	U_{iso} (x10^2) Å^2	Fractional Occupancy
Ti	0.762(2)	0.259(4)	0.5075(16)	17.9(7)	0.1400
Zr	0.762(2)	0.259(4)	0.5075(16)	17.9(7)	0.8600
P(1)	-0.012(2)	0.695(5)	0.6250(15)	0.17(3)	
P(2)	0.463(3)	0.253(5)	0.1152(17)	0.17(3)	
O(1)	0.147(5)	0.701(8)	0.5561(37)	0.61(1)	
O(2)	1.155(5)	0.452(8)	0.7367(42)	0.61(1)	
O(3)	0.879(6)	0.989(8)	0.5929(43)	0.61(1)	
O(4)	0.159(5)	0.907(7)	0.7270(38)	0.61(1)	
O(5)	0.343(6)	0.137(8)	0.0711(31)	0.61(1)	
O(6)	0.413(6)	0.505(9)	0.0879(45)	0.61(1)	
O(7)	0.541(4)	0.286(9)	0.2142(27)	0.61(1)	
O(8)	0.357(5)	0.777(9)	0.9324(40)	0.61(1)	
O(9)	0.302(6)	0.169(9)	0.2862(33)	4.18(9)	

Table 4: Fractional atomic coordinates and isotropic thermal displacement parameters with estimated standard deviations for phase 2 from the Rietveld refinement.

atom	*x*	*y*	*z*	U_{iso} (x10^2) Å^2	Fractional Occupancy
Ti	0.7347(7)	0.234(2)	0.4881(5)	0.19(8)	0.6800
Zr	0.7347(7)	0.234(2)	0.4881(5)	0.19(8)	0.3200
P(1)	-0.0379(14)	0.725(4)	0.6016(8)	0.16(3)	
P(2)	0.4987(16)	0.297(3)	0.6099(9)	0.16 (3)	
O(1)	0.1111(28)	0.765(6)	0.5830(14)	0.61(6)	
O(2)	-0.0631(36)	0.477(6)	0.5850(21)	0.61(6)	
O(3)	0.8318(34)	0.940(6)	0.5562(21)	0.61(6)	
O(4)	1.0145(23)	0.748(6)	0.7163(15)	0.61(6)	
O(5)	0.3552(31)	0.406(6)	0.6018(19)	0.61(6)	
O(6)	0.4672(36)	-0.037(5)	0.5845(17)	0.61(6)	
O(7)	0.6000(31)	0.218(6)	0.5612(20)	0.61(6)	
O(8)	0.6016(27)	0.303(6)	0.7113(16)	0.61(6)	
O(9)	0.2440(27)	0.258(6)	0.7314(13)	1.39(10)	

$Ti_{0.4}Zr_{0.6}(HPO_4)_2.H_2O$:

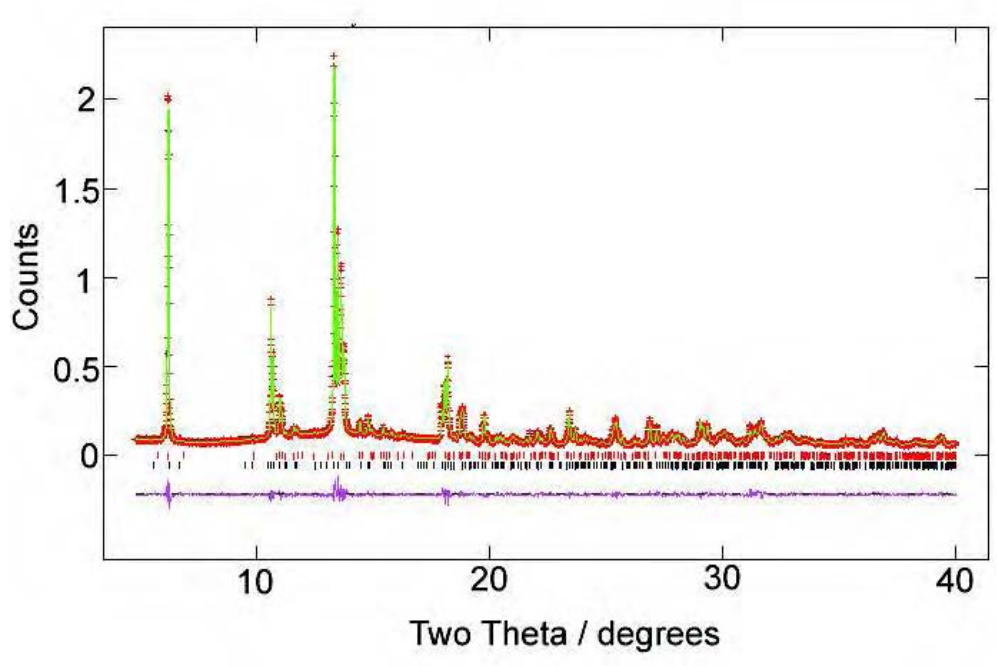

Figure 2: Refinement profile for $Ti_{0.4}Zr_{0.6}(HPO_4)_2.H_2O$. Vertical tick marks indicate allowed reflections for each phase. Phase 1 (red) and Phase 2 (black).

Table 5: Fractional atomic coordinates and isotropic thermal displacement parameters with estimated standard deviations for phase 1 from the Rietveld refinement.

atom	*x*	*y*	*z*	U_{iso} (x10^2) Å^2	Fractional Occupancy
Ti	0.7613(4)	0.2648(11)	0.5154(21)	2.13(11)	0.1400
Zr	0.7613(4)	0.2648(11)	0.5154(21)	2.13(11)	0.8600
P(1)	-0.0033(9)	0.7293(25)	0.6161(5)	0.35(16)	
P(2)	0.4746(9)	0.2402(26)	0.1082(5)	0.35(16)	
O(1)	0.1117(17)	0.8122(28)	0.5664(11)	1.08(16)	
O(2)	0.9625(18)	0.4984(33)	0.6130(12)	1.08(16)	
O(3)	0.8814(19)	0.9587(33)	0.5924(13)	1.08(16)	
O(4)	0.1106(14)	0.8362(25)	0.7116(9)	1.08(16)	
O(5)	0.3553(22)	0.0792(29)	0.0748(12)	1.08(16)	
O(6)	0.4093(19)	0.5179(30)	0.0707(11)	1.08(16)	
O(7)	0.5003(12)	0.2816(37)	0.2071(8)	1.08(16)	
O(8)	0.3881(15)	0.7898(34)	0.9064(8)	1.08(16)	
O(9)	0.2595(23)	0.2746(46)	0.2655(12)	4.76(53)	

Table 6: Fractional atomic coordinates and isotropic thermal displacement parameters with estimated standard deviations for phase 2 from the Rietveld refinement.

atom	*x*	*y*	*z*	U_{iso} (x10^2) Å^2	Fractional Occupancy
Ti	0.7408(9)	0.239(2)	0.4859(5)	1.80(23)	0.6800
Zr	0.7408(9)	0.239(2)	0.4859(5)	1.80(23)	0.3200
P(1)	-0.0315(16)	0.715(4)	0.5985(9)	1.18(34)	
P(2)	0.4987(16)	0.297(3)	0.6099(9)	1.18(34)	
O(1)	0.1254(32)	0.820(5)	0.5879(14)	0.19(27)	
O(2)	-0.1087(38)	0.476(5)	0.5598(24)	0.19(27)	
O(3)	0.8215(36)	0.928(6)	0.5657(22)	0.19(27)	
O(4)	1.0174(22)	0.779(7)	0.7135(14)	0.19(27)	
O(5)	0.3491(38)	0.406(5)	0.5731(20)	0.19(27)	
O(6)	0.4478(36)	-0.013(5)	0.5866(22)	0.19(27)	
O(7)	0.5989(31)	0.276(7)	0.5584(17)	0.19(27)	
O(8)	0.5988(25)	0.275(7)	0.7016(16)	0.19(27)	
O(9)	0.2316(28)	0.282(7)	0.7367(13)	1.66(66)	

$Ti_{0.3}Zr_{0.7}(HPO_4)_2.H_2O$:

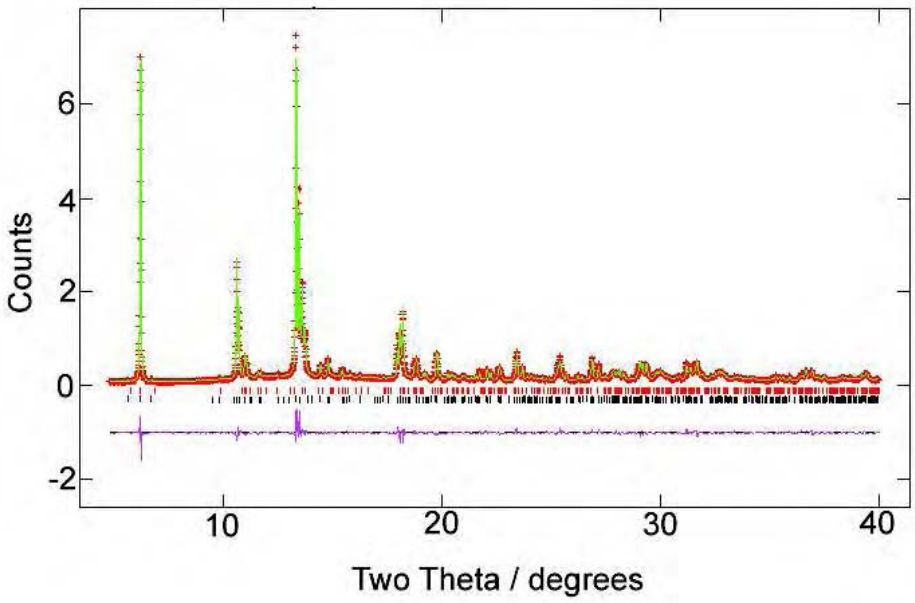

Figure 3: Refinement profile for $Ti_{0.3}Zr_{0.7}(HPO_4)_2.H_2O$. Vertical tick marks indicate allowed reflections for each phase. Phase 1 (red) and Phase 2 (black)

Table 7: Fractional atomic coordinates and isotropic thermal displacement parameters with estimated standard deviations for phase 1 from the Rietveld refinement.

atom	*x*	*y*	*z*	U_{iso} (x10^2) Å^2	Fractional Occupancy
Ti	0.7616(3)	0.2552(10)	0.5151(15)	1.16(7)	0.1400
Zr	0.7616(3)	0.2552(10)	0.5151(15)	1.16(7)	0.8600
P(1)	-0.0008(7)	0.7252(21)	0.6177(3)	0.24(13)	
P(2)	0.4726(7)	0.2318(22)	0.1063(4)	0.24(13)	
O(1)	0.1057(14)	0.7980(29)	0.5681(8)	1.14(6)	
O(2)	0.9503(18)	0.5020(31)	0.6099(11)	1.14(6)	
O(3)	0.8786(18)	0.9488(31)	0.5935(11)	1.14(6)	
O(4)	0.1090(11)	0.8096(26)	0.7169(7)	1.14(6)	
O(5)	0.3554(20)	0.0625(28)	0.0742(11)	1.14(6)	
O(6)	0.4146(19)	0.5150(28)	0.0722(10)	1.14(6)	
O(7)	0.5011(11)	0.2687(44)	0.2075(7)	1.14(6)	
O(8)	0.3799(14)	0.8070(29)	0.9057(7)	1.14(6)	
O(9)	0.2634(16)	0.2823(35)	0.2664(8)	2.70(40)	

Table 8: Fractional atomic coordinates and isotropic thermal displacement parameters with estimated standard deviations for phase 2 from the Rietveld refinement.

atom	*x*	*y*	*z*	U_{iso} (x10^2) Å^2	Fractional Occupancy
Ti	0.7276(11)	0.234(3)	0.4919(6)	1.13(26)	0.6800
Zr	0.7276(11)	0.234(3)	0.4919(6)	1.13(26)	0.3200
P(1)	-0.0379(24)	0.748(9)	0.6020(14)	2.49(11)	
P(2)	0.5079(24)	0.290(5)	0.5991(13)	2.49(11)	
O(1)	0.1120(40)	0.811(9)	0.5810(22)	1.69(8)	
O(2)	-0.0941(56)	0.491(9)	0.5603(39)	1.69(8)	
O(3)	0.8655(50)	0.927(9)	0.5720(37)	1.69(8)	
O(4)	1.0806(32)	0.747(12)	0.7012(18)	1.69(8)	
O(5)	0.3434(59)	0.378(8)	0.5769(29)	1.69(8)	
O(6)	0.4378(59)	-0.018(7)	0.5715(33)	1.69(8)	
O(7)	0.6217(51)	0.343(9)	0.5623(29)	1.69(8)	
O(8)	0.5334(31)	0.270(11)	0.7167(18)	1.69(8)	
O(9)	0.2160(34)	0.252(11)	0.7323(20)	1.73(9)	

$Ti_{0.2}Zr_{0.8}(HPO_4)_2.H_2O$:

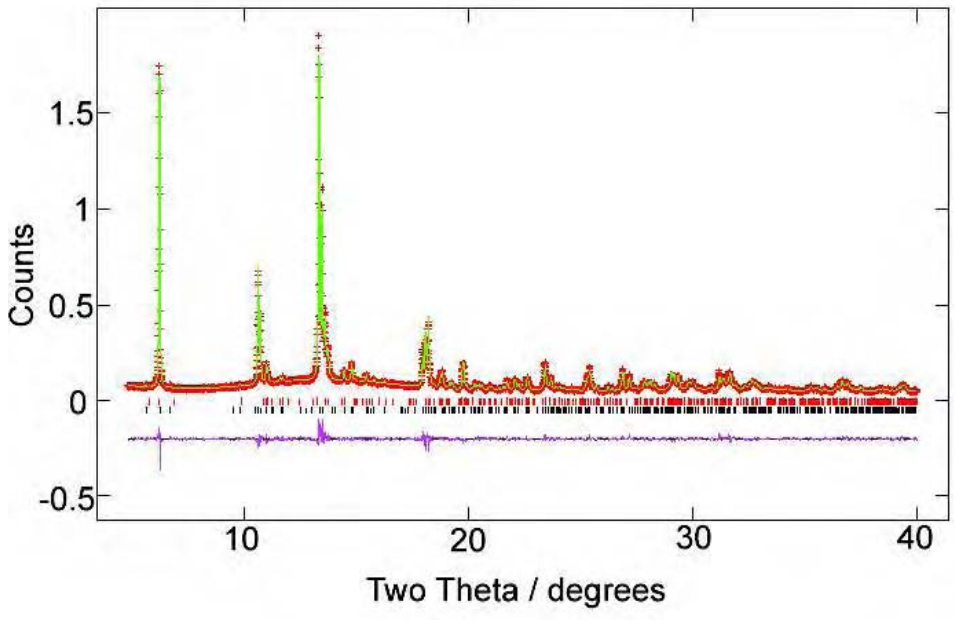

Figure 4: Refinement profile for $Ti_{0.2}Zr_{0.8}(HPO_4)_2.H_2O$. Vertical tick marks indicate allowed reflections for each phase.

Table 9: Fractional atomic coordinates and isotropic thermal displacement parameters with estimated standard deviations for phase 1 from the Rietveld refinement.

atom	*x*	*y*	*z*	U_{iso} (x10^2) Å^2	Fractional Occupancy
Ti	0.7608(4)	0.2545(14)	0.5150(2)	1.19(9)	0.1400
Zr	0.7608(4)	0.2545(14)	0.5150(2)	1.19(9)	0.8600
P(1)	-0.0013(9)	0.7286(30)	0.6165(5)	0.42(17)	
P(2)	0.4729(9)	0.2308(31)	0.1066(5)	0.42(17)	
O(1)	0.1077(20)	0.7978(40)	0.5659(12)	1.32(8)	
O(2)	0.9550(23)	0.4973(41)	0.6109(15)	1.32(8)	
O(3)	0.8759(25)	0.9516(42)	0.5903(14)	1.32(8)	
O(4)	0.1077(16)	0.8143(34)	0.7158(9)	1.32(8)	
O(5)	0.3502(27)	0.0651(38)	0.0720(15)	1.32(8)	
O(6)	0.4115(26)	0.5104(39)	0.0709(14)	1.32(8)	
O(7)	0.5013(14)	0.2654(63)	0.2066(9)	1.32(8)	
O(8)	0.3805(20)	0.8122(38)	0.9066(9)	1.32(8)	
O(9)	0.2665(23)	0.2739(52)	0.2659(11)	2.60(50)	

Table 10: Fractional atomic coordinates and isotropic thermal displacement parameters with estimated standard deviations for phase 2 from the Rietveld refinement.

atom	*x*	*y*	*z*	U_{iso} (x10^2) Å^2	Fractional Occupancy
Ti	0.735(3)	0.238(5)	0.496(2)	0.24(4)	0.6800
Zr	0.735(3)	0.238(5)	0.496(2)	0.24(4)	0.3200
P(1)	-0.037(5)	0.736(9)	0.600(3)	1.06(1)	
P(2)	0.513(5)	0.314(8)	0.602(3)	1.06(1)	
O(1)	0.112(11)	0.849(14)	0.579(6)	2.43(7)	
O(2)	-0.088(9)	0.470(13)	0.549(6)	2.43(7)	
O(3)	0.847(9)	0.855(16)	0.581(6)	2.43(7)	
O(4)	1.093(6)	0.756(18)	0.704(4)	2.43(7)	
O(5)	0.351(11)	0.415(17)	0.560(7)	2.43(7)	
O(6)	0.423(11)	-0.017(15)	0.570(7)	2.43(7)	
O(7)	0.611(11)	0.294(19)	0.572(6)	2.43(7)	
O(8)	0.523(6)	0.267(20)	0.717(4)	2.43(7)	
O(9)	0.228(10)	0.251(23)	0.733(5)	8.69(9)	

- *Germanium-Titanium phosphates*

$Ti_{0.7}Ge_{0.3}(HPO_4)_2.H_2O$:

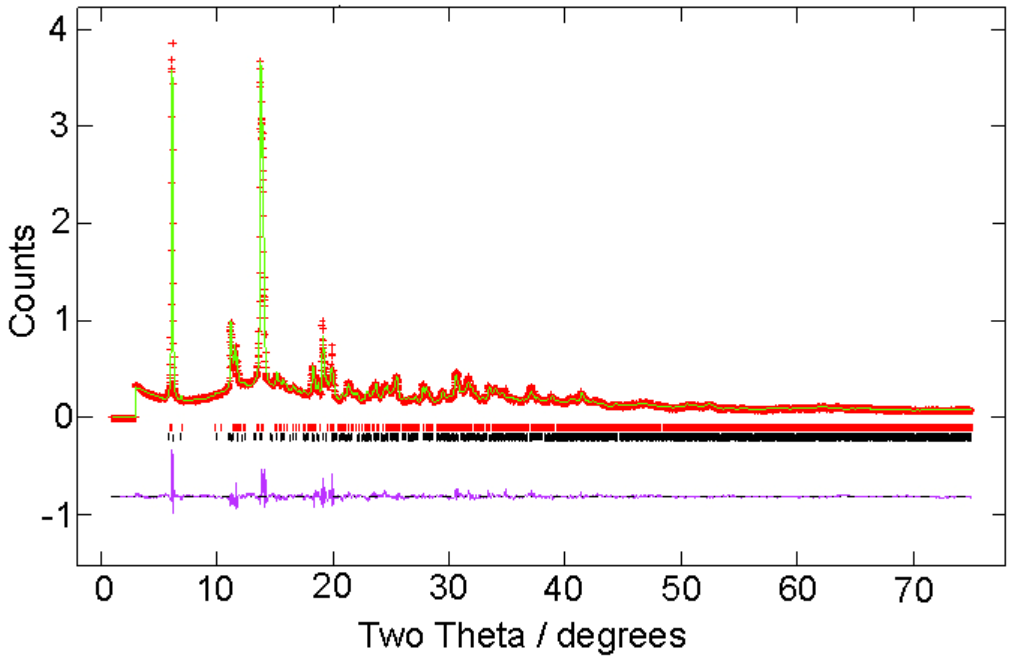

Figure 5: Refinement profile for $Ti_{0.7}Ge_{0.3}(HPO_4)_2.H_2O$. Vertical tick marks indicate allowed reflections for each phase.

Table 11: Fractional atomic coordinates and isotropic thermal displacement parameters with estimated standard deviations for phase 1 from the Rietveld refinement.

atom	*x*	*y*	*z*	U_{iso} (x10^2) Å^2	Fractional Occupancy
Ti	0.7521(18)	0.293(4)	0.4870(12)	3.00(60)	0.7200
Ge	0.7521(18)	0.293(4)	0.4870(12)	3.00(60)	0.2800
P(1)	-0.0334(28)	0.790(5)	0.5942(13)	0.01(34)	
P(2)	0.4945(29)	0.255(6)	0.1060(12)	0.01(34)	
O(1)	0.1331(46)	0.793(7)	0.5870(25)	1.72(30)	
O(2)	0.9423(56)	0.468(8)	0.5905(29)	1.72(30)	
O(3)	0.8106(54)	0.930(8)	0.5658(29)	1.72(30)	
O(4)	-0.0026(41)	0.779(8)	0.6998(23)	1.72(30)	
O(5)	0.3151(51)	0.081(7)	0.0868(28)	1.72(30)	
O(6)	0.3974(57)	0.535(8)	0.0895(31)	1.72(30)	
O(7)	0.6365(46)	0.235(8)	0.2096(23)	1.72(30)	
O(8)	0.4006(44)	0.834(8)	0.9478(25)	1.72(30)	
O(9)	0.2259(30)	0.232(6)	0.2316(16)	3.30(46)	

Table 12: Fractional atomic coordinates and isotropic thermal displacement parameters with estimated standard deviations for phase 2 from the Rietveld refinement.

atom	*x*	*y*	*z*	U_{iso} (x10^2) Å^2	Fractional Occupancy
Ti	0.7552(21)	0.243(4)	0.5023(13)	3.90(40)	0.1900
Ge	0.7552(21)	0.243(4)	0.5023(13)	3.90(40)	0.8100
P(1)	-0.0308(33)	0.702(6)	0.5987(14)	0.10(40)	
P(2)	0.4847(35)	0.289(6)	0.5875(12)	0.10(40)	
O(1)	0.1140(60)	0.913(11)	0.5822(26)	2.54(33)	
O(2)	-0.0380(50)	0.323(11)	0.5545(26)	2.54(33)	
O(3)	0.8630(60)	0.957(9)	0.5591(34)	2.54(33)	
O(4)	-0.0730(60)	0.774(8)	0.6951(28)	2.54(33)	
O(5)	0.3040(70)	0.476(9)	0.5798(34)	2.54(33)	
O(6)	0.4400(70)	-0.025(10)	0.5513(30)	2.54(33)	
O(7)	0.6340(60)	0.340(10)	0.5701(26)	2.54(33)	
O(8)	0.5460(50)	0.199(10)	0.6930(22)	2.54(33)	
O(9)	0.2520(40)	0.329(6)	0.7302(17)	3.99(47)	

$Ti_{0.6}Ge_{0.4}(HPO_4)_2.H_2O$:

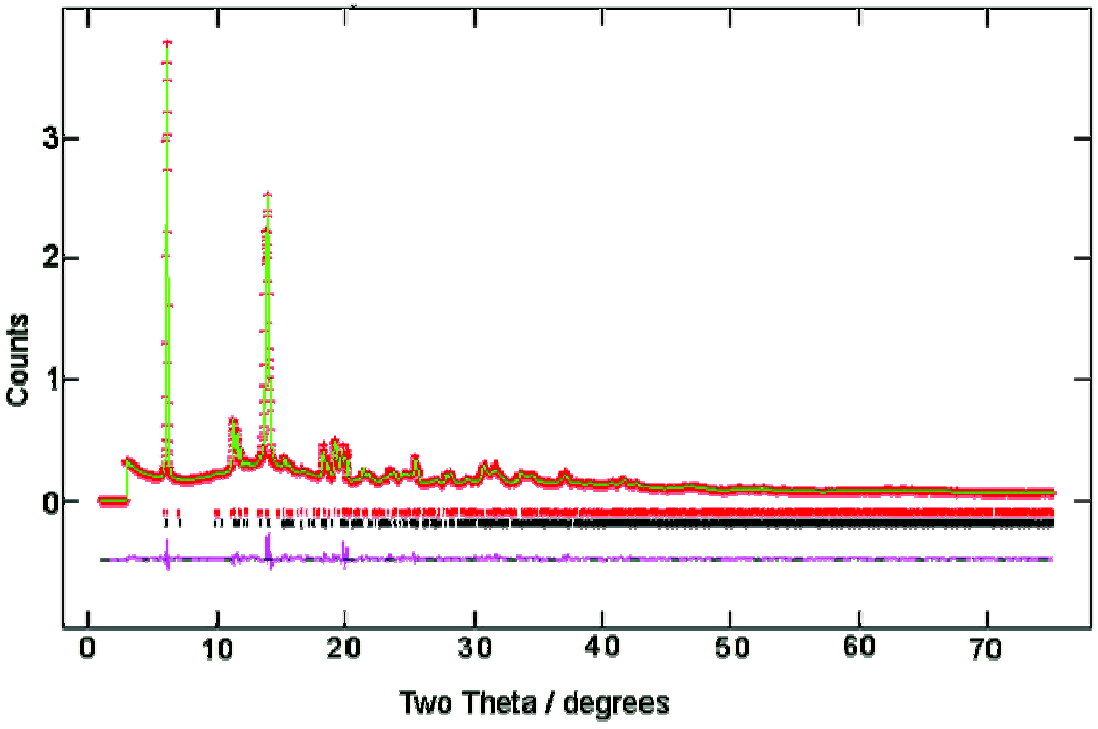

Figure 6: Refinement profile for $Ti_{0.6}Ge_{0.4}(HPO_4)_2.H_2O$. Vertical tick marks indicate allowed reflections for each phase.

Table 13: Fractional atomic coordinates and isotropic thermal displacement parameters with estimated standard deviations for phase 1 from the Rietveld refinement.

atom	*x*	*y*	*z*	U_{iso} (x10^2) Å^2	Fractional Occupancy
Ti	0.7593(7)	0.2412(22)	0.5119(4)	1.12(16)	0.7200
Ge	0.7593(7)	0.2412(22)	0.5119(4)	1.12(16)	0.2800
P(1)	0.0094(15)	0.7442(31)	0.6102(5)	0.42(14)	
P(2)	0.4657(11)	0.2544(31)	0.6008(5)	0.42(14)	
O(1)	0.0899(18)	0.8180(32)	0.5639(12)	1.93(11)	
O(2)	-0.0792(22)	0.4952(35)	0.5763(11)	1.93(11)	
O(3)	0.8431(20)	0.8772(35)	0.5947(12)	1.93(11)	
O(4)	0.1021(16)	0.7993(39)	0.7049(9)	1.93(11)	
O(5)	0.3217(23)	0.4536(33)	0.5693(13)	1.93(11)	
O(6)	0.4352(25)	-0.0856(34)	0.5738(15)	1.93(11)	
O(7)	0.6404(21)	0.3257(32)	0.5900(11)	1.93(11)	
O(8)	0.5148(15)	0.2740(47)	0.7105(8)	1.93(11)	
O(9)	0.2646(26)	0.2080(17)	0.7715(12)	0.82(35)	

Table 14: Fractional atomic coordinates and isotropic thermal displacement parameters with estimated standard deviations for phase 2 from the Rietveld refinement.

atom	*x*	*y*	*z*	U_{iso} (x10^2) Å^2	Fractional Occupancy
Ti	0.7522(12)	0.2223(18)	0.5006(5)	2.82(20)	0.1900
Ge	0.7522(12)	0.2223(18)	0.5006(5)	2.82(20)	0.8100
P(1)	-0.0497(16)	0.6913(31)	0.5891(8)	0.37(12)	
P(2)	0.4330(16)	0.3103(32)	0.0859(4)	0.37(12)	
O(1)	0.0683(26)	0.784(5)	0.6394(13)	2.84(14)	
O(2)	0.9330(28)	0.439(5)	0.5722(13)	2.84(14)	
O(3)	0.8772(26)	1.034(4)	0.5811(14)	2.84(14)	
O(4)	0.1218(25)	0.841(5)	0.7171(12)	2.84(14)	
O(5)	0.2743(26)	0.077(4)	0.0216(13)	2.84(14)	
O(6)	0.4740(30)	0.611(4)	0.0926(14)	2.84(14)	
O(7)	0.5474(25)	0.229(4)	0.1893(11)	2.84(14)	
O(8)	0.4299(24)	0.797(5)	0.9568(14)	2.84(14)	
O(9)	0.2947(39)	0.233(7)	0.2779(20)	2.49(98)	

$Ti_{0.5}Ge_{0.5}(HPO_4)_2.H_2O$ (GeP method):

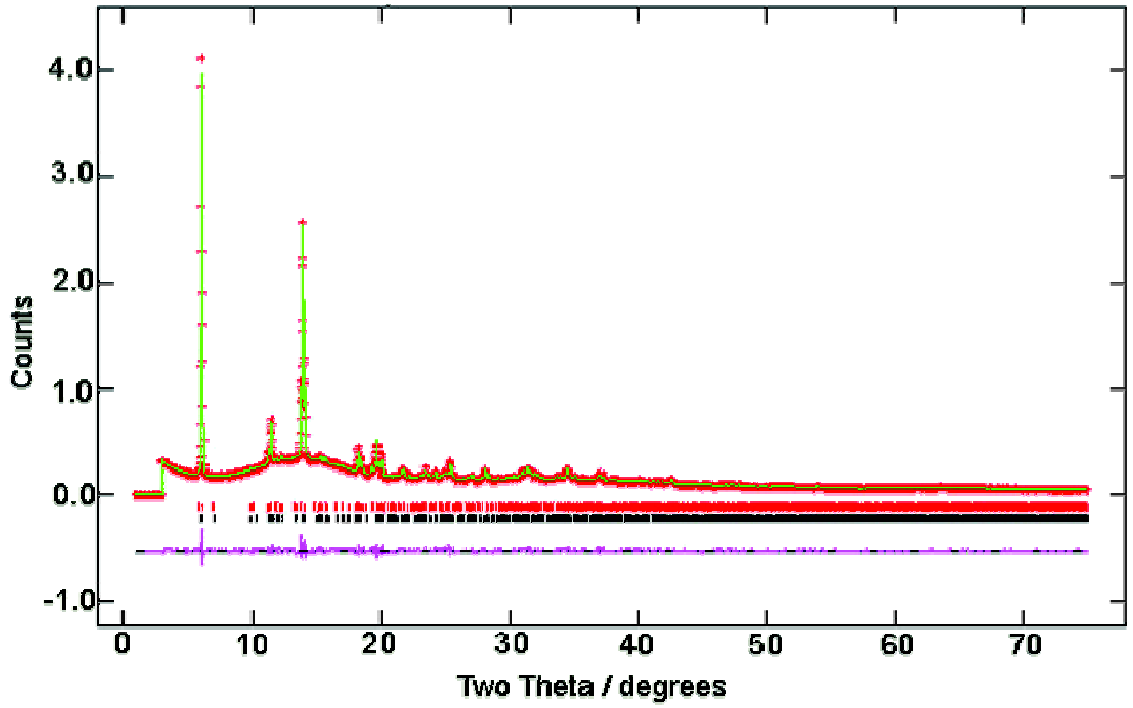

Figure 7: Refinement profile for $Ti_{0.5}Ge_{0.5}(HPO_4)_2.H_2O$. Vertical tick marks indicate allowed reflections for each phase.

Table 15: Fractional atomic coordinates and isotropic thermal displacement parameters with estimated standard deviations for phase 1 from the Rietveld refinement.

atom	*x*	*y*	*z*	U_{iso} (x10^2) Å^2	Fractional Occupancy
Ti	0.727(6)	0.274(10)	0.474(3)	2.70(18)	0.7200
Ge	0.727(6)	0.274(10)	0.474(3)	2.70(18)	0.2800
P(1)	-0.043(3)	0.639(6)	0.584(2)	2.65(30)	
P(2)	0.452(4)	0.226(6)	0.603(2)	2.65(30)	
O(1)	0.118(10)	0.848(20)	0.597(6)	2.70(6)	
O(2)	-0.087(11)	0.428(18)	0.587(6)	2.70(6)	
O(3)	0.782(10)	0.985(20)	0.602(6)	2.70(6)	
O(4)	0.060(11)	0.795(18)	0.688(5)	2.70(6)	
O(5)	0.322(12)	0.316(16)	0.597(5)	2.70(6)	
O(6)	0.415(10)	-0.105(18)	0.566(6)	2.70(6)	
O(7)	0.553(11)	0.384(19)	0.528(5)	2.70(6)	
O(8)	0.617(12)	0.043(17)	0.710(5)	2.70(6)	
O(9)	0.299(8)	0.140(14)	0.801(4)	4.40(12)	

Table 16: Fractional atomic coordinates and isotropic thermal displacement parameters with estimated standard deviations for phase 2 from the Rietveld refinement.

atom	*x*	*y*	*z*	U_{iso} (x10^2) Å^2	Fractional Occupancy
Ti	0.744(3)	0.222(4)	0.4954(13)	6.2(5)	0.1900
Ge	0.744(3)	0.222(4)	0.4954(13)	6.2(5)	0.8100
P(1)	-0.047(4)	0.656(4)	0.5913(17)	0.3(4)	
P(2)	0.470(3)	0.285(4)	0.0930(14)	0.3(4)	
O(1)	0.021(6)	0.961(11)	0.6381(30)	0.8(5)	
O(2)	0.921(7)	0.432(11)	0.5572(33)	0.8(5)	
O(3)	0.814(6)	0.860(10)	0.5537(31)	0.8(5)	
O(4)	0.167(5)	0.828(11)	0.7299(30)	0.8(5)	
O(5)	0.359(6)	-0.028(12)	0.0593(35)	0.8(5)	
O(6)	0.408(6)	0.532(13)	0.0840(34)	0.8(5)	
O(7)	0.546(6)	0.191(11)	0.1936(28)	0.8(5)	
O(8)	0.370(7)	0.992(8)	0.9318(31)	0.8(5)	
O(9)	0.238(4)	0.238(7)	0.2383(17)	3.2(4)	

$Ti_{0.5}Ge_{0.5}(HPO_4)_2.H_2O$ (TiP method):

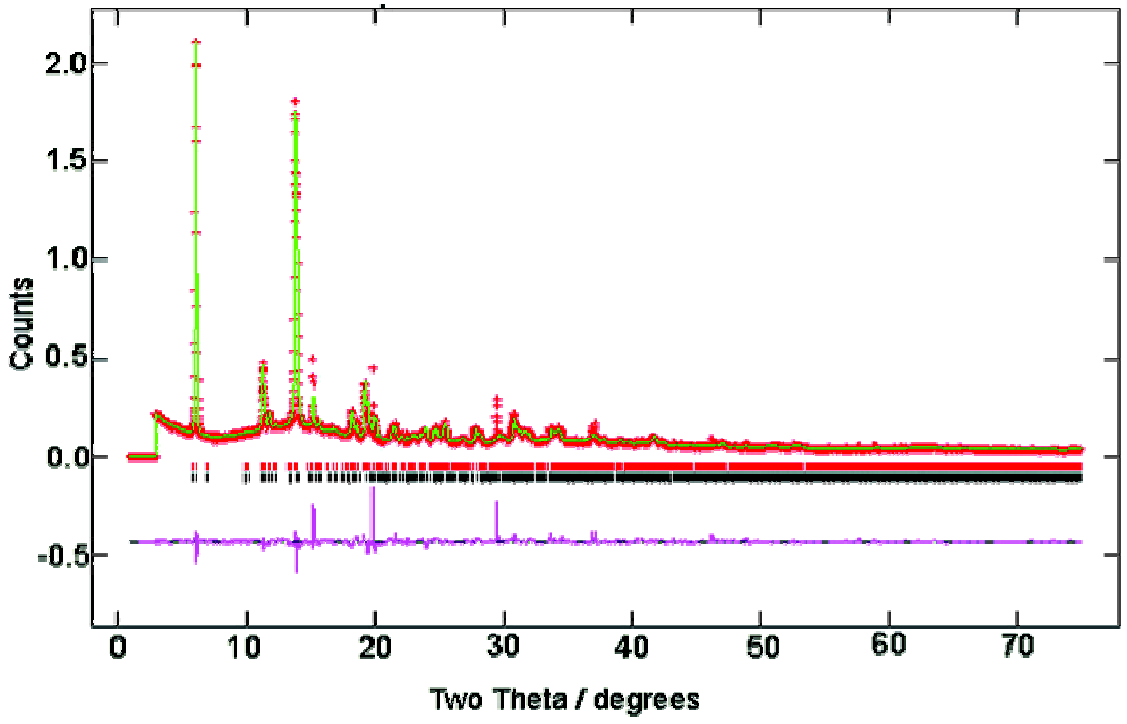

Figure 8: Refinement profile for $Ti_{0.5}Ge_{0.5}(HPO_4)_2.H_2O$. Vertical tick marks indicate allowed reflections for each phase.

Table 17: Fractional atomic coordinates and isotropic thermal displacement parameters with estimated standard deviations for phase 1 from the Rietveld refinement.

atom	*x*	*y*	*z*	U_{iso} (x10^2) Å^2	Fractional Occupancy
Ti	0.7315(12)	0.257(3)	0.4928(7)	5.15(30)	0.7200
Ge	0.7315(12)	0.257(3)	0.4928(7)	5.15(30)	0.2800
P(1)	-0.0169(18)	0.742(4)	0.5941(8)	2.11(20)	
P(2)	0.4822(17)	0.238(3)	0.1120(7)	2.11(20)	
O(1)	0.0933(35)	0.849(6)	0.5751(16)	2.25(28)	
O(2)	0.9115(37)	0.501(6)	0.5999(17)	2.25(28)	
O(3)	0.8091(33)	0.858(5)	0.5545(16)	2.25(28)	
O(4)	-0.0015(33)	0.733(7)	0.6916(16)	2.25(28)	
O(5)	0.1803(36)	0.073(5)	0.0500(17)	2.25(28)	
O(6)	0.3956(36)	0.556(6)	0.0572(19)	2.25(28)	
O(7)	0.5865(39)	0.115(5)	0.2009(18)	2.25(28)	
O(8)	0.4123(35)	0.836(5)	0.9507(19)	2.25(28)	
O(9)	0.2238(44)	0.193(8)	0.2626(24)	1.77(13)	

Table 18: Fractional atomic coordinates and isotropic thermal displacement parameters with estimated standard deviations for phase 2 from the Rietveld refinement.

atom	*x*	*y*	*z*	U_{iso} (x10^2) Å^2	Fractional Occupancy
Ti	0.7330(30)	0.224(5)	0.4959(18)	5.70(11)	0.1900
Ge	0.7330(30)	0.224(5)	0.4959(18)	5.70(11)	0.8100
P(1)	-0.0507(27)	0.738(4)	0.6003(13)	1.58(30)	
P(2)	0.5051(28)	0.242(5)	0.6229(15)	1.58(30)	
O(1)	0.0534(49)	0.677(8)	0.6018(26)	0.37(30)	
O(2)	-0.0747(55)	0.407(8)	0.5889(26)	0.37(30)	
O(3)	0.8659(49)	1.026(7)	0.6192(25)	0.37(30)	
O(4)	0.1160(46)	0.856(7)	0.7271(26)	0.37(30)	
O(5)	0.3337(49)	0.397(8)	0.5500(23)	0.37(30)	
O(6)	0.5149(52)	-0.116(7)	0.6365(28)	0.37(30)	
O(7)	0.6464(53)	0.106(8)	0.6948(29)	0.37(30)	
O(8)	0.7240(53)	0.072(7)	0.7663(27)	0.37(30)	
O(9)	0.1747(30)	0.278(5)	0.6975(14)	4.01(37)	

$Ti_{0.4}Ge_{0.6}(HPO_4)_2.H_2O$ (GeP method):

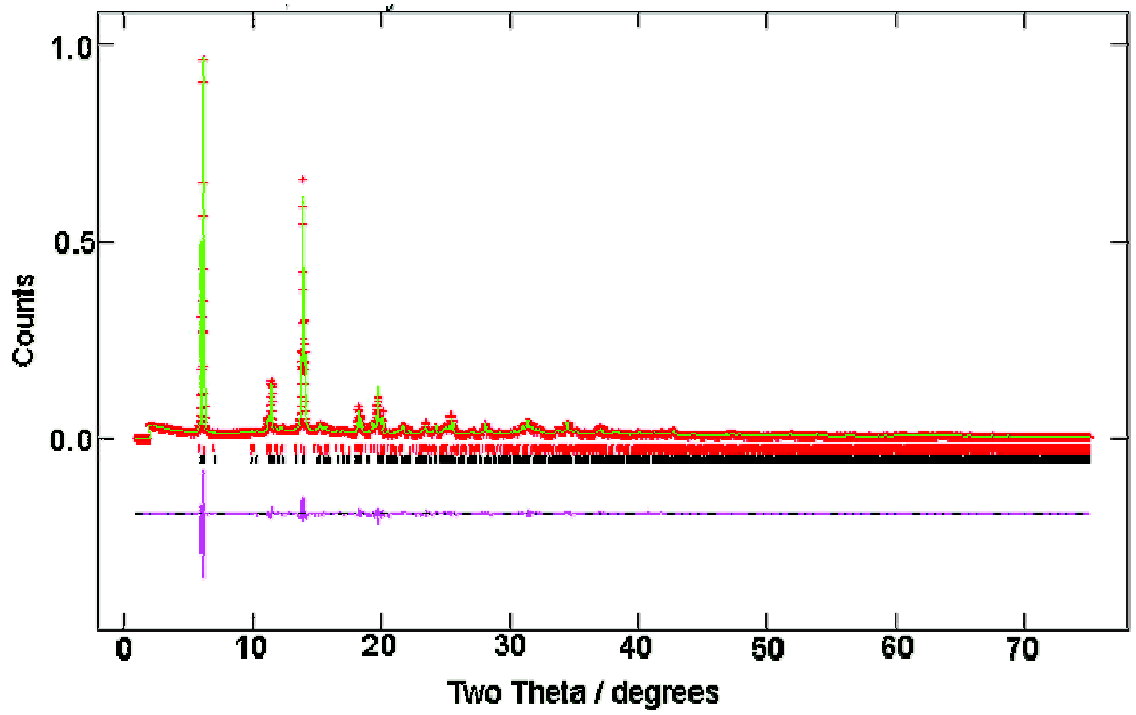

Figure 9: Refinement profile for $Ti_{0.4}Ge_{0.6}(HPO_4)_2.H_2O$. Vertical tick marks indicate allowed reflections for each phase.

Table 19: Fractional atomic coordinates and isotropic thermal displacement parameters with estimated standard deviations for phase 1 from the Rietveld refinement.

atom	*x*	*y*	*z*	U_{iso} (x10^2) Å^2	Fractional Occupancy
Ti	0.7401(23)	0.2520(40)	0.4944(12)	5.80(90)	0.7200
Ge	0.7401(23)	0.2520(40)	0.4944(12)	5.80(90)	0.2800
P(1)	-0.0450(19)	0.7430(25)	0.6013(9)	0.48(25)	
P(2)	0.4531(18)	0.3003(30)	0.6106(10)	0.48(25)	
O(1)	0.1641(29)	1.0297(47)	0.6922(19)	0.24(19)	
O(2)	-0.0335(33)	0.4313(44)	0.5918(18)	0.24(19)	
O(3)	0.8658(31)	1.0622(48)	0.5800(19)	0.24(19)	
O(4)	0.0876(30)	0.6935(49)	0.6807(17)	0.24(19)	
O(5)	0.2736(31)	0.4225(49)	0.5382(18)	0.24(19)	
O(6)	0.4139(29)	-0.0037(42)	0.5699(21)	0.24(19)	
O(7)	0.5992(30)	0.2981(46)	0.5533(19)	0.24(19)	
O(8)	0.6592(31)	0.1530(49)	0.7228(17)	0.24(19)	
O(9)	0.2840(18)	0.2266(27)	0.7672(9)	4.48(23)	

Table 20: Fractional atomic coordinates and isotropic thermal displacement parameters with estimated standard deviations for phase 2 from the Rietveld refinement.

atom	*x*	*y*	*z*	U_{iso} (x10^2) Å^2	Fractional Occupancy
Ti	0.7479(9)	0.2326(11)	0.4991(4)	1.17(11)	0.1900
Ge	0.7479(9)	0.2326(11)	0.4991(4)	1.17(11)	0.8100
P(1)	-0.0603(15)	0.6458(20)	0.5697(6)	0.50(17)	
P(2)	0.4614(12)	0.2819(20)	0.0871(5)	0.50(17)	
O(1)	0.0256(22)	0.8074(37)	0.6100(10)	2.57(11)	
O(2)	0.9215(23)	0.4234(37)	0.5596(11)	2.57(11)	
O(3)	0.8184(21)	0.9996(34)	0.5702(10)	2.57(11)	
O(4)	0.0963(21)	0.8178(30)	0.7348(9)	2.57(11)	
O(5)	0.3830(21)	-0.0366(36)	0.1012(10)	2.57(11)	
O(6)	0.4274(21)	0.5742(34)	0.0659(11)	2.57(11)	
O(7)	0.5332(18)	0.2165(35)	0.1807(9)	2.57(11)	
O(8)	0.3916(22)	0.9432(32)	0.9443(10)	2.57(11)	
O(9)	0.2269(30)	0.2138(48)	0.2228(10)	1.24(51)	

$Ti_{0.4}Ge_{0.6}(HPO_4)_2.H_2O$ (TiP method):

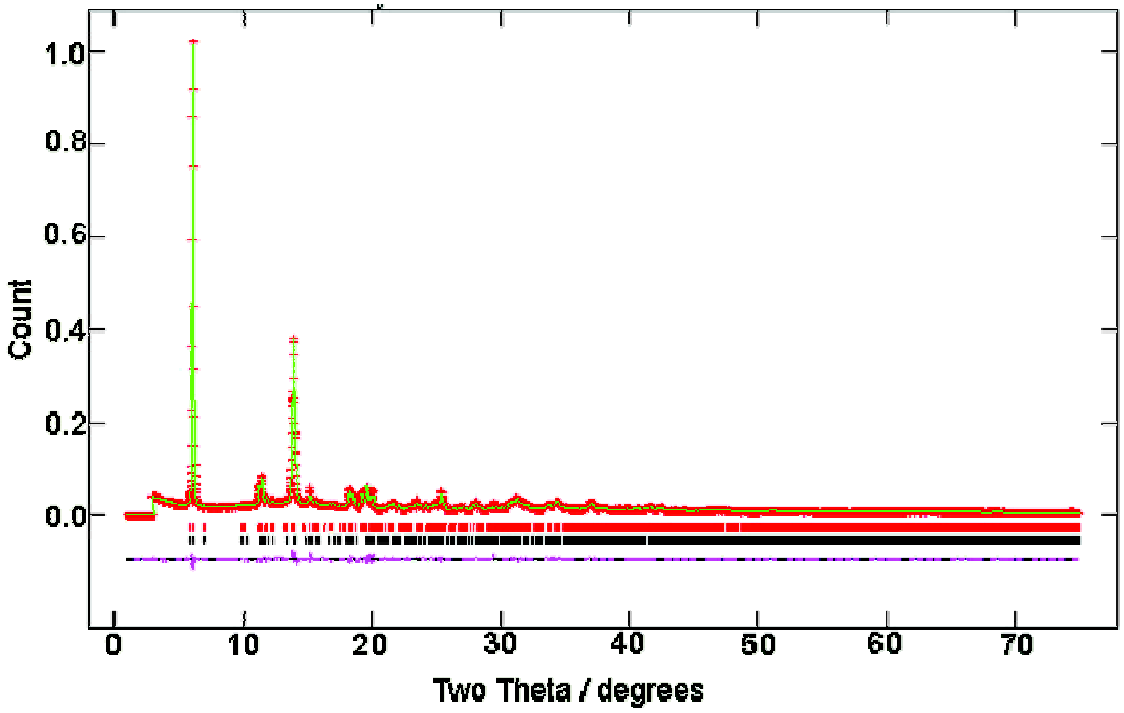

Figure 10: Refinement profile for $Ti_{0.4}Ge_{0.6}(HPO_4)_2.H_2O$. Vertical tick marks indicate allowed reflections for each phase.

Table 21: Fractional atomic coordinates and isotropic thermal displacement parameters with estimated standard deviations for phase 1 from the Rietveld refinement.

atom	*x*	*y*	*z*	U_{iso} (x10^2) Å^2	Fractional Occupancy
Ti	0.7403(12)	0.2241(25)	0.4885(7)	4.99(35)	0.7200
Ge	0.7403(12)	0.2241(25)	0.4885(7)	4.99(35)	0.2800
P(1)	-0.0412(16)	0.7518(31)	0.5884(8)	0.80(19)	
P(2)	0.4773(14)	0.2382(30)	0.1005(7)	0.80(19)	
O(1)	0.1399(23)	0.8082(40)	0.5895(12)	2.29(13)	
O(2)	0.8673(28)	0.5192(43)	0.5554(15)	2.29(13)	
O(3)	0.8001(27)	0.9138(43)	0.5617(14)	2.29(13)	
O(4)	0.0304(23)	0.7619(46)	0.6929(11)	2.29(13)	
O(5)	0.2661(24)	0.0492(36)	0.0773(13)	2.29(13)	
O(6)	0.4278(24)	0.5519(35)	0.0835(15)	2.29(13)	
O(7)	0.6264(25)	0.1345(37)	0.2025(13)	2.29(13)	
O(8)	0.4001(26)	0.8315(35)	0.9370(13)	2.29(13)	
O(9)	0.2042(19)	0.2875(37)	0.2249(11)	3.08(35)	

Table 22: Fractional atomic coordinates and isotropic thermal displacement parameters with estimated standard deviations for phase 2 from the Rietveld refinement.

atom	*x*	*y*	*z*	U_{iso} (x10^2) Å^2	Fractional Occupancy
Ti	0.7528(16)	0.252(2)	0.4992(9)	4.56(23)	0.1900
Ge	0.7528(16)	0.252(2)	0.4992(9)	4.56(23)	0.8100
P(1)	-0.0314(17)	0.698(3)	0.5993(8)	0.78(18)	
P(2)	0.4862(18)	0.272(3)	0.5907(7)	0.78(18)	
O(1)	0.0961(29)	0.835(5)	0.5827(13)	3.36(13)	
O(2)	-0.0117(25)	0.378(5)	0.5521(15)	3.36(13)	
O(3)	0.8739(26)	1.073(4)	0.5633(12)	3.36(13)	
O(4)	-0.1052(25)	0.821(4)	0.6893(14)	3.36(13)	
O(5)	0.2902(26)	0.492(4)	0.5782(16)	3.36(13)	
O(6)	0.4651(27)	-0.052(4)	0.5563(15)	3.36(13)	
O(7)	0.6044(28)	0.397(5)	0.5613(15)	3.36(13)	
O(8)	0.5495(29)	0.201(4)	0.6970(11)	3.36(13)	
O(9)	0.2669(34)	0.332(5)	0.7254(16)	2.30(70)	

$Ti_{0.3}Ge_{0.7}(HPO_4)_2.H_2O$ (GeP method):

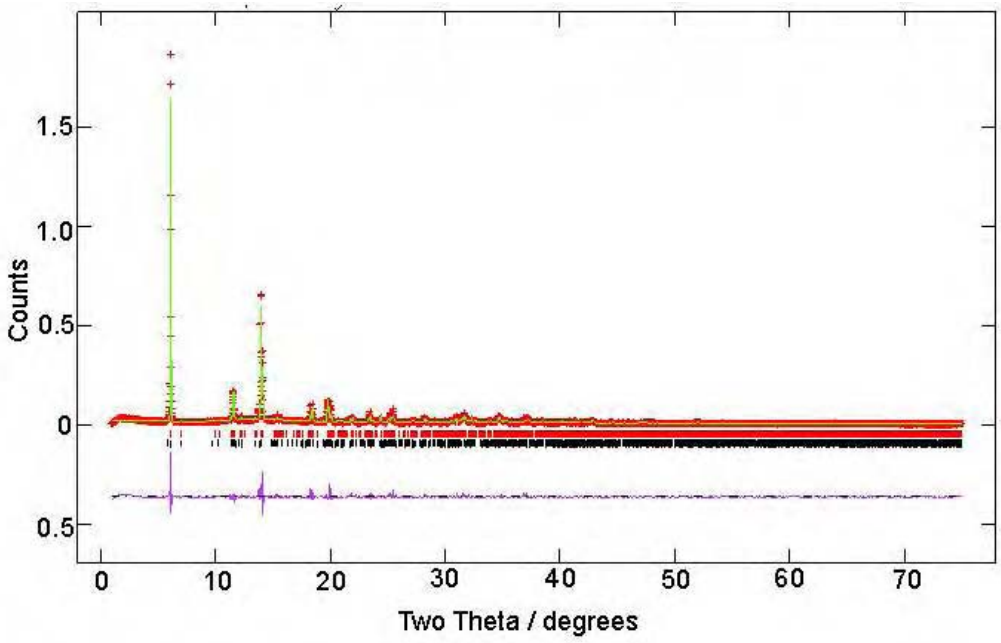

Figure 11: Refinement profile for $Ti_{0.3}Ge_{0.7}(HPO_4)_2.H_2O$. Vertical tick marks indicate allowed reflections for each phase.

Table 23: Fractional atomic coordinates and isotropic thermal displacement parameters with estimated standard deviations for phase 1 from the Rietveld refinement.

atom	*x*	*y*	*z*	U_{iso} (x10^2) Å^2	Fractional Occupancy
Ti	0.778(13)	0.322(20)	0.5000(70)	9.40(60)	0.7200
Ge	0.778(13)	0.322(20)	0.5000(70)	9.40(60)	0.2800
P(1)	-0.057(7)	0.788(13)	0.5692(28)	4.80(70)	
P(2)	0.451(8)	0.191(17)	0.5369(24)	4.80(70)	
O(1)	-0.057(9)	1.045(16)	0.5310(36)	0.31(40)	
O(2)	-0.097(9)	0.285(20)	0.5461(33)	0.31(40)	
O(3)	0.824(10)	1.017(16)	0.5839(39)	0.31(40)	
O(4)	0.043(9)	0.828(14)	0.6751(33)	0.31(40)	
O(5)	0.348(9)	0.143(15)	0.5857(39)	0.31(40)	
O(6)	0.313(8)	-0.204(22)	0.5590(31)	0.31(40)	
O(7)	0.398(9)	0.374(16)	0.5938(36)	0.31(40)	
O(8)	0.579(8)	0.259(17)	0.6721(31)	0.31(40)	
O(9)	0.149(8)	-0.297(14)	0.7241(4)	7.58(10)	

Table 24: Fractional atomic coordinates and isotropic thermal displacement parameters with estimated standard deviations for phase 2 from the Rietveld refinement.

atom	*x*	*y*	*z*	U_{iso} (x10^2) Å^2	Fractional Occupancy
Ti	0.7466(8)	0.262(2)	0.4940(3)	1.33(9)	0.1900
Ge	0.7466(8)	0.262(2)	0.4940(3)	1.33(9)	0.8100
P(1)	-0.0096(17)	0.728(4)	0.5955(7)	3.03(18)	
P(2)	0.4953(16)	0.270(5)	0.1015(7)	3.03(18)	
O(1)	-0.0498(33)	0.857(5)	0.6116(15)	0.86(20)	
O(2)	0.9208(29)	0.446(6)	0.5656(13)	0.86(20)	
O(3)	0.8120(32)	0.977(5)	0.5600(13)	0.86(20)	
O(4)	0.0002(25)	0.685(5)	0.7038(11)	0.86(20)	
O(5)	0.3396(30)	0.065(5)	0.0902(14)	0.86(20)	
O(6)	0.4460(32)	0.553(5)	0.0897(14)	0.86(20)	
O(7)	0.5806(23)	0.267(7)	0.2063(10)	0.86(20)	
O(8)	0.3781(29)	0.842(5)	0.9263(11)	0.86(20)	
O(9)	0.2469(32)	0.270(7)	0.2409(14)	0.18(40)	

$Ti_{0.3}Ge_{0.7}(HPO_4)_2.H_2O$ (TiP method):

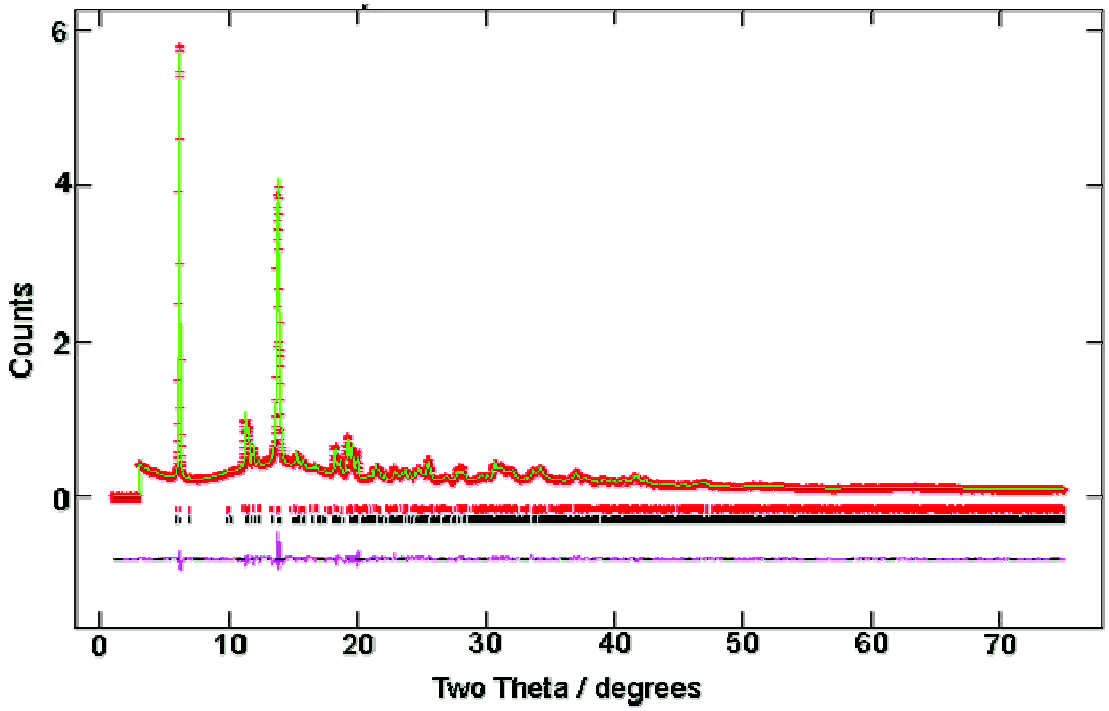

Figure 12: Refinement profile for $Ti_{0.3}Ge_{0.7}(HPO_4)_2.H_2O$. Vertical tick marks indicate allowed reflections for each phase.

Table 25: Fractional atomic coordinates and isotropic thermal displacement parameters with estimated standard deviations for phase 1 from the Rietveld refinement.

atom	*x*	*y*	*z*	U_{iso} (x10^2) Å^2	Fractional Occupancy
Ti	0.750(9)	0.238(23)	0.490(5)	3.8(22)	0.7200
Ge	0.750(9)	0.238(23)	0.490(5)	3.8(22)	0.2800
P(1)	-0.055(11)	0.708(26)	0.594(5)	0.5(15)	
P(2)	0.489(11)	0.235(23)	0.108(5)	0.5(15)	
O(1)	0.098(24)	0.854(45)	0.596(10)	0.5(17)	
O(2)	0.946(25)	0.404(36)	0.594(13)	0.5(17)	
O(3)	0.820(24)	0.882(38)	0.557(12)	0.5(17)	
O(4)	0.039(19)	0.777(36)	0.694(10)	0.5(17)	
O(5)	0.315(25)	0.043(41)	0.070(13)	0.5(17)	
O(6)	0.401(22)	0.522(45)	0.073(11)	0.5(17)	
O(7)	0.650(19)	0.128(36)	0.199(10)	0.5(17)	
O(8)	0.394(22)	0.837(45)	0.937(13)	0.5(17)	
O(9)	0.212(16)	0.209(32)	0.231(8)	3.2(32)	

Table 26: Fractional atomic coordinates and isotropic thermal displacement parameters with estimated standard deviations for phase 2 from the Rietveld refinement.

atom	*x*	*y*	*z*	U_{iso} (x10^2) Å^2	Fractional Occupancy
Ti	0.721(19)	0.294(30)	0.506(9)	1.0(29)	0.1900
Ge	0.721(19)	0.294(30)	0.506(9)	1.0(29)	0.8100
P(1)	0.038(36)	0.670(50)	0.601(17)	1.5(40)	
P(2)	0.493(10)	0.2373(28)	0.1106(4)	1.5(40)	
O(1)	0.110(80)	0.830(16)	0.586(46)	2.3(51)	
O(2)	0.020(10)	0.525(14)	0.582(56)	2.3(51)	
O(3)	0.913(10)	0.960(12)	0.623(54)	2.3(51)	
O(4)	0.009(9)	0.595(15)	0.687(44)	2.3(51)	
O(5)	0.140(10)	0.739(17)	0.612(52)	2.3(51)	
O(6)	0.472(10)	0.160(16)	0.588(50)	2.3(51)	
O(7)	0.670(8)	0.205(14)	0.592(41)	2.3(51)	
O(8)	0.568(9)	0.270(14)	0.709(45)	2.3(51)	
O(9)	0.322(21)	0.343(50)	0.731(17)	5.1(30)	

$Ti_{0.2}Ge_{0.8}(HPO_4)_2.H_2O$:

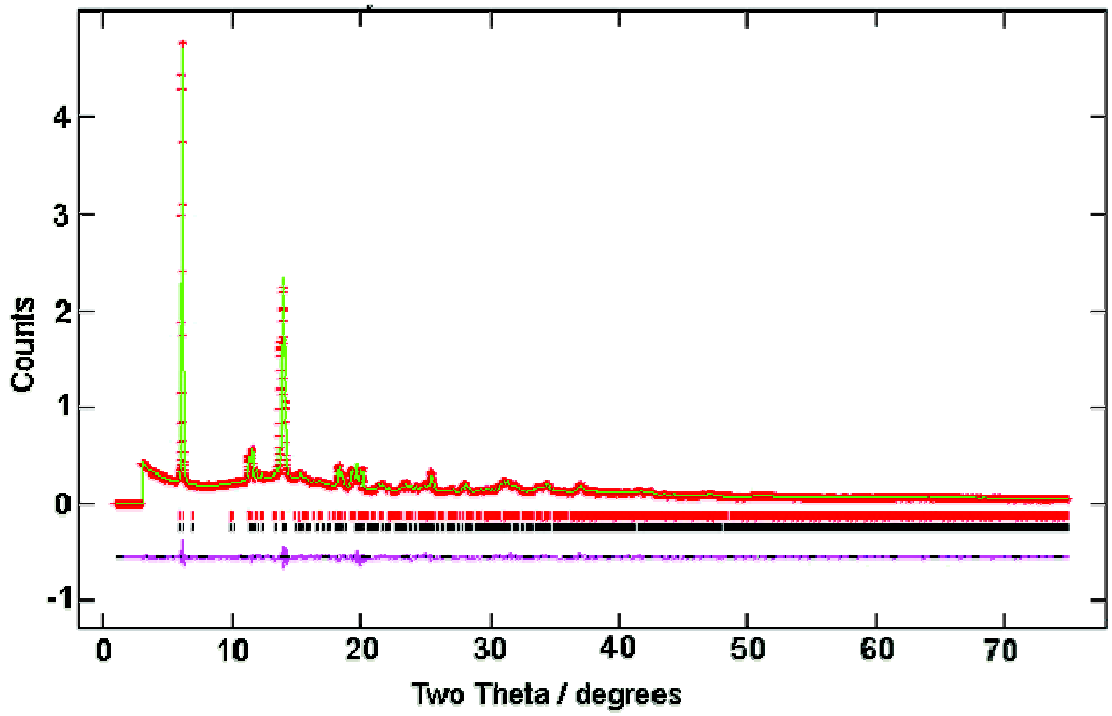

Table 27: Fractional atomic coordinates and isotropic thermal displacement parameters with estimated standard deviations for phase 1 from the Rietveld refinement.

atom	*x*	*y*	*z*	U_{iso} (x10^2) Å^2	Fractional Occupancy
Ti	0.7521(18)	0.293(4)	0.4870(12)	3.00(60)	0.7200
Ge	0.7521(18)	0.293(4)	0.4870(12)	3.00(60)	0.2800
P(1)	-0.0334(28)	0.790(5)	0.5942(13)	0.01(34)	
P(2)	0.4945(29)	0.255(6)	0.1060(12)	0.01(34)	
O(1)	0.1331(46)	0.793(7)	0.5870(25)	1.72(30)	
O(2)	0.9423(56)	0.468(8)	0.5905(29)	1.72(30)	
O(3)	0.8106(54)	0.930(8)	0.5658(29)	1.72(30)	
O(4)	-0.0026(41)	0.779(8)	0.6998(23)	1.72(30)	
O(5)	0.3151(51)	0.081(7)	0.0868(28)	1.72(30)	
O(6)	0.3974(57)	0.535(8)	0.0895(31)	1.72(30)	
O(7)	0.6365(46)	0.235(8)	0.2096(23)	1.72(30)	
O(8)	0.4006(44)	0.834(8)	0.9478(25)	1.72(30)	
O(9)	0.2259(30)	0.232(6)	0.2316(16)	3.30(46)	

Table 28: Fractional atomic coordinates and isotropic thermal displacement parameters with estimated standard deviations for phase 2 from the Rietveld refinement.

atom	*x*	*y*	*z*	U_{iso} (x10^2) Å^2	Fractional Occupancy
Ti	0.755(2)	0.243(4)	0.5023(13)	3.90(40)	0.1900
Ge	0.755(2)	0.243(4)	0.5023(13)	3.90(40)	0.8100
P(1)	-0.031(3)	0.702(6)	0.5987(14)	0.09(14)	
P(2)	0.485(4)	0.289(6)	0.5875(12)	0.09(14)	
O(1)	0.114(6)	0.913(11)	0.5822(26)	2.54(33)	
O(2)	-0.038(5)	0.323(11)	0.5545(26)	2.54(33)	
O(3)	0.863(6)	0.957(9)	0.5591(34)	2.54(33)	
O(4)	-0.073(6)	0.774(8)	0.6951(28)	2.54(33)	
O(5)	0.304(7)	0.476(9)	0.5798(34)	2.54(33)	
O(6)	0.440(7)	-0.025(10)	0.5513(30)	2.54(33)	
O(7)	0.634(6)	0.340(10)	0.5701(26)	2.54(33)	
O(8)	0.546(5)	0.199(10)	0.6930(22)	2.54(33)	
O(9)	0.252(4)	0.329(6)	0.7302(17)	3.99(47)	

Appendix 5: Variable Temperature XRD Patterns

- *Titanium-Zirconium Phosphates*

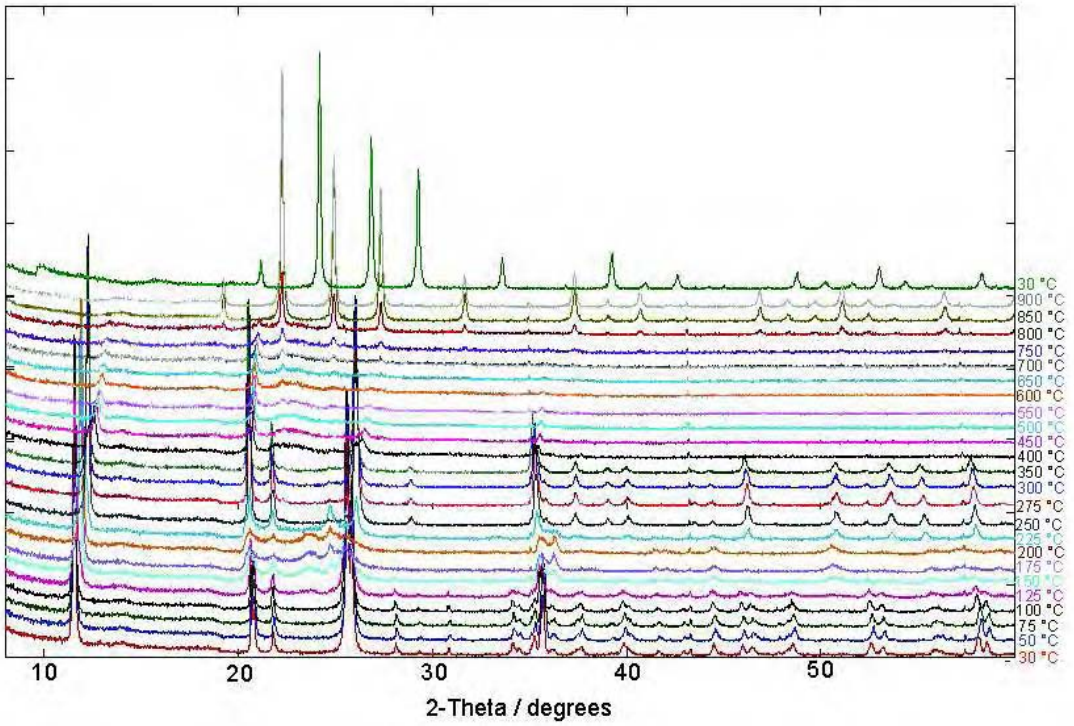

Figure 1: The in-situ XRD patterns of $Ti_{0.9}Zr_{0.1}(HPO_4)_2.H_2O$ recorded as a function of temperature

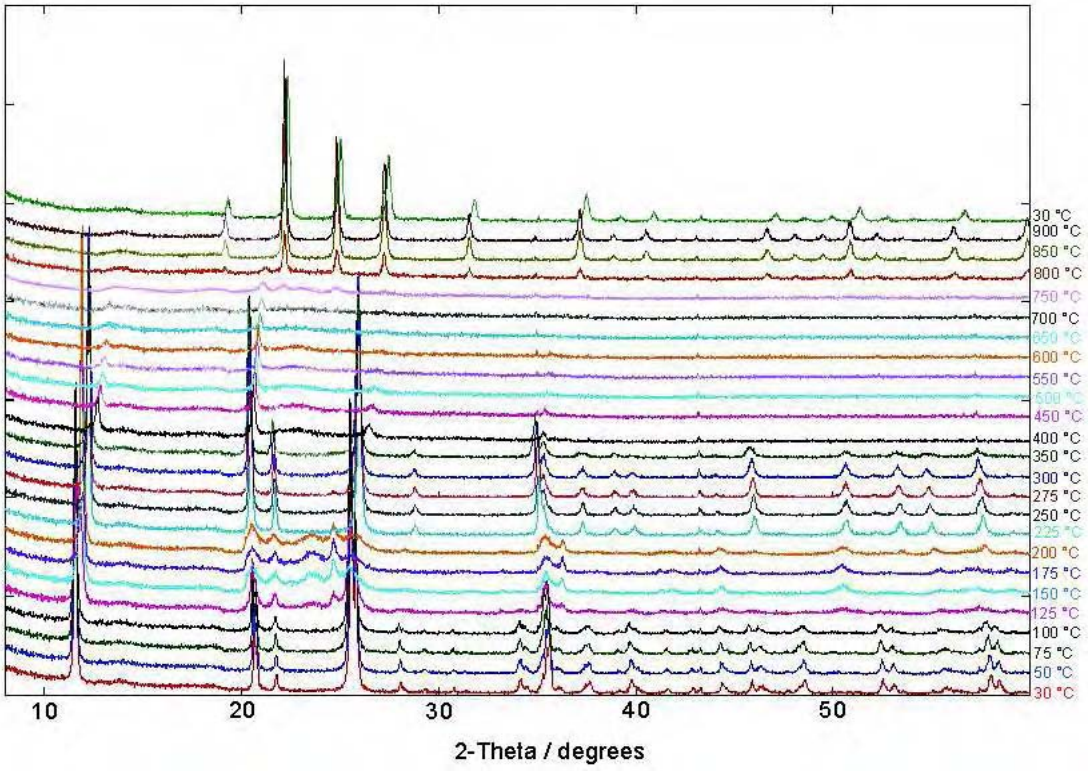

Figure 2: The in-situ XRD patterns of $Ti_{0.8}Zr_{0.2}(HPO_4)_2.H_2O$ recorded as a function of temperature

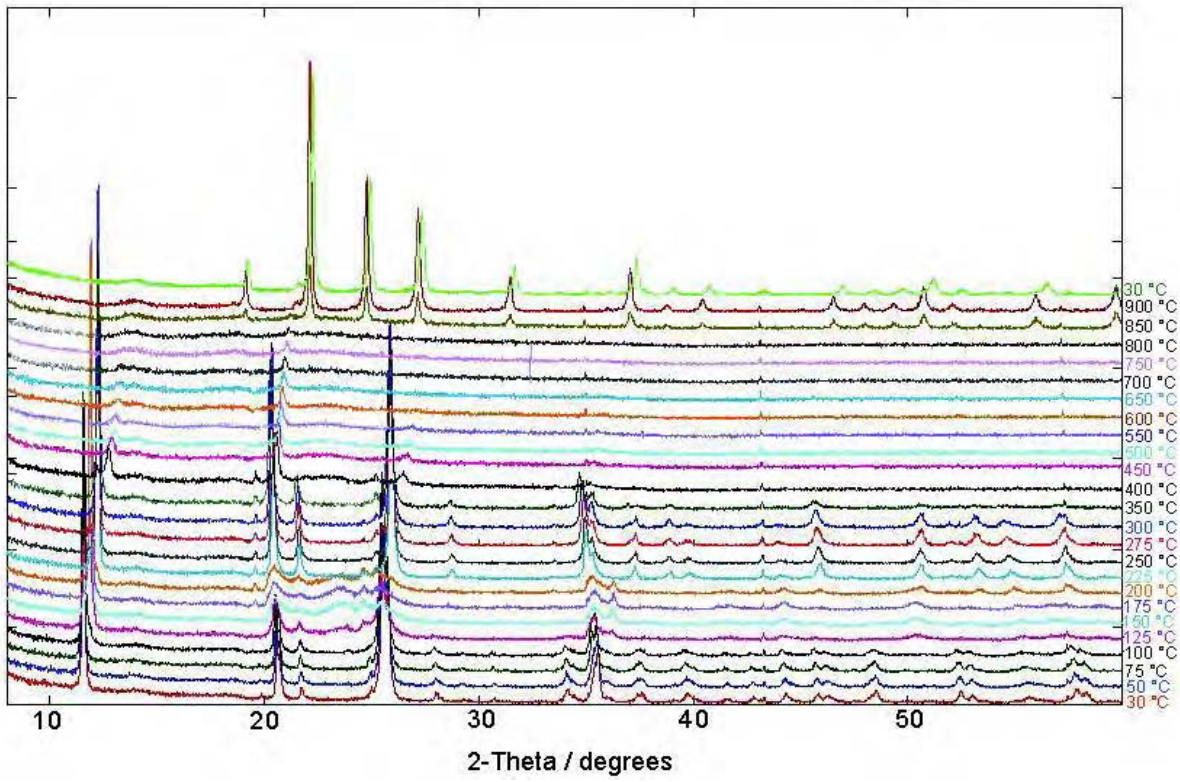

Figure 3: The in-situ XRD patterns of $Ti_{0.7}Zr_{0.3}(HPO_4)_2.H_2O$ recorded as a function of temperature

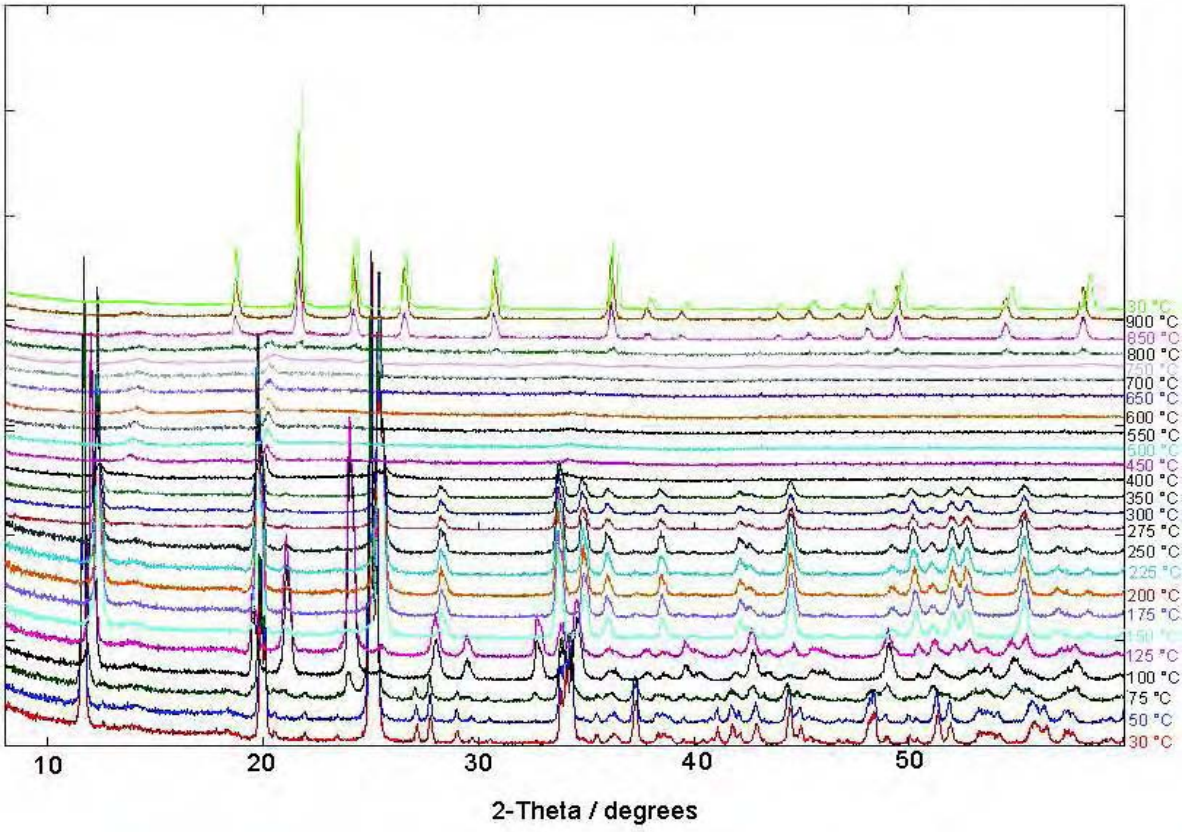

Figure 4: The in-situ XRD patterns of $Ti_{0.1}Zr_{0.9}(HPO_4)_2.H_2O$ recorded as a function of temperature

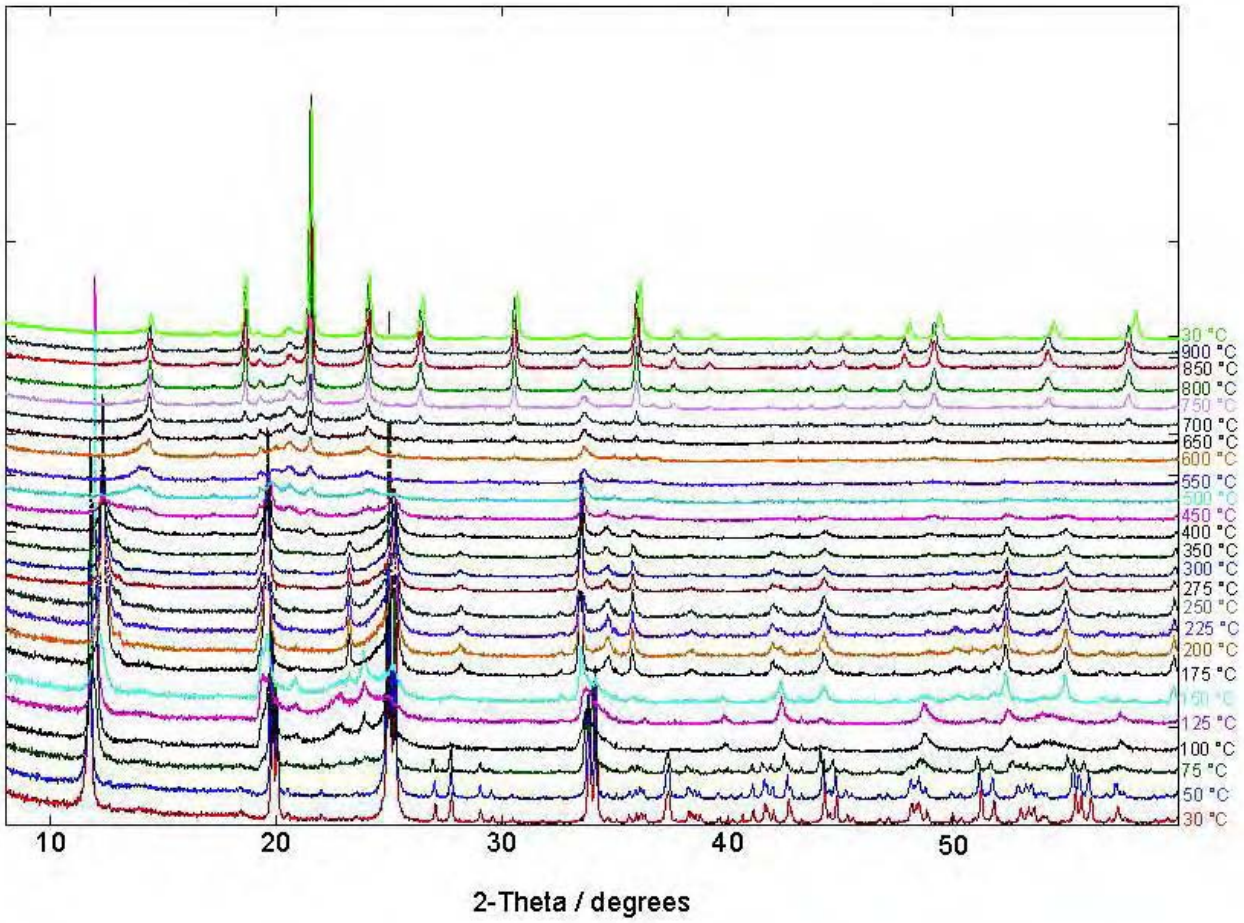

Figure 5: The in-situ XRD patterns of $Zr(HPO_4)_2.H_2O$ recorded as a function of temperature

- *Germanium-Titanium Phosphates*

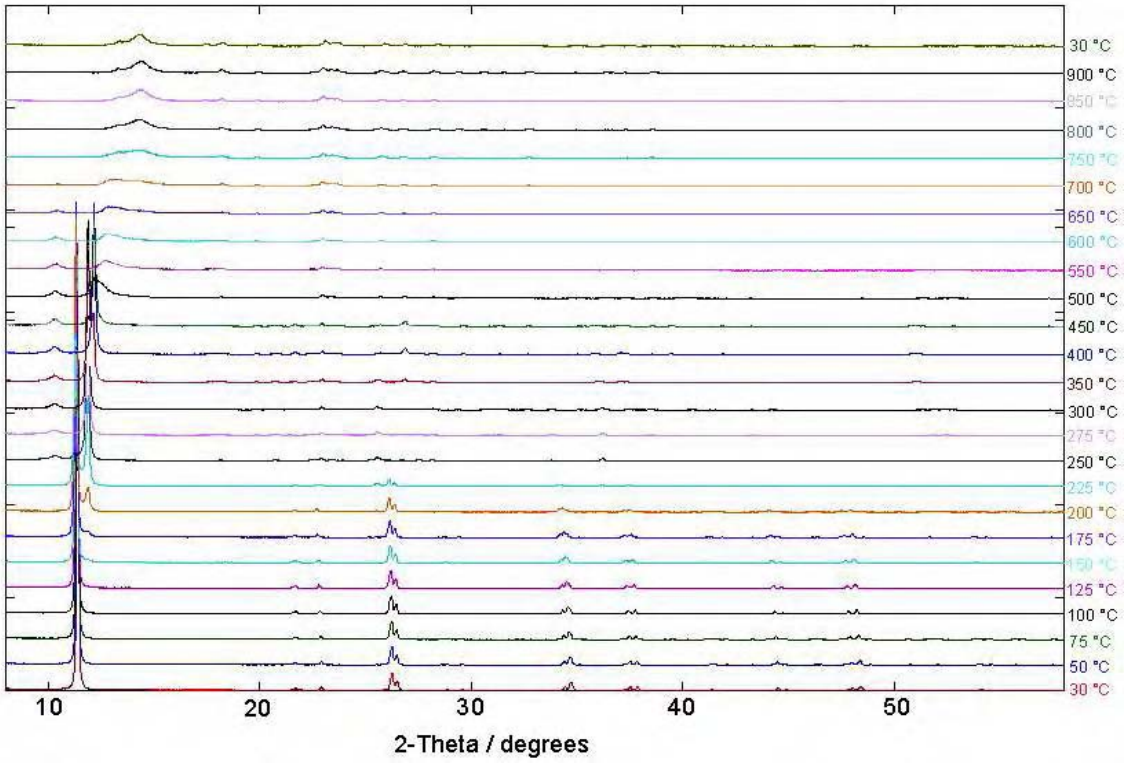

Figure 6: The in-situ XRD patterns of $Ge_{0.9}Ti_{0.1}(HPO_4)_2.H_2O$ (GeP method) recorded as a function of temperature

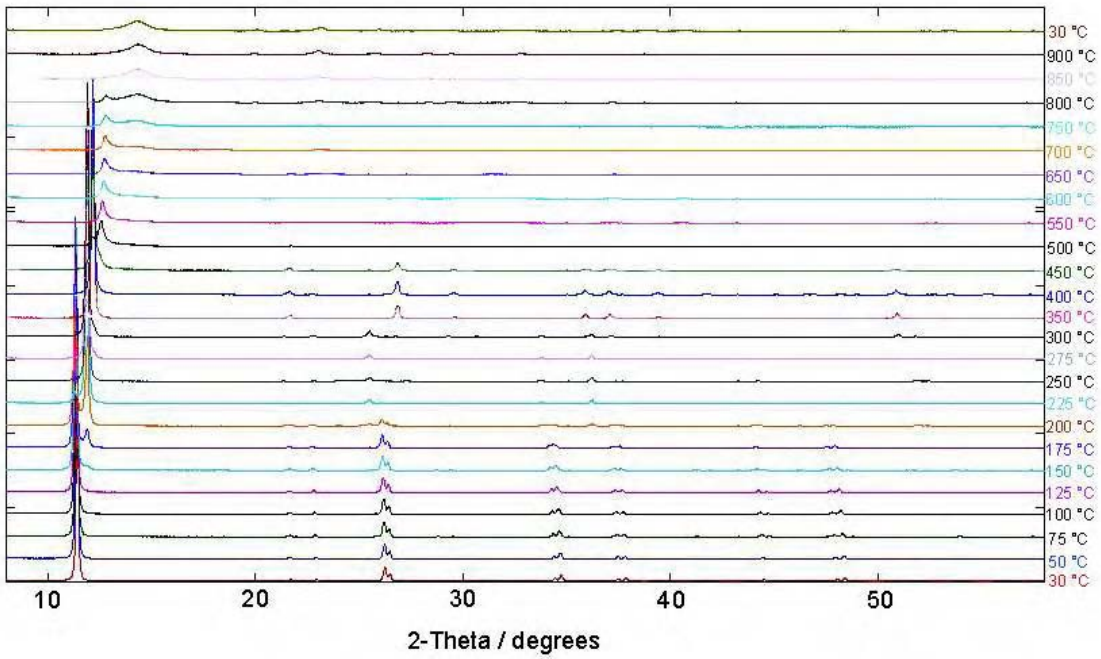

Figure 7: The in-situ XRD patterns of $Ge_{0.8}Ti_{0.2}(HPO_4)_2.H_2O$ (GeP method) recorded as a function of temperature

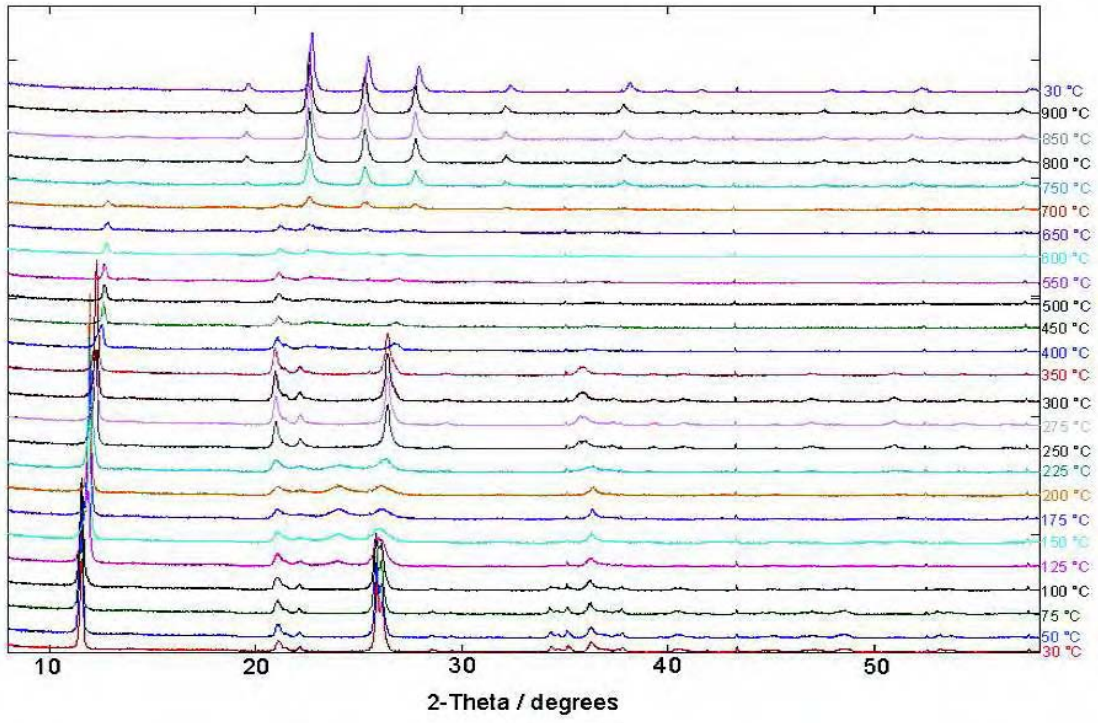

Figure 8: The in-situ XRD patterns of $Ge_{0.4}Ti_{0.6}(HPO_4)_2.H_2O$ (TiP method) recorded as a function of temperature

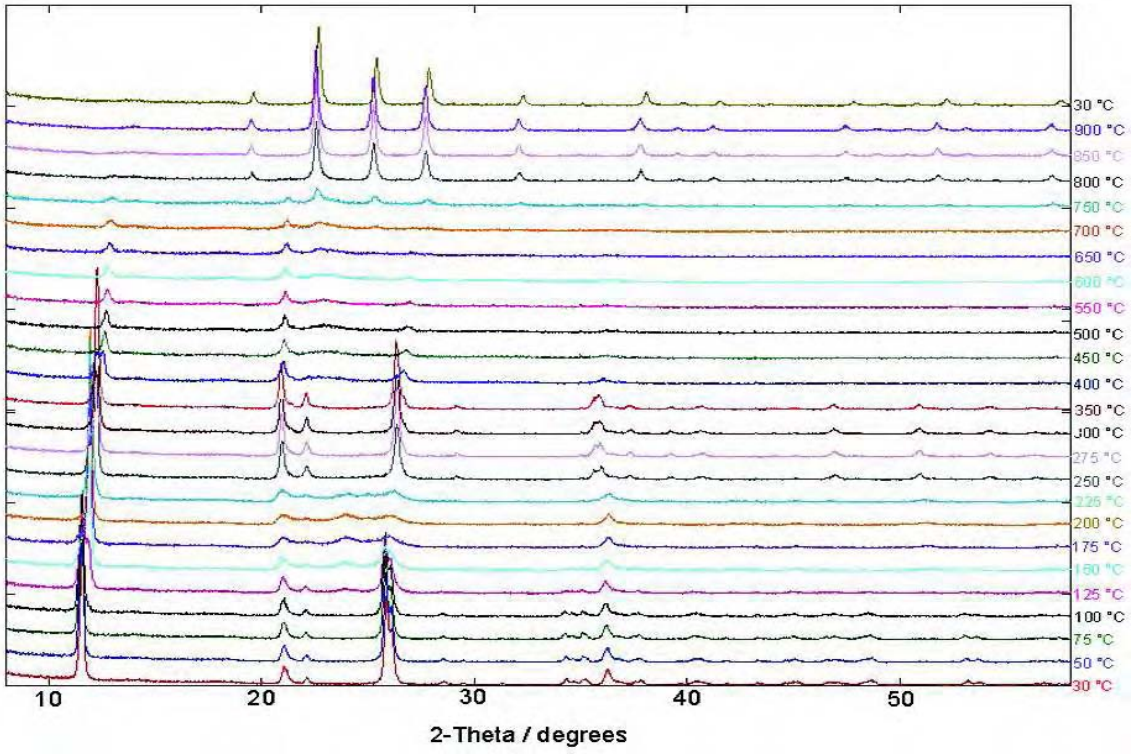

Figure 9: The in-situ XRD patterns of $Ge_{0.3}Ti_{0.7}(HPO_4)_2.H_2O$ (TiP method) recorded as a function of temperature

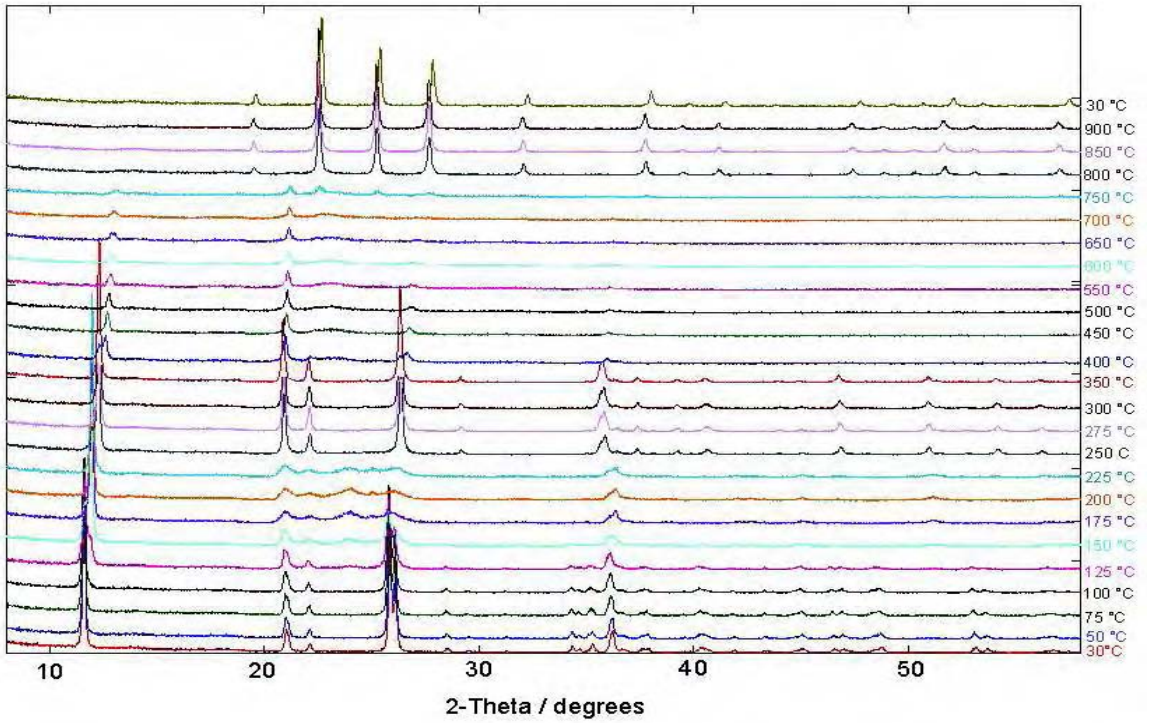

Figure 10: The in-situ XRD patterns of $Ge_{0.2}Ti_{0.8}(HPO_4)_2.H_2O$ (TiP method) recorded as a function of temperature

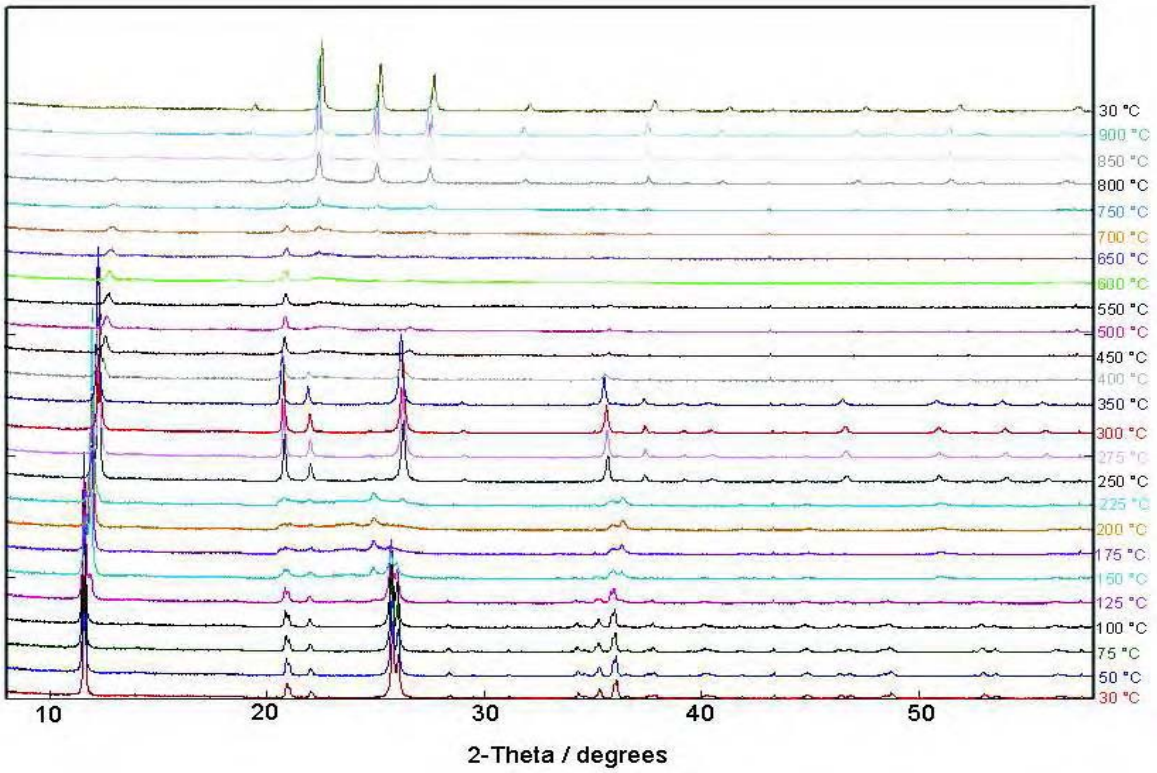

Figure 11: The in-situ XRD patterns of $Ge_{0.1}Ti_{0.9}(HPO_4)_2.H_2O$ (TiP method) recorded as a function of temperature

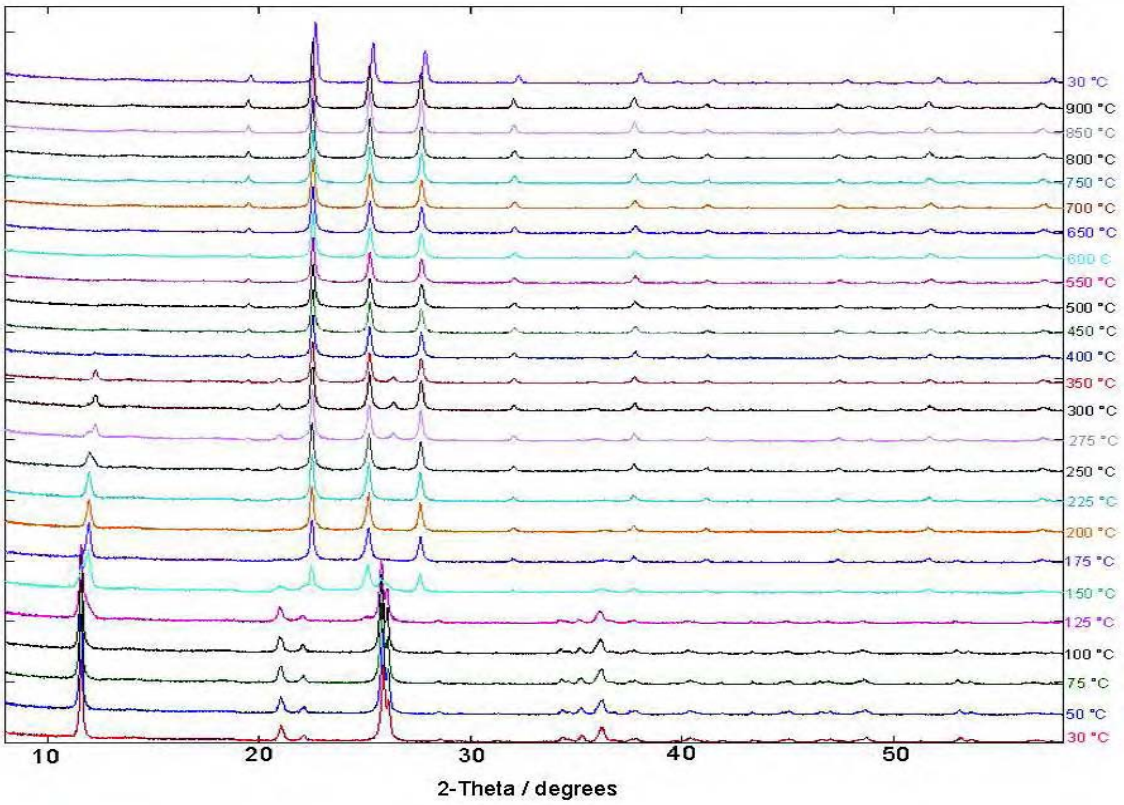

Figure 12: The in-situ XRD patterns of $Ge_{0.1}Ti_{0.9}(HPO_4)_2.H_2O$ (GeP method) recorded as a function of temperature

Appendix 6: Papers Arising From this Work

- "Synthesis and structural characterisation using Rietveld and pair distribution function analysis of layered mixed titanium-zirconium phosphates", V. A. Burnell, J. E. Readman, C. C. Tang, J. E. Parker, S. P. Thompson and J. A. Hriljac, *Journal of Solid State Chemistry*, **183**, 2196 (2010).